UNIVERSIDAD DE GRANADA

PhD THESIS

DESIGN AND ANALYTICAL CHARACTERIZATION OF CAPILLARY MICROFLUIDIC DEVICES

PhD Programme in Chemistry

Inmaculada Ortiz Gómez

Doctoral Thesis in Chemistry
National and International Mention

GRANADA
2020

UNIVERSITY OF GRANADA
FACULTY OF SCIENCES
Department of Analytical Chemistry
"Profesor Fermín Capitán García"

ECsens
Electronic and Chemical sensing solutions

El doctorando/ The doctoral candidate Inmaculada Ortiz Gómez y los directores de la tesis / and the thesis supervisor/s Alfonso Salinas Castillo e Ignacio de Orbe Payá

Garantizamos, al firmar esta tesis doctoral, que el trabajo ha sido realizado por el doctorando bajo la dirección de los directores de la tesis y hasta donde nuestro conocimiento alcanza, en la realización del trabajo, se han respetado los derechos de otros autores a ser citados, cuando se han utilizado sus resultados o publicaciones.

Guarantee, by signing this doctoral thesis, that the work has been done by the doctoral candidate under the direction of the thesis supervisor/s and, as far as our knowledge reacher, in the performance of the work, the rights of other authors to be cited (when their results or publications have been used) have been respected.

Lugar y fecha / Place and date:

Director/es de la Tesis / Thesis supervisor/s; Doctorando/ Doctoral candidate:

Firma / Signed Firma / Signed

UNIVERSITY OF GRANADA

FACULTY OF SCIENCES

Department of Analytical Chemistry

"*Profesor Fermín Capitán Garcia*"

Research Group FQM-118 "Electronic and Chemical sensing solutions, ECsens"

Official PhD Programme in Chemistry

Design and analytical characterization of capillary microfluidic devices

Doctoral Thesis in Chemistry National and International Mention

Inmaculada Ortiz Gómez

Doctoral Thesis directed by

Dr. D. Alfonso Salinas Castillo Dr. D. Ignacio de Orbe Payá

Editor: Universidad de Granada. Tesis Doctorales
Autor: Inmaculada Ortiz Gómez
ISBN: 978-84-1306-601-1
URI: http://hdl.handle.net/10481/63588

UNIVERSIDAD
DE GRANADA

D. Alfonso Salinas Castillo, y D. Ignacio de Orbe Payá ambos Profesores Titulares del Departamento de Química Analítica de la Facultad de Ciencias de la Universidad de Granada

CERTIFICAMOS QUE:

El trabajo de investigación recogido en la presente Memoria, titulada "Desing and analytical characterization of capillary microfluidic devices", y presentada por Inmaculada Ortiz Gómez para optar al grado de doctor por la Universidad de Granada, ha sido realizado en su totalidad bajo nuestra dirección en el Departamento de Química Analítica de la Universidad de Granada.

Dr. Alfonso Salinas Castillo
Profesor de Universidad

Dr. Ignacio de Orbe Payá
Profesor de Universidad

Dña. Inmaculada Ortiz Gómez
Doctoranda

Granada, x de 2020

A mi familia.

ÍNDICE

ORGANIZACIÓN DE LA TESIS DOCTORAL XII

OBJETIVOS XXXII

RESEARCH OBJETIVES XXXVII

RESUMEN XL

SUMMARY XLVIII

INTRODUCCIÓN 1

1. Nanociencia y Nanotecnología 3

1.1. Definición de Nanociencia y Nanotecnología 4

1.2. Nanociencia, Nanotecnología y Química Analítica 5

1.3. Nanomateriales 7

1.3.1. 44Clasificación de los nanomateriales 7

1.3.2. Propiedades de los nanomateriales 11

1.3.3. Métodos de síntesis de los nanomateriales 13

1.3.4. Técnicas de caracterización de los nanomateriales 14

1.3.5. Aplicaciones de los nanomateriales 19

2. Sensores 21

2.1. Definición de sensor 21

2.2. Sensores desechables 23

2.2.1. Materiales para el desarrollo de sensores desechables 25

2.2.2. Sistemas de detección de los sensores desechables 27

2.2.3. Elementos de reconocimiento en el desarrollo de sensores desechables 31

2.2.4. Campos de aplicación de los sensores desechables 33

3. Sensores portátiles para análisis no invasivos 43

3.1. Sensores portátiles dérmicos 45

4. Sistemas microfluídicos 47

4.1. Clasificación de los sistemas microfluídicos 50
4.2. Sistemas microfluídicos basados en papel 52
4.2.1. Técnicas de fabricación de µPADs 55
4.2.2. Métodos de detección de los µPADs 60
4.2.2.1. Detección óptica 60
4.2.2.2. Detección electroquímica 72
5. Análisis del color 74
5.1. Espacios de color 75
5.2. Dispositivos digitales para la medida del color 79
5.3. Smartphone como dispositivos ópticos de detección 81
REFERENCIAS 86
ÍNDICE DE FIGURAS 100
ÍNDICE DE TABLAS 102
EXPERIMENTAL 104
Capítulo 1: TETRAZINE-BASED CHEMISTRY FOR NITRITE DETERMINATION IN A PAPER MICROFLUIDIC DEVICE 108
1. Introduction 111
2. Materials and methods 114
2.1. Reagents and materials 114
2.2. Synthesis of 3, 6-bis (3, 5-dimethyl-1H-pyrazol-1-yl) -1, 4-dihydro-1, 2, 4, 5-tetrazine (DHBPTz) 115
2.3. Apparatus and instruments 116
2.4. Preparation of the µPAD 116
2.5. Image capture 117
2.6. Image-processing 117
2.7. Measurement protocol 118
3. Results and discussion 119
3. 1. µPAD preparation 119

3.2. µPAD measurement conditions 121

3.3. Analytical characterization 123

3.4. Interferences 125

3.5. Validation 126

4. Conclusions 127

REFERENCES 128

ÍNDICE DE FIGURAS 134

ÍNDICE DE TABLAS 135

Capítulo 2: MICROFLUIDIC PAPER-BASED DEVICE FOR COLORIMETRIC DETERMINATION OF GLUCOSE BASED ON A METAL-ORGANIC FRAMEWORK ACTING AS PEROXIDASE MIMETIC 138

1. Introduction 142

2. Experimental 144

2.1. Reagents and materials 144

2.2. Apparatus, instruments and software 145

2.3. Synthesis and characterization of the metal organic framework 145

2.4. Production of the µPAD 145

2.5. Image capture and processing 146

2.6. Analytical protocol 147

3. Results and discussion 147

3.1. µPAD preparation 149

3.2. Optimization of method 150

3.3. Choice of materials and analytical characterization 151

3.4. Interferences 154

3.5. Validation 155

4. Conclusions 155

5. Electronic supplementary material 156

5.1. XRPD analysis of Fe-MIL-101 MOF 156

5.2. Image-processing 157

5.3. Selection of materials for µpad fabrication 159

5.4. Location of reagents on the µPAD 159

5.5. Optimization of factors affecting the glucose µPAD 160

5.6. Reaction time 162

5.7. Influence of sample volume added on the µPAD 162

5.8. Comparison of detection parameters of several glucose procedures based on peroxidase mimetics 163

5.9. Dependence of saturation with concentration obtained using a smartphone and a digital camera 164

5.10. Influence of ionic strength 164

REFERENCES 165

ÍNDICE DE FIGURAS 173

ÍNDICE DE TABLAS 175

Capítulo 3: IN SITU SYNTHESIS OF FLUORESCENT SILICON NANODOTS FOR gLUCOSE AND FRUCTOSE MONITORING IN A PAPER MICROFLUIDIC DEVICE COMBINED WITH Laser induced grapheme HEATER 178

1. Introduction 183

2. Experimental 185

2.1. Reagents and materials 185

2.2. Instruments and software 185

2.3. Electronic device design 186

2.4. Fabrication of the LIG heater 188

2.5. µPAD preparation 188

2.6. Measurement procedure 189

2.7. Treatment of real samples 190

3. Results and discussion 191

3.1. Heater characterization 191

3.2. Characterization of SNDs 193
3.3. Optimization of method 195
3.4. Calibration and analytical parameters 196
3.5. Study and evaluation of potential interferences 198
3.6. Analysis of real samples 198
4. Conclusion 200
REFERENCES 201
ÍNDICE DE FIGURAS 208
ÍNDICE DE TABLAS 209
Capítulo 5: A VINYL SULFONE CLICKED CARBON-DOT-ENGINEERED MICROFLUIDIC PAPER-BASED ANALYTICAL DEVICE FOR FLUOROMETRIC DETERMINATION OF BIOTHIOLS 241
1. Introduction 244
2. Materials and methods 246
2.1. Materials and reagents 246
2.2. Apparatus, instruments and software 247
2.3. Preparation of CDs-paper: VS-click immobilization of CDs 247
2.4. Preparation of CDs-I-paper 248
2.5. Image capture and processing 248
2.6. Analytical protocol 249
3. Results and discussion 249
3.1. Paper selection for CDs immobilization 249
3.2. Fabrication of CDs-immobilized cellulose (CDs-paper) 250
3.3. Evaluation of the sensing capabilities of CDs-paper 253
3.4. Characterization of CDs and functionalized papers 254
3.5. Fabrication of the μPAD 256
3.6. Optimization of method 256
3.7. Analytical characterization of μPAD for biothiols assay 257

3.8. Interferences 261
3.9. Analysis of real samples 262
4. Conclusions 262
5. Electronic supplementary material 263
5.1. Synthesis of NH_2-CDs 263
5.2. Characterization of CDs 263
5.3. Schematic representation of the fluorescence measurement 264
5.4. Optimization of ISO for digital camera 265
5.5. Selection of the substrate for immobilizing of CDs 266
5.6. Evaluation of the CDs immobilization methodology 267
5.7. Evolution of immobilization methodology 268
5.8. XPS composition data 269
5.9. Elemental mapping scanning transmission electron microscopy 270
5.10. Fluorescence emission spectrum of CDs-paper versus CDs-I-paper 271
5.11. Optimization of the methodology 271
5.12. Optimization of GSH determination by the 3D µPAD 274
REFERENCES 275
ÍNDICE DE FIGURAS 280
ÍNDICE DE TABLAS 283
Capítulo 6: IONOPHORE-BASED OPTICAL SENSOR FOR URINE CREATININE DETERMINATION 287
Objetivo 288
1. Introduction 290
2. Experimental section 292
2.1. Reagent and materials 292
2.2. Intruments and software 293
2.3. Membrane preparation 293

2.4. Measurement setup 293
2.5. Analysis of real samples 294
3. Results and discussion 294
3.1. Optimization of the response 296
3.1.1. Membrane optimization 296
3.2. Reaction parameters 297
3.3. Analytical characterization 298
3.4. Analysis of real samples 301
4. Conclusiones 302
5. Electronic supporting information 302
5.1. Calix[4]pyrrole ionophore structure 302
5.2. Anionic salt optimization 303
5.3. Membrane thickness 305
5.4. pH optimization 306
5.5. Response time 306
5.6. Selectivity study and maximum tolerable error 307
5.7. Method comparison 309
5.8. Real sample analysis 309
REFERENCES 310
ÍNDICE DE FIGURAS 315
ÍNDICE DE TABLAS 317
Capítulo 7: LUMINESCENT CALCIUM PHOSPHATE NANOPARTICLES DOPED WITH EUROPIUM FOR THE QUANTIFICATION OF CREATININE 321
1. Introduction 324
2. Experimental 326
2.1. Chemicals and reagents 326
2.2. Synthesis of europium-doped amorphous calcium phosphate 326

2.3. Characterisation of the nanoparticles 327

2.4. Luminescence measurements 328

2.5. Creatinine quantification 329

3. Results and discussion 329

3.1. Synthesis and detailed characterisation of eu-acp 329

3.2. Optimizing the photo-luminescence emission of Eu-ACP 333

3.3. Analytical performance of Eu-ACP 335

3.4. Selectivity assay 338

3.5. Detection of creatinine in human urine 338

4. Conclusion 339

REFERENCES 340

ÍNDICE DE FIGURAS 347

ÍNDICE DE TABLAS 349

ANEXO: WEARABLE POTENTIOMETRIC ION PATCH FOR ON-BODY ELECTROLYTE MONITORING IN SWEAT: A VALIDATION STRATEGY TO ENSURE PHYSIOLOGICAL RELEVANCE 352

1. Introduction 355

2. Experimental section 358

2.1. Fabrication of the electrode array 358

2.2. Implementation of the electrodes into the sampling cell for on-body measurements 359

3. Results and discussion 360

3.1. In vitro performance of the WPISs 360

3.2. Off-site evaluation of the wpiss performance 362

3.3. Validation of the WPISs 365

4. Conclusions 372

REFERENCES 373

5. Electronic supplementary material 381

5.1. Reagents, materials and instrumentation 381

5.2. Potentiometric measurements 383

5.3. Fabrication of the all-solid-state wearable potentiometric ion sensors 384

5.4. Implementation of the sampling cell 385

5.5. On-body tests 386

5.6. Sweat collection 387

REFERENCES 402

ÍNDICE DE FIGURAS 408

ÍNDICE DE TABLAS 411

CONCLUSIONES 414

MAIN CONCLUSIONS 422

ACRóNIMOS 430

INFORME DEL FACTOR DE IMPACTO 436

ORGANIZACIÓN DE LA TESIS DOCTORAL

ORGANIZACIÓN DE LA TESIS DOCTORAL

Esta Tesis Doctoral se presenta bajo el sistema de reagrupamiento de publicaciones de acuerdo a las reglas para de la obtención del título de Doctor por la Universidad de Granada. Los principales resultados del estudio conducente en esta Tesis Doctoral han sido presentados como ocho trabajos de investigación enviados y/o publicados en revistas de investigación relevantes en el campo de la Química Analítica.

A continuación, se detalla la estructura de esta Tesis haciendo énfasis en la organización de la misma.

- **OBJETIVOS**

  En el primer apartado de la presente Memoria se recoge el objetivo general y los objetivos específicos que se han perseguido durante la realización de los diferentes trabajos de investigación que componen cada uno de los Capítulos de esta Tesis Doctoral.

- **RESUMEN**

  En el segundo apartado de esta Memoria se indica de forma resumida los aspectos más destacados de los temas que componen la introducción y los trabajos de investigación que se han llevado a cabo durante la realización de esta Tesis.

- **INTRODUCCIÓN**

  La introducción de esta Memoria está divida en 5 partes, de la Sección 1 a la Sección 5. La Sección 1 incluye una revisión bibliográfica acerca de los aspectos más relevantes en Nanociencia y Nanotecnología, así como, del empleo de nanomateriales en diversas aplicaciones químicas y principalmente analíticas. Seguidamente, la Sección 2 se centra en la definición, clasificación y campos de aplicación de los sensores químicos. Por otro lado, la Sección 3 destaca la importancia del desarrollo de sensores portátiles, flexibles y estirables para el análisis no invasivo de

biomarcadores en fluidos biológicos. Del mismo modo, la Sección 4 trata sobre el desarrollo de dispositivos microfluídicos basados en papel y empleados como soporte en análisis químico. En último lugar, en la Sección 5 se recoge información referente al uso del color como parámetro analítico en la detección óptica llevada a cabo por dispositivos de captura de imagen de uso común como cámaras fotográficas o cámaras de teléfonos móviles.

- **EXPERIMENTAL**

La sección experimental de esta Memoria recoge los diferentes trabajos de investigación llevados a cabo en el transcurso de esta Tesis Doctoral. Estos trabajos han sido organizados por Capítulos como se indica a continuación:

- **CAPÍTULO 1**

El primer Capítulo de esta Memoria trata sobre el diseño, desarrollo y caracterización de un dispositivo microfluídico basado en papel (µPAD) implementado con la tetrazina (1, 2-dihidro-3, 6-bis (3, 5-dimetil-1H-pirazol-1-il) 1, 2, 4, 5-tetrazina, DHBPTz) que actúa como reactivo de reconocimiento en la determinación colorimétrica de nitrito. Este trabajo surgió de una colaboración con el Grupo de Investigación de Carbohidratos (FQM-208) del Departamento de Química Orgánica de la Universidad de Granada dirigido por catedrático D. Francisco Santoyo González y del cual forma parte el Doctor Mariano Ortega Muñoz. Dicho grupo de investigación sintetizó y caracterizó la tetrazina DHBPTz que se implementó en el µPAD y se empleó como reactivo cromogénico en la determinación de nitrito.

El trabajo presentado en este Capítulo ha resultado en la publicación de un artículo científico. De acuerdo con el sistema de compendios de publicaciones, el primer artículo de la presente Tesis tiene como título “Tetrazine-based chemistry for nitrite determination in a paper microfluidic device” y ha sido publicado en Talanta, revista científica de primer cuartil (11/84) en el campo Química Analítica. 4.916 (JCR 2018).

Artículo:

Inmaculada Ortiz-Gómez, Mariano Ortega-Muñoz, Alfonso Salinas-Castillo, José Antonio Álvarez-Bermejo, María Ariza-Avidad, Ignacio de Orbe-Payá, Francisco Santoyo-González, Luís Fermín Capitán-Vallvey, Tetrazine-based chemistry for nitrite determination in a paper microfluidic device, Talanta, 160 (2016) 721-728.

Contribuciones a congresos:

1. III Simposio de Jóvenes Investigadores en Espectroscopia Aplicada

Organización	Sociedad de Espectroscopia Aplicada
Título	Dispositivo microfluídico en papel para la determinación de nitrito en agua
Autores	Inmaculada Ortiz-Gómez, María Ariza-Avidad, Alfonso Salinas-Castillo, Mariano Ortega-Muñoz, Francisco Santoyo-González, Ignacio de Orbe-Paya y Luís Fermín Capitán Vallvey
Presentación	Oral
Ámbito	Nacional
Celebración	Toledo
Fecha	2/09/2015 – 4/09/2015

- **CAPÍTULO 2**

El segundo Capítulo trata sobre el desarrollo de un dispositivo microfluídico basado en papel para la determinación colorimétrica de glucosa empleando el Metal Organic Framework (MOF) Fe-MIL-101 como mimético de la peroxidasa. En este caso, el trabajo se llevó a cabo gracias a la colaboración con el grupo de investigación de Química de la Coordinación y Análisis Estructural (FQM 195) del Departamento de Química Inorgánica de la Universidad de Granada del que forma parte el Profesor D.

Antonio Rodríguez Diéguez. El grupo de investigación FQM 195 se encargó de la síntesis y caracterización del MOF Fe-MIL-101, compuesto que presenta actividad mimética al enzima Horseradish Peroxidase (HRP) y que ha sido utilizado en este trabajo para catalizar la reacción de oxidación del reactivo cromogénico 3,3',5,5'-tetrametilbenzidina (TMB) en la determinación colorimétrica de glucosa.

El trabajo presentado en este Capítulo resultó en la publicación de un artículo científico que tiene como título "Microfluidic paper-based device for colorimetric determination of glucose based on a metal-organic framework acting as peroxidase mimetic" y ha sido publicado en la revista científica de primer cuartil (9/84) en el campo Química Analítica, Microchimica Acta. 5.479 (JCR 2018).

Artículo:

Inmaculada Ortiz-Gómez, Alfonso Salinas-Castillo, Amalia García, Jose Antonio Álvarez-Bermejo, Ignacio de Orbe-Payá, Antonio Rodríguez-Diéguez, Luís Fermín Capitán-Vallvey, Microfluidic paper-based device for colorimetric determination of glucose based on a metal-organic framework acting as peroxidase mimetic, Microchimica Acta, 185 (2018) 1-8.

Contribuciones a congresos:

1. XV Reunión del Grupo Regional de la Sociedad Española de Química Analítica

Organización	Grupo Regional Andaluz de la Sociedad Española de Química Analítica
Título	Determinación colorimétrica de glucosa basada en un MOF como mimético de la peroxidasa implementado en un sistema microfluídico
Autores	Inmaculada Ortiz-Gómez, Alfonso Salinas-Castillo, Belén Fernández, Ignacio de Orbe-Payá y Luís Fermín Capitán-Vallvey

ISSN/ISBN/DOI 978-84-16642-28-1

Presentación Oral

Ámbito Nacional

Celebración Almería

Fecha 30/06/2016 – 1/07/2016

2. I Congreso de Jóvenes Químicos y Bioquímicos Terapéuticos "I QuimBioquim"

Organización QuimBioquim

Título Microfluidic paper-based analytical device for colorimetric determination of glucose based on metal-organic framework as peroxidase mimetic

Autores Inmaculada Ortiz-Gómez, Alfonso Salinas-Castillo, Belén Fernández, Ignacio de Orbe-Payá y Luís Fermín Capitán-Vallvey

Presentación Oral

Ámbito Nacional

Celebración Granada

Fecha 3/10/2016 – 4/10/2016

3. I Congreso de Jóvenes Químicos y Bioquímicos Terapéuticos "Quimbioquim"

Organización Universidad de Granada

Título Microfluidic paper-based analytical device for colorimetric determination of glucose base on metal-organic framework as peroxidase mimetic

Autores	Inmaculada Ortiz-Gómez, Alfonso Salinas-Castillo, Belén Fernández, Ignacio de Orbe-Payá y Luís Fermín Capitán-Vallvey
Presentación	Oral
Ámbito	Nacional
Celebración	Granada
Fecha	03/10/2017 – 04/10/2017

4. II Jornadas de Investigadores en Formación "JIFFI"

Organización	Universidad de Granada
Título	Determinación colorimétrica de glucosa basada en un MOF como mimético de la peroxidasa implementado en un sistema microfluídico en papel.
Autores	Inmaculada Ortiz-Gómez, Alfonso Salinas-Castillo, Belén Fernández, Ignacio de Orbe-Payá y Luís Fermín Capitán-Vallvey
ISSN/ISBN/DOI	978-84-16929-82-5
Presentación	Oral
Ámbito	Regional
Celebración	Granada
Fecha	17/05/2017 – 19/05/2017

- **CAPÍTULO 3**

En el tercer capítulo de esta Memoria se describe la síntesis de silicon nanodot (SNDs) fluorescentes en un dispositivo microfluídico de papel que incorpora un calentador de grafeno fabricado por láser para la monitorización de la concentración de glucosa y fructosa en diferentes muestras. Este trabajo surgió de la colaboración con el grupo

de investigación en dispositivos electrónicos de la Universidad de Granada, del cual forma parte el Profesor D. Diego P. Morales. Aquí este grupo de investigación se encargó del diseño, fabricación y caracterización del calentador de grafeno inducido por láser implementado en el sistema para la síntesis de los SNDs fluorescentes.

El trabajo presentado en este Capítulo tiene como título "In situ synthesis of fluorescent silicon nanodots for glucose and fructose monitoring in a paper microfluidic device combined with laser induce grapheme heater" y ha sido enviado para su publicación a la revista científica de primer cuartil (4/84) en el campo Química Analítica ACS Sensors. 6.944 (JCR 2018).

- **CAPÍTULO 4**

El cuarto Capítulo de esta Tesis describe el diseño y desarrollo de un dispositivo microfluídico basado en papel para la determinación colorimétrica de glutation empleando un sistema basado en el complejo Ag(I)-TMB, de forma que el reconocimiento de glutation se produce por un cambio de color en la zona de detección del dispositivo microfluídico, e implementado con una etiqueta NFC para la transferencia de datos a un Smartphone utilizado como sistema de detección, almacenamiento y tratamiento de datos en la determinación. Este trabajo surgió de la colaboración con el grupo de investigación en dispositivos electrónicos anteriormente citado y del que forma parte la Dra. Dña. Almudena Rivadeneyra, la cual se encargó de la fabricación e implementación de la etiqueta NFC en el dispositivo microfluídico.

El trabajo presentado en este Capítulo tiene como título "Near fied communication for colorimetric determination of glutathione in a microfluidic paper-based analytical device" y ha sido enviado para su publicación a la revista científica de primer cuartil (4/84) en el campo Química Analítica Sensors and Actuator B-Chemical. 6.393 (JCR 2018).

Contribuciones a congresos:

1. XV Reunión del Grupo Regional Andaluz de la Sociedad Española de Química Analítica

Organización	Grupo Regional de la Sociedad Española de Química Analítica (GRASEQA)
Título	Dispositivo microfluídico en papel para la determinación colorimétrica de glutation basada en la reacción Ag (I)-TMB
Autores	Inmaculada Ortiz-Gómez, Alfonso Salinas-Castillo, Ignacio de Orbe-Paya y Luís Fermín Capitán Vallvey
ISSN/ISBN/DOI	978 – 84 – 16642 – 28 – 1
Presentación	Póster
Ámbito	Regional
Celebración	Almería
Fecha	30/06/2016 – 1/07/2016

2. XXV National Spectroscopy Meeting (RNE) and IX Iberian Spectroscopy Conference (CIE)

Organización	Sociedad de Espectroscopia Aplicada (SEA), Comité de Espectroscopia de la Sociedad Española de Óptica (SEDOPTICA), Sociedad Española de Química Analítica (SEQA), Sociedad Portuguesa de Bioquímica (SPB), Sociedad Portuguesa de Química (SPQ) y la Universidad de Alicante (UA)
Título	Paper-based microfluidic device for colorimetric detection of glutathione based on Ag(I) - TMB
Autores	Inmaculada Ortiz-Gómez, Alfonso Salinas-Castillo, Ignacio de Orbe-Paya y Luís Fermín Capitán Vallvey

Presentación	Póster
Ámbito	Internacional
Celebración	Alicante
Fecha	20/07/2016 – 22/07/2016

3. II Congreso de Jóvenes Químicos y Bioquímicos Terapéuticos, "II QuimBioQuim"

Organización	Universidad Rey Juan Carlos
Título	Determinación colorimétrica de glutation basada en la reacción Ag(I)-TBM implementado en un sistema microfluídico en papel
Autores	Inmaculada Ortiz-Gómez, Alfonso Salinas-Castillo, Ignacio de Orbe-Paya y Luís Fermín Capitán Vallvey
Presentación	Oral
Ámbito	Regional
Celebración	Móstoles, Madrid
Fecha	04/10/2017 – 5/10/2017

- **CAPÍTULO 5**

El Capítulo 5 trata sobre el desarrollo de un dispositivo microfluídico basado en papel que integra carbon dots inmovilizados covalentemente en el papel y que posteriormente han sido funcionalizados para la determinación de biotioles, en concreto glutatión, cisteina y homocisteina a través de un proceso tipo turn-off/turn-on. Este trabajo surgió de la colaboración con el Grupo de Investigación de Carbohidratos citado anteriormente. En este caso, este Grupo de Investigación se encargó de la inmovilización covalente de los carbon dots en la celulosa del papel y su posterior funcionalización.

El trabajo presentado en este capítulo ha resultado en la publicación de un artículo científico que tiene como título "A vinyl sulfone clicked carbon-dot-engineered microfluidic paper-based analytical device for fluorometric determination of biothiols" y ha sido publicado en la revista científica de primer cuartil (9/84) en el campo Química Analítica, Microchimica Acta. 5.479 (JCR 2018).

Artículo:

Inmaculada Ortiz-Gomez, Mariano Ortega-Muñoz, Antonio Marín-Sánchez, Ignacio de Orbe-Payá, Fernando Hernandez-Mateo, Luis Fermin Capitan-Vallvey, Francisco Santoyo-Gonzalez, Alfonso Salinas-Castillo, A vinyl sulfone clicked carbon-dot-engineered microfluidic paper-based analytical device for fluorometric determination of biothiols. Aceptado para su publicación el 27/5/2020 con la referencia Ms. No. MIAC-D-20-00239R1.

Contribuciones a congresos:

1. II Simposio de la Unidad de Excelencia de Química Aplicada a Biomedicina y Medio Ambiente "Materiales nanoestructurados de carbono: desafíos sintéticos y aplicaciones en nanotecnología

Organización	Unidad de Excelencia de Química Aplicada a Biomedicina y Medio Ambiente
Título	Inmovilización de carbon quantum dots sobre papel para la determinación de glutation
Autores	Inmaculada Ortiz-Gómez, María Ariza-Avidad, Alfonso Salinas-Castillo, Mariano Ortega-Muñoz, Francisco Santoyo-González, Ignacio de Orbe-Paya y Luís Fermín Capitán Vallvey
Presentación	Póster
Ámbito	Regional
Celebración	Granada

Fecha	18/01/2018

2. I Congreso sobre Materiales Multifuncionales para Jóvenes

Organización	Universidad de Granada
Título	Carbon dots inmovilizados sobre papel y funcionalizados para la determinación de glutation
Autores	Inmaculada Ortiz-Gómez, Alfonso Salinas Castillo, Ignacio de Orbe Paya, Mariano Ortega-Muñoz, Francisco Santoyo-González, y Luís Fermín Capitán Vallvey
Presentación	Oral
Ámbito	Regional
Celebración	Granada
Fecha	3/09/2018 – 04/09/2018

3. XVI Reunión del Grupo Regional Andaluz de la Sociedad Española de Química Analítica

Organización	Grupo Regional Andaluz de la Sociedad Española de Química Analítica, GRASEQA
Título	Inmovilización de carbon dots sobre papel para la determinación de glutation
Autores	Alfonso Salinas Castillo, Inmaculada Ortiz-Gómez, Ignacio de Orbe Paya, Mariano Ortega-Muñoz, Francisco Santoyo-González, y Luís Fermín Capitán Vallvey
ISSN/ISBN/DOI	978 – 84 – 17293 – 62 – 8
Presentación	Póster
Ámbito	Nacional

Celebración	Granada
Fecha	04/10/2018 – 05/10/2018

4. V Congreso de Estudiantes de Investigación Biosanitaria (CEIBS)

Organización	CEIBS
Título	Highly sensitive and selective fluorimetric detection of glutathione in urine based on functionalized cellulose paper
Autores	Ignacio de Orbe-Paya, Inmaculada Ortiz-Gómez, Mariano Ortega-Muñoz Alfonso Salinas-Castillo, , Francisco Santoyo-González, y Luís Fermín Capitán Vallvey
ISSN/ISBN/DOI	
Presentación	Póster
Ámbito	Regional
Celebración	Granada
Fecha	13/03/2019 – 16/03/2019

5. XXII Reunión de la Sociedad Española de Química Analítica

Organización	Sociedad Española de Química Analítica, SEQA
Título	3D µPAD based on carbon dots-iodoacetyl conjugates as fluorescence probe for the detection of glutathione
Autores	Ignacio de Orbe-Paya, Inmaculada Ortiz-Gómez, Mariano Ortega-Muñoz Alfonso Salinas-Castillo, , Francisco Santoyo-González, y Luís Fermín Capitán Vallvey
Presentación	Póster
Ámbito	Nacional

Celebración Valladolid

Fecha 17/07/2019 – 19/07/2019

- **CAPÍTULO 6**

En el sexto capítulo de esta Memoria se describe el desarrollo de un nuevo sensor óptico desechable para la determinación de creatinina en orina. El mecanismo de detección tiene lugar gracias a la incorporación del ionoforo calix[4]pirrol en la membrana óptica a través de un mecanismo de cambio iónico. Este estudio surgió de la colaboración con el Grupo de investigación Laboratory of Nanosensors de la Universidad Rovira i Virgili (URV) de Tarragona dirigido por el Profesor D. Javier Andrade. En este caso, el grupo de investigación se encargó de la síntesis y caracterización del ionoforo calix[4]pirrol empleado en la fabricación de la membrana sensora para poder llevar a cabo la determinación de creatinina.

El trabajo presentado en este capítulo ha resultado en la publicación de un artículo científico. De acuerdo con el sistema de compendios de publicaciones, el sexto artículo de la presente Memoria tiene como título "Ionophore-based optical sensor for urine creatinine determination" y ha sido publicado en la revista científica ACS Sensors que se encuentra en el primer cuartil (4/84) en el campo Química Analítica. 6.944 (JCR 2018).

Articulo:

Miguel M. Erenas, Inmaculada Ortiz-Gomez, Ignacio de Orbe-Paya, Daniel Hernandez-Alonso, Pablo Ballester, Pascal Blondeau, Francisco J. Andrade, Alfonso Salinas-Castillo, Luis Fermín Capitan-Vallvey, Ionophore-based optical sensor for urine creatinine determination, ACS Sensors, 4, (2019), 421-426.

Contribuciones a congresos:

1. VI Minisimposio de Investigación en Ciencias Experimentales

Organización	Universidad de Almería
Título	Disposable sensor for creatinine based on new ionophore
Autores	I. Ortiz Gómez, P. Siles Fernandez, A. Salinas Castillo, M. Erenas Rodriguez, T. Guinovart, P. Blondeau, F. Rius, F. J. Andrade, L.F. Capitán Vallvey
ISSN/ISBN/DOI	978 – 84 – 16642 – 96 – 0
Presentación	Póster
Ámbito	Regional
Celebración	Almería
Fecha	14/11/2017 – 15/11/2017

2. IV Desgranando Ciencia

Organización	Universidad de Granada
Título	Sensor desechable para la determinación de creatinina basado en un nuevo ionoforo
Autores	I. Ortiz Gómez, P. Siles Fernandez, A. Salinas Castillo, M. Erenas Rodriguez, T. Guinovart, P. Blondeau, F. Rius, F. J. Andrade, L.F. Capitán Vallvey
Presentación	Póster
Ámbito	Regional
Celebración	Granada

- **Capítulo 7**

En el Capítulo 7 se describe el desarrollo de un sensor óptico para la determinación de creatinina en orina basado en un mecanismo on/off debido al cambio de las propiedades luminiscentes de nanoparticulas de fosfato de calcio dopadas con europio en presencia de creatinina. Este trabajo surgió de la colaboración con el Grupo de Investigación BioNanoMet (FQM 368) del que forma parte el Profesor D. José Manuel Delgado López y la Dra. Dña. Gloria B. Ramírez Rodríguez. Este Grupo de Investigación se encargó de la síntesis y caracterización de nanopartículas de fosfato cálcico amorfo dopadas con europio (Eu-ACP) que son utilizadas en el trabajo aquí presentado para la determinación fosforimétrica de creatinina.

El trabajo presentado en este Capítulo tiene como título "Luminiscent calcium phosphate nanoparticles doped with europium for the quantification of creatinine" y ha sido enviado para su publicación a la revista científica de primer cuartil (5/14) en el campo Ciencia de los materiales y biomateriales, Colloids and Surfaces B: Biointerfaces. 3.973 (JCR 2018).

Contribuciones a congresos:

1. III Simposio de la Unidad de Excelencia de Química Aplicada a Biomedicina y Medioambiente

Organización	Universidad de Granada
Título	Determinación de creatinina basada en el empleo de nanopartículas de fosfato de calcio dopadas con europio como biomimético fluorescente
Autores	I. Ortiz Gómez, G. B. Ramírez-Rodríguez, A. Salinas Castillo, J. M. Delgado López, I. de Orbe Paya, L.F. Capitán Vallvey
Presentación	Póster
Ámbito	Regional
Celebración	Granada

Fecha 18/01/2019

2. IX International Congress on Analytical Nanoscience and Nanotechnology

Organización Universidad de Zaragoza

Título Determinación de creatinina basada en el empleo de nanopartículas de fosfato de calcio como biomimético fluorescente

Autores I. Ortiz Gómez, G. B. Ramírez-Rodríguez, A. Salinas Castillo, J. M. Delgado López, I. de Orbe Paya, L.F. Capitán Vallvey

ISSN/ISBN/DOI

Presentación Póster

Ámbito Internacional

Celebración Zaragoza

Fecha 2/07/2019 – 4/07/2019

- **ANEXO**

Como trabajo complementario de esta Memoria, aunque sin formar parte de los artículos presentados, se incluye un estudio sobre el desarrollo de un parche potenciométrico portátil para la determinación multi-ión de potasio, sodio, cloruro y pH de forma selectiva en sudor. Este trabajo de investigación surge con motivo de la estancia internacional realizada durante el desarrollo de esta Tesis para poder optar a la mención Doctorado Internacional. Así, este trabajo se llevó a cabo en el grupo de investigación del Profesor Gastón Crespo, *Department of Chemistry at the School of Engineering Sciences in Chemistry, Biotechnology and Healt del Royal Institute of technology KTH*, en Estocolmo, Suecia.

El trabajo presentado en este anexo ha resultado en la publicación de un artículo científico titulado "Wearable Potentiometric Ion Patch for On-Body Electrolyte Monitoring in Sweat: Toward a Validation Strategy to Ensure Physiological Relevance" y ha sido publicado en Analytical Chemistry, revista científica de primer cuartil (7/84) en el campo Química Analítica. 6.350 (JCR 2018).

Artículos:

M. Parrilla, I. Ortiz-Gómez, R. Cánovas, A. Salinas-Castillo, M. Cuartero, G.A. Crespo, Wearable Potentiometric Ion Patch for On-Body Electrolyte Monitoring in Sweat: Toward a Validation Strategy to Ensure Physiological Relevance, Analytical Chemistry, 91 (2019) 8644-8651.

Contribuciones a congresos:

1. I Congreso sobre Materiales Multifuncionales para Jóvenes

Organización	Universidad de Granada
Título	Sensor potenciométrico basado en un parche para la detección multi-iónica en sudor
Autores	M. Parrilla, I. Ortiz-Gómez, R. Cánovas, A. Salinas-Castillo, M. Cuartero, G.A.
Presentación	Póster
Ámbito	Regional
Celebración	Granada
Fecha	2/09/2018 – 3/09/2018

- **CONCLUSIONES**

La sección dedicada a las conclusiones incluye los objetivos alcanzados en el desarrollo de la Tesis.

OBJETIVOS

OBJETIVOS

El objetivo general de esta Tesis Doctoral es el diseño y caracterización analítica de dispositivos microfluídicos capilares empleados para la detección y monitorización de diferentes analitos de interés clínico, alimentario y medioambiental. Para ello se utilizarán nanomateriales novedosos con diferentes funcionalidades que se puedan implementar fácilmente en dispositivos robustos, miniaturizables, de fácil uso, bajo costo, portátiles, de aplicación directa, que no requieran el empleo de grandes volúmenes de muestra y reactivos y que permitan una detección rápida presentando unas buenas prestaciones analíticas.

Para alcanzar este objetivo general se plantean un conjunto de objetivos específicos que desarrollaran diferentes aspectos del mismo:

1. Desarrollar químicas de reconocimiento basadas en la utilización de nanomateriales funcionales de baja toxicidad, cuyas rutas sintéticas sean rápidas y fáciles de llevar a cabo, y que permitan un reconocimiento químico con una buena sensibilidad y selectividad para la identificación y determinación de analitos de interés biológico, ambiental y alimentario.

2. Diseñar y fabricar dispositivos microfluídicos basados en papel principalmente, mediante técnicas de fabricación sencillas, escalables y sostenibles, que permitan definir las diferentes partes del sensor, así como, implementar la química de reconocimiento desarrollada con el propósito de mejorar las prestaciones analíticas de los sistemas de análisis atendiendo a las características indicadas en el objetivo general.

3. Inmovilizar los nanomateriales que constituyen o forman parte de las fases sensoras para el reconocimiento químico en zonas específicas del dispositivo microfluídico con el objetivo de definir las áreas de reconocimiento del sistema sensor.

4. Optimizar las variables experimentales que puedan afectar a la respuesta de los dispositivos desarrollados entre los que se encuentran: temperatura, pH, tiempo

de reacción y tipo de soporte utilizado para la implementación de la química de reconocimiento.

5. Caracterizar bajo el punto de vista analítico, evaluar la selectividad y validar los dispositivos químicos desarrollados para la detección de diferentes analitos de interés en el campo clínico, ambiental o alimentario.

6. Evaluar las diferentes coordenadas de los espacios de color RGV y HSV obtenidas a partir de imágenes de los dispositivos empleando sistemas de captura de imagen para su uso como parámetro analítico.

7. Utilizar diferentes herramientas de captura de imagen digital como cámaras fotográficas y Smartphones para obtener imágenes de los dispositivos desarrollados permitiendo de este modo mejorar las prestaciones de portabilidad del sensor, así como, permitir el almacenamiento y la transferencia de datos.

RESEARCH OBJETIVES

RESEARCH OBJECTIVES AND SCOPE

The general objective of this PhD Thesis is the design and analytical characterization of capillary microfluidic devices used for the detection and monitoring of different analytes of clinical, food and environmental interest. For this, novel nanomaterials with different functionalities can be easily implemented in robust, miniaturizable, easy to use, low cost, portable analytical devices which let direct application, do not require the use of large volumes of sample and reagents and allow rapid detection, presenting good analytical performance.

To achieve this general objective, a set of specific objectives are proposed which will develop different aspects of it:

1. Developing of recognition chemicals based on the use of low toxicity functional nanomaterials, with quick and easy to carry out synthetic routes, and which allow chemical recognition with good sensitivity and selectivity for the identification and determination of analytes of biological, environmental and food interest.

2. Design and fabricating paper-based microfluidic devices, through simple, scalable and sustainable manufacturing techniques, which allow defining the different parts of the device, as well as implementing the recorgnition chemistry developed with the purpose of improving the analytical performance of analysis systems according to the characteristics indicated in the general aim.

3. Immobilization of nanomaterials used in the manufacturing of the device in specific areas of the microfluidic device with the aim of defining the areas of recognition.

4. Optimization of the experimental variables which can affect the operation of the developed sensors, among which are: temperature, pH, reaction time, type of support used for the implementation of the recognition chemistry, etc.

5. Analytical characterization, selectivity evaluation and validation of the developed capillary microfluidic devices for the detection of different analytes of interest in the clinical, environmental and food fields.

6. Evaluating the different coordinates of the RGV and HSV color spaces obtained from image capture devices for use as analytical parameter in optical sensors.

7. Use of different digital image capture devices, such as cameras and Smartphones to obtain images of the developed optical sensors, thus allowing the portability of the sensor, as well as the storage and data transfer in the case to use a Smartphone.

RESUMEN

RESUMEN

La Memoria aquí presentada expone y detalla los resultados obtenidos durante la realización del trabajo de investigación que ha conducido a la elaboración de la Tesis Doctoral titulada Design and analytical characterization of capillary microfluidic devices.

Esta Memoria se ha estructurado en dos partes principales, introducción y desarrollo experimental. A continuación, se describen los contenidos principales de cada parte:

La introducción engloba aspectos generales y de mayor relevancia a considerar relacionados con la Nanociencia y la Nanotecnología, incluyendo la definición y clasificación de los nanomateriales, así como, detallando sus propiedades, métodos de síntesis, técnicas de caracterización y campos de aplicación. Asimismo, también se incluye una definición y clasificación de los sensores químicos centrándose esta clasificación en los sensores desechables o de un solo uso. Del mismo modo, se detallan las principales características de éstos tipos de sensores, así como, los sistemas de detección que utilizan, los elementos de reconocimiento que incorporan y los campos de aplicación más relevantes en los que se emplean los sensores desechables en la actualidad.

A continuación, se indica la utilización y desarrollo de sensores portátiles, flexibles y estirables que se adaptan a la piel para la monitorización de biomarcadores a través del análisis del sudor. Del mismo modo, se recoge información acerca del desarrollo y la clasificación de los sistemas microfluídicos utilizados en las plataformas de análisis químico, resaltando la importancia de la utilización de los dispositivos microfluídicos capilares basados en papel en el desarrollo de sensores. Además, se clasifican y ordenan las diferentes técnicas de fabricación existentes para el desarrollo de sistemas microfluídicos capilares, así como, los métodos de detección óptica y electroquímica que utilizan las plataformas microfluídicas de análisis.

Para terminar, en la última parte de la introducción se hace especial hincapié en el análisis del color como parámetro analítico; se recoge información de los diferentes espacios de

color, así como, de los dispositivos digitales para la medida del color existentes y se propone la utilización del Smartphone como dispositivo óptico de detección.

Por otro lado, la parte experimental de esta Memoria incluye los procedimientos llevados a cabo para alcanzar los objetivos propuestos en la realización de la Tesis Doctoral aquí presentada, los resultados obtenidos y una discusión detallada de los mismos. Esta parte experimental se ha dividido en siete bloques que componen cada uno de los Capítulos de esta Memoria y un anexo.

El primer trabajo (Talanta, 2016, 160, 721-728) describe el desarrollo de un nuevo método de detección colorimétrica de nitrito utilizando un dispositivo microfluídico basado en papel implementado con una tetrazina que actúa como elemento de reconocimiento y permite llevar a cabo la determinación de éste compuesto en muestras de agua empleando como dispositivos de captura de imagen una cámara fotográfica y un Smartphone. Tras optimizar los diferentes parámetros influyentes en la reacción (pH de trabajo, concentración de tetrazina, volumen de muestra, etc.) el método analítico desarrollado presenta un límite de detección de 2.05 µM y un rango dinámico lineal comprendido entre 5 y 500 µM, siendo el tiempo de reacción de 5 minutos.

El segundo trabajo (Microchimica Acta, 2018, 185, 1-8) se centra en el diseño, desarrollo y validación de un dispositivo microfluídico basado en papel (µPAD) para la determinación colorimétrica de glucosa, en muestras de suero y orina, implementado con un MOF que actúa como mimético de la peroxidasa (HRP). Bajo condiciones experimentales óptimas se ha observado un rango lineal para concentraciones de glucosa hasta 150 µM, con un límite de detección y cuantificación de 2.5 µM y 10.6 µM, respectivamente. Asimismo, el tiempo necesario para completar ésta reacción de determinación es de 15 minutos.

El tercer trabajo (en escritura para enviarlo a ACS Sensors) introduce la síntesis in situ de silicon nanodots fluorescentes, empleando (3-Aminopropil) trietoxisilano y sacarosa, en un µPAD implementado con un calentador de grafeno inducido por láser para la

determinación de la concentración de sacarosa en muestras de suero y orina, así como, en zumos y tés comerciales mediante el empleo de una lámpara UV y un Smartphone. El método desarrollado presenta un rango dinámico lineal de 10 a 200 µM para glucosa y de 10 a 100 µM para fructosa con un límite de detección de 0.8 µM y 0.51 µM, respectivamente.

En el cuarto trabajo (en escritura para enviarlo a Sensor and Actuator B) se lleva a cabo el desarrollo de un µPAD para la determinación colorimétrica de glutation. Esta determinación se basa en el hecho de que la Ag(I) puede oxidar al reactivo 3,3',5,5'-tetrametilbencina (TMB) generando un cambio de color de la forma reducida (incolora) a la forma oxidada (azul) de éste reactivo. Asimismo, la presencia de glutatión en este sistema tiende a formar complejos con la Ag (I) impidiendo o dificultando por tanto la oxidación del TMB y permitiendo así su determinación. Además, una etiqueta NFC ha sido incorporada al dispositivo microfluídico de forma que la información analítica de éste sistema puede ser enviada a un Smartphone que analiza el color de la zona de detección del µPAD y genera los resultados cuantitativos del análisis. Bajo condiciones experimentales óptimas el método desarrollado presenta un rango dinámico lineal 0.72 a 250 µM para glutatión y un límite de detección de 0.72 µM.

En el quinto trabajo (Aceptado en Microchimica Acta, 27/05/2020) informa sobre el desarrollo de un µPAD para la detección fluorometrica off/on de biotioles. El ensayo descrito se basa en la unión covalente de carbon dots fluorescentes a la celulosa del papel y la posterior funcionalización de los carbon dots empleando ácido yodo acético de forma que, tras la funcionalización, pierden sus propiedades lumínicas (fluorescencia) por efecto de átomo pesado al incorporar en su estructura átomos de iodo. Así, esta detección es posible debido a que los carbon dots recuperan la fluorescencia en presencia de biotioles como glutatión, cisteína o homocisteina. Bajo condiciones experimentales óptimas el µPAD desarrollado presenta un rango dinámico lineal de 1 a 200 µM para glutatión y de 5 a 200 µM para cisteína y homocisteina. Además, este dispositivo presenta un límite de detección de 0.3 µM para glutatión y cisteína y de 0.4 µM para homocisteina.

El sexto trabajo (ACS Sensor, 2019, 4, 421-426) propone un nuevo método de determinación óptica de creatinina en muestras de orina. Este trabajo se centra en el desarrollo de un sensor desechable para la determinación colorimétrica de creatinina basado en un novedoso ionoforo de tipo calix[4]pirrol debido a su excelente selectividad hacia el ion creatininio. El mecanismo de detección de este sistema se basa en el reconocimiento del ion creatininio por el ionoforo calix[4]pirrol presente en la membrana sensora. Este ionoforo está acoplado a un indicador de pH lipofílico, que actúa como transductor en el reconocimiento de creatinina, ya que preserva la electroneutralidad de la membrana al incorporarse el ión creatininio al ionoforo, produciendo un intercambio catiónico que genera un cambio en el espectro de absorción de la fase sensora. Así, bajo condiciones optimas experimentales el rango dinamico lineal en la determinación de creatinina esta comprendido entre $1x10^{-5}$ – $1x10^{-2}$ M y el límite de detección calculado es de $1x10^{-5}$ M.

El séptimo trabajo de esta Memoria (enviado a Colloids and Surfaces B: Biointerfaces) se centra en la síntesis y caracterización de un novedoso sistema de detección luminiscente basadado en la utilización de nanoparticulas de fosfato de calcio dopadas con europio para la detección de creatinina. El sensor desarrollado se basa en un mecanismo on/off de las propiedades luminiscentes (fosforescencia) de las nanoparticulas de fosfato de calcio dopadas con europio en presencia de creatinina. En condiciones experimentales optimas se ha demostrado que las nanoparticulas permiten la determinación luminiscente de creatinina con una respuesta lineal en el rango de 1 a 120 µM, y con un limite de detección y cuantificación de 0.07 µM y 0.22 µM, respectivamente.

Como anexo a esta Memoria se ha incluido el trabajo publicado en (Anal. Chem. 2019, 91, 13, 8644-8651) que surge como consecuencia de la estancia predoctoral realizada en el *Department of chemistry, school of engineering science in chemistry, biochemistry and health of Royal institute of technology (KTH) in Stockholm, Sweden*. Este trabajo de investigación rompe con el esquema establecido de desarrollo de sistemas microfluídicos basados en papel para la detección óptica, centrándose en el desarrollo de un parche potenciométrico para la monitorización multi-iónica de electrolitos en sudor. Los electrodos incorporados en el parche han sido fabricados sobre un sustrato de poliuretano

e imprimidos con tinta de carbono estirable mediante serigrafía. Las membranas selectivas de iones implementadas en los electrodos permiten la monitorización de pH, Cl^-, Na^+ y K^+ en sudor en rangos de pH 4.5 – 7, y de concentraciones de 10-100 mM para Cl^-, Na^+ y K^+ mostrando una repuesta Nernsiana. La celda de muestreo que conforma el parche potenciométrico ha sido diseñada para recoger el sudor evitando problemas de contaminación y evaporación de la muestra al tiempo que proporciona un flujo constante de sudor a los electrodos para llevar a cabo el análisis. Por último, se escribe la validación in situ y ex situ del parche potenciométrico desarrollado que permite establecer la precisión del dispositivo.

SUMMARY

SUMMARY

The Manuscript shows and explains the results obtained during the research work that has led to the elaboration of the Doctoral Thesis entitled Design and analytical characterization of capillary microfluidic devices.

This Report has been structured in two main parts, introduction and experimental part. The main contents of each part are described below:

The introduction includes general and more relevant aspects to consider related to Nanoscience and Nanotechnology, including the definition and classification of nanomaterials, as well as, detailing their properties, synthesis methods, characterization techniques and fields of application. In addition, a definition and classification of chemical sensors is also included, focusing this classification on disposable or single-use sensors. In the same way, the main characteristics of these types of sensors are detailed, as well as the detection systems they use, the incorporated recognition elements and the most relevant fields of application in which disposable sensors are used.

Below, information on the development and classification of microfluidic systems used in chemical analysis platforms is collected, highlighting the importance of using paper-based microfluidic devices in the development of sensors. In addition, the different fabrication techniques for the development of microfluidic systems are classified, as well as the different optical and electrochemical detection methods that are implemented in the microfluidic analysis platforms are cited in this part.

Finally, in the last part of the introduction, it describes the importance of color analysis as an analytical parameter; information about the different color spaces is collected, as well as it propose the use of digital devices for color measurement such as Smartphone.

The experimental part of this Manuscript includes the procedures carried out to achieve the proposed objectives, the results obtained during the realization of this Thesis, and a detailed discussion about them. This experimental part has been divided in seven sections or chapters and an annex.

The first work (Talanta, 2016, 160, 721-728) describes the development of a new nitrite colorimetric detection method using a paper-based microfluidic device implemented with a tetrazine that acts as a recognition element and allows the determination of nitrite in water samples using a photographic camera or a smartphone as image capture devices.

After processing the different influencing parameters in the reaction (pH, tetrazine concentration, volume of sample, etc.), the developed analytical procedure has a detection limit of 2.05 µM and a linear dynamic range of between 5 and 500 µM, with 5 minutes reaction time.

The second work (Microchimica Acta, 2018, 185, 1-8) focuses on the design, development and validation of a paper-based microfluidic device (µPAD) for the colorimetric determination of glucose in serum and urine samples. The device was implemented with a MOF that acts as a peroxidase mimetic (HRP). Under optimal experimental conditions, a linear range for glucose up to 150 µM has been observed, with a detection and quantification limit of 2.5 µM and 10.6 µM, respectively. Also, the time required to complete this determination was 15 minutes.

The third work (in process to submit to ACS Sensors) introduces the in situ synthesis of fluorescent silicon nanodots, using (3-Aminopropyl) triethoxysilane and saccharose, in an implemented µPAD with a laser-induced grapheme heater for the determination of saccharose concentration in serum and urine samples, as well as in commercial juices and teas through the use of the µPAD under a UV lamp and taking a device photo with a digital camera and a Smartphone. The developed method presents a linear dynamic range of 10 to 200 µM for glucose and 10 to 100 µM for fructose with a detection limit of 0.8 µM and 0.51 µM, respectively.

The fourth work (in process to submit to Sensors and Actuator B-Chemical) is carried out the development of a µPAD for the colorimetric determination of glutathione. This determination is based on the fact that Ag (I) can oxidize 3, 3 ', 5, 5'-tetramethylbenzine (TMB) generating a color change from the reduced form of this reagent (colorless) to the oxidized form (blue). Similarly, the presence of glutathione in this system affects the formation of complexes with Ag (I), thus preventing or hindering the TMB oxidation. Furthermore, an NFC tag has been incorporated into the microfluidic device so that the analytical information from this µPAD can sent to a smartphone that analyzes the color of the detection area of the µPAD and generates the quantitative results of the analysis.

In the fifth work (Accepted manuscript in Microchimica Acta, 27/05/2020), reports the development of a µPAD for the off / on fluorometric detection of biothiols such as glutathione, cysteine and homocysteine using the µPAD under an UV lamp and a digital camera as an image capture device. The described method is based on the covalent

bonding of fluorescent carbon dots on cellulose paper and their functionalization using acetic iodine acid so that the carbon dots lose their luminesce properties (fluorescence) due to the heavy atom effect. Thus, this detection is possible because the carbon dots recover the fluorescence in the presence of biothiols. Under optimal experimental conditions, the developed µPAD presents a linear dynamic range of 1 to 200 µM for glutathione and 5 to 200 µM for cysteine and homocysteine. Furthermore, the µPAD has a detection limit of 0.3 µM for glutathione and cysteine and 0.4 µM for homocysteine.

The sixth work (ACS Sensor, 2019, 4, 421-426) proposes a new optical method for creatinine determination in urine samples. This work focuses on the development of a disposable sensor for the colorimetric determination of creatinine based on a novel calix [4] pyrrole ionophore due to its excellent selectivity towards the creatininium ion. The detection mechanism of this system is based on the recognition of the creatininium ion by the calix [4] pyrrole ionophore presents in the selective membrane. This ionophore is coupled to a lipophilic pH indicator, which acts as a transducer in the creatinine recognition, since it preserves the membrane electroneutrality when the creatininium ion is incorporated into the ionophore, producing a cation exchange that generates a change in the absorption spectrum of the selective membrane. Thus, under optimal experimental conditions, the linear dynamic range of creatinine determination is between 1x10-5 - 1x10-2 M and the calculated detection limit is 1x10-5 M.

The seventh work of this Manuscript (Submitted to Colloids and Surface B) focuses on the synthesis and characterization of a novel luminescent detection system based on the use of europium-doped calcium phosphate nanoparticles for the detection of creatinine. The developed sensor is based on an on / off mechanism of the luminescent (phosphorescence) properties of europium-doped calcium phosphate nanoparticles in the presence of creatinine. Under optimal experimental conditions, nanoparticles have been shown to allow the luminescent determination of creatinine with a linear range between 1 to 120 µM, and a detection and quantification limit of 0.07 µM and 0.22 µM, respectively.

Last, as annexed material, the work published in (Anal. Chem. 2019, 91, 13, 8644-8651) that arises as a consequence of the predoctoral stay in Department of Chemistry at the School of Engineering Sciences in Chemistry, Biotechnology and Healt of Royal Institute of technology, KTH (Stockholm, Sweden), has been included in this Manuscript. This research work breaks with the established scheme of development of paper-based

microfluidic systems for optical detection, focusing on the development and validation of a potentiometric patch for multi-ionic monitoring of electrolytes in sweat. The electrodes incorporated in the patch have been manufactured on a polyurethane substrate and printed with stretchable carbon ink by screen printing. The implemented ion selective membranes in the electrodes allow the monitoring of pH, Cl^-, Na^+ and K^+ in sweat in pH ranges 4.5 - 7, and concentrations of 10-100 mM for Cl^-, Na^+ and K^+ showing a Nernsian response. The implemented sampling cell on the potentiometric patch has been designed to collect sweat, avoiding contamination problems and evaporation of sweat, while providing a sample flow to the electrodes to carry out the analysis. Finally, the in situ and ex situ validation of the developed potentiometric patch is written, which allows establishing the precision of the developed device.

INTRODUCCIÓN

1. Nanociencia y Nanotecnología

En 1959 el físico Richard Feynman introdujo por primera vez el concepto de Nanotecnología en su conferencia "*There's plenty of room at the bottom*" [1]. Años más tarde, en 1974, Norio Taniguchi definió el término Nanotecnología para indicar la capacidad de utilizar materiales a nivel nanométrico. Desde entonces hasta la actualidad ha habido un gran número de avances y desarrollos científicos [2] que han demostrado la idea de Feynman de poder utilizar la materia de forma individual, es decir, al nivel de moléculas y átomos [3]. El gran desarrollo científico de la Nanociencia y la Nanotecnología en los últimos años se ha llegado a considerar como la "Revolución Industrial del siglo XXI".

La Nanociencia y la Nanotecnología se basan, por tanto, en la manipulación de átomos y moléculas individuales para producir materiales a escalas nanométricas. El prefijo "nano" deriva de la palabra griega "*enano*". Un nanómetro (nm) es igual a una milmillonésima de metro (10^{-9} m). De esta forma, según recoge la Internantional Organization for Standarization (ISO) la definición de "nanoescala" es el intervalo de tamaños comprendidos entre 1 y 100 nm [4]. En esta dimensión, la Figura 1 muestra el nanómetro en contexto. En comparativa, un cabello humano tiene 80000 nm de ancho aproximadamente, mientras que un glóbulo rojo puede llegar a tener 7000 nm de ancho.

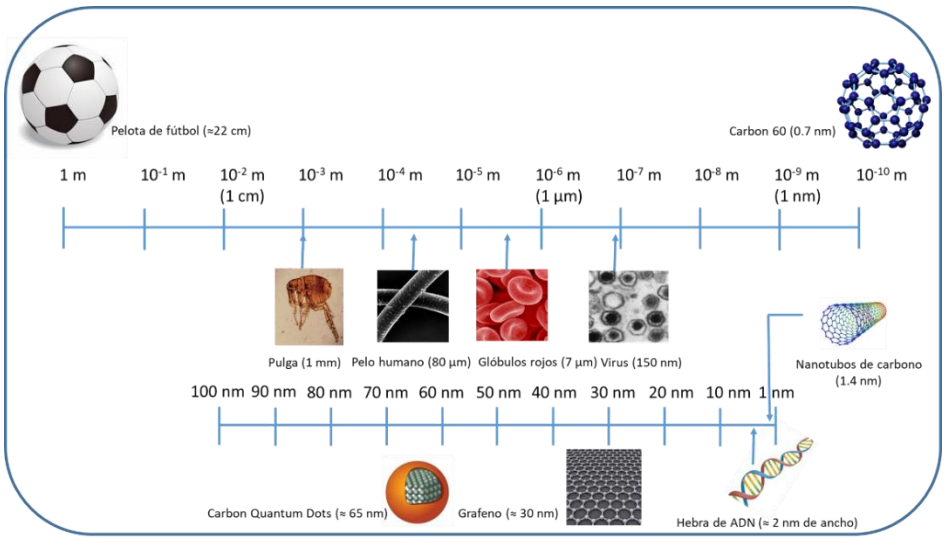

Figura 1. Escala de longitud que muestra el nanómetro.

En este contexto, el rango de tamaño que mayor interés presenta va típicamente desde 100 nm hasta el nivel atómico, es decir, aproximadamente 0.2 nm. Este rango se establece debido a que los materiales que lo conforman pueden tener propiedades diferentes o mejoradas en comparación con los mismos materiales en un mayor tamaño. Las principales razones que producen este cambio en el comportamiento del material son un aumento relativo del área superficial y el dominio de los efectos cuánticos. Por un lado, un aumento en el área superficial da como resultado un aumento en la reactividad química. Esto hace que algunos nanomateriales, por ejemplo, sean útiles como catalizadores para mejorar la eficiencia de pilas y baterías. Por otro lado, dado que el tamaño del material se reduce, los efectos cuánticos pueden cambiar significativamente, modificando las propiedades ópticas, magnéticas o eléctricas del material [5].

1.1. Definición de Nanociencia y Nanotecnología

Existe una amplia variedad de definiciones de Nanociencia. Sin embargo, una de las definiciones de Nanociencia más aceptada es la que considera esta disciplina como el estudio y manipulación de diversos materiales a nivel atómico, molecular o macromolecular, donde las propiedades químicas o físicas difieren significativamente de las que presenta el mismo material a mayor escala. Otra definición más general considera la Nanociencia como la disciplina que se encarga de la síntesis, caracterización y exploración de materiales nanoestructurados.

Por otro lado, el termino Nanotecnología se relaciona con la gestión de las características del material como el tamaño, morfología, composición química y configuración molecular para mejorar sus propiedades. En cuanto a su significado, la Royal Society define la Nanotecnología como el diseño, caracterización, producción y aplicación de estructuras, dispositivos y sistemas a través del control de la forma y el tamaño a nivel nanométrico. Otra definición referida al término Nanotecnología es aquella que considera el conjunto de técnicas de investigación y desarrollo a nivel atómico, molecular y supramolecular cuyo objetivo es crear estructuras, dispositivos y sistemas con nuevas propiedades y funciones que surgen del comportamiento de la materia cuando su tamaño disminuye a escalas nanométricas [3].

1.2. Nanociencia, Nanotecnología y Química Analítica

En los últimos años los avances científicos han logrado el desarrollo de nuevas herramientas que nos han permitido diseñar, fabricar y caracterizar materiales nanométricos con gran precisión. En este contexto, las aplicaciones de la Nanotecnología se han extendido a todos los ámbitos científicos presentando un gran auge en disciplinas como la Biotecnología, Química, Electrónica, Ciencia de los Materiales, etc. (Figura 2). De hecho, el impacto de la Nanotecnología ha generado importantes avances en medicina, electrónica, comunicaciones, producción y almacenamiento, seguridad y defensa [6]. Todo ello ha provocado un gran interés en sectores públicos y privados derivando en un crecimiento exponencial en Investigación y Desarrollo por parte de estos organismos. Actualmente, existe un gran interés a nivel mundial de fomentar la investigación en Nanociencia y Nanotecnología por lo que las inversiones que se realizan en esta área de la ciencia llegan a alcanzar más de 17.000 millones de euros solo a nivel europeo.

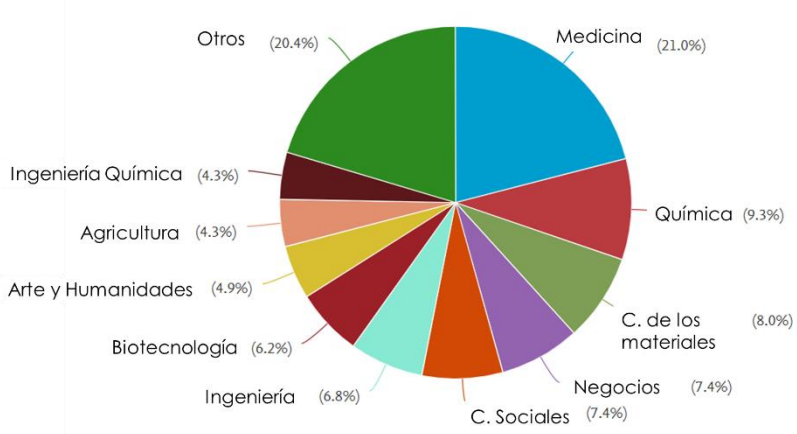

Figura 2. Áreas de aplicación extraída de la base de datos Scopus para el término "Nanotecnología" desde 2000 al 2019.

En concordancia, el desarrollo de estas disciplinas ha favorecido en gran medida la incorporación de nanomateriales en numerosos productos de consumo diario entre los que se encuentran alimentos, cosméticos y pinturas. Este hecho ha despertado una cierta inquietud en la población derivada del riesgo para la salud y el medio ambiente que puede suponer una exposición prolongada de este tipo de materiales. Por todo ello, surge la necesidad de evaluar y controlar los efectos a corto y largo plazo asociados con las aplicaciones nanotecnológicas.

Hoy en día, se hace evidente la necesidad de realizar estudios que nos permitan identificar y cuantificar los posibles riesgos de la utilización de nanomateriales [7]. Por otro lado, es importante poder determinar las posibles consecuencias de la liberación de estos materiales al medio ambiente. Por todo ello, es necesario incorporar estrategias que reduzcan o anticipen los posibles efectos negativos de los nanomateriales sobre la salud y poder establecer medidas preventivas convenientes.

Si bien cabe destacar, uno de los objetivos principales de la Química Analítica es el desarrollo de nuevos métodos de análisis, ya sea para mejorar los métodos existentes o para introducir estrategias de análisis alternativas que pongan solución a los nuevos problemas sociales y económicos que se presentan.

En consecuencia, a lo lago de los años la Química Analítica ha tomado un mayor rol en Nanociencia y Nanotecnología. Por un lado, gracias a la Química Analítica podemos obtener información de la composición química y caracterización de los nanomateriales generados [8]. Así mismo, los productos nanotecnológicos pueden emplearse en el desarrollo de nuevas herramientas y procedimientos de análisis químico con unas prestaciones diferentes a los actualmente existentes. Esta idea queda reflejada en la Figura 3.

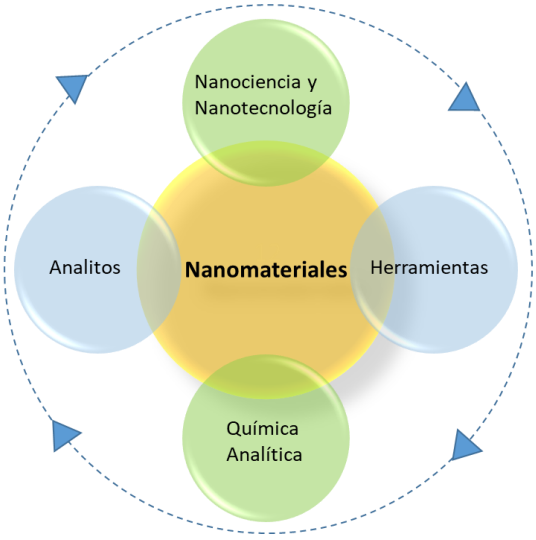

Figura 3. Vínculo entre la Química Analítica y la Nanociencia y Nanotecnología.

Tales herramientas de análisis pueden ser útiles para caracterizar las propiedades fisicoquímicas de los nuevos nanomateriales que se desarrollan en las distintas disciplinas científicas. Además, el desarrollo de métodos analíticos basados en Nanotecnología puede contribuir a la simplificación y/o el mejoramiento de los procesos analíticos existentes o del desarrollo de nuevos métodos de análisis.

En resumen, los nanomateriales pueden participar en las distintas etapas del proceso analítico gracias a sus propiedades, es por ello que la Nanociencia y la Nanotecnología se encuentran integradas en los fines de la Química Analítica actual [9].

1.3. Nanomateriales

Existen numerosas definiciones relacionadas con el término nanomaterial [5], [10], [11]. Sin embargo, el Comité Científico de la Unión Europea categoriza la definición de nanomaterial basada en el tamaño [12]. Por ende, un nanomaterial se define como un *material natural, accidental o fabricado que contenga partículas, sueltas o formando un agregado o aglomerado y en el que el 50% o más de las partículas en la distribución de tamaños presente una o más dimensiones externas en el intervalo de tamaños comprendidos entre 1 nm y 100 nm*.

1.3.1. Clasificación de los nanomateriales

De forma general, los nanomateriales se categorizan como aquellos materiales con dimensiones inferiores a 100 nm. Dentro de esta variedad de productos se encuentran nanopartículas (NPs), nanocristales, nanotubos, grafeno, dendrímeros, liposomas, fullerenos y nanoconos, entre otros muchos.

De este modo, existen diferentes criterios de clasificación de los nanomateriales. De acuerdo a su origen o naturaleza, los nanomateriales se pueden clasificar en naturales, donde se incluyen los fullerenos, óxidos de hierro y las cenizas volcánicas; accidentales u originados como consecuencia de la actividad humana como los óxidos de titanio, aluminio o sílice y fabricados de forma intencionada

como las nanopartículas de plata o los nanotubos de carbono. Sin embargo, una de las clasificaciones más extendidas de los nanomateriales es aquella que atiende a sus dimensiones [13]. Así, los nanomateriales se pueden clasifican en:

a) Nanomateriales en una dimensión

En este grupo se encuentran los nanomateriales unidimensionales como películas delgadas, capas y superficies. Este tipo de materiales se han desarrollado y utilizado ampliamente a lo largo de los años en la fabricación de dispositivos electrónicos, en ingeniería y en química.

- **Quantum Dots**

  Los Quantum Dots (QDs) teorizados en la década de 1970 e inicialmente creados en el principio de los ochenta son nanomateriales constituidos por nanocristales semiconductores coloidales. Los QDs tienen forma esférica con un tamaño entre 1 y 12 nm. El núcleo de los QDs está formado por material inorgánico rodeado de una capa exterior de moléculas de ligandos que evita su agregación en medios líquidos. Si las partículas semiconductoras que forman los QDs son suficientemente pequeñas, entran en juego los efectos cuánticos, que limitan las energías a las que los electrones y los defectos pueden existir en las partículas. Como la energía está relacionada con la longitud de onda (o color), esto significa que las propiedades ópticas de la partícula pueden ajustarse dependiendo de su tamaño. Por lo tanto, se pueden sintetizar partículas que puedan emitir o absorber a una longitud de onda específica (colores), simplemente controlando su tamaño. Recientemente, se han encontrado QDs con aplicaciones en células solares y etiquetas biológicas fluorescentes empleadas para rastrear diferentes tipos de moléculas biológicas [14]–[16].

b) Nanomateriales en dos dimensiones

Los nanomateriales bidimensionales han generado un gran interés entre la comunidad científica en los últimos años gracias a sus novedosas propiedades. Tienen dimensiones micro/macrométricas y forman parte de ellos diferentes materiales entre los que se encuentran:

- **Nanotubos de carbono (CNT)**

  Estas estructuras fueron observadas por primera vez en 1991 por Sumio Iijima. Los nanotubos de carbono son láminas de grafeno enrolladas presentando un diámetro de entre 10 y 6 micrómetros. Existen dos tipos de CNT; los de pared simple compuestos por un solo tubo y los de pared múltiple formados por varios tubos concéntricos. Se trata de materiales con unas excelentes propiedades físico-químicas. Son mecánicamente muy fuertes y tan rígidos como el diamante, cuentan con una gran flexibilidad sobre su eje y pueden conducir electricidad extremadamente bien. Todas estas propiedades hacen especialmente potente el uso de CNT en el desarrollo de dispositivos electrónicos, nanoelectrónica y sensores [17].

- **Nanotubos inorgánicos**

  Son materiales basados en compuestos en capas como el fullereno inorgánico y el disulfuro de molibdeno. Tienen excelentes propiedades tribológicas, resistencia al impacto de ondas de choque, reactividad catalítica y una gran capacidad para el almacenamiento de litio e hidrógeno. Un ejemplo son los nanotubos de óxido, como el dióxido de titanio los cuales están siendo utilizados para aplicaciones en catálisis, fotocatálisis y en el almacenamiento de energía [18].

- **Nanocables**

  Los nanocables son cables ultrafinos o conjuntos lineales de puntos formados por autoensamblaje. Los nanocables semiconductores compuestos por silicio, nitruro de galio y fosfuro de indio han demostrado tener un alto potencial en óptica, electrónica y magnetismo. Por ejemplo, los nanocables tienen una potencial aplicación en el almacenamiento de datos con alta densidad, ya sea como cabezales de lectura magnéticos o como nanodispositivos electrónicos y optoelectrónicos, para interconexiones metálicas de dispositivos cuánticos y nanodispositivos. En la preparación de estos nanocables se utilizan técnicas de crecimiento sofisticadas, que incluyen procesos de autoensamblaje, estrategia que permite la formación de estructuras complejas mediante la interacción de

los bloques de construcción, átomos o moléculas de forma precisa dando lugar a la estructura deseada.

c) Nanomateriales en tres dimensiones

Este tipo de nanomateriales están constituidos por agrupaciones de nanomateriales en una y dos dimensiones. Dentro de esta clasificación podemos encontrar:

- **Nanopartículas**

  Las nanopartículas se pueden encontrar de forma natural en el mundo, por ejemplo, como los productos de los procesos fotoquímicos que realizan plantas y algas o como productos de la actividad volcánica. Durante miles de años se han generado como productos de combustión y cocción de alimentos. Por otro lado, las nanopartículas también han sido fabricadas de forma intencionada por el hombre, un claro ejemplo de ello son los óxidos metálicos. Este tipo de nanopartículas presentan un gran interés debido a sus propiedades químicas y su comportamiento óptico. Por ejemplo, el dióxido de titanio y el óxido de zinc se convierten en transparentes a nanoescala, son capaces de absorber y reflejar la luz UV por lo que son de gran utilizad como protectores solares. Las nanopartículas tienen un gran potencial en diversas aplicaciones a corto plazo, por ejemplo, en la fabricación de nuevos cosméticos, textiles y pinturas, y a largo plazo en métodos de focalización y transporte de medicamentos donde podrían ser utilizados para transportar fármacos a un sitio específico del cuerpo.

- **Fullerenos**

  Se trata de una nueva clase de materiales de carbono con morfología esférica de aproximadamente 1 nm de diámetro que comprenden 60 átomos de carbono dispuestos como 20 hexágonos y 12 pentágonos; presentan una configuración de un balón de fútbol. Los fullerenos cuentan con múltiples aplicaciones entre las que destacan su capacidad de actuar

como lubricante para superficies, vehículos de liberación de medicamentos y son de gran utilidad en circuitos electrónicos.

- **Dendrímeros**

  Los dendrímeros son moléculas poliméricas esféricas. Hay muchos tipos de dendrímeros; el más pequeño tiene varios nanómetros de tamaño. Los dendrímeros se usan en aplicaciones convencionales como recubrimientos y tintas, pero también tienen una gama de propiedades interesantes que podría conducir a aplicaciones de gran utilidad. Por ejemplo, los dendrímeros pueden actuar como moléculas transportadoras a nanoescala y como tal podrían utilizarse en la administración de medicamentos. Además, los dendrímeros presentan un gran potencial en su utilización para la limpieza ambiental ya que pueden atrapar iones metálicos. De esta forma se podrían utilizar para la purificación de agua.

1.3.2. Propiedades de los nanomateriales

Dos factores principales causan diferencias entre un nanomaterial y el mismo material pero de mayor tamaño: el área de superficial y los efectos cuánticos, como se ha comentado anteriormente. Estos factores pueden cambiar o mejorar las propiedades del material, por ejemplo, reactividad, resistencia y características eléctricas del mismo, etc. [19].

A medida que una partícula disminuye de tamaño, una mayor proporción de los átomos se encuentran en la superficie en comparación con aquellos de mayor tamaño, provocando un cambio en las propiedades del material. Por ejemplo, una partícula de un tamaño de 30 nm tiene el 5% de sus átomos en su superficie pero cuando el tamaño de la partícula es 10 nm el 20% de sus átomos están en la superficie, y así sucesivamente. Por ello, los nanomateriales tienen un área de superficie mucho mayor por unidad de masa en comparación con partículas más grandes. Muchas de las reacciones químicas ocurren en la superficie de los materiales, esto significa que una masa dada de material en forma de nanomaterial

será mucho más reactivo que la misma masa de material compuesta de partículas más grandes alterando así las propiedades del material.

Las nanopartículas de origen metálico exhiben propiedades ópticas que dependen notablemente de la forma y el tamaño del nanomaterial siendo distintas de los metales cuando se encuentran en la escala macroscópica. Cuando se hace incidir un haz de luz sobre la superficie de una nanopartícula, los electrones libres de la banda de conducción se excitan produciendo un desplazamiento de cargas negativas con respecto a las cargas positivas del núcleo provocando una polarización de la partícula. Los niveles de energía en las moléculas nanométricas están cuantizados y la banda prohibida (bandgap) de los electrones está directamente relacionado con el tamaño de la nanopartícula. Cuanto menor es el tamaño de ésta el bandgap es mayor y por tanto la longitud de onda de emisión menor. Estos electrones libres en las nanopartículas actúan como osciladores de resonancia del plasmón superficial (SPR).

En este sentido, las nanopartículas metálicas cambian de color debido a la excitación de todos los electrones libres dentro de la banda de conducción de la superficie de la nanopartícula (Figura 4.). Esta característica hace que las nanopartículas sean útiles para aplicaciones biomédicas.

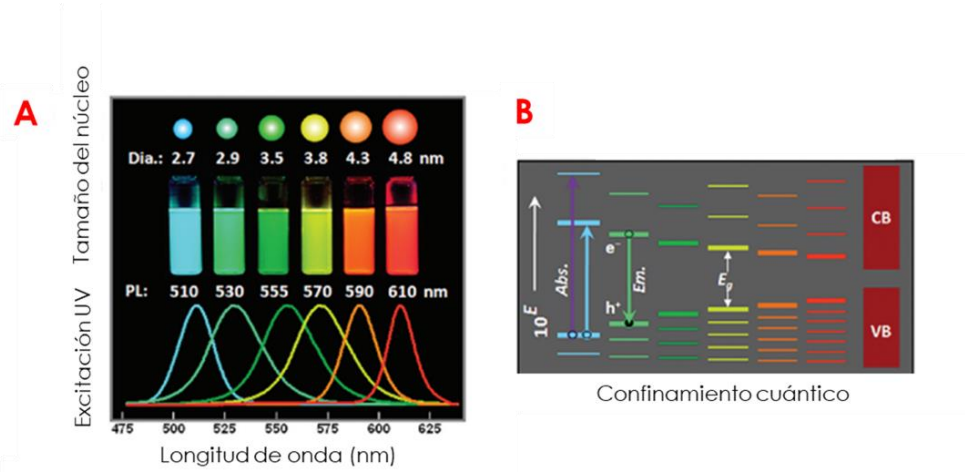

Figura 4. Espectros de emisión de nanopartículas de diferente tamaño. Imagen modificada de [20].

1.3.3. Métodos de síntesis de los nanomateriales

Los continuos avances en Nanociencia y Nanotecnología han permitido el desarrollo de una amplia variedad de nanomateriales funcionales con unas propiedades únicas y bien definidas. El empleo de estos materiales nanométricos ha producido grandes progresos en la miniaturización, permitiendo así el desarrollo de dispositivos tecnológicos con múltiples aplicaciones [21], [22].

En general, hay dos formas de diseñar entidades complejas de dimensiones reducidas basadas en enfoques ascendentes y descendentes como muestra la Figura 5. Estas metodologías de síntesis se conocen comúnmente como Bottom-up (de abajo hacia arriba) y Top-down (de arriba hacia abajo). Ambas alternativas de síntesis permiten la fabricación de nanomateriales de forma fiable, precisa y reproducible.

- **Bottom-up**

  Dicha fabricación consiste en la manipulación de átomos y moléculas para formar las estructuras deseadas, es decir, formar estructuras directamente a partir de mecanismos de crecimiento del material como la deposición de la capa atómica. Los objetivos de este tipo de síntesis son alcanzar una máxima precisión ya que casi todos los átomos se distribuyen en el lugar correcto y en el espacio adecuado; diseñar estructuras complejas molecularmente y reducir los costos de fabricación a poco más que el costo de lo requerido, materias primas y energía.

- **Top-down**

  Esta alternativa de síntesis emplea procedimientos de fabricación de nanomateriales mediante la reducción de tamaño de otros materiales de mayor tamaño. Esta estrategia requiere la utilización de instrumentación más compleja que en el caso de la síntesis Bottom-up ya que parte del material

másico se va descomponiendo o dividiendo en unidades más pequeñas para dar lugar al nanomaterial que se quiere obtener.

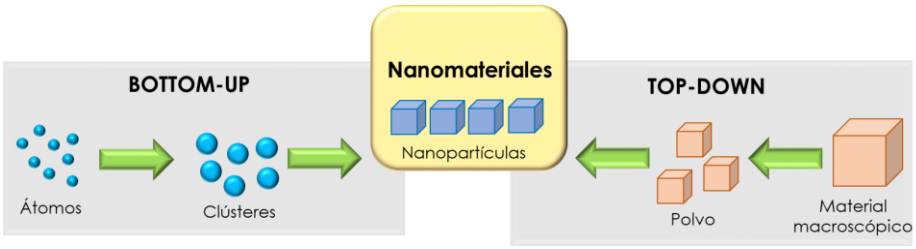

Figura 5. Alternativas de síntesis de nanomateriales.

1.3.4. Técnicas de caracterización de los nanomateriales

La caracterización de los nanomateriales se centra en la determinación de su forma, tamaño, distribución, propiedades químicas y mecánicas. Por tanto, la caracterización de un material tiene como objetivo el control de la calidad del material. En consecuencia, el conjunto de técnicas de caracterización existentes nos permiten observar y medir las propiedades de un material a nivel de nanoescala [23], [24].

En cuanto a las diferentes formas de caracterizar un nanomaterial estas se dividen en:

- **Caracterización morfológica y estructural**

  Las características morfológicas de los nanomateriales suscitan gran interés debido a la influencia de la morfología en las propiedades del material. De esta forma, podemos observar los átomos que conforman un material, así como, analizar la relación entre su forma y sus propiedades permitiendo el control de procesos en la nanoescala.

  Existen diferentes herramientas de caracterización para el estudio morfológico (tamaño y forma) de un material [25]. Las técnicas microscópicas, por ejemplo, son muy fiables en la caracterización de nanomateriales. Estas técnicas consisten en el bombardeo del material con

un haz de electrones. En el caso de la microscopia electrónica de barrido (SEM) se analizan los electrones secundarios que proceden de la superficie del material ya que nos proporcionan información sobre el tamaño y la forma del nanomaterial. A menudo, la caracterización morfológica de un material mediante esta técnica permite que el microscopio este acoplado a un espectrómetro de energía dispersada (EDX). De esta forma, este dispositivo es capaz de monitorizar los rayos X que son emitidos por el material cuando está siendo bombardeado por el haz de electrones. Gracias a este acoplamiento se puede llevar a cabo un análisis cualitativo y cuantitativo del material en diferentes secciones del mismo.

Otra posibilidad en la caracterización morfológica de nanomateriales es el empleo del microscopio electrónico de transmisión (TEM). En este caso se generan imágenes a partir de un haz de electrones que atraviesa el nanomaterial, es por ello que el espesor de la muestra es un parámetro a tener en cuenta en este tipo de análisis. De igual forma si se emplea la microscopia electrónica de transmisión de alta resolución (HRTEM) se puede obtener una mayor precisión en el tamaño del material, visualizar los límites del entramado cristalino, obtener información cristalográfica del mismo y obtener los parámetros estructurales de los nanocristales que forman el material [26]. Además de todo esto, es posible acoplar una unidad de barrido por transmisión (STEM) al microscopio de forma que podamos obtener mapas composicionales del nanomaterial.

De igual forma otra alternativa para obtener información morfológica de un material es la microscopia de fuerza atómica (AFM). Esta técnica de análisis se basa en el empleo de una sonda que cuenta con una punta muy fina que es guiada por la superficie de la muestra de forma que realiza el análisis en modo contacto -no contacto, es decir, monitoriza las interacciones entra la punta y el nanomaterial. Esta técnica permite monitorizar materiales conductores y no conductores obteniendo información sobre la topografía superficial del material [27], [28].

En conclusión, puede afirmarse que las técnicas basadas en microscopia resultan de gran utilidad en la caracterización morfológica de los nanomateriales. Sin embargo, la etapa de preparación de la muestra a menudo resulta tediosa y puede afectar a la morfología original del material. Esto es debido a que existe la necesidad de depositar la muestra sobre un soporte sólido o rejilla y, a continuación, someter la muestra a condiciones de vacío y sequedad, y por último llevar a cabo su metalización; por ello, la estructura nativa del nanomaterial puede sufrir algún tipo de alteración o pueden darse casos de agregados de las partículas que conforman el material.

Una técnica complementaria a los análisis morfológicos realizados mediante técnicas microscópicas son las medidas de dispersión de luz (Dynamic Light Scattering, DLS) [29]. Esta técnica presenta la ventaja de ser una técnica simple, no invasiva, no destructiva y asequible económicamente. Mediante DLS se puede obtener información de la estructura, morfología, estado de agregación y conformación molecular de los nanomateriales o sus bioconjugados. El análisis mediante DLS resulta especialmente interesante cuando se necesita obtener información acerca de la distribución de tamaños de las nanopartículas. La información que se obtiene mediante DLS se corresponde con el diámetro hidrodinámico de las nanopartículas, es decir, el núcleo, los ligandos que lo rodean y las moléculas de disolvente. Por su parte, se basa en la medida de las fluctuaciones en la intensidad de la luz dispersada que se relaciona directamente con el tamaño hidrodinámico del material.

El equipo de DLS a menudo esta acoplado a una unidad de medida de potencial Z de esta forma se puede determinar la carga neta superficial de un nanomaterial disperso. En este caso se aplica un campo eléctrico a través de la muestra y se mide la velocidad a la que se mueven las especies cargadas hacia un electrodo. Este parámetro está influenciado por la concentración de nanopartículas, la presencia de tensoactivos, la

naturaleza de los ligandos superficiales, la temperatura y el pH del medio en el que se encuentra disperso el nanomaterial. Resulta de especial interés conocer el valor de la carga neta superficial de las nanopartículas ya que proporciona información acerca de la estabilidad de la dispersión coloidal en el medio en el que se encuentra. De forma general, se utiliza como valor de referencia ± 30 mV; valores superiores indican que la dispersión que conforma la muestra es estable. Valores inferiores indican la tendencia de la muestra a formar agregados.

El estudio de las características estructurales de un nanomaterial es muy importante ya que nos permite conocer la composición y la naturaleza de los materiales de unión que lo forman. Entre las distintas técnicas existentes, se encuentra la difracción de rayos X (XRD). Se trata de una técnica de rutina empleada para obtener información acerca de la estructura de materiales cristalinos, resulta de gran utilidad para identificar sustancias desconocidas ya que se pueden comparar los datos de difracción obtenidos con la base de datos del International Centre for Diffraction Data (ICDD). Esta técnica permite obtener información sobre la estructura cristalográfica, la identificación de fases cristalinas y parámetros de red mediante un tratamiento matemático de los difractogramas obtenidos.

- **Caracterización composicional**

Actualmente existe un gran interés en conocer la composición de un material de forma cualitativa y cuantitativa, por ello resulta interesante el análisis de una muestra mediante EDX. Como se mencionó anteriormente, esta técnica nos permite conocer la composición elemental del material y se utiliza ampliamente para dar soporte a SEM y TEM, entre otras. Se trata de una técnica sencilla, rápida, directa y resulta muy fácil interpretar sus resultados en la caracterización de la composición de nanopartículas. Esta técnica de análisis se basa en la detección de la radiacción X que emite un material excitado por un haz de electrones enfocado en un área muy pequeña de la muestra. De forma que estos electrones producen

transiciones energéticas en los átomos que involucran los niveles atómicos más internos generando fotones en el espectro de los rayos X que son característicos de cada tipo de átomo permitiendo así su identificación.

Otra técnica ampliamente utilizada en la caracterización composicional de un nanomaterial es la espectroscopia fotoelectrónica de rayos X (XPS). Se trata de una técnica no destructiva muy útil en el análisis de la composición de superficies. Esta técnica requiere condiciones de ultra-vacío ya que la muestra es bombardeada mediante un haz monocromático de rayos X de alta energía. Cuenta con un analizador de electrones de alta resolución donde se determinan los fotoelectrones que abandonan la muestra. En este tipo de análisis se obtiene un espectro con los picos correspondientes a los fotoelectrones desprendidos. La energía de enlace de los picos es característica de cada elemento, es por ello que se puede determinar la composición superficial de una muestra.

Por otro lado, la espectroscopia infrarroja de transformada de Fourier (FTIR) es una técnica poderosa para obtener información de los enlaces químicos entre los ligandos de las nanoestructuras, de esta forma se puede tener información sobre la presencia y ausencia de grupos funcionales específicos y determinadas estructuras químicas. Además, los desplazamientos en la frecuencia de absorción de las bandas y los cambios en la intensidad indican cambios en la estructura química de las moléculas. Así, FTIR proporciona un espectro de reflexión de las bandas de los grupos funcionales de sustancias orgánicas e inorgánicas. De esta forma es posible realizar una identificación de los materiales.

- **Caracterización del área superficial**

La técnica por excelencia para la caracterización del área superficial de una muestra es la resonancia magnética nuclear (RMN). Esta técnica proporciona información física, química, estructural acerca de las

interacciones de los ligandos de una molécula con otra. El RMN se basa en medidas del momento magnético de ciertos núcleos magnéticos entre los que se encuentran el hidrogeno (^{1}H), carbono (^{13}C) y el fósforo (^{31}P) cuando se le aplica un campo magnético. Además, el RMN permite llevar a cabo la monitorización de reacciones de intercambio de ligando sobre la superficie de un nanomaterial aunque no es adecuada para nanopartículas con una solubilidad baja.

- **Caracterización óptica**

  Las propiedades ópticas de un material son muy importantes en numerosas aplicaciones, es por ello que resulta de gran interés su estudio. Estas caracterizaciones se basan en ley de Beer-Lambert y los principios básicos de la luz. Estas técnicas dan información sobre las propiedades de absorción, reflexión y luminiscencia de un material. De entre los instrumentos ópticos más utilizados en el estudio de las propiedades ópticas de un material se encuentran el espectrofotómetro ultravioleta-visible (UV-Vis), espectrofluorímetro y el elipsómetro. La espectrofotometría de absorción molecular ultravioleta-visible (UV-vis) es importante en la caracterización de las propiedades ópticas y espectroscópicas de un material. Esta técnica a menudo se emplea para evaluar la concentración, tamaño y estado de agregación de nanomateriales. Los desplazamientos en los espectros de absorción y emisión de nanomateriales provocados por un cambio en el entorno de los ligandos o en la composición del disolvente constituyen la base para el desarrollo de una gran cantidad de sensores ópticos.

1.3.5. Aplicaciones de los nanomateriales

Gran parte de la Nanociencia está relacionada con la comprensión de las propiedades de los materiales en el nanoescala y los efectos de disminuir el tamaño de los materiales o los componentes estructurados de materiales. Las partículas a nanoescala pueden exhibir, por ejemplo, diferentes propiedades eléctricas, ópticas

o magnéticas de grandes partículas del mismo material como se ha comentado anteriormente. Estas propiedades inherentes de los nanomateriales aumentan sus posibilidades para ser utilizados en diversas aplicaciones dentro de las distintas disciplinas científicas [30].

La síntesis de nuevos nanomateriales ofrece nuevas oportunidades para el avance en el desarrollo de una nueva generación de herramientas que permite la detección selectiva de biomoléculas. El uso de nanomateriales en el desarrollo de sensores y biosensores se debe principalmente a sus propiedades especiales. Los nanomateriales presentan una estructura estable, compatibilidad biológica, alto rendimiento catalítico y gran área superficial específica [31].

En este sentido, existe una gran variedad de nanopartículas de metales nobles [32], óxidos metálicos [33], así como, nanotubos de carbono [34] y grafeno [35] que presentan actividad similar a la peroxidasa e incluso a otros enzimas como la glucosa oxidasa (GOx) [36]. Su aplicación en el desarrollo de biosensores tiene un gran interés ya que pueden sustituir a las enzimas naturales debido a su alta estabilidad y actividad catalítica similar. Se consideran como nanomateriales miméticos enzimáticos y son ideales para la detección rápida en el desarrollo de biosensores colorimétricos. El grafeno y sus derivados exhiben actividad catalítica similar a la peroxidasa de rábano picante (HRP) por lo que se utilizan como sustrato para catalizar reacciones de oxidación de reactivos cromógenicos como la o-fenilendiamina (OPD), el 3,3’,5 ,5’-tetrametilbencidina (TMB) o el 2,2′-azino-bis (ácido 3-etilbenzotiazolina-6-sulfónico (ABTS) con peróxido de hidrogeno (H_2O_2) generando cambios de color proporcionales a la concentración de H_2O_2. Este hecho permite el desarrollo de biosensores colorimétricos para la detección de glucosa [37], ácido ascórbico (AA) [38], peróxido de hidrógeno [39], glutation [40] y ADN [41].

Nanomateriales como los carbon dots (CDs) se utilizan en el desarrollo de sensores electroquímicos gracias a su capacidad para acelerar electrones en los

procesos de transferencia de carga entre la interfaz de detección y el electrodo, promoviendo así procesos redox. Además, los CDs pueden combinarse con diferentes metales para obtener híbridos metálicos proporcionando propiedades superiores y aumentando así los campos de aplicación de éstos materiales. Por ejemplo, híbridos de CDs y nanopartículas de oro (CDs/AuNPs) se han utilizado para la detección electroquímica de nitrito [42].

Por otro lado, existen numerosas aplicaciones bioanalíticas descritas que utilizan QDs como marcadores luminiscentes en la detección de ácidos nucleicos, proteínas, oligonucleótidos, anticuerpos, y otras biomoléculas debido a sus propiedades fotoluminiscentes [43], [44]. Esta detección se lleva a cabo normalmente por una conjugación producida entre los QDs y la biomolécula a través de enlaces con los grupos funcionales del nanomaterial como son los grupos amino, carboxilo o tioles.

2. Sensores

2.1. Definición de sensor

Un sensor se define como un dispositivo miniaturizado que puede proporcionar información en tiempo real sobre la presencia de compuestos o iones específicos en muestras complejas (Figura 6). Los sensores químicos contienen dos componentes básicos conectados entre sí: un receptor, sistema de reconocimiento químico que interacciona específicamente con una sustancia química determinada, y un transductor fisicoquímico que interpreta dicha interacción y la transforma en una señal medible a partir de la cual se obtiene información analítica específica cuantitativa o semicuantitativa. En este sentido, un sensor debe presentar las siguientes características: precisión, exactitud, selectividad, sensibilidad, reversibilidad, capacidad para simplificar el proceso analítico, respuesta rápida y en tiempo real, estabilidad operativa, capacidad de integración, simplicidad, robustez y bajo coste.

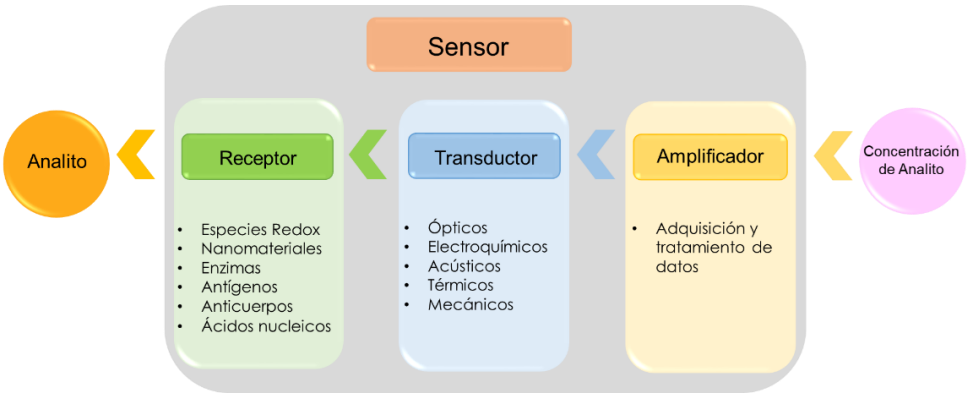

Figura 6. Esquema de funcionamiento de un sensor.

- **Receptor:** es el elemento de reconocimiento, componente principal de un sensor, permite la interacción selectiva con la especie a determinar. El elevado grado de selectividad que presenta el receptor hacia un analito concreto permite que pueda ser utilizado en matrices complejas sin necesidad de etapas de tratamiento de la muestra.

- **Transductor:** se trata de un sistema con capacidad de convertir la información química en una señal eléctrica que contenga información analítica sobre el analito. El transductor no debe interferir en la reacción de reconocimiento y su respuesta debe ser rápida.

- **Amplificador:** sistema que lleva a cabo la amplificación y tratamiento de la señal para que podamos obtener los resultados de forma adecuada y que puedan ser interpretados.

En los últimos años, el desarrollo de sensores ha sido uno de los campos que ha evolucionado más rápidamente debido al gran impacto que supone el desarrollo de dispositivos de análisis en diversas aplicaciones: biomedicina, análisis clínico, control ambiental y alimentario, etc. En la actualidad, los sensores constituyen una línea de mercado en expansión donde la industria sanitaria constituye una gran parte [45].

2.2. Sensores desechables

Los sensores desechables son dispositivos de detección utilizados para obtener información rápida, accesible y confiable diferenciándose de las técnicas de análisis convencionales en las características básicas recogidas en la Tabla 1. Entre las áreas de aplicación de los sensores desechables se encuentran: farmacia, agricultura, control de calidad ambiental, análisis de alimentos y en ciencias forenses. Los sensores desechables son dispositivos baratos, fáciles de usar y asequibles. Esta clase de sensores de bajo costo permiten obtener información de forma rápida en cualquier lugar y en cualquier momento. La creciente demanda de análisis puntuales fuera de los laboratorios ha experimentado un enorme crecimiento especialmente en el caso de los diagnósticos médicos, control de calidad de alimentos y monitorización ambiental de contaminantes. Por todo ello, una amplia gama de dispositivos desechables, como pruebas de embarazo, medidores de glucosa y demás se han integrado en nuestra vida diaria.

El descubrimiento de diferentes materiales y el desarrollo de nuevas tecnologías de detección tienen un papel fundamental en la implementación de nuevos sensores. La utilización de materiales novedosos en el desarrollo de sensores permite reducir los costes, el impacto medioambiental y mejorar el rendimiento y la aplicabilidad de los sensores desechables.

Por lo tanto, los sensores desechables deben cumplir una serie de requisitos: utilizar materiales baratos, sostenibles o biodegradables; permitir la producción en masa a bajo coste; ser compactos con una alta modularidad y menos componentes; permitir la portabilidad; tener una respuesta de análisis rápida; ser fáciles de utilizar u ofrecer un manejo automatizado, minimizando así, la intervención del usuario y además, deben permitir la entrega de resultados precisos de acuerdo con las normas de calidad establecidas [46].

Tabla 1. Comparación de las técnicas convencionales de análisis con el uso de sensores desechables.

Análisis	Ventajas	Desventajas
Sensores desechables	Detección rápida Aplicación directa Portabilidad Fácil uso Reutilizable Económico Menor volumen de muestra y reactivos No es necesario el pretratamiento de la muestra	Menor sensibilidad Menor especificidad
Técnicas convencionales	Alta sensibilidad Alta sensibilidad	Largos tiempos de espera de los resultados Costosos Necesidad de desplazar la muestra al laboratorio Personal de laboratorio cualificado Aparatos de alta tecnología Necesidad de pretratamiento de muestra No reutilizable Generación de residuos elevada Grandes volúmenes de muestra y reactivos son requeridos Necesario una fuente de alimentación constante

2.2.1. Materiales para el desarrollo de sensores desechables

Los avances científicos en el desarrollo de materiales han permitido ampliar la utilización de diferentes compuestos en la fabricación de sensores desechables. Entre los materiales más utilizados en el desarrollo de sensores de un solo uso se encuentran los materiales estándar como el silicio, el vidrio o la cerámica, polímeros sintéticos, materiales basados en celulosa y materiales híbridos.

- **Materiales estándar**

  Los materiales estándar utilizados en el desarrollo de microelectrónica como el silicio, vidrio, cerámica y metales presentan excelentes propiedades eléctricas, mecánicas y térmicas por lo que su uso se ha extendido en el desarrollo de sensores de presión, quimio y biosensores a gran escala y bajo costo. Sin embargo, en comparación con otros materiales utilizados en la fabricación de sensores desechables, éstos materiales son más costosos, complejos de procesar, su fabricación requiere equipos específicos y productos químicos peligrosos. Además, la utilización de estos materiales es limitada en cuanto a su flexibilidad y estirabilidad. A pesar de ello, la aplicación de materiales estándar en la construcción de sensores desechables se ha mantenido debido a las caídas recientes en el precio y las mejoras de las propiedades de estos materiales [47].

- **Polímeros sintéticos**

  En contraposición a los materiales estándar, los polímeros sintéticos son generalmente más baratos y permiten la fabricación en masa, de forma rápida y a un bajo costo de sensores desechables. Existe una gran variedad de materiales poliméricos disponibles con diferentes propiedades, capacidad de estiramiento, transparencia, etc. es por ello que son ampliamente utilizados en el desarrollo de sensores de un solo uso.

  A diferencia de los elastómeros, los polímeros termoestables se caracterizan por su rigidez y por su resistencia al calor y la luz. El ejemplo

más extendido es la poliimida, comúnmente conocida como Kapton, la cual se utiliza para crear barreras en los dispositivos microfluídicos y en la fabricación de sensores desechables. Entre las ventajas que presentan los materiales termoestables se encuentran la gran estabilidad química que presentan y la transparencia óptica. Sin embargo, se trata de materiales más caros que otros polímeros por lo que su aplicación en sensores desechables es limitada [48].

Los materiales termoplásticos, por otro lado, son polímeros termoendurecibles, es decir, se pueden moldear y reformarse por encima de la temperatura de transición vítrea, presentan una gran rigidez y resistencia química a disolventes orgánicos. Además, son muy utilizados en la industria para la producción en masa a través de procesos de estampado en caliente o de moldeo por inyección. Se emplean en la fabricación de sensores desechables polímeros termoplásticos como el polipropileno (PP), poliestireno (PS), polimetacrilato de metilo (PMMA) y el poli(tereftalato de etileno) (PET), entre otros.

- **Materiales basados en celulosa**

El papel es un material atractivo en el desarrollo de sensores desechables debido a sus propiedades: bajo costo, disponibilidad, ligereza, flexibilidad, biodegradabilidad, compatibilidad con diversos métodos de fabricación, permite la fabricación de estructuras microfluídicas y se puede plegar en forma 3D (origami). Estas características hacen que el papel se emplee ampliamente en el desarrollo de sensores desechables [49], [50].

Los papeles de celulosa y nitrocelulosa se utilizan en la fabricación de tiras reactivas y otros ensayos como el test de embarazo. Se trata de materiales opacos y de bajo coste. Otros materiales de celulosa muy utilizados en el desarrollo de sensores son el celofan, materiales de nanocelulosa y textiles a base de celulosa. El celofan se puede emplear como sustrato para la

fabricación escalable y de bajo costo de sensores desechables [51]. La nanocelulosa puede estar hecha de nanofibras de celulosa o nanocelulosa bacteriana [52], [53]. Estos materiales se pueden constituir fácilmente en películas, hidrogeles o aerosoles con porosidad seleccionable, hidrofilia, flexibilidad y transparencia y pueden servir como sustrato biodegradable. Los textiles a base de celulosa a menudo se utilizan como sustrato para sensores portátiles. En contraste con el papel, los textiles pueden ser más duraderos, flexibles y pueden adaptarse mejor al cuerpo, siendo esta característica muy importante en el desarrollo de sensores desechables portátiles [54], [55].

- **Materiales híbridos**

  Para mejorar las propiedades de los materiales empleados en sensores de un solo uso en la mayoría de los casos se recurre a la utilización de materiales híbridos que mejoran el rendimiento de los sensores en comparación con los materiales únicos. Generalmente, los materiales híbridos se componen de un polímero específico combinado con materiales estándar, papel [56], [57] u otros polímeros [58].

En resumen, los materiales empleados en la fabricación de los sensores desechables deben elegirse considerando: la técnica de detección que se utiliza, los requisitos de la detección (flexibilidad, transparencia, etc.) y las características de los materiales [59].

2.2.2. Sistemas de detección de los sensores desechables

Los sensores desechables suelen emplear diferentes sistemas de detección para la transducción de señales entre los que se encuentran los sistemas ópticos, electroquímicos, mecánicos, magnéticos, termométricos y microgravimétricos. A pesar de la gran variedad de métodos de detección existentes empleados por los

sensores desechables los sistemas de detección de tipo óptico y electroquímico son los más utilizados.

- **Métodos ópticos:** los sensores ópticos llevan a cabo el reconocimiento de un compuesto por un cambio en sus propiedades ópticas (color, fluorescencia, fosforescencia o quimioluminiscencia), ver Figura 7. La señal producida puede observarse a simple vista o puede ser recogida por un fotodetector que convierte la señal óptica en una señal eléctrica [60], [61]. Se trata de un método de detección sencillo, rápido, fiable, sensible, no destructivo y que permite la multiplexación [62].

- Por otra parte, los métodos ópticos presentan dos inconvenientes principales, la susceptibilidad a la interferencia ambiental, como por ejemplo la degradación de las moléculas fotoactivas, y el uso de materiales ópticos costosos y frágiles que requieren un manejo cuidadoso. Sin embargo, los métodos ópticos son cada vez más utilizados para el desarrollo de sensores desechables, especialmente en combinación con Smartphones [63]. Esta combinación permite no solo la detección óptica del compuesto de interés sino que permite la transferencia y el almacenamiento de los resultados lo cual supone una mejora en las prestaciones del propio sensor. Entre los materiales funcionales más utilizados para la detección óptica se pueden incluir nanopartículas de oro y plata, Quantum Dots, cristales fotónicos y nanomateriales de grafeno [64].

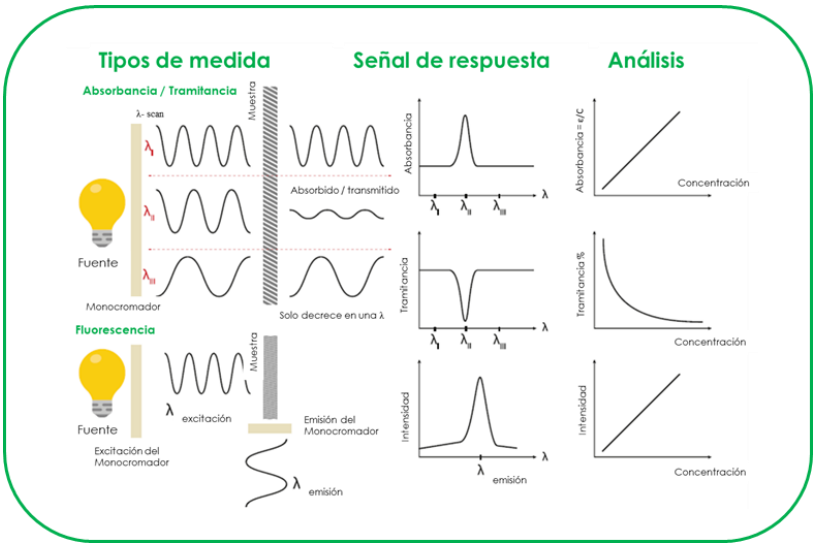

Figura 7. Sistemas de transducción óptica [46].

- **Métodos electroquímicos:** en los métodos electroquímicos el analito genera directa o indirectamente una señal electroquímica proporcional a su concentración. De entre las diferentes técnicas electroquímicas más destacadas se encuentran la potenciometría, amperometría, voltamperometría, espectroscopía de impedancia y conductimetría (Figura 8).

  Los sistemas potenciométricos miden los cambios en el potencial entre dos electrodos en equilibrio, electrodo de trabajo o working electrode (WE) y electrodo de referencia o reference electrode (RE) de potencial constante, causado por la concentración del analito [65]. Por otro lado, los sistemas amperométricos y voltamperométricos son métodos dinámicos que emplean un tercer electrodo (auxiliar), se trata de un electodo de conteo o counter electrode (CE) que en un sistema potenciostático sirve para establecer el voltaje deseado en el electrodo de trabajo. En los sistemas amperométricos, la corriente derivada de la oxidación o reducción de moléculas electroactivas, se mide a un potencial constante o potencial escalonado en el tiempo. Sin embargo, los sistemas voltamperométricos miden la corriente durante un barrido de potencial que puede ser lineal, cíclico o combinado con pulsos. Así mismo, la espectroscopia de impedancia mide un potencial sinusoidal

en un rango de frecuencia aplicado a la celda electroquímica, es decir, se mide la respuesta de la corriente, la resistencia y la capacidad del sistema permitiendo el estudio de la superficie y las propiedades del material. Por último, en conductimetría se registra la resistencia de un electrolito mediante el uso de un potencial alterno [66].

La elección del material para el electrodo de trabajo es uno de los factores más importantes al diseñar un sensor electroquímico. Los electrodos deben ser adecuados para la aplicación, por ejemplo, deben ser químicamente resistentes a la muestra y deben ofrecer una buena sensibilidad, selectividad y estabilidad a largo plazo. Por todo ello, los materiales comúnmente utilizados para la fabricación de los electrodos en los sensores desechables incluyen: metales inertes (oro, plata, paladio o platino); metales semiconductores como, los óxidos de zinc, dióxido de estaño, trióxido de tungsteno y estaño u óxido de iridio y materiales a base de carbono incluyendo carbón vítreo, diamante o tinta de carbono [67].

En ocasiones los materiales utilizados en el desarrollo de los electrodos se pueden modificar con otros materiales para mejorar sus características de detección. Por ejemplo, el empleo de nanopartículas metálicas a base de carbono como los nanotubos de carbono o el grafeno permiten una mejor conductividad eléctrica y mejoran la especificidad de los electrodos en comparación con los electrodos no modificados.

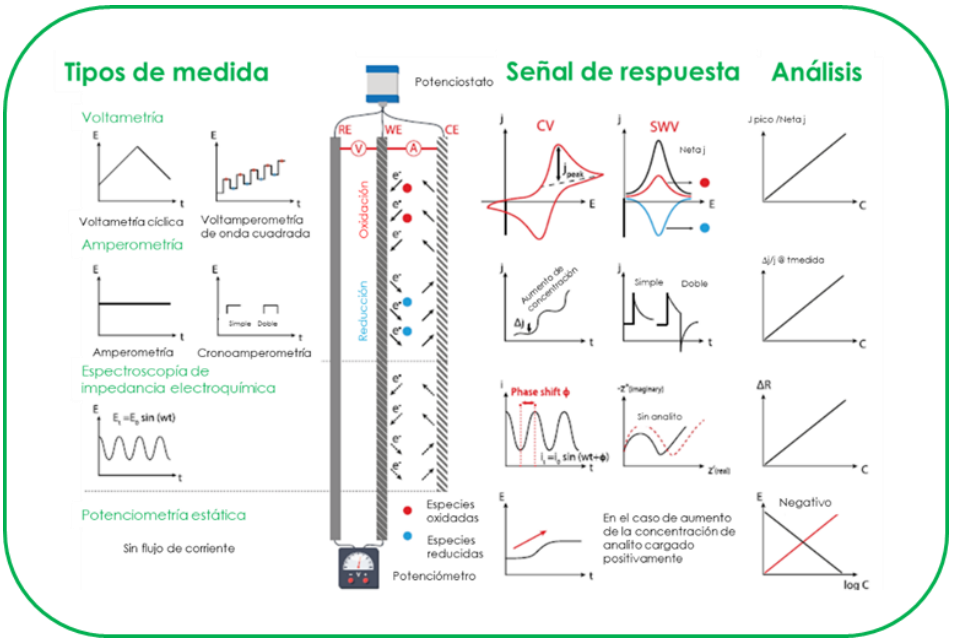

Figura 8. Sistemas de transducción electroquímica [46].

2.2.3. Elementos de reconocimiento en el desarrollo de sensores desechables

La conversión de la información química o bioquímica en una señal que pueda ser medida implica un reconocimiento molecular o biomolecular del compuesto de interés en una determinada muestra. Para ello, existen diferentes elementos de reconocimiento que permiten la detección del compuesto de interés entre los que se encuentran los receptores naturales y artificiales [68], Figura 9.

- **Receptores naturales:** los elementos de reconocimiento natural son moléculas que se encuentran de forma natural en organismos vivos, tales como ácidos nucleicos, enzimas, anticuerpos, orgánulos, células o tejidos. A pesar de su alta especificidad, su producción a gran escala suele conllevar grandes costes económicos por lo que su fabricación a nivel industrial tiende a ser difícil. Además, los elementos de reconocimiento natural exhiben un alto grado de variabilidad biológica, baja estabilidad y actividad en condiciones no fisiológicas (pH y temperatura extremos o presencia de disolventes orgánicos).

- **Receptores artificiales:** el avance en aplicaciones de ingeniería y biología han permitido el diseño y la síntesis de receptores artificiales que pueden sustituir o mejorar las variantes naturales. Dentro de este grupo se encuentran aptámeros, polímeros de impronta molecular (MIP), ionóforos, receptores supramoleculares y péptidos sintéticos, entre otros. En contraposición a los receptores naturales, los receptores artificiales ofrecen una estabilidad mejorada y una alta afinidad a un menor costo. Estas características hacen que los receptores artificiales sean ideales en el desarrollo de sensores desechables.

En este sentido, la selección de los elementos de reconocimiento en el desarrollo de sensores desechables viene definidas por:

- **La molécula objetivo:** pueden ser entidades complejas como células y macromoléculas o sustancias pequeñas como metabolitos.

- **Los requisitos de la detección:** condiciones de trabajo no fisiológicas o monitorización continua de la medida.

- **Las características de los elementos de reconocimiento:** alta sensibilidad, posibilidad de realizar medidas a largo plazo, afinidad analito/receptor, selectividad, influencia del efecto matriz en el reconocimiento, estabilidad y coste del receptor.

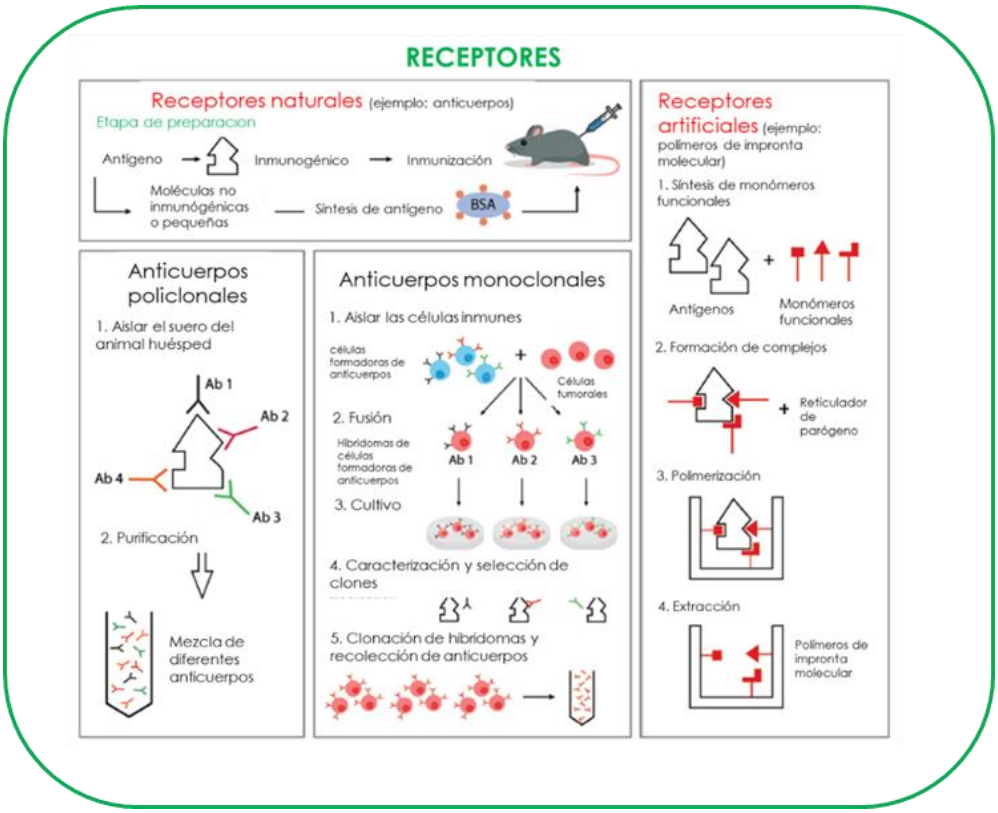

Figura 9. Esquema de producción de elementos de reconocimiento [46].

2.2.4. Campos de aplicación de los sensores desechables

Los sensores desechables se han utilizado en diversas aplicaciones entre las que se encuentran:

- **Diagnóstico de enfermedades**

  El desarrollo de sensores desechables ha facilitado en gran medida la descentralización del análisis clínico, ha reducido el tiempo de espera de los resultados y ha permitido reducir el coste de los análisis. Tradicionalmente, el diagnóstico de enfermedades requería de numerosos pasos hasta la obtención de los resultados. Estos pasos incluían la toma de muestras de los pacientes en hospitales, consultorios y clínicas; una etapa de preparación de las muestras extraídas a los pacientes y el envío, en numerosas ocasiones, de las muestras a una instalación central para su análisis. Todo ello puede traducirse en largos periodos de espera hasta obtener los resultados, retrasando de esta forma una intervención rápida y

eficaz en caso de ser necesario. Añadido a este problema podemos incluir la necesidad de una segunda cita médica para discutir los resultados de los análisis y tomar las medidas pertinentes.

Esta situación puede ser extremadamente complicada para individuos que viven en zonas rurales, personas de avanzada edad o con pocos recursos económicos, o situaciones excepcionales generadas como consecuencia de epidemias o pandemias. Por todo ello, se considera de especial interés el desarrollo de puntos de atención, denominados Point of Care (POC), que permiten el uso de dispositivos de análisis portátiles y desechables para analizar muestras de fluidos corporales en apenas varios minutos lo que se traduce en diagnósticos más rápidos [69].

Para lograr esta descentralización del análisis clínico los nuevos dispositivos desarrollados deben cumplir una serie de características: ser altamente sensibles; requerir de pequeñas cantidades de muestra para la realización del análisis; permitir tiempos de respuesta cortos para acelerar la intervención médica; ser económicos y accesibles; fáciles de usar por los profesionales de la salud o usuarios capacitados para realizar la prueba con éxito; ser desechables y no necesitar un pretratamiento de la muestra aunque este requisito no siempre se puede evitar [70]. En este caso, el empleo de sensores desechables basados en sistemas microfluídicos se presenta como una posible solución ya que su objetivo es automatizar y miniaturizar diferentes métodos de laboratorio en sistemas portátiles, compactos, independientes y de un solo uso. Es por ello que la mayoría de las pruebas de puntos de atención o Point of Care Test (POCT) tienen una unidad microfluídica desechable (cartucho, tira reactiva, etc.) para el análisis *in situ*.

Convencionalmente, los dispositivos POCT se pueden clasificar en cuatro categorías principalmente [71]:

1) Aquellos cuya rapidez es el atributo más valioso que presentan para reforzar la decisión de actuación en el tratamiento de afecciones letales, por ejemplo meningitis.

2) Aquellos cuyo tiempo de ensayo es corto pero también es un elemento crucial para la toma de medidas para contener un brote de una enfermedad.

3) Aquellos para la verificación de los causantes de una enfermedad.

4) Aquellos para el autocontrol de pacientes que no asisten a los seguimientos de tratamientos como por ejemplo, en el caso de pacientes con enfermedades de transmisión sexual.

Sin embargo, los dispositivos POCT disponibles en el mercado actualmente permiten la detección de compuestos de interés en el análisis clínico pero suelen presentar algunas limitaciones como su precio y la dificultad de uso para permitir la monitorización de la salud personal diariamente, (Figura 10). Una tendencia emergente para mejorar estos inconvenientes es el uso de teléfonos inteligentes en el análisis. Esta inclusión de los Smartphone en el análisis clínico es posible ya que estos dispositivos cuentan con cámaras, potentes microprocesadores, permiten la comunicación inalámbrica de alta velocidad y largo alcance (3G/4G, Wi-Fi, Bluetooth) [72], [73].

Por otro lado, para mejorar la accesibilidad, reducir costos y complejidad en el análisis el papel y las membranas de nitrocelulosa han sido ampliamente utilizadas en el desarrollo de dispositivos POCT desechables [74]. Los sistemas basados en papel son de bajo costo y relativamente fáciles de fabricar. Además, el papel es biodegradable, se puede incinerar eliminando la posible propagación de productos biológicos y químicos contaminantes [75]–[77]. Otra característica importante en el uso del papel para el desarrollo de dispositivos POCT es la posibilidad de plegar en diferentes geometrías 3D el papel para generar diferentes formas y simplificar el manejo del mismo.

El análisis basado en papel puede ser de tipo colorimétrico sin necesidad de emplear dispositivos de detección específicos ya que la señal puede ser registrada a simple vista reduciendo el costo total y la complejidad del análisis. No obstante, el empleo de dispositivos de imagen (Smartphones, scanners, etc.) pueden mejorar la sensibilidad en la detección [78] .

Figura 10. Ejemplos de dispositivos POCT comerciales [46].

Por último, el diagnóstico portátil basado en POCT acerca un poco más al individuo a las plataformas de análisis ya que estos pequeños dispositivos están conectados directamente al usuario. El formato más empleado para los dispositivos de diagnóstico portátil conocidos como wearables (vestibles) son parches, vendajes o tatuajes que se aplican directamente sobre la piel (Figura 11). Estos se utilizan, por ejemplo, para controlar el estado de recuperación de una herida ya que permiten la medida de la temperatura corporal, conocer valor de pH y la medida de la concentración de diferentes electrolitos [79]. Además, es posible conectar una placa de circuito impreso al apósito para mantener bajo vigilancia de

forma inalámbrica y utilizando un teléfono móvil la recuperación de la herida. De esta forma se podrían monitorizar y controlar los estadios de recuperación de heridas crónicas, como por ejemplo úlceras, que requieren mucho tiempo para su recuperación. Una prospección de futuro indica que las próximas generaciones de dispositivos desechables permitirán no solo la monitorización de heridas sino también el tratamiento en tiempo real de las mismas mediante el suministro de medicamentos.

El análisis químico no invasivo de electrolitos, pH o glucosa y lactato en muestras biológicas como el sudor es otra área de aplicación de los sensores desechables portátiles. En este sentido, la monitorización continua de determinados analitos mediante un análisis no invasivo en muestras de sudor, saliva, lágrimas u orina, abordan los posibles problemas que otros dispositivos de análisis no pueden solventar [80]. Un claro ejemplo es el control de los niveles de glucosa mediante el empleo de tiras reactivas o de un glucómetro portátil. Los sensores basados en dispositivos vestibles son capaces de llevar a cabo un control en continuo permitiendo también la transferencia de datos a dispositivos móviles de forma inalámbrica para advertir al usuario si su concentración de glucosa es alta o baja.

No obstante, la monitorización de parámetros bioquímicos a partir de muestras de sudor presenta dos desventajas principalmente. La primera desventaja deriva de la necesidad de producir sudor. Se necesita aumentar la temperatura corporal, por ejemplo, mediante el desarrollo de actividad física para poder obtener información analítica a partir del sudor. El segundo inconveniente está asociado a la concentración o nivel ciertos analitos en el sudor ya que éste puede no correlacionarse estrechamente con los niveles en sangre. Otra forma comúnmente utilizada para aumentar la sudoración de la piel es mediante iontoforesis. Esta técnica consiste en introducir iones de sustancias activas a través de la piel mediante la aplicación de una pequeña corriente eléctrica en una zona del cuerpo empleando para ello dos electrodos a un voltaje de 1.5 mA durante 5 minutos aproximadamente. Así, las sustancias ionicas del cuerpo tienden a desplazarse hacia el polo de signo contrario del electrodo situado en la piel aumentando por

tanto la sudoración excesiva. La iontoforesis conocida comúnmente como el test del sudor es una técnica muy utilizada para el diagnóstico de enfermedades como la fibrosis quística.

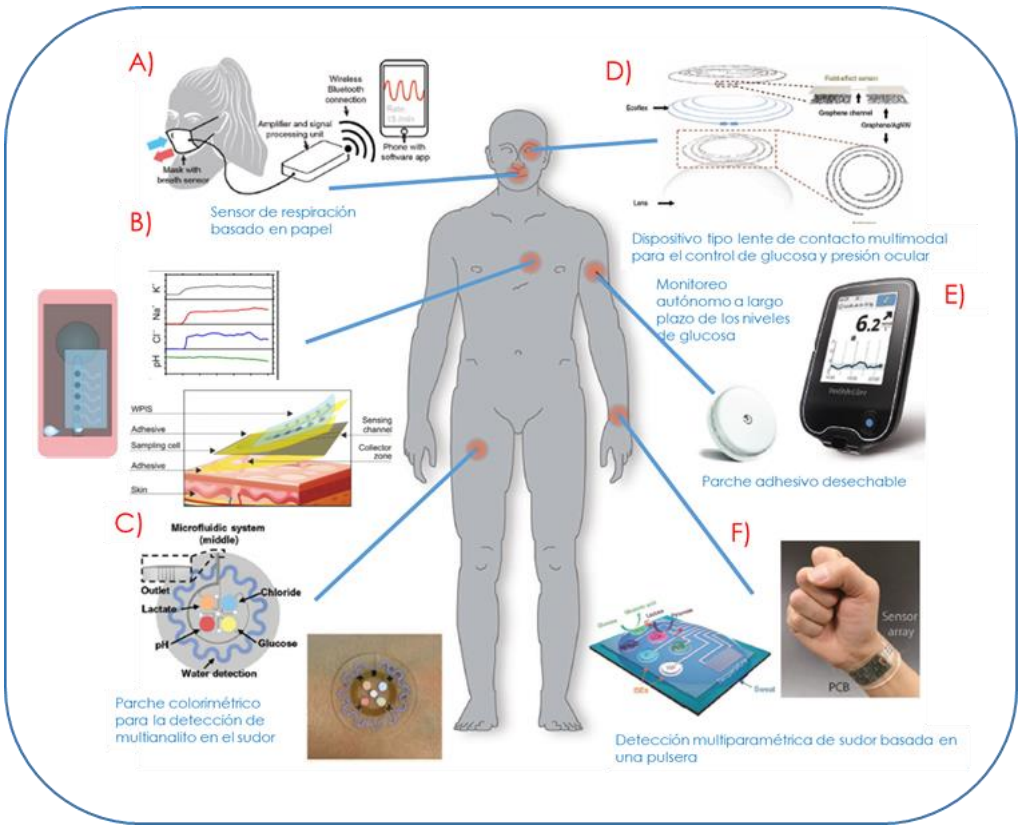

Figura 11. Dispositivos de diagnóstico portátiles [46].

Por otro lado, existe una amplia gama de dispositivos portátiles que tienen como objetivo la monitorización de señales físicas. Por ejemplo, la aceleración, tensión, radiación o frecuencia del pulso. Para la medida de este tipo de parámetros se suelen utilizar dispositivos portátiles en forma de pulsera o con forma de tatuaje. Además, estos sensores se pueden equipar con sistemas de comunicación de campo cercano, Near Field Communication (NFC) que permiten el almacenamiento y la transferencia de datos [81]. Los sensores dotados de sistemas NFC pueden transmitir información digital a un Smartphone, como se ha indicado anteriormente, de forma inalámbrica sin necesidad de una fuente de energía o batería adicional [82].

- **Análisis de alimentos**

  Garantizar la seguridad y la calidad de los alimentos resulta de gran importancia dentro y fuera de la industria alimentaria. La aparición de organismos genéticamente modificados, alimentos orgánicos y nutracéuticos hace que los consumidores estén cada vez más interesados en conocer la composición y el estado de los alimentos que ingieren. Los alimentos se envían a menudo desde diferentes partes del mundo como resultado directo de la globalización por lo que la contaminación de los alimentos recibidos puede provocar escenarios inesperados y por tanto el control en seguridad de los alimentos se convierte en algo prioritario (Figura 12).

  Aunque la mayoría de las pruebas que se realizan a los alimentos pueden llevarse a cabo en grandes laboratorios, existen algunos inconvenientes o dificultades que pueden surgir derivadas del análisis. En primer lugar, debido a la amplia gama de analitos presentes en los alimentos incluso los laboratorios centralizados pueden estar especializados en un único número de contaminantes. Principalmente, existen cuatro categorías de analitos en el análisis de alimentos: contaminantes, ingredientes nutricionales, aditivos alimentarios y alérgenos. Para el análisis de estos analitos los alimentos deben enviarse a diferentes laboratorios al mismo tiempo. Por otro lado, las muestras deben enviarse en un medio altamente controlado para evitar posibles alteraciones que puedan influir en la calidad del alimento lo cual incrementa el coste del análisis.

  El desarrollo de sensores desechables portátiles reduce la necesidad de transportar los alimentos a los laboratorios para analizar sus componentes. Por ejemplo, los sensores electroquímicos pueden analizar muestras liquidas extraídas de los alimentos sólidos. Los sensores colorimétricos, por su parte, pueden ser de utilidad en el análisis de muestras liquidas o gaseosas liberadas de los alimentos [83].

Contaminantes biológicos, como patógenos y toxinas, o contaminantes no biológicos, como metales pesados, pesticidas y productos veterinarios son la mayor preocupación para los productores, minoristas y consumidores [84]. La contaminación biológica por patógenos y parásitos puede detectarse mediante el análisis destructivo de muestras líquidas midiendo la concentración de toxinas producidas a través de ensayos de flujo continuo. La contaminación microbiana y la degradación de carnes frescas puede ser monitorizada de manera no destructiva mediante la detección de aminas biogénicas volátiles utilizando sensores desechables incorporados en los recipientes de almacenaje de los alimentos. La utilización de este tipo de sensores en el análisis alimentario supone una detección más rápida, fácil de ejecutar y menos costosa que un análisis convencional llevado a cabo en un laboratorio. No obstante, el análisis de alimentos mediante métodos tradicionales, como la cromatografía líquida, proporcionan resultados más precisos sobre este tipo de contaminantes.

Pese a las ventajas inherentes que presenta el uso de sensores desechables para el análisis de alimentos desafortunadamente el número de sensores disponibles en el mercado para dicho análisis es reducido. Esto se debe en gran medida a la dificultad derivada de la extracción y preparación de las muestras para el análisis por personal no cualificado. Una alternativa puede ser la utilización de etiquetas colorimétricas que se puedan adherir al embalaje de los alimentos y permitan su análisis sin necesidad de tratar las muestras.

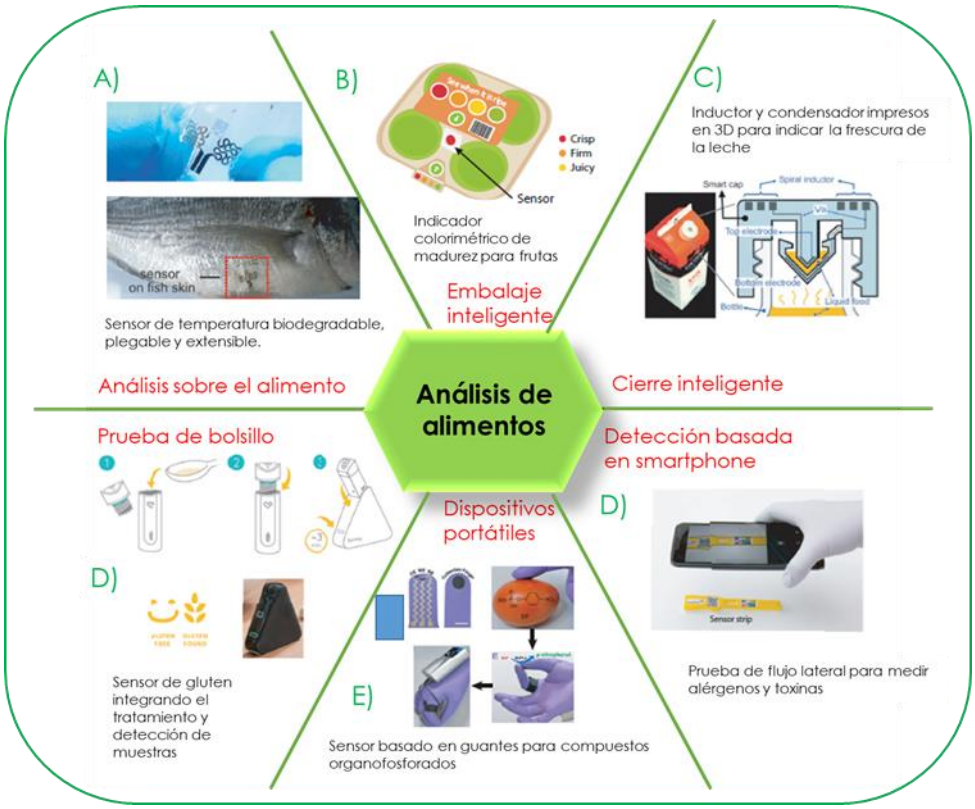

Figura 12. Sensores desechables para el análisis de alimentos[46].

- **Análisis medioambiental**

Otra área de aplicación donde el empleo de sensores desechables y portátiles tiene una gran importancia es sin duda la medioambiental (Figura 13). De todos es conocida la importancia de detectar y cuantificar la contaminación ambiental que amenaza los ecosistemas en todo el mundo. Los contaminantes son transportados por aire, suelo y agua moviéndose de un medio a otro de forma natural o mediante la acción del hombre. En los países industrializados la contaminación ambiental es predominante mientras que en áreas menos desarrolladas los problemas derivados de la contaminación suelen hacerse notorios en la calidad del agua [85].

Los contaminantes ambientales se pueden clasificar en tres grandes grupos: los contaminantes inorgánicos (metales como el plomo o el cadmio y no metales como fosfatos o nitritos) [77], productos químicos

orgánicos (pesticidas o productos farmacéuticos) y contaminantes biológicos (virus, bacterias, hongos, etc.).

La detección de contaminantes inorgánicos, especialmente de metales pesados en muestras de agua y suelo son quizás una de las aplicaciones más importantes de los sensores desechables en el análisis del medioambiente. Los compuestos inorgánicos se pueden detectar ópticamente, empleando dispositivos colorimétricos basados en papel, sustratos poliméricos, silicio o vidrio [86], [87].

Los contaminantes emergentes (productos farmacéuticos, pesticidas, etc.) presentes en las aguas residuales perjudican la calidad de la red hidráulica, además de dañar organismos acuáticos y humanos, por lo tanto, se hace imprescindible controlar sus concentraciones en este medio [88]. En este sentido, el empleo de sensores desechables basados en polímeros de impronta molecular (MIP) permiten detectar estos contaminantes [89]. Estos sensores generalmente reconocen toxinas cuya concentración se relaciona con la señal generada por el sensor [90].

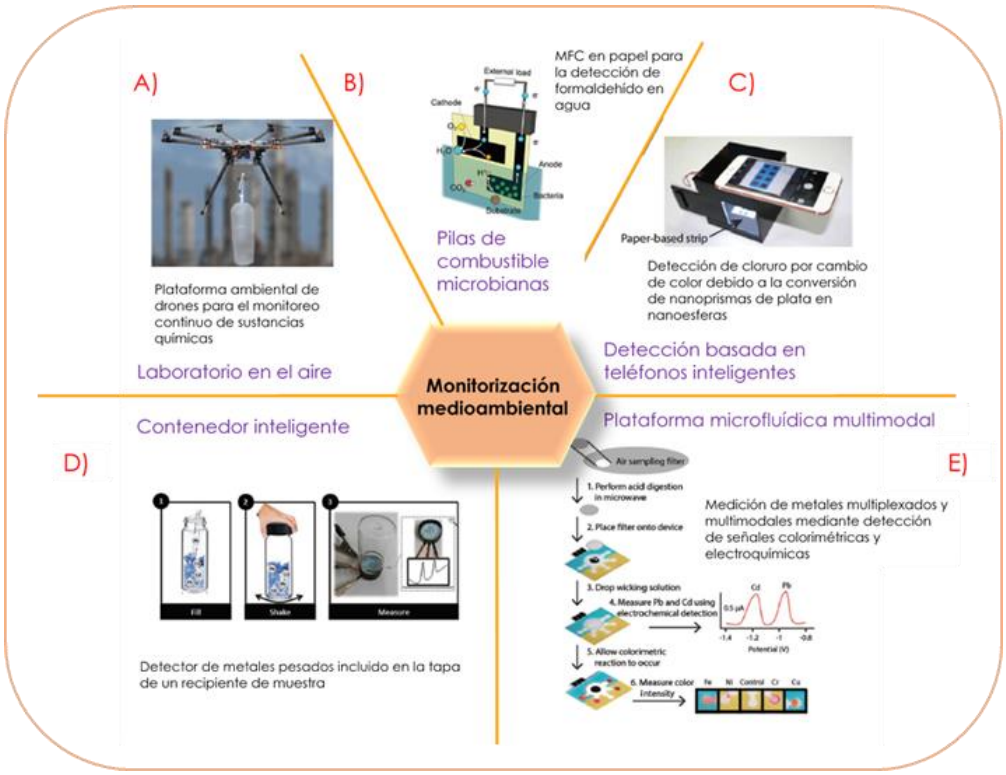

Figura 13. Sensores desechables empleados en el control medioambiental [46].

3. Sensores portátiles para análisis no invasivos

Actualmente, el desarrollo de sensores y biosensores que permitan conocer el estado fisiológico de una persona de forma no invasiva o mínimamente invasiva, permitiendo la monitorización en tiempo real y en continuo de un determinado biomarcador que proporcione información analítica, a través del análisis de fluidos corporales como sudor, lagrimas, saliva u orina, es un factor principal en la detección de enfermedades [91]. En este sentido, los sensores flexibles y portátiles, como los wearable, presentan un gran potencial al interactuar con la piel para extraer información analítica de los biofluídos, y por lo tanto, poder mejorar la calidad de vida de estas personas como se ha indicado anteriormente [92].

De este modo, se puede decir que los sensores portátiles deben presentar una serie de características básicas para conseguir este propósito; ser fáciles de usar, de pequeño tamaño y biocompatibles, no requerir, en la medida de lo posible, el empleo de una batería

para la alimentación del sensor, permitir el análisis no invasivo de forma continua y simultánea, así como, la transferencia de datos de forma inalámbrica [93]. Además, los sensores químicos portátiles deben poder detectar los analitos de interés de forma rápida, con tiempos de respuesta cortos correspondientes a la variación de la concentración del analito. Este requisito también exige que la mayoría de los sensores portátiles posean una respuesta reversible proporcionando datos precisos con histéresis insignificante. Del mismo modo, la selectividad del sensor debe ser alta, esto quiere decir, que debe ser capaz de discriminar entre el analito objetivo y la posible interferencia producida por ciertos componentes de la muestra que se comportan de manera similar a éste.

Cada sensor debe ser diseñado para funcionar sobre un rango dinámico que abarque la concentración medible más baja y más alta de analito en la muestra. Otra característica importante de los sensores portátiles es la estabilidad. Uno de los problemas más comunes a los que se enfrentan los sensores químicos portátiles y muchos sensores mecánicos es que se deforman al estirarse debido al movimiento de del cuerpo o la exposición continua a los biofluídos que pueden conducir a incrustaciones, cambios químicos irreversibles o la adsorción en la superficie del transductor de determinados compuestos lo que resulta en la degradación mecánica del material y el deterioro del sensor.

En este sentido, el desarrollo de dispositivos basados en sustratos flexible es un factor principal en la fabricación de sensores portátiles de estas características ya que permiten el contacto directo con el cuerpo brindando la posibilidad de realizar movimientos sin afectar a la fiabilidad de la medida del sensor o sin alterar la muestra en su recogida [94].

En base a todo esto, se han desarrollado varios sensores portátiles y dispositivos comerciales que permiten la monitorización del estado fisiológico dinámico de pacientes con determinadas enfermedades. Por ejemplo, existen sensores que permiten controlar la perdida excesiva de sodio en el sudor durante un esfuerzo intenso. Conocer este dato es muy importante para pacientes con fibrosis quística ya que una perdida excesiva de sodio aumenta considerablemente la probabilidad de sufrir una hiponatremia que puede derivar en una insuficiencia cardíaca y en la muerte del paciente. Otros biomarcadores de interés

en el campo de aplicación de los sensores portátiles (Figura 14.) son la determinación de glucosa, lactato, urea, Ca^{2+}, K^{+}, pH, oxígeno y determinados parámetros metabólicos como los signos vitales (respiración y movimientos corporales, expresiones faciales, temperatura de la piel y pulso de la muñeca, entre otros) [95], [96], [97], [98]. Por ejemplo, una concentración anómala de electrolitos en el sudor se puede correlacionar con determinadas enfermedades como daño hepático, disfunción renal, hipocalcemia e hipocloremia. Así, una tendencia actual es la fabricación de sensores que permiten la detección simultánea multivariante para aportar mayor información y fiabilidad en los resultados de los análisis al determinar diferentes parámetros en una misma muestra [99].

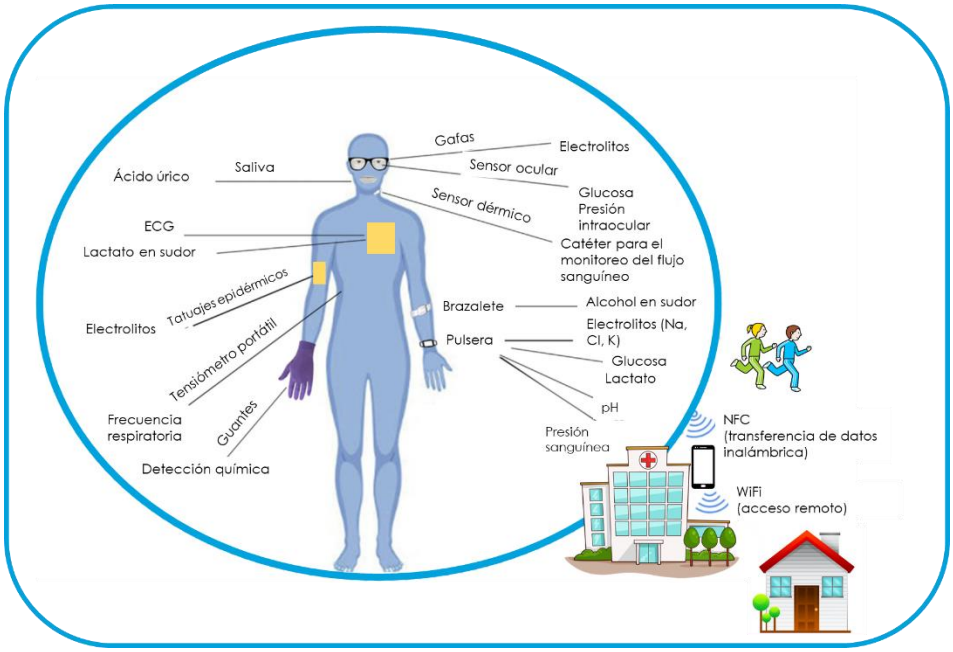

Figura 14. Biosensores portátiles no invasivos para el control de parámetros biométricos. Figura modificada de [100].

3.1. Sensores portátiles dérmicos

Actualmente, la atención médica personalizada ha llevado a la demanda de dispositivos portátiles que permitan el control en tiempo real del estado fisiológico de los seres humanos a través del análisis del sudor. En este sentido, la epidermis es una barrera de información extraordinaria debido a que es la primera línea de defensa en nuestro sistema inmune y dado que sirve como barrera para la perdida de agua y nutrientes circulantes en la sangre, Figura 15. Por estas razones, la epidermis, a través

del análisis del sudor, es una fuente de información ideal para los sensores químicos portátiles.

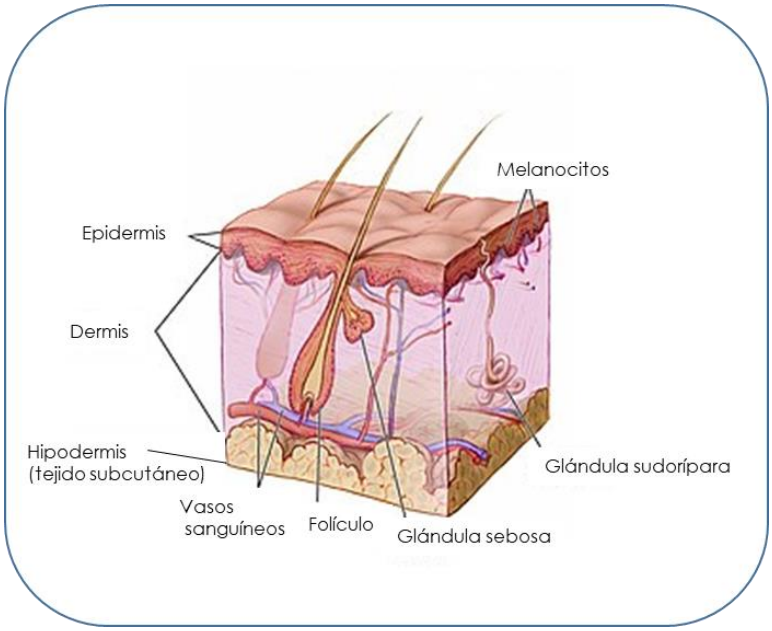

Figura 15. Diagrama de la sección transversal de la piel humana.

Los sensores más empleados en el análisis del sudor suelen utilizar técnicas electroquímicas, amperométricas y potenciométricas principalmente en la monitorización de electrolitos entre los que se encuentran los ya citados, K^+, Na^+, Cl^- y NH_4^+ ya que un trastorno en los niveles de éstos electrolitos pueden ser indicadores de hipercalemia o hipernatremia, entre otros. Se han desarrollado numerosos dispositivos para analizar estos electrolitos en sudor de forma no invasiva que incorporan baterías recargables para la alimentación, así como sistemas de transmisión de datos Bluetooth o la incorporación de etiquetas NFC para la transferencia de datos.

Uno de los inconvenientes que presentan este tipo de sensores portátiles es la dificultad que supone miniaturizar los diferentes módulos del sensor añadido a la baja compatibilidad que presentan para su apego a la piel. En consecuencia, para desarrollar un sensor portátil se debe tener en cuenta la selección del sustrato, biocompatibilidad y capacidad de estiramiento que presenta, así como, la técnica de fabricación que se lleva a cabo de forma que su desarrollo suponga un menor costo.

La piel humana presenta gran elasticidad, sin embargo, esta varía enormemente con la edad, hidratación del individuo y zona corporal. Por todo ello, la elección del material para la fabricación del sensor es esencial. De este modo el empleo de materiales intrínsecamente estirables como elastómeros, compuestos poliméricos y compuestos con cargas metálicas son los más empleados ya que proporcionan la robustez mecánica necesaria, así como, una alta escalabilidad en la fabricación del dispositivo. Por ejemplo, poliimida, tereftalato de polietileno (PET), naftalato de polietileno y poliuretano (PU), polidimetilsiloxano (PDMS), Ecoflex, papel, seda y textiles en general, entre otros, han sido ampliamente utilizados en el desarrollo de sensores vestibles o portátiles [101], [102]. En cuanto a las técnicas de fabricación de los sensores portátiles las más comunes debido a su simplicidad y escalabilidad son la litografía, serigrafía e impresión 3D.

Otro problema asociado a la utilización de sensores portátiles para el análisis del sudor es la posibilidad de contaminación de la muestra. La piel no solo sirve de barrera para proteger los órganos del cuerpo y extraer sustancias de desecho de éste, sino que también está cubierta por bacterias que tienen un papel protector y que se alimentan de estos desechos. Se estima que en la piel se encuentran 10.000.000 de bacterias por centímetro cuadrado, las cuales se alimentan de la glucosa extraída en el sudor secretando proteínas y otros productos de desecho que se encuentran en la piel. Por otro lado, se ha demostrado que los electrolitos del sudor se acumulan en las capas superficiales de la epidermis y en los conductos del sudor antes de que se produzca la sudoración. Esta acumulación de electrolitos y productos de desecho puede suponer problemas de contaminación del sudor y por consiguiente un análisis erróneo del mismo por parte del sensor. Sin embargo, estos inconvenientes pueden mitigarse si se lleva a cabo un lavado de la piel antes de aplicar el sensor para el análisis del sudor.

4. Sistemas microfluídicos

Una de las tendencias actuales en Química Analítica consiste en mejorar las técnicas de análisis de forma que implique una automatización, miniaturización y simplificación de los procesos analíticos. Años atrás, las técnicas de análisis estaban dirigidas hacia la

mejora de los parámetros de calidad, es decir, exactitud, precisión, sensibilidad y representatividad.

Actualmente, dado la enorme evolución que ha experimentado la era digital y las necesidades de la sociedad actual, las técnicas de análisis se centran principalmente en la búsqueda de una mayor portabilidad y rapidez, así como, en el carácter desechable de los dispositivos de análisis, tal y como se ha ido comentando a lo largo de esta introducción. Todo ello ha supuesto un gran cambio en las tendencias de la Química Analítica tradicional y ha favorecido la descentralización del análisis químico y el desarrollo de sistemas que favorecen el flujo de información entre el lugar donde se realiza el análisis y el especialista. Además, ha permitido el uso de materiales más baratos y/o asequibles por un mayor número de personas.

De esta forma, la miniaturización y simplificación han ganado mayor importancia y han permitido la disminución de los costes de los análisis químicos. Tanto es así que estas tendencias se relacionan entre sí como puede verse en la Figura 16. Por tanto, cuando se transforma un método manual en automático, por regla general aumenta el grado de miniaturización, simplificación y, por lo general, la disminución del coste. Esto es así porque se reduce el volumen de reactivos, muestras y desechos, así como, el tiempo y el número de equipos e instrumentos necesarios para llevar a cabo el análisis.

De este modo, el uso de tecnologías que satisfacen estas tendencias conducen a la mejora de la calidad analítica de los resultados. De forma general, se puede decir que las nuevas tecnologías provocan una disminución en el tiempo y en el coste de los análisis y permiten reducir la participación de personal cualificado en la utilización de los mismos. La sencillez, la portabilidad y la capacidad de poder compartir información con facilidad hacen posible que personal no cualificado pueda usar los sistemas de análisis en el lugar donde se origina el problema. Todo ello facilita y favorece la descentralización y por ende disminuye el tiempo de respuesta de los resultados.

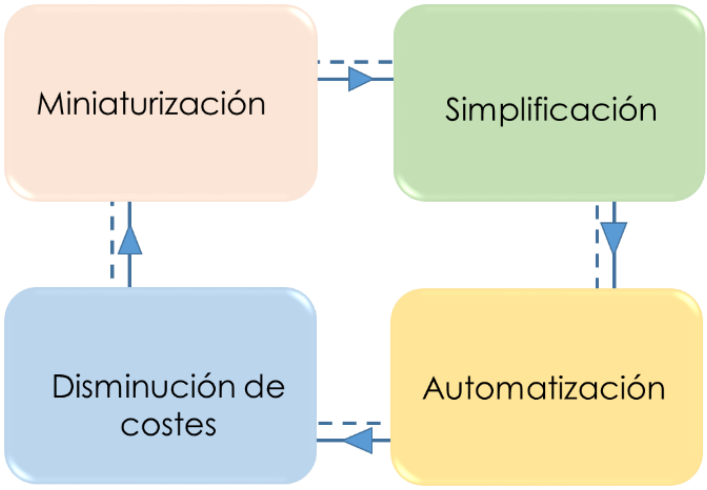

Figura 16. Tendencias actuales de la Química Analítica.

El desarrollo de nuevas tecnologías de microfabricación ha permitido el crecimiento de sistemas de análisis miniaturizados tipo Lab-on-a-Chip (LOC) que conlleva una disminución en el tamaño de los analizadores, un menor volumen de muestra y de reactivos necesarios para el análisis químico, así como la posibilidad de integrar diferentes pasos del proceso analítico: tratamiento de muestra, separación y detección de los analitos en el mismo dispositivo, reduciendo de este modo el tiempo de análisis sin aumentar la complejidad del ensayo.

Las plataformas microfluídicas son una alternativa para la fabricación de dispositivos analíticos miniaturizados de bajo costo y fabricación sencilla que pueden ser utilizados en una gran variedad de áreas de aplicación entre las que se incluyen diagnóstico clínico, control de la calidad de alimentos y vigilancia ambiental.

Actualmente, el desarrollo de procedimientos basados en sistemas microfluídicos para la detección de analitos en sectores como el clínico [103], alimentario [104] o medioambiental [105] que permitan una rápida respuesta presenta una gran importancia. El continuo avance de sistemas y procesos analíticos para mejorar la salud humana ha derivado en el desarrollo de instrumentación portátil, reutilizable y efectiva entre los que se encuentran las plataformas miniaturizadas como las ya mencionadas Point-of-care (POC) o Point-of-Need (PoN). Este avance tecnológico supone un gran cambio en el

paradigma del diagnóstico tradicional. Este hecho es debido a que esta forma de análisis basada en POC, proporciona información diagnóstica de forma rápida y precisa, brindando la posibilidad de una rápida intervención.

Según la Organización Mundial de la Salud (WHO) las pautas requeridas para desarrollar un sistema POC eficiente deben satisfacer el acrónimo inglés ASSURED, es decir, el sistema debe ser asequible (Affordable), sensible, (Sensitive), especifico (Specific), fácil de utilizar por el usuario (User friendly), rápido (Rapid) para poder tomar decisiones de forma inmediata, robusto (Robust) para transportarlo y distribuirlo sin que se altere su funcionamiento, sin equipamientos específicos (Equipment-free) y debe permitir la entrega directa de los resultados a los usuarios (Delivered).

4.1. Clasificación de los sistemas microfluídicos

Atendiendo al principio que utilicen para la propulsión de líquidos, los sistemas microfluídicos se pueden clasificar en: capilares, impulsados por presión, centrífugos, electrocinéticos y acústicos como se muestra en la Figura 17 [106].

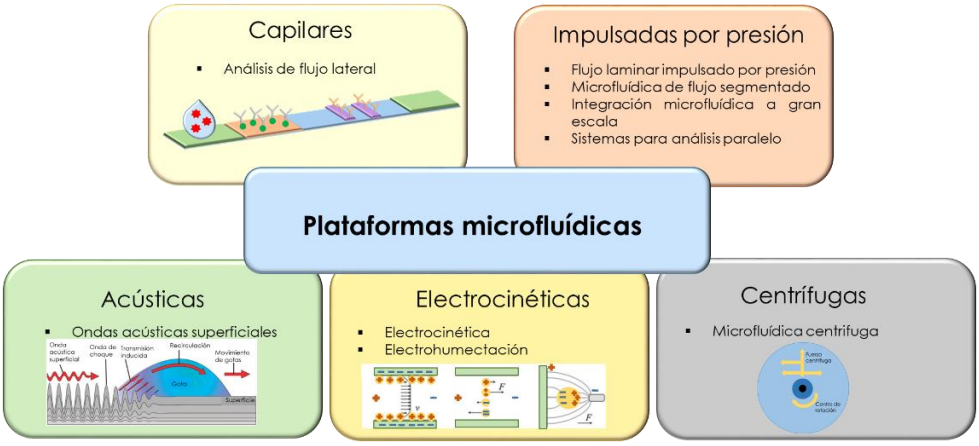

Figura 17. Clasificación de las plataformas microfluídicas.

- **Sistemas microfluídicos capilares**

  Dentro de este grupo de plataformas microfluídicas se encuentran los test de flujo lateral también conocidos como tiras reactivas. El ejemplo más

extendido de este tipo de sistemas son los test de embarazo. Mediante estos sistemas los líquidos son impulsados por la fuerza capilar desde un extremo de la tira al extremo opuesto de la misma. El movimiento del líquido está controlado por la humectabilidad y el tamaño del sustrato poroso o microestructurado que forma la tira. Todos los reactivos químicos requeridos para el ensayo se distribuyen a lo largo de del sistema microfluídico ocupando una posición estratégica para que reaccionen con la muestra y generen la señal analítica. Normalmente, se trata de una señal óptica como puede ser un cambio de color en el área de detección del sistema microfluídico.

Los test de flujo lateral presentan un puerto de entrada y una ventana de detección. La muestra se introduce en el dispositivo a través de una almohadilla absorbente y el fluido migra por capilaridad hacia una zona donde se han inmovilizado anticuerpos conjugados que reaccionan con ella como puede verse en la Figura 18. A continuación, la muestra llega a una zona de captura donde el complejo analito anticuerpo-conjugado se une a anticuerpos inmovilizados produciendo una línea visible. Pasada esta línea la muestra continúa migrando hasta que llega a la zona de control donde un exceso de anticuerpo conjugado se une y produce una segunda línea visible, es decir, la línea de control que nos indica que la muestra ha migrado a través del sistema como se deseaba. Cuando finaliza el ensayo se observan dos líneas siendo esto indicativo de un resultado positivo o bien una si es negativo.

Este tipo de sistemas microfluídicos ofrece una serie de ventajas ya que requiere pequeños volúmenes de muestra y reactivos, se trata de sistemas desechables, de fácil manejo y cuyos resultados se generan en cuestión de minutos. Estas características los convierten en aptos para cualquier tipo de usuario, capacitados o no. Sin embargo, la simplicidad de la tira reactiva también presenta un inconveniente. Los protocolos de ensayo dentro de los sistemas capilares siguen un esquema de proceso fijo con un número

limitado de operaciones unitarias. Además, la dependencia capilar de la muestra líquida en el sistema microfluídico supone una disminución en la precisión debido a la aparición de falsos positivos o falsos negativos.

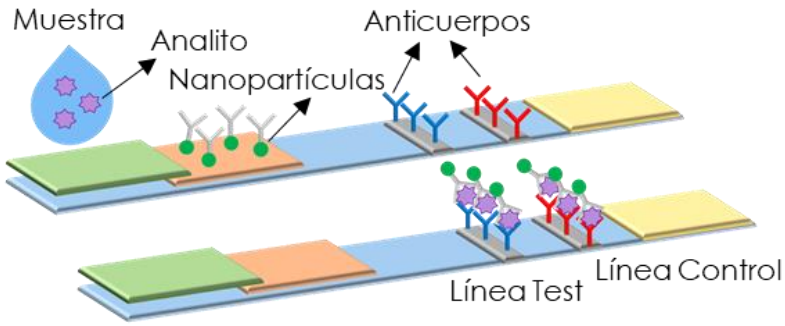

Figura 18. Test de flujo lateral.

4.2. Sistemas microfluídicos basados en papel

El papel se ha usado en Química Analítica desde hace mucho tiempo, siendo el ejemplo más representativo el papel indicador de pH en sus diversas variantes o papeles impregnados para el análisis de otros analitos en agua u orina. Sin embargo, su uso en ensayos microfluídicos no fue significativo hasta que el grupo de Whitesides en 2007 desarrollara por primera vez dispositivos con zonas delimitadas en sustratos de nitrocelulosa a los que denomino "Microfluidic Paper-based Analytical Device" (µPAD). El primer µPAD diseñado por Whitesides en la Universidad de Harvard, fue un ensayo para la determinación de glucosa y proteína diseñado mediante litografía como el que se muestra en la Figura 19. Desde entonces, una gran variedad de técnicas de fabricación se han desarrollado y aplicado. Este dispositivo llevó a muchos investigadores a considerar el papel como un material con grandes posibilidades para diversas aplicaciones analíticas.

Desde entonces los µPADs se consideran una nueva alternativa tecnológica para la fabricación de dispositivos microfluídicos portátiles y desechables. A lo largo de los años su utilización ha aumentado en diversas aplicaciones como el desarrollo de sensores y (bio)sensores [74], Figura 20.

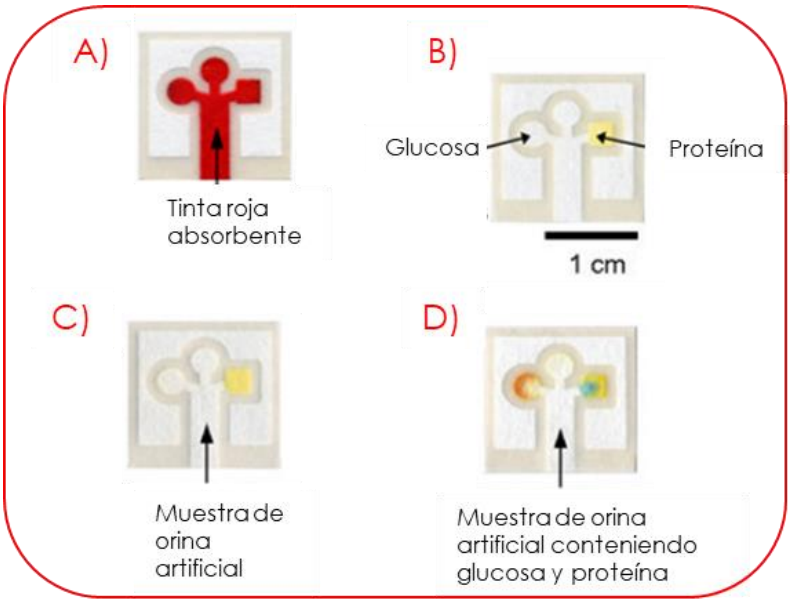

Figura 19. Representación de las partes y respuesta del µPAD. Imagen extraída de [107].

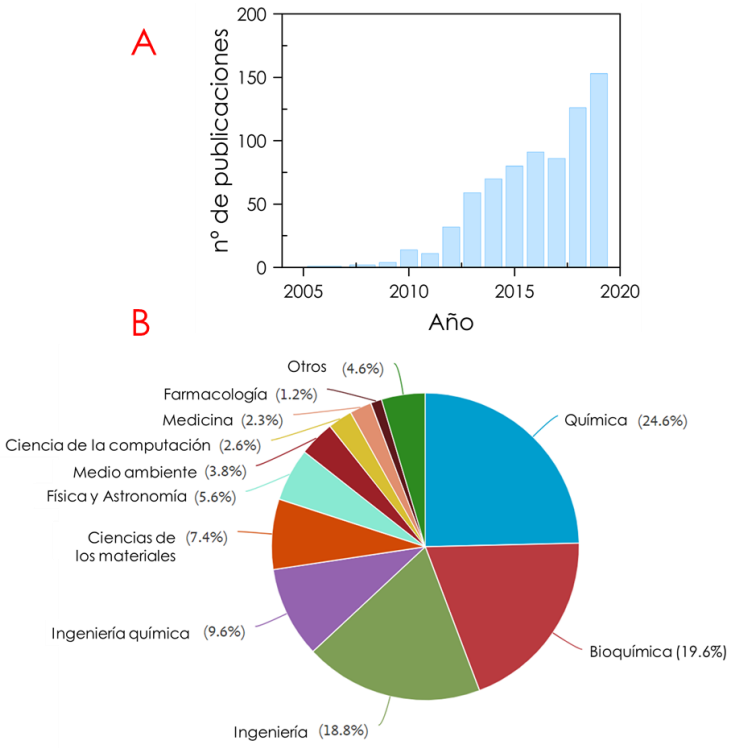

Figura 20. Número de publicaciones científicas entre 2005 y 2019 obtenido de la base de datos de Scopus para el término "Microfluidic Paper-based Analytical Device", A) Publicaciones científicas por año B) Publicaciones científicas por área de aplicación.

Las razones por las que el papel se convierte en un sustrato atractivo para la fabricación de este tipo de dispositivos se debe a diversos factores:

- **Bajo coste:** se trata de un producto que se extrae de la madera o el algodón por lo que es muy abundante y económico.

- **Gran biodegradabilidad:** tanto el papel como los productos derivados de éste pueden ser desechados mediante incineración sin producir efectos nocivos para el medioambiente como sí ocurre por ejemplo con los residuos plásticos.

- **Biocompatibilidad:** esta propiedad inherente del papel hace posible la inmovilización de biomoléculas y el cultivo de organismos.

- **Extremada ligereza, flexibilidad y pequeño espesor:** el papel presenta excelentes propiedades mecánicas que permiten una perfecta distribución y almacenamiento.

- **Estructura porosa y elevada área superficial:** la estructura del papel permite el almacenamiento o retención de compuestos, así como, su distribución. Estas características permiten una modificación sencilla de las propiedades químicas del papel. Por ejemplo, mediante la adsorción de compuestos con grupos funcionales de interés. El papel se produce a partir de una suspensión acuosa diluida de fibras de celulosa que se drenan a través de un tamiz, se presionan y secan para producir una lámina formada por una red de fibras entrelazadas al azar. Su estructura fibrosa y porosa permite el transporte de líquidos a su través sin necesidad de una fuerza externa. Además, la estructura fibrosa de éste facilita la absorción de reactivos dentro de las fibras de celulosa por lo que es compatible con muchas químicas y es fácil de modificar químicamente.

- **Hidrofilia:** esta característica del papel simplifica el sistema microfluídico ya que permite la capilaridad y no es necesario un equipo de propulsión, como

por ejemplo una bomba, para desplazar un líquido de un extremo del papel al otro lado.

- **Versatilidad de diseño:** existen numerosas técnicas que nos permiten la fabricación a gran escala de dispositivos cuya forma y tamaño es de fácil modificación. Las distintas áreas del µPAD diseñado nos permiten realizar distintas operaciones del proceso analítico (tratamiento de la muestra, separación, reacción, detección, etc.).

En los últimos años se ha producido un cambio en el diseño de los dispositivos microfluídicos debido al empleo de técnicas de fabricación más avanzadas que permiten obtener resultados más precisos y cuantitativos. Así, los µPADs son herramientas analíticas fabricadas con papel capaces de analizar cantidades complejas y pequeñas de muestras empleando la microfluídica para el transporte, clasificación y separación de la muestra. Teniendo en cuenta las sorprendentes propiedades del papel, los µPADs se presentan como una tecnología innovadora para el manejo y análisis de fluidos, con una amplia gama de aplicaciones, que ofrecen bajo costo, facilidad de fabricación, operación e independencia de equipos.

4.2.1. Técnicas de fabricación de µPADS

Existen numerosas técnicas para la fabricación de dispositivos microfluídicos en papel. En general se basan en la fabricación de canales hidrófobos en la superficie del papel. Esto se puede hacer mediante dos tipos de técnicas principalmente: la técnica de hidrofobización y la técnica de corte. La hidrofobización del papel se puede llevar a cabo de diversas formas como pueden ser por bloqueo físico de los poros del papel, por deposición física de un reactivo hidrofobizante en la superficie de la fibra de celulosa o mediante la modificación de la superficie de la fibra del papel [108], [109].

La fabricación de µPADs debe cumplir una serie de requisitos relacionados con la elección de las técnicas de fabricación y el tipo de materiales a utilizar buscando en todo caso bajo coste, sencillez de fabricación y un proceso de producción eficiente.

Hay diversas técnicas de fabricación que implican la modificación química y/o la deposición física que podrían ser utilizados para ajustar las propiedades del papel, de tal manera que quede disponible para su modificación adicional o su uso directo en una amplia gama de aplicaciones. Dependiendo del objetivo que se persiga en los dispositivos basados en papel, los métodos de fabricación y las técnicas de análisis se pueden ajustar para cumplir las necesidades del usuario final, ver Figura 21.

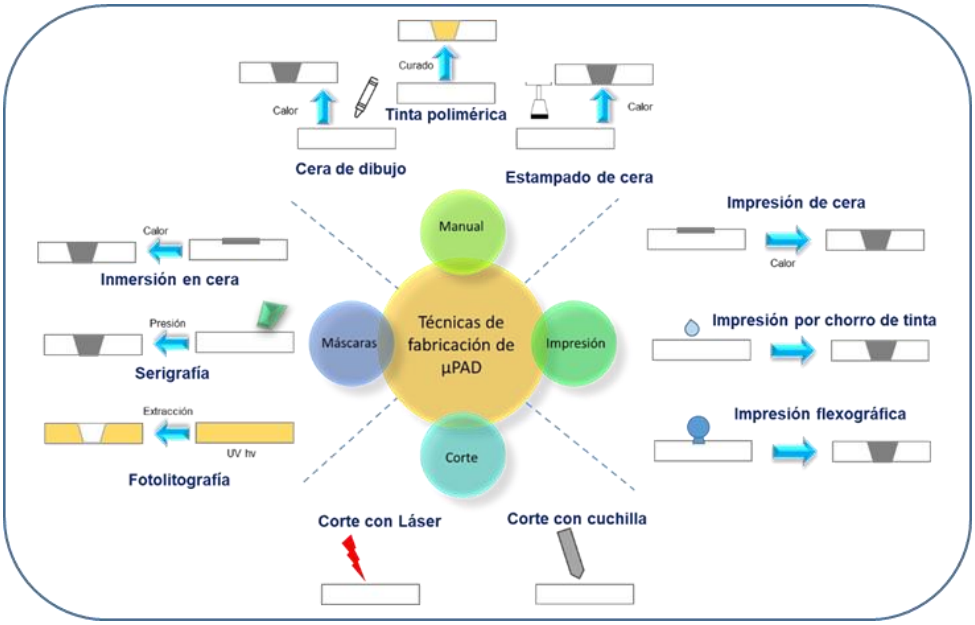

Figura 21. Esquema de las principales técnicas de fabricación de µPAD.

Entre las técnicas de fabricación existentes de µPADs se encuentran las siguientes (Figura 22.):

- **Fotolitografía:** técnica mediante la cual se crea canales microfluídicos utilizando una resina hidrófoba fotosensible y una máscara o plantilla con la geometría de los canales que se quieren definir en el sustrato. Para crear los canales hidrófobos se coloca la máscara sobre la superficie del papel

que esta a su vez recubierta por la resina hidrófoba. A continuación, se irradia el conjunto con radiación ultravioleta durante unos minutos y por último se retira la resina del papel empleando un disolvente orgánico. El canal hidrófobo define la vía de penetración del fluido en el sustrato, ya que el líquido hidrófilo se confina dentro de las paredes hidrófobicas. El líquido se mueve a través del sustrato de papel por la acción del flujo capilar [107]. La fotolitografía es una técnica de impresión fácil de llevar a cabo y mediante la cual se obtienen diseños con una buena definición. Sin embargo, la principal desventaja de esta técnica deriva de la necesidad de emplear resinas y disolventes orgánicos en el proceso de fabricación de los canales hidrófobos.

- **Grabado mediante chorro de tinta:** técnica que permite la hidrofobización completa del papel empleando un polímero, normalmente poliestireno [110]. A continuación, se produce la disolución selectiva del poliestireno con tolueno que se inyecta a través de una impresora de chorro de tinta para fabricar los canales hidrofóbicos. Esta técnica permite la fabricación de dispositivos microfluídicos en papel a gran escala. Además, los dispositivos fabricados mediante esta técnica presentan una buena definición incluso cuando su tamaño es muy reducido. Sin embargo, la utilización de disolventes orgánicos volátiles en el proceso de fabricación de los µPADs aumenta la peligrosidad de la técnica [111].

- **Tratamiento con plasma:** mediante esta técnica de impresión se deposita sobre el papel un dímero de alquil ceteno (AKD) y heptano para generar los canales hidrófobos mediante la modificación química de las fibras de celulosa. Así, la AKD reacciona con los grupos hidroxilo de la celulosa generando zonas hidrófobas en el papel. Esta impresión requiere una etapa de curado de los patrones hidrófobos que se lleva a cabo calentando el papel en un horno a 100ºC durante 45 minutos para curar la AKD. Mediante esta técnica se generan canales hidrófobos invisibles de hasta 300 µm. La formación de dispositivos microfluídicos basados en papel mediante la impresión con AKD tiene el potencial de ampliarse para su uso comercial [112].

- **Impresión por cera:** los canales hidrófobos en el papel se generan mediante la impresión de los patrones utilizando una impresora de cera. A continuación, el papel se calienta para que la cera funda y genere los canales hidrofóbicos [113]. Como fuente de calor se puede emplear un horno, una placa caliente o una pistola de calor para fundir cera. El proceso de calentamiento permite que la cera penetre tanto verticalmente como horizontalmente dentro de la matriz de papel [114]. Otra alternativa a la utilización de una impresora de cera puede ser la utilización de lápices de cera para dibujar los canales hidrófobos manualmente. Este proceso también implica una etapa de calentamiento para que la cera funda y penetre en el papel. Si la geometría de los canales no es muy compleja, es una técnica de fabricación de µPADs muy fácil de llevar a cabo y económica [115].

- **Impresión por flexografía:** utiliza un polímero como el poliestireno disuelto en un disolvente orgánico volátil como el tolueno o el xileno para hidrofobizar directamente el papel. La impresión flexográfica de poliestireno permite la producción directa de dispositivos microfluídicos en papel. Esta técnica flexográfíca emplea un rodillo cilíndrico para distribuir la solución de poliestireno e imprimir los patrones microfluídicos en el papel. Este método requiere al menos dos ciclos de impresión secuenciales para obtener barreras impermeables. Así, el ancho nominal del canal obtenido por este método es de 1 mm aproximadamente. La impresión flexográfica es compatible con la producción a gran escala, con velocidades de impresión de hasta 60 m/min. A pesar de esto, esta técnica puede presentar algunas limitaciones, pues se requieren múltiples etapas de impresión para definir completamente los canales, afectando esto a la resolución y a la reproducibilidad de la técnica.

- **Serigrafía:** técnica que permite la hidrofobización selectiva del papel de forma sencilla. Consiste en transferir tinta a través de una malla tensada con los patrones que se quieren imprimir. Para transferir la tinta a través de la malla se requiere la utilización de una regleta que ejerce presión sobre la malla haciendo que la tinta pase y se marque en el papel. Normalmente,

después de imprimir los patrones de tinta sobre el papel se requiere una etapa de curado para lo que se utiliza un horno o estufa. La temperatura del horno depende de la composición de la tinta empleada para la fabricación de los canales hidrófobos en el papel. La serigrafía es una técnica sencilla y fácilmente escalable aunque la resolución de las líneas puede ser baja y exige una pantalla diferente para cada diseño [116].

- **Técnica de corte:** se trata de una técnica diferente a las anteriores ya que no necesita productos químicos para definir los límites de flujo en el papel. Esta técnica hace uso de una impresora de corte con una cuchilla o un plotter XY controlado por un ordenador. El plotter de corte gira sobre un adaptador para cortar el papel en diferentes formas y ángulos. Después del proceso de corte se puede retirar manualmente las secciones no deseadas del papel. Cabe destacar que estos dispositivos no son mecánicamente rígidos y, por lo tanto, requieren recubrir el papel con películas de vinilo o poliéster como sustratos de respaldo o sellado. Así, la técnica de corte presenta ciertas ventajas frente a las técnicas anteriores: es una técnica sostenible con el medio ambiente, ya que no genera residuos al no utilizar disolventes orgánicos ni reactivos químicos para definir los límites de flujo en el papel; es fácil de usar y no requiere etapas de lavado del papel al finalizar el proceso de fabricación del dispositivo. No obstante, la continua utilización del plotter de corte de la impresora genera desgastes en la cuchilla por lo que hay que estar constantemente cambiándola o limpiándola [117].

- **Tratamiento con láser:** emplea un láser de dióxido de carbono que corta el papel con la forma desea [118]. La zona hidrófoba del papel está delimitada por el propio corte del láser. El equipo utilizado en esta técnica para realizar el corte del papel es fácil de utilizar, de bajo coste y está ampliamente disponible. El láser de la impresora es capaz de cortar a diferentes presiones y ángulos, los cuales varían dependiendo de la aplicación. Una desventaja que presenta esta técnica surge de la acción propia de cortar, ya que puede causar deformaciones en el papel. Además, se requiere de etapas de lavado del papel después de realizar el corte con

el láser ya que éste quema el sustrato al cortarlo generando cenizas que oscurecen el papel.

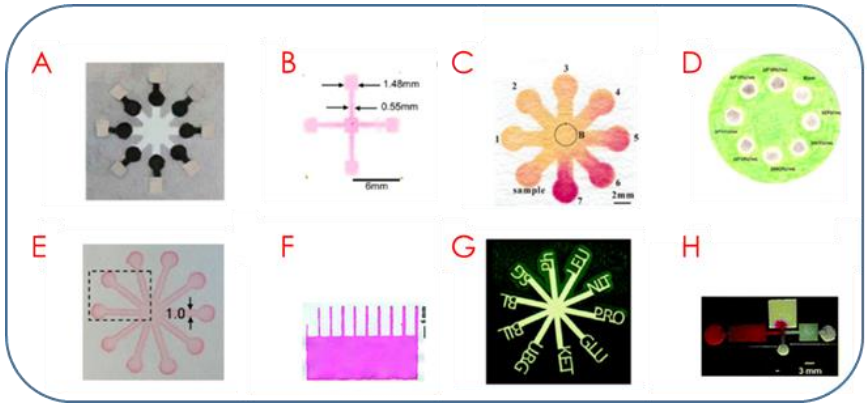

Figura 22. Ejemplos de µPADs diseñados mediante: A) Fotolitografía, B) grabado con chorro de tinta, C) tratamiento con plasma, D) impresión con cera, E) impresión por flexografía, F) serigrafía, G) corte con plotter, H) impresión por corte con láser. Figuras extraídas de [74] y [119].

4.2.2. Métodos de detección de los µPADS

Dentro de la amplia variedad de métodos de detección empleados en los dispositivos microfluídicos basados en papel (electroquímicos [120], espectroscópicos [121], espectroelectroquímicos [122], etc.) el sistema de detección más utilizado en este tipo de dispositivos es mayoritariamente de tipo óptico y sobre todo colorimétrico bien mediante observación visual o por medida de color con sensores de color de algún dispositivo de imagen tipo escáner, webcam, cámara fotográfica o Smartphone. La rápida respuesta que se genera, la sencillez de este tipo de reacciones y la posibilidad de obtener resultados de forma semicuantitativa hacen que este tipo de detección sea una de los más utilizadas actualmente.

4.2.2.1. Detección óptica

Los sistemas de detección óptica utilizados en el desarrollo de los µPADs se basan en técnicas como la absorción UV-visible, la luminiscencia y la resonancia de plasmón superficial (SPR).

- **Detección espectrofotométrica**

Las técnicas de absorción se basan en el hecho de hacer incidir sobre la muestra un haz de radicación de forma que parte de la radiación incidente es absorbida por la muestra. Así, la intensidad de la radiación transmitida es distinta a la radiación incidente. De esta forma, la cantidad de radiación absorbida permite establecer la relación entre la intensidad de radiación incidente y la transmitida (Ecuación 1).

$$A = log \frac{I_o}{I} \qquad \text{Ecuación 1}$$

Donde A es la absorbancia, I_o es la intensidad de radiación incidente y I es la intensidad de radiación transmitida.

La concentración de una determinada especie en una muestra se puede determinar mediante la ley de Lambert-Beer (Ecuación 2). Esta ley se basa en el hecho de que la absorción de una muestra depende de la longitud de onda. De este modo, es posible determinar diferentes especies de una misma muestra siempre y cuando posean distintos espectros de absorción.

$$A = \varepsilon \cdot l \cdot c \qquad \text{Ecuación 2}$$

Donde A es la absorbancia, ε es el coeficiente de absortividad molar del analito, l es el paso de la luz a través de la muestra y c es la concentración de analito en la muestra.

Esta técnica óptica permite la determinación directa e indirecta de especies absorbentes o sin capacidad de absorción pero que pueden

transformarse en otras que si son capaces de absorber. Así, existen determinados métodos de absorción basados en la determinación indirecta de sustratos de enzimas. El ejemplo más extendido es la determinación óptica de glucosa. Esta determinación se basa en la degradación de la glucosa por el enzima glucosa oxidasa (GOx) con la consiguiente formación del producto oxidado y la liberación de peróxido de hidrógeno. Así, ninguno de los compuestos implicados presenta una absorción de radiación suficiente como para llevar a cabo su determinación de forma directa, es por ello que surge la necesidad de acoplar determinados reactivos que sí son capaces de absorber la radiación. Se trata de indicadores colorimétricos conocidos comúnmente como reactivos cromogénicos que cambian su espectro de absorción en función de su estado de oxidación. En ésta determinación óptica de glucosa, reactivos como el TMB y el APTS se utilizan como reactivos de acoplamiento para ser oxidados por el H_2O_2 generado en la degradación de la glucosa. De esta forma cambian su espectro de absorción y permiten la determinación indirecta de la concentración de glucosa en una muestra, ver Figura 23.

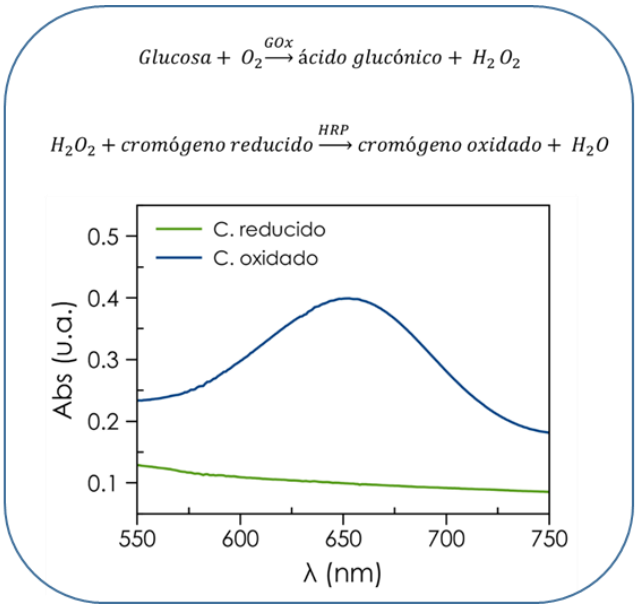

Figura 23. Reacciones catalíticas implicadas en la determinación óptica de glucosa. Espectros de absorción del TMB en la determinación de glucosa.

La detección óptica en µPADs implica el movimiento pasivo del analito contenido en una muestra a la zona de detección del µPAD por capilaridad. Una vez en la zona de detección reacciona con los reactivos necesarios para producir un cambio de color detectable tal y como se ha indicado anteriormente. En general, las imágenes de la zona de detección en los métodos ópticos son recogidas por dispositivos de imagen convencionales tales como, Smartphones, escáneres o cámaras digitales y luego son transferidas a un ordenador que las analiza y extrae la información de interés con la ayuda de algún editor de imágenes [123].

Existen numerosas publicaciones científicas en las que proponen el uso de teléfonos móviles, en concreto Smartphones, para la detección óptica en µPADs. Por ejemplo, Lopez-Ruíz y col. [124] desarrollaron un dispositivo microfluídico basado en papel para la determinación colorimétrica de nitrito y pH en muestras de agua, ver Figura 24. El µPAD desarrollado comprende siete áreas de detección donde se inmovilizan los reactivos correspondientes para producir cambios de color selectivos cuando se deposita una muestra en el área de muestreo y por capilaridad llega hasta las zonas de detección. Trabajando bajo condiciones de luminosidad controlada se captura una imagen del µPAD con la cámara de un teléfono móvil. A continuación, se procesa la imagen capturada utilizando un algoritmo desarrollado para la detección de color en las múltiples de las áreas de detección. El procesamiento de las imágenes permite reducir la influencia de la fuente de luz y el posicionamiento del µPAD en la imagen.

La detección colorimétrica presenta inherentes ventajas entre las que se encuentran su simplicidad, fácil utilización, rapidez en la obtención de la respuesta y bajo coste. Sin embargo, la detección colorimétrica en ocasiones puede presentar una baja sensibilidad y selectividad por lo que otros métodos ópticos como las medidas de luminiscencia están siendo utilizadas.

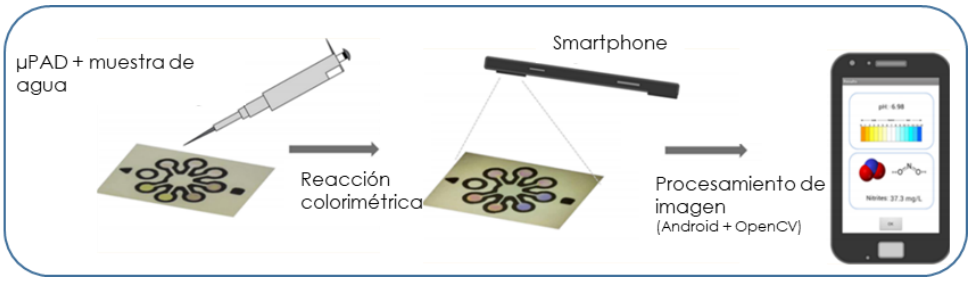

Figura 24. Ilustración esquemática del µPAD usado para la determinación de nitrito y pH en muestras de agua usando un teléfono móvil para la detección colorimétrica. Esquema extraído de [104].

- **Detección luminiscente**

  La determinación de numerosos analitos se lleva a cabo mediante la emisión o atenuación (quenching) luminiscente de estos compuestos mejorando significativamente la selectividad, sensibilidad, límites de detección y el rango lineal en comparación con las técnicas de absorción. En este sentido, el desarrollo de µPADs cuyo sistema de detección se basa en fenómenos luminiscentes (fluorescencia y fosforescencia) para la determinación cualitativa y cuantitativa de analitos está siendo ampliamente utilizado.

  Tanto la fluorescencia y como la fosforescencia son procesos de emisión que tienen lugar cuando las moléculas absorben energía procedente de una radiación incidente a una determinada longitud de onda y posteriormente emiten esa radiación a una longitud de onda mayor [125]. El conocido diagrama de Jablonski (Figura 25) representa los procesos de emisión de estos fenómenos luminiscentes mostrando los distintos niveles electrónicos de una molécula y las posibles transiciones electrónicas que tienen lugar entre estos niveles.

  Como indica el diagrama la absorción de la radiación por parte de las moléculas produce la excitación de algunos electrones desde el estado fundamental S_0 hasta niveles electrónicos más energéticos. ($S_0 \rightarrow S_1$) y ($S_0 \rightarrow S_2$). A su vez, los electrones excitados pueden regresar al estado fundamental o a niveles menos energéticos mediante procesos

de desactivación radiante y no radiante como las conversiones internas y externas, la relajación vibracional y el entrecruzamiento entre sistemas.

En este sentido, la relajación vibracional se produce como consecuencia de las colisiones entre las moléculas excitadas y el disolvente. De esta forma el exceso de energía vibracional de las moléculas excitadas se transfiere a las moléculas del disolvente produciéndose transiciones electrónicas a niveles de menor energía dentro de un mismo nivel electrónico. De manera conjunta también pueden ocurrir procesos de conversión interna y externa los cuales involucran transiciones intermoleculares en las cuales las moléculas pasan de un estado electrónico más energético a otro inferior sin emisión de la radiación ($S_2 \rightarrow S_1$).

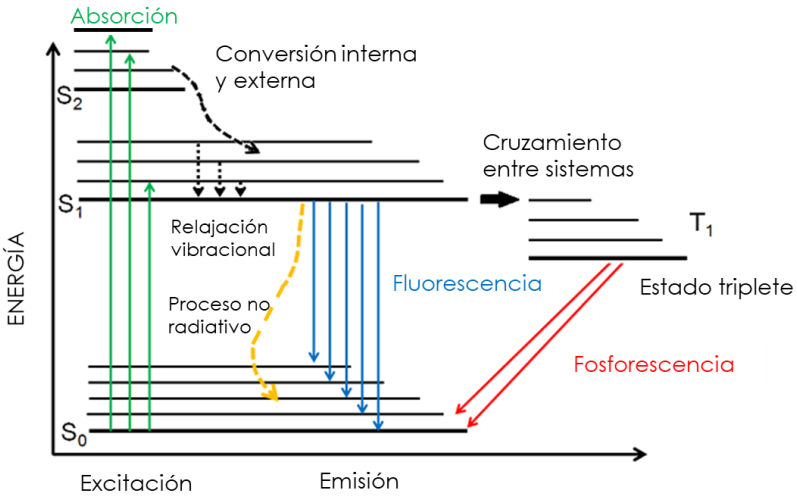

Figura 25. Diagrama de Jablonski.

Por otra parte, los procesos radiantes provocan la emisión de fluorescencia y fosforescencia. La fluorescencia se basa en la transición de los electrones desde estados excitados al estado fundamental con emisión directa de radiación ($S_1 \rightarrow S_0$), así mismo, la fosforescencia implica un cambio en el espín de los electrones excitados mediante de un proceso de entrecruzamiento de sistemas. Este entrecruzamiento

implica un cambio en la multiplicidad de la molécula generando una transición entre el estado singlete excitado S_1 y el estado triplete excitado T_1 ($S_1 \rightarrow T_1$; $S_2 \rightarrow T_2$). Los procesos de entrecruzamiento entre sistemas que originan emisión fosforescente requieren de la presencia de átomos pesados que favorezcan el cambio de espín entre los electrones excitados.

Entre los factores que afectan a los procesos de emisión luminiscente podemos encontrar, la estructura de las moléculas, el tipo de disolvente, el pH, la temperatura y el oxígeno disuelto. La presencia de grupos aromáticos o dobles enlaces favorecen la emisión luminiscente. De forma general, un incremento en el número de anillos aromáticos, así como, el grado de condensación originan mayores rendimientos cuánticos por lo que aumenta la relación entre el número de moléculas que emiten y el número de moléculas excitadas. La rigidez estructural de las moléculas provoca una disminución en la velocidad a la que se producen los procesos de conversión interna haciendo disminuir la desactivación no radiante. La viscosidad del disolvente en el que se encuentran disueltas las moléculas facilita o dificulta la probabilidad de colisiones entre ellas y las moléculas de disolvente.

En este sentido, cuanto menor sea la viscosidad del disolvente las probabilidades de choque de las moléculas será más alto y los procesos de desactivación no radiante estarán más favorecidos. Por otro lado, cambios en la acidez o basicidad del medio en el que se encuentran las moléculas provocan cambios en la emisión luminiscente de las mismas. Así, la presencia de oxígeno disuelto en ocasiones provoca la formación de complejos con las especies luminiscentes dando lugar a procesos de atenuación de la luminiscencia. Esta atenuación se produce como consecuencia de la transferencia de energía de excitación desde las moléculas excitadas a las moléculas de oxígeno.

Estas diferencias en los mecanismos de las transiciones electrónicas ocurren más rápido en la emisión de fluorescencia que en la emisión de fosforescencia. En contraposición, la emisión de fosforescencia continua después de que la radiación incidente haya cesado.

La detección fluorescente en µPADs se basa en la interacción del analito con diversos marcadores fluorescentes (fluoróforos) [126]. El proceso de detección implica el uso de una fuente de luz de una longitud de onda apropiada para inducir la luminiscencia de los fluoróforos. La luz resultante se filtra para aislar la emisión de fotones excitados y la intensidad de los fotones de emisión se mide y se usa como indicador de la concentración de analito de interés.

Así, el reconocimiento de diversos analitos entre los que se encuentran los metales pesados se lleva a cabo empleado sistemas de detección fluorescente en µPADs. En la determinación de metales se suelen utilizar agentes quelantes, por ejemplo, receptores que tienen una fuerte interacción con los analitos. Además, estas unidades quelantes están conectadas con un fluoróforo para generar el reconocimiento fluorescente ya sea mejorando la intensidad de fluorescencia del fluoroforo o mediante el quenching de la fluorescencia. Esta forma de detección permite el reconocimiento de metales a nivel de trazas de forma rápida. Por ejemplo, Liu y col [127] han desarrollado un sensor para la determinación de cobre utilizando nanoclusters de AgNCs inmovilizados en papel de celulosa. Las propiedades fluorescentes de AgNCs son atenuadas en presencia de iones Cu^{2+} estableciéndose una excelente relación lineal entre la respuesta fluorescente y la concentración de iones Cu^{2+} presente en la muestra utilizando como sistema de medida un espectrofluorímetro.

- **Resonancia de plasmón superficial**

Los sistemas de resonancia de plasmón superficial (SPR) se basan en la medida de los cambios del índice de refracción de un haz de radiación cuando éste se proyecta sobre una superficie metálica [128]. Así, este tipo de sistemas SPR constan de una lámpara, un prisma acoplado a una superficie de vidrio recubierta con una lámina fina de oro, plata, cobre o aluminio donde tiene lugar la interacción con el analito, un sistema de flujo y un detector (Figura 26.).

El funcionamiento de los sistemas SPR consiste en una excitación colectiva de los electrones libres de la banda de conducción de la superficie de las nanopartículas metálicas cuando un haz de luz incidente se proyecta sobre ellas. La excitación de los electrones libres tiene lugar debido a la fuerte interacción del haz de luz sobre las nanopartículas provocando una excitación electromagnética conocida como polaritón del plasmón de superficie.

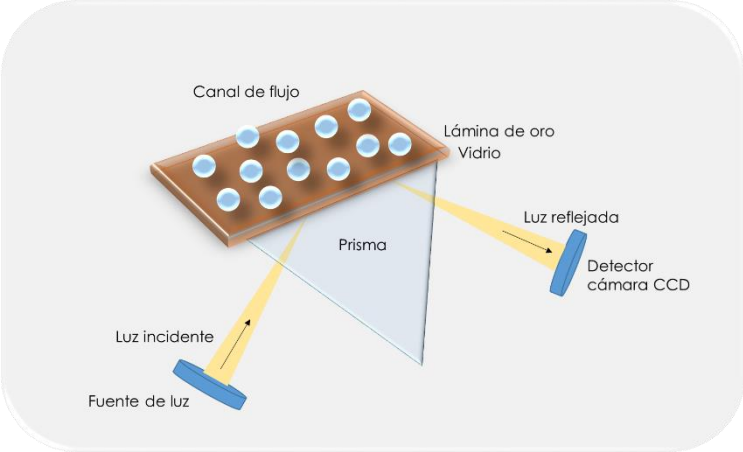

Figura 26. Esquema de los componentes de un sistema SPR.

Para determinadas frecuencias de la energía incidente, se produce un acoplamiento entre las frecuencias de la onda incidente y la onda de oscilación del polaritón, este fenómeno recibe el nombre de resonancia del plasmón de superficie y tiene la capacidad de absorber

ciertas frecuencias de la luz incidente, así como de transmitir las frecuencias no absorbidas que se asocian a un determinado color.

En el caso de nanopartículas de metales nobles como el oro y la plata la resonancia es máxima y su frecuencia se produce en el campo visible del espectro electromagnético. Cuando el tamaño de las nanopartículas es menor que la longitud de onda de la radiación incidente tiende a producirse esta resonancia ya que tienen lugar excitaciones dipolares fuertes de los electrones libres en la superficie de la partícula con la resonancia del plasmón generándose un fuerte acoplamiento de los electrones libres con el haz de luz incidente. Cabe señalar que la frecuencia de resonancia y la anchura de la banda de absorción del plasmón dependen del tamaño y de la forma de las nanopartículas. Así, esta dependencia permite seleccionar frecuencias de la luz reflejada a las que van asociadas distintas energías y colores. La posibilidad de alterar las frecuencias de resonancia es el principio de las importantes propiedades óptico-electrónicas de las nanopartículas metálicas.

La respuesta óptica de las nanopartículas metálicas está relacionada con la oscilación de los electrones libres de la superficie dentro de un potencial de Coulomb, formado por el núcleo iónico de la nanopartícula cargado positivamente. Así, la resonancia de plasmón superficial depende fuertemente de otros factores como la concentración de nanopartículas, la distribución espacial de las mismas y las propiedades de la matriz que rodea a las partículas metálicas. La energía de la resonancia del plasmón superficial depende a su vez de la densidad del plasma de electrones libres y de la propiedad dieléctrica del medio que rodea a las partículas, esta energía aumenta con la frecuencia de resonancia a medida que disminuye el diámetro de la nanopartícula. Para nanopartículas con un diámetro menor de 20 nm, el ancho de banda del plasmón aumenta a

medida que disminuye el tamaño de las partículas y cuando el diámetro es mayor de 20 nm la anchura de banda se desliza a longitudes de onda más largas y se producen multipolos y oscilaciones más complejas. Por tanto, la modificación de la frecuencia transmitida de las nanopartículas puede ser llevarse a cabo modificando su tamaño. En una dispersión coloidal de nanopartículas de oro de tamaño inferior a 30 nm la resonancia de plasmón superficial absorbe la luz de la zona visible del espectro electromagnético de color azul-verde y produce una luz reflejada de color rojo.

A medida que las nanopartículas de oro aumentan su tamaño la longitud de onda de la resonancia de plasmón superficial se desplaza hacia la zona visible del espectro electromagnético de longitudes de onda de menor energía que corresponden con el color rojo, de esta forma, se absorbe la luz roja y se refleja la luz azul, ver Tabla 2.

Como la frecuencia de la resonancia de plasmón superficial depende en gran medida de la constante dieléctrica del medio que rodea a las partículas también el color de éstas puede cambiar con el valor de la constante dieléctrica del disolvente.

Por todo ello, las nanopartículas metálicas tienen propiedades ópticas, eléctricas y térmicas únicas y son muy importantes en aplicaciones como sensores biológicos y químicos en diversos campos como la biología, medicina, etc.

Uno de los inconvenientes que presenta esta técnica de detección es la dificultad para detectar compuestos de bajo peso molecular ya que las moléculas pequeñas originan cambios en el ángulo de resonancia que resultan difíciles de detectar. No obstante, este problema puede

solventarse incrementando la relación señal-ruido del sistema de detección.

Por otro lado, la principal ventaja que presentan los sistemas SPR deriva de su capacidad para medir en tiempo real las interacciones que tienen lugar entre las moléculas y la superficie del metal. De esta forma, resulta posible monitorizar dicho procedimiento de forma fácil y se puede implementar en sistemas miniaturizados y portátiles para la detección *in situ* se diversos compuestos de interés clínico, ambiental y alimentario.

Tabla 2. Longitudes de onda asociados a los colores absorbidos y reflejados.

Longitud de onda (nm)	Color absorbido	Color reflejado
650 – 780	Rojo	Azul – verde
595 – 650	Naranja	Turquesa
560 - 595	Amarillo - Verde	Púrpura
500 – 560	Verde	Magenta
490 – 500	Verde azulado	Rojo
480 – 490	turquesa	Naranja
435 - 480	Azul	Amarillo
380 – 435	violeta	Amarillo - verde

En este sentido, los sistemas SPR se han implementado en el desarrollo de µPADs para la determinación de diversos compuestos. En el trabajo de Vahid H. y col [129], por ejemplo, se desarrolla un µPAD para la determinación de ácido úrico cuyo mecanismo de detección se basa en la interacción ácido úrico con nanopartículas de plata (AgNPs), Figura 27. El color amarillo originado de la absorción de luz visible en la superficie de resonancia del plasmón de AgNPs se detecta a simple vista y se cuantifica utilizando un escáner como sistema de detección.

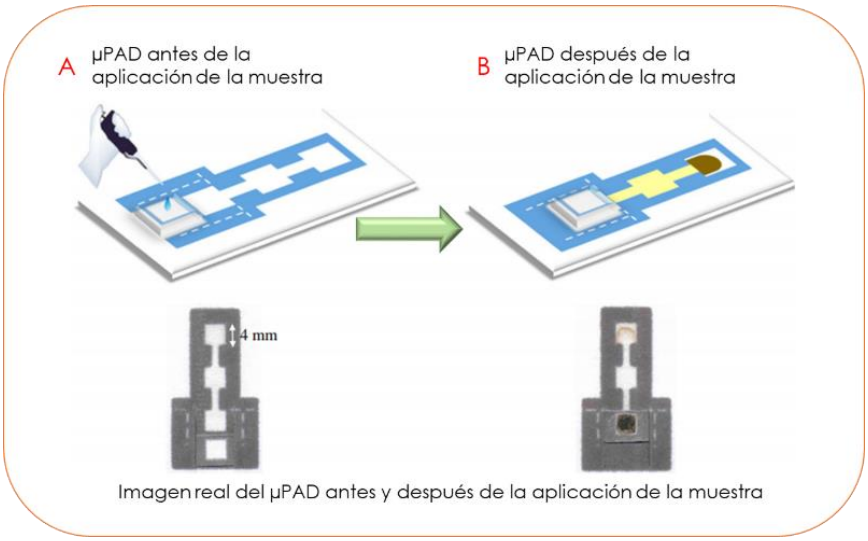

Figura 27. µPAD para la determinación de ácido úrico basado en un sistema SPR empleando nanopartículas de plata. Imagen extraída y modificada de [109].

4.2.2.2. Detección electroquímica

La detección electroquímica es un método de detección muy utilizado en desarrollo de sistemas microfluídicos en papel debido a sus inherentes características: bajo costo, portabilidad, alta selectividad, buena sensibilidad, y simplicidad de la instrumentación que resulta en un bajo consumo de energía eléctrica. Por todo ello, es eminente su adecuación en µPADs para la determinación de compuestos biomédicos como glucosa, lactato, ácido úrico y colesterol.

En este sentido, los dispositivos microfluídicos basados en papel que utilizan este tipo de sistemas de detección reciben comúnmente el nombre de "Paper-based Electrochemical Devices" (PEDs). Este tipo de sistemas registran el cambio en las propiedades eléctricas del medio como la corriente, el potencial, la conductividad, etc. producido como consecuencia de la reacción de reconocimiento entre el analito y el sustrato. Así, los sistemas de detección electroquímico se pueden clasificar en función de la propiedad eléctrica medida por el transductor: amperométricos, potenciométricos y conductimétricos.

La detección electroquímica en sistemas PEDs implica la impresión sobre el papel de tres electrodos: el electrodo de referencia (RE), el electrodo de trabajo

(WE) y un electrodo de conteo (CE) [120]. Para la fabricación de los electrodos suelen utilizarse tintas conductoras de carbono y plata principalmente que se imprimen sobre el papel mediante técnicas como la serigrafía. Una vez definido el electrodo de trabajo se modifica su superficie para que sea selectiva en la determinación del biomarcador de interés.

Estas técnicas de detección permiten el análisis de los procesos que ocurren en la membrana selectiva depositada en la superficie del electro de trabajo. El análisis de la muestra generalmente se lleva a cabo mediante deposición por gota de las soluciones que portan la muestra sobre el electrodo. La información analítica que generan las técnicas electroquímicas viene dada por la corriente eléctrica generada como respuesta a la diferencia de potencial establecida entre el electrodo de referencia y el electrodo de trabajo en una determinada escala de tiempo. De esta forma, la corriente medida puede proceder de la migración de iones para compensar cargas fijas en la superficie del electrodo de trabajo o de la reacción de oxidación-reducción que sufren ciertas moléculas como resultado del potencial electroquímico aplicado.

Con respecto a la parte microfluídica, normalmente se fabrican dispositivos 3D en un solo sustrato de papel. El montaje del papel se lleva a cabo doblando el papel a mano. Desde que en 2011 Richard M. Crooks y col. desarrollaran el primer dispositivo 3D se ha vuelto muy popular ya que este diseño permite reducir los volúmenes de reactivos y muestras y evita la contaminación de los electrodos cuando se modifica el electrodo de trabajo ya que estos están separados en dos pestañas diferentes, una para el electrodo de trabajo y otra para el electrodo de referencia y el contador. En el trabajo de Richard M. Crooks y col se desarrolló un inmunosensor desechable de impedancia para la detección de un interferón gamma humano (IFN-γ) utilizando papel de filtro Whatman no. 1 como sustrato. El dispositivo se diseñó mediante impresión por cera, y para aumentar la sensibilidad del inmunosenor se usó tinta de grafeno para la fabricación del electrodo de trabajo que después se modificó con polianilina para inmovilizar covalentemente los anticuerpos monoclonales

IFN- γ. Una vez funcionalizado, las dos pestañas del dispositivo se plegan quedando una sobre la otra y la celda electroquímica completa.

5. Análisis del color

El color ha sido usado desde hace mucho tiempo en Química Analítica como una de las principales propiedades organolépticas que incluye información cualitativa y semicuantitativa en reacciones de separación y de identificación, así como para indicar el punto final en volumetrías. Desde el siglo XVIII se han propuesto una gran cantidad de ensayos que usan tanto reactivos en disolución como papeles impregnados de reactivos que originan o modifican su color en presencia del analito [130].

Estos ensayos son esencialmente cualitativos y en general poco sensibles y en cualquier caso, subjetivos. Por su parte, los ensayos semicuantitativos o cuantitativos generalmente operan por comparación con cartas de color. El desarrollo instrumental ocurrido en el siglo XX propició el desarrollo del denominado análisis instrumental y relegó estos ensayos a unas cuantas, aunque importantes, áreas tales como urianálisis o los ensayos inmunocromatográficos.

A finales del siglo XX el desarrollo de los detectores de color y los sensores de imagen que duplican y mejoran la visión humana al percibir y describir una imagen por vía electrónica y la puesta a punto de nuevas químicas de reconocimiento, ha abierto la puerta a nuevas estrategias y oportunidades en Química Analítica [131].

La intensidad de los colores de las sustancias, presentes en una membrana sensora, puede ser evaluada a partir de las imágenes tomadas de esta membrana empleando cámaras fotográficas, escáneres o cualquier otro dispositivo de imagen. A partir de estas imágenes se expresan los colores como datos numéricos, definiendo para ello una región de interés dentro del área sensora de dicha membrana que es donde se encuentra la información química. El promedio del color de los píxeles puede ser empleado para relacionar la

intensidad o la tonalidad del color con la concentración de sustancia presente mediante una función de calibrado [132].

5.1. Espacios de color

Los colores expresan cualidades resultantes de experiencias visuales y pueden cuantificarse midiendo la distribución de energía espectral de la luz que origina el color utilizando una serie de métodos o espacios de color que especifican el color de una sustancia en base a los tres colores primarios (rojo, verde, azul), de forma similar a la percepción humana del color. La retina del ojo es sensible a tres longitudes de onda correspondientes a la luz roja, verde y azul. Las señales eléctricas de las células de la retina (conos y bastones) se combinan en el cerebro originando las diferentes sensaciones de color: saturación, tono, luminosidad, textura, tamaño, localización, etc.

Por lo general, un color se define como una combinación lineal de los principales componentes de color utilizados en un espacio de color, entendiendo por espacio de color, una representación matemática grafica que nos ayuda a clasificar los colores según sus características y que nos sirve para recoger información de color de escáneres, monitores, cámaras y demás dispositivos electrónicos. En este sentido, podemos definir un color a partir de la medida física de la potencia radiante utilizando para ello detectores térmicos y fotónicos como los dispositivos de carga acoplada (CCD) o los dispositivos tipo Complementary Metal Oxide Semiconductor (CMOS).

En base a esto, es posible clasificar los espacios de color en cuatro grupos diferentes los cuales se relacionan entre sí aplicando diferentes transformaciones:

- Triestímulo lineales: CIE XYZ y RGB
- Cromáticos xy: CIE xyY
- Perceptualmente uniformes: CIE L*u*v, el CIE L*a*b* y el R'G'B' no lineal
- Orientados al tono: HLS y el HSV

De entre los espacios de color mencionados, los más utilizados en aplicaciones analíticas son los espacios de color triestímulo RGB y los orientados al tono HSV. Estos modelos matemáticos describen los colores como secuencias de números empleando tres coordenadas para representar la posición de cada color específico.

Los colores se caracterizan por: la luminosidad o saturación, es decir, la intensidad luminosa de la luz por unidad de área; la cromaticidad, que se denota como la proporción entre los tres estímulos de color que son necesarios para describir un color y la tonalidad que es la cualidad que distingue los colores por la longitud de onda de la luz que se percibe como dominante [133].

- **Espacio de color RGB**

  El espacio de color RGB es una forma de representación del color usado por la TV, escáneres, monitores, videocámaras y proyectores de vídeo, entre otros. La mayoría de las cámaras de color empleadas para la adquisición de imágenes digitales utilizan este espacio de color. Las imágenes del mismo consisten en tres planos de imagen, uno por cada color primario que cuando llegan a un monitor RGB se combinan para producir una imagen en color.

  Este modo es el que más se usa en la iluminación artificial y en la mayoría de monitores, proporcionando la mayoría de la radiación del espectro visible mezclando los colores rojos, verdes y azules. Estos tres colores primarios forman el blanco cuando se combinan simultáneamente; por eso se llaman también aditivos (ver Figura 28). Al mezclarse dos a dos, crean los colores secundarios. Si la mezcla es en diferentes proporciones de estos colores básicos, se van originando los diferentes tonos de la gama del espectro.

  Este espacio de color es muy utilizado en análisis químico ya que se usa en diversos dispositivos, como los anteriormente mencionados, para la

detección, representación y exhibición de imágenes en sistemas electrónicos o informáticos.

Mediante este modelo se representa el color como una mezcla aditiva de los tres colores primarios, rojo (R), verde (G) y azul (B), por lo que se emplean tres coordenadas para definir el color relacionando cada coordenada con un color. De esta forma se le asigna un valor numérico a cada color, de forma que el valor 0 significa que no interviene el color en la mezcla y a medida que ese valor aumenta, se entiende que aporta más intensidad a ésta [134].

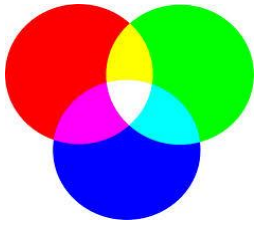

Figura 28. Síntesis aditiva del color en el espacio de color RGB.

El principal inconveniente que presenta el espacio de color RGB es que definen el color como una mezcla de colores básicos y a menudo se obtiene información solo de un color o del cociente de varias coordenadas de color con lo cual se pierde información de los colores no utilizados. Esta pérdida de información supone una disminución en la robustez de la señal por lo que para solventar este problema se utiliza el espacio de color HSV el cual define los colores como una combinación del tono (H), saturación (S) y luminosidad (V). En este caso, el color se define por una coordenada, por ejemplo, el tono mientras que las otras coordenadas solo añaden un matiz a ésta. Así, podemos definir el tono de un sensor mediante una sola coordenada sin estar influenciado por otras haciendo el parámetro analítico más robusto.

- **Espacio de color HSV**

El espacio de color HSV es una representación alternativa derivada del espacio RGB. Se trata de una representación de tres parámetros como son el tono (H), la saturación (S) y el brillo (V) representados mediante un sistema coordenado.

El tono se representa como un ángulo cuyo valor varía entre 0º y 360º (Figura 29). En ciertas aplicaciones, los posibles valores referidos al tono se normalizan de 0 a 1, de forma que todos los posibles tonos se encuentran entre esos valores. Los valores posibles referidos a la saturación van del 0 a 100%. Cuanto menor sea el valor referido a la saturación de un color, mayor tonalidad grisácea presentará. La saturación es una propiedad del color que puede ser usada como parámetro analítico en diversas aplicaciones, pues el valor de saturación depende únicamente de la intensidad luminosa. La luminosidad toma valores desde 0 a 100% donde el cero representa el negro y el 100 el blanco [135].

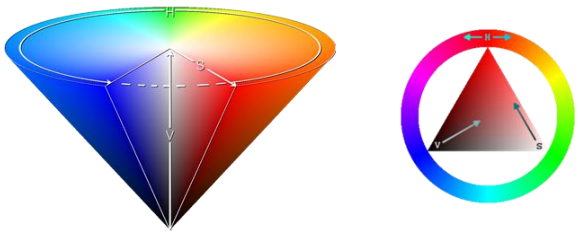

Figura 29. Representación del espacio de color HSV.

Dado que la mayoría de los dispositivos de captura proporcionan información RGB, es necesario definir las ecuaciones (Figura 30) que permiten realizar las diferentes transformaciones entre los espacios de color RGB y HSV anteriormente citados[136].

$$M = \max(R, G, B)$$
$$m = \min(R, G, B)$$
$$\mathrm{C} = \mathrm{M} - \mathrm{m}$$
$$\mathrm{H} = 60º \times \begin{cases} \text{indefinido si } \mathrm{C} = 0 \\ \dfrac{\left(\dfrac{\mathrm{G} - \mathrm{B}}{\mathrm{C}}\right)}{6}, \text{si } \mathrm{M} = \mathrm{R} \\ \dfrac{\left(\dfrac{B - R}{C} + 2\right)}{6}, si\ M = G \\ \dfrac{\left(\dfrac{R - G}{C} + 4\right)}{6}, si\ M = R \end{cases}$$
$$\mathrm{S} = \begin{cases} 0\ si\ C = 0 \\ \dfrac{C}{V} \end{cases}$$
$$\mathrm{V} = \max(\mathrm{R}, \mathrm{G}, \mathrm{B})$$

Figura 30. Ecuaciones para la transformación de los espacios de color RGB y HSV.

5.2. Dispositivos digitales para la medida del color

Los dispositivos digitales para la medida del color son sensores de imagen que convierten una imagen óptica en una señal electrónica mediante la generación de una corriente eléctrica o voltaje que es proporcional a la intensidad de la radiación óptica incidente. Esta señal electrónica generada, por lo general, se convierte en un código digital que caracteriza las coordenadas de color correspondientes.

Existen diferentes dispositivos de imagen para recopilar información acerca del color, entre los más utilizados se encuentran: escáneres, cámaras digitales, cámaras CCD, microscopios basados en una cámara CCD, teléfonos con cámara, smartphones, tabletas, cámaras web y colorímetros, entre otros.

Los sensores CCD son sensores de color compuestos por un sustrato de silicio sobre el cual se dispone una matriz de fotodiodos MOS (Metal-Oxide-Semiconductor) dispuestos uno al lado del otro. En la arquitectura de CCD existen tres funciones básicas: recogida de carga, transferencia de carga y conversión de la carga en tensión medible. La carga creada en cada bloque elemental de un sistema CCD es proporcional a la luz incidente. La carga se transfiere píxel a píxel de forma secuencial hasta que llega al amplificador. Con el fin de obtener y dividir la información del color, la mayoría de las cámaras CCD utilizan un filtro de Bayer. El filtro de Bayer es una cuadrícula de filtros rojos, verdes y azules que se sitúan delante de los elementos que componen el detector y hacen llegar la radiación transmitida por cada filtro, proporcionando información sobre la intensidad de radiación en cada una de las zonas rojas, verdes y azules del espectro, que por síntesis aditiva permitirá establecer el color de cada píxel.

La proporción de filtros de cada color en el filtro de Bayer no es igual, sino que existen un 50% de filtros verdes, 25% de rojos y 25% de azules. La razón de que se use mayor cantidad de puntos verdes es que el ojo humano es más sensible a ese color. Debido a esta distribución, el color de cada píxel que compone la imagen va a venir dado por la interpolación de la tonalidad de cuatro fotodiodos, dos verdes, uno azul y otro rojo.

Una alternativa a los sensores CCD son los dispositivos CMOS. La principal ventaja que presentan estos tipos de dispositivos frente a los CCD es que se puede integrar más de un transistor en cada píxel. Los sensores CMOS ofrecen tiempos de respuesta más bajos, así como un menor consumo en un tamaño más pequeño pero, por lo general, las características de ruido y los límites de detección son peores que en el caso de los sensores CCD. Por otra parte, los sensores de imagen CMOS se diferencian en el diseño de fabricación de los CCD, pues los sensores CMOS incorporan un amplificador de la señal eléctrica en cada fotosito, siendo común incluir el conversor analógico digital en el propio chip.

Actualmente, la adquisición de imágenes con estos sensores juega un papel importante en campos como el de la alimentación, medio ambiente, seguridad y salud. Las cámaras CCD han sido usadas para la detección de niveles bajos de explosivos [137], para la determinación de bacterias en alimentos [138] así como para la determinación de diversos iones como el calcio, el magnesio, el potasio, el sodio, el mercurio o el cloruro en agua empleando medidas de fluorescencia sobre microplacas [139], entre otras.

5.3. Smartphone como dispositivos ópticos de detección

El término Smartphone fue introducido en 1997 para caracterizar a los teléfonos inteligentes siendo dispositivos portátiles que tenían la capacidad de conectarse a Internet y que poseían cámaras fotográficas integradas. Desde entonces hasta la actualidad, los servicios que estos dispositivos ofrecen han ido en aumento, y hoy en día, constituyen una herramienta indispensable en una serie de campos tanto de la telecomunicación como de la ciencia, así como en la vida diaria de millones de ciudadanos de todo el mundo. Los Smartphones son pequeños ordenadores portátiles con una memoria interna extensa que permite el almacenamiento de datos y cámaras con lentes de alta calidad para fotografiar imágenes.

Actualmente, aproximadamente el 80% de los teléfonos móviles que existen en el mundo son Smartphones. La rápida aceptación de estos dispositivos es debida a la combinación del incremento de sus características, cada vez más sofisticadas, y a la gran cantidad de aplicaciones que aprovechan los sensores del teléfono, pantalla táctil, cámara/s integrada/s, batería de alto rendimiento, conexión a Internet y almacenamiento de datos.

Debido al creciente desarrollo de la tecnología empleada en la fabricación de los Smartphones, éstos se han empezado a utilizar con diferentes propósitos como alternativa a otros tipos de instrumentación más compleja. Gracias a la capacidad de la cámara de los Smartphones para tomar imágenes a color de gran resolución y a la presencia de sensores de bajo coste integrados, estos dispositivos se pueden usar para

la detección y cuantificación de sustancias en una gran variedad de muestras (Figura 31). Los Smartphones son herramientas potencialmente accesibles y más baratas que los dispositivos analíticos portátiles de laboratorio. Estos dispositivos se pueden utilizar para ejecutar pruebas de rutina, que generalmente realizan personal cualificado utilizando instrumentación de laboratorio tales como microscopios y espectrofotómetros. El desarrollo de los sistemas POC ha incentivado el uso de los Smartphones en el análisis clínico ofreciendo una mejora en el diagnóstico y el tratamiento de patologías [140].

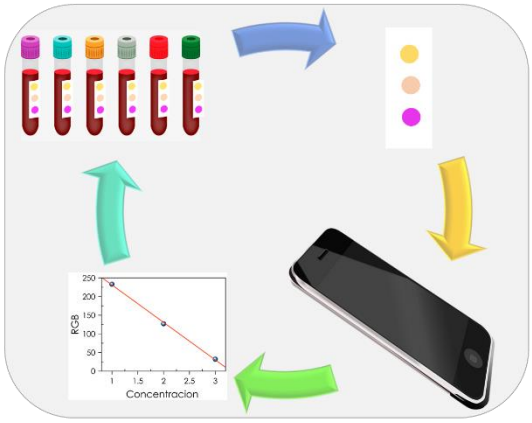

Figura 31. Esquema del análisis de una muestra empleando un Smartphone.

El uso de cámaras basadas en sensores de imagen tipo CMOS incorporadas en Smartphones como detectores ha aumentado notablemente en los últimos tiempos, siendo las imágenes obtenidas utilizadas para diferentes propósitos, pudiendo citarse como ejemplo la determinación de oxígeno usando el color de un sensor a partir de la imagen tomada con un teléfono móvil o la determinación simultanea de glucosa y medida del pH empleando un dispositivo microfluídico en papel basado en la medida de color [141].

Este incremento del uso de Smartphones como dispositivos de análisis del color se debe en gran medida a la disponibilidad de estos dispositivos por parte de los usuarios, la facilidad de manejo que presentan y la sofisticada tecnología que utilizan en su fabricación ya que poseen cámaras fotográficas integradas de gran resolución

permitiendo, además, la conexión a Internet y la transferencia de datos, lo cual se convierte en una ventaja para enviar información. Así, la mejora continua de la electrónica de los teléfonos inteligentes y el desarrollo de nuevas aplicaciones ha estimulado la investigación de detectores basados en Smartphone mediante el uso de la cámara del teléfono como un detector inteligente. Casi todos los métodos ópticos de análisis como absorbancia, reflectancia, fluorescencia, SPR, bioluminiscencia y electroquimioluminiscencia se han integrado en Smartphones para el desarrollo de diversas aplicaciones [142].

Los Smartphones pueden utilizarse como microscopios portátiles sin necesidad de utilizar lentes especiales u otros componentes ópticos, simplificando de esta forma la arquitectura del sistema de detección. Por ejemplo, mediante la toma de una fotografía de una muestra de sangre iluminada con un LED se pueden detectar micropartículas, glóbulos rojos y blancos, plaquetas y la presencia de parásitos en la muestra. La luz LED se dirige verticalmente hacia la zona del dispositivo de análisis que contiene la muestra que queremos analizar. De esta forma la luz se dispersa y refracta por la muestra. Las ondas de luz que pasan a través de los distintos componentes de la muestra crean un holograma que el teléfono puede detectar con la cámara tomando una fotografía de la misma [143]. Este sistema de detección tiene importantes características donde se incluye la compacidad, ligereza y rentabilidad lo que lo hace muy adecuado para su uso descentralizado en la fabricación de sistemas POC. Por otro lado, la resolución de las imágenes está limitada por el tamaño de los pixeles del sensor, lo que hace que el sistema sea menos preciso que un microscopio estándar. Además, la obtención de las imágenes reales requiere de un algoritmo de reconstrucción holográfica que podría reducir drásticamente la velocidad de procesamiento del teléfono afectando esto al proceso de reconstrucción holográfica.

Otro componente de los Smartphones que tiene una gran aplicabilidad en la detección óptica es la posibilidad de utilizar el flash del teléfono para iluminar las muestras al tomar la fotografía. La principal ventaja de su utilización es la homogeneidad de la luz que permite aumentar la robustez del sistema de medida [144].

Una alternativa para la utilización de los teléfonos inteligentes en aplicaciones analíticas surge de la posibilidad de conectarlos con los dispositivos de análisis a través de un puerto USB, Bluetooth o Wi-Fi. De esta manera, el dispositivo realiza la medida y el teléfono se utiliza para controlar la configuración experimental y mostrar el resultado de la prueba en la pantalla de igual forma que un miniordenador portátil [145].

La sensibilidad basada en colores ha atraído mucha atención debido a su bajo costo, simplicidad y practicidad. Las cámaras de los Smartphones usan matrices CMOS de bajo costo que responden a los niveles de los colores básicos rojo, verde y azul (RGB) produciendo resultados visuales estables de forma simple. Además, estas cámaras integran algunas funciones como el balance de blancos automático (AWB) que está diseñado para equilibrar los niveles de RGB de una fotografía con el objetivo de proporcionar una correcta reproducción del color ajustando los valores detectados con independencia del tipo de luz que ilumina la muestra.

Sin embargo, de forma general las cámaras que integran los Smartphones presentan baja sensibilidad, aunque cuentan con funciones de equilibrio de color integrados para fotografía con luz ambiental, en ocasiones resulta difícil controlar las condiciones de iluminación durante la imagen [146]. Esto es especialmente cierto fuera de ambientes controlados, tales como laboratorios y por eso es difícil realizar medidas cuantitativas precisas. Además, analizar las imágenes no siempre es fácil especialmente cuando hay pequeños cambios de color. En estos casos, no siempre es posible utilizar el espacio de color RGB por lo que se debe utilizar una alternativa como el espacio de color HSV o el CIE. Por todas estas razones, al utilizar Smartphones como sistemas de detección en el desarrollo de pruebas colorimétricas se suelen utilizar carcasas externas específicas que se acoplan al teléfono y minimizan la variación en las condiciones de iluminación y posicionamiento de la cámara. La tecnología de impresión 3D resulta muy útil para fabricar accesorios para Smartphones evitando que la luz ambiental interfiera en la imagen.

Además, el empleo de software específicos y componentes adicionales como baterías y lentes LED para la reflexión y transmisión pueden superar estas limitaciones y permitir que se realicen medidas precisas [147]. No obstante, la sensibilidad y resolución de la cámara del teléfono mejoran continuamente. Los nuevos modelos CMOS con sensores de iluminación trasera (BSI-CMOS) mejoran la calidad de la imagen. A pesar de esto su sensibilidad es aún menor que la de un CCD.

Por otro lado, el incremento del número de aplicaciones móviles que se han ido desarrollando a lo largo de los años ha aumentado las posibilidades de utilización de los Smartphones como sistema de detección. Numerosas aplicaciones permiten editar fotografías, analizar el color RGB y procesar imágenes, entre otras. Estas aplicaciones permiten el análisis de imágenes digitales y la recopilación de datos cuantitativos midiendo los cambios de color e intensidades de una fotografía [148].

REFERENCIAS

[1] R. Feynman, "There's plenty of room at the bottom," *Feynman Comput.*, pp. 63–76, 2018.

[2] N. Taniguchi, "On the Basic Concept of Nanotechnology," *Proc. Int. Conf. Prod. Eng.*, pp. 18–23, 1974.

[3] J. The Royal Society Engineering, The Royal Academy of Dowling, A Clift, R Grobert, N Hutton, D Oliver, R O'neill, O Pethica, J Pidgeon, N Porritt and E. Ryan, J Al., "Nanoscience and nanotechnologies: opportunities and uncertainties," *London R. Soc. R. Acad. Eng. Rep.*, vol. 46, no. July, pp. 618–618, 2004.

[4] I. I. 12805:2011, "Nanotechnologies-Materials specifications- Guidance on specifying nano-objects.," *Internet*, 2011.

[5] G. Guisbiers, S. Mejía-Rosales, and L. Francis, "Nanomaterial Properties: Size and Shape Dependencies," *J. Nanomater.*, vol. 2012, Dec. 2012.

[6] A. Correia, M. Pérez, J. Sáenz, and P. Serena, "Nanotechnology applications: A driving force for R&D investment," *Phys. status solidi*, vol. 204, pp. 1611–1622, Jun. 2007.

[7] A. Lapresta-Fernández, A. Fernandez, and J. Blasco, "Public concern over ecotoxicology risks from nanomaterials: Pressing need for research-based information," *Environ. Int.*, vol. 39, pp. 148–149, Feb. 2012.

[8] F. Adams and C. Barbante, "Chapter 4 - Nanotechnology and Analytical Chemistry," in *Chemical Imaging Analysis*, vol. 69, F. Adams and C. B. T.-C. A. C. Barbante, Eds. Elsevier, 2015, pp. 125–157.

[9] M. Valcárcel, B. M. Simonet, and S. Cárdenas, "Analytical nanoscience and nanotechnology today and tomorrow.," *Anal. Bioanal. Chem.*, vol. 391, no. 5, pp. 1881–1887, Jul. 2008.

[10] "Nanomaterials definition matters," *Nat. Nanotechnol.*, vol. 14, no. 3, p. 193, 2019.

[11] M. J. Pitkethly, "Nanomaterials – the driving force," *Mater. Today*, vol. 7, no. 12, Supplement, pp. 20–29, 2004.

[12] M. Bleeker, Eric A J Jong, Wim H Re, Geertsma Groenewold and A. Heugens, Evelyn Koers-Jacquemijns, Marjorie Van de meent, D Popma, Jan Rietveld, Anton Wijnhoven, Susan Cassee, Flemming Oomen, "Considerations on the EU definition of a nanomaterial: Science to support policy making," *Regul. Toxicol. Pharmacol.*, vol. 65, Nov. 2012.

[13] Z. Abdullaeva, "Classification of Nanomaterials," 2017, pp. 27–56.

[14] J. Costa-Fernandez, R. Pereiro, and A. Sanz-Medel, "The Use of Luminescent Quantum Dots for Optical Sensing," *TrAC Trends Anal. Chem.*, vol. 25, pp. 207–218, Mar. 2006.

[15] C. Carrillo-Carrión, S. Cárdenas, B. Simonet, and M. Valcárcel, "Quantum dots luminescence enhancement due to illumination with UV/Vis light," *Chem. Commun. (Camb).*, vol. 35, pp. 5214–5226, Oct. 2009.

[16] J. J. Michalet, X Pinaud, Fabien Bentolila, Laurent Tsay, J Doose, S Li and S. Gobalakrishnan, Sundaresan Wu, A M Gambhir, Shweta Weiss, "Quantum Dots for Live Cells, In Vivo Imaging, and Diagnostics," *Science*, vol. 307, pp. 538–544, Feb. 2005.

[17] J. A. García-Calzón and D. G. Marta Elena, "Synthesis and analytical potential of silica nanotubes," *TrAC Trends Anal. Chem.*, vol. 35, pp. 27–38, May 2012.

[18] M. Valcárcel and B. M. Simonet, "Nanomaterials for improved analytical processes," *Anal. Bioanal. Chem.*, vol. 399, no. 1, pp. 1–2, 2011.

[19] I. Khan, K. Saeed, and I. Khan, "Nanoparticles: Properties, applications and toxicities," *Arab. J. Chem.*, vol. 12, no. 7, pp. 908–931, 2019.

[20] W. R. Algar, K. Susumu, J. B. Delehanty, and I. L. Medintz, "Semiconductor Quantum Dots in Bioanalysis: Crossing the Valley of Death," *Anal. Chem.*, vol. 83, no. 23, pp. 8826–8837, Dec. 2011.

[21] G. Ganachari, Dr. Sharanabasava Banapurmath, Nagaraj Salimath, Basavaraja Yaradoddi, Jayachandra Shettar, Ashok Hunashyal, A M Abbaraju, Venkataraman Patil, Parvathi Shoba, H Hiremath, "Synthesis Techniques for Preparation of Nanomaterials," 2017.

[22] C. P. Devatha and A. K. Thalla, "Chapter 7 - Green Synthesis of Nanomaterials," in *Micro and Nano Technologies*, S. Mohan Bhagyaraj, O. S. Oluwafemi, N. Kalarikkal, and S. B. T.-S. of I. N. Thomas, Eds. Woodhead Publishing, 2018, pp. 169–184.

[23] S. Mourdikoudis, R. M. Pallares, and N. T. K. Thanh, "Characterization techniques for nanoparticles: comparison and complementarity upon studying nanoparticle properties," *Nanoscale*, vol. 10, no. 27, pp. 12871–12934, 2018.

[24] P.-C. Lin, S. Lin, P. C. Wang, and R. Sridhar, "Techniques for physicochemical characterization of nanomaterials," *Biotechnol. Adv.*, vol. 32, no. 4, pp. 711–726, 2014.

[25] B. Zhang and B. Yan, "Analytical strategies for characterizing the surface chemistry of nanoparticles," *Anal. Bioanal. Chem.*, vol. 396, no. 3, pp. 973–982, Feb. 2010.

[26] R. Ghosh Chaudhuri and S. Paria, "Core/Shell Nanoparticles: Classes, Properties, Synthesis Mechanisms, Characterization, and Applications," *Chem. Rev.*, vol. 112, no. 4, pp. 2373–2433, Apr. 2012.

[27] C. Barth, A. S. Foster, C. R. Henry, and A. L. Shluger, "Recent Trends in Surface Characterization and Chemistry with High-Resolution Scanning Force Methods," *Adv. Mater.*, vol. 23, no. 4, pp. 477–501, Jan. 2011.

[28] K. E. Sapsford, K. M. Tyner, B. J. Dair, J. R. Deschamps, and I. L. Medintz, "Analyzing Nanomaterial Bioconjugates: A Review of Current and Emerging Purification and Characterization Techniques," *Anal. Chem.*, vol. 83, no. 12, pp. 4453–4488, Jun. 2011.

[29] J. Tepale, Nancy Fernández-Escamilla, Víctor V. A. Carreon-Alvarez, Clara González-Coronel, Valeria J. Luna-Flores, Adan Carreon Alvarez, Alejandra Aguilar, "Nanoengineering of Gold Nanoparticles: Green Synthesis, Characterization, and Applications," *Crystals*, vol. 9, no. 12, p. 612, Nov. 2019.

[30] A. Bratovcic, "Different Applications of Nanomaterials and Their Impact on the Environment," *Int. J. Mater. Sci. Eng.*, vol. 5, pp. 1–7, Mar. 2019.

[31] J. Li, Haikuo Huang, Jiehuan Lv, Junhong An, Hongjie Zhang, Xiaodong Zhang, Zhizhou Fan, Chunhai Hu, "Nanoparticle PCR: Nanogold-assisted PCR with enhanced specificity," *Angew. Chemie - Int. Ed.*, vol. 44, no. 32, pp. 5100–5103, 2005.

[32] S. Chen, X. Hai, X.-W. Chen, and J.-H. Wang, "In Situ Growth of Silver Nanoparticles on Grapheme Quantum Dots for Ultrasensitive Colorimetric Detection of H2O2 and Glucose," *Anal. Chem.*, vol. 86, no. 13, pp. 6689–6694, Jul. 2014.

[33] Y. Liu, M. Yuan, L. Qiao, and R. Guo, "An efficient colorimetric biosensor for glucose based on peroxidase-like protein-Fe3O4 and glucose oxidase nanocomposites," *Biosens. Bioelectron.*, vol. 52, pp. 391–396, 2014.

[34] K. Komori, T. Terse-Thakoor, and A. Mulchandani, "Bioelectrochemistry of Heme Peptide at Seamless Three-Dimensional Carbon Nanotubes/Grapheme Hybrid Films for Highly Sensitive Electrochemical Biosensing," *ACS Appl. Mater. Interfaces*, vol. 7, no. 6, pp. 3647–3654, Feb. 2015.

[35] X. Kang, J. Wang, H. Wu, I. A. Aksay, J. Liu, and Y. Lin, "Glucose Oxidase–grapheme–chitosan modified electrode for direct electrochemistry and glucose sensing," *Biosens. Bioelectron.*, vol. 25, no. 4, pp. 901–905, 2009.

[36] C. Luo, Weijie Zhu, Changfeng Su, Shao Li, Di He, Yao Huang, Qing Fan, "Self-Catalyzed, Self-Limiting Growth of Glucose Oxidase-Mimicking Gold Nanoparticles," *ACS Nano*, vol. 4, no. 12, pp. 7451–7458, Dec. 2010.

[37] G. Lin, Tianran Zhong, Liangshuang Wang, Jing Guo, Liangqia Wu, Hanyin Guo, Qingquan Fu, FengFu Chen, "Graphite-like carbon nitrides as peroxidase mimetics and their applications to glucose detection," *Biosens. Bioelectron.*, vol. 59, pp. 89–93, 2014.

[38] L. Chen, Jing Ge, Jia Zhang, Lin Li, Zhaohui Li, Jianjun Sun, Yanjun Qu, "Reduced grapheme oxide nanosheets functionalized with poly(styrene sulfonate) as a peroxidase mimetic in a colorimetric assay for ascorbic acid," *Microchim. Acta*, vol. 183, no. 6, pp. 1847–1853, 2016.

[39] F. Li, Siliang Li, Hua Chen and B. Liu, Jian Zhang, Haoli Yang, Zhengyin Wang, "Strong coupled palladium nanoparticles decorated on magnetic grapheme nanosheets as enhanced peroxidase mimetics for colorimetric detection of H2O2," *Dye. Pigment.*, vol. 125, pp. 64–71, 2016.

[40] J. Liu, L. Meng, Z. Fei, P. J. Dyson, X. Jing, and X. Liu, "MnO2 nanosheets as an artificial enzyme to mimic oxidase for rapid and sensitive detection of glutathione," *Biosens. Bioelectron.*, vol. 90, pp. 69–74, 2017.

[41] Y. Tao, Y. Lin, J. Ren, and X. Qu, "Self-assembled, functionalized grapheme and DNA as a universal platform for colorimetric assays," *Biomaterials*, vol. 34, no. 20, pp. 4810–4817, 2013.

[42] Z. Zhuang, H. Lin, X. Zhang, F. Qiu, and H. Yang, "A glassy carbon electrode modified with carbon dots and gold nanoparticles for enhanced electrocatalytic oxidation and detection of nitrite," *Microchim. Acta*, vol. 183, no. 10, pp. 2807–2814, 2016.

[43] C. Herrera, Vanessa Hsu, Ssu-Chieh Joseph Rahim, Maha K Chen and J. B. Nguyen, Lisa Liu, Wendy F Haun, "Pushing the limits of detection for proteins secreted from single cells using quantum dots," *Analyst*, vol. 144, no. 3, pp. 980–989, 2019.

[44] X.-E. Ma, Yingxin Mao, Guobin Huang, Weiren Wu, Guoqiang Yin, Wen Ji, Xinghu Deng, Zishi Cai, Zhiming Zhang and Z. He, Zhike Cui, "Quantum Dot

Nanobeacons for Single RNA Labeling and Imaging," *J. Am. Chem. Soc.*, vol. 141, no. 34, pp. 13454–13458, Aug. 2019.

[45] P. Mehrotra, "Biosensors and their applications - A review," *J. oral Biol. craniofacial Res.*, vol. 6, no. 2, pp. 153–159, 2016.

[46] F. Dincer, Can Bruch, Richard Costa-Rama, Estefanía Fernández-Abedul, Maria Teresa Merkoçi, Arben Manz, Andreas Urban, Gerald Anton Güder, "Disposable Sensors in Diagnostics, Food, and Environmental Monitoring," *Adv. Mater.*, vol. 31, no. 30, 2019.

[47] M. Madou and M. Madou, *Fundamentals of microfabrication and nanotechnology*. 2012.

[48] Y. S. Rim, S.-H. Bae, H. Chen, N. De Marco, and Y. Yang, "Recent Progress in Materials and Devices toward Printable and Flexible Sensors.," *Adv. Mater.*, vol. 28, no. 22, pp. 4415–4440, Jun. 2016.

[49] Y. Yang, E. Noviana, M. P. Nguyen, B. J. Geiss, D. S. Dandy, and C. S. Henry, "Paper-Based Microfluidic Devices: Emerging Themes and Applications," *Anal. Chem.*, vol. 89, no. 1, pp. 71–91, Jan. 2017.

[50] M. M. Hamedi, A. Ainla, F. Güder, D. C. Christodouleas, M. T. Fernández-Abedul, and G. M. Whitesides, "Integrating Electronics and Microfluidics on Paper.," *Adv. Mater.*, vol. 28, no. 25, pp. 5054–5063, Jul. 2016.

[51] M. M. Hamedi, B. Ünal, E. Kerr, A. C. Glavan, M. T. Fernandez-Abedul, and G. M. Whitesides, "Coated and uncoated cellophane as materials for microplates and open-channel microfluidics devices," *Lab Chip*, vol. 16, no. 20, pp. 3885–3897, 2016.

[52] H. Golmohammadi, E. Morales-Narváez, T. Naghdi, and A. Merkoçi, "Nanocellulose in Sensing and Biosensing," *Chem. Mater.*, vol. 29, no. 13, pp. 5426–5446, Jul. 2017.

[53] A. Morales-Narváez, Eden Golmohammadi, Hamed Naghdi, Tina Yousefi, Hossein Kostiv, Uliana Horák, Daniel Pourreza, Nahid Merkoçi, "Nanopaper as an Optical Sensing Platform," *ACS Nano*, vol. 9, no. 7, pp. 7296–7305, Jul. 2015.

[54] M. Parrilla, R. Cánovas, I. Jeerapan, F. J. Andrade, and J. Wang, "A Textile-Based Stretchable Multi-Ion Potentiometric Sensor.," *Adv. Healthc. Mater.*, vol. 5, no. 9, pp. 996–1001, May 2016.

[55] M. Stoppa and A. Chiolerio, "Wearable electronics and smart textiles: a critical review.," *Sensors (Basel).*, vol. 14, no. 7, pp. 11957–11992, Jul. 2014.

[56] J.-W. Shangguan, Y. Liu, J.-B. Pan, B.-Y. Xu, J.-J. Xu, and H.-Y. Chen, "Microfluidic PDMS on paper (POP) devices.," *Lab Chip*, vol. 17, no. 1, pp. 120–127, Dec. 2016.

[57] M. Dou, D. C. Dominguez, X. Li, J. Sanchez, and G. Scott, "A versatile PDMS/paper hybrid microfluidic platform for sensitive infectious disease diagnosis.," *Anal. Chem.*, vol. 86, no. 15, pp. 7978–7986, Aug. 2014.

[58] P. P. Imani, Somayeh Bandodkar, Amay J Mohan, A M Vinu Kumar, Rajan Yu, Shengfei Wang, Joseph Mercier, "A wearable chemical-electrophysiological hybrid biosensing system for real-time health and fitness monitoring.," *Nat. Commun.*, vol. 7, p. 11650, May 2016.

[59] K. Gao, Wei Emaminejad, Sam Nyein, Hnin Yin Yin Challa, Samyuktha Chen, D. Peck, Austin Fahad, Hossain M. Ota, Hiroki Shiraki, Hiroshi Kiriya, G. A. Lien, Der Hsien Brooks, and A. Davis, Ronald W. Javey, "Fully integrated wearable sensor arrays for multiplexed in situ perspiration analysis," *Nature*, vol. 529, no. 7587, pp. 509–514, 2016.

[60] C. Guner, Hasan Ozgur, Erol Kokturk, Guzin Celik, Mehmet Esen, Elif Topal, Ahmet E Ayas, Sencer Uludag, Yildiz Elbuken and A. Dana, "A smartphone based surface plasmon resonance imaging (SPRi) platform for on-site biodetection," *Sensors Actuators B Chem.*, vol. 239, pp. 571–577, 2017.

[61] M. A. Aćimović, Srdjan S Ortega and R. Sanz, Vanesa Berthelot, Johann Garcia-Cordero, Jose L Renger, Jan Maerkl, Sebastian J Kreuzer, Mark P Quidant, "LSPR chip for parallel, rapid, and sensitive detection of cancer markers in serum.," *Nano Lett.*, vol. 14, no. 5, pp. 2636–2641, May 2014.

[62] G. Zanchetta, R. Lanfranco, F. Giavazzi, T. Bellini, and M. Buscaglia, "Emerging applications of label-free optical biosensors," *Nanophotonics*, vol. 6, Jan. 2017.

[63] D. Quesada-González and A. Merkoçi, "Mobile phone-based biosensing: An emerging 'diagnostic and communication' technology.," *Biosens. Bioelectron.*, vol. 92, pp. 549–562, Jun. 2017.

[64] D. Quesada-González and A. Merkoçi, "Nanomaterial-based devices for point-of-care diagnostic applications," *Chem. Soc. Rev.*, vol. 47, no. 13, pp. 4697–4709, 2018.

[65] J. Wang, "Electrochemical biosensors: Towards point-of-care cancer diagnostics," *Biosens. Bioelectron.*, vol. 21, no. 10, pp. 1887–1892, 2006.

[66] A. J. Bard, L. R. Faulkner, E. Swain, and C. Robey, *Fundamentals and*

Applications. .

[67] Q. Han, Su-Ting Peng, Haiyan Sun, K.-S. Venkatesh, Shishir Chung, and V. A. L. Lau, Siu Chuen Zhou, Ye Roy, "An Overview of the Development of Flexible Sensors.," *Adv. Mater.*, vol. 29, no. 33, Sep. 2017.

[68] M. Zourob, *Recognition Receptors in Biosensors*. 2010.

[69] J. Yang, K. Wang, H. Xu, W. Yan, Q. Jin, and D. Cui, "Talanta Detection platforms for point-of-care testing based on colorimetric , luminescent and magnetic assays : A review," *Talanta*, vol. 202, no. April, pp. 96–110, 2019.

[70] P. Yager, G. J. Domingo, and J. Gerdes, "Point-of-Care Diagnostics for Global Health," *Annu. Rev. Biomed. Eng.*, vol. 10, no. 1, pp. 107–144, Jul. 2008.

[71] C. A. Holland and F. L. Kiechle, "Point-of-care molecular diagnostic systems — past, present and future," *Curr. Opin. Microbiol.*, vol. 8, no. 5, pp. 504–509, 2005.

[72] E. Aronoff-Spencer, A. G. Venkatesh, A. Sun, H. Brickner, D. Looney, and D. A. Hall, "Detection of Hepatitis C core antibody by dual-affinity yeast chimera and smartphone-based electrochemical sensing.," *Biosens. Bioelectron.*, vol. 86, pp. 690–696, Dec. 2016.

[73] G. M. Ainla, Alar Mousavi, Maral P S Tsaloglou, Maria-Nefeli Redston, Julia Bell, Jeffrey G Fernández-Abedul, M Teresa Whitesides, "Open-Source Potentiostat for Wireless Electrochemical Detection with Smartphones.," *Anal. Chem.*, vol. 90, no. 10, pp. 6240–6246, May 2018.

[74] A. K. Yetisen, M. S. Akram, and C. R. Lowe, "Paper-based microfluidic point-of-care diagnostic devices," *Lab Chip*, vol. 13, no. 12, pp. 2210–2251, 2013.

[75] E. Gabriel, P. Garcia, F. Lopes, and W. Coltro, "Paper-Based Colorimetric Biosensor for Tear Glucose Measurements," *Micromachines*, vol. 8, Mar. 2017.

[76] M.-N. Verma, Mohit S Tsaloglou, D. Sisley, Tyler Christodouleas, and G. M. Chen, Austin Milette, Jonathan Whitesides, "Sliding-strip microfluidic device enables ELISA on paper.," *Biosens. Bioelectron.*, vol. 99, pp. 77–84, Jan. 2018.

[77] D. M. Cate, S. D. Noblitt, J. Volckens, and C. S. Henry, "Multiplexed paper analytical device for quantification of metals using distance-based detection.," *Lab Chip*, vol. 15, no. 13, pp. 2808–2818, Jul. 2015.

[78] M. O. Ismail, Abdulghani Araújo, F. Chagas, Cyro L S Griveau, Sophie D'Orlyé, Fanny Varenne, Anne Bedioui, and W. K. T. Coltro, "Colorimetric analysis of the decomposition of S-nitrosothiols on paper-based microfluidic devices," *Analyst*, vol. 141, no. 22, pp. 6314–6320, 2016.

[79] R. M. Koh, Ahyeon Kang, Daeshik Xue, Yeguang Lee, Seungmin Pielak *et al.*, "A soft, wearable microfluidic device for the capture, storage, and colorimetric sensing of sweat," *Sci. Transl. Med.*, vol. 8, no. 366, 2016.

[80] M. Parrilla, I. Ortiz-Gómez, R. Cánovas, A. Salinas-Castillo, M. Cuartero, and G. A. Crespo, "Wearable Potentiometric Ion Patch for On-Body Electrolyte Monitoring in Sweat: Toward a Validation Strategy to Ensure Physiological Relevance," *Anal. Chem.*, vol. 91, no. 13, pp. 8644–8651, Jul. 2019.

[81] D. Zhang and Q. Liu, "Biosensors and bioelectronics on smartphone for portable biochemical detection," *Biosens. Bioelectron.*, vol. 75, pp. 273–284, 2016.

[82] C. Xu, Gang Cheng, L. Yuan, Wei Liu, Zhaoyang Zhu, Z. Li, Xintong Lu, Yanli Chen, J. Liu, Jinglong Cui, Zheng Liu, and Q. Men, Hong Liu, "Smartphone-based battery-free and flexible electrochemical patch for calcium and chloride ions detections in biofluids," *Sensors Actuators B Chem.*, vol. 297, p. 126743, 2019.

[83] G. Fuertes, I. Soto, R. Carrasco, M. Vargas, J. Sabattin, and C. Lagos, "Intelligent Packaging Systems: Sensors and Nanosensors to Monitor Food Quality and Safety," *J. Sensors*, vol. 2016, p. 4046061, 2016.

[84] A. Mishra, Rupesh K Hubble, Lee J Martín, Aida Kumar, Rajan Barfidokht and J. Kim, Jayoung Musameh, Mustafa M Kyratzis, Ilias L Wang, "Wearable Flexible and Stretchable Glove Biosensor for On-Site Detection of Organophosphorus Chemical Threats.," *ACS sensors*, vol. 2, no. 4, pp. 553–561, Apr. 2017.

[85] M. I. G. S. Almeida, B. M. Jayawardane, S. D. Kolev, and I. D. McKelvie, "Developments of microfluidic paper-based analytical devices (μPADs) for water analysis: A review," *Talanta*, vol. 177, pp. 176–190, 2018.

[86] A. Yakoh, P. Rattanarat, W. Siangproh, and O. Chailapakul, "Simple and selective paper-based colorimetric sensor for determination of chloride ion in environmental samples using label-free silver nanoprisms.," *Talanta*, vol. 178, pp. 134–140, Feb. 2018.

[87] D. Martín-Yerga, I. Álvarez-Martos, M. C. Blanco-López, C. S. Henry, and M. T. Fernández-Abedul, "Point-of-need simultaneous electrochemical detection of lead and cadmium using low-cost stencil-printed transparency electrodes.," *Anal. Chim. Acta*, vol. 981, pp. 24–33, Aug. 2017.

[88] J. Chouler, Á. Cruz-Izquierdo, S. Rengaraj, J. L. Scott, and M. Di Lorenzo, "A screen-printed paper microbial fuel cell biosensor for detection of toxic compounds in water.," *Biosens. Bioelectron.*, vol. 102, pp. 49–56, Apr. 2018.

[89] C. Warwick, A. Guerreiro, and A. Soares, "Sensing and analysis of soluble phosphates in environmental samples: A review," *Biosens. Bioelectron.*, vol. 41, pp. 1–11, 2013.

[90] J. Van Dorst, Bieke Mehta, R. Bekaert, Karen Rouah-Martin, Elsa De Coen, Wim Dubruel, Peter Blust, and J. Robbens, "Recent advances in recognition elements of food and environmental biosensors: A review," *Biosens. Bioelectron.*, vol. 26, no. 4, pp. 1178–1194, 2010.

[91] A. Salim and S. Lim, "Recent advances in noninvasive flexible and wearable wireless biosensors," *Biosens. Bioelectron.*, vol. 141, p. 111422, Sep. 2019.

[92] W. Dang, L. Manjakkal, W. T. Navaraj, L. Lorenzelli, V. Vinciguerra, and R. Dahiya, "Stretchable wireless system for sweat pH monitoring," *Biosens. Bioelectron.*, vol. 107, pp. 192–202, Jun. 2018.

[93] Z. Luo, Q. Qi, L. Zhang, R. Zeng, L. Su, and D. Tang, "Branched Polyethylenimine-Modified Upconversion Nanohybrid-Mediated Photoelectrochemical Immunoassay with Synergistic Effect of Dual-Purpose Copper Ions," *Anal. Chem.*, vol. 91, no. 6, pp. 4149–4156, Mar. 2019.

[94] R. Zhao, S. Lin, H. Yuk, and X. Zhao, "Kirigami enhances film adhesion," *Soft Matter*, vol. 14, no. 13, pp. 2515–2525, 2018.

[95] K. Gao, Wei Emaminejad, Sam Nyein, Hnin Yin Yin Challa, Samyuktha Chen, D. Peck, Austin Fahad, Hossain M. Ota, Hiroki Shiraki, Hiroshi Kiriya, G. A. Lien, Der-Hsien Brooks, and A. Davis, Ronald W. Javey, "Fully integrated wearable sensor arrays for multiplexed in situ perspiration analysis," *Nature*, vol. 529, no. 7587, pp. 509–514, Jan. 2016.

[96] J. Jia, Wenzhao Bandodkar, Amay J. Valdés-Ramírez, Gabriela Windmiller, Joshua R. Yang, Zhanjun Ramírez, Julian Chan, Garrett Wang, "Electrochemical Tattoo Biosensors for Real-Time Noninvasive Lactate Monitoring in Human Perspiration," *Anal. Chem.*, vol. 85, no. 14, pp. 6553–6560, Jul. 2013.

[97] D. Bandodkar, Amay J. Molinnus and J. Mirza, Omar Guinovart, Tomás Windmiller, Joshua R. Valdés-Ramírez, Gabriela Andrade, Francisco J. Schöning, Michael J. Wang, "Epidermal tattoo potentiometric sodium sensors with wireless signal transduction for continuous non-invasive sweat monitoring," *Biosens. Bioelectron.*, vol. 54, pp. 603–609, Apr. 2014.

[98] J. Sempionatto, Juliane R. Nakagawa, Tatsuo Pavinatto, Adriana Mensah, Samantha T. Imani, Somayeh Mercier, Patrick Wang, "Eyeglasses based wireless

electrolyte and metabolite sensor platform," *Lab Chip*, vol. 17, no. 10, pp. 1834–1842, 2017.

[99] K. Gao, Wei Emaminejad, Sam Nyein, Hnin Yin Yin Challa, Samyuktha Chen and A. Peck, Austin Fahad, Hossain M. Ota, Hiroki Shiraki, Hiroshi Kiriya, Daisuke Lien, Der-Hsien Brooks, George A. Davis, Ronald W. Javey, "Fully integrated wearable sensor arrays for multiplexed in situ perspiration analysis," *Nature*, vol. 529, no. 7587, pp. 509–514, 2016.

[100] A. Salim and S. Lim, "Recent advances in noninvasive flexible and wearable wireless biosensors," *Biosens. Bioelectron.*, vol. 141, no. June, p. 111422, 2019.

[101] Z. Yu, Y. Tang, G. Cai, R. Ren, and D. Tang, "Paper Electrode-Based Flexible Pressure Sensor for Point-of-Care Immunoassay with Digital Multimeter," *Anal. Chem.*, vol. 91, no. 2, pp. 1222–1226, Jan. 2019.

[102] J. Heikenfeld, J. Jajack, A. Rogers, J. Gutruf, P. Tian, L. Pan, T. Li, R. Khine, M. Kim, J. Wang, J. Kim, J. Rogers, J. Gutruf, P. Tian, L. Pan, T. Li, R. Khine, M. Kim, J. Wang, J. Kim, "Wearable sensors: modalities, challenges, and prospects," *Lab Chip*, vol. 18, no. 2, pp. 217–248, 2018.

[103] A. M. Foudeh, T. Fatanat Didar, T. Veres, and M. Tabrizian, "Microfluidic designs and techniques using lab-on-a-chip devices for pathogen detection for point-of-care diagnostics," *Lab Chip*, vol. 12, no. 18, pp. 3249–3266, 2012.

[104] J.-Y. Yoon and B. Kim, "Lab-on-a-Chip Pathogen Sensors for Food Safety," *Sensors (Basel).*, vol. 12, pp. 10713–10741, Dec. 2012.

[105] R. Pol, F. Céspedes, D. Gabriel, and M. Baeza, "Microfluidic lab-on-a-chip platforms for environmental monitoring," *TrAC Trends Anal. Chem.*, vol. 95, pp. 62–68, 2017.

[106] D. Mark, S. Haeberle, G. Roth, F. von Stetten, and R. Zengerle, "Microfluidic lab-on-a-chip platforms: requirements{,} characteristics and applications," *Chem. Soc. Rev.*, vol. 39, no. 3, pp. 1153–1182, 2010.

[107] A. W. Martinez, S. T. Phillips, M. J. Butte, and G. M. Whitesides, "Patterned paper as a platform for inexpensive, low-volume, portable bioassays.," *Angew. Chem. Int. Ed. Engl.*, vol. 46, no. 8, pp. 1318–1320, 2007.

[108] D. M. Cate, J. A. Adkins, J. Mettakoonpitak, and C. S. Henry, "Recent developments in paper-based microfluidic devices," *Anal. Chem.*, vol. 87, no. 1, pp. 19–41, 2015.

[109] Y. Xia, J. Si, and Z. Li, "Fabrication techniques for microfluidic paper-based

analytical devices and their applications for biological testing: A review.," *Biosens. Bioelectron.*, vol. 77, pp. 774–789, Mar. 2016.

[110] K. Abe, K. Suzuki, and D. Citterio, "Inkjet-Printed Microfluidic Multianalyte Chemical Sensing Paper," *Anal. Chem.*, vol. 80, no. 18, pp. 6928–6934, Sep. 2008.

[111] K. Maejima, S. Tomikawa, K. Suzuki, and D. Citterio, "Inkjet printing: an integrated and green chemical approach to microfluidic paper-based analytical devices," *RSC Adv.*, vol. 3, no. 24, pp. 9258–9263, 2013.

[112] X. Li, J. Tian, T. Nguyen, and W. Shen, "Paper-Based Microfluidic Devices by Plasma Treatment," *Anal. Chem.*, vol. 80, no. 23, pp. 9131–9134, Dec. 2008.

[113] W. Dungchai, O. Chailapakul, and C. S. Henry, "A low-cost, simple, and rapid fabrication method for paper-based microfluidics using wax screen-printing.," *Analyst*, vol. 136, no. 1, pp. 77–82, Jan. 2011.

[114] E. Carrilho, A. W. Martinez, and G. M. Whitesides, "Understanding Wax Printing: A Simple Micropatterning Process for Paper-Based Microfluidics," *Anal. Chem.*, vol. 81, no. 16, pp. 7091–7095, Aug. 2009.

[115] Y. Lu, W. Shi, L. Jiang, J. Qin, and B. Lin, "Rapid prototyping of paper-based microfluidics with wax for low-cost, portable bioassay.," *Electrophoresis*, vol. 30, no. 9, pp. 1497–1500, May 2009.

[116] U. T. Sriram, Ganesan Bhat, Mahesh P Patil, Pravin Uthappa, T. M. Jung, Ho-Young Altalhi, Tariq Kumeria, Tushar Aminabhavi, and M. D. Pai, Ranjith Krishna Madhuprasad Kurkuri, "Paper-based microfluidic analytical devices for colorimetric detection of toxic ions: A review," *TrAC Trends Anal. Chem.*, vol. 93, pp. 212–227, 2017.

[117] E. M. Fenton, M. R. Mascarenas, G. P. López, and S. S. Sibbett, "Multiplex Lateral-Flow Test Strips Fabricated by Two-Dimensional Shaping," *ACS Appl. Mater. Interfaces*, vol. 1, no. 1, pp. 124–129, Jan. 2009.

[118] J. Nie, Y. Liang, Y. Zhang, S. Le, D. Li, and S. Zhang, "One-step patterning of hollow microstructures in paper by laser cutting to create microfluidic analytical devices," *Analyst*, vol. 138, no. 2, pp. 671–676, 2013.

[119] D. M. Cate, J. A. Adkins, J. Mettakoonpitak, and C. S. Henry, "Recent Developments in Paper-Based Microfluidic Devices," *Anal. Chem.*, vol. 87, no. 1, pp. 19–41, Jan. 2015.

[120] W. Dungchai, O. Chailapakul, and C. S. Henry, "Electrochemical detection for paper-based microfluidics.," *Anal. Chem.*, vol. 81, no. 14, pp. 5821–5826, Jul.

2009.

[121] G. G. Morbioli, T. Mazzu-Nascimento, A. M. Stockton, and E. Carrilho, "Technical aspects and challenges of colorimetric detection with microfluidic paper-based analytical devices (μPADs) - A review.," *Anal. Chim. Acta*, vol. 970, pp. 1–22, Jun. 2017.

[122] J. L. Delaney, C. F. Hogan, J. Tian, and W. Shen, "Electrogenerated Chemiluminescence Detection in Paper-Based Microfluidic Sensors," *Anal. Chem.*, vol. 83, no. 4, pp. 1300–1306, Feb. 2011.

[123] E. F. M. Gabriel, P. T. Garcia, F. M. Lopes, and W. K. T. Coltro, "Paper-Based Colorimetric Biosensor for Tear Glucose Measurements," *Micromachines*, vol. 8, no. 4, p. 104, Mar. 2017.

[124] L. F. Lopez-Ruiz, Nuria Curto, Vincenzo F. Erenas, Miguel M. Benito-Lopez, Fernando Diamond, Dermot Palma, Alberto J. Capitan-Vallvey, "Smartphone-based simultaneous pH and nitrite colorimetric determination for paper microfluidic devices.," *Anal. Chem.*, vol. 86, no. 19, pp. 9554–9562, Oct. 2014.

[125] J. R. Lakowicz and B. R. Masters, "Principles of Fluorescence Spectroscopy, Third Edition," *J. Biomed. Opt.*, vol. 13, no. 2, p. 029901, 2008.

[126] K. Yamada, S. Takaki, N. Komuro, K. Suzuki, and D. Citterio, "An antibody-free microfluidic paper-based analytical device for the determination of tear fluid lactoferrin by fluorescence sensitization of Tb3+," *Analyst*, vol. 139, no. 7, pp. 1637–1643, 2014.

[127] X. Liu, C. Zong, and L. Lu, "Fluorescent silver nanoclusters for user-friendly detection of Cu2+ on a paper platform," *Analyst*, vol. 137, no. 10, pp. 2406–2414, 2012.

[128] H. H. Nguyen, J. Park, S. Kang, and M. Kim, "Surface plasmon resonance: a versatile technique for biosensor applications.," *Sensors (Basel).*, vol. 15, no. 5, pp. 10481–10510, May 2015.

[129] V. Hamedpour, G. J. Postma, E. van den Heuvel, J. J. Jansen, K. Suzuki, and D. Citterio, "Chemometrics-assisted microfluidic paper-based analytical device for the determination of uric acid by silver nanoparticle plasmon resonance," *Anal. Bioanal. Chem.*, vol. 410, no. 9, pp. 2305–2313, 2018.

[130] Y. A. Zolotov, V.M.Ivanov, and V. Amelin, *Chemical test methods of analysis*. 2002.

[131] R. E. Oesper, "History of analytical chemistry (Szabadvary, Ferenc)," *J. Chem.*

Educ., vol. 44, no. 1, p. A62, Jan. 1967.

[132] C.-M. Martinez, Andres W Phillips, Scott T Nie, Zhihong Cheng and G. M. Carrilho, Emanuel Wiley, Benjamin J Whitesides, "Programmable diagnostic devices made from paper and tape.," *Lab Chip*, vol. 10, no. 19, pp. 2499–2504, Oct. 2010.

[133] S. Cotton, "Colour, colour spaces and the human visual system," *Univ. Birmingham, Sch. Comput. Sci. …*, 1995.

[134] D. Pascale, "A review of RGB color spaces... from xyY to R'G'B'," *Babel Color*, pp. 1–35, 2003.

[135] G. Schleyer, G. Lefranc, C. Cubillos, G. Millán, and R. Osorio, "A new method for colour image segmentation," *Int. J. Comput. Commun. Control*, vol. 11, p. 860, Oct. 2016.

[136] A. Ford and A. R. Alanrobertsrdbbccouk, "Colour Space Conversions," vol. 1998, pp. 1–31, 1998.

[137] M. O. Salles, G. N. Meloni, W. R. de Araujo, and T. R. L. C. Paixão, "Explosive colorimetric discrimination using a smartphone{,} paper device and chemometrical approach," *Anal. Methods*, vol. 6, no. 7, pp. 2047–2052, 2014.

[138] V. K. Rajendran, P. Bakthavathsalam, and B. M. Jaffar Ali, "Smartphone based bacterial detection using biofunctionalized fluorescent nanoparticles," *Microchim. Acta*, vol. 181, no. 15, pp. 1815–1821, 2014.

[139] L. F. García, Antonio Erenas, M M Marinetto, Eugenio D Abad, Carlos A de Orbe-Paya, Ignacio Palma, Alberto J Capitán-Vallvey, "Mobile phone platform as portable chemical analyzer," *Sensors Actuators B Chem.*, vol. 156, no. 1, pp. 350–359, 2011.

[140] A. Roda, E. Michelini, M. Zangheri, M. Di Fusco, D. Calabria, and P. Simoni, "Smartphone-based biosensors: A critical review and perspectives," *TrAC Trends Anal. Chem.*, vol. 79, pp. 317–325, 2016.

[141] U. M. Jalal, G. J. Jin, and J. S. Shim, "Paper–Plastic Hybrid Microfluidic Device for Smartphone-Based Colorimetric Analysis of Urine," *Anal. Chem.*, vol. 89, no. 24, pp. 13160–13166, Dec. 2017.

[142] P. P. Gallegos, Dustin Long, Kenneth D Yu, Hojeong Clark and B. T. Lin, Yixiao George, Sherine Nath, Pabitra Cunningham, "Label-free biodetection using a smartphone," *Lab Chip*, vol. 13, no. 11, pp. 2124–2132, 2013.

[143] A. Tseng, Derek Mudanyali, Onur Oztoprak, Cetin Isikman, Serhan O Sencan,

Ikbal Yaglidere, Oguzhan Ozcan, “Lensfree microscopy on a cellphone,” *Lab Chip*, vol. 10, no. 14, pp. 1787–1792, 2010.

[144] V. Oncescu, M. Mancuso, and D. Erickson, “Cholesterol testing on a smartphone,” *Lab Chip*, vol. 14, no. 4, pp. 759–763, 2014.

[145] E. Stedtfeld, Robert D Tourlousse, Dieter M Seyrig, Gregoire Stedtfeld, Tiffany M Kronlein, Maggie Price, Scott Ahmad, Farhan Gulari and S. A. Tiedje, James M Hashsham, “Gene-Z: a device for point of care genetic testing using a smartphone,” *Lab Chip*, vol. 12, no. 8, pp. 1454–1462, 2012.

[146] L. Shen, J. A. Hagen, and I. Papautsky, “Point-of-care colorimetric detection with a smartphone,” *Lab Chip*, vol. 12, no. 21, pp. 4240–4243, 2012.

[147] A. I. Barbosa, P. Gehlot, K. Sidapra, A. D. Edwards, and N. M. Reis, “Portable smartphone quantitation of prostate specific antigen (PSA) in a fluoropolymer microfluidic device,” *Biosens. Bioelectron.*, vol. 70, pp. 5–14, 2015.

[148] Y. Liu, Tao Zhang, Shuxin Liu, Wei Zhao, Shun Lu, Zhiwei Wang and H. Wang, Guangtu Zou, Ping Wang, Xianxiang Zhao, Qingbiao Rao, “Smartphone based platform for ratiometric fluorometric and colorimetric determination H2O2 and glucose,” *Sensors Actuators B Chem.*, vol. 305, p. 127524, 2020.

ÍNDICE DE FIGURAS

Figura 1. Escala de longitud que muestra el nanómetro 3
Figura 2. Áreas de aplicación extraída de la base de datos 5
Figura 3. Vínculo entre la Química Analítica y la Nanociencia y Nanotecnología . 6
Figura 4. Espectros de emisión de nanopartículas de diferente tamaño. Imagen modificada de [20] 12
Figura 5. Alternativas de síntesis de nanomateriales 14
Figura 6. Esquema de funcionamiento de un sensor 22
Figura 7. Sistemas de transducción óptica [41] 29
Figura 8. Sistemas de transducción electroquímica [41] 31
Figura 9. Esquema de producción de elementos de reconocimiento [41] 33
Figura 10. Ejemplos de dispositivos POCT comerciales [41] 36
Figura 11. Dispositivos de diagnóstico portátiles [41] 38
Figura 12. Sensores desechables para el análisis de alimentos[41] 41
Figura 13. Sensores desechables empleados en el control medioambiental [41] ... 43
Figura 14. Biosensores portátiles no invasivos para el control de parámetros biométricos. Figura modificada de [94] 45
Figura 15. Diagrama de la sección transversal de la piel humana 46
Figura 16. Tendencias actuales de la Química Analítica 49
Figura 17. Clasificación de las plataformas microfluídicas 50
Figura 18. Test de flujo lateral 52
Figura 19. Representación de las partes y respuesta del µPAD. Imagen extraída de [101] 53
Figura 20. Número de publicaciones científicas entre 2005 y 2019 obtenido de la base de datos de Scopus para el término "Microfluidic Paper-based Analytical Device", A) Publicaciones científicas por año B) Publicaciones científicas por área de aplicación 53
Figura 21. Esquema de las principales técnicas de fabricación de µPAD 56
Figura 22. Ejemplos de µPADs diseñados mediante: A) Fotolitografía, B) grabado con chorro de tinta, C) tratamiento con plasma, D) impresión con cera, E) impresión por flexografía, F) serigrafía, G) corte con plotter, H) impresión por corte con láser. Figuras extraídas de [69] y [113] 60

Figura 23. Reacciones catalíticas implicadas en la determinación óptica de glucosa. Espectros de absorción del TMB en la determinación de glucosa 62
Figura 24. Ilustración esquemática del µPAD usado para la determinación de nitrito y pH en muestras de agua usando un teléfono móvil para la detección colorimétrica. Esquema extraído de [104]..... 64
Figura 25. Diagrama de Jablonski 65
Figura 26. Esquema de los componentes de un sistema SPR 68
Figura 27. µPAD para la determinación de ácido úrico basado en un sistema SPR empleando nanopartículas de plata. Imagen extraída y modificada de [109] 72
Figura 28. Síntesis aditiva del color en el espacio de color RGB 77
Figura 29. Representación del espacio de color HSV 78
Figura 30. Ecuaciones para la transformación de los espacios de color RGB y HSV 79
Figura 31. Esquema del análisis de una muestra empleando un Smartphone..... 82

ÍNDICE DE TABLAS

Tabla 1. Comparación de las técnicas convencionales de análisis con el uso de sensores desechables. 24
Tabla 2. Longitudes de onda asociados a los colores absorbidos y reflejados. 71

EXPERIMENTAL

Capítulo 1

TETRAZINE-BASED CHEMISTRY FOR NITRITE DETERMINATION IN A PAPER MICROFLUIDIC DEVICE

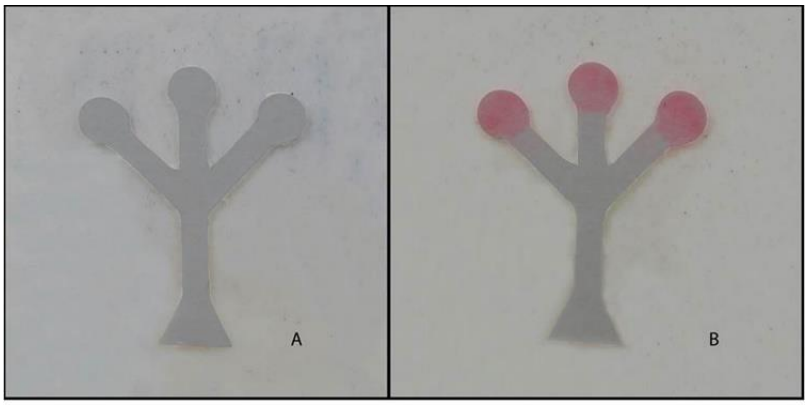

Published in Talanta 2016, 160, 721-728

CAPÍTULO 1: TETRAZINE-BASED CHEMISTRY FOR NITRITE DETERMINATION IN A PAPER MICROFLUIDIC DEVICE

Inmaculada Ortiz-Gomez[a], Mariano Ortega-Muñoz[b] Alfonso Salinas-Castillo[a], Maria Ariza Avidad[a], Ignacio de Orbe-Payá[a], Francisco Santoyo-Gonzalez[b], Luis Fermin Capitan-Vallvey[a]

[a]Department of Analytical Chemistry, Campus Fuentenueva, Faculty of Sciences, 18071, University of Granada, Spain.

[b]Department of Organic Chemistry, Campus Fuentenueva, Faculty of Sciences, 18071, University of Granada, Spain.

Planteamiento

Altas concentraciones de nitrito en agua son comunes debido a la utilización intensiva de fertilizantes que contienen compuestos nitrogenados. Esta incorporación excesiva de nitrito en agua afecta a su calidad y supone un riesgo para la salud humana. Por tanto, la determinación de nitrito en agua presenta una gran importancia debido principalmente al efecto perjudicial que puede provocar su ingesta en el cuerpo humano. Se ha comprobado que el nitrito puede reaccionar con compuestos hidrosolubles del cuerpo formando N-nitrosaminas cancerígenas e interfiriendo en el transporte de oxígeno en la sangre lo que conlleva a una metahemoglobinemia entre otros efectos dañinos sobre la salud [1]. En este sentido, la Agencia de protección del medio ambiente de la Unión Europea ha establecido como nivel máximo de nitrito en agua una concentración de 0. 5 mg/L o una concentración de 1 mg/L medido como nitrógeno, considerándose contaminante concentraciones superiores a la establecida [2], [3].

En consecuencia, numerosas técnicas analíticas donde se incluye la espectrofotometría UV-vis, luminiscencia, electroquímica y técnicas de separación como la cromatografía o la electroforesis capilar se han empleado para la determinación de nitrito en agua. Sin embargo, estas técnicas de análisis a menudo implican una laboriosa y lenta preparación de las muestras para el análisis y requieren personal altamente cualificado. Por todo ello, surge hoy en día, la necesidad del desarrollo de nuevas técnicas de análisis más rentables para la monitorización de forma rápida de este tipo de contaminantes.

Así, el desarrollo de µPADs se ha propuesto en numerosas publicaciones científicas [4]–[10] como dispositivos idóneos para satisfacer estas características en el análisis de nitrito

en agua, alimentos (encurtidos y vegetales) y muestras biológicas como saliva, sudor, orina, etc.

En este sentido, los µPADs desarrollados se basan en la determinación colorimétrica de nitrito mediante la reacción de Griess. Esta reacción implica la formación de una sal de diazonio de estructura general $R{-}N_2^+X^-$ por reacción de nitrito en medio ácido con una amina aromática primaria como es el ácido sulfanílico y la posterior reacción de la sal de diazonio con α-naftilamina originando una azoderivado de color magenta (R-N=N-R') [11].

En los últimos años se han publicado numerosos trabajos científicos donde se desarrollan métodos colorimétricos basados en esta reacción pero incorporando ciertas modificaciones. Un claro ejemplo de esto, es el trabajo de Thiago M. G y col. [10]. En este estudio, se propone como método de análisis un µPAD para la determinación de nitrito en tres tipos de muestras: agua, alimentos y saliva. La reacción colorimétrica de determinación de nitrito en este trabajo se basa en la reacción de Griess modificada, en la que se reemplaza el ácido sulfanílico por sulfanilamida de esta forma la cinética de la reacción es más rápida y la estabilidad del colorante formado mejora notablemente. Thiago y col. se basan en los resultados de Bhakta y col. [12] los cuales aseguran que cuanto más fuerte es el ácido empleado en la reacción mayor es la sensibilidad analítica del método. No obstante, el principal inconveniente que presenta el reactivo de Griess en la determinación colorimétrica de nitrito, es su baja estabilidad. De esta forma, las características analíticas del µPAD desarrollado pueden verse afectadas según el tipo de almacenamiento y el modo de uso de éste.

Por todo ello, teniendo en cuenta estas consideraciones en este Capítulo proponemos una alternativa a la reacción de Griess para determinación colorimétrica de nitrito implementada en un µPAD con el fin de obtener una fase sensora más estable, con mejores características analíticas y capacidad de ser aplicada satisfactoriamente en el análisis y la determinación de nitrito en muestras reales.

Objetivo

El objetivo del primer capítulo de esta Memoria es desarrollar un nuevo método de determinación de nitrito utilizando un dispositivo microfluídico basado en papel (µPAD) incorporando una tetrazina como elemento de reconocimiento selectivo y utilizando como propiedad analítica el color medido al analizar una fotografía del µPAD, después de adicionar la muestra y que tenga lugar la reacción colorimétrica, con una cámara fotográfica o bien un Smartphone.

Para lograr este objetivo, se trabajo en colaboración con el Grupo de Investigación FQM-208 pertenecientes al Departamento de Química Orgánica de la Universidad de Granada con quienes se llevó a cabo la síntesis y caracterización del compuesto 1, 2-dihidro-3, 6-bis (3, 5-dimetil-1H-pirazol-1-il) 1, 2, 4, 5-tetrazina (DHBPTz) que ha sido empleado como reactivo cromogénico para la determinación colorimétrica de nitrito. A continuación, se llevó a cabo el diseño del µPAD de forma que incorpore todas las operaciones analíticas necesarias para la reacción y medida de nitrito. Asimismo, se ha realizado un estudio de todas las variables influyentes sobre la reacción y sobre la medida de color en esta determinación y, por último, se ha realizado una caracterización del método propuesto. Además, se ha llevado a cabo la determinación colorimétrica de nitrito en muestras reales de distintos tipos de agua (embotellada y agua corriente). Por último, se han comparado los resultados obtenidos del análisis cuantitativo de nitrito haciendo uso de una cámara fotográfica con los resultados obtenidos mediante el empleo de un Smartphone.

Las etapas de las que consta este trabajo pueden resumirse en:

1. Síntesis y caracterización de 1, 2-dihidro-3, 6-bis (3, 5-dimetil-1H-pirazol-1-il) 1, 2, 4, 5-tetrazina (DHBPTz).
2. Diseño y fabricación del µPAD.
3. Optimización de las variables influyentes en la determinación de nitrito.
4. Caracterización analítica del método propuesto.
5. Determinación de nitrito en muestras de agua.
6. Comparativa del empleo utilizando una cámara fotográfica y un Smartphone como sistemas de detección.

TETRAZINE-BASED CHEMISTRY FOR NITRITE DETERMINATION IN A PAPER MICROFLUIDIC DEVICE

Abstract

We present a new chemistry to determine nitrites implemented in a microfluidic paper-based analytical device (μPAD). The device is fabricated in cellulose paper with a sample reception area and three replicate detection areas with recognition chemistry immobilized by adsorption. The method involves the use of nitrite in an acid medium reaction to generate nitrous acid, which produces the oxidation of s-dihydrotetrazine: 1, 2-dihydro-3, 6 - bis (3, 5-dimethyl-1H-pyrazol-1-yl) -1, 2, 4, 5-tetrazine (DHBPTz), which change the detection zone from colorless to pink. We used a digital camera for the quantitative analysis of nitrite with the color coordinate S of the HSV color space as the analytical parameter. Parameters such as concentration and volume of s-dihydrotetrazine, pH, sample volume and reaction time were studied. The detection limit for this method is 1.38 μM nitrite. To estimate the selectivity of the method an interference study of common ions in water samples was performed. The procedure was applied to natural water and compared with reference procedures.

Keywords: Tetrazine · Photographic camera and smartphone · Colorimetric assay · Microfluidic paper-based device · Nitrite determination

1. Introduction

Nitrite is a ubiquitous and naturally occurring species that plays an important role in different physiological, food, environmental and industrial systems. Different approaches have been used for analysis, with the most common being spectrophotometric, luminescent, potentiometric, amperometric, and separative procedures [11], [13], [14]. Most spectrophotometric methods use the Griess reaction based on azo dye formation [15] in different variants because it offers the right balance between simplicity, instrumental needs, cost and sensitivity [12]. These methods, however, have several drawbacks such as the need to control the pH, the temperature, the use of multiple reagents, some of them carcinogenic, and a long reaction time [16]. To overcome some

of these disadvantages, we have developed a user-friendly paper-based device based on a new s-tetrazine-based chemistry for nitrite determination that is being presented for the first time, to the best of our knowledge.

s-Tetrazines, a class of high-nitrogen organic compounds, have received much synthetic attention because of their inherent biological potential [17], [18]. They have also been frequently used as building blocks in organic transformations or as bridging ligands in metal complexes [17], [19], [20]. In particular, 1, 2, 4, 5-tetrazines [21], [22] are the most important class of tetrazines that, due to the four electronegative nitrogen atoms in the tetrazine ring, have great synthetic utility and are capable of participating in strain-promoted inverse-electron-demand Diels–Alder cycloaddition reactions with an applicability in bioconjugation [23]–[25]. They also provide access to a wide range of other heterocycles such as dihydropyridazine and pyridazine systems [26].

In the actual state-of-the-art, the s-tetrazine ring is always obtained indirectly by oxidation of its 1, 2- or1, 4-dihydro (or even in rare cases its tetrahydro) counterpart, which can be prepared by various methods. Five main different strategies have been reported to date [27], but the long used Pinner synthesis and a modified version of it [28], [29] are still the most commonly used. The Pinner synthesis involves the reaction of hydrazine with a nitrile, always leading to a dihydrotetrazine that has to be further oxidized into the fully aromatic tetrazine. An versatile alternative strategy is that introduced by Scott based on the preparation of 1, 2-dihydro-3, 6- bis (3, 5-dimethyl-1*H*-pyrazol-1-yl) -1, 2, 4, 5-tetrazine (DHBPTz) [11]. This heterocycle is readily prepared via a condensation reaction of a triaminoguanidinum salt and acetylacetone in water [30]–[33].

Analytical applications of tetrazines are few and derived from three characteristics of their most stable form (1, 2, 4, 5 isomer; s-tetrazines) : a) the strong electron deficient character of the ring which leads it to accept electrons and protons simultaneously, producing dihydrotetrazines via anion radical [18], [34]; b) the low-lying π^* orbital resulting in highly colored compounds, typically red, due to an n-π^* transition in the visible light; additionally, some tetrazines, namely those replaced by electronegative heteroatoms (F, Cl, O) directly on the ring, show fluorescence both in solution and in the solid state with medium quantum yield ($\Phi_f < 0.4$) and a lifetime typically in the 10-160 ns range in solution [20], [31], [35], [36]; c) the presence of at least four nitrogen donor atoms at the

molecule that result in a coordination ability characterized by electron and charge transfer phenomena and efficient metal-metal bridging capacity [20], [37]. Chung et al. identified gram-positive bacteria using a two-step labeling procedure by reacting by cycloaddition, nanoparticles labeled with a fluorescent tetrazine with bacteria bonded to the bacterial cell wall with vancomycin or daptomycin derivatives [38].

A colorimetric sensing material for VOCs has been developed based on a nanotubular metal-organic framework (MOF) including 3, 6-di (pyridin-4-yl) -1, 2, 4, 5-tetrazine and $WS_4Cu_4^{2+}$ units. The combination of a sieving function along with solvatochromism makes it possible to discriminate small solvent molecules, both liquid and vapors, which is ascribed to its strong π-acceptor property and labile electronic structure to solvent polarity [39].

The strong electron-deficient character of tetrazines is more prominent in their first excited state, which means that fluorescent tetrazines can be quenched by electron donors [18]. The quenching that occurs between the tetrazine excited state and the donor through electron transfer has been proposed for the determination of different protic and aprotic compounds in solution such as amines, PAH, phenols, etc [35], [40]. Malinge et al. used the extinction of fluorescence by the photoinduced electron transfer of silica nanoparticles functionalized with trialkoxysilane tetrazines for low-molecular weight amine sensing [36].

There are few examples of the use of tetrazines as chromogenic reagents for metal ions, the earliest being the paper by Schilt et al. on ferroin-type reagents for Fe (II) , Cu (II) and Co (II) that include some pyridyltetrazines [41]. Samanta et al. [42] used pyridyl tetrazines for the selective determination of Cu (II), Ni (II) and Ag (I) in aqueous solution through a different approach that increases their solubility in water through a facile synthesis of tetrazine capped silver nanoparticles. Complexation of metal ions by tetrazine moieties from adjacent NPs causes aggregation shifting in the plasmon band energy at longer wavelengths, making it possible to determine the metal ions both in solution and in test paper format. The coordination ability of tetrazines has been used by Roushani et al. to develop a polyacrilic ion imprinted polymer including DHBPTz moieties for extraction and the pre-concentration of Fe (III) [43].

The change in color of dihydro-tetrazines by oxidation has been proposed only once to the best of our knowledge for sensing of oxidant gases. The dihydro-1, 2, 4, 5-tetrazine-3, 6-dicarboxylate was introduced into a chemically stable UiO-66-based MOF structure by a post-synthetic linker exchange reaction [44]. The tetrazine functionalized zirconium MOF can be oxidized by nitrous gases with a concomitant drastic color change from yellow to pink and regenerated by treatment with dithionite, making it a potential sensing material for oxidant gases. Inspired by this development and the easy preparation of DHBPTz [30]–[33], it was hypothesized that the use of DHBPTz in a microfluidic analytical device can produce a simple new procedure for nitrite determination.

This work demonstrates a paper-based microfluidic colorimetric sensor for the determination of nitrite in water samples based on the dihydrotetrazine chemistry and the redox character of nitrite using a very simple operational procedure. Microfluidic analytical devices have some advantages over other analytical approaches such as providing reliable measurements with efficiency and speed using small volumes of sample solutions [45]. Microfluidic paper-based analytical devices (μPAD) are based on the creation of hydrophilic micro-channels on cellulose-type substrates by means of two main types of techniques that form hydrophobic boundaries using materials such as wax, polymers and inks on hydrophilic paper or by forming physical boundaries by means of laser or knife cutting [46], [47].

2. Materials and methods

2.1. Reagents and materials

Nitrite stock solution (80 mM) was prepared in water from sodium nitrite (CAS No, 7632-00-0, Merck, Darmstadt, Germany) dried at 105°C. The solution was periodically standardized by titration with potassium permanganate. Solutions of lower concentration were prepared by appropriate dilution with water. This solution was stable for at least one month and was kept in a refrigerator in a stopped amber bottle. Other standards were 1000 mg L^{-1} stock solutions of the ions: Al (III), Pb (II), Cu (II), Fe (III), Zn (II), Mg (II), Ca (II), and Na (I) (as nitrates) and chloride, fluoride, sulfate, nitrate, phosphate and hypochlorite as sodium salts, all purchased from Merck (Merck, Spain). Other chemicals were ethanol (CAS No, 64-17-5) , hydrochloric acid (CAS No, 7647-01-0) and anhydrous citric acid (CAS No, 77-92-9) obtained from Panreac (PanreacQuímica S. A., Spain);

tetrahydrofuran (CAS No, 109-99-9) from Sigma Aldrich (Sigma-Aldrich Química S. A., Spain); and acetonitrile (CAS No, 75-05-8), acetone (CAS No, 67-64-1), methanol (CAS No, 67-56-1) and ethyl acetate (CAS No, 141-78-6) supplied by Lab Scan (Lab–Scan, Spain). All reagents were of analytical-reagent-grade unless stated otherwise. All aqueous solutions were made using reverse-osmosis type quality water (Mili-RO 12 plus Milli-Q station from Millipore, conductivity 18. 2 MΩ·cm).

Filter paper (ref. 1420, basis weight 80 g/m^2; thickness 170 µm; retention 14-18 µm) from Filter-Lab, Barcelona, Spain, double-sided adhesive tape from Miarco (Valencia, Spain) and transparent sheets from Schwan-Stabilo (Heroldsberg, Germany) were used to create the µPAD.

2.2. Synthesis of 3, 6-bis (3, 5-dimethyl-1H-pyrazol-1-yl) -1, 4-dihydro-1, 2, 4, 5-tetrazine (DHBPTz)

- ***Triaminoguanidinemonohydrochloride*** [33]***:***

Hydrazine monohydrate 6. 82 g (136. 4 mmol) was added to a suspension of 3.82 g (40.0 mmol) of guanidine hydrochloride in 1, 4-dioxane (20 mL) at room temperature. The reaction mixture was then stirred under reflux for 2 h. The reaction mixture was cooled to room temperature, filtered, washed with 1, 4-dioxane and dried 5.0 g (85%) of white powder was obtained.

- ***3, 6-Bis (3, 5-dimethylpyrazol-1-yl) -1, 2-dihydro-1, 2, 4, 5-tetrazine*** [33]**:**

3.04 g (21.5 mmol) of triaminoguanidinemonohydrochloride in 25 mL of water was added in drops to 4.53 g (45.3 mmol) of 2, 4-pentanedione. The mixture was then stirred for 1h, with the temperature then increased to 80ºC slowly, heating and stirring for an additional 1 h. Afterward, the solution was cooled down to room temperature slowly, filtering and washing with sufficient distilled water and dried, producing 1. 76 g (30%) of pure product, mp 138–139 ºC (Lit. 130-131ºC) [32]; ^{1}H-NMR (d_6-DMSO, 300 MHz): d (ppm) 2.18 (s, 2CH_3), 2.41 (s, 2CH_3), 6.15 (s, 2CH), 8.82 (s,

2NH); ^{13}C-NMR (d_6-DMSO, 75 MHz): d (ppm) 13.68, 13.96, 110.15, 142.39, 146.00, 150.09.

2.3. Apparatus and instruments

The color change in the µPAD was measured with a Canon PowerShot G12 digital camera (Canon Inc., Tokio, Japan). The transflectance measurements of the µPAD were obtained using an Ocean Optics USB2000 UV-Vis spectrophotometer connected by an optical fiber to an ISP-R integrating sphere with fiber ports at 90º to the spectrometer and 8º to the light source (LS-1 tungsten halogen light source).

2.4. Preparation of the µPAD

The fabrication process of the µPAD was performed by a craft-cutting technique, because it is cost-efficient, simple and reproducible, using standard laboratory filter paper (Filter-Lab, ref. 1420). The pattern was first designed using Illustrator software (Adobe Systems) and the design was exported as an FS file to the controller software of an X-Y knife plotter (Secabo GmbH, Wolnzach, Germany). For the production, a piece of paper was affixed using double-sided adhesive tape to a plastic sheet to avoid tearing and then was cut with a single pass of the knife. To optimize the procedure and the substrate used, the µPAD elements were produced in 4x32 replicas by cutting the acetate-backed cellulose with a 75% success rate, confirming the viability of the design. The removal of weeding was performed manually.

The device is tree-shaped, as shown in Figure 1, containing two separates zones, one for the sampling and the second for detection by triplicate, where the chromogenic reagent DHBPTz is immobilized. Once prepared, the plastic back of the µPAD was peeled off and adhered to a rigid plastic support for use.

The device was prepared by drop casting the needed reagents in each sensing area under ambient atmospheric conditions. To prepare the device, 1 µL of 1.5 M citric acid was dispensed twice onto the three detection zones after drying each time. Next, 1 µL of 22 mM DHBPTz solution was added, then dried at room temperature for 5 min and the

µPAD stored in the dark until use. Between consecutive castings of the reagents it is important to let the device dry to avoid the reverse flow of the reagents into the channel.

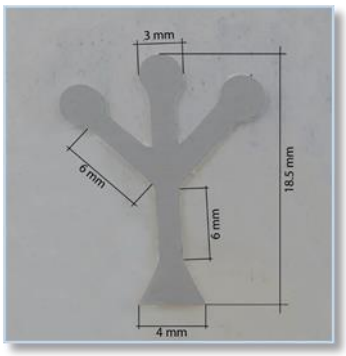

Figure 1. Picture of the µPAD indicating dimensions.

2.5. Image capture

To evaluate the color change of the µPAD after reacting with the nitrite solution, a picture was taken in JPEG format using a digital camera. The optimized setting conditions used to photograph the device were: macro, ISO 100, shutter speed 1/500 s, aperture value f/4 and focal length of 6. 1 mm. To keep all the image-gathering conditions the same, a Cube Light Box [48] was used with the camera placed in front of a homemade white wooden box with two LED 6500 K lamps placed at 45º with respect to the digital camera, with the µPAD in a fixed position inside the box to isolate it from external radiation.

An additional readout method was used to determine the nitrite using a CMOS sensor based on the HSV color variation acquired and processed with a smartphone. An iPhone 4.0 with a 5-megapixel still camera was set to flash "off" and the image was saved as a JPEG in the smartphone memory.

2.6. Image-processing

Using GIMP 2.8.10 Adobe digital editing software, the images were processed and treated to remove the areas that contained no relevant information and to calculate the analytical parameter, the saturation value S of the HSV color space. Each of the sensing areas of the picture of the µPAD was selected using the editor's color picker tool. Each

channel was normalized independently to calculate the RGB values as well as the S parameter of the HSV color space [49] and their corresponding standard deviations from a region of interest (ROI) slightly smaller than the detection area, around 6000 pixels.

This analysis provides analytical data in the form of basic HSV color from the smartphone, which can be used for quantitative analysis. A ColorAssit application was used to capture the HSV values, resulting in a much shorter analysis time than other commonly used programmes such as Matlab, Visual basic, GIMP and Adobe Photoshop.

2.7. Measurement protocol

To initiate the reactions that produce color changes in the sensing areas of the μPAD, 10 μL of a solution of known nitrite concentration for calibration and unknown for validation were dropped in the lower sampling area of the microfluidic device. Due to the capillarity of the filter paper, the solution flowed towards the three sensing areas where the reagents were placed. During use, the device was kept in a horizontal position and over a non-absorbent surface. In this way, the flow of the solution did not favor any direction and there was no absorption of the reagents or sample solution in the supporting material below the device. Five minutes were needed to complete the reaction on each sensing area where a pink color appeared on the white detection areas (Figure 2). Once all the sensing areas were allowed to react, a picture of the microfluidic device was captured using a digital camera as noted above to maintain controlled illumination conditions. In both cases the concentration was calculated from the calibration curve obtained with the nitrite standards.

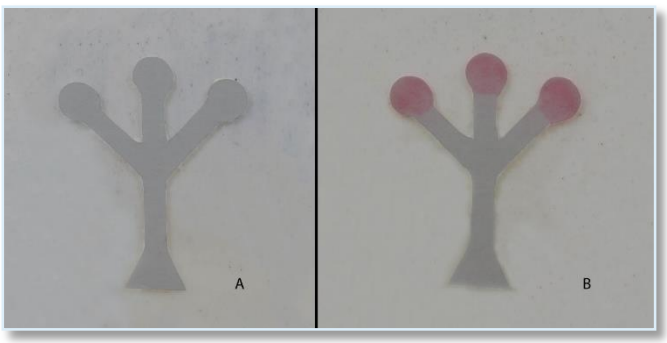

Figure 2. μPAD before (A) and after (B) reaction with nitrite.

3. Results and discussion

Tetrazines are the electron-poorest aromatic system of the classical heterocyclic aromatic rings, which makes tetrazine rings a strong electron attractor with a relative strong oxidizing power (E^o -0.96 V DHBPTz in dichloromethane) [17]; consequently s-tetrazines can be easily reduced. The electrochemical reduction of tetrazines produces a stable anion radical by reversibly accepting one electron or a dihydrotetrazine by accepting a second electron in a non-electrochemically reversible process [17]. Nevertheless, this process is chemically reversible, for example when using sodium dithionite [49]. A common synthetic method for tetrazines is based on the oxidation of dihydrotetrazines with oxidants such as chlorine gas, trichloroisocyanuric acid, manganese dioxide, nitrous gas, or sodium nitrite [17], [50], [51]. The oxidation of dihydrotetrazines produces an intense color change, typically from pale yellow to red, due to the appearance of a low-lying π* orbital in the tetrazine that leads to an→π* transition in the visible light. In this study we use DHBPTz as a reagent for nitrite determination based on its immobilization by adsorption on cellulose fibers, in this way overcoming the problem of insolubility in water (solubility 0.30 g/l; 25ºC). The reaction of DHBPTz with nitrite in acetone produces a red solution (Fig. 3) with a maximum at 516 nm [17] while the diffuse reflectance spectrum of BPTz in cellulose after reaction with nitrite shows a maximum at 472 nm.

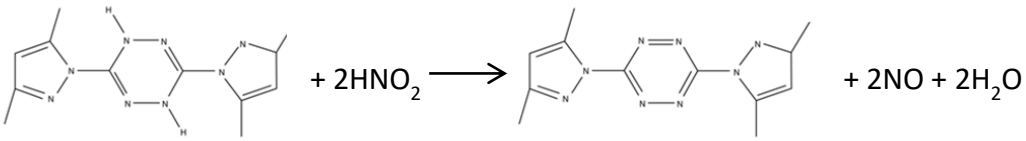

Figure 3. Reaction of DHBPTz with nitrite in acidic medium.

3. 1. µPAD preparation

The µPAD for nitrite is a single-channel-type device with a sampling area at the bottom of the device and a triple detection area containing the recognition chemistry immobilized by adsorption on the cellulose and deposited with a micropipette from a DHBPTz organic solution. This design makes it possible to carry out the necessary operations to analyze

the nitrite present in the aqueous samples. Moreover, thanks to this design three replicates from the same solution can be measured simultaneously, thus improving accuracy.

Different materials were tested for membrane selection as the support for the nitrite μPAD with no leaching of reagents or the reaction product and a homogeneous distribution of color in the reaction areas. Materials tested for the preparation and measurement of nitrite μPAD were quantitative filter papers of different filtration and retention capacity (10 types ranging from 1 to 30 μm pore size) and hydrophilic nylon membranes (amphoteric, cationic and anionic). The best results for color intensity and the homogeneous distribution of the dye were obtained with a cellulosic membrane with a medium filtration rate and 14-18 μm pore size.

The areal size, number of recognition areas and layout of the μPAD were designed to: 1) minimize color reading errors (3 mm-diameter detection area with some 6000 pixels); 2) obtain a suitable collection of the sample (triangular reception area for 10 μL sample); 3) obtain replicate measurements from the same solution (tree-type device with three detection areas).

To model the fluid movement within the selected paper, the Washburn equation was used (equation 1) where Υ is the interfacial tension, θ is the contact angle between the liquid and the paper surface, D is the effective capillary diameter and μ is the viscosity of the liquid.

$$L = \sqrt{\frac{(\gamma \cos\theta) D t}{4\mu}}$$

The fit to the Washburn equation was obtained by fitting the experimental data, for a piece of paper 10 cm long and 0.3 mm wide, with a square root function ($L=A\sqrt{t}$) resulting A = 0.5698 (R^2 = 0.9975). The experimental data of the device without considering the two arms of the μPAD show some Washburn-type behavior because of the change of the channel length along the device. The average time needed to wet the μPAD was 8 s.

3.2. µPAD measurement conditions

The reagent DHBPTz was deposited on the detection areas of the µPAD from an acetonic solution because of its high solubility and evaporation rate in this solvent. The optimum DHBPTz amount immobilized was studied by casting 1 µL per detection area of a solution with concentrations ranging between 11 and 66 mM (Fig. 4A). The concentration selected as optimal was 22 mM because higher concentrations increased the blank signal as shown in Fig. 4A; this figure was 6 µg DHBPTz per recognition area or 0. 64 µg/mm^2.

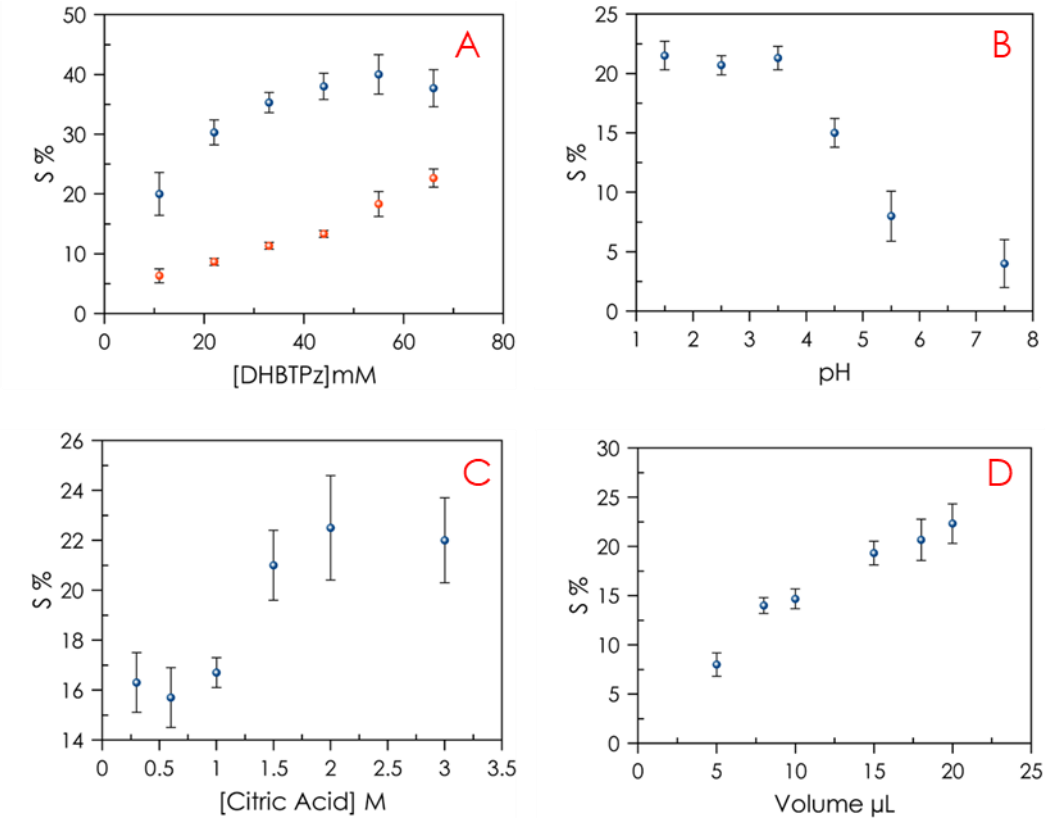

Figure 4. Influencing factors for nitrite µPAD. A) Influence of DHBPTz immobilized on µPAD using 1 µL of acetonic solutions of different concentrations. Citric acid 1 µL 1.5 M; nitrite 10 µL 1000 µM; Lower curve: blank signal evolution; B) pH dependence on nitrite recognition. pH adjusted with 0.5 µL twice per recognition area of 1 M citric acid/ citrate buffers. Nitrite 10 µL 200 µM; C) Influence of citric acid concentration. pH = 2.0; 1 µL citric acid various concentrations per recognition area; nitrite 10 µL 200 µM; D) Influence of nitrite volume. Nitrite 100 µM.

As nitrite recognition is pH dependent, a study of the pH influence using the prepared µPAD was performed, selecting citric acid as the reagent because it is acid enough to trigger the reaction and be immobilized on cellulose. The study was performed with citric acid or citrate buffers with a pH between 2.0 and 7.5. Fig. 4B shows that the reaction only

proceeds in an acid medium. As the working pH, 2.0 adjusted by citric acid was selected in good agreement with the acidity constant for nitrous acid (pK_a= 3.25).

A study of the optimum citric acid concentration performed between 0.5 and 3.0 M (Figure 4C) revealed that concentrations higher than 1.5 M worsen the precision and do not increase the S signal. Thus, the µPAD was prepared by adding 0.5 µL twice with drying between additions of 1.5 M citric acid, i.e., 288 µg citric acid per recognition area or 40.7 µg/mm^2.

Two possible areas were tested for citric acid placement: the recognition area and the transport channel. In both cases 0.5 µL of the citric acid was dispensed two times to prevent spreading. The results show a 30% increase in the S value on average for acid immobilized on the detection area instead of the transport channel; consequently all reagents were deposited in the detection area.

Different volumes of nitrite solution were dispensed on the sampling area of the µPAD (Figure 4D), selecting 10 µL as the optimal sample volume as it is enough to wet the device with reasonable drying time and good precision.

The reaction time was studied by extracting the frames from a video of the µPAD after adding the sample containing nitrite (Figure 5). As a reaction time, 5 min was selected because it was sufficient to complete the reaction and dry the paper to obtain the picture.

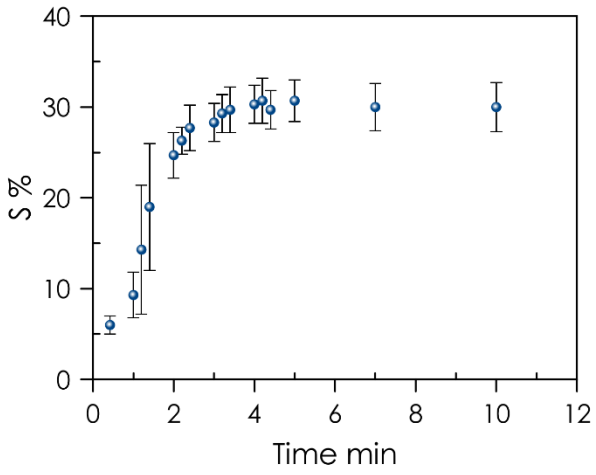

Figure 5. Kinetic study of nitrite assay color intensity (Nitrite 10 µL 1000 µM).

3.3. Analytical characterization

The color of the µPAD changes from white, because the DHBPTz reagent is almost colorless, to pink by reaction with nitrite. This monotonal change was fitted to the saturation coordinate S of the HSV color space after imaging the device with a digital camera. The S value increases with nitrite concentration. The analytical function was obtained by means of a calibration set composed of 11 standards with 3 replicates obtained with the same device between 10 and 1000 µM with a 5 minute reaction time (Figure 6). The observed dependence between the S value and nitrite concentration is a logarithmic dependence that is linearized using: S = a·log[nitrite] + b. Additionally Figure 6 (black dots and bars) includes the same calibration acquired with a smartphone in order to show the viability of the proposal with this device. The performance characteristics of the µPAD developed are presented in Table 1.

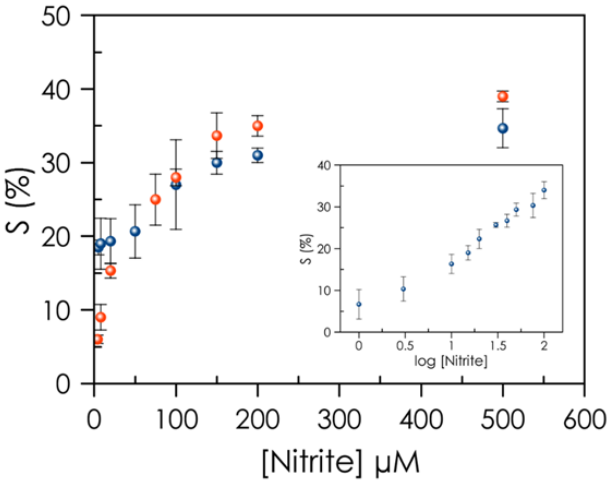

Figure 6. Dependence of nitrite concentration (A) obtained with digital camera (red) and smartphone (black). Logarithmic calibration function (B) with digital camera (red) and smartphone (black).

The detection limits (DL) were obtained using the standard criteria [52], [53] DL = y_b + 3s_b, where y_b is the average blank signal and s_b is the standard deviation of the blank, which was determined from 24 blanks (relative standard deviation (RSD) 2.6 %). With this criterion, the value of the DL was 1.38 µM (0.10 mg/L) and the quantification limit 2.60 µM (0.18 mg/L), acceptable values taking into account the drinking water standard value of 0.5 mg/L [6], [10]. The repeatability, as RSD, obtained using 7 different µPADs

at 100 µM nitrite was 9.7%, an acceptable precision considering the measuring system used.

The lifetime of the µPAD was studied for 21 days using two series of prepared devices, regularly checking their response to a 100 µM nitrite concentration. One series was protected from light and preserved at 4ºC and the other protected from light in a desiccator at room temperature. During the study period, it was observed that the signal is maintained when protected from light at 4ºC, decreasing only 10.1%, while at room temperature the device has a lifetime of some 2 weeks decreasing 35% at the end of the study. The cost of the µPAD considering only the reagents and paper to make the device is around 0.10 €/unit.

Table 1. Analytical characteristics of µPAD for nitrite.

Analytical Parameter	Value
Measurement range (µM)	5 - 500
Slope, (b)	17.30
Intercept, (a)	-6.47
LOD (µM)	1. 30
LQ (µM)	2. 20
Precision (%)	3.5 (10 µM)
	4.5 (100 µM)
	4.7 (200 µM)
Lifetime (days)	21

A comparative study of different microfluidic devices from the literature is presented in Table 2, showing that the tetrazine-based µPAD described here has advantages such as: 1) a wide range and good detection limit, typically one magnitude order better than Griess; 2) a better stability since the degradation of the Griess reagent results in a pink shade [12]; 3) a shorter reaction time (5 min) [6]; and 4) a similar lifetime [6].

Table 2. Colorimetric microfluidic-based nitrite assays.

Chromogenic reagent	Microfluidic device type	Range	LOD	Precision	Measurement system	Application	Ref.
NED	µPAD	86-1850 µM	11. 3 µM	---	Smartphone	---	[54]
NED	µTAD	100-1000 µM	---	---	Ruler	Artificial urine	[55]
NED	µPAD	20-160 µM	7. 8 µM	---	Scanner	Saliva	[56]
NED	µPAD	0-100 µM	11. 3 µM	---	Scanner	Saliva	[57]
NED	µPAD	10-1000 µM	10 µM	---	Scanner	Saliva	[12]
NED	µPAD	3-50 mM	2. 8 mM	---	Scanner	Urine, saliva	[58]
NED	µPAD	156-1250 µM	-	---	Phone camera	Water	[59]
NED	µPAD	10-150 µM	1 µM	2. 9 %	Scanner	Water	[6]
DHBPTz	µPAD	10-1000 µM	1. 38 µM	9. 7 %	Camera Phone	Water	This work

NED: N- (1-naphthyl) -ethylenediamine; µTAD: Thread-based microfluidic device

3.4. Interferences

In order to discover any potential interferences in water that could modify the analytical signal of the tetrazine-based µPAD, we specifically studied the effect of some species that are common in water, namely: Na (I), Ca (II), Mg (II), Cu (II), Zn (II), Pb (II), Al (III), Fe (III), Cl^-, SO_4^{2-}, NO_3^-, PO_4^{3-}, F^- and ClO^-. Solutions containing 200 µM nitrite and 5 mg/L interference (Ca (II), Mg (II), Cu (II), Zn (II), Pb (II), Al (III), Fe (III)) or 50 mg/L interference (Na (I), Cl^-, SO_4^{2-}, NO_3^-, PO_4^{3-}, F^-) were analyzed in triplicate, showing good selectivity (Figure7) except for Fe (III) and ClO^-. The tolerance (amount of interfering species that produces an error equal to the RSD of the procedure) calculated for both ClO^- and Fe (III) was 4 mg/L. The interference of Fe (III) can be eliminated by adding 10 µL of 10 mg/L EDTA as a masking agent to the recognition area.

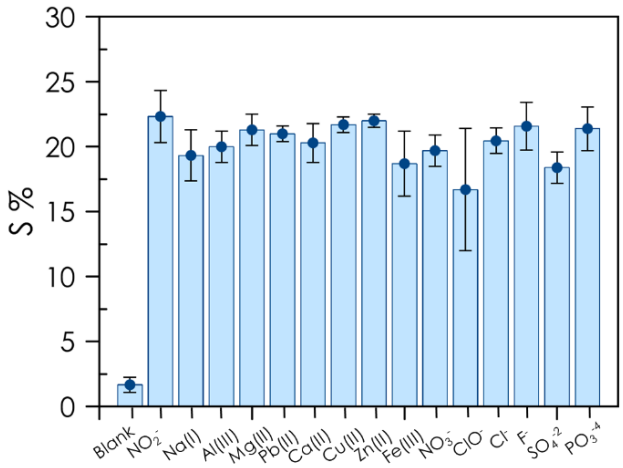

Figure 7. The selectivity of µPAD for 200 µM nitrite in the presence of interferents at 5 mg/L (Ca (II), Mg (II), Cu (II), Zn (II), Pb (II), Al (III), Fe (III) or 50 mg/L (Na (I), Cl^-, SO_4^{2-}, NO_3^-, PO_4^{3-}, F^-).

3.5. Validation

The prepared µPAD was applied to determine nitrite in different types of water. Two different water samples obtained in the cities of Granada and Malaga (Spain) and some mineral water were analyzed. 10 µL of each sample was placed in the sampling area of the microfluidic device and, after 5 minutes, a picture was taken. Since no nitrite was detected in those water samples, they were spiked at 200 µM analyte concentration prior to reaction in the µPAD. The samples were analyzed following the general procedure and the recovery results obtained are shown in Table 3, with values ranging from 97% to 105%, demonstrating the high potential of the novel optical µPAD assay for the analysis of trace levels of nitrite in real samples.

Table 3. Recovery study for nitrite in water.

Sample	Nitrite added, µM	Nitrite found, µM	Recovery, %
Mineral water	200	195 ± 1.1	97.5
	100	102.5 ± 0.6	102.5
	10	9.0 ± 1.0	90.0
Tap water, Granada	200	195 ± 2.8	97.5
	100	105.0 ± 2.1	105.0
	10	9.7 ± 0.6	97.0
Tap water, Malaga	200	210 ± 2.3	105.1

4. Conclusions

We have successfully designed a colorimetric assay for nitrite in aqueous media based on a tetrazine chemistry used for the first time for this determination with advantages over the commonly used Griess reaction of similar sensitivity, non-carcinogenic reagents and a short reaction time. The system was implemented in a microfluidic paper-based analytical device (µPAD). In order to simplify the assay, the change in color after reaction for 5 min with a water sample and measurement with a photographic camera is evaluated by the coordinate S of the HSV color space. The assay presents good sensitivity for nitrite with a detection limit of 1.38 µM. The µPAD was stable for 21 days when protected from light and preserved at 4ºC.

REFERENCES

[1] M. Habs and D. Schmähl, "Diet and cancer," *Journal of Cancer Research and Clinical Oncology*. 1980.

[2] U. S. E. P. Agency and O. Water, "2018 Edition of the Drinking Water Standards and Health Advisories Tables," no. March, 2018.

[3] Y. Song, G. F. Deng, X. R. Xu, Y. H. Chen, F. Chen, and H. Bin Li, "Nitrate and nitrite content in bottled beverages by ion-pair high-performance liquid chromatography," *Food Addit. Contam. Part B Surveill.*, 2013.

[4] E. Vidal, A. S. Lorenzetti, A. G. Lista, and C. E. Domini, "Micropaper-based analytical device (μPAD) for the simultaneous determination of nitrite and fluoride using a smartphone," *Microchem. J.*, vol. 143, pp. 467–473, 2018.

[5] E. Trofimchuk, Y. Hu, A. Nilghaz, M. Z. Hua, S. Sun, and X. Lu, "Development of paper-based microfluidic device for the determination of nitrite in meat," *Food Chem.*, vol. 316, p. 126396, 2020.

[6] B. M. Jayawardane, S. Wei, I. D. McKelvie, and S. D. Kolev, "Microfluidic Paper-Based Analytical Device for the Determination of Nitrite and Nitrate," *Anal. Chem.*, vol. 86, no. 15, pp. 7274–7279, Aug. 2014.

[7] P. Garcia, T. Cardoso, C. Garcia, E. Carrilho, and W. Coltro, "A handheld stamping process to fabricate microfluidic paper-based analytical devices with chemically modified surface for clinical assays," *RSC Adv.*, Aug. 2014.

[8] F. Pena-Pereira, Ó. Matesanz, I. Lavilla, and C. Bendicho, "A paper-based gas sensor for simultaneous non-instrumental colorimetric detection of nitrite and sulfide in waters," *J. Sep. Sci.*, Feb. 2020.

[9] C.-K. Chiang, A. Kurniawan, C.-Y. Kao, and M.-J. Wang, "Single step and mask-free 3D wax printing of microfluidic paper-based analytical devices for glucose and nitrite assays," *Talanta*, vol. 194, pp. 837–845, 2019.

[10] T. M. G. Cardoso, P. T. Garcia, and W. K. T. Coltro, "Colorimetric determination of nitrite in clinical{,} food and environmental samples using microfluidic devices stamped in paper platforms," *Anal. Methods*, vol. 7, no. 17, pp. 7311–7317, 2015.

[11] M. J. Moorcroft, J. Davis, and R. G. Compton, "Detection and determination of nitrate and nitrite: a review.," *Talanta*, vol. 54, no. 5, pp. 785–803, Jun. 2001.

[12] S. A. Bhakta, R. Borba, M. J. Taba, C. D. Garcia, and E. Carrilho, "Determination of nitrite in saliva using microfluidic paper-based analytical devices.," *Anal. Chim. Acta*, vol. 809, pp. 117–122, Jan. 2014.

[13] L. Lauko and B. Ernest, "Analytical Methods for the Determination of Nitrites," *Chem. List.*, vol. 109, pp. 191–197, Mar. 2015.

[14] M. Oms, A. Cerdà, and V. Cerdà, "Analysis of nitrates and nitrites," 2000, pp. 201–222.

[15] R. B. P. Weselsky, *No Title*, 12th ed. Ber. Dtsch: Chem. Ges., 1897.

[16] M. Porche, *Spectrophotometric determination of nitrite by derivatization with captopril*. 2014.

[17] G. Clavier and P. Audebert, "s-Tetrazines as Building Blocks for New Functional Molecules and Molecular Materials," *Chem. Rev.*, vol. 110, no. 6, pp. 3299–3314, Jun. 2010.

[18] P. Bleehen, N M Newlands, E S Lee, S M Thatcher, N Selby and M. F. Calvert, A H Rustin, G J Brampton, M Stevens, "Cancer Research Campaign phase II trial of temozolomide in metastatic melanoma.," *J. Clin. Oncol.*, vol. 13, no. 4, pp. 910–913, Apr. 1995.

[19] K. Parimal, E. Witlicki, and A. Flood, "Interconverting Two Classes of Architectures by Reduction of a Self-Sorting Mixture," *Angew. Chem. Int. Ed. Engl.*, vol. 49, pp. 4628–4632, Jun. 2010.

[20] W. Kaim, "The coordination chemistry of 1,2,4,5-tetrazines," *Coord. Chem. Rev.*, vol. 230, no. 1, pp. 127–139, 2002.

[21] N. Saracoglu, "Recent advances and applications in 1,2,4,5-tetrazine chemistry," *Tetrahedron*, vol. 63, no. 20, pp. 4199–4236, 2007.

[22] A. M. Churakov and V. A. Tartakovsky, "Progress in 1,2,3,4-Tetrazine Chemistry," *Chem. Rev.*, vol. 104, no. 5, pp. 2601–2616, May 2004.

[23] J. Šečkutė and N. K. Devaraj, "Expanding room for tetrazine ligations in the in

vivo chemistry toolbox," *Curr. Opin. Chem. Biol.*, vol. 17, no. 5, pp. 761–767, 2013.

[24] N. K. Devaraj and R. Weissleder, "Biomedical Applications of Tetrazine Cycloadditions," *Acc. Chem. Res.*, vol. 44, no. 9, pp. 816–827, Sep. 2011.

[25] N. Devaraj, R. Upadhyay, J. Haun, S. Hilderbrand, and R. Weissleder, "Fast and Sensitive Pretargeted Labeling of Cancer Cells through a Tetrazine/trans-Cyclooctene Cycloaddition," *Angew. Chem. Int. Ed. Engl.*, vol. 48, pp. 7013–7016, Sep. 2009.

[26] V. N. Tolshchina, S G Ishmetova, R I Ignatenko, N K Korotina, A V Slepukhin, P A Rusinov, G L Charushin, "Synthesis and transformations of cyanomethyl-1,2,4,5-tetrazines," *Chem. Heterocycl. Compd.*, vol. 49, no. 4, pp. 604–617, 2013.

[27] W. P. W. J. G. Erickson, P. Wiley, *The Chemistry of Heterocyclic Compounds: A Series of Monographs*. New York: Interscience Publishers Inc, 1956.

[28] N. O. Abdel, M. A. Kira, and M. N. Tolba, "A direct synthesis of dihydrotetrazines," *Tetrahedron Lett.*, vol. 9, no. 35, pp. 3871–3872, 1968.

[29] P. Audebert, Pierre Sadki, Saïd Miomandre, Fabien Clavier, Gilles Vernières, Marie Saoud, Merzaka Hapiot, "Synthesis of new substituted tetrazines: Electrochemical and spectroscopic properties," *New J. Chem.*, vol. 28, pp. 387–392, Mar. 2004.

[30] M. Coburn, G. Buntain, B. Harris, M. Hiskey, K.-Y. Lee, and D. Ott, "ChemInform Abstract: An Improved Synthesis of 3,6-Diamino-1,2,4,5-tetrazine. Part 2. From Triaminoguanidine and 2,4-Pentanedione.," *Cheminform*, vol. 23, p. 228, May 2010.

[31] G. Gong, Yonghua Miomandre, Fabien Méallet-Renault, Rachel Badré, Sophie Galmiche, Laurent Tang, Jie Audebert, Pierre Clavier, "Synthesis and Physical Chemistry of s-Tetrazines: Which Ones are Fluorescent and Why?," *European J. Org. Chem.*, vol. 2009, pp. 6121–6128, Oct. 2009.

[32] Y. Li, A. Asadi, and D. M. Perrin, "Hydrolytic stability of nitrogenous-heteroaryltrifluoroborates under aqueous conditions at near neutral pH," *J. Fluor. Chem.*, vol. 130, no. 4, pp. 377–382, 2009.

[33] M. Adib, M. Soheilizad, L. G. Zhu, and J. Wu, "A one-pot, three-component synthesis of 3-(1 H -pyrazol-1-yl)-4 H,7 H -[1,2,4,5]tetraazino[6,1- b][1,3]benzoxazin-7-ones under solvent-free conditions," *Synlett*, vol. 26, no. 2, pp. 177–182, 2015.

[34] S. Samanta and P. Biswas, "Metal free visible light driven oxidation of alcohols to carbonyl derivatives using 3,6-di(pyridin-2-yl)-1,2,4,5-tetrazine (pytz) as catalyst," *RSC Adv.*, vol. 5, no. 102, pp. 84328–84333, 2015.

[35] P. Audebert, F. Miomandre, G. Clavier, M.-C. Vernières, S. Badré, and R. Méallet-Renault, "Synthesis and Properties of New Tetrazines Substituted by Heteroatoms: Towards the World's Smallest Organic Fluorophores," *Chemistry*, vol. 11, pp. 5667–5673, Sep. 2005.

[36] J. Malinge, C. Allain, L. Galmiche, F. Miomandre, and P. Audebert, "Preparation, Photophysical, Electrochemical, and Sensing Properties of Luminescent Tetrazine-Doped Silica Nanoparticles," *Chem. Mater.*, vol. 23, no. 20, pp. 4599–4605, Oct. 2011.

[37] L. E. Kreno, K. Leong, O. K. Farha, M. Allendorf, R. P. Van Duyne, and J. T. Hupp, "Metal–Organic Framework Materials as Chemical Sensors," *Chem. Rev.*, vol. 112, no. 2, pp. 1105–1125, Feb. 2012.

[38] R. Chung, Hyun Jung Reiner, Thomas Budin, Ghyslain Min, Changwook Liong, Monty Issadore, David Lee, Hakho Weissleder, "Ubiquitous Detection of Gram-Positive Bacteria with Bioorthogonal Magnetofluorescent Nanoparticles," *ACS Nano*, vol. 5, no. 11, pp. 8834–8841, Nov. 2011.

[39] Z.-Z. Lu, R. Zhang, Y.-Z. Li, Z.-J. Guo, and H.-G. Zheng, "Solvatochromic Behavior of a Nanotubular Metal−Organic Framework for Sensing Small Molecules," *J. Am. Chem. Soc.*, vol. 133, no. 12, pp. 4172–4174, Mar. 2011.

[40] R. A. King, G. Vacek, and H. F. Schaefer, "1,3,5-Trisilabenzene: has it been synthesized?," *J. Mol. Struct. THEOCHEM*, vol. 358, no. 1, pp. 1–14, 1995.

[41] A. A. Schilt, W. E. Dunbar, B. W. Gandrud, and S. E. Warren, "New chromogens of the ferroin type—VI: Some derivatives of 1- and 3-cyanoisoquinoline and substituted 2-cyanopyridines," *Talanta*, vol. 17, no. 7, pp. 649–653, 1970.

[42] S. Samanta, S. Das, and P. Biswas, "Synthesis of 3,6-di(pyridin-2-yl)-1,2,4,5-tetrazine (pytz) capped silver nanoparticles using 3,6-di(pyridin-2-yl)-1,4-dihydro-1,2,4,5-tetrazine as reducing agent: Application in naked eye sensing of Cu2+, Ni2+ and Ag+ ions in aqueous solution and paper pl," *Sensors Actuators B Chem.*, vol. 202, pp. 23–30, 2014.

[43] M. Roushani, T. M. Beygi, and Z. Saedi, "Synthesis and application of ion-imprinted polymer for extraction and pre-concentration of iron ions in environmental water and food samples," *Spectrochim. Acta Part A Mol. Biomol. Spectrosc.*, vol. 153, pp. 637–644, 2016.

[44] G. Nickerl, I. Senkovska, and S. Kaskel, "Tetrazine functionalized zirconium MOF as an optical sensor for oxidizing gases," *Chem. Commun.*, vol. 51, no. 12, pp. 2280–2282, 2015.

[45] T. Yager, Paul Edwards and B. H. Fu, Elain Helton, Kristen Nelson, Kjell Tam, Milton R Weigl, "Microfluidic diagnostic technologies for global public health.," *Nature*, vol. 442, no. 7101, pp. 412–418, Jul. 2006.

[46] S. Caté, Antoine Mercier Langevin, Patrick Ross, Pierre-Simon Duff and B. Hannington, Mark Gagne, Simon Dubé, *Insight on the chemostratigraphy of the volcanic and intrusive rocks of the Lalor auriferous VMS deposit host succession, Snow Lake, Manitoba*. 2014.

[47] C. L. Cassano and Z. H. Fan, "Laminated paper-based analytical devices (LPAD): fabrication, characterization, and assays," *Microfluid. Nanofluidics*, vol. 15, no. 2, pp. 173–181, 2013.

[48] M. Ariza-Avidad, A. Salinas-Castillo, M. P. Cuéllar, M. Agudo-Acemel, M. C. Pegalajar, and L. F. Capitán-Vallvey, "Printed Disposable Colorimetric Array for Metal Ion Discrimination," *Anal. Chem.*, vol. 86, no. 17, pp. 8634–8641, Sep. 2014.

[49] R. W. G. Hunt, "Colour Science: Concepts and Methods, Quantitative Data and Formulas," *Opt. Acta Int. J. Opt.*, vol. 15, no. 2, p. 197, 1968.

[50] M. D. Helm, A. Plant, and J. P. A. Harrity, "A novel approach to functionalised pyridazinone arrays," *Org. Biomol. Chem.*, vol. 4, no. 23, pp. 4278–4280, 2006.

[51] M. Tutak, A. Disli, and A. Alicilar, "Monochlorotetrazinyl Reactive Dyes: Synthesis and Characterization," *Asian J. Chem.*, vol. 21, pp. 6513–6524, Oct. 2009.

[52] N. J. Miller, J.C. Miller, *Estadística y Quimiometría para Química Analítica, 4 ed., Prentice Hall, Madrid, 2002.* .

[53] *Eu Commission, EU Water Framework Directive, 237, OJEU 2000, pp. 1-73.* .

[54] L. F. Lopez-Ruiz, Nuria Curto, Vincenzo F. Erenas, Miguel M. Benito-Lopez, Fernando Diamond, Dermot Palma, Alberto J. Capitan-Vallvey, "Smartphone-based simultaneous pH and nitrite colorimetric determination for paper microfluidic devices.," *Anal. Chem.*, vol. 86, no. 19, pp. 9554–9562, Oct. 2014.

[55] A. Nilghaz, D. R. Ballerini, X.-Y. Fang, and W. Shen, "Semiquantitative analysis on microfluidic thread-based analytical devices by ruler," *Sensors Actuators B Chem.*, vol. 191, pp. 586–594, 2014.

[56] Y. Jiang, Z. Hao, Q. He, and H. Chen, "A simple method for fabrication of microfluidic paper-based analytical devices and on-device fluid control with a portable corona generator," *RSC Adv.*, vol. 6, no. 4, pp. 2888–2894, 2016.

[57] T. Cardoso, P. Garcia, and W. Coltro, "Colorimetric determination of nitrite in clinical, food and environmental samples using microfluidic devices stamped in paper platform," *Anal. methods*, vol. 7, Apr. 2015.

[58] S. A. Klasner, A. K. Price, K. W. Hoeman, R. S. Wilson, K. J. Bell, and C. T. Culbertson, "Paper-based microfluidic devices for analysis of clinically relevant analytes present in urine and saliva," *Anal. Bioanal. Chem.*, vol. 397, no. 5, pp. 1821–1829, 2010.

[59] B. Wang, Z. Lin, and M. Wang, "Fabrication of a Paper-Based Microfluidic Device To Readily Determine Nitrite Ion Concentration by Simple Colorimetric Assay," *J. Chem. Educ.*, vol. 92, pp. 733–736, Apr. 2015.

ÍNDICE DE FIGURAS

Capítulo 1

Figure 1. Picture of the µPAD indicating dimensions 117
Figure 2. µPAD before (A) and after (B) reaction with nitrite 118
Figure 3. Reaction of DHBPTz with nitrite in acidic medium 119
Figure 4. Influencing factors for nitrite µPAD. A) Influence of DHBPTz immobilized on µPAD B) pH dependence on nitrite recognition. C) Influence of citric acid concentration. D) Influence of nitrite volume. Nitrite 100 µM. 121
Figure 5. Kinetic study of nitrite assay color intensity. Nitrite 10 µL 1000 µM 122
Figure 6. Calibration graph for nitrite 123
Figure 7. The selectivity of µPAD for 200 µM nitrite in the presence of interferents at 5 mg/L 126

ÍNDICE DE TABLAS

Table 1. Analytical characteristics of µPAD for nitrite 124
Table 2. Colorimetric microfluidic-based nitrite assays..... 125
Table 3. Recovery study for nitrite in water 126

Capítulo 2

MICROFLUIDIC PAPER-BASED DEVICE FOR COLORIMETRIC DETERMINATION OF GLUCOSE BASED ON A METAL -ORGANIC FRAMEWORK ACTING AS PEROXIDASE MIMETIC

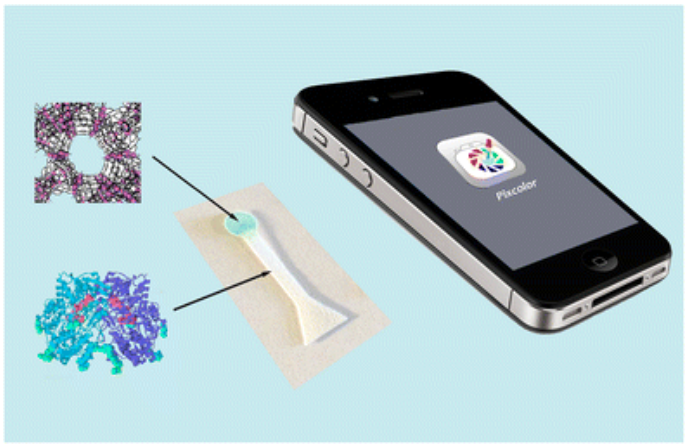

Published in Microchimica Acta, 2018,185, 1-8

CAPÍTULO 2: MICROFLUIDIC PAPER-BASED DEVICE FOR COLORIMETRIC DETERMINATION OF GLUCOSE BASED ON A METAL-ORGANIC FRAMEWORK ACTING AS PEROXIDASE MIMETIC

Inmaculada Ortiz-Gómez[a], Alfonso Salinas-Castillo[a], Amalia García García[b], José Antonio Álvarez-Bermejo[c], Ignacio de Orbe-Payá[a], Antonio Rodríguez-Diéguez[b] and Luis Fermín Capitán-Vallvey[a].

[a]ECsens, Department of Analytical Chemistry; [b]Department of Inorganic Chemistry, Campus Fuentenueva, Faculty of Sciences, 18071 University of Granada, Spain.

[c]Department of Information Technology, Cañada de San Urbano, 04120, University of Almeria, Spain.

Planteamiento

Los metal-organic frameworks (MOF) son una clase de polímeros de coordinación de estructura porosa compuestos por un metal como núcleo inorgánico conectados por ligando orgánicos de diversa naturaleza como los grupos carboxílicos, amino y fosfatos [1]–[3]. Esta estructura hibrida resultante proporciona a los MOF propiedades excepcionales como una elevada flexibilidad, porosidad y área superficial específica, buena estabilidad térmica y mecánica, así como una buena actividad catalítica [4]–[6].

En consecuencia, los MOF han sido utilizados en numerosas aplicaciones como almacenamiento, catálisis, procesos de separación, aplicaciones biológicas y el desarrollo de sensores químicos [7], [8]. En este sentido, recientemente se ha demostrado que algunos MOF presentan actividad mimética siendo capaces de imitar la actividad de ciertas encimas en procesos catalíticos. Por ejemplo, L. Ai y col. [9] demostraron que el MOF MIL-53 presenta actividad similar a la peroxidasa y que por tanto, en presencia de peróxido de hidrogeno (H_2O_2) podría catalizar la reacción de oxidación de determinados compuestos como el 3,3',5, 5'-tetrametilformamida (TMB), el O-fenilendiamina (OPD) y el 1, 2, 3-trihidroxibenceno (THB) generando cambios de color de los estos reactivos al pasar a su estado oxidado y pudiendo relacionar la concentración de H_2O_2 con este cambio de color. Del mismo modo, MOF basados en hierro como el MOF Co/2Fe y el MOF MIL-101 se han utilizado para la detección colorimétrica de H_2O_2, glucosa, ácido úrico y biotioles [10]–[12].

En este sentido, la utilización de MOF como catalizadores biomiméticos expanden las aplicaciones de estos compuestos en el desarrollo de sensores y biosensores ya que los MOF pueden utilizarse como enzimas artificiales en diversas plataformas de detección. Las enzimas artificiales son muy populares en el campo de la investigación porque se pueden producir y purificar fácilmente con buena estabilidad. Además, se pueden utilizar muchas veces sin necesidad de estar preparando el material con frecuencia.

En este contexto, la posibilidad de implementar un MOF que actúa como imitador de una enzima en un sistema microfluídico basado en papel ofrece ciertas ventajas incluyendo simplicidad y compatibilidad junto con portabilidad en el análisis [13]. El papel es un material atractivo en el desarrollo de sensores químicos y se acepta como una plataforma tecnológica innovadora en el desarrollo de sistemas de detección debido a su flexibilidad, ligereza y bajo coste, entre otras como se ha comentado en la introducción de esta Memoria.

Por todo ello, la implementación de un compuesto con actividad imitadora de enzimas como es el MOF Fe-MIL-101 es importante en el desarrollo de sensores químicos de estas características ya que la eliminación de una enzima hace que el sensor más estable frente a cambios de pH, temperatura, etc. Asimismo, la posibilidad de sintetizar este nanomaterial directamente sobre el papel aporta simplicidad, mejora la operatividad del sistema y reduce el coste del dispositivo ya que no se requieren operaciones de preparación y purificación en la síntesis del compuesto [14].

Por otro lado, la utilización de una cámara digital y la función iOS de un Smartphone para la detección de determinados compuestos aporta nuevamente simplicidad en el análisis y permite mantener la portabilidad del sistema de detección. Así, debido a las capacidades de los Smartphone (sensores, cámaras digitales, potencia de procesamiento, aplicaciones, conectividad, portabilidad, etc.) la utilización de estos dispositivos como detectores ofrecen dispositivos de diagnóstico analítico rápidos, de bajo costo y fáciles de utilizar [15]–[18].

En este sentido, el acoplamiento de sensores portátiles y Smartphones proporcionan las medidas precisas para la detección colorimétrica de compuestos de interés en diversos campos de aplicación como el diagnóstico de enfermedades. Estos sensores se utilizan para caracterizar e identificar la concentración de compuestos químicos y biológicos en

función de sus interacciones con moléculas especificas tales como, colorantes, enzimas y anticuerpos [19], [20].

Objetivo

En el segundo trabajo de esta Memoria se describe el diseño y desarrollo de un µPAD para la determinación colorimétrica de glucosa implementado con el MOF Fe-MIL-101, que actúa como mimético de la peroxidasa (HRP), y empleando como dispositivo de detección una cámara fotográfica y un Smartphone.

Con este fin se llevó a cabo la síntesis del MOF Fe-MIL-101 en papel utilizando ácido tereftálico y tricloruro de hierro en dimetilformamida (DMF). Seguidamente se evaluaron las características estructurales de este compuesto, así como su actividad catalítica frente al enzima HRP en la reacción colorimétrica de determinación de glucosa. Asimismo, se estableció como parámetro analítico la coordenada de saturación (S) obtenida del despacio de color HSV para determinar la concentración de glucosa de una muestra. A continuación, se optimizaron las variables influyentes en la reacción de determinación de glucosa entre las que se encuentran: concentración óptima de MOF Fe-MIL-101, TMB, GOx, pH de la reacción, distribución de los reactivos en el µPAD, tiempo de reacción y volumen de muestra empleado. Una vez optimizado el sistema se procedió a la caracterización analítica del mimo. Además, se estudió la estabilidad del dispositivo desarrollado, así como la selectividad que presenta el mismo en la determinación de glucosa. Por otro lado, se comprobó la viabilidad de utilizar como dispositivo de imagen para la medida del color un Smartphone. Finalmente, se evaluó la utilidad del µPAD propuesto para la determinación colorimétrica de glucosa mediante el análisis de muestras reales de suero y orina.

En definitiva, las etapas de las que consta este trabajo pueden resumirse en:

1. Síntesis y caracterización del MOF Fe-MIL-101.
2. Fabricación y preparación del µPAD.
3. Optimización de las variables influyentes en la determinación de glucosa.
4. Caracterización analítica del método propuesto para la determinación colorimétrica de glucosa.
5. Empleo de una cámara fotográfica y un Smartphone como sistemas de análisis para extraer la información analítica del µPAD de forma fácil y rápida.
6. Determinación de glucosa en muestras de suero y orina.

MICROFLUIDIC PAPER-BASED DEVICE FOR COLORIMETRIC DETERMINATION OF GLUCOSE BASED ON A METAL-ORGANIC FRAMEWORK ACTING AS PEROXIDASE MIMETIC

Abstract

This work presents a microfluidic paper-based analytical device (µPAD) for glucose determination using a supported metal-organic framework (MOF) acting as a peroxidase mimic. The catalytic action of glucose oxidase (GOx) on glucose causes the formation of H_2O_2, and the MOF causes the oxidation of 3,3',5,5'-tetramethylbenzidine (TMB) by H_2O_2 to form a blue-green product with an absorption peak at 650 nm in the detection zone. A digital camera and the iOS feature of a smartphone are used for the quantitation of glucose with the S coordinate of the HSV colour space as the analytical parameter. Different factors such as the concentration of TMB, GOx and MOF, pH and buffer, sample volume, reaction time and reagent position in the µPAD were optimized. Under optimal conditions, the value for the S coordinate increases linearly up to 150 $\mu mol \cdot L^{-1}$ glucose concentrations, with a 2.5 $\mu mol \cdot L^{-1}$ detection limit. The µPAD remains stable for 21 days under conventional storage conditions. Such an enzyme mimetic-based assay to glucose determination using Fe-MIL-101 MOF implemented in a microfluidic paper-based device possesses advantages over enzyme-based assays in terms of costs, durability and stability compared to other existing glucose determination methods. The procedure was applied to the determination of glucose in (spiked) serum and urine.

Keywords: µPADs · Enzyme mimic · Photographic camera · Smartphone app · Colorimetric assay · Glucose monitoring · 3,3',5,5'-Tetramethylbenzidine

1. Introduction

The use of biomimetic catalysts to imitate natural enzymes by using alternative materials in analytical devices is of great interest for reducing costs and increasing stability, robustness and recyclability. The materials developed by biomimetic chemistry include

nanozymes [21], such as nanomaterial-based artificial enzymes and nanomaterials with enzyme-like activities. The main groups of nanozymes consist of artificial hydrolytic enzymes, such as metallocolloids or dendrimers [22], and artificial redox enzymes that mainly mimic superoxide oxidase, catalase, oxidase or peroxidase activity. These nanozymes have many applications in fields ranging from biosensing to immunoassays, cancer diagnostics and therapy [23].

Focusing on peroxidases and especially horseradish peroxidase (HRP), an important heme-containing enzyme, many analogs have been described as HRP mimics [24] such as magnetic nanoparticles [25], cerium oxide nanoparticles [26], Co_3O_4 nanoparticles [27], Au@ Pt core-shell nanohybrids [28], Ag_3PO_4 nanocrystals, metal-organic frameworks (MOF) [29], carboxyl-modified grapheme oxide [30], single-walled carbon nanotubes [31], helical carbon nanotubes [32], and carbon dots [33].

MOFs are highly porous materials composed of extended structures of metal ions connected by coordination bonds to multi-topic organic molecules, which can lead to a potentially huge number of possible combinations [34]. Their essential characteristics are: high porosity and high surface area, structural versatility, and ability to present specific functionality [35].

Metal nodes for MOF include transition, rare-earth, alkaline or alkaline-earth metal ions and size, coordination geometry, and angularity of the multi-topic ligands and metal clusters define the crystal structure of the MOFs [34]. Due to its porosity, MOFs can provide active sites and channels for transport for reactants and products, creating a catalytic microenvironment with highly tunable properties [36]. However, the characteristics of the MOF not only depends on the chemical composition, but also on the microstructure, morphology and size; hence the type of chemical synthesis used is important [37].

Two types of MOF-based biomimetic catalysts were used: 1) MOF frameworks themselves; and 2) catalytically active species or compounds/complexes encapsulated into MOFs. Examples of type 1 include Fe(III)-based MOFs, namely MIL-53(Fe) [38] or HAP@MIL-100(Fe) [39] for glucose determination in solution. Examples of type 2 include the hemin molecule encapsulated into MOFs such as the amino-containing MIL-

101 and HKUST-1 proposed for glucose determination [40], although a further step would be the encapsulation of heme-based enzymes into MOFs [35] or the embedding of multiple enzymes (GOx/HRP) in Zn(II) imidazolate framework [41].

This work demonstrates a paper-based microfluidic colorimetric device for the determination of glucose in serum and urine samples based on Fe-MIL-101 MOF as the HRP mimic. The microfluidic paper-based devices (μPADs) are currently emerging as a very interesting platform in biosensing applications because they are low-cost, disposable, rapid and technically simple, have high throughput and low sample consumption [42]. In short, μPADs have been recognized as a good solution for point-of-care (POC) diagnostic devices in health care and other sectors, so-called point-of-need (PON) testing [43].

2. Experimental

2.1. Reagents and materials

D(+)–Glucose; D(+)-fructose; D(+)-maltose-1-hydrate; D(+)-sucrose; sodium chloride and hydrogen peroxide 30% w/v from Panreac (http://www.panreac.es). D(+)-Mannose; D(+)-galactose; glucose oxidase from Aspergillus niger; terephthalic acid; DL-cysteine; 3,3',5,5'-tetramethylbenzidine (TMB); TRIS hydrochloride; glacial acetic acid; N,N-dimethylformamide (DMF); tetrahydrofuran (THF); ethanol; sodium hydroxide; sodium acetate; sodium phosphate; sodium hydrogenphosphate; sodium dihydrogenphosphate; anhydrous calcium chloride; iron trichloride hexahydrate; uric acid; urea; albumin bovine serum (BSA) and chitosan from Sigma-Aldrich (http://www.sigmaaldrich.com).

All reagents were of analytical-reagent-grade unless stated otherwise. All aqueous solutions were made using reverse-osmosis type quality water (Milli-RO 12 plus Milli-Q station from Millipore, conductivity 18.2 MΩ·cm). Filter paper (ref. 1240, basis weight 85 $g \cdot m^{-2}$; thickness 200 μm; retention 14-18 μm) from Filter-Lab (www.fanoia.com), double-sided adhesive tape from Miarco (http://www.miarco.com) and transparent sheets from Schwan-Stabilo (http://www.schwan-stabilo.com) were used to manufacture the μPAD.

2.2. Apparatus, instruments and software

The colour of the μPAD was measured with a Canon PowerShot S5 IS digital camera (Canon Inc., Tokio, Japan) as well as an iPhone 4.0 smartphone (Apple Inc., Cupertino, CA, USA). ImageJ (National Institutes of Health) software was used to analyse the region of interest (ROI) of the image along with the Color Space Converter plugin (http://rsb.info.nih.gov/ij/plugins/color-space-converter.html). Objective-C was used for the development of application software. The laboratory evaluations of μPAD in serum samples were completed for validation purposes, using Accu-Chek Aviva Nano (Roche, Switzerland) glucose-meter provided with test-strips ref. 111.

2.3. Synthesis and characterization of the metal organic framework

Fe-MIL-101 was prepared as described in the literature [44], [45] with some minor modifications. In a typical synthesis, a mixture of 0.270 g (1 mmol) of $FeCl_3 \cdot 6H_2O$, 0.166 mg of terephthalic acid (1 mmol), and 15 mL DMF was heated at 110 ºC for 20 h in a Teflon-lined stainless steel bomb. The resulting brown solid was filtered off, and purified by washing in hot ethanol (60 ºC, 3 h, 2 times), filtered off, and dried in an oven (70 ºC, 30 min). The mean yield was around 20%. The synthesized Fe-MIL-101 was characterized with X-ray diffraction (XRD) (Fig. S1).

2.4. Production of the μPAD

The devices were produced in a paper sheet using a craft-cutting technique as a cost-efficient, simple and reproducible process. The μPAD pattern was first designed using Illustrator software (Adobe Systems) and the design was exported as an FS file to the controller software of a desktop laser engraver with a 12 W CO_2 laser source (Rayjet, www.rayjetlaser.com). For the production, a piece of selected paper was affixed at the ends of the base of the laser printer using adhesive tape to prevent tearing, and then was cut with a single pass of the laser beam. To optimize the procedure and the substrate used, the μPAD elements were produced in 4x32 replicas by cutting the plastic-backed cellulose paper (203 mm x 254 mm) and removing the weeding manually. The rate of success was 99 %, thus confirming the viability of the design.

The device (Fig. 1) consists of three separate zones, one for sampling, a transport channel where the cocktail with glucose oxidase and buffer are immobilized, and a detection zone where the chromogenic reagent and MOF are immobilized. The device was taped to a rigid plastic support using double-sided adhesive tape.

The device was prepared by drop casting the needed reagents in each respective zone under ambient atmospheric conditions. To prepare the detection zone, 1 µL of 2.5 mmol·L^{-1} TMB was dispensed onto the detection zone and then dried. Next, 1 µL of 0.75 mg·mL^{-1} MOF suspension in 2 mg·mL^{-1} aqueous chitosan was added. Then, the transport channel was prepared by adding 1 µL of a cocktail containing 105 µL of pH 7.4 phosphate buffer 1 mmol·L^{-1}, 15 µL of 2 mg·mL^{-1} aqueous chitosan and 1.5 µL of 1993.9 U·mL^{-1} of GOx, then dried at room temperature for 5 min. The µPADs were stored in a dry environment at 4 °C in the dark until use.

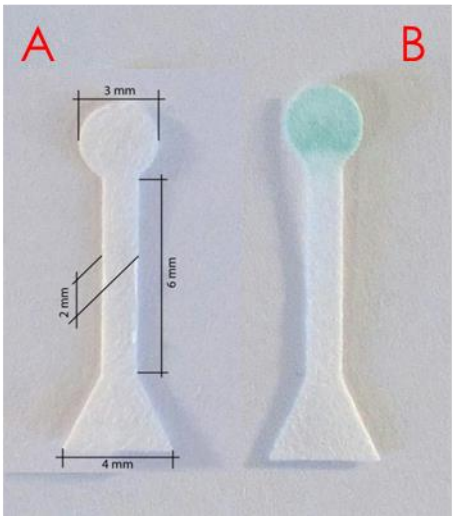

Figure 1. Picture of the µPAD indicating dimensions. µPAD before (A) and after (B) reaction with glucose.

2.5. Image capture and processing

The µPADs were imaged with a digital camera after reacting with glucose containing samples or standards. The optimized setting conditions used to acquire the picture of the devices were: ISO 100, shutter speed 1/500 s, aperture value f/4 and focal length of 6.1 mm, automatic white balance; resolution 3264x2998; super-macro mode. To maintain all the image-gathering conditions constant, a Cube Light Box was used with the camera

placed in the front of a homemade white wooden box with two LED 6500 K lamps placed at 45º with respect to the digital camera, with the μPAD in a fixed position inside the box to isolate it from external radiation. The captures were obtained in JPEG format.

An additional readout method was used to determine glucose with a CMOS sensor based on the HSV variation acquired and processed with a smartphone. An iPhone 4.0 with a 5-megapixel still camera was set with the flash "off" and the image was saved as a JPEG in the smartphone memory.

The captured images were processed (see Supporting Information) to obtain the region of interest (ROI) that contains the relevant analytical information and the mode value of the S value of pixels presents in the ROI was used as analytical parameter.

2.6. Analytical protocol

For glucose determination, 10 μL of a solution of different concentrations of glucose is dropped onto the sampling area of the microfluidic device. After the solution flows by capillarity towards the zones where the reagents are placed, twenty minutes are needed to complete the reaction, when a blue colour appears in the white detection zone (Fig. 1). Once the sensing area is allowed to react, a picture of the microfluidic device is captured using a digital camera, as indicated above, to maintain controlled light conditions. The concentration is calculated from the calibration curve obtained with glucose standards. During use, the device is maintained in a horizontal position over a non-absorbent surface to keep the solution from flowing in a particular direction.

3. Results and discussion

Among the various Fe(III)-terephthalic acid metal-organic frameworks described, the Fe-MIL-101 is notable for its good catalytic properties. It has a rigid zeolite-type structure, with rigid terephthalate ligands (BDC), consisting of cages of two (29 and 34 Å) modes accessible through microporous windows of 12 and 16 Å. With framework formula Fe_3-(μ_3-O)Cl(H_2O)$_2$(BDC)$_3$ [45], the MOF consists of Fe(III) carboxylate trimeric clusters with terminal water molecules [46]. Removing the water by heating creates unsaturated

coordination sites. Together with the large pores of Fe-MIL-101, which allows access to the active MOF sites where the Fe(III) acts as a Lewis acid, this justifies the catalytic activity.

To control the size and shape of the MOF, which determines its chemical and physical properties, different modulators are added during the synthesis to the adjust acidity, ion-strength, and/or polarity of the reaction medium [47]. In this case, the mild solvothermal synthesis of the MOF produces Fe-MIL-101, which has a typical octahedron morphology, although the use of modulators like sodium acetate or glycerol produces spindle-shape and bipyramidal hexagonal-shape MOFs, respectively [44].

The peroxidase-like catalytic activity of Fe-MIL-101 in solution has been studies by Chen et al. [48] with the substrates TMB and H_2O_2 as the model reaction system. The apparent Michaelis constant K_m found with TMB as the substrate (0.158 mmol·L^{-1}) and H_2O_2 as the substrate (0.006 mmol·L^{-1}) was lower than that of the natural enzyme HRP (0.434 mmol·L^{-1} and 3.7 mmol·L^{-1}, respectively), indicating that this MOF has a high binding affinity, mainly to H_2O_2. Another interesting feature of Fe-MIL-101 is its high affinity to H_2O_2 over a broad pH range, especially at neutral pH, for which reason we selected this MOF as the HRP mimetic in a glucose assay. The catalytic mechanism of Fe-MIL-101 studied with photoluminescence [48] suggests the decomposition of H_2O_2 activated by MOF to generate ·OH radicals, which are released before they react with the second substrate TMB, which is probably adsorbed onto the MOF via π-π and hydrogen bond interactions in a ping–pong mechanism, as described for MIL-53(Fe) [38], [49].

To the best of our knowledge, no paper device has been described for the quantitative determination of analytes using MOFs as a mimic of enzymes, except for the proposal by Chen et al. using hydroxyapatite nanowires-MIL-100(Fe) MOF core/shell nanofibers fixed on paper by filtration for the visual semiquantitative determination of glucose [39]. Additionally, the selected MOF Fe-MIL-101 has been primarily used in synthetic chemistry as a catalyst, such as for the allylic oxidation of cyclohexane, alkenes, acetalization of aldehydes, and sulfoxidation of aryl sulphides [46], [50], in environmental remediation as visible light photocatalysts of dyes [51] and in drug delivery [45].

The purpose of this study is to prepare a capillary platform that includes a nanozyme to mimic the enzyme role, thus improving the analytical characteristics, the stability of the analysis and cutting costs. As the model system, the enzymatic glucose determination based on GOx and Fe- MIL-101 as peroxidase mimic was selected.

The capillary platforms attain passive liquid transport via capillary forces acting in a single capillary or in the capillaries of fibrous materials or microstructured surfaces [52]. Different materials have been used such as paper, thread and cloth fabrics which, although they share capillary action, differ in characteristics such as the length of the fibres, interfibre bonding and porous channel structures [52]. In this case, we developed a paper-based analytical assay (µPAD) in combination with a digital camera to quantify the analyte by colour measurement [42].

3.1. µPAD preparation

For the selection of the µPAD membrane, different materials were tested, looking for the following conditions: no reagent or reaction product leaching and a homogeneous distribution of colour in the detection area. The materials tested for both the µPAD preparation and colour measurement included quantitative filter papers of different filtration and retention capacity (8 types from 1 to 30 µm pore size, and 80-100 $gr \cdot m^{-2}$ basis weight). The best results in terms of colour intensity, the difference between blank and signal and the homogeneous distribution of dye were obtained with cellulosic membrane (ref. 1240) with fast filtration, 80 $gr \cdot m^{-2}$ basis weight, 14-18 µm pore size, and 0.170 mm thickness (Fig. S3).

To select the most appropriate location of the reagents in the µPAD, several alternatives were studied between the transport channel and the detection zone. Table S1 and Fig. S4 show that the separation between the recognition reaction and the transduction reaction in the presence of chitosan in both location is the one that has the best results with the lowest standard deviation.

The size of each area and the layout of the µPAD were designed to obtain a suitable collection of the sample, to minimize the impact of the separation between the glucose

recognition zone and H_2O_2 detection zone and to minimize colour reading errors. Therefore, the nanozyme μPAD for glucose was a single-channel-type device with a triangular sampling area at the bottom of the device for a 10 μL sample, a transport channel containing the recognition chemistry immobilized by adsorption on the cellulose and a detection area with chemistry immobilized, with 7 mm from the middle of the transport channel to the middle of the detection area. In addition, the detection area was 3 mm-diameter, i.e. ROIs of some 6000 pixels.

The movement of the water within the selected paper fits the Washburn equation ($L=A\sqrt{t}$) with A = 0.5698 (R^2 = 0.9975). The experimental data for the designed μPAD shows some Washburn-type behaviour because of the change in channel length along the device, with the average time needed to wet the μPAD being 9.5 ± 0.7 s.

3.2. Optimization of method

Different peroxidase substrates were tested for catalytic oxidation with MOF [38], [44], [48] in the glucose μPAD, such as 2,2′-azino-bis(3-ethylbenzothiazoline-6-sulfonic acid) diammonium salt (ABTS), o-phenylenediamine (OPD) and 3,3′,5,5′-tetramethylbenzidine (TMB). TMB was selected and the drawback of the inhomogeneous colour distribution in the detection area [52] is overcome by including chitosan, which is retained by electrostatic adsorption and hydrogen bonding in the cellulose along with oxidized TMB [53].

The chemical conditions under which the glucose test is carried out are the result of balancing the conditions needed for both the recognition and transduction steps. The nanozyme Fe- MIL-101 used as a peroxidase mimetic in the μPAD was deposited on the paper from an aqueous dispersion retained on the cellulosic fibres, as shown in the SEM images in which MOF has an octahedral morphology with an average diameter of 250±30 nm (Fig. 2 and Fig. S5).

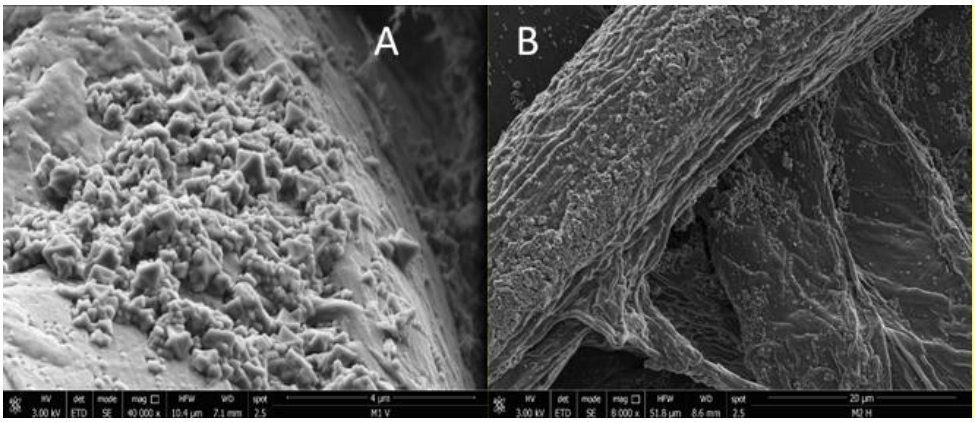

Figure 2. SEM images of the Fe-MIL-101 MOF in cellulosic support.

The following parameters were optimized: a) TMB concentration; b) MOF concentration; c) sample pH value and d) GOx concentration. The following experimental conditions were found to give best results: a) the concentration selected as optimum for TMB was 2.5 mmol·L^{-1}, i.e. 0.60 µg TMB per recognition area or 85 ng·mm^{-2}, b) the optimum for MOF was 0.75 mg·mL^{-1}, i.e. 0.75 µg MOF per recognition area or 106 ng·mm^{-2}, c) a sample pH value of 7.4, d) the concentration selected as optimum for GOx was 16.6 U·mL^{-1}. Respective data are given in the Electronic Supporting Material Figure S6.

By monitoring the colour change in the µPAD (Fig. S7) we observed that the reaction time required to complete the assay is 15 min, which is less time than when using the MOF procedures in solution, which is typically 20 min at 40-45ºC, as shown in Table S2. The decrease in saturation after 15 min is due to the drying of µPAD, which produces a colour change.

To study the sample volume, different volumes of glucose solution were dispensed on the sampling area of the µPAD, and 10 µL was selected as the working volume, as it is sufficient to wet the device with good precision (Fig. S8).

3.3. Choice of materials and analytical characterization

We have selected MOFs as peroxidase mimetic in µPAD format by three general reasons: good mimetic activity, not used on µPAD devices and low toxicity and namely the Fe-MIL-101 MOF by different reasons: good stability, cheap cost, facile and reproducible synthesis, right size to be immobilized in paper at the same time that allow the diffusion

of sample through cellulosic membranes with different porosity, and good biomimetic ability according to literature.

The colour of the detection area of the device changes from colourless on the white background of the paper, because the small amount of MOF present is not perceptible, to blue from the oxidized TMB. This monotonal colour change is followed by the saturation coordinate S of the HSV colour space after imaging the device with a digital camera. The S value increases with glucose concentration. The analytical function is obtained by means of a calibration set composed of 8 glucose standards between 1 and 150 µmol·L^{-1} with 3 replicates each and using 20 min as the reaction time (Fig. 3).

$$\frac{1}{S} = a\frac{1}{[Glucose]} + b \quad (1)$$

The dependence between the S value and glucose concentration, obtained with a digital camera, is a Michaelis Menten-type dependence, which fits well with a rectangular hyperbolic equation that is linearized using a Lineweaver-Burk transformation. The linear relationship (R^2 = 0.958) holds up to 150 µmol·L^{-1}.

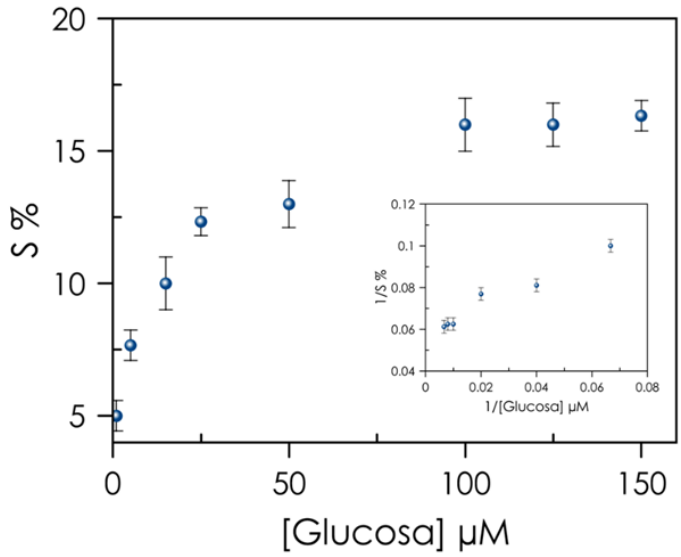

Figure 3. External calibration for the glucose µPAD with digital camera. Data points are the mean of 3 assays. The data were fit with Eq. (1) and the inset shows the linear calibration using a Lineweaver-Burk transformation.

Fig. S9 includes the same calibration acquired with a Pixcolor application smartphone to show the viability of the proposal with this device. The performance characteristics of the device are presented in Table 1.

The detection limit (DL) was obtained using the standard criteria from a relative standard deviation of the blanks (n=8) of 1.8 %, giving 2.5 $\mu mol \cdot L^{-1}$ (0.45 $mg \cdot L^{-1}$) and a quantification limit of 10.6 $\mu mol \cdot L^{-1}$ (1.92 $mg \cdot L^{-1}$), acceptable values taking into account the normal values in biological fluids.

The repeatability, as RSD, obtained using 8 different µPADs working at 25 $\mu mol \cdot L^{-1}$ and 100 $\mu mol \cdot L^{-1}$ glucose is 1.8 %, an acceptable precision considering the measuring system used. The lifetime of the µPAD was studied for 21 days using two series of prepared devices, regularly checking their response to a 100 $\mu mol \cdot L^{-1}$ glucose concentration. One series was protected from light and preserved at 4ºC and the other protected from light in a desiccator at room temperature. During the study period, it was observed that the signal is maintained when protected from light at 4ºC, only decreasing 10 %, while at room temperature the device has a lifetime of some 3 weeks, decreasing 73 % at the end of the study. Additionally, the cost of the µPAD considering only the reagents and paper is around 2 cents/unit and 0.03 cents/unit considering MOF only.

Table 4. Analytical characteristics of µPAD for glucose.

Analytical Parameter	Value
Measurement range ($\mu mol \cdot L^{-1}$)	10.6-150
Slope (b)	0.04
Intercept (a)	13.79
LOD ($\mu mol \cdot L^{-1}$)	2.5
LOQ ($\mu mol \cdot L^{-1}$)	10.6
Precision (%) 25 $\mu mol \cdot L^{-1}$	1.9
Precision (%) 100 $\mu mol \cdot L^{-1}$	1.8
Lifetime (days)	21

A comparative study of different procedures using mimetic materials in solution and in paper-based microfluidic devices from the literature is presented in Table S2. The methods for glucose in solution using peroxidase mimetics are more sensitive in general due to the use of spectrophotometer. Compared to µPAD assays based on the whole bienzymatic system (GOx+HRP) or on GOx and mimetic, the sensitivity is greatly reduced. From the few µPAD described in literature for glucose determination that use mimetics, the here presented offer the best sensitivity, both in detection limit and in slope of calibration function.

3.4. Interferences

To check potential interferences in serum and urine that can affect the analytical signal of the MOF-based µPAD, we specifically studied the effect of some species common in theses samples. D(+)maltose, sacarose, D(+)fructose, D(+)mannose, D(+)galactose, uric acid, urea, BSA, NaCl, $CaCl_2$, solutions containing 2000 µmol·L^{-1} interference and 100 µmol·L^{-1} glucose were analysed in triplicate showing good selectivity (Fig. 4 and Fig. S10).

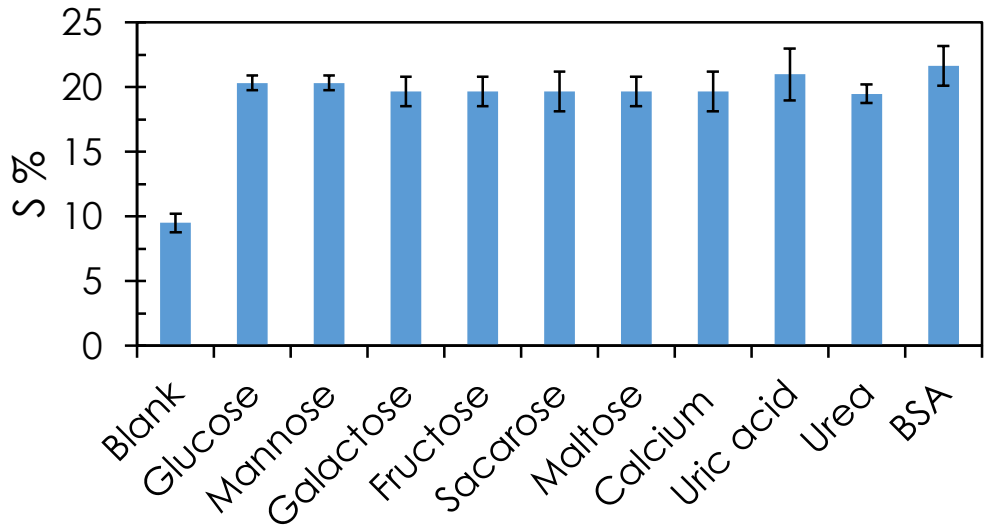

Figure 4. Selectivity of µPAD for 100 µmol·L^{-1} glucose in the presence of 2000 µmol·L^{-1} interferents.

3.5. Validation

To test the capabilities of developed µPAD assay, the determination of glucose in two biological fluids (serum and urine) was performed. Samples of blood and urine obtained from anonymous healthy volunteers were analysed. The results obtained by the proposed method agree with those obtained by glucose-meter, confirming the reliability and precision of the proposed method for glucose detection in real samples. The spiked recoveries of glucose in serum samples have been investigated and the results are shown in Table 2. These results suggest that the colorimetric method proposed in this work can be used for the determination of glucose in real samples obtaining good recovery percentage and precision.

Table 5. Real samples glucose determination[a].

	Glucose content µmol·L^{-1}			Recovery study		
Samples	**Glucometer**	**µPAD**	**Test t[b] t_{exp}**	**Added µmol·L^{-1}**	**Found µmol·L^{-1}**	**Recovery %**
Serum	33 ± 3.1	40 ± 3.2	2.722	100	130 ± 7.5	92.8
	35 ± 1.0	31 ± 2.3	2.762		135 ± 2.3	103.1
	33 ±1.7	32 ± 3.6	0.435		129 ± 6.1	97.6
	48 ± 3.1	49 ± 4.2	0.332		152 ± 2.1	102.5
Urine	---	4 ± 1.7	---	100	113 ± 4.0	108.6
	---	1.3 ± 0.6	---		104 ± 1.1	102.7
	---	3.2 ± 0.6	---		109 ± 1.5	105.2

[a]The sample treatment was a 1:10 dilution for urine and serum and a previous filtration through 0.20 µm for urine. 10 µL of each sample of serum or urine were placed in the sampling area of the microfluidic device and, after 20 min, a picture was taken with the digital camera. n=3. [b]Comparison of means with Student's t, $t_{tab(0.05,4)}$ =2.776.

4. Conclusions

The present work studies the design and characterization of a paper based microfluidic colorimetric assay for glucose. The assay is based on Fe-MIL-101 MOF to mimic the immobilized peroxidase on commercial cellulose paper. The assay is simple to prepare and use, low cost and allows accurate determination of glucose using a small sample volume (10 µl). The images were acquired with a digital camera, or alternatively with a smartphone, that was processed in the latter case on the same device with a developed iOS application. The use of MOF as a peroxidase mimetic in µPAD, demonstrated in this work for the first time to the best to our knowledge, has advantages over enzyme-based

assays in terms of cost, durability and stability compared to other existing glucose determination methods and in terms of cost (0.03 cents/unit) comparing with those using other mimetic materials. These advantages open the way for the use of MOF materials in microfluidic capillary devices combined with consumer electronics devices for POC and PON applications.

5. Electronic supplementary material

5.1. XRPD analysis of Fe-MIL-101 MOF

The sample was gently deposited in the hollow of an aluminium holder equipped with a zero background plate. Diffraction data (Cu $K\alpha$, λ = 1.5418 Å) were collected on a θ:θ Bruker AXS D8 vertical scan diffractometer equipped with primary and secondary Soller slits, a secondary beam curved graphite monochromator, a Na(Tl)I scintillation detector, and pulse height amplifier discrimination. The generator was operated at 40 kV and 40 mA. The optics used were the following: divergence 0.5°, antiscatter 0.5°, receiving 0.2 mm. A scan was performed with 5 < 2θ < 23° with t = 0.5 s and $\Delta 2\theta$ = 0.02°. The bail refinement (Fig. S1) was obtained with the unit cell of Fe-MIL-101 material with TOPAS [54] [cubic *Fd*-3*m*, a = 89,902 Å]. The XRD pattern for Fe-MIL-101 MOF (Figure S1) were in agreement with the literature [44], [55] and with the pattern calculated from the crystallographic data.

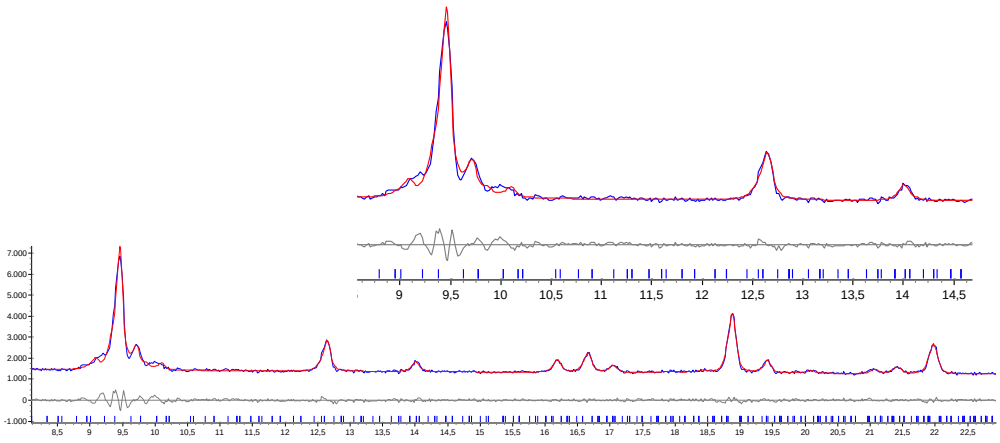

Figure S1. LeBail refinement results for sample as appreciable from experimental (blue), calculated (red), and difference (gray) diffraction patterns. For the sake of clarity, the portion above 9-15° has been magnified (3X). Horizontal axis: 2Θ, deg.

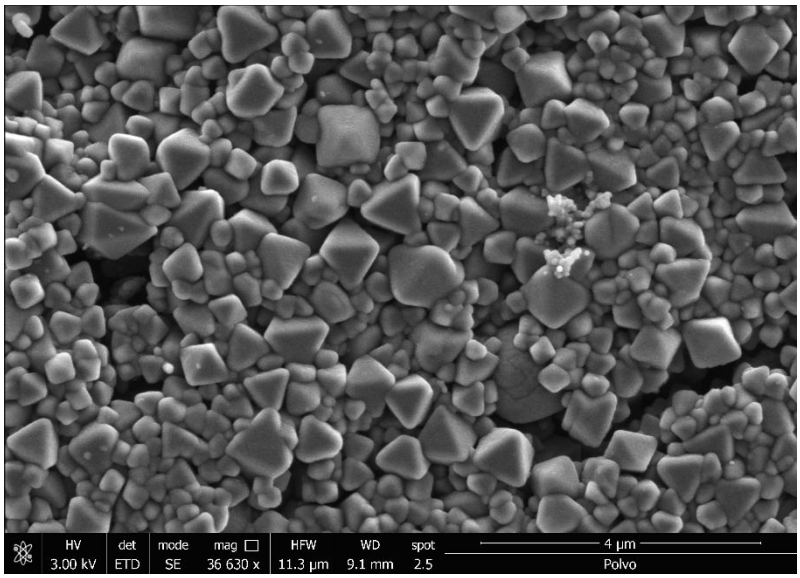

Figure S2. SEM images of as prepared octahedral Fe-MIL-101 MOF obtained at high magnification.

5.2. Image-processing

The images were processed using the digital editing software GIMP 2.8.10 Adobe by selecting the region of interest (ROI) that contains the relevant analytical information. The ROI of each picture was selected using the colour picker tool of the editor from a circle slightly smaller than the detection area of the µPAD, which typically contains around 6000 pixels. Each colour channel was normalized independently to calculate the RGB values as well as the S parameter of the HSV colour space [56], which was used as the analytical parameter, and their corresponding standard deviations.

A mobile application called "Pixcolor" was developed for an iPhone device with the iOS operating system. The software that we embedded in the device uses the image captured by the CCD sensor to retrieve the colorimetric information. The processing is done in two separate stages; the first is submitted to conventional algorithms that extract the CCD sensed image into a separate memory area where it can be processed normally. For the sake of image quality, the processing should be done as soon as possible to prevent the operating system of the device from post-processing the image, which would apply compression algorithms to the image, causing it to take information from the sensor.
Once the image is prepared in the memory, the HSV coordinates are calculated from the RGB coordinates [57], [58], and the saturation value is used for quantitative analysis. Fig.

S2 shows an image of the image processing done by the application. The main menu of the application is customized to offer the possibility of taking a new picture of the microfluidic device or analyse a previous saved picture from the gallery. The selection of the detection zone can be done manually using zoom and pressing “done” to analyse the selection; Figure S2E presents the results of the analysis.

Additionally, this app implements the second stage of the processing, which consists of correcting the image according to the deviation of the specific CCD from the ideal CCD sensor. Two identical CCD sensors do not interpret the scene into the same image, due to variations in the manufacturing process, which makes each CCD sensor unique. The embedded software models the image as in [59] to obtain a footprint of the deviation resulting from a particular sensor. This deviation is used to correct the image as much as possible.

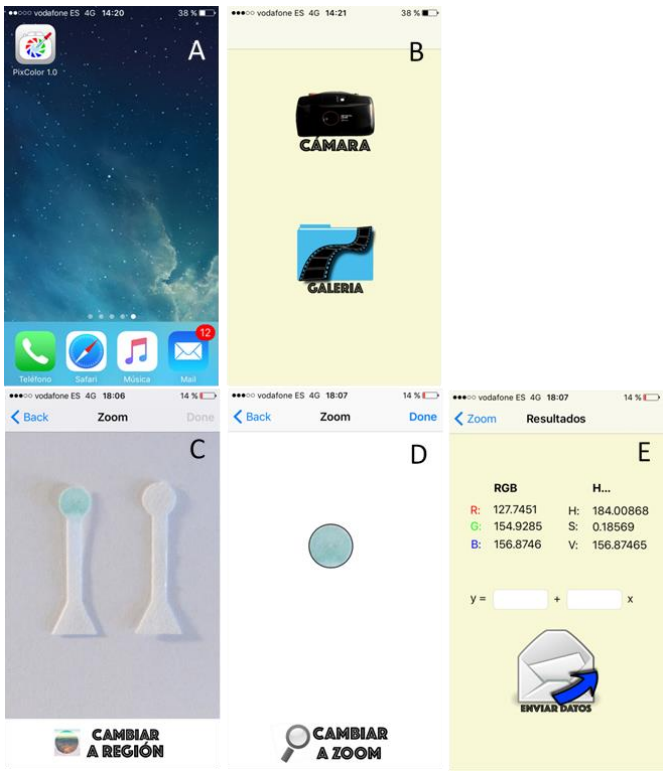

Figure S3. Screen captures of the developed iOS application: (A) iPhone menu app, (B) main menu Pixcolor, (C) acquisition process, (D) sensing area detection and (E) final results obtained after image processing.

5.3. Selection of materials for µpad fabrication

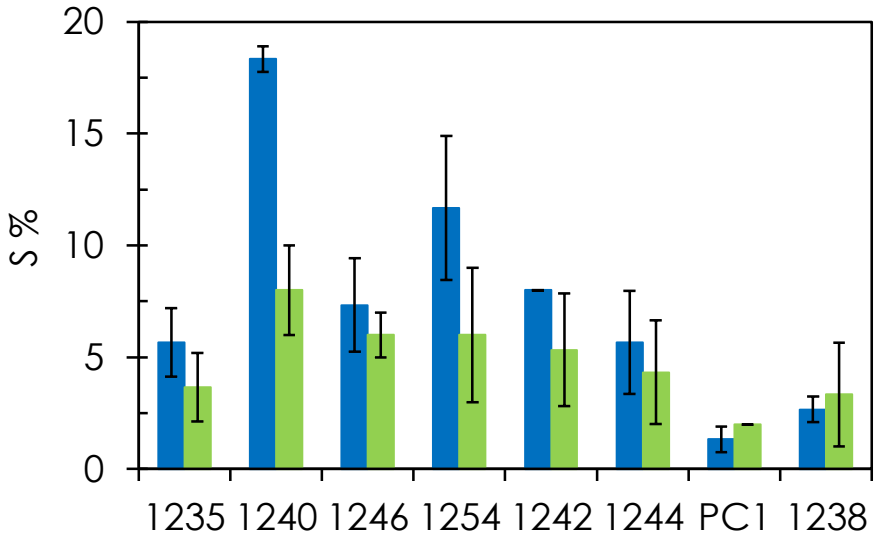

Figure S4. Selection of materials for µPAD fabrication. Conditions: 1.0 µL of TMB solution 2.5 mmol·L^{-1}; 1.0 µL MOF dispersion 0.75 mg·mL^{-1}; 30 µL phosphate buffer pH 7.4 1 mmol·L^{-1}; 1.5 µL GOx 1993.9 U·mL^{-1}; 15 µL chitosan 2 mg·mL^{-1}. Blue bars: with 10 µL glucose 100 µmol·L^{-1}; Green bars: 10 µL water. S% is the coordinate S (saturation) of colour space HSV.Figure S4. Selection of materials for µPAD fabrication. Conditions: 1.0 µL of TMB solution 2.5 mmol·L^{-1}; 1.0 µL MOF dispersion 0.75 mg·mL^{-1}; 30 µL phosphate buffer pH 7.4 1 mmol·L^{-1}; 1.5 µL GOx 1993.9 U·mL^{-1}; 15 µL chitosan 2 mg·mL^{-1}. Blue bars: with 10 µL glucose 100 µmol·L^{-1}; Green bars: 10 µL water. S% is the coordinate S (saturation) of colour space HSV.

5.4. Location of reagents on the µPAD

Table S1. Reagents location on the µPAD.

Test	Detection zone	Transport channel	S	S.D.
1	TMB, MOF, chitosan	GOx, pH 7.4, chitosan	20.0	1.41
2	TMB, MOF, GOx	pH 7.4	19.5	2.12
3	TMB, MOF, GOx, pH 4	pH 7.4	15.5	0.71
4	TMB, MOF, pH 7.4	GOx, chitosan	14.0	1.41
5	TMB, MOF	GOx, pH 7.4	13.0	0.1
6	TMB, MOF, pH 4	GOx, pH 7.4	9.5	0.70
7	TMB, MOF, pH 4	GOx	6.5	2.12

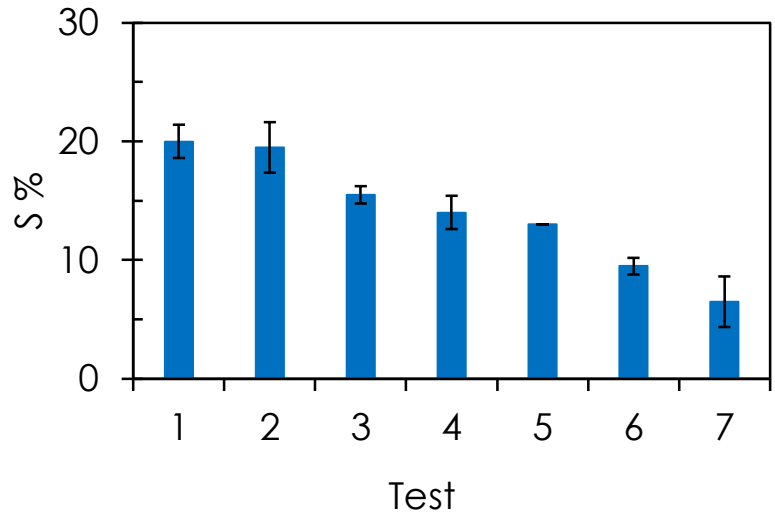

Figure S5. Reagents location on the µPAD. Conditions: 1.0 µL of TMB solution 2.5 mmol·L^{-1}. 1.0 µL MOF dispersion 0.75 mg·mL^{-1}; 30 µL phosphate buffer pH 7.4 1 mmol·L^{-1}; 1.5 µL GOx 1993.9 U·mL^{-1}; 15 µL chitosan 2 mg·mL^{-1} and 10 µL glucose 100 µmol·L^{-1}. S% is the coordinate S (saturation) of colour space HSV.

5.5. Optimization of factors affecting the glucose µPAD

The reagent TMB is deposited on the µPAD detection area from an ethanolic solution, because of its high solubility and evaporation rate in this solvent. Then the MOF is deposited on the same area of the µPAD from an aqueous solution containing chitosan. The optimum amounts of TMB and MOF were studied in separate experiments preparing the devices by casting 1 µL of a TMB solution with concentrations ranging between 1 and 15 mmol·L^{-1} (Fig. S3A) and later preparing devices with 1 µL of an aqueous dispersion with the concentration ranging from 0.10 to 2 mg·mL^{-1} of MOF (Fig. S3B). The concentration selected as optimum for TMB was 2.5 mM, i.e. 0.60 µg TMB per recognition area or 85 ng·mm^{-2}, and the optimum for MOF was 0.75 mg·mL^{-1}, i.e. 0.75 µg MOF per recognition area or 106 ng·mm^{-2}.

The pH was adjusted by placing a buffer in the transport channel of the device along with the enzyme GOx. Like other peroxidase nanozymes, the activity of the Fe-MIL-101 MOF was remarkably dependent on the pH, although usually the maximum for Fe MOF catalytic activity appears between 3.5-4.0, as occurs with MIL-53(Fe) [38], [49], [60]. However, Fe-MIL-101 catalyses effectively over a wider pH range, between 3.0 and 7.0 [48]. A study of the pH dependence made with different devices prepared with GOx in phosphate buffers with the pH ranging from 5.4 to 9.5 deposited in the transport channel

shows a maximum between 7.0 and 7.5, selecting as working pH 7.4 (Fig. S3C), a value that agrees with other glucose devices [61], [62].

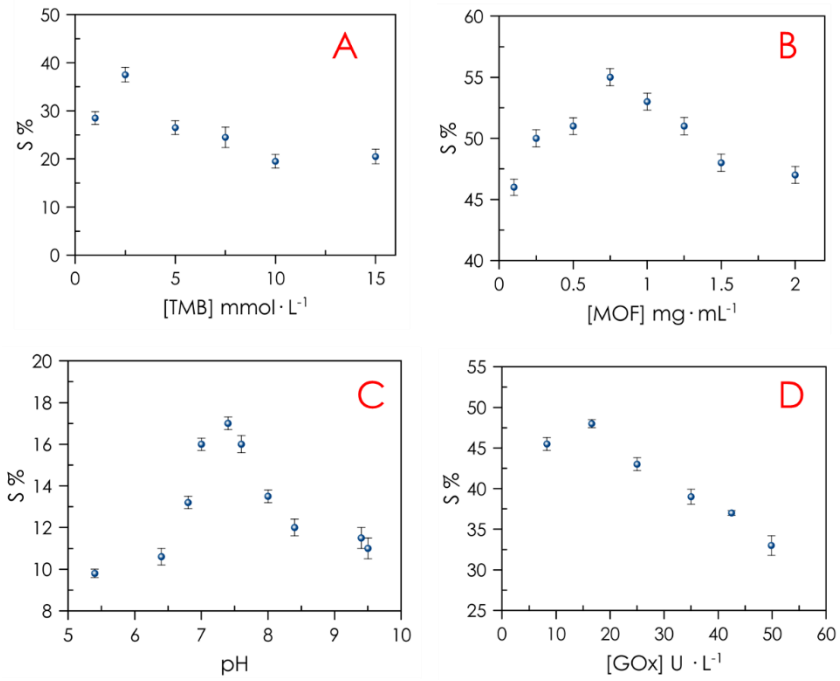

Figure S6. Influencing factors for glucose µPAD: A) Influence of TMB concentration. Conditions: 1.0 µL of different concentrations of TMB; 1.0 µL MOF dispersion 0.75 mg·mL^{-1}; 30 µL phosphate buffer pH 7.4 1 mmol·L^{-1}; 3µL GOx 1049.4 U·mL^{-1}; 15 µL chitosan 2 mg·mL^{-1}; 10 µL glucose 500 µmol·L^{-1}. B) Influence of MOF concentration. Conditions: 1.0 µL of MOF dispersion of different concentrations; 1.0 µL TMB 2.5 mmol·L^{-1}; 30 µL phosphate buffer pH 7.4 1 mmol·L^{-1}; 3µL GOx 1049.4 U·mL^{-1}; 15 µL chitosan 2 mg·mL^{-1}; 10 µL glucose 500 µmol·L^{-1}; C) Influence of pH. Conditions: 1.0 µL TMB 2.5 mmol·L^{-1}; 1.0 µL MOF dispersion 0.75 mg·mL^{-1}; 1.5 µL GOx 1993.9 U·mL^{-1}; 15 µL chitosan 2 mg·mL^{-1}; 10 µL glucose 250 µmol·L^{-1}. D) Influence of GOx concentration. Conditions: 1.0 µL of GOx with different concentrations; 1.0 µL TMB 2.5 mmol·L^{-1}; 1.0 µL MOF dispersion 0.75 mg·mL^{-1}; 30 µL phosphate buffer pH 7.4 1 mmol·L^{-1}; 15 µL chitosan 2 mg·mL^{-1}; 10 µL glucose 500 µmol·L^{-1}. S% is the coordinate S (saturation) of colour space HSV.

The concentration of the enzyme deposited on the transport channel was optimized using devices prepared with 1 µl of GOx solution prepared in 7.4 buffers with concentrations ranging between 8.31 and 49.84 U·mL^{-1} (Fig. S3C). The optimum selected was 16.6 U·mL^{-1}. Although the catalytic activity of Fe-MIL-101 increases with the reaction temperature with a maximum between 35 and 45 ºC as a result of the increase in kinetic energy and the diffusion rate of the H_2O_2 and, hence, an increase in the collisions with the catalytic centres of the MOF [49], [48] this test conducted on paper was done at room temperature (22 ±2 ºC).

5.6. Reaction time

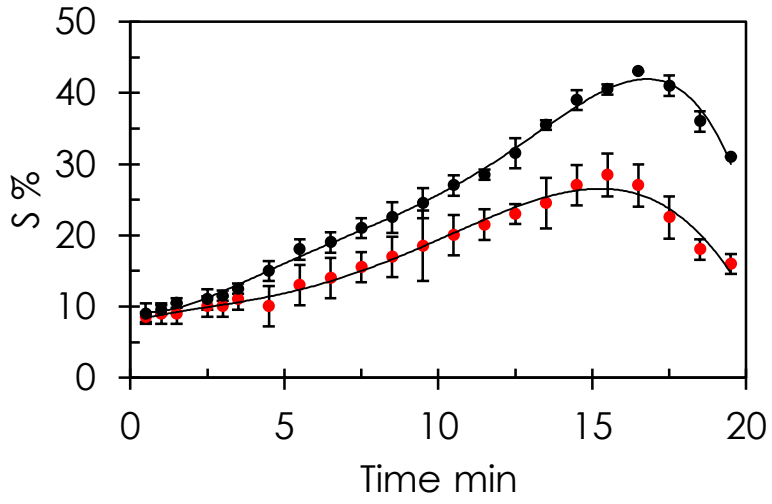

Figure S7. Evolution of saturation coordinate S with time. Conditions: 1.0 µL of TMB solution 2.5 mmol·L^{-1}. 1.0 µL MOF dispersion 0.75 mg·mL^{-1}; 30 µL phosphate buffer pH 7.4 1 mmol·L^{-1}; 1.5 µL GOx 1993.9 U·mL^{-1}; 15 µL chitosan 2 mg·mL^{-1} and 10 µL glucose 500 and 150 µmol·L^{-1}. S% is the coordinate S (saturation) of colour space HSV.

5.7. Influence of sample volume added on the µPAD

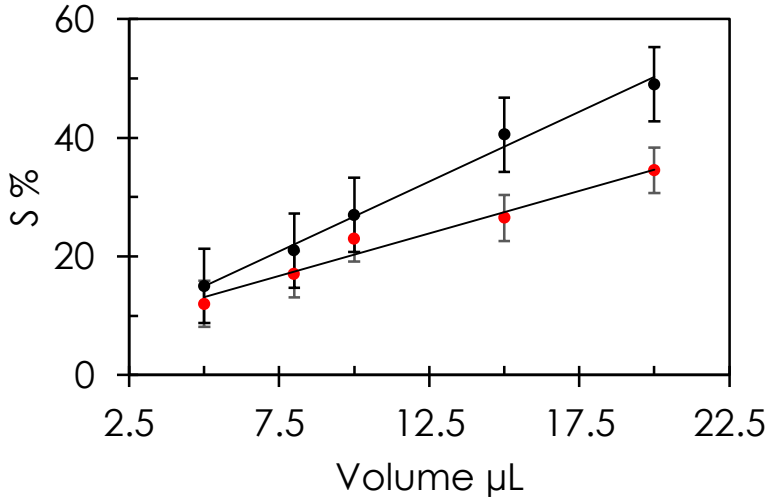

Figure S8. Influence of sample volume added. Conditions: 1.0 µL of ethanolic TMB solution; 1.0 µL MOF dispersion 0.75 mg·mL^{-1}; 30 µL phosphate buffer 1 mmol·L^{-1} pH 7.4; 1.5 µL GOx 1993.9 U·mL^{-1}; 15 µL chitosan 2 mg·mL^{-1}. The red dots correspond to 500 µmol·L^{-1} of glucose and the black dots correspond to 150 µmol·L^{-1} of glucose. S% is the coordinate S (saturation) of colour space HSV.

5.8. Comparison of detection parameters of several glucose procedures based on peroxidase mimetics

Table S2. Analytical figures of merit of recent colorimetric glucose procedures based on peroxidase mimetics.

Analytical System	Chromogenic reagent	Range $\mu mol \cdot L^{-1}$	LOD $\mu mol \cdot L^{-1}$	Medium	Reaction time	Measurement system	Ref.
GOx Fe_3O_4 MNPs	ABTS	50-1000	30	S	30 min (37ºC)	Spectrophotometer	[63]
GOx $ZnFe_2O_4$ MNPs	TMB	1.25-18.75	0.3	S	30 min (37ºC)	Spectrophotometer	[64]
GOx - Co_3O_4 NPs	TMB	10-10000	5	S	20 min (45ºC)	Spectrophotometer	[27]
GOx - HRP NFs	TMB	0–50	0.2	S	25 min (37ºC)	Spectrophotometer	[65]
GOx - HRP NFs	ABTS	0-20	0.3	S	5 min (RT)	Spectrophotometer	[66]
GOx - Hemin/WS_2-NSs	TMB	5-200	1.5	S	30 min (37ºC)	Spectrophotometer	[67]
GOx-MIL - 53(Fe)	TMB	0.25-20	0.25	S	20 min (40ªC)	Spectrophotometer	[38]
GOx-$Cu_2(OH)_3Cl$-CeO_2	TMB	100-2000	50	S	60 min (40ºC)	Spectrophotometer	[68]
GOx-glycine-MIL-53(Fe)	TMB	0.25-10	0.13	S	20 min (40ºC)	Spectrophotometer	[60]
HAP@MIL-100(Fe) NFs	TMB	2-50	25	S	30 min (37ºC)	Spectrophotometer	[39]
GOx - HRP gelatin filter	TBHBA + 4-AAP	1000-55055	---	P	2 min (RT)	Reflectance spectrophotometer	[69]
GOx - HRP SNP with APTS	KI with trehalose	500 – 10000	500	µPAD	15 min (RT)	Scanner	[70]
GOx - HRP	KI	0-20000	---	µPAD	10 min (RT)	Camera/smartphone	[71]
GOx - HRP	4-AAP - MAOS	0-20000	700	µPAD	150 s (RT)	Smartphone	[72]
GOx - HRP NFs	TMB	0-300	15.6	µPAD	15 min (RT)	Digital camera	[73]
GOx - HRP NFs	TMB	100-10000	25	µPAD	10 min (RT)	Digital camera	[74]
GOx - HRP	KI	4000-20000	1470	µPAD	10 min (RT)	Camera phone	[75]
GOx - HRP trehalose	HBA + 4-AAP	0-20000	150	µPAD	10 min (RT)	Camera phone	[76]
GOx-CeO_2 NPs silanized paper	ABTS	< 100000	500	P	10 min (RT)	Scanner	[77]
GOx – Qdots	Fluor. quenching	278-11100	50	P	15 min	Digital camera	[78]
GOx - Fe-MIL-101	TMB	10.6-150	2.5	µPAD	15 min	Digital camera	This paper

AAP: 4-amine antipyrine; ABTS: 2,20-azino-bis(3-ethylbenzthiazoline-6-sulfonic acid; APTS: aminopropyltriethoxysilane; HAP@MIL-100(Fe) NFs: hydroxyapatite nanowires@MOF core/shell nanofibers; Hemin/WS_2-NSs: hemin-functionalized WS_2 nanosheets; HBA: 4-hydroxybenzoic acid; MAOS: N-ethyl-N-(2-hydroxy-3-sulfopropyl)-3,5-dimethylaniline; NFs: nanoflowers; MNPs: magnetic nanoparticles; P: in paper; µPAD: paper-based microfluidic device; RT: room temperature; SNPs: silica nanoparticles; S: in solution; TBHBA: 2,4,6-tribromo-3-hydroxy benzoic acid.

5.9. Dependence of saturation with concentration obtained using a smartphone and a digital camera

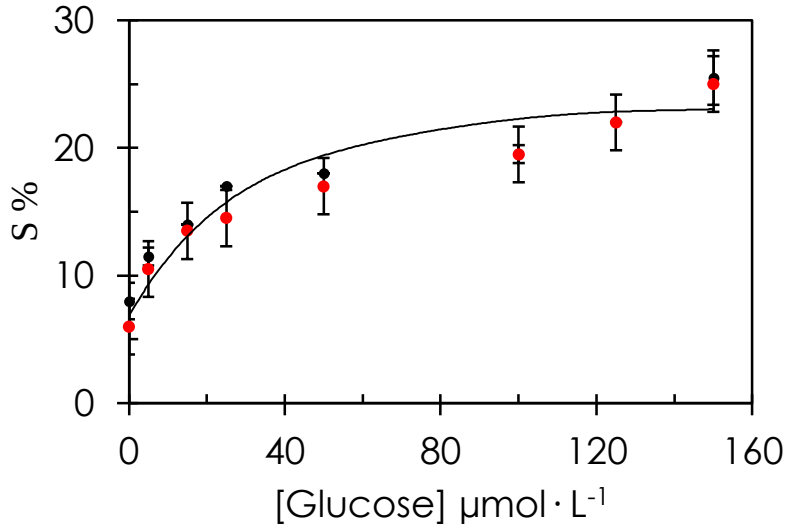

Figure S9. Dependence of saturation with glucose concentration obtained using a smartphone (black dots) and a digital camera (red dots) as analytical devices. Conditions: 1.0 µL of ethanolic TMB solution; 1.0 µL MOF dispersion 0.75 mg·mL^{-1}; 30 µL phosphate buffer 1 mmol·L^{-1} pH 7.4; 1.5 µL GOx 1993.9 U·mL^{-1}; 15 µL chitosan 2 mg·mL^{-1}. S% is the coordinate S (saturation) of colour space HSV.

5.10. Influence of ionic strength

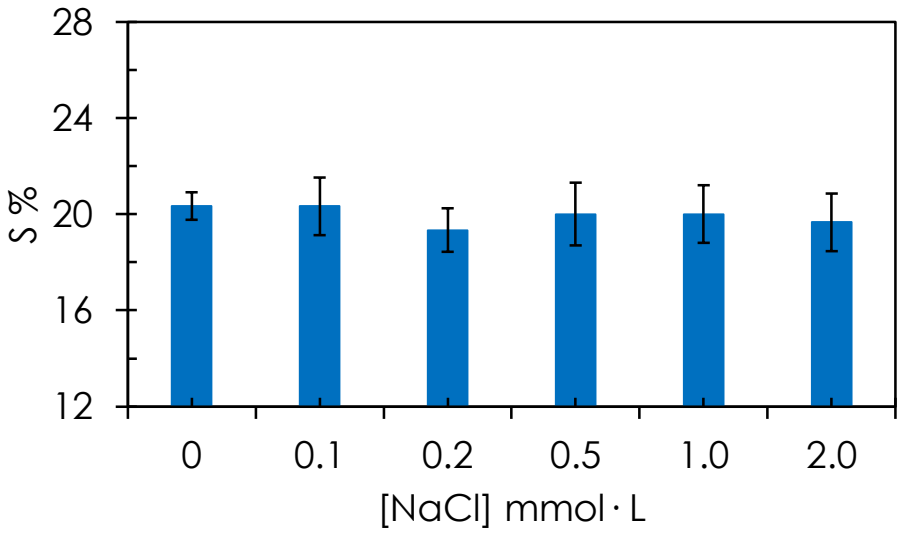

Figure S10. Ionic strenght. Conditions: 1.0 µL of ethanolic TMB solution; 1.0 µL MOF dispersion 0.75 mg·mL^{-1}; 30 µL phosphate buffer 1 mmol·L^{-1} pH 7.4; 1.5 µL GOx 1993.9 U·mL^{-1}; 15 µL chitosan 2 mg·mL^{-1}. Glucose 100 µmol·L^{-1}. S%: coordinate S (saturation) of HSV colour space.

REFERENCES

[1] H.-C. "Joe" Zhou and S. Kitagawa, "Metal–Organic Frameworks (MOFs)," *Chem. Soc. Rev.*, vol. 43, no. 16, pp. 5415–5418, 2014.

[2] H.-S. Wang, "Metal–organic frameworks for biosensing and bioimaging applications," *Coord. Chem. Rev.*, vol. 349, pp. 139–155, Oct. 2017.

[3] M. Giménez-Marqués, T. Hidalgo, C. Serre, and P. Horcajada, "Nanostructured metal–organic frameworks and their bio-related applications," *Coord. Chem. Rev.*, vol. 307, pp. 342–360, 2016.

[4] O. M. Eddaoudi, Mohamed Moler, David B Li, Hailian Chen, Banglin Reineke, Theresa M O'Keeffe, Michael Yaghi, "Modular Chemistry: Secondary Building Units as a Basis for the Design of Highly Porous and Robust Metal−Organic Carboxylate Frameworks," *Acc. Chem. Res.*, vol. 34, no. 4, pp. 319–330, Apr. 2001.

[5] S. Qiu and G. Zhu, "Molecular engineering for synthesizing novel structures of metal–organic frameworks with multifunctional properties," *Coord. Chem. Rev.*, vol. 253, no. 23, pp. 2891–2911, 2009.

[6] Q. Yang, Q. xu, and H.-L. Jiang, "Metal-organic frameworks meet metal nanoparticles: Synergistic effect for enhanced catalysis," *Chem. Soc. Rev.*, vol. 46, Jun. 2017.

[7] U. Anik, S. Timur, and Z. Dursun, "Metal organic frameworks in electrochemical and optical sensing platforms: a review," *Microchim. Acta*, vol. 186, Feb. 2019.

[8] S. Li and F. Huo, "Metal–organic framework composites: from fundamentals to applications," *Nanoscale*, vol. 7, no. 17, pp. 7482–7501, 2015.

[9] L. Ai, L. Li, C. Zhang, J. Fu, and J. Jiang, "MIL-53(Fe): A Metal-Organic Framework with Intrinsic Peroxidase-Like Catalytic Activity for Colorimetric Biosensing," *Chemistry*, vol. 19, pp. 15105–15108, Nov. 2013.

[10] Y. Wang, Y. Zhu, A. Binyam, M. Liu, Y. Wu, and F. Li, "Discovering the enzyme mimetic activity of metal-organic framework (MOF) for label-free and colorimetric sensing of biomolecules," *Biosens. Bioelectron.*, vol. 86, pp. 432–438, 2016.

[11] X. Qi, H. Tian, X. Dang, Y. Fan, Y. Zhang, and H. Zhao, "A bimetallic Co/Mn metal–organic-framework with a synergistic catalytic effect as peroxidase for the colorimetric detection of H2O2," *Anal. Methods*, vol. 11, no. 8, pp. 1111–1124,

2019.

[12] H. Yang, R. Yang, P. Zhang, Y. Qin, T. Chen, and F. Ye, "A bimetallic (Co/2Fe) metal-organic framework with oxidase and peroxidase mimicking activity for colorimetric detection of hydrogen peroxide," *Microchim. Acta*, vol. 184, pp. 4629–4635, 2017.

[13] G. C. Ilacas, A. Basa, K. J. Nelms, J. D. Sosa, Y. Liu, and F. A. Gomez, "Paper-based microfluidic devices for glucose assays employing a metal-organic framework (MOF)," *Anal. Chim. Acta*, vol. 1055, pp. 74–80, 2019.

[14] Y. Guo and W. Zhao, "In situ formed nanomaterials for colorimetric and fluorescent sensing," *Coord. Chem. Rev.*, vol. 387, Apr. 2019.

[15] D. Wei, Qingshan Qi, Hangfei Luo, Wei Tseng and A. Ki, So Jung Wan, Zhe Göröcs, Zoltán Bentolila, Laurent A Wu, Ting-Ting Sun, Ren Ozcan, "Fluorescent Imaging of Single Nanoparticles and Viruses on a Smart Phone," *ACS Nano*, vol. 7, no. 10, pp. 9147–9155, Oct. 2013.

[16] A. F. Coskun, R. Nagi, K. Sadeghi, S. Phillips, and A. Ozcan, "Albumin testing in urine using a smart-phone," *Lab Chip*, vol. 13, no. 21, pp. 4231–4238, 2013.

[17] A. Roda, M. Guardigli, D. Calabria, M. M. Calabretta, L. Cevenini, and E. Michelini, "A 3D-printed device for a smartphone-based chemiluminescence biosensor for lactate in oral fluid and sweat," *Analyst*, vol. 139, no. 24, pp. 6494–6501, 2014.

[18] A. Navruz, Isa Coskun, Ahmet F Wong, Justin Mohammad, Saqib Tseng, Derek Nagi, Richie Phillips, Stephen Ozcan, "Smart-phone based computational microscopy using multi-frame contact imaging on a fiber-optic array," *Lab Chip*, vol. 13, no. 20, pp. 4015–4023, 2013.

[19] S. K. Vashist, P. B. Luppa, L. Y. Yeo, A. Ozcan, and J. H. T. Luong, "Emerging Technologies for Next-Generation Point-of-Care Testing," *Trends Biotechnol.*, vol. 33, no. 11, pp. 692–705, 2015.

[20] A. Chib, M. H. van Velthoven, and J. Car, "mHealth Adoption in Low-Resource Environments: A Review of the Use of Mobile Healthcare in Developing Countries," *J. Health Commun.*, vol. 20, no. 1, pp. 4–34, Jan. 2015.

[21] F. Manea, F. Houillon, L. Pasquato, and P. Scrimin, "Nanozymes: Gold-Nanoparticle-Based Transphosphorylation Catalysts," *Angew. Chem. Int. Ed. Engl.*, vol. 43, pp. 6165–6169, Nov. 2004.

[22] F. Mancin, L. Prins, P. Pengo, L. Pasquato, P. Tecilla, and P. Scrimin, "Hydrolytic

Metallo-Nanozymes: From Micelles and Vesicles to Gold Nanoparticles," *Molecules*, vol. 21, p. 1014, Aug. 2016.

[23] E. Wei, Hui Wang, "Nanomaterials with enzyme-like characteristics (nanozymes): next-generation artificial enzymes," *Chem. Soc. Rev.*, vol. 42, no. 14, pp. 6060–6093, 2013.

[24] M. Nasir, M. H. Nawaz, U. Latif, M. Yaqub, A. Hayat, and A. Rahim, "An overview on enzyme-mimicking nanomaterials for use in electrochemical and optical assays," *Microchim. Acta*, vol. 184, no. 2, pp. 323–342, 2017.

[25] C. Ding, Y. Yan, D. Xiang, C. Zhang, and Y. Xian, "Magnetic Fe3S4 nanoparticles with peroxidase-like activity, and their use in a photometric enzymatic glucose assay," *Microchim. Acta*, vol. 183, no. 2, pp. 625–631, 2016.

[26] A. Asati, S. Santra, C. Kaittanis, S. Nath, and J. Perez, "Oxidase-Like Activity of Polymer-Coated Cerium Oxide Nanoparticles," *Angew. Chem. Int. Ed. Engl.*, vol. 48, pp. 2308–2312, Mar. 2009.

[27] J. Mu, Y. Wang, M. Zhao, and L. Zhang, "Intrinsic peroxidase-like activity and catalase-like activity of Co3O4 nanoparticles," *Chem. Commun.*, vol. 48, no. 19, pp. 2540–2542, 2012.

[28] N. Pan, W. Li-Ying, L.-L. Wu, C.-F. Peng, and Z.-J. Xie, "Colorimetric determination of cysteine by exploiting its inhibitory action on the peroxidase-like activity of Au@Pt core-shell nanohybrids," *Microchim. Acta*, vol. 184, no. 1, pp. 65–72, 2017.

[29] J.-W. Zhang, H.-T. Zhang, Z.-Y. Du, X. Wang, S.-H. Yu, and H.-L. Jiang, "Water-stable metal–organic frameworks with intrinsic peroxidase-like catalytic activity as a colorimetric biosensing platform," *Chem. Commun.*, vol. 50, no. 9, pp. 1092–1094, 2014.

[30] Y. Song, K. Qu, C. Zhao, J. Ren, and X. Qu, "Grapheme Oxide: Intrinsic Peroxidase Catalytic Activity and Its Application to Glucose Detection," *Adv. Mater.*, vol. 22, pp. 2206–2210, May 2010.

[31] Y. Song, X. Wang, C. Zhao, K. Qu, J. Ren, and X. Qu, "Label-Free Colorimetric Detection of Single Nucleotide Polymorphism by Using Single-Walled Carbon Nanotube Intrinsic Peroxidase-Like Activity," *Chemistry*, vol. 16, pp. 3617–3621, Mar. 2010.

[32] R. Cui, Z. Han, and J.-J. Zhu, "Helical Carbon Nanotubes: Intrinsic Peroxidase Catalytic Activity and Its Application for Biocatalysis and Biosensing," *Chemistry*,

vol. 17, pp. 9377–9384, Aug. 2011.

[33] Y. Shi, Wenbing Wang, Qinlong Long, Yijuan Cheng, Zhiliang Chen, Shihong Zheng, Huzhi Huang, "Carbon nanodots as peroxidase mimetics and their applications to glucose detection," *Chem. Commun.*, vol. 47, no. 23, pp. 6695–6697, 2011.

[34] P. Kumar, A. Deep, and K.-H. Kim, "Metal organic frameworks for sensing applications," *TrAC Trends Anal. Chem.*, vol. 73, pp. 39–53, 2015.

[35] Y. Chen and S. Ma, "Biomimetic catalysis of metal–organic frameworks," *Dalt. Trans.*, vol. 45, no. 24, pp. 9744–9753, 2016.

[36] J. Liu, L. Chen, H. Cui, J. Zhang, L. Zhang, and C.-Y. Su, "Applications of metal–organic frameworks in heterogeneous supramolecular catalysis," *Chem. Soc. Rev.*, vol. 43, no. 16, pp. 6011–6061, 2014.

[37] V. V Butova, M. A. Soldatov, A. A. Guda, K. A. Lomachenko, and C. Lamberti, "Metal-organic frameworks: structure, properties, methods of synthesis and characterization," *Russ. Chem. Rev.*, vol. 85, no. 3, pp. 280–307, 2016.

[38] W. Dong, X. Liu, W. Shi, and Y. Huang, "Metal–organic framework MIL-53(Fe): facile microwave-assisted synthesis and use as a highly active peroxidase mimetic for glucose biosensing," *RSC Adv.*, vol. 5, no. 23, pp. 17451–17457, 2015.

[39] F.-F. Chen, Y.-J. Zhu, Z.-C. Xiong, and T. Sun, "Hydroxyapatite Nanowires@Metal-Organic Framework Core/Shell Nanofibers: Templated Synthesis, Peroxidase-Like Activity, and Derived Flexible Recyclable Test Paper," *Chem. - A Eur. J.*, vol. 23, Mar. 2017.

[40] F.-X. Qin, S.-Y. Jia, F.-F. Wang, S.-H. Wu, J. Song, and Y. Liu, "Hemin@metal–organic framework with peroxidase-like activity and its application to glucose detection," *Catal. Sci. Technol.*, vol. 3, no. 10, pp. 2761–2768, 2013.

[41] X. Wu, J. Ge, C. Yang, M. Hou, and Z. Liu, "Facile synthesis of multiple enzyme-containing metal–organic frameworks in a biomolecule-friendly environment," *Chem. Commun.*, vol. 51, no. 69, pp. 13408–13411, 2015.

[42] G. G. Morbioli, T. Mazzu-Nascimento, A. M. Stockton, and E. Carrilho, "Technical aspects and challenges of colorimetric detection with microfluidic paper-based analytical devices (μPADs) - A review.," *Anal. Chim. Acta*, vol. 970, pp. 1–22, Jun. 2017.

[43] E. Petryayeva and W. R. Algar, "Toward point-of-care diagnostics with consumer electronic devices: the expanding role of nanoparticles," *RSC Adv.*, vol. 5, no. 28,

pp. 22256–22282, 2015.

[44] Y. Liu, P. Gao, C. Huang, and Y. Li, "Shape- and size-dependent catalysis activities of iron-terephthalic acid metal-organic frameworks," *Sci. China Chem.*, vol. 58, no. 10, pp. 1553–1560, 2015.

[45] K. M. L. Taylor-Pashow, J. Della Rocca, Z. Xie, S. Tran, and W. Lin, "Postsynthetic Modifications of Iron-Carboxylate Nanoscale Metal−Organic Frameworks for Imaging and Drug Delivery," *J. Am. Chem. Soc.*, vol. 131, no. 40, pp. 14261–14263, Oct. 2009.

[46] M. Yang, J. Tang, Q. Ma, N. Zheng, and L. Tan, "High activity Fe-MIL-101 solid acid catalyst for acetalization of aldehydes with methanol and enamination of β-dicarbonyl compounds," *J. Porous Mater.*, vol. 22, no. 5, pp. 1345–1350, 2015.

[47] G. Horcajada, Patricia Gref, Ruxandra Baati, Tarek Allan, Phoebe K Maurin and C. Couvreur, Patrick Férey, Gérard Morris, Russell E Serre, "Metal–Organic Frameworks in Biomedicine," *Chem. Rev.*, vol. 112, no. 2, pp. 1232–1268, Feb. 2012.

[48] Y. Chen, Daomei Li, Bin Jiang, Liang Duan, Deliang Li, Yizhou Wang, Jiaqiang He, Jiao Zeng, "Highly efficient colorimetric detection of cancer cells utilizing Fe-MIL-101 with intrinsic peroxidase-like catalytic activity over a broad pH range," *RSC Adv.*, vol. 5, no. 119, pp. 97910–97917, 2015.

[49] J. Lu, Y. Xiong, C. Liao, and F. Ye, "Colorimetric detection of uric acid in human urine and serum based on peroxidase mimetic activity of MIL-53(Fe)," *Anal. Methods*, vol. 7, no. 23, pp. 9894–9899, 2015.

[50] K. O. Skobelev IY, Sorokin AB, Kovalenko KA, Fedin VP, *Solvent-free allylic oxidation of alkenes with O2 mediated by Fe-MIL and Cr-MIL-101*, J Catal: 2013.

[51] K. G. M. Laurier, F. Vermoortele, R. Ameloot, D. E. De Vos, J. Hofkens, and M. B. J. Roeffaers, "Iron(III)-Based Metal–Organic Frameworks As Visible Light Photocatalysts," *J. Am. Chem. Soc.*, vol. 135, no. 39, pp. 14488–14491, Oct. 2013.

[52] D. Mark, S. Haeberle, G. Roth, F. Von Stetten, and R. Zengerle, "Microfluidic lab-on-a-chip platforms: Requirements, characteristics and applications," *Chem. Soc. Rev.*, vol. 39, no. 3, pp. 1153–1182, 2010.

[53] H. Orelma, I. Filpponen, L.-S. Johansson, J. Laine, and O. J. Rojas, "Modification of Cellulose Films by Adsorption of CMC and Chitosan for Controlled Attachment of Biomolecules," *Biomacromolecules*, vol. 12, no. 12, pp. 4311–4318, Dec. 2011.

[54] T.-R. Bruker AXS, "General profile and structure analysis software for powder

diffraction data." 2009.

[55] K. Taylor-Pashow, J. Rocca, Z. Xie, S. Tran, and W. Lin, "Post-Synthetic Modifications of Iron-Carboxylate Nanoscale Metal-Organic Frameworks for Imaging and Drug Delivery," *J. Am. Chem. Soc.*, vol. 131, pp. 14261–14263, Oct. 2009.

[56] G. Wyszecki and W. Stiles, "Color Science: Concepts and Methods, Quantitative Data and Formulae, 2nd Edition," *Color Sci. Concepts Methods, Quant. Data Formulae, 2nd Ed. by Gunther Wyszecki, W. S. Stiles, pp. 968. ISBN 0-471-39918-3. Wiley-VCH , July 2000.*, Jul. 2000.

[57] K. Cantrell, M. M. Erenas, I. de Orbe-Payá, and L. F. Capitán-Vallvey, "Use of the Hue Parameter of the Hue, Saturation, Value Color Space As a Quantitative Analytical Parameter for Bitonal Optical Sensors," *Anal. Chem.*, vol. 82, no. 2, pp. 531–542, Jan. 2010.

[58] L. F. Capitan-Vallvey, N. López-Ruiz, A. Martínez Olmos, M. Erenas, and A. Palma, "Recent developments in computer vision-based analytical chemistry: A tutorial review," *Anal. Chim. Acta*, vol. 899, Oct. 2015.

[59] G. Hammouri and B. Sunar, "Generating unique identifiers for smartphones using software," *Electron. Lett.*, vol. 50, pp. 938–939, Jun. 2014.

[60] W. Dong, L. Yang, and Y. Huang, "Glycine post-synthetic modification of MIL-53(Fe) metal–organic framework with enhanced and stable peroxidase-like activity for sensitive glucose biosensing," *Talanta*, vol. 167, pp. 359–366, 2017.

[61] K. Schilling, A. Lepore, J. Kurian, and A. Martinez, "Correction to Fully Enclosed Microfluidic Paper-Based Analytical Devices," *Anal. Chem.*, vol. 84, p. 3484, Mar. 2012.

[62] Z. Chen, Xi Chen, Jin Wang, Fubin Xiang, Xia Luo, Ming Ji, Xinghu He, "Determination of glucose and uric acid with bienzyme colorimetry on microfluidic paper-based analysis devices," *Biosens. Bioelectron.*, vol. 35, no. 1, pp. 363–368, 2012.

[63] H. Wei and E. Wang, "Fe 3 O 4 Magnetic Nanoparticles as Peroxidase Mimetics and Their Applications in H 2 O 2 and Glucose Detection," *Anal. Chem.*, vol. 80, pp. 2250–2254, Apr. 2008.

[64] li Su, J. Feng, X. Zhou, C. Ren, H. Li, and X. Chen, "Colorimetric Detection of Urine Glucose Based ZnFe2O4 Magnetic Nanoparticles," *Anal. Chem.*, vol. 84, pp. 5753–5758, Jun. 2012.

[65] Z. Sun, Jiayu Ge, Jiechao Liu, Weimin Lan, Minhua Zhang, Hongyan Wang, Pengfei Wang, Yanming Niu, "Multi-enzyme co-embedded organic-inorganic hybrid nanoflowers: Synthesis and application as a colorimetric sensor," *Nanoscale*, vol. 6, Nov. 2013.

[66] Z. Li, Y. Zhang, Y. Su, P. Ouyang, J. Ge, and Z. Liu, "Spatial co-localization of multi-enzymes by inorganic nanocrystal-protein complexes," *Chem. Commun.*, vol. 50, Aug. 2014.

[67] Q. Chen, J. Chen, C. Gao, M. Zhang, J. Chen, and H. Qiu, "Hemin-functionalized WS2 nanosheets as highly active peroxidase mimetic for label-free colorimetric detections of H2O2 and glucose," *Analyst*, vol. 140, Feb. 2015.

[68] N. Wang, J. Sun, L. Chen, H. Fan, and S. Ai, "A Cu2(OH)3Cl-CeO2 nanocomposite with peroxidase-like activity, and its application to the determination of hydrogen peroxide, glucose and cholesterol," *Microchim. Acta*, vol. 182, May 2015.

[69] R. Cha, D. Wang, Z. He, and Y. Ni, "Development of cellulose paper testing strips for quick measurement of glucose using chromogen agent," *Carbohydr. Polym.*, vol. 88, pp. 1414–1419, May 2012.

[70] E. Evans, E. Gabriel, T. E. Benavidez, W. Coltro, and C. Garcia, "Modification of Microfluidic Paper-Based Devices with Silica Nanoparticles," *Analyst*, Aug. 2014.

[71] J. Cai, Longfei Wang, Yong Wu, Yunying Xu, Chunxiu Zhong, Minghua Lai, Heyun Huang, "Fabrication of a microfluidic paper-based analytical device by silanization of filter cellulose using a paper mask for glucose assay.," *Analyst*, vol. 139, no. 18, pp. 4593–4598, Sep. 2014.

[72] H. J. Chun, Y. Park, Y. D. Han, Y. Jang, and H. Yoon, "Paper-based glucose biosensing system utilizing a smartphone as a signal reader," *Biochip J.*, vol. 8, pp. 218–226, Oct. 2014.

[73] M. Ariza-Avidad, A. Salinas-Castillo, and L. F. Capitán-Vallvey, "A 3D μPAD based on a multi-enzyme organic-inorganic hybrid nanoflower reactor," *Biosens. Bioelectron.*, 2016.

[74] X. Zhu, J. Huang, J. Liu, H. Zhang, J. Jiang, and R. Yu, "A dual enzyme–inorganic hybrid nanoflower incorporated microfluidic paper-based analytic device (μPAD) biosensor for sensitive visualized detection of glucose," *Nanoscale*, vol. 9, no. 17, pp. 5658–5663, 2017.

[75] D.-H. Xue, Yuan-Yuan Zhang, Wentao Zhang, Meng-Yue Liu, Li-Zhi Zhu, Wen-

Xin Yan, Ling-Zhi Wang, Jing Wang, Yan-Ru Wang, Jian-Long Zhang, "Development of a paper-based microfluidic analytical device by a more facile hydrophobic substrate generation strategy," *Anal. Biochem.*, vol. 525, Mar. 2017.

[76] V. F. Curto, N. Lopez-Ruiz, L. F. Capitan-Vallvey, A. J. Palma, F. Benito-Lopez, and D. Diamond, "Fast prototyping of paper-based microfluidic devices by contact stamping using indelible ink," *RSC Adv.*, vol. 3, no. 41, pp. 18811–18816, 2013.

[77] M. Ornatska, E. Sharpe, D. Andreescu, and S. Andreescu, "Paper Bioassay Based on Ceria Nanoparticles as Colorimetric Probes," *Anal. Chem.*, vol. 83, pp. 4273–4280, Jun. 2011.

[78] G. Durán, T. E. Benavidez, Á. Ríos, and C. Garcia, "Quantum Dot-Modified Paper-Based Assay for Glucose Screening," *Microchim. Acta*, vol. 183, Dec. 2015.

ÍNDICE DE FIGURAS

Capítulo 2

Figure 1. Picture of the µPAD indicating dimensions. µPAD before (A) and after (B) reaction with glucose. 146
Figure 2. SEM images of the Fe-MIL-101 MOF in cellulosic support. 151
Figure 3. External calibration for the glucose µPAD with digital camera. Data points are the mean of 3 assays. The data were fit with Eq. (1) and the inset shows the linear calibration using a Lineweaver-Burk transformation. 152
Figure 4. Selectivity of µPAD for 100 µmol·L^{-1} glucose in the presence of 2000 µmol·L^{-1} interferents..... 154

Figure S1. LeBail refinement results for sample as appreciable from experimental (blue), calculated (red), and difference (gray) diffraction patterns. For the sake of clarity, the portion above 9-15° has been magnified (3X). Horizontal axis: 2Θ, deg..... 156
Figure S2. SEM images of as prepared octahedral Fe-MIL-101 MOF obtained at high magnification. 157
Figure S3. Screen captures of the developed iOS application: (A) iPhone menu app, (B) main menu Pixcolor, (C) acquisition process, (D) sensing area detection and (E) final results obtained after image processing. 158
Figure S4. Selection of materials for µPAD fabrication. Conditions: 1.0 µL of TMB solution 2.5 mmol·L^{-1}; 1.0 µL MOF dispersion 0.75 mg·mL^{-1}; 30 µL phosphate buffer pH 7.4 1 mmol·L^{-1}; 1.5 µL GOx 1993.9 U·mL^{-1}; 15 µL chitosan 2 mg·mL^{-1}. Blue bars: with 10 µL glucose 100 µmol·L^{-1}; Green bars: 10 µL water. S% is the coordinate S (saturation) of colour space HSV.Figure S4. Selection of materials for µPAD fabrication. Conditions: 1.0 µL of TMB solution 2.5 mmol·L^{-1}; 1.0 µL MOF dispersion 0.75 mg·mL^{-1}; 30 µL phosphate buffer pH 7.4 1 mmol·L^{-1}; 1.5 µL GOx 1993.9 U·mL^{-1}; 15 µL chitosan 2 mg·mL^{-1}. Blue bars: with 10 µL glucose 100 µmol·L^{-1}; Green bars: 10 µL water. S% is the coordinate S (saturation) of colour space HSV..... 159
Figure S5. Reagents location on the µPAD. Conditions: 1.0 µL of TMB solution 2.5 mmol·L^{-1}. 1.0 µL MOF dispersion 0.75 mg·mL^{-1}; 30 µL phosphate buffer pH 7.4 1 mmol·L^{-1}; 1.5 µL GOx 1993.9 U·mL^{-1}; 15 µL chitosan 2 mg·mL^{-1} and 10 µL glucose 100 µmol·L^{-1}. S% is the coordinate S (saturation) of colour space HSV. 160

Figure S6. Influencing factors for glucose µPAD: A) Influence of TMB concentration. Conditions: 1.0 µL of different concentrations of TMB; 1.0 µL MOF dispersion 0.75 mg·mL^{-1}; 30 µL phosphate buffer pH 7.4 1 mmol·L^{-1}; 3µL GOx 1049.4 U·mL^{-1}; 15 µL chitosan 2 mg·mL^{-1}; 10 µL glucose 500 µmol·L^{-1}. B) Influence of MOF concentration. Conditions: 1.0 µL of MOF dispersion of different concentrations; 1.0 µL TMB 2.5 mmol·L^{-1}; 30 µL phosphate buffer pH 7.4 1 mmol·L^{-1}; 3µL GOx 1049.4 U·mL^{-1}; 15 µL chitosan 2 mg·mL^{-1}; 10 µL glucose 500 µmol·L^{-1}; C) Influence of pH. Conditions: 1.0 µL TMB 2.5 mmol·L^{-1}; 1.0 µL MOF dispersion 0.75 mg·mL^{-1}; 1.5 µL GOx 1993.9 U·mL^{-1}; 15 µL chitosan 2 mg·mL^{-1}; 10 µL glucose 250 µmol·L^{-1}. D) Influence of GOx concentration. Conditions: 1.0 µL of GOx with different concentrations; 1.0 µL TMB 2.5 mmol·L^{-1}; 1.0 µL MOF dispersion 0.75 mg·mL^{-1}; 30 µL phosphate buffer pH 7.4 1 mmol·L^{-1}; 15 µL chitosan 2 mg·mL^{-1}; 10 µL glucose 500 µmol·L^{-1}. S% is the coordinate S (saturation) of colour space HSV. 161

Figure S7. Evolution of saturation coordinate S with time. Conditions: 1.0 µL of TMB solution 2.5 mmol·L^{-1}. 1.0 µL MOF dispersion 0.75 mg·mL^{-1}; 30 µL phosphate buffer pH 7.4 1 mmol·L^{-1}; 1.5 µL GOx 1993.9 U·mL^{-1}; 15 µL chitosan 2 mg·mL^{-1} and 10 µL glucose 500 and 150 µmol·L^{-1}. S% is the coordinate S (saturation) of colour space HSV. 162

Figure S8. Influence of sample volume added. Conditions: 1.0 µL of ethanolic TMB solution; 1.0 µL MOF dispersion 0.75 mg·mL^{-1}; 30 µL phosphate buffer 1 mmol·L^{-1} pH 7.4; 1.5 µL GOx 1993.9 U·mL^{-1}; 15 µL chitosan 2 mg·mL^{-1}. The red dots correspond to 500 µmol·L^{-1} of glucose and the black dots correspond to 150 µmol·L^{-1} of glucose. S% is the coordinate S (saturation) of colour space HSV. 162

Figure S9. Dependence of saturation with glucose concentration obtained using a smartphone (black dots) and a digital camera (red dots) as analytical devices. Conditions: 1.0 µL of ethanolic TMB solution; 1.0 µL MOF dispersion 0.75 mg·mL^{-1}; 30 µL phosphate buffer 1 mmol·L^{-1} pH 7.4; 1.5 µL GOx 1993.9 U·mL^{-1}; 15 µL chitosan 2 mg·mL^{-1}. S% is the coordinate S (saturation) of colour space HSV. 164

Figure S10. Ionic strenght. Conditions: 1.0 µL of ethanolic TMB solution; 1.0 µL MOF dispersion 0.75 mg·mL^{-1}; 30 µL phosphate buffer 1 mmol·L^{-1} pH 7.4; 1.5 µL GOx 1993.9 U·mL^{-1}; 15 µL chitosan 2 mg·mL^{-1}. Glucose 100 µmol·L^{-1}. S%: coordinate S (saturation) of HSV colour space. 164

ÍNDICE DE TABLAS

Capítulo 2

Table 1. Analytical characteristics of µPAD for glucose. 153
Table 2. Real samples glucose determination[a]..... 155

Capítulo 3

IN SITU SYNTHESIS OF FLUORESCENT SILICON NANODOTS FOR GLUCOSE ANF FRUCTOSE MONITORING IN A PAPER MICROFLUIDIC DEVICE COMBINED WITH LASER INDUCED GRAPHEME HEATER

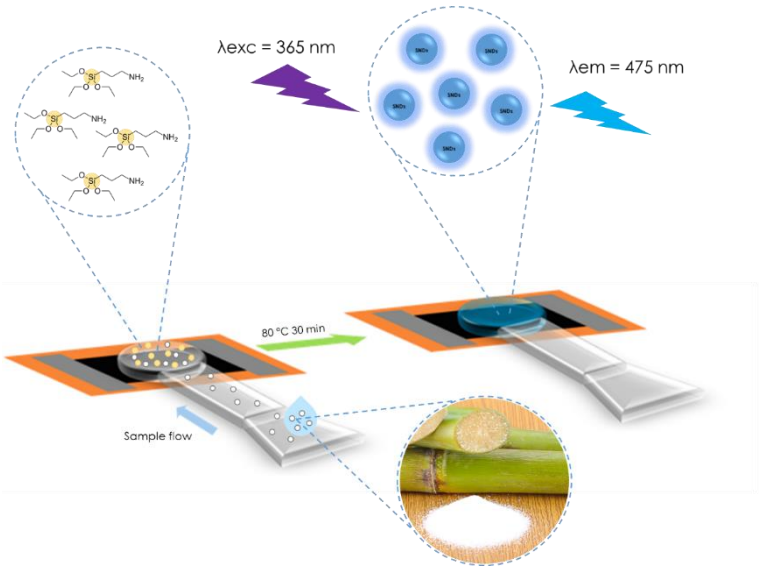

Submit to ACS Sensors

CAPÍTULO 3: IN SITU SYNTHESIS OF FLUORESCENT SILICON NANODOTS FOR GLUCOSE AND FRUCTOSE MONITORING IN A PAPER MICROFLUIDIC DEVICE COMBINED WITH LASER INDUCED GRAPHEME HEATER

Inmaculada Ortiz-Gómez [a, c], Víctor Toral-López [b,d], Francisco J Maldonado [b,d] ,Ignacio de Orbe-Payá [a, c], Antonio García [b], Noel Rodríguez [b,d], Luís Fermín Capitán-Vallvey [a, c], Diego P Morales [b], Alfonso Salinas-Castillo [a, c]

[a]ECsens, Department of Analytical Chemistry, Faculty of Sciences, 18071 University of Granada, Granada, Spain.

[b]Electronic Devices Research Group, Department of Electronics and Computer Technology, Faculty of Sciences, 18071 University of Granada, Spain

[c]Unit of Excellence in Chemistry applied to Biomedicine and the Environment, University of Granada, Spain

[d]Pervasive Electronics Advanced Research Laboratory, University of Granada, 18071 Granada, Spain

Planteamiento

El tratamiento de la diabetes requiere de una frecuente monitorización de los niveles de glucosa en sangre [1]. Por eso, los sensores de glucosa deben operar de forma simple y el coste de los análisis debe ser lo más bajo posible. En base a lo expuesto, existen varios métodos de determinación de glucosa entre los que se encuentran los basados en técnicas electroquímicas, espectroscopia Raman mejorada en superficie (Surface Enhanced Raman Spectroscopy; SERS) y técnicas ópticas como las basadas en colorimetría y fluorimetría, que permiten una determinación de forma rápida y sencilla [2]–[6].

Así, los métodos colorimétricos empleados en la mayoría de sensores desarrollados para la determinación de glucosa se basan en dos reacciones de oxidación combinadas en las que participan las enzimas glucosa oxidasa (GOx) y peroxidasa de rabano picante (HRP) o en su defecto, algún compuesto con actividad mimética como se ha indicado anteriormente en esta Memoria. De esta forma, la determinación enzimática de glucosa

involucra tres procesos: a) la generación de peróxido de hidrogeno (H_2O_2) y ácido glucónico, a través de la reacción de oxidación de la glucosa catalizada por el enzima GOx en presencia de oxígeno atmosférico; b) la oxidación del reactivo cromogénico utilizado en la determinación por el H_2O_2 generado, a través de la reacción catalizada por la enzima HRP y c) la medida del color originado por el reactivo cromogénico en función de la concentración de H_2O_2 generado en la oxidación de la glucosa presente en la muestra [7].

Estos métodos de determinación de glucosa presentan una elevada especificidad debido al empleo de enzimas en la reacción de reconocimiento; sin embargo, la actividad de las enzimas puede sufrir alteraciones debido a las condiciones medioambientales, es decir, el efecto de la temperatura, el pH, la humedad del ambiente o la presencia de compuestos químicos interferentes [8]. Además, la utilización de enzimas presenta algunas desventajas intrínsecas tales como una baja estabilidad debido a su fácil y rápida desnaturalización. En este sentido, el desarrollo de la nanotecnología ha permitido la síntesis en el laboratorio de nuevos compuestos que mimetizan la actividad de las enzimas y que se pueden utilizar en la reacción de determinación de la glucosa presentando una actividad similar al empleo de enzimas incluso en condiciones extremas [9]. Entre estos materiales podemos encontrar nanopartículas de metales nobles como el oro, la plata o el platino, nanomateriales formados por óxidos de metales como Fe_3O_4, CeO_2, etc., metal-organic framework (MOF), nanohojas en dos dimensiones como el óxido de grafeno (GO) y el sulfuro de molibdeno (MoS_2), quantum dots semiconductores y nanodots basados en carbono [10]–[14]. Sin embargo, la mayoría de estos nanomateriales presentan solo actividad similar a la enzima HRP, no pudiendo por tanto reemplazar al enzima GOx en esta reacción de determinación de glucosa. Por esta razón, el desarrollo de sensores libres de enzimas para la determinación óptica de glucosa resulta de gran interés.

Recientemente se han desarrollado sensores ópticos que permiten la determinación de glucosa mediante sistemas libres de enzimas empleando principalmente moléculas fluorescentes con grupos como el ácido boronico que pueden unirse a la glucosa mediante enlace covalente. Sin embargo, esta unión covalente puede originar señales de fondo en la detección óptica de glucosa perjudicando la sensibilidad del sistema [15]–[19]. Por lo tanto, todavía existe un gran interés en el desarrollo de nuevas estrategias de determinación óptica de glucosa para hacer frente a estos inconvenientes.

Los puntos cuánticos de sílice (silicon nanodots, SNDs) fluorescentes han surgido como nanomateriales novedosos para construir sondas fluorescentes en la determinación óptica de analitos debido a sus inherentes propiedades entre las que se incluyen, proceder de una fuente abundante de silicio, posibilidad de modificación de su superficie de forma controlable, alta luminiscencia, gran fotoestabilidad, buena biocompatibilidad y baja toxicidad, entre otras. En cuanto a los métodos de síntesis de los SNDs, estos se basan en reacciones hidrotermales entre compuestos con un alto contenido en silicio, como es el caso del (3-aminopropil) trietoxisilano (APTS) y un compuesto de carbono que actúan como reductor para la formación de estas nanopartículas [17].

De este modo, la síntesis de SNDs puede emplearse en la detección óptica de glucosa como un sistema libre de enzimas. Además, a través la síntesis *in situ* de estas partículas se puede conseguir una síntesis más sencilla, facilidad de operación y bajo costo en el desarrollo del sensor. En el procedimiento de detección, la formación del nanomaterial y la detección de glucosa tienen lugar simultáneamente, sin el requerimiento de mano de obra intensiva, operaciones de preparación y purificación, y exhibiendo, por tanto, prometedoras aplicaciones en este campo del análisis [20]. En este sentido, la síntesis de SNDs tiene lugar mediante la reacción de óxido-reducción entre la glucosa o fructosa de una muestra y el silicio procedente del APTS, existiendo una relación directa entre la concentración de monosacarido que presenta una muestra y la cantidad de nanopartículas de silicio que se forman.

Objetivo

El tercer capítulo de esta Memoria describe la síntesis *in situ* de silicon nanodots fluorescentes, a partir de APTS y glucosa o fructosa, en un µPAD que incluye un calentador de grafeno preparado por láser para la monitorización de la concentración de glucosa de muestras biológicas y bebidas comerciales mediante el uso de una lámpara UV y un Smartphone.

En base a este objetivo se realizó el diseño del µPAD de forma que permitiera llevar a cabo la síntesis de los SNDs, así como la medida de la concentración de glucosa y/o fructosa de una muestra. Para suministra la energía necesaria al µPAD para llevar a cabo la síntesis de los SNDs fluorescentes se diseñó y caracterizó un calentador de grafeno fabricado por láser. Seguidamente se llevó a cabo la síntesis y caracterización estructural de SNDs empleando APTS y glucosa. A continuación, se optimizaron las condiciones químicas bajo las cuales se realiza la determinación de sacarosa: concentración de APTS, pH de la reacción, temperatura y volumen de muestra empleado. Posteriormente, se procedió a la caracterización analítica del µPAD y se evaluó la posibilidad de utilizar el µPAD desarrollado para la determinación de glucosa y fructosa en muestras biológicas y alimentos.

En resumen, las etapas de las que consta este trabajo pueden resumirse en:

1. Diseño del µPAD.
2. Fabricación del calentador de grafeno inducido por láser.
3. Fabricación del µPAD.
4. Síntesis y caracterización estructural de los SNDs.
5. Optimización de las variables influyentes en la determinación de glucosa y fructosa.
6. Caracterización analítica del µPAD.
7. Determinación de glucosa en muestras de suero y orina, así como la determinación de glucosa y fructosa en zumos y tés comerciales.

IN SITU SYNTHESIS OF FLUORESCENT SILICON NANODOTS FOR GLUCOSE AND FRUCTOSE MONITORING IN A PAPER MICROFLUIDIC DEVICE COMBINED WITH LASER INDUCED GRAPHEME HEATER

Inmaculada Ortiz-Gómez [a, c], Víctor Toral-López [b,d], Francisco J Romero [d], Ignacio de Orbe-Payá [a, c], Antonio García [b], Noel Rodríguez [b,d], Luís Fermín Capitán-Vallvey [a, c], Diego P Morales [b,c], Alfonso Salinas-Castillo [a, c]

[a]ECsens, Department of Analytical Chemistry, Faculty of Sciences, 18071 University of Granada, Granada, Spain.

[b]Research Group, Department of Electronics and Computer Technology, Faculty of Sciences, 18071 University of Granada, Spain

[c]Unit of Excellence in Chemistry applied to Biomedicine and the Environment, University of Granada, Spain

[d]Pervasive Electronics Advanced Research Laboratory, University of Granada, 18071 Granada, Spain

Abstract

We report a simple, rapid, low-resource and one-step method for formation of fluorescent silicon nanodots (SNDs) in a microfluidic paper-based analytical device (µPAD) incorporated in a reusable, portable and flexible heater for glucose and fructose monitoring. The synthesis of SNDs is based on the redox reaction between (3-aminopropyl) triethoxysilane (APTS) reagent and glucose or fructose, which acts as a reductive. The grapheme-based heater was fabricated by laser ablation of Kapton polyimide. Thereby, the developed system heat the µPAD during the synthesis of SNDs at 80ºC for 30 min. The blue emitting SNDs formed have an emission peak wavelength at 475 nm. We used a digital camera and smartphone for the quantitative analysis of glucose and fructose with the grey scale value as the analytical parameter. Under the optimal conditions, the method has a low detection limit (0.80 µM for glucose and 0.51 µM for fructose, respectively), and a linear response in a concentration range from (10-200 µM for glucose and 10-100 µM for fructose, respectively). This method has been

applied to the determination of glucose in biological fluids (serum and urine samples). In addition, determination of glucose and fructose in commercial juices and teas have been carried out.

Keywords: Silicon nanoparticles · Glucose · Fructose · Color measurement · µPAD · Smartphone · LIG Heater · Laser-scribing

1. Introduction

Microfluidic paper-based analytical devices (µPADs) [21] have recently received a huge attention for the design of chemistry analysis platforms due to their inherent advantages such as, eco-friendly support, manipulate small volumes of fluids reducing the consumption of samples and reagents, minimize the complexity of analyse procedures, reduce the assay time, portability, wearability, lower cost per test, higher sensibility and integration into miniaturized analytical devices, among other [22], [23].

Thereby, microfluidic technologies have been employed in developing point of care (POC) diagnostics [24], [25], [26]. µPADs integrate with diverse emerging functional nanomaterials have opened the possibility to expanding their potential. For example, the advanced diagnostic technologies, such as POC diagnostics use nanomaterial for optical or electrochemical detection of multiple analytes or markers [27]. Moreover, multiple conventional detection techniques, such as colorimetric detection [28],[29], fluorescence, electrochemical detection, surface-enhanced Raman Spectroscopy have been integrated into µPAD for POCT assays [30],[31], [32].

In this way, semiconductor materials such as silicon, have emerged as a new nanomaterial to construct luminescent probes on the basis of their intrinsic properties: size, shape, composition, surface modification, high luminescence, strong photostability, good biocompatibility and low toxicity [33], [34]. Current research trends focus on the development of silicon materials for a diverse range of applications, such as batteries, photocatalysis, plasmon enhanced spectroscopy, optical devices, biological imaging screening and sensors, among others [35]–[38]. In this sense, silicon nanodots (SNDs) have a great potential as novel nanomaterials to fabricate fluorescent probes for sensing. However, studies on SNDs are limited due to the complicated synthetic procedures, strict

experimental conditions and use of costly equipment involved in the synthesis [33], [39]–[41]. Different versatile methods have been developed to produce silicon nanodots, for example solution-phase reductive strategy, sonochemical synthesis, microware irradiation, mechanochemical method, laser ablation, microemulsion, and plasma-assisted aerosol precipitation [42]–[47]. Theses methodologies require complicated procedures, harsh experiment conditions and costly equipment. For example, microwave method required high temperature (~ 160ºC), high pressure (~ 10-15 times atmospheric pressure) and costly microware equipment to produce silicon nanoparticles [48].

Thus, simple and eco-friendly synthesis strategies which eliminate or reduce the use of chemical compounds as well as energy exhaustive processes are highly desirable [49]. For all this, the possibility to implement chemical reagent for nanomaterials in microfluidic platforms such as µPAD could minimize these drawbacks, allowing the in situ generation of the SNDs which reduces its aging and so, assures the reliability of the measuring process.

In this direction, the develop of flexible film heaters [50], which have been fabricated with new materials as grapheme nano-aggregates and nanowires combined with inkjet printing and laser scribing techniques, among others, ease and increase the development of healthcare applications [51], [52],[53].

Thus, this work investigates the possibility of combination handheld readers such as smartphone with these devices to control a chemical reaction or process in a microfluidic system that increases their capabilities. Specifically, we present an application of a heater in combination with a smartphone to control a chemical reaction. A flexible Laser Induced Grapheme (LIG) heater studied in a previous work [54] is combined with electronic hardware to create a system with communications capabilities that can control the temperature of the reaction. The result of this combination is a cost-effective, reusable system to control the chemical reaction to determine glucose and fructose.

In summary, this work describes a µPAD for directly monitoring the level of glucose and fructose by one-step synthesizing fluorescent SNDs using a reusable, cost-effective, flexible and portable LIG heater. The novelty of the proposed assay is based on the combination of paper-based microfluidic device and LIG heater, which provides the energy necessary to heat the paper and facilitate the synthesis of SNDs. Thereby, this non-enzymatic method for the determination of monosacaride (glucose or fructose) is based

on the possibility to relate the increase of fluorescence intensity SNDs with the concentration of monosacaride in a sample. Therefore, the measurement of glucose and fructose content in different samples by take a photography of the µPAD using a digital camera or a smartphone under UV-vis lamp. In view of the operation simplicity from the synthesis of SNDs in this assay, this method it possible to monitor human glucose levels in biological samples such as serum and urine. Also, the proposed assay also results suitable able to estimate significant glucose and fructose content in soft drinks. Thus, the results show that the proposed device is affordable, sensitive, quick and robust, portable, simple to use and green-friendly for the use of fluorescence tools in the point of care testing.

2. Experimental

2.1. Reagents and materials

Glucose, galactose, mannose, sacarose, fructose, maltose, trehalose, serine, histidine, lysine, arginine, asparagine, uric acid, urea, sodium hydroxide, sodium chloride, potassium chloride, calcium chloride, magnesium chloride, disodium hydrogen phosphate, sodium sulfate, (3-Aminopropyl) triethoxysilane (APTS), Tris-HCl from Sigma Aldrich (Madrid, Spain). All reagents used were of analytical-reagent-grade unless stated otherwise. Kapton® HN polymide films with a thickness of 125 µm was purchased from DuPont™ (Constantine, MI, USA). Conductive silver/silver chloride (Ag/AgCl) ink from Loctite (Henkel). Whatman grade 1 chromatography paper from Sigma-Aldrich was used to manufacture the µPAD. All aqueous solutions were made using doubly deionized water (18.2 MΩ·cm resistance) was obtained from a Milli-RO 12 plus Milli-Q station (Millipore, Bedford, MA, USA).

2.2. Instruments and software

The fluorescence intensity of SNDs was measured with a Sony Cyber-shot DSC-HX 300 digital camera (Sony, Tokio, Japan) and a Huawei Mate 10 lite Smartphone (Huawei Technologies Co. Ltd., Shenzhen, China) after illumination with an UV transilluminator

220 V (MUV 21 series). ImageJ software was used to converter the fluorescence intensity to colour and analyse the region of interest (ROI) of the image along with the Color Space Converter plugin. The analytical devices were fabricated on paper using a craft-cutting technique as a cost-efficient, simple and reproducible process using a 12 W CO_2 laser engraver (Rayjet, Barcelona, Spain).

The temperature response of the heater was also measured by applying voltage steps with Precision Source/Measure Unit B2902 (Keysight Technologies, USA) while measuring temperature with IR camera Fluke TiS75 (Fluke Corporation, USA).

Fluorescence spectrum was collected using a Varian Cary Eclipse luminescence spectrometer (Varian Ibérica, Madrid, Spain). Absorbance spectrum were obtained using a Hewlett Packard diode array spectrophotometer (model 8453; Norwalk, CT, USA). Fourier-transform infrared (FT-IR) spectra were obtained using a Bruker Tensor 27 spectrometer under Attenuated Total Reflection (ATR) configuration with spectral resolution of 2 cm-1 by accumulating 25 scans in the 4000–500 cm-1 range. To investigate the size of SNDs, dynamic light scattering (DLS) assay was performed and Zeta potential measurements of SNDs in solutions at different pH values were measured by a Malvern zetasizer. The chemical composition of SNDs synthetized on paper (Si, C, O and N) was analyzed by X-ray photoelectron spectroscopy (XPS). The XPS spectra measurements were performed by Kratos Axis ultra-DLD. Also, by energy dispersive X-ray spectroscopy (EDX) measurements, the chemical composition of SNDs was contrasted. In addition, the distribution and compositional zonation of chemical elements in the paper was elucidated by an element mapping performed by energy-dispersive X-ray spectroscopy (EDS). SEM images were recorded with a QuenScan 650F FEI© electronic microscope together with an Everhart-Thornley detector 8ETD). Raman spectra were acquired with a JASCO 108 NRS-5100 dispersive micro-Raman spectrometer (from JASCO, Inc., Tokio, Japan). All these studies were done at the Centre for Scientific Instrumentation (University of Granada).

2.3. Electronic device design

A device for temperature control has been developed. This device must be able to measure and change the temperature of the heater and communicate with a smartphone that will

be the user interface. PSoC4 (Cypress Semiconductors, USA), has been selected for this purpose as it has Bluetooth 4.0 capabilities and analog and digital reconfigurable capabilities. Thanks to this interface, the user can use the smartphone to enable or disable the heat in the device and select the temperature of the heater when it is active. Also, the actual temperature of the heater is communicated to the user through this interface.

To supply power to the heater a current controlled DC/DC converter is employed. This device is controlled by a PWM generated by PSoC4 with calculates the duty depending on the temperature measurement which is obtained from an IR thermopile sensor. The power can be supplied from two sources, a micro-USB connector or a Li-ion battery of 680 mAh which can supply the system for 13.6 hours. The micro-USB connector permits the use of any USB device or even an external battery for extended working time.

The electronics are integrated in a rigid-flex PCB of 22.5x32.5 mm as the one shown in the Figure 1A. The rigid-flex PCB allow the integration of the temperature sensor in the housing to measure the heater temperature just over it. The heater is connected through two pads in the bottom layer. To ensure a good contact, the housing press over these pads fixing the heater at the same time.

Temperature sensor is the thermopile sensor TSD305-1C55, which allows noncontact temperature sensing and I2C connection with the microcontroller. This sensor is connected through a flexible strip to place it over the heater as shown in Figure 1B. Figure 1C shows the aspect of the housing created in 3D to encapsulate the system, a window is open in this case to illuminate µPADs and measure fluorescence.

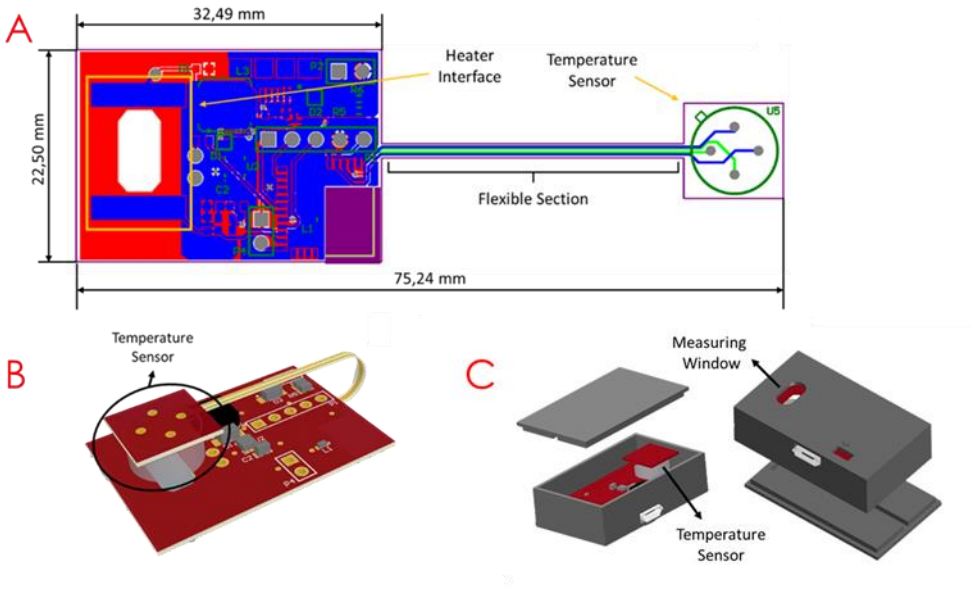

Figure 1. Hardware characteristics. (A) Board dimensions and distribution; (B) Folder state of the board inside the housing; (C) Housing made for the board.

2.4. Fabrication of the LIG heater

Heaters were fabricated using Kapton® HN (DuPontTM) polyimide films with a thickness of 125 µm as raw material. A CO_2 laser was used to ablate this polyimide and obtain conductive patterns. The laser employed was a 12W CO_2 laser engraver with a fixed wavelength of 10.6 µm (Rayjet, Barcelona, Spain). The laser was regulated at 20% of its maximum power and a 10% of its maximum speed, which means a power of 2.4W and a speed of 0.15 $m \cdot s^{-1}$. The substrate was placed at 5.08 cm from the laser head, allowing spatial resolution of 25 µm. With these parameters, is possible to obtain LIG films with a sheet resistance of $90 \Omega \cdot sq^{-1}$, while avoiding permanent deformations on the substrate. The sheet resistances were measured with B2901A Keysight source measuring unit (SMU) in a four-point measure configuration [55].

2.5. µPAD preparation

The µPADs were produced in a paper sheet using standard laboratory filter paper (Whatman no 1) by craft cutting technique. The device as shown in Figure 2, containing three separates areas, one for the sampling, the second for transport the sample and third for the synthesis of SNDs and detection of glucose and fructose.

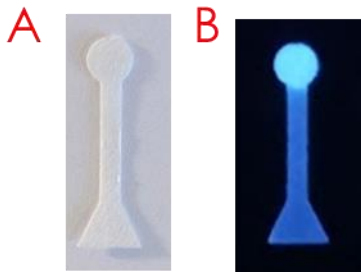

Figure 2. (A) Microfluidic paper-based analytical device for glucose and fructose monitoring; (B) µPAD with synthetized SNDs under UV-lamp (λ_{exc}= 365 nm).

2.6. Measurement procedure

Detection and quantitation of glucose were performed under the optimized conditions. The device was prepared by drops casting of 1 µL 98% of APTS solution onto the detection area. After, 7.5 µL of different concentrations of glucose and fructose (ranging from 10 to 1000 µM) were dropped onto the sampling area. The monosacaride solution go through to the detection area by capillarity. Then, the detection area of the µPAD was heating at 80ºC for 30 min to ensure complete reaction between APTS and glucose or fructose to synthetize the SNDs (Figure 3).

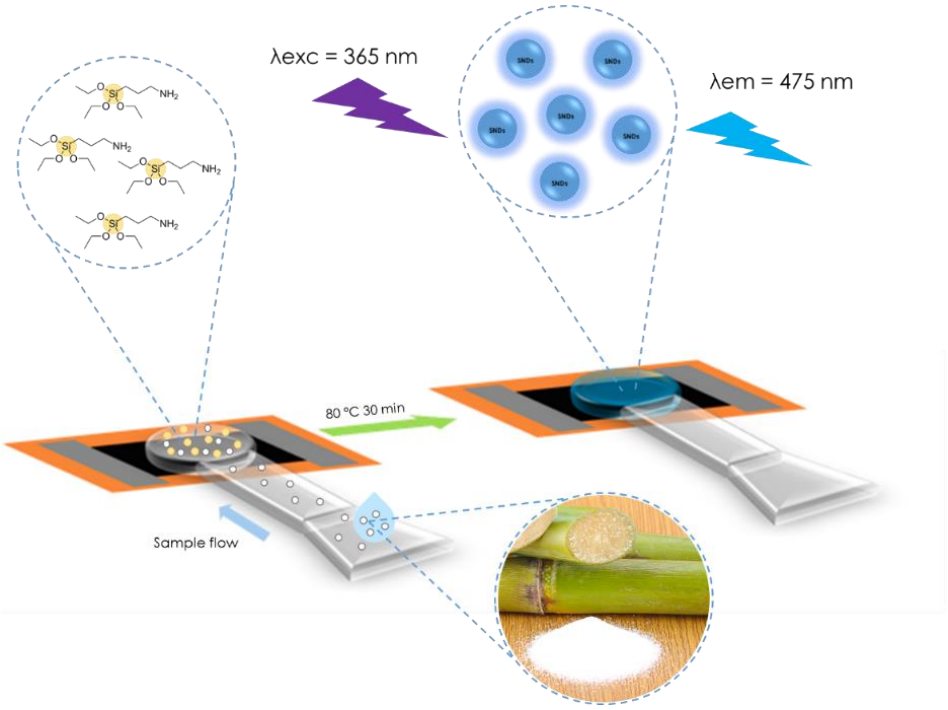

Figure 3. Schematic illustration of SNDs synthesis from APTS and glucose or fructose.

For the analysis of SNDs fluorescence intensity, the µPADs were placed under a UV lamp at 365 nm wavelength and 220 W using a homemade accessory designed and made by us. This accessory avoid that the light from the lamp interferes in the measurement of SNDs fluorescence intensity. Thereby, the accessory has a hole of 4 mm diameter to let the measure of SNDs fluorescence on the detection area of the µPAD with a digital camera or Smartphone. The camera was placed in front of the accessory with the µPAD at a fixed distance of 10 cm. After that, the detection area of the µPADs were imaged after reacting with standards or real samples containing glucose or fructose. The setting conditions used to photograph the detection area were: ISO 1600, shutter speed 1/80 s, aperture value f/2.8 and focal length of 4 mm using a digital camera. Thus, the setting conditions for Smartphone were: ISO 500, shutter speed 1/13s, aperture value f/2.20 and focal length of 35 mm.

The images acquired were saved in JPEG (joint photographic experts group) format. After that, images were converted to gray scale using a script and analyzed by ImagenJ software (National Institutes of Health). The fluorescence intensity was analyzed using ImagenJ function to obtain the region of interest (ROI) that contains the analytical information in the detection area of 4 mm diameter. Then, the program transformed each ROI into the gray scale space as the average of R, G and B coordinates from RGB (Red, Green, Blue) color space and this value was denoted by Gray scale. Thus, an average of the gray scale coordinate from the pixels considered was calculated and used to glucose and fructose determination.

2.7. Treatment of real samples

To evaluate the feasibility of the developed µPADs, the proposed method was applied to the determination of glucose in urine and serum, and total glucose and fructose content in juices and teas samples. The urine samples were obtained from healthy volunteers. All the urine samples were analyzed after prior dilution at 1:10 ratio in Milli-Q and filtered by a 0.22 µm pore diameter filter. For glucose analysis in serum samples, artificial human serum was prepared according to the following composition: 137.5 mM NaCl, 4.2 mM $NaHCO_3$, 3 Mm KCl, 0.5 mM Na_2HPO_4, 0.5 Mm $MgCl_2$, 2.64 mM $CaCl_2$ and 0.5 mM Na_2SO_4. The pH value of the artificial serum samples were adjusted at 7.4. Also, four different soft-drinks were purchased in local markets: pineapple juice, orange juice,

tomato juice, black tea and green tea were also used to validate the sensor response. The samples were shaken before opening, diluted 1:1000 with Milli-Q water and filtered by a 0.22 µm pore diameter filter.

3. Results and discussion

3.1. Heater characterization

LIG heater was obtained from ablation of Kapton polyimide. As seen in Figure 4A the heaters have a dimension of 10x15mm with two contacts of Ag/Cl ink, keeping a heating surface of around 10x10mm. Heaters was characterized physically and electrically to determine its composition and behaviour. In Figure 4C and Figure 4D, SEM images of this heater are shown. As can be appreciated in the edge, laser changes the material for a uniform material with smooth surface to a poruous irregular material. In detailed image this porosity can be appreciated more clearly. To confirm the grapheme nature of the material obtained, Raman spectroscopy was employed, whose results are shown in Figure 4B. As shown, the spectrum is composed by 4 peaks which confirm the grapheme nature of the structure. The coexistence of D and 2D peaks demonstrate that the structure differs of a monolayer grapheme. Moreover, the structure has several defects in the crystalline structure, confirmed by an ID/IG ratio close to 1, and is composed by several layers of grapheme, explained by the ratio I2D/IG. The results show that the obtained material is derived from grapheme, so it has some electrical conductivity.

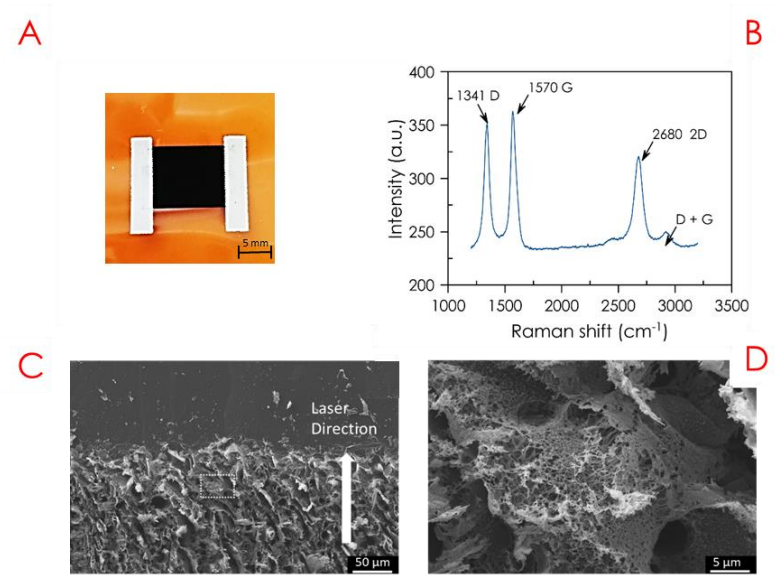

Figure 4. Heater physical characterization. (A) Real heater image; (B) Raman spectrum of LIG heater; (C) SEM image of the edge of heater; (D) SEM image detail (dashed square in (C) figure).

The temperature response of the heater was also measured by applying voltage steps with Precision Source/Measure Unit B2902 while measuring temperature with IR camera Fluke TiS75. The results are shown in Figure 5. As can be seen in Figure 5A, the setting time is around 7 seconds. Power density needed for each temperature is shown in Figure 5B, it varies from 0 to 1.4 W·cm^{-2} for temperatures from ambient to 300°C. Temperature vs voltage applied to the heater is shown in Figure 5C.

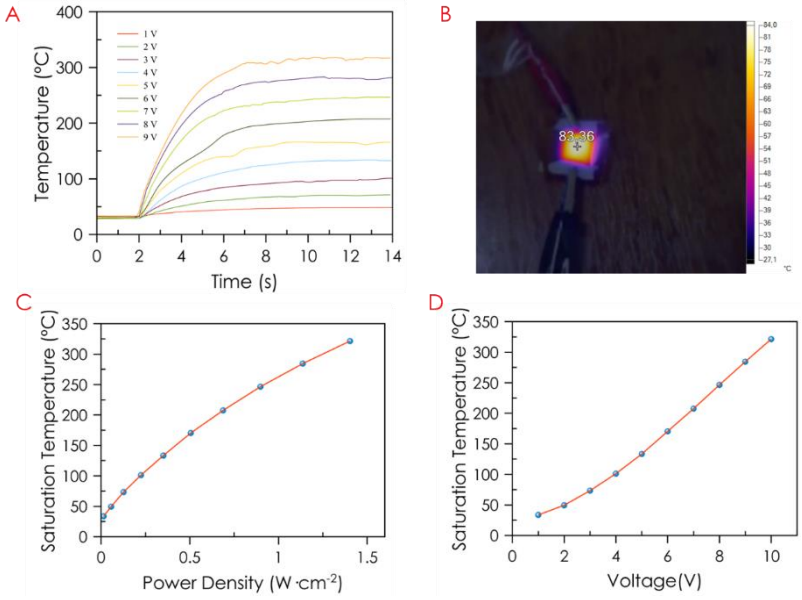

Figure 5. Electrical characterization of the heater. (A) Temporal evolution of temperature for different voltages; (B) Infrared thermal imaging of heater (C) Saturation temperature vs Power density; (D) Saturation temperature vs Voltage.

3.2. Characterization of SNDs

Silicon nanodots were synthesized in the detection area of the µPAD through the reaction between APTS and glucose using a LIG heater. The nanoparticles were obtained after 30 min heating at 80ºC, as indicated the results of XPS analysis (Figure 6). The Figure 6A presents five peaks at 101.2, 152.3, 284.4, 397.5 and 531.2 eV corresponded to Si 2p, Si 2s, C 1s, N 1s and O 1s, respectively. The high-resolution scans show four different chemical bonds for C 1s at 283.2, 284.3, 285.6 and 286.8 eV corresponding to the presence of C-Si, C-C/C=C, C-N and C-OH/C-O-C groups, as a shown in Figure 6B. The high-resolution N 1s spectrum present three different peaks at 398.4, 399.2 and 400.5 eV which were associated with N-Si, C-N-C and C-N=C groups (Figure 6C). Three peaks at 528.2, 531.2 and 533.5 eV were attributed to Si-O, and C-O in the high-resolution XPS spectrum of O 1s (Figure 6D). The Si 2p spectrum present three peaks at 100.1, 101.2 and 102.2 eV, which were associated with Si-C, Si-N and Si-O groups, respectively (Figure 6E).

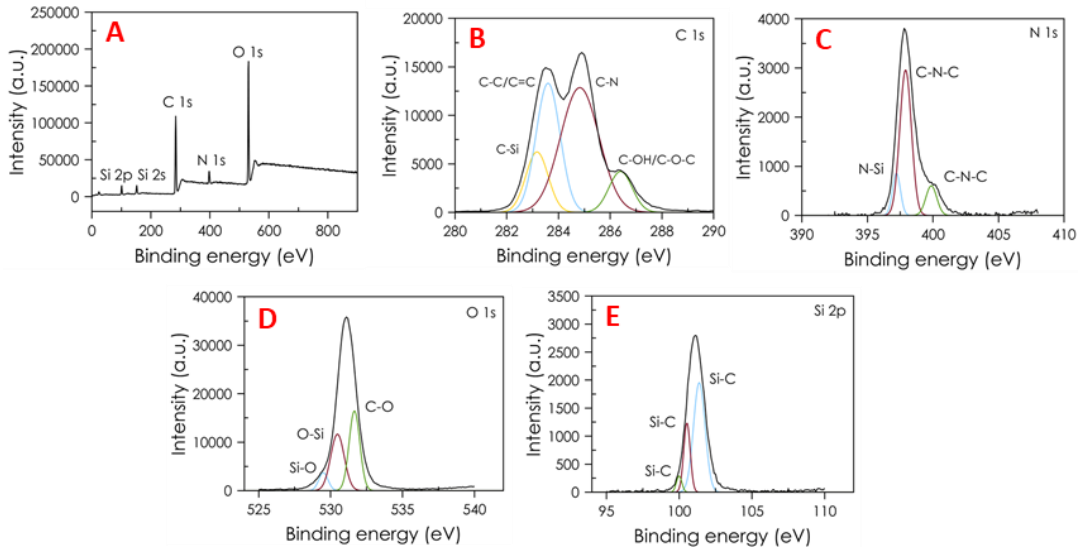

Figure 6. High-resolution XPS spectrum of the SNDs synthetized on the cellulose paper. (A) Full range; (B) C 1s; (C) N 1s; (D) O 1s and (E) Si 2p respectively.

FT-IR spectrum over the range 500-4000 cm-1 confirm the presence of various chemical bonds in SNDs as shown in Figure 7A. The FT-IR spectra of the µPAD containing the synthetized SNDs were recorded, which several distinct absorption peaks in the range of 1000-3500 cm-1. The characteristic peaks of the stretching vibration of Si-C and Si-O

were showed at 1250 and 1050 cm-1 respectively. The strong peaks at 1500 and 3300 cm-1 are assigned to the N-H bending vibration. It is indicated the presence of SNDs on the paper surface.

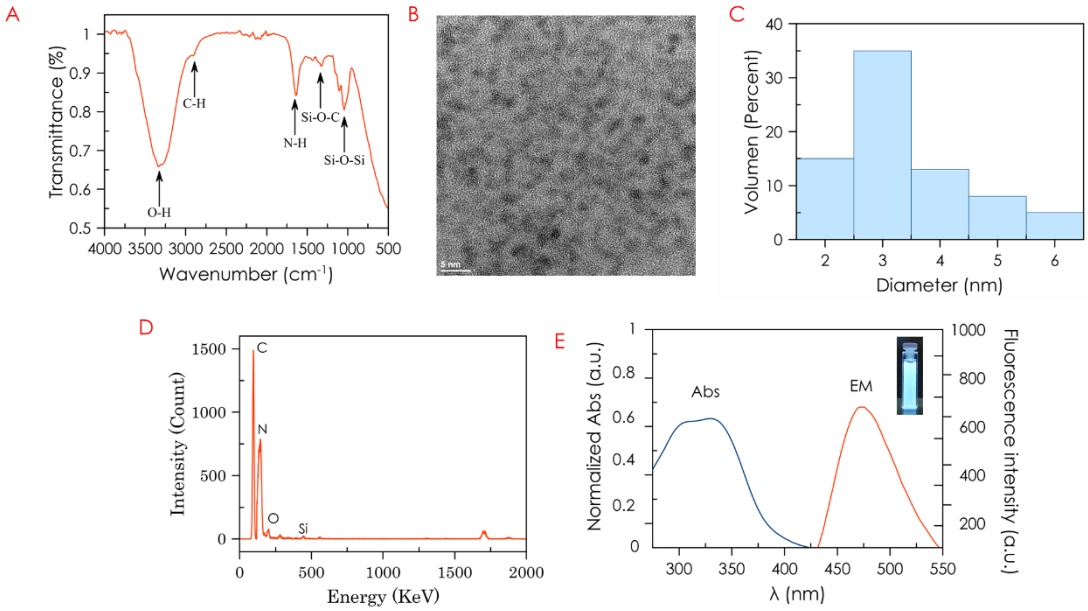

Figure 7. (A) FT-IR spectrum synthetized SNDs on the µPAD; (B) TEM image, (C) Size distribution of SNDs; (D) EDX spectrum SNDs; (E) Fluorescence emission spectra (line red) and UV-Vis spectra (line blue) of SNDs in water. Insert: Cuvette photography λ_{exc}= 365 nm.

In order to know the size of synthetized SNDs, transmission electron microscopy (TEM) and DLS assay was performed. As shown in Figure 7B, the diameters of SNDs ranged from 1 to 6 nm with uniform dispersion. This results is consistent with that from DLS. In this case, the SNDs were synthetized on the µPAD under optimal condition using nine different µPADs. After that, the µPADs were immersed on distil water to dissolve the synthetized SNDs. As shown in Figure 7C. The diameters of SNDs ranged from 3 to 6 nm with uniform dispersion. This results are consistent with the values reported in the bibliography. In addition, zeta potential measurements of SNDs in solutions at three different pH values 1, 7 and 12 were measured by a Malvern zetasizer. Data were acquired in the phase analysis light scattering mode following solution equilibration at 25ºC. The changes of zeta potential values measured using for synthetized SNDs on paper. It was observed that at pH 1 the zeta potential of SNDs was +18.9 mV. However, when the pH

was raised to 7 or 12 the zeta potential was reduced to 1.2 mV or -4.6 mM, respectively due to the reduced number of protonated amine groups.

On the other hand, the optical properties of SNDs were investigated, UV-Vis spectra of SNDs was collected by using Agilent Cary UV-Vis spectrometer. Figure 7D is the UV-vis absorption spectrum of SNDs synthetized on the µPAD and dissolved on distil water. The spectrum exhibits a strong absorption peak centered at 330 nm. Fluorescence spectra of SNDs were measured from 300 to 400 nm. As shown in Figure 7E the maximum emission peak at 475 nm under the excitation of 410 nm.

3.3. Optimization of method

The chemical conditions under which the glucose determination is carried out are the result of balancing the conditions needed for both the recognition and transduction steps therefore the following parameters were optimized: concentration of APTS, pH of reaction, temperature, reaction time and volume of sample.

In a first instance, the concentration of APTS used for the synthesis of SNDs was selected to a range from 0.11 to 1.48 $mmol \cdot mm^{-2}$ as shown in Figure 8A. It was found that, the fluorescence intensity increase when the concentration of APTS increase until 0.88 $mmol \cdot mm^{-2}$, so this concentration was selected as optimal. Next, the pH-luminescence behaviour of SNDs was investigated to pH range from 1 to 12. The Figure 8B demonstrate the strong pH-stability of the SNDs. After, the reaction temperature was studied in the range 40-100 ºC. The results shows that the paper fluorescence intensity increase from 40 to 80ºC and decrease for higher temperatures. For that, 80ºC was selected as optimal because of the fluorescence intensity was maximum for this temperature as shows the Figure 8C. Also, the reaction time required for the determination of glucose was studied in a range between 5 to 90 min. As a reaction time 30 min was selected because it was sufficient to complete the reaction such as shown in the Figure 8D. Finally, the volume of sample needed to complete the reaction detection between glucose and APTS in the µPAD was studied in a range between 1 to 10 µL. As show the Figure 8E, the value of 7.5 µL of glucose solution was selected as optimal. It was found that, for higher volumes than 7.5 µL the fluorescence intensity decrease because the sample removed the APTS to the sampling area of the µPAD inducing a fluorescence intensity decrees.

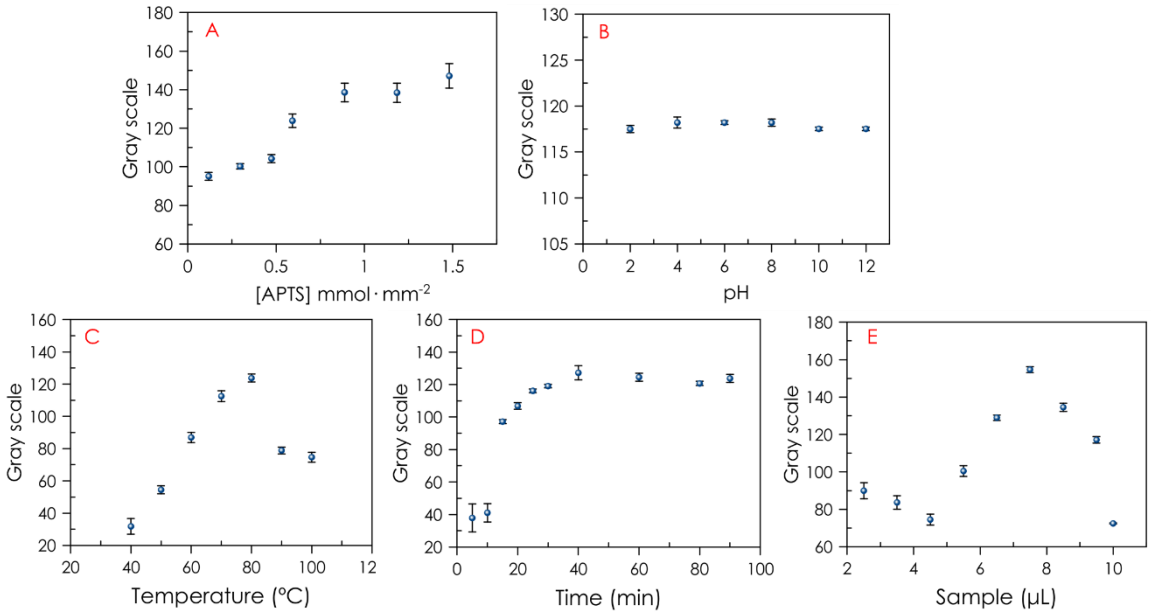

Figure 8. Optimization of parameters: (A) APTS concentration: 7.5 µL glucose 200 µM heating at 80ºC for 30 min; (B) pH dependent intensity behavior of SNDs: 1 µL APTS and 7.5 µL glucose 200 µM heating at 80ºC for 30 min; (C) Temperature: 1 µL APTS and 7.5 µL glucose 200 µM for 30 min heating; (D) Reaction time for glucose determination: 1 µL APTS and 7.5 µL glucose 200 µM heating at 80ºC; (E) Volume of sample: 1 µL APTS heating at 80ºC for 30 min. λ_{exc}= 365 nm. Data points are the mean of 3 assays in each optimization.

3.4. Calibration and analytical parameters

The developed µPAD is based on the synthesis of silicon nanodots prepared after adding APTS and glucose or fructose by heating with a flexible, portable and reusable LIG heater. SNDs synthesized by redox reaction between reducer monosacaride such as glucose or fructose, which acts as reducer, and APTS exhibited high blue fluorescence with an emission peak wavelength of 475 nm. The fluorescence intensity of SNDs increase when the concentration of reducer monosacaride increase. This increase of fluorescence can be quantified by correlating the grey intensity of the µPAD with the concentration of glucose and fructose present in the sample, Figure 9. For this determination, a photography of the µPAD was carried out after reaction with glucose or fructose using a digital camera or a Smartphone. The analytical functions were obtained by means of a calibration set composed of 12 standards with 3 replicates obtained with a new µPAD each time between 10 and 200 µM for glucose and 10 to 100 µM for fructose. The performance analytical characteristics of the µPAD developed are presented in Table 1.

Table 1. Analytical characteristics of µPAD for glucose or fructose determination.

Analytical parameter	Values for glucose	Values for fructose
Measurement range, µM	10 - 200	10 – 100
Slope	0.51	0.79
Intercept	20.56	6.82
LOD, µM	0.80	0.51
LOQ, µM	2.68	1.55
Precision, %	2.65	1.85

The limit of detection (LOD) was obtained using the standard criteria LOD = 3σ/slope where σ is the standard deviation of the blank, which was determined from 12 blanks (relative standard deviation (RSD) 1.13). With this criterion, the value of the LOD was 0.8 µM for glucose and 0.51 µM for fructose and the limit of quantification (LOQ) 2.68 µM and 1.55 µM for glucose and fructose, respectively. The repeatability as RSD, obtained using 8 different µPADs at 40 µM and 100 µM glucose, was 2.65% and 4.28%, an acceptable precision considering the measuring system used.

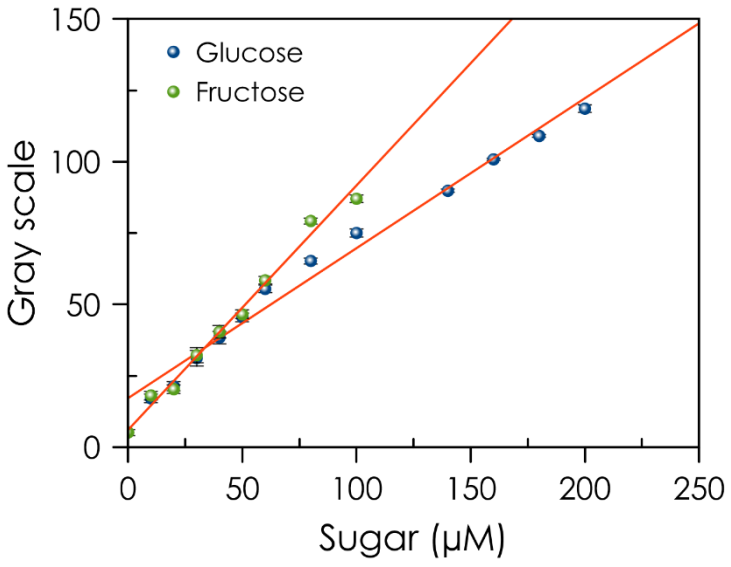

Figure 9. Calibration curve for (A) glucose and (B) fructose. Conditions: 1 µL APTS; heating at 80ºC for 30 min; 7.5 µL of glucose or fructose solutions; λ_{exc}= 365 nm. Data points are the mean of 3 assays.

3.5. Study and evaluation of potential interferences

The effect of different compounds commonly present in biological samples such as serine, histidine, lysine, arginine, asparagine, uric acid, urea, NaCl, KCl, $CaCl_2$, $MgCl_2$, Na_2HPO_4, Na_2SO_4 and monosaccharides and disaccharides such as galactose, fructose, sucrose, maltose, trealose, and mannose were evaluated Figure 10. The data shows that the SNDs exhibited excellent properties as a fluorescence probe for glucose and fructose over other amino acids and inorganic salts. The fluorescence intensity increases when glucose, fructose, galactose, sucrose, maltose, trehalose, and mannose were presented on the sample. However, the concentration of theses sugars in normal human serum and urine is at least ten times lower than that of glucose. Therefore, this method can be applied as a selective probe for glucose detection without significant interferences [34].

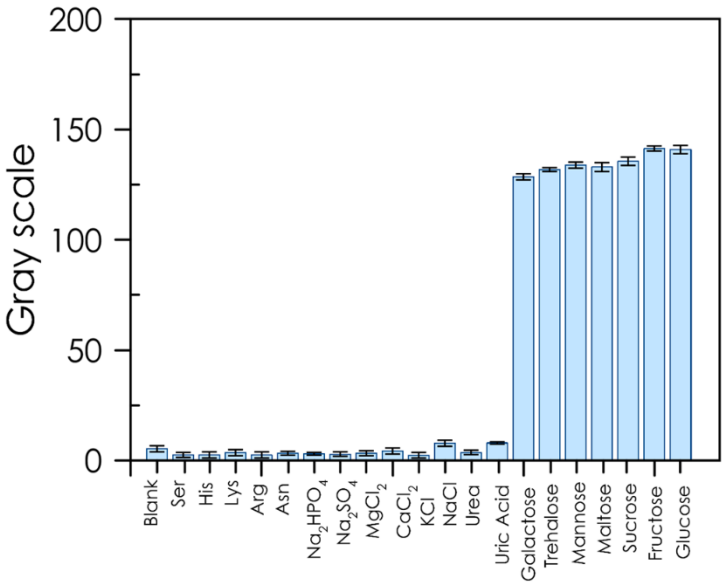

Figure 50. Response of different interferences and sugars. Conditions: 1 µL APTS; heating at 80ºC for 30 min; 7.5 µL of interference solutions 250 µM; λ_{exc}= 365 nm. Data points are the mean of 3 assays.

3.6. Analysis of real samples

Glucose plays an important role in the life system. For example, to know the glucose concentration is essential for the care of people with diabetes. For that, the human serum and urine samples were often used as test samples to investigate the glucose concentration levels. Thus, serum samples from healthy human have a normal content of glucose between 3.9 and 6.1 mmol·L^{-1}[56]. On the other hand, the normal fasting urine glucose

level in the healthy human urine are around 0.8 mmol·L^{-1}[57]. In this way, in order to evaluate the feasibility of practical application of the developed µPAD in the analysis of a biological samples such as urine and serum, the recovery experiments of standard addition were carried out. The detection results for glucose are shown in Table 2. For urine samples, the recovery experiment was carried out by spiking of 10, 20 and 30 µM of standard glucose. Also, the artificial serum samples were spiked of 10, 20, 30 and 50 µM of standard glucose solutions. Thereby, the recoveries obtained for urine and serum samples are in the range of 99.23 – 109.70 % and 103.46 –113.80%, respectively. The results demonstrate that the method proposed in this work can be used for determination of glucose in real samples obtaining good recovery percentage and precision.

Table 2. Determination of glucose in human urine samples.

Sample	Found, µM	Added, µM	Total found, µM	Recovery, %
Urine 1	25.56	30	55.33	99.23
		20	46.07	102.55
		10	36.53	109.70
Urine 2	30.90	30	61.94	103.46
		20	53.66	113.80
		10	41.49	105.9
Serum	-	10	10.74	107.40
		20	19.47	97.33
		30	30.27	100.92
		50	50.00	99.99

On the other hand, the determination of glucose and fructose content in foodstuff such as soft-drinks, mainly juices and teas, which have a high level of these monosacarides, is an important issue in food quality control [58]. In this way, we have evaluated the amount

of glucose and fructose present in three different juices and two teas. These samples content three different types of sugar mainly: sucrose, fructose and glucose. Thereby, the acidic pH of these drinks generally leads to the slow conversion of sucrose into its two constituent sugars: glucose and fructose, whereas in natural samples, glucose and fructose naturally results the most representative sugars [58]. In this way, we have determinate the global content of glucose and fructose as an index of reducer monosacarides present in these samples. The detection results from the present method are basically consistent with the known contents. The values reported are the average of the measurements performed using 9 different sensors. The results found are satisfactory when it compared with the labelled of the drinks such as shown in the Table 3.

Table 3. Determination of total glucose and fructose in commercial juices and teas (n = 9).

Samples	Labelled g·mL^{-1}	Found g·mL^{-1}
Pineapple juice	0.026	0.024 ± 0.003
Orange juice	0.102	0.089 ± 0.011
Tomato juice	0.035	0.036 ± 0.006
Black tea	0.045	0.044 ± 0.003
Green tea	0.082	0.79 0.002

4. Conclusion

In summary, a sensitive, highly robust and cost-efficient µPAD for glucose and fructose detection has been designed. The device is based on the synthesis of fluorescent silicon nanodots by heating the µPAD with APTS and reducer monosacaride using a flexible, portable and reusable LIG heater. The sensing is operative by redox reaction between APTS and glucose or fructose, which acts such as reducer, the resulting fluorescence intensity let the rapid screening of glucose and fructose by the use of a UV lamp and a digital camera or smartphone. We expect that this method may open up a new avenue in developing low-cost and ecofriendly method for biological diagnostics application.

REFERENCES

[1] G. A. Nichols, K. Bell, T. M. Kimes, and M. O\textquoterightKeeffe-Rosetti, "Medical Care Costs Associated With Long-term Weight Maintenance Versus Weight Gain Among Patients With Type 2 Diabetes," *Diabetes Care*, vol. 39, no. 11, pp. 1981–1986, 2016.

[2] J. Hu, Yihui Cheng, Hanjun Zhao, Xiaozhi Wu, Jiangjiexing Muhammad, Faheem Lin, Shichao He, C. Zhou, Liqi Zhang, and H. Deng, Yu Wang, Peng Zhou, Zhengyang Nie, Shuming Wei, "Surface-Enhanced Raman Scattering-Active Gold Nanoparticles with Enzyme Mimicking Activities for Measuring Glucose and Lactate in Living Tissues," *ACS Nano*, vol. 11, May 2017.

[3] X. Wang, Zao Cao, Xiaoqin Liu, Danni Hao, Shuai Du, Gu Asiri, Abdullah M Sun, "Ternary NiCoP nanosheet array on Ti mesh: a high-performance electrochemical sensor for glucose detection," *Chem. Commun.*, vol. 52, Nov. 2016.

[4] M. Grembecka, A. Lebiedzińska, and P. Szefer, "Simultaneous separation and determination of erythritol, xylitol, sorbitol, mannitol, maltitol, fructose, glucose, sucrose and maltose in food products by high performance liquid chromatography coupled to charged aerosol detector," *Microchem. J.*, vol. 117, pp. 77–82, 2014.

[5] Q. Wu, X. Wang, C. Liao, Q. Wei, and Q. Wang, "Microgels Coating Magnetic Nanoparticles via Bienzyme-mediated Free-radical Polymerization for Colorimetric Detection of Glucose," *Nanoscale*, vol. 7, Oct. 2015.

[6] J. Wang, "Electrochemical glucose biosensors.," *Chem. Rev.*, vol. 108, no. 2, pp. 814–825, Feb. 2008.

[7] F. Li, X. Wang, J. Liu, Y. Hu, and J. He, "Double-layered microfluidic paper-based device with multiple colorimetric indicators for multiplexed detection of biomolecules," *Sensors Actuators B Chem.*, vol. 288, pp. 266–273, 2019.

[8] K. Schügerl, B. Hitzmann, H. Jurgens, T. Kullick, R. Ulber, and B. Weigal, "Challenges in integrating biosensors and FIA for on-line monitoring and control," *Trends Biotechnol.*, vol. 14, no. 1, pp. 21–31, 1996.

[9] H. Wu, Jiangjiexing Wang, Xiaoyu Wang, Quan Lou, Zhangping Li, Sirong Zhu, Yunyao Qin, Li Wei, "Nanomaterials with enzyme-like characteristics

(nanozymes): next-generation artificial enzymes (II)," *Chem. Soc. Rev.*, vol. 48, no. 4, pp. 1004–1076, 2019.

[10] li Su, J. Feng, X. Zhou, C. Ren, H. Li, and X. Chen, "Colorimetric Detection of Urine Glucose Based ZnFe2O4 Magnetic Nanoparticles," *Anal. Chem.*, vol. 84, pp. 5753–5758, Jun. 2012.

[11] Y. Song, K. Qu, C. Zhao, J. Ren, and X. Qu, "Grapheme Oxide: Intrinsic Peroxidase Catalytic Activity and Its Application to Glucose Detection," *Adv. Mater.*, vol. 22, pp. 2206–2210, May 2010.

[12] Y. Shi, Wenbing Wang, Qinlong Long, Yijuan Cheng, Zhiliang Chen, Shihong Zheng, Huzhi Huang, "Carbon nanodots as peroxidase mimetics and their applications to glucose detection," *Chem. Commun.*, vol. 47, no. 23, pp. 6695–6697, 2011.

[13] H. Wei and E. Wang, "Fe3O4 magnetic nanoparticles as peroxidase mimetics and their applications in H2O2 and glucose detection," *Anal. Chem.*, vol. 80, no. 6, pp. 2250–2254, 2008.

[14] Y. Jv, B. Li, and R. Cao, "Positively-charged gold nanoparticles as peroxidiase mimic and their application in hydrogen peroxide and glucose detection," *Chem. Commun.*, vol. 46, no. 42, pp. 8017–8019, 2010.

[15] L. Du, Z. Li, J. Yao, G. Wen, C. Dong, and H.-W. Li, "Enzyme free glucose sensing by amino-functionalized silicon quantum dot," *Spectrochim. Acta Part A Mol. Biomol. Spectrosc.*, vol. 216, pp. 303–309, 2019.

[16] B. Sharma and S. Tanwar, "One Pot Green Synthesis of Si Quantum Dots and Catalytic Au Nanoparticle-Si Quantum Dot Nanocomposite," *ACS Sustain. Chem. Eng.*, vol. 7, Jan. 2019.

[17] Q. Cai, H. Meng, Y. Liu, and Z. Li, "Fluorometric determination of glucose based on a redox reaction between glucose and aminopropyltriethoxysilane and in-situ formation of blue-green emitting silicon nanodots," *Microchim. Acta*, vol. 186, Jan. 2019.

[18] H. Chen *et al.*, "One-step rapid synthesis of fluorescent silicon nanodots for a hydrogen peroxide-related sensitive and versatile assay based on the inner filter

effect," *Analyst*, vol. 144, no. 13, pp. 4006–4012, 2019.

[19] L. Ding, Z. Gong, M. Yan, J. Yu, and X. Song, "Determination of glucose by using fluorescent silicon nanoparticles and an inner filter caused by peroxidase-induced oxidation of o-phenylenediamine by hydrogen peroxide," *Microchim. Acta*, vol. 184, Nov. 2017.

[20] Y. Guo and W. Zhao, "In situ formed nanomaterials for colorimetric and fluorescent sensing," *Coord. Chem. Rev.*, vol. 387, Apr. 2019.

[21] A. W. Martinez, S. T. Phillips, M. J. Butte, and G. M. Whitesides, "Patterned paper as a platform for inexpensive, low-volume, portable bioassays.," *Angew. Chem. Int. Ed. Engl.*, vol. 46, no. 8, pp. 1318–1320, 2007.

[22] D. Mark, S. Haeberle, G. Roth, F. Von Stetten, and R. Zengerle, "Microfluidic lab-on-a-chip platforms: Requirements, characteristics and applications," *Chem. Soc. Rev.*, vol. 39, no. 3, pp. 1153–1182, 2010.

[23] Y. Xia, J. Si, and Z. Li, "Fabrication techniques for microfluidic paper-based analytical devices and their applications for biological testing: A review.," *Biosens. Bioelectron.*, vol. 77, pp. 774–789, Mar. 2016.

[24] F. Hu, Jie Wang, ShuQi Wang, Lin Li, Fei Pingguan-Murphy, Belinda Lu, Tian Jian Xu, "Advances in paper-based point-of-care diagnostics," *Biosens. Bioelectron.*, vol. 54, pp. 585–597, 2014.

[25] A. K. Yetisen, M. S. Akram, and C. R. Lowe, "Paper-based microfluidic point-of-care diagnostic devices," *Lab Chip*, vol. 13, no. 12, pp. 2210–2251, 2013.

[26] D. Mark, S. Haeberle, G. Roth, F. von Stetten, and R. Zengerle, "Microfluidic lab-on-a-chip platforms: requirements{,} characteristics and applications," *Chem. Soc. Rev.*, vol. 39, no. 3, pp. 1153–1182, 2010.

[27] V. Gubala, L. F. Harris, A. J. Ricco, M. X. Tan, and D. E. Williams, "Point of Care Diagnostics: Status and Future," *Anal. Chem.*, vol. 84, no. 2, pp. 487–515, Jan. 2012.

[28] L. Shen, J. A. Hagen, and I. Papautsky, "Point-of-care colorimetric detection with a smartphone," *Lab Chip*, vol. 12, no. 21, pp. 4240–4243, 2012.

[29] B. M. Jayawardane, I. D. McKelvie, and S. D. Kolev, "Development of a Gas-Diffusion Microfluidic Paper-Based Analytical Device (μPAD) for the Determination of Ammonia in Wastewater Samples," *Anal. Chem.*, vol. 87, no. 9, pp. 4621–4626, May 2015.

[30] D. M. Cate, J. A. Adkins, J. Mettakoonpitak, and C. S. Henry, "Recent Developments in Paper-Based Microfluidic Devices," *Anal. Chem.*, vol. 87, no. 1, pp. 19–41, Jan. 2015.

[31] L. Syedmoradi, M. Daneshpour, M. Alvandipour, F. A. Gomez, H. Hajghassem, and K. Omidfar, "Point of care testing: The impact of nanotechnology," *Biosens. Bioelectron.*, vol. 87, pp. 373–387, 2017.

[32] F. Dincer, Can Bruch, Richard Costa-Rama, Estefanía Fernández-Abedul, Maria Teresa Merkoçi, Arben Manz, Andreas Urban, Gerald Anton Güder, "Disposable Sensors in Diagnostics, Food, and Environmental Monitoring," *Adv. Mater.*, vol. 31, no. 30, 2019.

[33] B. Sharma, S. Tanwar, and T. Sen, "One Pot Green Synthesis of Si Quantum Dots and Catalytic Au Nanoparticle-Si Quantum Dot Nanocomposite," *ACS Sustain. Chem. Eng.*, vol. 7, no. 3, pp. 3309–3318, 2019.

[34] Q. Cai, H. Meng, Y. Liu, and Z. Li, "Fluorometric determination of glucose based on a redox reaction between glucose and aminopropyltriethoxysilane and in-situ formation of blue-green emitting silicon nanodots," *Microchim. Acta*, vol. 186, no. 2, 2019.

[35] J. G. Croissant, Y. Fatieiev, A. Almalik, and N. M. Khashab, "Mesoporous Silica and Organosilica Nanoparticles: Physical Chemistry, Biosafety, Delivery Strategies, and Biomedical Applications," *Adv. Healthc. Mater.*, vol. 7, no. 4, p. 1700831, Feb. 2018.

[36] S. Chandra, Y. Masuda, N. Shirahata, and F. M. Winnik, "Transition-Metal-Doped NIR-Emitting Silicon Nanocrystals," *Angew. Chemie Int. Ed.*, vol. 56, no. 22, pp. 6157–6160, May 2017.

[37] J. G. Croissant, X. Cattoën, J.-O. Durand, M. Wong Chi Man, and N. M. Khashab, "Organosilica hybrid nanomaterials with a high organic content: syntheses and applications of silsesquioxanes," *Nanoscale*, vol. 8, no. 48, pp. 19945–19972,

2016.

[38] B. F. P. McVey and R. D. Tilley, "Solution Synthesis, Optical Properties, and Bioimaging Applications of Silicon Nanocrystals," *Acc. Chem. Res.*, vol. 47, no. 10, pp. 3045–3051, Oct. 2014.

[39] T. Bose, Sandeep Ganayee, Mohd. Azhardin Mondal, Biswajit Baidya, Avijit Chennu, Sudhakar Mohanty, Jyoti Sarita Pradeep, "Synthesis of Silicon Nanoparticles from Rice Husk and their Use as Sustainable Fluorophores for White Light Emission," *ACS Sustain. Chem. Eng.*, vol. 6, no. 5, pp. 6203–6210, May 2018.

[40] J. Zhang and S.-H. Yu, "Highly photoluminescent silicon nanocrystals for rapid, label-free and recyclable detection of mercuric ions," *Nanoscale*, vol. 6, Mar. 2014.

[41] Y. Zhong, Yiling Sun, Xiaotian Wang, Siyi Peng, Fei Bao, Feng Su, Yuanyuan Li, Youyong Lee, Shuit-Tong He, "Facile, Large-Quantity Synthesis of Stable, Tunable-Color Silicon Nanoparticles and Their Application for Long-Term Cellular Imaging," *ACS Nano*, vol. 9, no. 6, pp. 5958–5967, Jun. 2015.

[42] Y. Zhong, Yiling Sun, Xiaotian Wang, Siyi Peng, Fei Bao, Feng Su, Yuanyuan Li, Youyong Lee, Shuit-Tong He, "Facile, Large-Quantity Synthesis of Stable, Tunable-Color Silicon Nanoparticles and Their Application for Long-Term Cellular Imaging," *ACS Nano*, vol. 9, no. 6, pp. 5958–5967, Jun. 2015.

[43] L. Mohapatra, Pratyasha Mendivelso-Perez, Deyny Bobbitt, Jonathan M. Shaw, Santosh Yuan, Bin Tian, Xinchun Smith, Emily A. Cademartiri, "Large-Scale Synthesis of Colloidal Si Nanocrystals and Their Helium Plasma Processing into Spin-On, Carbon-Free Nanocrystalline Si Films," *ACS Appl. Mater. Interfaces*, vol. 10, no. 24, pp. 20740–20747, Jun. 2018.

[44] G. A. Mastronardi, Melanie L. Hennrich, Frank Henderson, Eric J. Maier-Flaig, Florian Blum, Carolin Reichenbach, Judith Lemmer, Uli Kübel, Christian Wang, Di Kappes, Manfred M. Ozin, "Preparation of Monodisperse Silicon Nanocrystals Using Density Gradient Ultracentrifugation," *J. Am. Chem. Soc.*, vol. 133, no. 31, pp. 11928–11931, Aug. 2011.

[45] X. Zhai, B. Song, B. Chu, Y. Su, H. Wang, and Y. He, "Highly fluorescent,

photostable, and biocompatible silicon theranostic nanoprobes against Staphylococcus aureus infections," *Nano Res.*, vol. 11, no. 12, pp. 6417–6427, Dec. 2018.

[46] Y. He, Yao Zhong, Yiling Peng, Fei Wei, Xinpan Su and S.-T. Lu, Yimei Su, Shao Gu, Wei Liao, Liangsheng Lee, "One-Pot Microwave Synthesis of Water-Dispersible, Ultraphoto- and pH-Stable, and Highly Fluorescent Silicon Quantum Dots," *J. Am. Chem. Soc.*, vol. 133, no. 36, pp. 14192–14195, Sep. 2011.

[47] X. Zhong, Yiling Peng, Fei Bao, Feng Wang, Siyi Ji and Y. Yang, Liu Su, Yuanyuan Lee, Shuit-Tong He, "Large-Scale Aqueous Synthesis of Fluorescent and Biocompatible Silicon Nanoparticles and Their Use as Highly Photostable Biological Probes," *J. Am. Chem. Soc.*, vol. 135, no. 22, pp. 8350–8356, Jun. 2013.

[48] Y. Zhong, Yiling Peng, Fei Wei, Xinpan Zhou, Yanfeng Wang, Jie Jiang, Xiangxu Su, Yuanyuan Su, Shao Lee, Shuit-Tong He, "Microwave-Assisted Synthesis of Biofunctional and Fluorescent Silicon Nanoparticles Using Proteins as Hydrophilic Ligands," *Angew. Chemie Int. Ed.*, vol. 51, no. 34, pp. 8485–8489, Aug. 2012.

[49] G. Chen, Haoyu Wu, Li Wan, Yuqi Huang, Lulu Li, Ningxing Chen, Jinyang Lai, "One-step rapid synthesis of fluorescent silicon nanodots for a hydrogen peroxide-related sensitive and versatile assay based on the inner filter effect," *Analyst*, vol. 144, no. 13, pp. 4006–4012, 2019.

[50] B. Li, Chang Xu, Yi-Tao Zhao and C. P. Jiang, Li Chen, Shi-Guo Xu, J B Fu, Xian-Zhu Sun, Rong Wong, "Flexible grapheme electrothermal films made from electrochemically exfoliated graphite," *J. Mater. Sci.*, vol. 51, Sep. 2015.

[51] S. Xie, T. Li, Z. Xu, Y. Wang, X. Liu, and W. Guo, "A high-response transparent heater based on a CuS nanosheet film with superior mechanical flexibility and chemical stability," *Nanoscale*, vol. 10, no. 14, pp. 6531–6538, 2018.

[52] K. Handique, "Microfluidic cartridge and method of making same," vol. 2, no. 12, pp. 1–8, 2004.

[53] V. Catto, Ariadne Da Silva, Luís Ribeiro, Caue Bernardini, Sandrine Aguir, Khalifa Longo, Elson Mastelaro, "An easy method of preparing ozone gas sensor based on ZnO nanorods," *RSC Adv.*, Feb. 2015.

[54] N. Romero, Francisco J. Rivadeneyra, Almudena Ortiz-Gomez, Inmaculada Salinas, Alfonso Godoy, Andrés Morales, Diego P. Rodriguez, "Inexpensive Grapheme Oxide Heaters Lithographed by Laser," *Nanomaterials*, vol. 9, no. 9, p. 1184, Aug. 2019.

[55] M. Bobinger, Marco R Romero, Francisco J Salinas-Castillo, Alfonso Becherer and A. Lugli, Paolo Morales, Diego P Rodríguez, Noel Rivadeneyra, "Flexible and robust laser-induced grapheme heaters photothermally scribed on bare polyimide substrates," *Carbon N. Y.*, vol. 144, pp. 116–126, 2019.

[56] Y. Qi, Y. Chen, J. He, and X. Gao, "Highly sensitive and simple colorimetric assay of hydrogen peroxide and glucose in human serum via the smart synergistic catalytic mechanism," *Spectrochim. Acta Part A Mol. Biomol. Spectrosc.*, vol. 234, p. 118233, 2020.

[57] D. O. F. Kidney, "Laboratory Assessment of Kidney Disease," *Pocket Companion to Brenner Rector's Kidney*, pp. 21–41, 2011.

[58] F. Della Pelle, A. Scroccarello, S. Scarano, and D. Compagnone, "Silver nanoparticles-based plasmonic assay for the determination of sugar content in food matrices," *Anal. Chim. Acta*, vol. 1051, pp. 129–137, 2019.

ÍNDICE DE FIGURAS

Capítulo 3

Figure 1. Hardware characteristics. (A) Board dimensions and distribution; (B) Folder state of the board inside the housing; (C) Housing made for the board..... 188
Figure 2. (A) Microfluidic paper-based analytical device for sugar monitoring; (B) µPAD with synthetized SNDs under UV-lamp (λ_{exc}= 365 nm). 189
Figure 3. Schematic illustration of SNDs synthesis from APTS and saccharose. 189
Figure 4. Heater physical characterization. (A) Real heater image; (B) Raman spectrum of LIG heater; (C) SEM image of the edge of heater; (D) SEM image detail (dashed square in (C) figure). 192
Figure 5. Electrical characterization of the heater. (A) Temporal evolution of temperature for different voltages; (B) Infrared thermal imaging of heater (C) Saturation temperature vs Power density; (D) Saturation temperature vs Voltage. 192
Figure 6. High-resolution XPS spectrum of the SNDs synthetized on the cellulose paper. (A) Full range; (B) C 1s; (C) N 1s; (D) O 1s and (E) Si 2p respectively. 193
Figure 7. (A) FT-IR spectrum synthetized SNDs on the µPAD; (B) TEM image, (C) Size distribution of SNDs; (D) EDX spectrum SNDs; (E) Fluorescence emission spectra (line red) and UV-Vis spectra (line blue) of SNDs in water. Insert: Cuvette photography λ_{exc}= 365 nm. 194
Figure 8. Optimization of parameters: (A) APTS concentration: 7.5 µL glucose 200 µM heating at 80ºC for 30 min; (B) pH dependent intensity behavior of SNDs: 1 µL APTS and 7.5 µL glucose 200 µM heating at 80ºC for 30 min; (C) Temperature: 1 µL APTS and 7.5 µL glucose 200 µM for 30 min heating; (D) Reaction time for glucose determination: 1 µL APTS and 7.5 µL glucose 200 µM heating at 80ºC; (E) Volume of sample: 1 µL APTS heating at 80ºC for 30 min. λ_{exc}= 365 nm. Data points are the mean of 3 assays in each optimization. 196
Figure 9. Calibration curve for (A) glucose and (B) fructose. Conditions: 1 µL APTS; heating at 80ºC for 30 min; 7.5 µL of glucose or fructose solutions; 197
Figure 10. Response of different interferences and sugars. Conditions: 1 µL APTS; heating at 80ºC for 30 min; 7.5 µL of interference solutions 250 µM; λ_{exc}= 365 nm. Data points are the mean of 3 assays. 198

ÍNDICE DE TABLAS

Capítulo 3

Table 1. Analytical characteristics of µPAD for glucose or fructose determination. .. 197
Table 2. Determination of glucose in human urine samples. 199
Table 3. Determination of total sugars in commercial juices and teas (n = 9). 200

Capítulo 4

NEAR FIELD COMMUNICATION FOR COLORIMETRIC DETERMINATION OF GLUTATHIONE IN A MICROFLUIDIC PAPER-BASED ANALYTICAL DEVICE

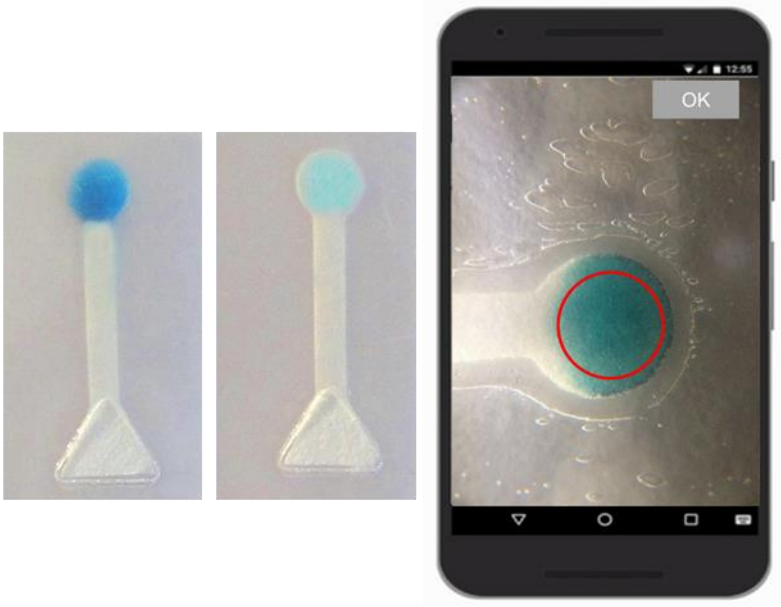

In process to submit to Sensor and Actuator B-Chemical

CAPÍTULO 5: NEAR FIELD COMMUNICATION FOR COLORIMETRIC DETERMINATION OF GLUTATHIONE IN A MICROFLUIDIC PAPER-BASED ANALYTICAL DEVICE

Inmaculada Ortiz-Gómeza [a,c], Almudena Rivadeneyra [b,c], Ignacio de Orbe-Payá [a,c], Luís Fermín Capitán-Vallvey [a,c], Alfonso Salinas-Castillo [a,c]

[a]ECsens, Department of Analytical Chemistry, Faculty of Sciences, University of Granada, 18071 Granada, Spain

[b]Electronic Devices Research Group, Department of Electronics and Computer Technology, Faculty of Sciences, University of Granada, 18071 Granada, Spain

[c]Unit of Excellence in Chemistry applied to Biomedicine and the Environment, Faculty of Science, University of Granada, 18071 Granada, Spain

Planteamiento

El glutatión (GSH) es un biotiol muy importante presente en los sistemas biológicos ya que está implicado en diversas funciones celulares entre las que se encuentra la de antioxidante, eliminando especies reactivas del oxígeno que presentan un electrón no apareado. Altos niveles de GSH en suero y orina humanos están vinculados al diagnóstico de diferentes enfermedades como cáncer, daño hepático, problemas cardíacos, psoriasis, y otras dolencias [1]. En consecuencia, la determinación de glutatión en diferentes muestras biológicas tales como sangre, plasma, suero, orina, etc. se considera muy importante para el diagnóstico de estas enfermedades. En este sentido, hasta la fecha se han desarrollado numerosas técnicas para la detección de glutatión en estas muestras entre las que podemos destacar, cromatografía de líquidos de alta resolución (HPLC), electroforesis capilar, electroquímica, quimioluminiscencia, espectroscopia de masas, etc [1]–[8]. A pesar de que estos métodos de determinación presentan una alta sensibilidad, se trata de metodologías costosas debido a los equipos e instrumentos de medida que utilizan, así como a los largos protocolos que se necesita llevar a cabo para preparar las muestras para el análisis y la necesidad de recurrir a personal cualificado para realizar los análisis. Por todo ello, hoy en día surge la necesidad de desarrollar nuevos métodos de detección más simples y novedosos para la determinación de glutatión. Como se ha venido comentando en la introducción de esta memoria la fabricación de dispositivos

microfluídicos basados en papel (µPAD) supone una alternativa ventajosa en el desarrollo de nuevos métodos de detección, simplificando el análisis y reduciendo el coste de los mismos. A este hecho, se suma la posibilidad de poder combinar estas plataformas de análisis con químicas de reconocimiento novedosas que permitan reducir el volumen de reactivos necesarios para llevar a cabo el análisis al implementarse en el µPAD y permitan una funcionalización del mismo. Hasta la fecha, se han empleado diversas técnicas analíticas que permiten la determinación de glutatión atendiendo a las características comentadas anteriormente, la mayoría de ellas se basan en métodos ópticos basados en cambios de color como consecuencia de la reacción del biotiol con algún nanomaterial implementado en el µPAD [9], [10]. Sin embargo, la aplicabilidad de los dispositivos desarrollados a menudo se ve afectada por la baja selectividad del sistema. Por lo tanto, se requiere del desarrollo de nuevo métodos colorimétricos para la determinación de glutatión que permitan mejorar todos estos aspectos. Así, en este capítulo se propone un nuevo método de determinación colorimétrica de glutatión basado en la reacción Ag (I)-3,3', 5, 5'-tetrametilbencidina utilizando un µPAD implementado con los reactivo necesarios para llevar a cabo la determinación y que además cuenta con una etiqueta NFC que permite la transferencia de datos de forma que se mejorando las prestaciones de análisis notablemente.

Objetivo

En el quinto capítulo de esta Memoria se describe el diseño y desarrollo de un µPAD para la determinación colorimétrica de glutation empleando un sistema basado en la reacción de oxido-reducción entre la Ag(I) y el 3,3',5,5'-tetrametilbencidina (TMB) generando un color azul intenso como consecuencia de la oxidación del TMB. En esta reacción la presencia de glutatión puede formar complejos con la Ag(I) y dificultar o impedir la reacción entre ambos de forma que se produce una disminución en la saturación de color. Esta diferencia de color puede ser analiza y relacionada con la concentración de glutation presente en una muestra si se toma una fotografía de la zona de detección del µPAD. Además, el sistema cuenta con una etiqueta NFC que permite la transferencia de datos a un Smartphone para llevar a cabo el almacenamiento y el tratamiento de las imágenes.

Por todo ello, para lograr este objetivo, se ha llevado a cabo el diseño y fabricación del µPAD para la determinación de glutation, se han estudiado las variables influyentes en la reacción de determinación y se ha realizado una caracterización analítica del dispositivo. Del mismo modo, se ha diseñado, caracterizado e integrado una etiqueta NFC en el µPAD que permite la transferencia de datos al Smartphone y analizar las imágenes para obtener los resultados. Además, se ha estudiado la selectividad del método colorimétrico desarrollado y se ha llevado a cabo la determinación de glutation en muestras de suero con objeto de demostrar la aplicabilidad del µPAD.

Las etapas de las que consta este trabajo pueden resumirse en:

1. Diseño y fabricación del µPAD.
2. Optimización de las variables influyente en la reacción de determinación de glutation.
3. Caracterización analítica del µPAD
4. Estudio de la selectividad del método propuesto para la determinación de glutation.
5. Diseño y caracterización de una etiqueta NFC para la transferencia de datos.
6. Implementación de la etiqueta NFC en el µPAD.
7. Determinación de glutation en muestras de suero.

NEAR FIELD COMMUNICATION FOR COLORIMETRIC DETERMINATION OF GLUTATHIONE IN A MICROFLUIDIC PAPER-BASED ANALYTICAL DEVICE

Abstract

Herein, we propose a microfluidic paper-based analytical device (μPAD) as a simple, rapid and selective colorimetric method for glutathione (GSH) determination. The proposed method was based on the fact that Ag^+ could oxidize 3, 3', 5, 5'-tetramethylbenzidine (TMB) to oxidized TMB and induce a blue color. Thus, the introduction of GSH could cause the reduction of oxidized TMB which resulted in a blue color fading. Based on this finding, we developed a method for the determination of GSH with a smartphone. This integration between μPAD and smartphone with a wireless communication electronic interfaces to digital image capture hardware serve as a means for quantitation. The proposed method shows a low detection limit of 0.72 μM with a digital camera and 1.0 μM with a smartphone. In addition, the most important of this non-enzymatic method is a simple, fast, portable and successfully de-termination of GSH within 20 min using a colorimetric signal.

Keywords: 3, 3', 5, 5'- Tetramethylbenzidine · Colorimetric assay · Glutathione · μPAD · NFC tag

1. Introduction

Glutathione (GSH), athiol-containing tripeptide (γ-L-glutamyl–cysteinyl–glycine), plays key roles in biological systems and serves many cellular functions to GSH and are important biomarkers related to many diseases such as cancer, liver damage, heart problems, psoriasis and other health problems. Thus, knowing the deficiency or increase of GSH is important to detect these diseases [11], [12], [13].

Nowadays, different analytical techniques are used for the detection of GSH as high performance liquid chromatography (HPLC) [14] and mass spectrometry [15]. Though most of these methods have high sensitivity, they suffer from the disadvantages of high

costs, time-consuming sample pretreatment and sophisticated instrument manipulation; in consequence, it is urgently needed to develop simple and novel GSH detection methods.

Currently, the use of microfluidic paper-based analytical devices (μPAD) has been shown high potential to be applied in a variety of bioanalytical studies involving sensing and diagnostic applications. This work demonstrates a paper-based microfluidic colorimetric sensor for the determination of GSH in biological samples based on the fact that Ag (I) serves as an oxidant for 3, 3′,5,5′,-tetramethylbenzidine (TMB) changing its colour to blue. However, the presence of GSH could cause the reduction of oxidized TMB along with a reaction with Ag (I) which resulting blue colour fading.

Microfluidic analytical devices have some advantages over other analytical approaches such as providing reliable measurements with efficiency and speed using small volumes of sample solutions [16]. Microfluidic paper-based analytical devices (μPAD) are based on the creation of hydrophilic micro-channels on cellulose-type substrates by means of two main types of techniques that form hydrophobic boundaries using materials such as wax, polymers and inks on hydrophilic paper or by forming physical boundaries by means of laser or knife cutting [17], [18]. In this work, the colour change of sensitive membranes based on TMB oxidation cause of presence of Ag (I) chemistry is studied in μPAD format for GSH determination in a simple operational procedure.

The interest of the Internet of Things (IoT) is growing these days. The fact that physical things can be connected to the Internet makes it possible to access data from a distance and to remotely control our physical world. In the IoT context, a smart object refers to an embedded system, which is connected to the Internet. Another technology that is emerging in the same direction is the RFID technology. This technology is a substitute of popular optical barcodes attached to many every-day products. In this case, a smart low-cost electronic ID-tag has to a product, so the product can be identified from a distance. By adding more capabilities to the ID tag, the tagged thing becomes a smart object [19].

Typically, RFID technology is classified according to the work frequency, as follows [20]–[22], in the frequency band of 13.56 MHz, we can find the Near Field Communication (NFC) protocol, designed for interactions between electronic devices in

close proximity (<10 cm) [23] and has the attractiveness of being implemented in many mobile devices, such as tablets and mobile phones. This later characteristic reduces the complexity of the traditional RFID readers where it is necessary to have not only a specific reader and a computer application to extract and process the read data. In this regard, we can take advantage of this technology and use a non-specific device to read a passive RFID tag with sensing capabilities where it is only necessary to install a mobile application to access to these functionalities.

In this context, Kassal et al.[24] presented a wireless smart tag for ultra low-power chemical sensing. In particular, this tag measures autonomously the electrode potential and stores this value in its internal memory. Then, these logged data can be transferred wirelessly to an RFID reader or a smart phone through near field communication (NFC). This RFID tag features are ultra-low power consumption, potentiometric sensing ability, autonomous data logging, and RFID/NFC compatible air interface, being useful for pH or ion-selective electrodes as stand-alone device or as part of sensor networks in the framework of the IoT. Kassal et al. [24] showed the pH determination as an experimental example of the capability of the tag. Another example shows a blood glucose measurement device wirelessly, which uses the 13.56 MHz magnetic field provided by the NFC interface to provide the electric energy required to power all electronic components of the system. Moreover, the measured data are transferred to a smart phone thanks to the NFC protocol. Due to the fact that no battery, display and storage are required, the size of the system as well as the consumption can be drastically reduced. The device is located over the NFC interface of a smartphone, supplying the device and extracting all the result of the blood glucose measurement as well as other relevant information of it to the smart phone. Once the smart phone gets all the information, it is shown on its display and saved on the phone in order to be accessed in the future or it can be sent to any other device via Internet [25].

Here, we present a passive NFC tag for chemical detection. This tag consists of a coil inductor as antenna and an RFID chip compatible with the NFC protocol. To this basic RFID tag, we have included a light emitter diode (LED) and a resistor as polarized element to develop the chemical optical sensor. The detection area of the µPAD is on top of the LED whose radiation response changes in presence of glutathione. The mechanism to extract the measurement is to locate the mobile phone with NFC capability in the

proximity of the tag, then the tag receives enough energy to power up the LED and the membrane changes its colorimetric response whose is captured by the camera of the mobile phone and later processes to extract the value. This is a simple system to easily extract colorimetric responses with a cheap and general-purpose device.

2. Experimental section

2.1. Reagents and materials

All reagents used were of analytical-reagent-grade unless stated otherwise and were obtained from Sigma-Aldrich (Sigma-Aldrich Química S.A., Madrid, Spain). All aqueous solutions were made using reverse-osmosis type quality water, Milli-RO 12 plus Milli-Q station from Millipore, conductivity 18.2 MΩ•cm, (Millipore, Bedford, MA, USA). 3,3',5,5'-tetramethylbenzidine (TMB); Acetic acid; sodium acetate; ethanol; L-gluthation (GSH); L-cysteine; L-glutamine (Gln); L-arginine (Arg); L-asparagine (Asn); DL-homocysteine (Hcys); L-glutamic acid (Glu); D-mannose (Man); galactose (Gal); D-lysine (Lys); L-serine (Ser) and L-histidine (His). Silver nitrate (AgNO3) from Merck (Darmstadt, Germany). Filter paper (ref. Whatman 1, qualitative circles 150 mm) from Sigma-Aldrich and transparent sheets 54x86 mm, quality strength protecting, 125 microns (Itaca, USA) were used to protect the μPAD.

2.2. Instruments and Software

The color change of the μPAD was measured with a Canon PowerShot G12 digital camera (Canon Inc., Tokio, Japan) and a LG Nexus 4 smartphone (Android). To keep all the image-gathering conditions the same, a Cube Light Box was used [26]. GIMP 2.8.22 software was used to analyze the region of interest (ROI) of the image along with the Color Space Converter plugin. A Rayjet Trotec Laser engraving printer (Rayjet, Trotec, Austria), commanded by Rayjet Commander Software, was used to design and fabricate the μPAD.

2.3. Preparation of µPAD

The devices were produced in a paper sheet by using a craft-cutting technique as cost-efficient, simple and reproducible process. The pattern of µPAD was first designed using Illustrator software (Adobe Systems) and the design was exported as an FS file to the controller software of a desktop Laser engraver with 12 W CO_2 laser source. To optimize the procedure and the substrate used, the µPAD elements were produced by cutting the cellulose paper (diameter 185 mm). The rate of success was 99 % confirming the viability of the design.

The device shown in Figure 1A consists of three separate areas, one for sampling, a transport channel where the $AgNO_3$ and buffer are immobilized, and a detection area where the chromogenic reagent is located. To prepare the µPAD for colorimetric detection of GSH firstly, 0.5 µL of 12.5 mM TMB was added to the detection area. Next, 0.5 µL of 15 mM $AgNO_3$ solution containing 100 µL of acetate buffer (100 mM, pH 4) was added over on the transport channel, then the µPAD was plasticized to avoid that the reagents undergo the processes of evaporation and degradation by means of a manual laminator at a temperature of 150 ºC using a thermoplastic material (54 x 86 mm). A hole in the sampling area of the µPAD let to the sample through the device. After that, the µPADs were stored in a dry environment at 4 °C in the dark until use.

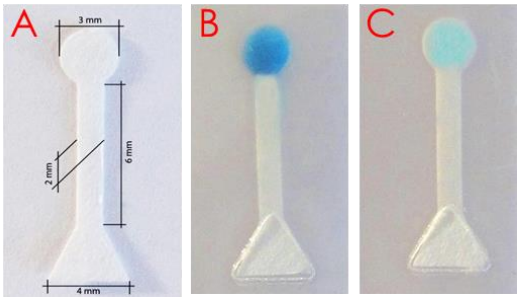

Figure 6. Picture of the µPAD (A) after adding a sample without GSH and (B) with GSH (C).

2.4. Image capture in cube light box and processing

The µPAD were imaged with a digital camera after reacting with GSH containing samples or standards. The images were processed by using the digital editing software GIMP 2.8.22 by selecting the region of interest (ROI) that contains relevant analytical

information. The ROI of each picture was selected by using the color picker tool of the editor from a circle slightly smaller than the detection area of the μPAD that typically contains around 6000 pixels. Each color channel was normalized independently to calculate the S parameter (saturation) of the HSV color space [27], which was used as analytical parameter, and their corresponding standard deviations.

2.5. Measurement protocol

For GSH determination, 10 μL of a solution of different concentrations were dropped in the sampling area of the microfluidic device. After that, the solution flow by capillarity towards the zones where the reagents are placed, twenty minutes are needed to complete the reaction decreasing the blue color on the detection zone (Figure 1B and Figure 1C). Once the sensing area was react, a picture of the microfluidic device was captured using a digital camera and a smartphone. The GSH concentration was calculated from the calibration function obtained with GSH standards. During the use the device is kept in horizontal position to non-favoured the flow of the solution and over a non-absorbent surface.

2.6. Tag design

The tag has been designed to resonate at the high frequency (HF) band, centred at 13.56 MHz. The operation mode in this frequency band is coupling, so that the antenna is a coil inductor. The Advanced Design System (ADS) software (Keysight Technologies, Santa Clara, CA, USA) based on momentum method was used for designing the antennas and for studying their RF electrical behaviour, taking into account their surface area roughness and the influence of the substrate [8].

The SL13a (ASM AG, Unterpremstaetten, Austria) was chosen as the RFID chip. It has a capacitance of approximately 25 pF at f0 = 13.56 MHz. Not considering the parasitic resistance, a value of 5.5 μH for the coil antenna should be achieved to enable the resonance at the desired frequency, avoiding the inclusion of an external capacitor [8].

This chip has an in-built temperature sensor with a non-linearity of ±0.5ºC with a maximum range from -40 ºC to 74 ºC.A10-bits Analog to Digital Converter (ADC) and an 8-kbit EEPROM are included in the chip.

Two different white LEDs have been tested in order to study the influence of the light source on the system. For this purpose, a NSPW310DS (Nichia Corporation, Japan) and a SMLP12WB (ROHM Semiconductor, USA) has been selected. The former has circular section with a diameter of 3.5 mm whereas the latter has a diameter of 0.6 mm.

Figure 2A presents the layout of this RFID tag. In order to provide the chemical sensing capabilities, we have included a light emitter diode (LED) between the VDD and VSS pins of this chip. A serial resistor has been added to polarize the LED. Figure 2B illustrates the inductance and quality of factor of the designed coil before placing the other components to the tag.

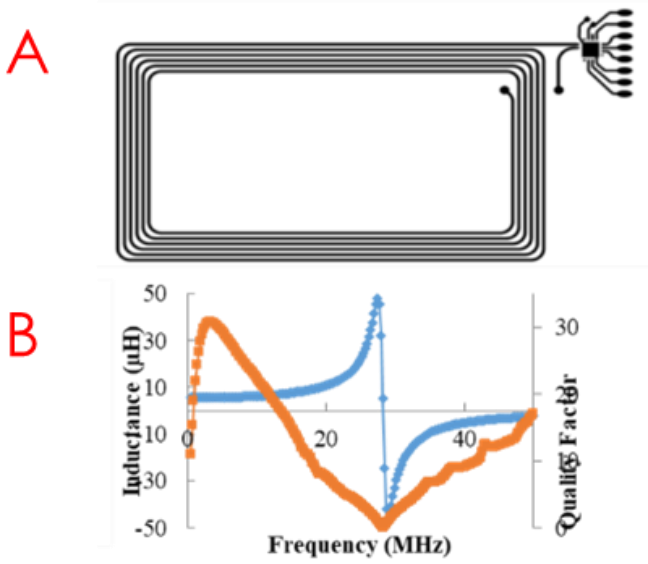

Figure 7. (A) Layout of the designed passive NFC tag with sensing capabilities. (B) Coil characterization: Inducance (L) and Quality Factor (Q).

2.7. Tag fabrication and characterization

This tag has been manufactured with a milling machine model S100 (LPKF Laser & Electronics AG, Garbsen, Germany) on FR-4 substrate. Accuracy on fabrication plays an important role on RF circuits, so specific RF tools were employed in the milling process.

Placement and soldering of the components were carried out by using an infrared solder station model IR/PL 550 (Kurtz Holding GmbH & Co., Kreuzwertheim, Germany).

In order to study the influence of the reader on the read range and LED power, three different commercial RFID readers has been using to test the system. In particular, an HF TRF7960 (Texas Instruments, USA) compatible with ISO 15693, a TRF7970 (Texas Instruments, USA)compatible with ISO 15693 and NFC protocol and a smart phone LG Nexus 4 (Google, USA) compatible with NFC has been employed in this work. The RFID readers power up and drive the tags using commands of the different protocols. The characterization of the coil inductor parameters have been carried out with an impedance analyser E42990A and an impedance probe kit (42941A) (Keysight Technologies., Santa Clara, CA, USA) by measuring its inductance and quality factor, using the four-wire measurement technique and using an excitation voltage of V_{DC} = 0 and V_{AC} = 500 mV.

2.8. Measurement protocol tag

The mechanism to extract the measurement is to locate the mobile phone with NFC capability in the proximity of the tag, then the tag receives enough energy to power up the LED and the membrane changes its colorimetric response whose is captured by the camera of the mobile phone and later processed it in the phone to extract the S parameter or saturation value of HSV color space. Once the saturation value is processed, it is shown in the mobile display and stored in the smart phone memory.

Although this procedure can be done with any HF RFID reader, we consider that using NFC provides a benefit to the system because any person can use this system with just having a smart terminal with NFC capabilities without requiring a specific device to perform the measurement.

2.9. Mobile application

The first step before the development of a mobile phone application is the selection of the operative system in which the application will run. In our case, Android has been chosen as operating system not only because of the ease of programming and being free license

against other proprietary operating systems, such as iOS (Apple Incorporation, California) or BlackBerry OS (BlackBerry, Ontario, Canada), but also because the vast majority of NFC terminal are supported in Android. Furthermore, operative system of smartphones is led by Android with almost 75% of the market [9]. Furthermore, our application requires the use of NFC protocol and the number of Android devices, which has incorporated this technology, is the largest.

In this work, a LG Nexus 4 (Google, USA) was selected as detection platform. This smartphone has a quad core processor, running the Android version 4.4.4. The phone has a display of 4.7 in. with 1280 x 768 pixels of resolution with total dimensions of 133.9 mm × 68.7 mm × 9.1 mm. This terminal has an in-built camera of 8 megapixels.

Following the same procedure as in [10], camera parameters were fixed in the developed application in order to avoid automatic configurations of the mobile phone. In addition, the application uses the autofocus option, which avoids capturing blurred and out of focus pictures of the microfluidic device.

The resolution of the pictures has been set to the highest available value in this phone, which is 3264 × 2448 pixels, in order to guarantee a high number of pixels for the analysis of the image. Despite the higher resolution, the time of processing has been also increased for this resolution. All the pictures are saved in Joint Photographic Experts Group (JPEG) format, which is the default format in most of the smart terminals, with a resolution of 96 dots per inch (dpi) and 8-bits per RGB channel. During the acquisition of the picture, the smartphone needs to be maintained in parallel position with the RFID tag in order to reduce distortions in the shape of the sensing areas due to the inclination of the mobile. Furthermore, the smartphone must be enough close to the RFID tag to provide enough energy to power up the LED. If the smartphone is not correctly placed, the LED does not provide emission.

In the case of smartphones with NFC capabilities, once this feature is activated, every time that an NFC tag or system is placed in the read range of the smartphone, the phone tries to establish communication with the other device via NFC protocol. Therefore, it is not necessary to include in the application any NFC code to power the LED unless we want to extract the ID, temperature value or other external connected sensor.

Nevertheless, we programmed the app to extract also the tag ID as well as the time and date when the measurement was performed so all these parameters together with the HSV coordinates could be stored in an internal database.

3. Results and discussion

3.1. Mechanism of GSH detection

The mechanism of the detection of GSH is shown in Scheme 1. Previous research [28] described that Ag^+ could directly oxidize TMB to the oxidized TMB (eqn (1)) and induce a blue color changing. Subsequently, the introduction of GSH of Ag^+-TMB system caused the reduction of oxidize TMB to form TMB (eqn(2)) which resulted in the fading of the blue color. On the other hand, GSH could also be responsive to bind to Ag^+ (eqn(3)), both of which suppress the oxidized TMB process

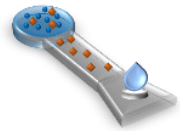

$$Ag^+ + TMB \rightarrow Ag^+ + TMB_{ox} \quad (1)$$

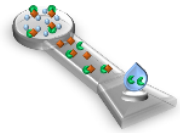

$$Ag^+ + GSH \rightarrow Ag^+ - GSH_{Complex} \quad (2)$$

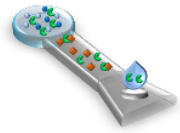

$$TMB_{ox} + 2GSH \rightarrow TMB + GSSH + 2H^+ \quad (3)$$

Scheme 1. Mechanism illustration for GSH detection.

To verify this mechanism, controlled testing was carried out at room temperature using 0.5 µL of 12.5 mM of TMB, 0.5 µL of 15 mM AgNO3 in 100 µL of acetate buffer 100 mM (pH 4) with 10 µL of different concentration of GSH. The results are displayed in Figure 3, the reagents (AgNO3 and TMB) not generate color change in the µPAD. Thus, a color blue in the detection area of the µPAD is strong and obvious in the TMB plus Ag+ system after adding 10 µL of sample without GSH, owing to the formation of TMBox. In

addition, the detection area of the µPAD changes the blue saturation when 10 µL of 150 µM and 250 µM of GSH were adding.

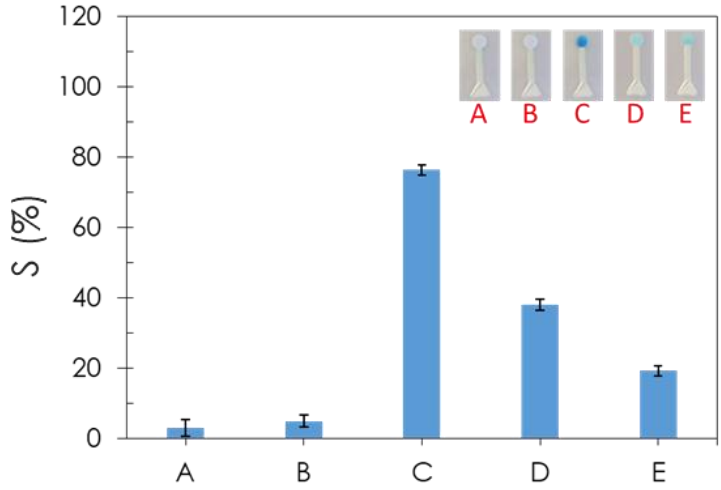

Figure 8. Response of the µPAD to AgNO3 (A), TMB (B), Ag^+ + TMB (C), Ag^+ + TMB + GSH 150 µM (D) and Ag^+ + TMB + GSH 250 µM (E). The insets show the corresponding photographic images of the µPAD in each case.

The results confirmed that TMBox could be reduced by GSH resulting in a decrease of saturation in the detection zone of the µPAD. Thus, a novel method for GSH determination could be established by using Ag^+-TMB system as a colorimetric assay.

3.2. Optimization of GSH detection conditions

Several aspects that affect the sensitivity of this method to detect GSH were optimized, such as the concentration of Ag^+ and TMB, pH value of the reaction buffer and reaction time (Figure 4.).

To study the effect of the concentration of immobilized Ag+ in the µPAD to the GSH detection, 0.5 µL of AgNO3 solution at concen-trations between 1.0 mM to 35 mM were added on the transport channel (Figure 4A). It can be obviously seen that the concentration of AgNO3 being too high or too low is not suitable for GSH detec-tion because the saturation is too low. The experiments show that the best saturation is obtained when the AgNO3 concentration is fixed at 15 mM.

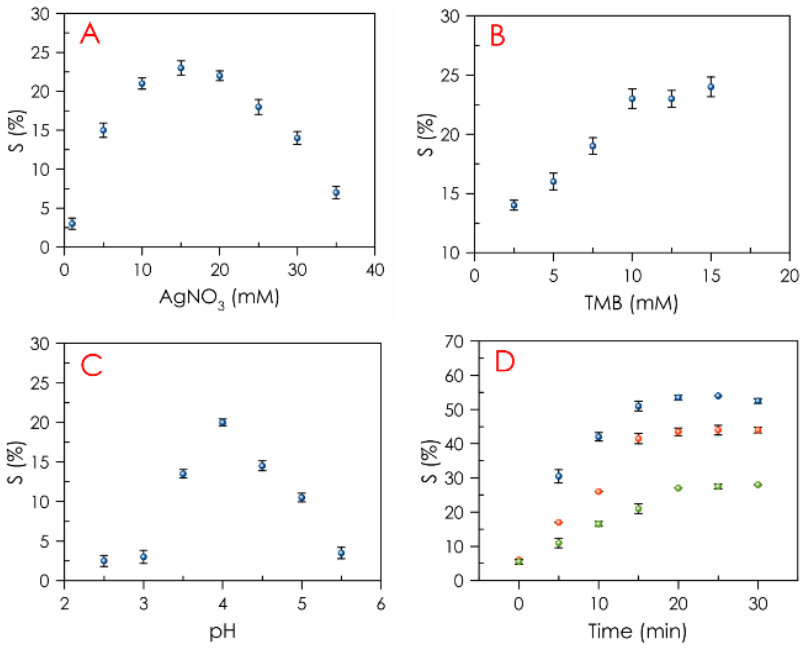

Figure 9. Optimization of the reaction conditions for GSH detection: (A) $AgNO_3$ concentration; (B) TMB concentration; (C) pH dependence on GSH recognition and (D) reaction time for 50 µM (blue dots), 150 µM (red dots) and 250 µM (green dots) of GSH.

The effect of the concentration of TMB was displayed in Figure 4B. The reagent TMB is deposited on detection area of µPAD from an ethanolic solution, because its high solubility and evaporation rate in this solvent. The optimum concentration of TMB was stud-ied in separate experiments preparing devices by drop casting 0.5 µL of a TMB solutions between 2.5 mM to 15 mM. Results showed that with the concentration of TMB increased, the color of the detection zone in the µPAD exhibited a significant change of saturation. According to the results, the selected concentration as optimum for TMB was 12.5 mM.

The effect of pH value in the GSH detection was investigated because pH has an important effect on the charge properties of amine, carboxyl and thiol groups of GSH [28], [29]. In addition, it was reported that the effect of pH on the Ag^+ oxidase-like activity catalytic could be used for TMB oxidation so extreme pH values are not suitable for this enzyme mimetic reaction. The pH was adjusted by placing a buffer in the transport channel of device along with the silver nitrate solution. As shown in Figure 4C the

influence of pH was investigated in the pH range of 2.5 to 5.5 using 100 mM of sodium acetate buffer. An increase in pH from 2.5 to 4 results in the increased saturation for oxidation of TMB in the detection zone in the µPAD furthermore the saturation value decrease when pH values are higher than 4 in consequently pH 4 was selected as an optimum for GSH detection.

The reaction time was studied by taking photos of µPAD during 30 min as shown in Figure 4D. Thus, the results indicate that after 15 min of reaction the saturation of the detection zone is maximum. For time higher than 15 min the saturation value, it seem constant. Consequently, 15 min was selected because it was sufficient to complete the reaction and dry the paper to obtain the picture.

3.3. Acquisition system characterization tag

The operation of the LED is limited by the maximum available power from the rectifier of the RFID chip. In the case of the SL13A, the maximum voltage is 3 V and the maximum current is 4 mA, so the ideal maximum available power is 12 mW.

Both LEDs have been chosen to work with a forward voltage as close as possible to 3V, taking in account the RFID chip power constraints. According to the manufacturer information for the maximum available current (4 mA), a forward voltage of about 2.6 V and 2.9V can be achieved for the 3 mm LED and SMD LED, respectively. When the tag with the 3 mm LED is placed at 10 mm distance of the reader, the polarization I-V point is 0.15 mA–1.66 V, leading to a power consumption of 0.25 mW. This gives us a luminance of XX cad according to the manufacturer. In a similar way, the SMD LED tag at this same distance, 10 mm, operates at 1.60 V and 0.14 mA. The power consumption is 0.21 mW and the associated luminance is XX cad.

The larger the distance between the reader and the tag, the lower the amount of power rectified by the chip, leading to a lower LED luminance. Figure 5 shows both LEDs operating point using three different commercial readers. There is a limit distance where the associated rectified power and luminance is not enough to acquire the sensor

information. The limit of luminance is XX cad, so the maximum distance is 8.0 cm for TRF7960/7970 readers and 4.0 cm for LG Nexus 4 reader. The highest read range is achieved with the TRF7960 and the lowest range with the smartphone. This result can be explained by the fact that the mobile terminal has a smaller an-tenna than the other two commercial readers do.

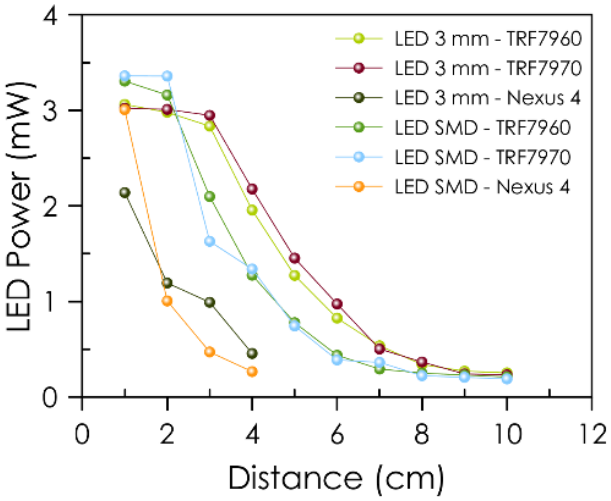

Figure 10. LED polarization as a function of the distance between the tag and the reader.

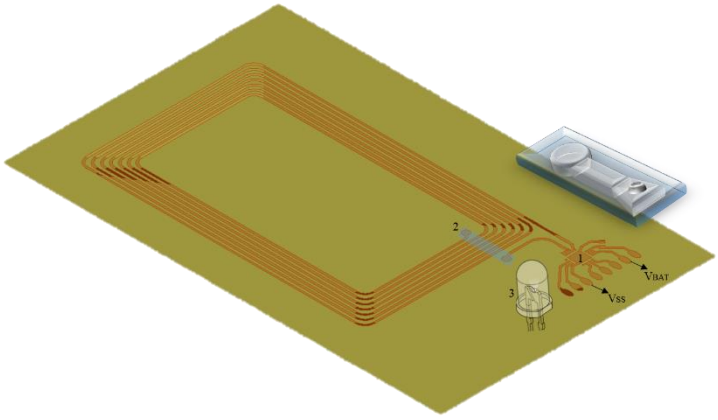

Figure 11. Schematic of the measurement system.

The measurement setup consists of the developed µPAD, the de-signed NFC tag with the LED and the smartphone with the An-droid application (see Figure 6). Once the app is initialized, the first we do is to check if NFC is enabled in the smartphone. If so, the user can select to get data or go to the database (DB) (Figure 7A). Once we are in the get data

menu and we place the phone next to the tag, we can see the ID, time and date (Figure 7B). Then, to acquire the HSV coordinates, we press such button and we are redirect it to the phone camera to take a picture (Figure 7C). Once we save the picture, we can select the area to be analysed with our fingertip (Figure 7D). If the user press OK, it is now redirected back to the former screen with both NFC and HSV data taken. All this information can be stored in the internal database by clicking on SAVE (Figure 7E).

Figure 12. (A) Home Screen; (B) Getting Data with NFC; (C) Selecting area of analysis.

3.4. Analytical characterization

Based on the relationship between saturation change of blue color of the detection zone in the device and GSH concentration, a sensi-tive colorimetric assay based on paper for GSH detection was established. This monotonal color change is followed by the satura-tion coordinate S of HSV color space after imaging the device with a smartphone. The S value decreases with glutathione concentration as shown in Figure 8A. The analytical function is obtained by means of a calibration set composed by 6 GSH standards between 0 and 250 µM with 3 replicates each and using 20 min as reaction time.

The experimental dependence between the S value and GSH con-centration, obtained with a digital camera and with a smartphone, are a lineal dependence. The regression equation with a digital camera is S = -0.24C + 76.19 with a correlation coefficient (R^2) of 0.9992 and with a smartphone is S = -0.19C + 74.94 with R^2=0.9965.

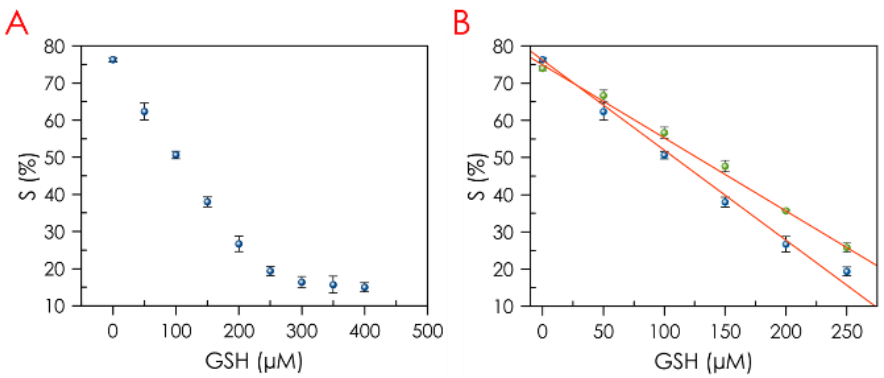

Figure 8. (A) Dependence of glutathione concentration obtained with digital camera and (B) calibration function with digital camera (blue dots) and with smartphone (green dots).

The detection limit of GSH was calculated in light of the 3σ/slope laws to be as low as 0.72 µM and 1.0 µM for a measurement with digital camera and smartphone, respectively. In addition, the quantification limit was calculated by 10σ/slope equation resulting 2.41 µM, acceptable values taking into account the normal values in biological fluids. The repeatability of the proposed method, as RSD, is obtained by 6 different µPAD working at 200 µM glutathione is 2.3 %, an acceptable precision considering the measuring system used. The cost of the µPAD considering only reagents, and paper for device making is around 0.05 cents/unit. The performance characteristics of the µPAD developed are presented in Table 1.

Table 6. Analytical characterization of µPAD for GSH determination.

Analytical parameters	D. camera	Smartphone
Measurement range (µM)	0-250	0-250
Slope (μM^{-1})	0.24	0.19
Intercept (a.u.)	76.19	74.94
LOD (µM)	0.72	1.0
LOQ (µM)	2.41	3.05
Precision (%) 200 µM	2.3	

A comparative study of different analytical performance for colori-metric detection of GSH is presented in Table 2, showing that the µPAD described has an ample range and good detection limit com-pared to other devices. As shown in Table 2, the linear range of

our method is wider than or comparable to some of theirs. The propose method providing a convenient and efficient detection sensor for GSH. The detection limit obtained in our method is lower compari-son with other. Our method provides an alternative to determination of GSH in real samples. Moreover, the detection time is much shorter than many previous reports. In summary, our method is feasible, fast and cost-effective.

Table 7. Comparison of different colorimetric methods for GSH detection.

Materials	Linear range (μM)	LOD (μM)	Reaction time (min)	References
Fe^{+3}-TMB	2.0-24.0	1.04	10	[31]
Rhodamine B-gold NPs	12 - 1384	1.0	60	[32]
Ag^{+}-TMB	0.05 – 8.0	0.05	10	[33]
MnO_2 NPs-TMB	0.26 - 26	0.1	15	[34]
Fe_3O_4-ABTS-H_2O_2	3.0 – 30	Not given	20	[35]
Ag^{+}-TMB	0-250	0.72	15	This work

3.5. Selectivity

In order to evaluate the selectivity of the proposed method, we examined the influence of some potential interferences in serum, including Cys, Hcy, Lys, Ser, His, Gln, Arg, Asn, Glu, mannose, galactose, homocysteine, lysine, serine and histidine. Solutions containing 100 μM glutathione and 100 μM interference were analyzed in triplicate, showing good selectivity (Figure 9). The reaction conditions are the same descripted in the section 2.3. The difference in the saturation values between the blank and interfer-ences was normalized, where S0 is the saturation value of the blank and S is the saturation value for each interference.

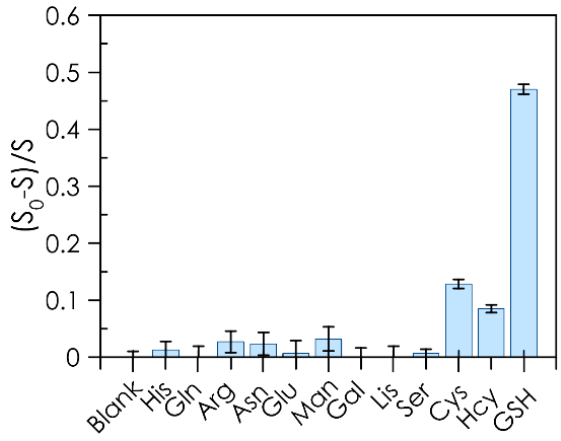

Figure 9. Normalized saturation changes of Ag^{+}-TMB assay.

3.6. Real samples analysis

To verify the possibility of the porous μPAD for quantitative determination of GSH in real samples, the concentration of GSH in human serum was studied. As we all know, the normal level of GSH is 7-21 μM in human serum [30]. Thus, the human serum samples were diluted 100 times, and the samples were spiked with different amounts of GSH. After that, 10 μL of each sample were placed in the sampling area of the microfluidic device and, after 15 minutes, a picture was taken. The results of detection are given in the Table 3. It can be seen that the measured values are consistent with the spiked values for the concentration of GSH in serum samples. The recoveries of different known amounts of added GSH are obtained from 98.31% to 104.56% for serum samples. All of these results indicate that the propose method is accurate and sensitive enough for the detection of biothiols in real samples.

Table 8. Recovery study for GSH in human serum samples.

Concentration of GSH (μM)			
Sample	**Amount added**	**Amount found**	**Recovery (%)**
	50	54.96	100.92
Serum 1	200	209.13	104.56
	250	254.96	101.98
	50	50.79	101.58
Serum 2	200	196.63	98.31
	250	254.96	101.98
	50	51.21	102.42
Serum 3	200	197.46	98.73
	250	254.96	101.98

4. Conclusion

In summary, we have settled a simple and low-cost assay for the colorimetric determination of glutathione using a microfluidic paper-based analytical device and a smartphone. The interaction of NFC interface with a smartphone let image processing and recording color changes onto the microfluidic paper-based analytical device and converting them into quantitative information were accomplished by digital image capture and analysis. Thus, our method presents a limit of detection of 1.0 µM for glutathione with a linear dynamic range from 10 – 250 µM. Moreover, this method is applied to the determination of glutathione in human serum sample and obtains satisfactory results.

REFERENCES

[1] F. Wang, Y. Zhu, J. Xu, Z. Xu, G. Cheng, and W. Zhang, "Highly selective and ratiometric fluorescent nanoprobe for the detection of cysteine and its application in test strips," *Anal. Bioanal. Chem.*, vol. 410, no. 20, pp. 4875–4884, Aug. 2018.

[2] R. Rajaram and J. Mathiyarasu, "An electrochemical sensor for homocysteine detection using gold nanoparticle incorporated reduced graphene oxide," *Colloids Surfaces B Biointerfaces*, vol. 170, pp. 109–114, Oct. 2018.

[3] X. Ji, W. Wang, X. Li, Y. Chen, and C. Ding, "Enhanced chemiluminescence detection of glutathione based on isoluminol-PSM nanoparticles probe," *Talanta*, vol. 150, pp. 666–670, Apr. 2016.

[4] S. Childs, N. Haroune, L. Williams, and M. Gronow, "Determination of cellular glutathione:glutathione disulfide ratio in prostate cancer cells by high performance liquid chromatography with electrochemical detection," *J. Chromatogr. A*, vol. 1437, pp. 67–73, Mar. 2016.

[5] J. B. Raoof, R. Ojani, H. Karimi-Maleh, M. R. Hajmohamadi, and P. Biparva, "Multi-wall carbon nanotubes as a sensor and ferrocene dicarboxylic acid as a mediator for voltammetric determination of glutathione in hemolysed erythrocyte," *Anal. Methods*, vol. 3, no. 11, p. 2637, 2011.

[6] P. Miao, L. Liu, Y. Nie, and G. Li, "An electrochemical sensing strategy for ultrasensitive detection of glutathione by using two gold electrodes and two complementary oligonucleotides," *Biosens. Bioelectron.*, vol. 24, no. 11, pp. 3347–3351, Jul. 2009.

[7] J. Kruusma, A. M. Benham, J. A. G. Williams, and R. Kataky, "An introduction to thiol redox proteins in the endoplasmic reticulum and a review of current electrochemical methods of detection of thiols," *Analyst*, vol. 131, no. 4, p. 459, 2006.

[8] L. Janeš, K. Lisjak, and A. Vanzo, "Determination of glutathione content in grape juice and wine by high-performance liquid chromatography with fluorescence detection," *Anal. Chim. Acta*, vol. 674, no. 2, pp. 239–242, Aug. 2010.

[9] M. Lin, Y. Guo, Z. Liang, X. Zhao, J. Chen, and Y. Wang, "Simple and fast determination of biothiols using Fe3+-3, 3′, 5, 5′-tetramethylbenzidine as a colorimetric probe," *Microchem. J.*, vol. 147, pp. 319–323, Jun. 2019.

[10] P. Ni *et al.*, "Highly sensitive and selective colorimetric detection of glutathione

based on Ag [I] ion–3,3′,5,5′-tetramethylbenzidine (TMB)," *Biosens. Bioelectron.*, vol. 63, pp. 47–52, Jan. 2015.

[11] C. Chen, W. Liu, C. Xu, and W. Liu, "A colorimetric and fluorescent probe for detecting intracellular biothiols," *Biosens. Bioelectron.*, vol. 85, pp. 46–52, 2016.

[12] H. Gallwitz, S. Bonse, A. Martinez-Cruz, I. Schlichting, K. Schumacher, and R. L. Krauth-Siegel, "Ajoene Is an Inhibitor and Subversive Substrate of Human Glutathione Reductase and Trypanosoma cruzi Trypanothione Reductase: Crystallographic, Kinetic, and Spectroscopic Studies," *J. Med. Chem.*, vol. 42, no. 3, pp. 364–372, Feb. 1999.

[13] S. C. Lu, "Regulation of glutathione synthesis.," *Curr. Top. Cell. Regul.*, vol. 36, pp. 95–116, 2000.

[14] K. P. Mitton and J. R. Trevithick, "High-performance liquid chromatography-electrochemical detection of antioxidants in vertebrate lens: glutathione, tocopherol, and ascorbate.," *Methods Enzymol.*, vol. 233, pp. 523–539, 1994.

[15] A. Mika, E. Skorkowski, and P. Stepnowski, "The Use of Different MS Techniques to Determine Glutathione Levels in Marine Tissues," *Food Anal. Methods*, vol. 6, no. 3, pp. 789–802, 2013.

[16] T. Yager, Paul Edwards and B. H. Fu, Elain Helton, Kristen Nelson, Kjell Tam, Milton R Weigl, "Microfluidic diagnostic technologies for global public health.," *Nature*, vol. 442, no. 7101, pp. 412–418, Jul. 2006.

[17] R. Ghosh, S. Gopalakrishnan, R. Savitha, T. Renganathan, and S. Pushpavanam, "Fabrication of laser printed microfluidic paper-based analytical devices (LP-µPADs) for point-of-care applications," *Sci. Rep.*, vol. 9, no. 1, p. 7896, 2019.

[18] A. K. Yetisen, M. S. Akram, and C. R. Lowe, "Paper-based microfluidic point-of-care diagnostic devices," *Lab Chip*, vol. 13, no. 12, pp. 2210–2251, 2013.

[19] N. Gershenfeld, R. Krikorian, and D. Cohen, "The Internet of Things," *Sci. Am.*, vol. 291, pp. 76–81, Nov. 2004.

[20] M. Ward and R. van Kranenburg, "RFID: Frequency, standards, adoption and innovation," *JISC Technol. Stand. Watch*, no. May, p. 36, 2006.

[21] K. Domdouzis, B. Kumar, and C. Anumba, "Radio-Frequency Identification (RFID) applications: A brief introduction," *Adv. Eng. Informatics*, vol. 21, no. 4, pp. 350–355, 2007.

[22] J. Landt, "The history of RFID," *Potentials, IEEE*, vol. 24, pp. 8–11, Nov. 2005.

[23] P. Peris-Lopez, J. Hernandez-Castro, J. Tapiador, and A. Ribagorda, *RFID*

Systems: A Survey on Security Threats and Proposed Solutions, vol. 4217. 2006.

[24] P. Kassal, I. M. Steinberg, and M. D. Steinberg, "Wireless smart tag with potentiometric input for ultra low-power chemical sensing," *Sensors Actuators B Chem.*, vol. 184, pp. 254–259, 2013.

[25] S. Cecil, M. Bammer, G. Schmid, K. Lamedschwandner, and A. Oberleitner, "Smart NFC-sensors for healthcare applications and further development trends," *e i Elektrotechnik und Informationstechnik*, vol. 130, pp. 191–200, Nov. 2013.

[26] M. Ariza-Avidad, A. Salinas-Castillo, M. P. Cuéllar, M. Agudo-Acemel, M. C. Pegalajar, and L. F. Capitán-Vallvey, "Printed Disposable Colorimetric Array for Metal Ion Discrimination," *Anal. Chem.*, vol. 86, no. 17, pp. 8634–8641, Sep. 2014.

[27] G. Wyszecki and W. Stiles, "Color Science: Concepts and Methods, Quantitative Data and Formulae, 2nd Edition," *Color Sci. Concepts Methods, Quant. Data Formulae, 2nd Ed. by Gunther Wyszecki, W. S. Stiles, pp. 968. ISBN 0-471-39918-3. Wiley-VCH , July 2000.*, Jul. 2000.

[28] S. Liu, J. Tian, L. Wang, and X. Sun, "Highly sensitive and selective colorimetric detection of Ag(I) ion using 3,3′,5,5′,-tetramethylbenzidine (TMB) as an indicator," *Sensors Actuators B Chem.*, vol. 165, no. 1, pp. 44–47, 2012.

[29] N. Zhang, F. Qu, H. Q. Luo, and N. B. Li, "Sensitive and selective detection of biothiols based on target-induced agglomeration of silvernanoclusters," *Biosens. Bioelectron.*, vol. 42, pp. 214–218, 2013.

[30] H. Liu *et al.*, "High performance fluorescence biosensing of cysteine in human serum with superior specificity based on carbon dots and cobalt-derived recognition," *Sensors Actuators B Chem.*, vol. 280, pp. 62–68, 2019.

[31] M. Lin, Y. Guo, Z. Liang, X. Zhao, J. Chen, and Y. Wang, "Simple and fast determination of biothiols using Fe3+-3, 3′, 5, 5′-tetramethylbenzidine as a colorimetric probe," *Microchem. J.*, vol. 147, pp. 319–323, 2019.

[32] H.-H. Cai, H. Wang, J. Wang, W. Wei, P.-H. Yang, and J. Cai, "Naked eye detection of glutathione in living cells using rhodamine B-functionalized gold nanoparticles coupled with FRET," *Dye. Pigment.*, vol. 92, no. 1, pp. 778–782, 2012.

[33] P. Ni *et al.*, "Highly sensitive and selective colorimetric detection of glutathione based on Ag [I] ion-3,3',5,5'-tetramethylbenzidine (TMB).," *Biosens. Bioelectron.*, vol. 63, pp. 47–52, Jan. 2015.

[34] X. Liu, Q. Wang, Y. Zhang, L. Zhang, Y. Su, and Y. Lv, "Colorimetric detection of glutathione in human blood serum based on the reduction of oxidized TMB," *New J. Chem.*, vol. 37, no. 7, pp. 2174–2178, 2013.

[35] Y. Ma, Z. Zhang, C. Ren, G. Liu, and X. Chen, "A novel colorimetric determination of reduced glutathione in A549 cells based on Fe3O4 magnetic nanoparticles as peroxidase mimetics," *Analyst*, vol. 137, no. 2, pp. 485–489, 2012

ÍNDICE DE FIGURAS

Capítulo 4

Figure 1. Picture of the µPAD (A) after adding a sample without GSH and (B) with GSH (C). 218

Figure 2. (A) Layout of the designed passive NFC tag with sensing capabilities. (B) Coil characterization: Inducance (L) and Quality Factor (Q). 220

Figure 3. Response of the µPAD to AgNO3 (A), TMB (B), Ag^+ + TMB (C), Ag^+ + TMB + GSH 150 µM (D) and Ag^+ + TMB + GSH 250 µM (E). The insets show the corresponding photographic images of the µPAD in each case. 224

Figure 4. Optimization of the reaction conditions for GSH detection: (A) $AgNO_3$ concentration; (B) TMB concentration; (C) pH dependence on GSH recognition and (D) reaction time for 50 µM (blue dots), 150 µM (red dots) and 250 µM (green dots) of GSH. 225

Figure 5. LED polarization as a function of the distance between the tag and the reader. 227

Figure 6. Schematic of the measurement system. 227

Figure 7. (A) Home Screen; (B) Getting Data with NFC; (C) Selecting area of analysis. 228

ÍNDICE DE TABLAS

Capítulo 4

Table 1. Analytical characterization of µPAD for GSH determination. 229
Table 2. Comparison of different colorimetric methods for GSH detection. 230
Table 3. Recovery study for GSH in human serum samples. 231

Capítulo 5

A VINYL SULFONE CLICKED CARBON-DOT-ENGINEERED MICROFLUIDIC PAPER-BASED ANALYTICAL DEVICE FOR FLUOROMETRIC DETERMINATION OF BIOTHIOLS

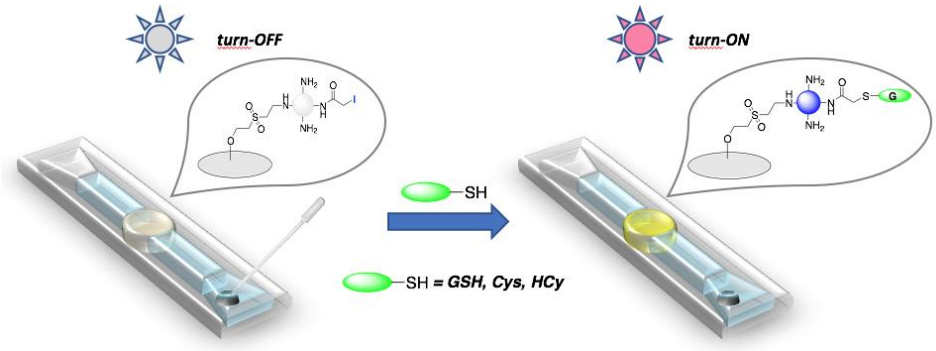

Published in Microchimica Acta 2020

CAPÍTULO 5: A VINYL SULFONE CLICKED CARBON-DOT-ENGINEERED MICROFLUIDIC PAPER-BASED ANALYTICAL DEVICE FOR FLUOROMETRIC DETERMINATION OF BIOTHIOLS

Inmaculada Ortiz-Gomez[1,3], Mariano Ortega-Muñoz[2,3], Antonio Marín-Sánchez[1,3], Ignacio de Orbe-Payá[1,3,] Fernando Hernandez-Mateo[2,3], Luis Fermin Capitan-Vallvey[1,3], Francisco Santoyo-Gonzalez[2,3], Alfonso Salinas-Castillo[1,3]

[1]Department of Analytical Chemistry, Faculty of Sciences, Campus Fuentenueva s/n, University of Granada, 18071 Granada, Spain

[2]Department of Organic Chemistry, Biotechnology Institute, Faculty of Sciences, Campus Fuentenueva s/n, University of Granada, 18071 Granada, Spain

[3]Unit of Excellence in Chemistry applied to Biomedicine and the Environment University of Granada, 18071 Granada, Spain

Planteamiento

Como se ha descrito en la introducción de esta Memoria, la utilización del papel de celulosa en el desarrollo de plataformas microfluídicas de diagnóstico para construir instrumentación portátil miniaturizada resulta de gran interés debido a las múltiples ventajas que presenta en la realización de análisis químicos y biológicos. De hecho, uno de los campos de aplicación de mayor interés de los dispositivos microfluídicos basados en papel (µPAD) es su empleo en aplicaciones biomédicas para el desarrollo de tecnologías Point of Care (POC) [1].

Por otro lado, la funcionalización de materiales de celulosa tiene un gran potencial debido a la capacidad de extender la funcionalidad y aplicabilidad de los µPADs en el desarrollo de nuevas plataformas de detección. La integración de nanomateriales en el papel mejora notablemente la capacidad de detección del dispositivo de análisis. En este sentido, la integración de µPADs con nanomateriales funcionales como, metales, óxidos metálicos, nanomateriales de carbono y polímeros de impresión molecular, ha sido notable en los últimos años. Todos estos nanomateriales poseen propiedades distintivas que mejoran el rendimiento de los µPADs y amplían considerablemente sus campos de aplicación [2].

La mayoría de las metodologías publicadas utilizando nanomateriales para la funcionalización del papel en el desarrollo de dispositivos de detección están dirigidas a la utilización de materiales químicos que poseen excelentes propiedades ópticas. Así, el empleo de nanopartículas de carbono, como los carbon dots (CDs) [3], se han utilizado como sondas fluorescentes en la detección de diversos analitos debido a su alta sensibilidad, buena especificidad, estabilidad química, buena biocompatibilidad, baja toxicidad y propiedades lumínicas únicas [4].

Por todo ello, en el quinto capítulo de esta Memoria se propone el desarrollo de un µPAD que integra CDs unidos covalentemente al papel y funcionalizados para el ensayo fluorometrico off/on de biotioles como glutation, cisteína y homocisteina.

Objetivo

El objetivo principal de este quinto capítulo es el desarrollo de un µPAD para la determinación fluorometrica off/on de biotioles. Este ensayo se basa en la unión covalente de CDs fluorescentes en papel de celulosa y su posterior funcionalización de forma que los CDs pierdan sus propiedades fluorescentes reactivándose la fluorescencia en presencia de biotioles.

Para alcanzar este objetivo, se ha llevado a cabo la síntesis, inmovilización covalente y funcionalización de los carbon dots fluorescentes al papel de celulosa, se han optimizados las variables influyentes en la reacción de determinación de biotioles y se ha caracterizado analíticamente el sistema para la detección de glutation, cisteína y homocisteina. Por último, se ha llevado a cabo la determinación de glutation en muestras de orina.

En la práctica, las etapas de las que consta este trabajo de investigación son las siguientes:

1. Síntesis y caracterización estructural de los CDs seleccionados en la química de reconocimiento de los biotioles.
2. Unión covalente de CDs al papel de celulosa.
3. Funcionalización de CDs inmovilizados y perdida de la fluorescencia.
4. Optimización de las variables influyentes en la detección de biotioles.
5. Caracterización analítica del µPAD en la determinación de glutation, cisteína y homocisteina.
6. Aplicación del µPAD para la determinación de glutation en muestras de orina.

A VINYL SULFONE CLICKED CARBON-DOT-ENGINEERED MICROFLUIDIC PAPER-BASED ANALYTICAL DEVICE FOR FLUOROMETRIC DETERMINATION OF BIOTHIOLS

Abstract

A microfluidic paper-based analytical device integrating carbon-dot (CDs) is fabricated and used for a fluorometric off-on assay of biothiols. Vinyl sulfone (VS) click immobilization of carbon dots (CDs) on paper was accomplished by a one-pot simplified protocol that uses divinylsulfone (DVS) as a homobifunctional reagent. This reagent mediated both the click oxa-Michael addition to the hydroxyl groups of cellulose and ulterior covalent grafting of the resulting VS-paper to NH_2-functionalized CDs by means of click aza-Michael addition. The resulting cellulose nanocomposite was used to engineer an inexpensive and robust microfluidic paper-based analytical device (μPAD) that is used for a reaction-based off-on fluorometric assay of biothiols (GSH, Cys and Hcy). The intrinsic blue fluorescence of CDs (with excitation/emission maxima at 365/450 nm) is turned off via the heavy atom effect of an introduced iodo group. Fluorescence is turned on again by the displacement of iodine by reaction with a biothiol. The increase in fluorescence is related to the concentration over a wide range (1 to 200 μM for GSH, and 5-200 μM for Cys and Hcy, respectively), and the assay exhibit a low detection limit (0.3 μM for GSH and for Cys and 0.4 μM Hcy, respectively). The method allows for rapid screening and can also be used in combination with a digital camera readout.

Keywords: Microfluidic paper-based device · Off-on assay · Carbon dots · Click immobilization · Vinyl sulfone · Biothiols determination · Glutathione · Photographic camera

1. Introduction

Microfluidics is nowadays a flourishing technology embraced by most engineering disciplines including chemical sensing and biosensing [5], [6].

Albeit traditional microfluidic (bio)sensing devices are typically made from silicon and glass, because of the geometrical precision and inertness for reuse that these materials provide, and polymer materials, recent trends have moved the interest to cellulose paper as an appealing analytical platform [7]–[9]. For these reasons, microfluidic paper-based analytical devices (μPADs), [10] while retaining the miniaturization and integration characteristics of their counterparts, are also powerful tools for point-of-care testing (POCT) as they accomplish the ASSURED (affordable, sensitive, specific, user-friendly, rapid and robust, equipment-free and deliverable to end users) criteria outlined by the World Health Organization (WHO) for POCT [11] Therefore, μPADs have emerged as a leading alternative for the development of portable and disposable diagnostic devices aimed to high-tech applications [12].

In order to provide conventional μPADs with higher versatility and multifunctional performance, the integration of diverse emerging functional nanomaterials into paper has been implemented to μPADs in the last decade expanding their potential [13]. Hybrid cellulose composites incorporating nanoparticles (NPs) has shown great potential for the fabrication of sophisticated (bio)chemical assay that exhibit excellent selectivity and sensitivity, and rapid response [2]. Nobel metal (Au and Ag), bimetals (including semiconductor quantum dots -QDs-) and metal oxides nanoparticles (NPs) as well as carbon nanomaterials (grapheme, carbon nanotubes and carbon dots -CDs-) have been successfully incorporated into paper leading to NP-based paper (bio)chemical sensors.

Although the detection methods commonly used in (bio)sensing have been integrated into μPADs, [14] optical techniques are still prevalent because of their sensitivity and operational simplicity. Among the different methods used to detect the optical response signal emitted from paper-based devices, [1] fluorescence spectroscopy in its numerous variations have attracted enormous interest and is nowadays a powerful tool [1]. As the majority of (bio)analytes do not exhibit fluorescence, the detection and quantification of these compounds using a fluorescent assay would require the mediation of fluorescent probes and for this purpose selected NPs are paradigmatic optical signal reporters. In this respect, QDs has been a rational choice for the preparation of fluorogenic paper nanocomposites. However, substantiated concerns about the toxicity of these heavy-metal

NPs have turned the attention to emergent CDs [15] as a valuable alternative to perform as fluorescent reporters in paper-based sensors because their low toxicity and other distinctive advantages: convenient synthesis, low toxicity, prominent biocompatibility, high resistance to photobleaching, colorful photoluminescence, high chemical resistance, high water solubility, easy functionalization, and low cost [16]. For this reason, in the actual state-of-the-art of paper-based (bio)chemical sensors, CDs-modified cellulose is becoming an appealing platform that, in the particular case of μPADs, have been applied in few reported cases [17], [18].

In this paper, we describe the vinyl sulfone (VS) click immobilization of CDs on paper by a one-pot simplified protocol that uses divinylsulfone (DVS) as a homobifunctional click reagent that allows the click oxa-Michael addition to the paper surface and ulterior covalent grafting of the resulting VS-cellulose to NH_2-functionalized CDs by means of click aza-Michael addition. Besides the well-known use of DVS as a cross-linking reagent of diverse (bio)polymers, [19] including cellulose with different purposes, the DVS-mediated immobilization of biomolecules, particularly enzymes, to cellulose is also a proven methodology [20]. However, the implementation of click VS click coupling for engineering CDs-based fluorogenic cellulose platform is described herein for the first time. As a proof-of-concept of the applicability of the novel platform, we fabricate an engineered fluorogenic CDs-based μPAD, and we demonstrate its applicability for a reaction-based off-on analytical evaluation of biothiols.

2. Materials and methods

2.1.Materials and reagents

L-Glutathione (GSH); L-cysteine (Cys); DL-homocysteine (Hcy); L-serine (Ser); L-histidine (His); L-galactose (Gal); L-lysine (Lys); L-arginine (Arg); L-asparagine (Asn); D-mannose (Man); ethanol; ethanolamine; triethylamine (TEA); dichloromethane (DCM); sodium hydrogenphosphate; sodium dihydrogenphosphate; sodium hydrogencarbonate; sodium carbonate; anhydrous citric acid (CA); iodoacetic acid (IAA); divinyl sulfone (DVS); branched polyethylenimine 25 kDa (25kPEI); N,N-dicyclohexylcarbodiimide (DCC); N,N-diisopropylethylamine (DIPEA) were purchased

from Sigma-Aldrich (www.sigmaaldrich.com). NH_2-functionalized CDs were prepared following a slightly modified reported hydrothermal synthesis starting form citric acid (CA) as the carbon source [21] (see ESM). All reagents were of analytical-reagent–grade unless stated otherwise. Whatman grade 1 chromatography paper from Sigma-Aldrich was used to manufacture the μPAD. All aqueous solutions were made using reverse-osmosis type quality water (Milli-RO 12 plus Milli-Q station from Millipore, conductivity 18.2 MΩ·cm).

2.2.Apparatus, instruments and software

The fluorescence intensity of the functionalized paper analytical device was measured with a Sony Cyber-shot DSC-HX 300 digital camera (Sony, Tokio, Japan) after illumination with an UV transilluminator 220 V (MUV 21 series). A script of MATLAB was used to analyze the region of interest (ROI) of the image along with the Color Space Converter. Fluorescence spectra were obtained using Cary Eclipse UV-Vis fluorescence spectrophotometer. A pH meter (Crison micro pH 2000) was utilized to measure the pH values of aqueous solutions. The analytical devices were fabricated on paper using a craft-cutting technique as a cost-efficient, simple and reproducible process using a 12 W CO_2 laser engraver (Rayjet, www.rayjetlaser.com). The size, morphology and characterization of the CDs were examined by high resolution transmission electron microscopy (HRTEM) using a FEI TITAN G2 microscope operating 200 kV. The XPS spectra measurements were performed on an X-ray photoelectron spectroscopy (Kratos Axis ultra-DLD) for characterization of the functionalized paper analytical device and CDs. The maps of the paper by elemental mapping scanning transmission electron microscopy (STEM) were carried out using scanning transmission electron microscopy Zeiss SUPRA 40 VP. All of these studies were carried out at the Centre of Scientific Instrumentation (University of Granada, Spain).

2.3.Preparation of CDs-paper: VS-click immobilization of CDs

The chemical immobilization of CDs into cellulose paper was carried out in a two-step procedure that use DVS as a homobifunctional cross-linker (Scheme 1). In detail, disks (3 mm-diameter) of Whatman grade 1 filters were first produced using a cutting technique

that was optimizing using a sheet paper (150 mm-diameter) for the production of 120 replicas. In a first step, twenty paper disks (3 mm-diameter) were first immersed into a buffer (3 mL, 0.5 M Na_2CO_3, pH 12) and, then, DVS (180 µL) was added. The mixture was shacked with a stirrer (250 rpm, 25 ºC, 12 h). The resulting **VS-paper** disks were washed with 1:1 ethanol/water and drying at room temperature. In a second step, the activated **VS-paper** disks were deposited into a phosphate buffer (1 mL, 10 mM, pH 7.4) containing **NH_2-CDs** (5 µL, $1.72x10^{-5}$ mg·mL^{-1}), and shacked with a stirrer (250 rpm, 25 ºC, 6 h). The resulting **CDs-paper** disks were washed with 1:1 ethanol/water and drying at room temperature. To block the unreacted free VS groups, the pieces of paper were shacked (10 min) with a mixture of ethanolamine (100 µL), and trimethylamine (20 µL) in water (3 mL). Finally, the papers were washed with 1:1 ethanol/water and dried under vacuum at room temperature and stored in a dry environment at 4 °C in the dark until use.

2.4.Preparation of CDs-I-paper

The **CDs-paper** disks were immersed into a solution of DCM (30 mL) containing IAA (3.72 mg·mL^{-1}), DCC (4.12 mg·mL^{-1}) and DIPEA (2.58 mg·mL^{-1}). The vessel with the mixture was covered with an aluminum foil to protect from the light and was orbital shook (6 h). After this time, the functionalization of the paper disks was estimated to be complete, and the resulting **CDs-I-paper** disks were washed with 1:1 ethanol/water and stored in a plastic box cover with aluminum foil to protect them from the light.

2.5.Image capture and processing

Cellulosic disks were imaged with a digital camera after reacting with standards or bioanalytes containing samples (Fig. ESM2). The optimized setting conditions used to photograph the devices were: ISO 1250, shutter speed 1/80 s, aperture value f/3.2 and focal length of 4 mm. The ISO parameter was investigated (Fig. ESM3) by increasing the fluorescence intensity from 400 to 4000 ISO because of the sensitivity of the camera increase. The imaging position of camera was also considered because of its effect on the imaging results, which should not be overlooked. Paper was placed under a UV lamp using a homemade accessory. This chamber has nine holes which let the fluorescence intensity of the paper through the box when we make a picture with a digital camera

avoiding that the light from the lamp interferes in the measurement (Fig. 1). The UV source was used at 365 nm wavelength and 220 W. For the analysis of **CDs-paper** the fluorescence intensities of the captured images were converted to grey scale using a new MATLAB function to obtain the region of interest (ROI) that contains the relevant analytical information in a circular area of 3.4 mm diameter. This MATLAB function has been developed to automatically detect the circular zones of the image, to establish a subarea of each detected circle containing the main pixels with relevant analytical information (this allows to discard the pixels of the edges and those corresponding to possible shadows of the image) and to calculate the grey scale of each circular subarea.

2.6.Analytical protocol

Biothiols determination were carried out, under the optimized conditions by using a **CDs-I-paper** disk or a µPAD device. For **CDs-I-paper,** the disk was immersed into a sample of the analyte (GSH, Cys or Hcy, 1 mL, 1:10 phosphate buffer, pH 7.4, 10 mM) under dark conditions and a nitrogen atmosphere for 30 min to ensure complete reaction. After this time, the disk paper was washed with Milli-Q water, dried under vacuum at room temperature, and the measurement performed as indicated in previous section. All of the measurements were performed at least three times and the standard deviation was plotted as the error bar. For the µPAD device, a solution (5 µL) of different concentrations of GSH, Cys or Hcy (ranging from 1-500 µM) was dropped onto the sampling area. After flowing of the solution by capillarity towards the **CDs-I-paper** disk the free iodine liberated in the reaction was removed after 30 min of reaction by washing with MilliQ water (3 x10 µL), and the measurement performed as indicated above. The procedure used for the detection of biothiols in human urine was the same as that described for standard solutions of GSH, Cys or Hcy.

3. Results and discussion

3.1.Paper selection for CDs immobilization

The selection of the paper substrate to be used was envisaged as the first step. According with the sensing functionality expected for the intended µPAD, the optimal material

selected should meet two criteria: a low fluorescence background and a homogeneous distribution of fluorescence in the detection area. With these requirements, a series of commercial quantitative filter papers of different filtration (6 types from 1 to 30 µm pore size, and an 80-100 $gr \cdot m^{-2}$ basis weight) and 3 types of Nylon membranes (1240, 1242, 1254, PC1, 1244, Whatman 1, Nytran SPC, Biodyne Plus, Biodyne C, respectively) were tested for their fluorescence properties (see Fig. ESM4). The data indicated that standard Whatman grade 1 filters show the lower fluorescence profile being selected as the optimal material for their engineering.

3.2.Fabrication of CDs-immobilized cellulose (CDs-paper)

The engineering of CDs-modified paper sensors requires CDs immobilization to the cellulose surface as one of the cornerstone steps to enable sensing applications. For this purpose, adsorption and covalent grafting are the most commonly used approaches. The adsorption of CDs on paper is mediated by the electrostatic and Van der Waals forces being a successful, simple and inexpensive methodology to functionalize cellulose. However, in preliminary studies carried out in this case for the immobilization of the CDs by adsorption on Whatman grade 1 standard paper do not give a good result, since the CDs are carried away by the aqueous solutions used, causing an irregular distribution of fluorescence. In Fig. ESM5 (A, B and C), we can see how as an aqueous sample passes through the paper with the CDs immobilized by adsorption, they are dragged in the direction of flow. This makes the fluorescence not homogeneous, causing a large experimental error in the measurements. However, the covalent immobilization of the CDs on the paper causes a uniform fluorescence when passing an aqueous sample through it, as shown in Figure ESM5 (D and E), which improves the reproducibility of the measurements.

Likewise, a fluorescence quenching study was carried out to check whether the covalently linked CDs continue to keep active the functional surface groups responsible for the fluorescence quenching. For this, Cu^{2+} was chosen whose ability to attenuate the fluorescence of CDs is well known [22] since the amino groups on the surface of CDs can bind Cu^{2+} ions to form amino complexes, which lead to a strong quenching of the fluorescence of the CDs by inner filter effect. It was observed that when passing a Cu^{2+}

solution through the derivatized paper there is a drastic reduction in fluorescence, but homogeneously throughout the paper (see Figure ESM5 F), which confirms the functionality of the paper.

Taking into account this finding, the covalent immobilization of CDs was envisaged as an alternative pathway. The chemical functionalization by covalent bonding provides better binding of CDs to the paper surface regardless of the major number of steps usually required and the plausible detrimental of the paper properties. Because of these drawbacks, the chemical conjugation approach of CDs has been scarcely used up to the present [23]–[25]. From the panoply of methodologies developed for the modification of cellulose in diverse scenarios, [7], [26] the synthetic strategies applied on the reported cases dealing with CDs combine the complementary reactivity of the abundant hydroxyl groups on cellulose with that of the surface functional groups of CDs (mainly carboxylates and amines). However, due to the inertness of the hydroxyl functions, a pre-activation step is required for the construction of cellulose-CDs covalent bridges. For CDs-modified cellulose oxidation of the hydroxyl groups for their transformation in more reactive carbonyl or carboxyl groups is the reported strategy that was followed by the formation of amide bridge with the CDs through common EDC/NHS reagents [23]–[25]. With this background, developing efficient methods for the covalent functionalization of CDs-cellulose composite materials is of utmost importance for engineering smart sensors.

In this context, the click-chemistry philosophy offers already unexplored possibilities for its implementation in the fabrication of novel CDs-modified cellulose materials. Owing to the remarkable attributes of simplicity, modularity, robustness and high conversion under mild reactions conditions, click chemistries have found significant utility in material science, including NP modification, [27] but a more limited application in the surface functionalization of cellulose. From the toolbox of click reactions, the prevalent Cu(I)-catalyzed azide-alkyne cycloadditions (CuAAC) and also thiol-ene reactions are the protocol most often employed for accessing clicked-cellulose materials [28], [29]. However, the introduction of the corresponding clickable groups, in both of the mentioned approaches, is a multi-step process that, despite the efficiency of the click assembly, discourages its application. Considering the bulk nature of cellulose paper and

in order to find simple click alternatives for its modification that also precludes any purification step, we envisaged the Michael-type addition of vinyl sulfone (VS), a less considered click reaction, as a valuable option to solve these problems because VS chemistry can perfectly combine the inherent functionality (hydroxyl for cellulose and amino for CDs) of the two assembling units.

With this background, we designed a reliable and straightforward one-pot two-step procedure for the fabrication of CDs-immobilized paper **CDs-paper**- (Scheme 1). For our purpose, divinylsulfone (DVS) is the reagent of choice as it can behave as a homobifunctional click reagent that will allow, first, its click oxa-Michael addition to the paper surface by reaction with the hydroxyl groups, and, later, the covalent grafting of the resulting reactive **VS-paper** to NH_2-functionalized CDs by means of a click aza-Michael addition. Among the broad panoply of aminated CDs described in the literature, NH_2-functionalized CDs were prepared following a reported hydrothermal synthesis (180 ºC, 10 h) that use citric acid (CA), as the carbon source, and the polyamine branched polyethylenimine 25kDa (25kPEI), as a N-doping agent and surface modifier [21]. The anchoring of the CDs to the surface of cellulose paper was, then, performed by a reliable and simple sequence of two steps: first, VS functionalization of disks papers -**VS-paper**- by immersion into a buffered (pH 12) DVS solution, and, then, covalent click conjugation of the NH_2-functionalized CDs by an additional immersion of the **VS-paper** into a buffered (pH 7.4) solution of the CDs. Covalent effectively improves the reproducibility of the reaction zone and the uniformity of fluorescence. Effectiveness of the immobilization was assessed by the quenching of the fluorescence mediated by Cu^{2+} [22] (Fig. ESM6) and by the physical characterization of the resulting **CDs-paper** (see below).

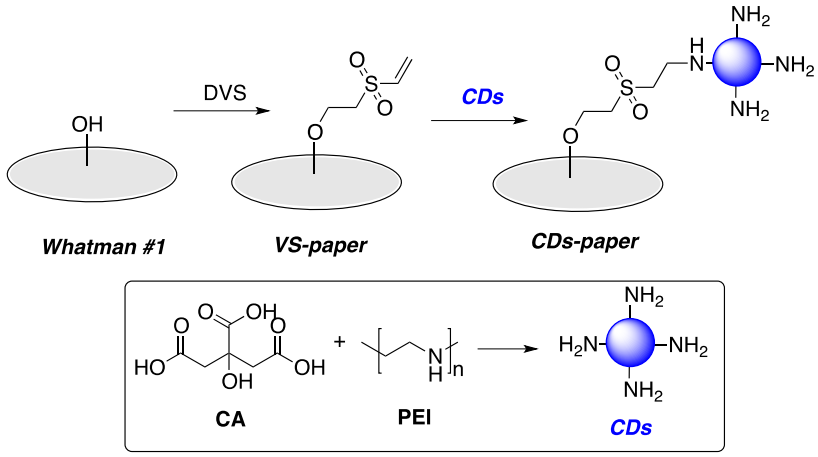

Scheme 1. VS-based click immobilization of CDs onto paper: Preparation of clicked **CDs-paper.**

3.3.Evaluation of the sensing capabilities of CDs-paper

To prove the sensing capabilities of the fabricated fluorogenic clicked **CDs-paper** in view to later engineering μPADs that use the immobilized CDs as signal reporters, the biothiols glutathione (GSH), cysteine (Cys), and homocysteine (Hcy) were chosen as bioanalytes of interest because they play an important role in cellular functions and maintaining the biological redox homeostasis. GSH is the most plentiful intracellular thiol and plays a vital role in maintaining biological homeostasis by acting as an essential endogenous redox regulator [30]. Abnormal level of cellular GSH is considered to be sign of many diseases, like liver damage, cancer, Alzheimer's and cardiovascular diseases. Deficiency of Cys is usually associated with leukocyte loss, hematopoiesis decrease, skin lesions etc. Furthermore, abnormal levels of Hcy can induce a risk factor for cardiovascular and Alzheimer's diseases [31], [32]. Although great efforts in fluorescent probes have been devoted to detect these biothiols selectively and efficiently in biological samples, the contributions based on CDs [33]–[35] or in paper-based analytical devices [36], [37]are limited. CDs-based biothiols sensors are usually fluorescence "off–on" devices that exploit a strategy based on the fluorescence quenching of the CDs by a sacrificial quencher (normally a metal ion: Au^{3+}, Ag^{+}, Cu^{2+}) and subsequent fluorescence revival by a reaction-based process with GSH, Cys or Hcy. However, in the context of our work the reported photochemical heavy-atom effect [38] exhibit by halogens (Cl, Br and I) that determines quenching of fluorescent probes (turn off) is a particularly appealing because of the easy halogen derivation of NH_2-functionalized CDs by reaction with monohalo-acetic acid. Later halogen nucleophilic displacement by a thiol-containing derivative

elicits a significant fluorescent increase (turn on), strategy that have been applied in the design of CDs fluorescence probes for the detection of biothiols [33]. On this basis, the **CDs-paper** was reacted with iodoacetic acid (IAA) being obtained the corresponding **CDs-I-paper** by a straightforward immersion protocol (Scheme 2). The absent of fluorescent emission observed (turn-off) for this halogen-modified material confirms the role of iodine as a quintessential fluorescence quencher confirming, furthermore, the chemical functionalization of the paper, in concordance with our expectative (see below). With the **CDs-I-paper** in hands, the recovery of the fluorescence intensity (turn-on) was evaluated and confirmed when the -SH group of GSH, Cys or Hcy causes nucleophilic substitution, and release of iodine anions.

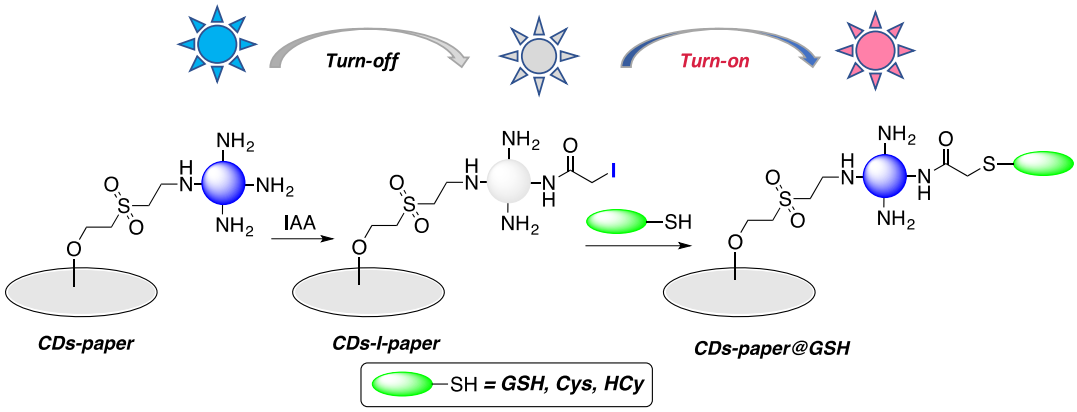

Scheme 2. Fabrication of fluorogenic off-on CDs-paper and its application in biosensing of biothiols (GSH, Cys, Hyc).

3.4.Characterization of CDs and functionalized papers

The CDs and the functionalized papers were characterized by means of techniques currently used in the characterization of CDs, namely, high-resolution transmission electron microscopy (HR-TEM), energy dispersive X-ray spectroscopy (EDX), and X-ray photoelectron spectroscopy (XPS). First, HR-TEM images of the CDs (Fig. ESM1A) were obtained to attain information about their size and morphology. The presence of lattice planes with an interplanar distance around 3.22 nm indicates a high crystallinity for the CDs. CDs size are distributed between 2-5 nm, with a 3 nm average particle size (Fig. ESM1B), and the NPs show a circular shape, in concordance with the literature [21]. Elemental analysis by energy dispersive X-ray spectroscopy (EDX) were next performed

to know the composition of CDs. The spectrum shows the presence of carbon, nitrogen, and oxygen atoms (Fig. ESM1C) and also a peak corresponding to uranium atoms, because of the use of uranyl acetate for the dye of CDs to improve their contrast for HRTEM analysis. Furthermore, the elemental composition of the CDs was also performed by XPS surface analysis. The results indicated the presence of carbon, oxygen and nitrogen in the CDs surface.

To attain information about the successful covalent click immobilization of CDs in cellulose paper, their iodine derivatization and their reactivity with biothiols, the surface of the corresponding paper disks was also characterized. To this aim, unmodified cellulose Whatman grade 1 paper was first characterized by XPS (Fig. ESM7). As expected, the obtained data for the elemental composition merely indicate the presence of carbon and oxygen atoms. After DVS treatment, the resulting **VS-paper** exhibit a typical doublet S_{2p} peak (168.0 eV) which is attributed to the sulfone group. In addition, the atomic quantification shows 8.25% S atoms corroborating the successful VS functionalization of the cellulose fibers (Fig. ESM7A). After VS-click immobilization of CDs, the XPS spectrum of **CDs-paper** show a predominant N_{1s} peak (400 eV), indicative also of the successful covalent anchoring of CDs (Fig. ESM7B). For the **CDs-I-paper** obtained after reaction with IAA, a I_{3d} peak (620 eV) confirms the incorporation of I atoms onto the cellulose with a 0.64% value. (Fig. ESM7C). After reaction of this I-functionalized cellulose with GSH for its determination, an 4.89% increase of S atom was quantified, data that confirms the substitution of iodine by the sulfur atom of the thiol group of GSH (Fig. ESM7D). The spatial distribution and compositional zonation of chemical elements in the samples of the different functionalized-papers was also elucidated by an element mapping performed by energy-dispersive X-ray spectroscopy (EDS) (Fig. ESM8). For **VS-paper**, the main constituents are C, O, and S and the mapping show a uniform distribution of S atoms on the paper surface (Fig. ESM8A). In addition, the elemental mapping for the **CDs-I-paper** reveals iodo signals after the IAA treatment surface (Fig. ESM8B).

Finally, fluorescence emission of **CDs-paper** and **CDs-I-paper** was evaluated (Fig. ESM9). In the first case, for a 330 nm wavelength excitation, the fluorescence spectrum

of **CDs-paper** shows a peak with a maximum emission wavelength of 450 nm. By the contrary, this peak disappears for **CDs-I-paper** after functionalization of the CDs by IAA.

3.5.Fabrication of the µPAD

The different zones that make up the device were designed using Illustrator software (Adobe Systems) and the design exported as a FS file to the controller software of 12W CO2 laser source. For the production, a paper sheet and adsorbent pad were affixed at the base of the laser printer using tape to prevent tearing, and both were cut with a single pass of laser beam. The different paper areas of the µPAD were produced in 120 replicates by cutting the cellulose paper (150 mm diameter). After cutting, the paper areas were washed with 1:1 ethanol/water and drying at room temperature until use it. For fabrication of µPAD, the different zones were aligned, assembled together and laminated with thermoplastic material (30 µ biaxially oriented polypropylene 30 film) with a clothes iron leaving a hole for sampling. The applied temperature of the clothes iron was 160 ºC for 2 minutes. After that, the plastic layers were sticked. Lamination improves the robustness of the paper device and also protects biothiols from atmospheric oxygen oxidation. The viability of the design is validated by a 95% rate of success.

(a) **(b)**

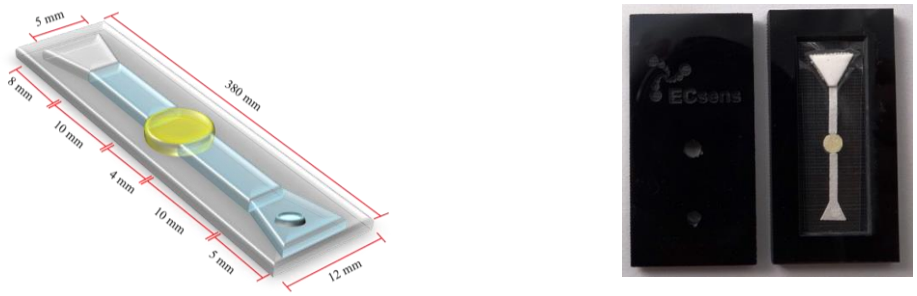

Figure 13. Microfluidic paper-based analytical device for biothiols. (a) Drawing of the µPAD indicating dimensions. (b) Picture of the µPAD for biothiols determination inside of a homemade accessory.

3.6.Optimization of method

To adjust the reactions and processes in order to ensure perfect performance of the µPAD device for the evaluation of biothiols, different variables involved in the engineered steps

were studied and optimized by using GSH: (a) paper substrate; (b) concentration of reagents; (c) pH; (d) reaction time of the two last reactive steps (iodine derivatization of immobilized CDs and reaction with GSH). Respective data and figures are given in the Electronic Supplementary Material. The following experimental conditions were found to give the best results: (a) Whatman 1 paper substrate; (b) $1.72x10^{-6}$ mg·mL^{-1} was chosen as the optimal CDs concentration and the 120 mM concentration was selected as optimal for IAA; (c) The results indicate the value of pH 7.4 as optimal for further experiments; (d) for the iodine displacement by GSH the reaction is complete in shorter reaction times of 30 min, as deduced for the observed invariability of the fluorescence after this time, which indicated complete assembly of the GSH to the NPs.

3.7.Analytical characterization of µPAD for biothiols assay

As mentioned, the fluorescence intensity of **CDs-I-paper** is recovered (turn-on) when the biothiols cause nucleophilic substitution and release of iodine anions. The increase of fluorescence can be quantified by correlating the grey intensity of the paper with the concentration of biothiols present in the sample (Fig. 2A). This determination was performed following the described analytical protocol and by taking a photography of the µPAD after the reaction with the different biothiols using a digital camera and a homemade accessory under UV lamp (wavelength of excitation = 365 nm) (Fig. 1B). The data show that the fluorescence intensity and the concentration of the biothiols exhibit a linearized logarithmic dependence according with the equation I = a·log[biothiol]+b (Fig. 2B) where a is the intercept and b is the slope. The fluorescence intensity of the blank was subtracted for each of the concentrations studied.

The analytical performance characteristics of the µPAD are included in Table 1. A calibration plot (12 standards with 3 replicates obtained with a new device each time) was performed to obtain the calibration function. The LOD was calculate using the standard criteria LOD = 3σ/slope where σ is the standard deviation of the blank, and respectively with the same criteria the quantification limit was 10σ/slope, which was calculated from 18 blanks. The limit of detection (LOD) of the device was then calculated for each biothiol (0.3 µM, 0.3 µM and 0.4 µM for GSH, Cys and Hcy, respectively) by a relative standard deviation (3.43%) of the blanks (n=18). Furthermore, the quantification limit

(LOQ) was calculated for each biothiol being obtained values (0.9 µM, 1.2 µM and 1.3 µM for GSH, Cys and Hcy, respectively) that are in the range of the normal values observed for biothiols in biological fluids. Thus, the normal level of GSH, Cys and Hcys in serum are lower than 5.8 µM, 287 µM and 12 µM, respectively (Blood levels of homocysteine, cysteine, glutathione, folic acid, and vitamin B12 in the acute phase of atherothrombotic stroke [39]. The repeatability (RSD), obtained using 18 different µPAD working at 200 µM GSH, is 5.4%, an acceptable precision considering the measuring system used. The lifetime of the device was also studied for 28 days by keeping a set of µPAD at room temperature in dark using a desiccator, and regularly checking their response to a 100 µM GSH concentration. The fluorescence intensity observed was constant during the studied period.

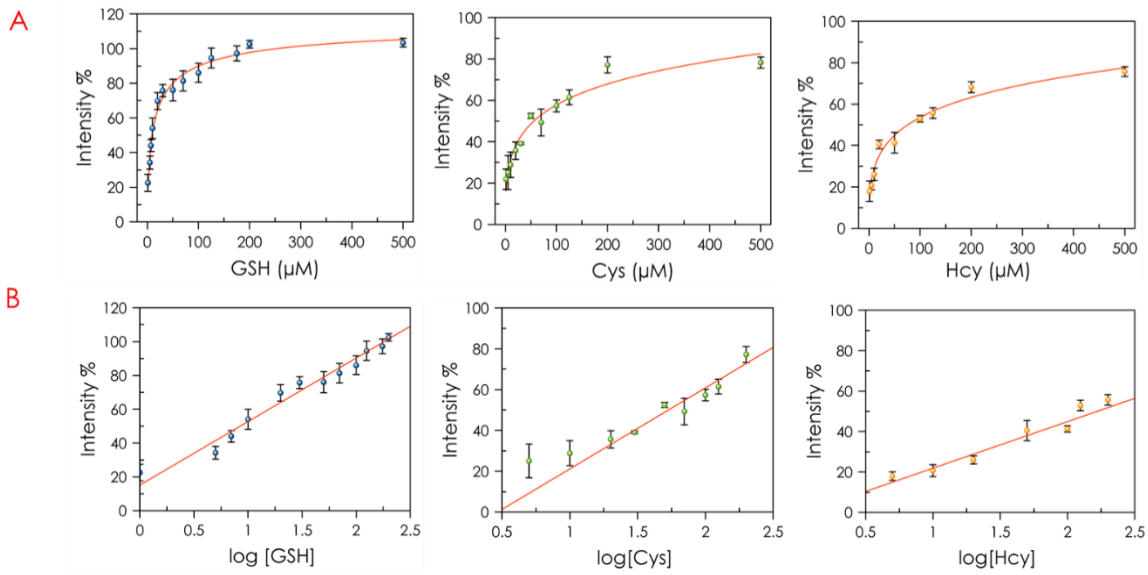

Figure 14. (A) Dependence of the intensity of the fluorescence with the biothiols concentration. (B) Linearization of calibration functions for biothiols. Data points are the mean of 3 assays. Conditions: paper disk with 1.72×10^{-6} mg·mL^{-1} of immobilized CDs and functionalized with 120 mM of IAA; 5 µL phosphate buffer pH 7.4 10 mM; 5 µL of sample (GSH, Cys or Hcys); reaction time 30 min.

Table 9. Analytical characteristics of µPAD for GSH, Cys and Hcy determination.

Analytical parameter	Value		
	GSH	**Cys**	**Hcy**
Measurement range (µM)	1-200	5-200	5-200
Slope (a)	35.8	39.7	23.0
Intercept (b)	29.3	18.5	1.14
LOD (µM)	0.3	0.3	0.4
LOQ (µM)	0.9	1.2	1.3

A comparison of the response of standards including a sole biothiol (5 µM Cys, Hcy and GSH) shows that Cys and Hcy induces modest fluorescence changes but lower than GSH for reasons that are unclear (Fig. 3). Results are consistent with those observed by Wu [40]. Experiments between GSH in the presence of Cys and/or Hcy, by using solutions containing equal concentration (5 µM) of each biothiol, indicate that the fluorescent response of **CDs-I paper** is almost additive reflecting the individual contribution of each biothiol. On this basis, µPADs based on **CDs-I paper** are appropriate for the evaluation of the total concentration of biothiols present in a sample. However, the concentration of biothiols varies significantly among different biological fluids (whole blood, plasma, urine) where the prevalence of a specific biothiol over the others is observed (GSH in blood, Cys in plasma and urine). This fact determines that the total concentration in each biological is influenced mainly by the predominant biothiol, anyway this assay can be useful the determine the global content as an index of biothiols presents.

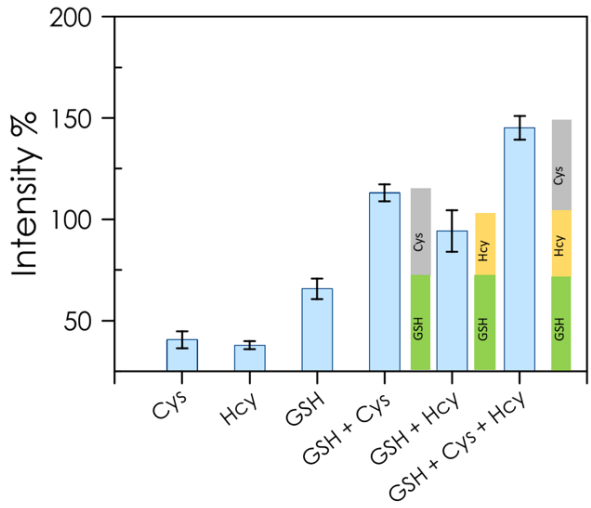

Figure 15. Comparison of the response of 5 µM Cys, Hcy and GSH, 5 µM GSH in the presence of 5 µM Cys, 5 µM of GSH in presence of 5 µM Hcy and 5 µM GSH en 5 µM Cys and Hcy. Coloured bar indicates theoretical values for the binary and tertiary systems obtained from the individual contribution of each biothiol according to the calibration function. Data points are the mean of 3 assays. Conditions: paper disk with 1.72×10^{-6} mg·mL^{-1} of immobilized CDs and functionalized with 120 mM of IAA; 5 µL phosphate buffer pH 7.4 10 mM; 5 µL of sample; reaction time 30 min.

A comparison of different reported methods to detect and quantify biothiols with the new method reported herein is presented in Table 2. The fluorescent systems collected in the Table shown attractive sensitivity, but they also exhibited some disadvantages. For example, g-C_3N_4-Ag^+ method present a good detection limit for GSH, Cys and Hcy and their detection in real samples is possible but the synthesis of reagent is difficult and the reaction time is longer than others [41]. On the other hand, PEI-AgNCs present a worse detection limit for GSH determination compared with others and the determination of Cys and Hcy present interference [42]. CdTe QDs-Hg^{2+} method exhibit a good linear range and detection limit for GSH, the reaction time is shorter than others but this methodology is designed only for cell [43]. In addition, some of the assays collected required in the use of Hg^{2+} for the construction of the sensor, which is harmful and should be avoided in routine analysis. While, the most important feature of the new sensing strategy developed is a good sensitivity for determination of GSH, Cys, and Hcy, a wide range and the reaction time than is shorter than other methods.

Table 2. Comparison between some selected assays for biothiols determination.

Material	GSH		Cys		Hcy		Reaction time (min)	Application	Ref.
	LR (µM)	LOD (µM)	LR (µM)	LOD (µM)	LR (µM)	LOD (µM)			
g-C_3N_4-Ag^+	0.02-100	0.0081	0.02-100	0.0064	0.02-100	0.0096	45	Urine	[41]
PEI-AgNCs	0.5-6	0.38	0.1-10	0.042	0.1-10	0.047	30	Plasma	[42]
CDs/Hg^{2+}	0.5-10	0.008	0.5-10	0.0076	0.5-10	0.0069	12	Plasma	[3]
Mu-Hg^{2+}	0.1-40	0.01	0.5-30	0.02	0.5-50	0.04	5	Urine	[44]
Hg^{2+}-Au^+	0-0.25	0.0094	0-0.25	0.0083	0-0.25	0.0149	15	Serum	[45]
CdTe QDs-Hg^{2+}	0.6-20	0.1	2.0-20	0.6	-	-	5	Cell	[43]
CDs-I	1-200	0.3	5-200	0.3	5-200	0.4	30	Urine	This work

LR = Linear range, LOD = Limit of detection

3.8. Interferences

The effect of different compounds commonly present in urine (Ser, His, Arg, Asn, Gal, and Man) for their plausible interference in the detection of biothiols was next evaluated. The data (Fig. 4) shows that the **CDs-I-paper** exhibited good properties as highly selective probe for biothiols over other amino acids (in Figure 4 red line indicate the maximum blank signal in this experiment), demonstrating their suitable application for the analysis of biothiols.

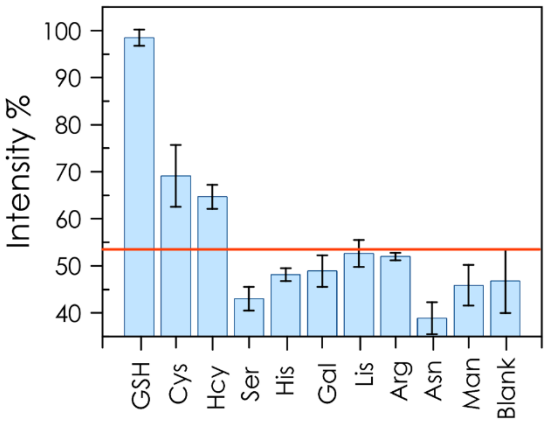

Figure 4. Response of GSH, Cys and Hcy and interferences (100 µM). Data points are the mean of 3 assays. Conditions: paper disk with $1.72x10^{-6}$ mg·mL^{-1} of immobilized CDs and functionalized with 120 mM of IAA; 5 µL phosphate buffer pH 7.4 10 mM; 5 µL of interferent; reaction time 30 min.

3.9. Analysis of real samples

To evaluate the feasibility of the µPADs in the analysis of a real biological sample, **CDs-I-paper** was applied to determinate biothiols in urine. The samples analyzed were collected from anonymous healthy volunteers. All the samples were filtered by a 0.22 µm pore diameter filter then, the samples were diluted 1:10 with phosphate buffer (pH 7.4, 10 mM). The recovery experiment was carried out by spiking after dilution with 30 and 60 µM of standard GSH in the urine samples values that are in order of normal concentrations [46]. The recoveries obtained are in the range of 98.6 - 111.5% and 100.2 -112.0%, respectively. The results demonstrate that the method proposed in this work can be used for determination of biothiols in real samples (Table 3).

Table 3. Recovery study for GSH in urine samples.

Sample	Concentration of GSH, µM		Recovery, %
	Amount added	Amount found*	
Urine 1	30	29.8 ± 2.1	98.6
Urine 2		31.9 ± 2.8	106.4
Urine 3		33.9 ± 4.1	111.5
Urine 4		33.5 ± 1.7	110.6
Urine 1	60	60.5 ± 1.4	100.2
Urine 2		61.2 ± 2.7	102.0
Urine 3		67.4 ± 2.4	112.0
Urine 4		63.6 ± 4.2	105.0

*Data points are the mean of 3 assays.

4. Conclusions

In the present work, we have successfully engineered a novel, inexpensive and highly robust µPAD that behaves as a fluorescent sensing system for the determination of biothiols such as GSH, Cys and Hcy. The device is based on the use of CDs as signal reporters that have been covalently immobilized on paper by VS click chemistry. The sensing is operative by turning off the intrinsic fluorescence of the CDs by exploiting the heavy-atom effect of their iodo derivative and the ulterior turning on by the displacement of this halogen by reaction with GSH, Cys or Hcy. The resulting increase of the

fluorescence correlates accurately with the concentration of the different biothiols in samples. The device allows the rapid screening of biothiols by the use of a UV lamp and a digital camera, avoiding specific instrumentation. Our results are useful for the rational design of fluorescent CD-based μPAD. In summary, the device shows great promise as a potent tool for clinical diagnosis and therapy related to GSH, Cys and Hcy.

5. Electronic supplementary material

5.1. Synthesis of NH_2-CDs

In brief, a mixture of CA (1.0 g) and 25k PEI (0.5 g) in Milli-Q water (5 mL) was heated (180 ºC, 10 h) in a Teflon-lined stainless steel bomb. After heating, the solution was cooled to room temperature and the crude product was subjected to dialysis (MW=3.5 KDa) to obtain the CDs. Physical characterization of CDs by HRTEM (Fig. ESM1) was in concordance with the reported data in literature.[19]

5.2. Characterization of CDs

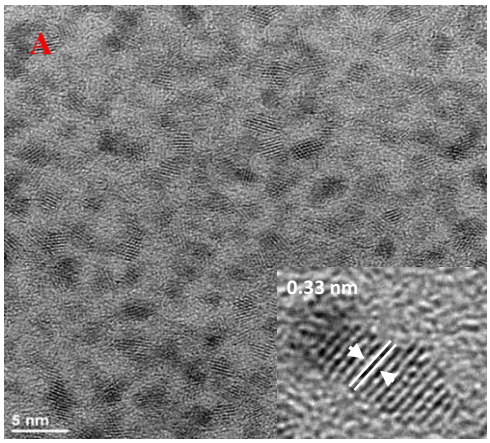

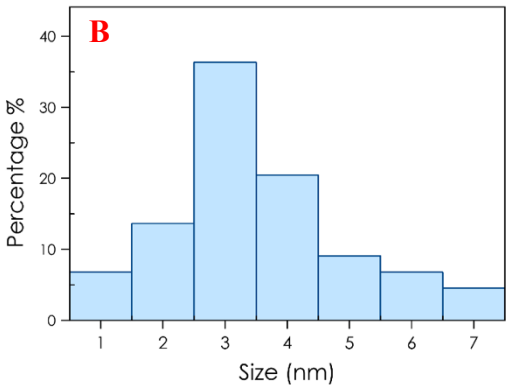

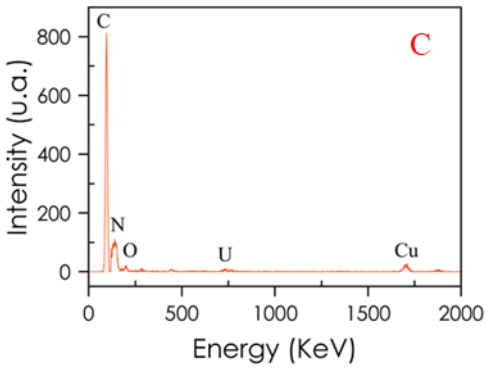

Fig ESM 1. Characterization of the CDs by HRTEM. A) HR-TEM image, B) Size distribution for CDs and C) EDX spectrum.

5.3. Schematic representation of the fluorescence measurement

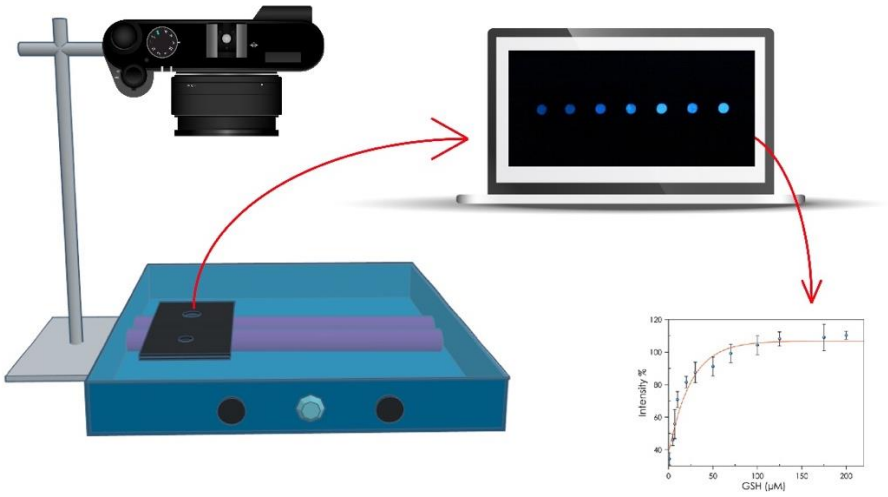

Fig ESM 2. The measurement system consists of a digital camera located at a distance of 10 cm from the UV transilluminator. The µPAD is placed inside the homemade accessory in the UV transilluminator. The captured images were converted to grayscale using a MATLAB script to obtain the region of interest (ROI) and with them the calibration function was calculated.

5.4. Optimization of ISO for digital camera

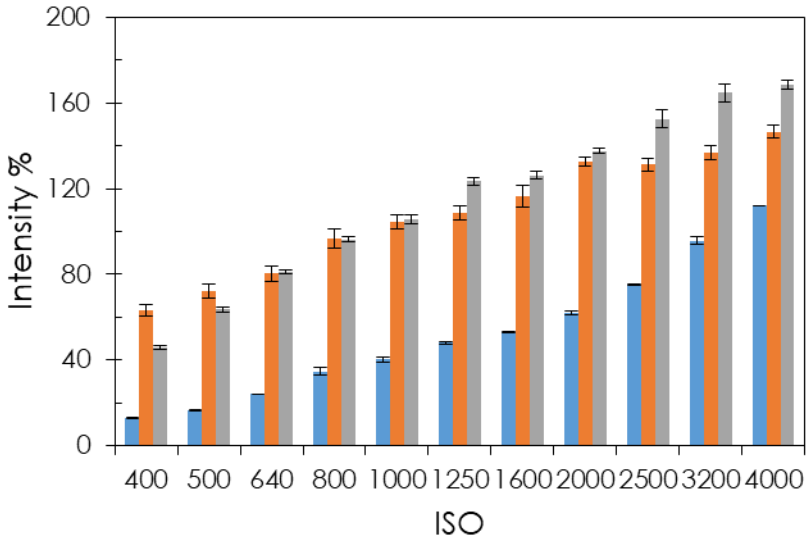

Fig ESM 3. Optimization of ISO for digital camera. Blue bars: CDs-I.-paper; orange bars: GSH 250 µM; gray bars: GSH 750 µM. The paper circles were put in a homemade accessory on the UV transilluminator and a picture was taken. The intensity of the papers was obtained using ISO ranging between 400–4000. Data points are the mean of 3 assays. Conditions: paper disk with 1.72×10^{-6} mg·mL^{-1} of immobilized CDs and functionalized with 120 mM of IAA; paper disks were buffered with phosphate buffer pH 7.4 10 mM, after that were dipped in GSH solutions; reaction time 30 min; λ_{exc}= 365 nm.

5.5. Selection of the substrate for immobilizing of CDS

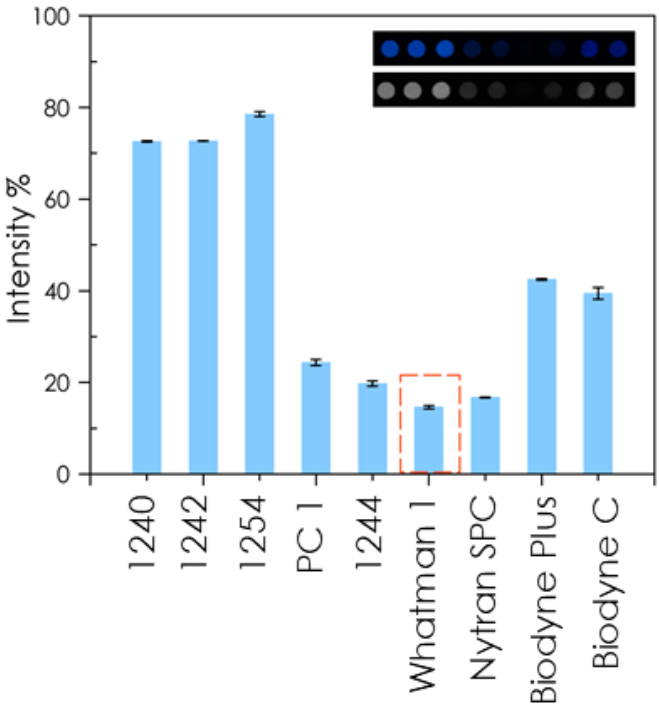

Fig ESM 4. Fluorescence profile of different commercial filter papers and nylon membranes: 1240, 1242, 1254, 1244, Whatman 1, PC1, Nytran SPC, Biodyne Plus, Biodyne C. Disks were placed in a homemade accessory, illuminated with a 365 nm wavelength UV lamp transilluminator and imaged with a digital camera (ISO 1250, shutter speed 1/80 s, aperture value f/3.2 and focal length of 4 mm). Inset: Image of the fluorescence emitted by the different substrates studied and the image in gray scale. Data points are the mean of 3 assays for each type of paper or nylon membranes.

5.6. Evaluation of the CDS immobilization methodology

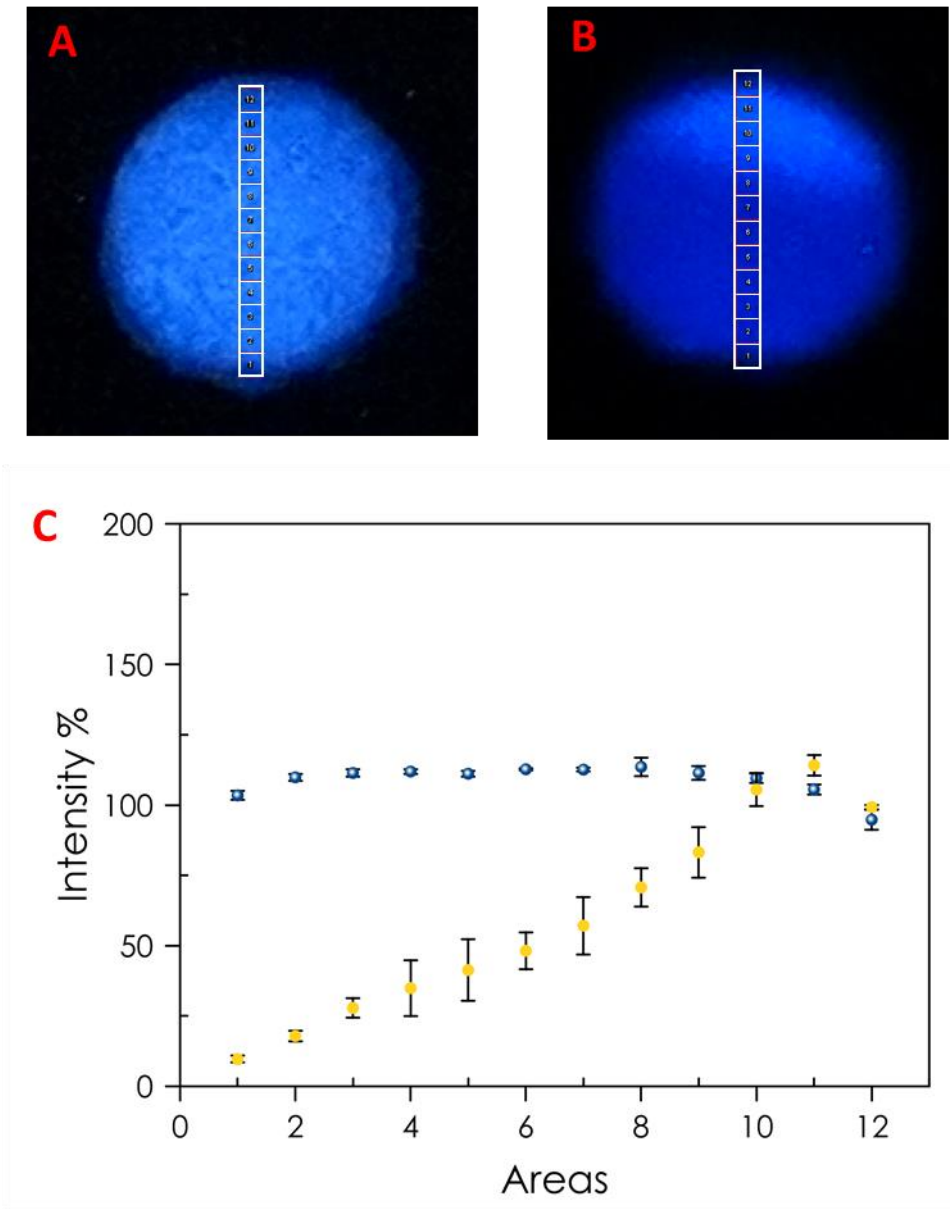

Fig ESM 5. Evaluation of immobilization methodology by Cu^{2+} quenching. A) Physical adsorption of CDs: Fluorescence intensity of a disk paper with CDs. B) Maintenance of fluorescence intensity after treatment of a disk paper with water C) Graphical comparative of fluorescence intensity along the diameter of paper disk prior (blue dots) and after (yellow dots) the treatment with water.

5.7. Evolution of immobilization methodology

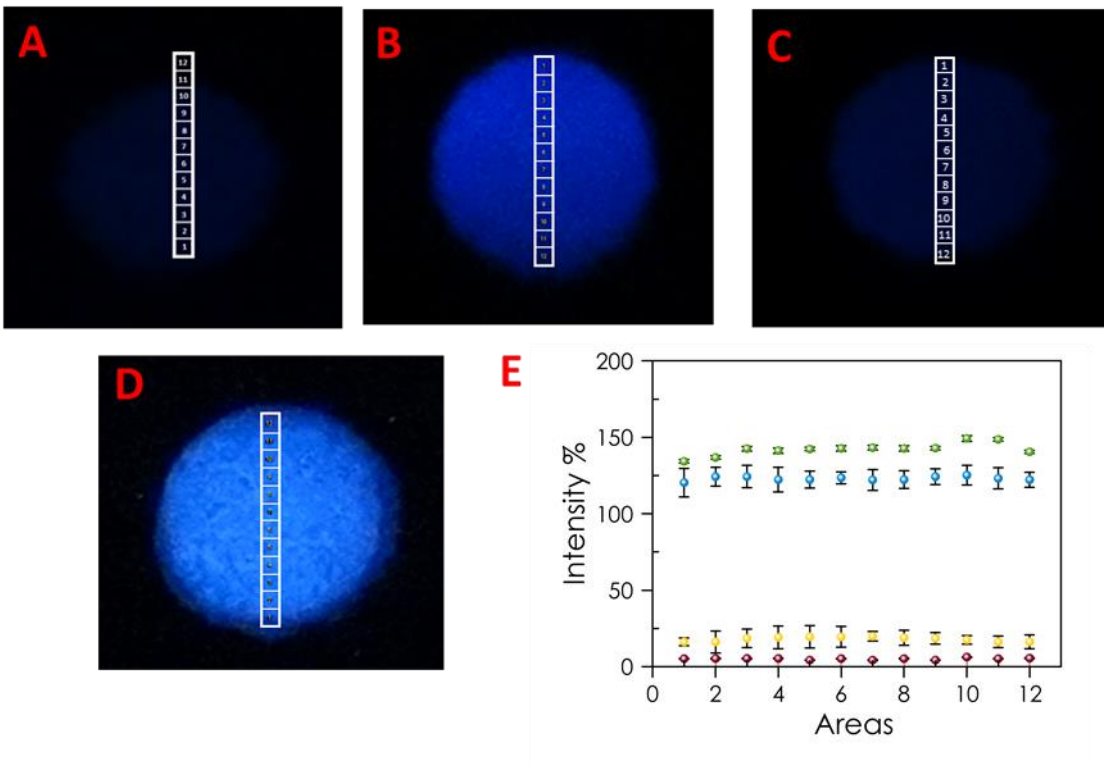

Fig ESM 6. Evaluation of immobilization methodology. A Fluorescence intensity of a disk paper. B Fluorescence intensity of a disk paper with CDs immobilized. C Maintenance of fluorescence intensity after treatment of a disk paper with a IAA. D Fluorescence intensity of a disk paper after GSH reaction. E Graphical comparative of fluoresce intensity for a disk paper (red dots) CDs-paper (green dots), CDs-I-paper (yellow dots) and CDs-paper@GSH (blue dots) with a 500 µM GSH solution.

5.8. XPS composition data

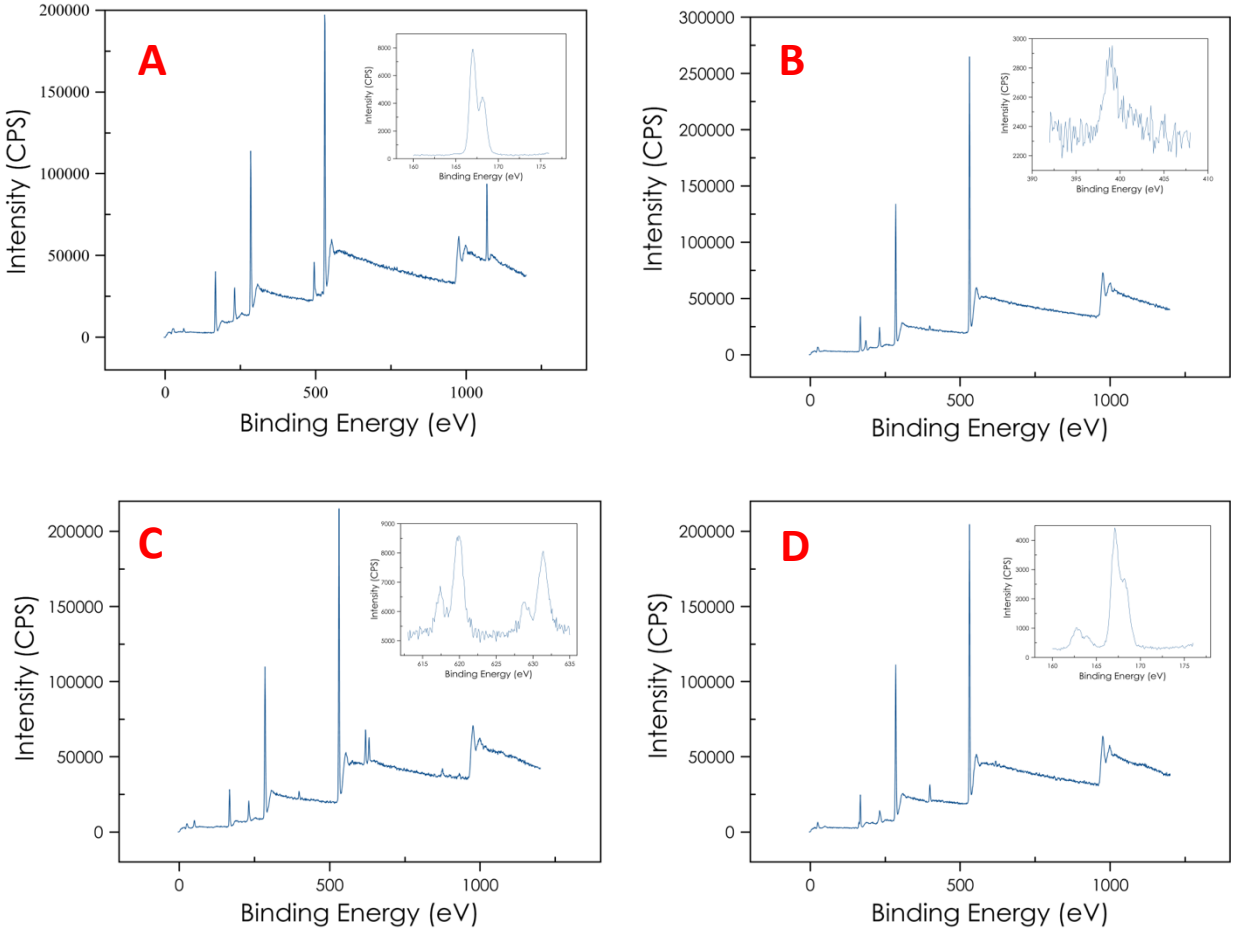

Fig ESM 7. XPS spectra. A) VS-paper, Inset: high resolution S_{2p} peak: 168 eV; B) CDs-paper, Inset: high resolution N_{1s} peak: 400 eV. C) CDs-I-paper, Inset: high resolution I_{3d} peak: 620 and 635 eV. D) CDs-I-paper@GSH; Inset: high resolution S_{2p} peak:165 eV.

5.9.Elemental mapping scanning transmission electron microscopy

A

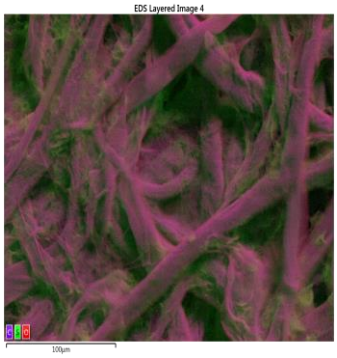

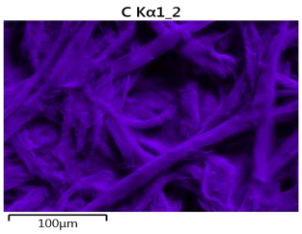

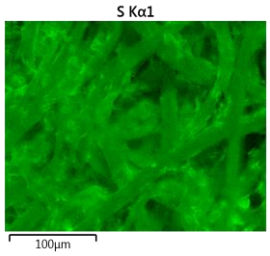

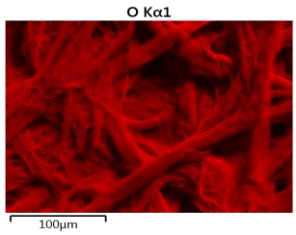

B

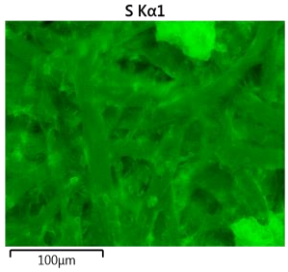

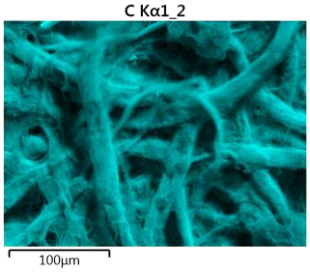

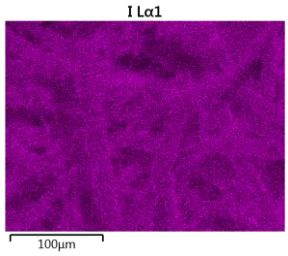

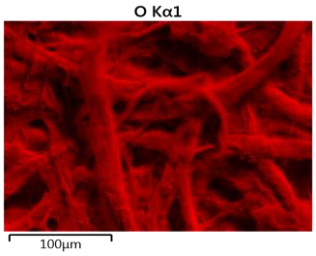

C

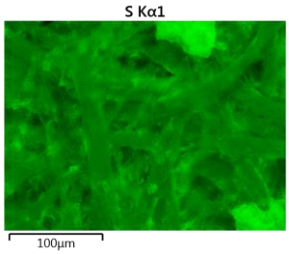

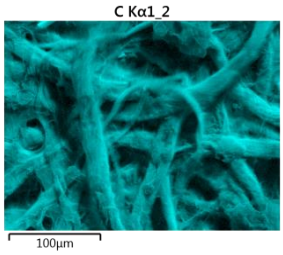

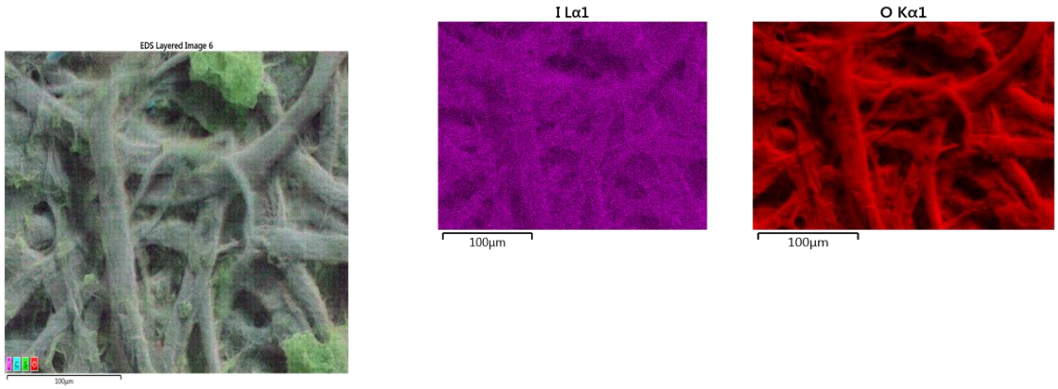

Fig ESM 8. Elemental mapping by scanning transmission electron microscopy. A) VS-paper; B) CDs-I-paper; C) CDs-I-paper after GSH reaction.

5.10. Fluorescence emission spectrum of CDs-paper versus CDs-I-paper

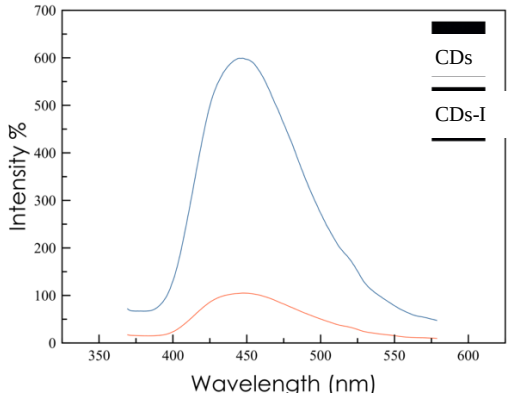

Fig ESM 9. Fluorescence emission spectrum of CDs-paper and CDs-I-paper using an excitation wavelength of 330 nm. Inset: Images of CDs-paper and CDs-I-paper.

5.11. Optimization of the methodology

To adjust the reactions and processes in order to ensure perfect performance of the µPAD device for the GSH determination, different variables involved in the engineered steps were studied and optimized. Concentration of reagents, pH, and reaction times of the two last reactive steps (iodine derivatization of immobilized CDs and reaction with GSH) were analyzed (Fig. ESM10). In a first instance, different concentrations (ranging from $1.72x10^{-6}$ to $8.6x10^{-5}$ mg·mL^{-1}) of the CDs solution used in the click immobilization step with **VS-paper** were assayed. For these experiments, a fluorescence intensity increase was observed for the **CDs-paper** in parallel with the augmentation of the concentration

of CDs in the range $1.72x10^{-6}$-$1.72x10^{-5}$ mg·mL^{-1} while for higher NPs concentrations the intensity remained constant (Fig. ESM10A). On this basis, the value of $1.72x10^{-6}$ mg·mL^{-1} was chosen as the optimal CDs concentration. Next, the IAA concentration used for the iodine functionalization of immobilized CDs was studied. Concentrations ranging from 20 to 140 mM were assayed. From the obtained data for the resulting **CDs-I-paper** (Fig. ESM10B), the 120 mM concentration was selected as optimal because of the significant decrease of the fluorescence intensity observed for this value. The effect of pH on the fluorescence intensity of **CDs-I-paper** prior and after GSH coupling was another parameter investigated (Fig. ESM10C). The results indicate an increasing and stable effect for the fluorescence in the 7.0-8.0 pH range being adopted the value of pH 7.4 as optimal for further experiments. Finally, the reaction times required were studied for their optimization. It was found that, for the iodine functionalization of CDs by reaction with IAA, a reaction time of 6 h is required to complete the derivatization (Fig. ESM10D). However, for the iodine displacement by GSH the reaction is complete in shorter reaction times of 30 min, as deduced for the observed invariability of the fluorescence after this time, which indicated complete assembly of the GSH to the NPs (Fig. ESM10E).

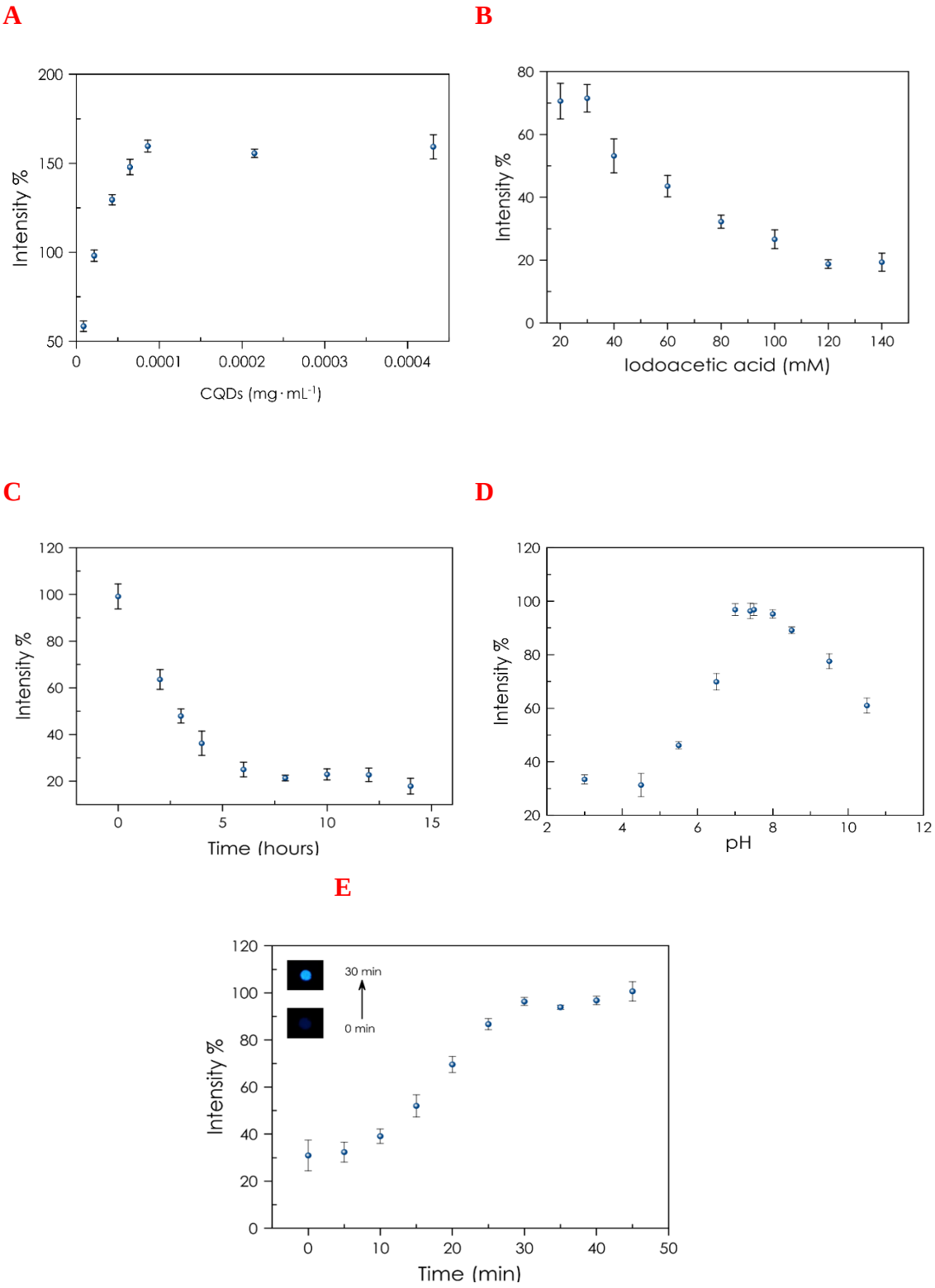

Fig ESM 10. Optimization of parameters: A) [CDs]: twenty disks of VS-paper, PBS buffer (1 mL, pH 7.4, 10 mM) and different concentrations of CDs 0.008 mg·mL^{-1}; B) [IAA]: twenty disks of CDs-paper, (30 mL); DCC (4.12 mg), DIPEA (2.58 mg) and different concentrations of IAA; C) pH. Conditions: disk of CDs-paper, IAA (120 mM) and GSH (500 µM); D) Reaction time for fabrication of CDs-I-paper: disk of CDs-paper and IAA (120 mM); E) Reaction time for conjugation of GSH: CDs-paper, IAA (120 mM), GSH (500 µM), PBS buffer (pH 7.4, 10 mM). All parameters were evaluated with a digital camera at ISO 1250.

5.12. Optimization of GSH determination by the 3D µPAD

In order to increase the intensity of the fluorescence signal emitted by the CDs immobilized on the paper disk after reaction with GSH, the free iodine generated on the detection area of the µPAD need to be removed through the adsorbent pad by using MilliQ water (10 µL). As shows the Fig. ESM11, three washes are optimal to obtain 100% of the signal after reaction with GSH. The experimental results indicate that more than three washing steps produce a decreasing of fluorescence intensity because the iodine free accumulate in the adsorbent pad was moved to the detection area again.

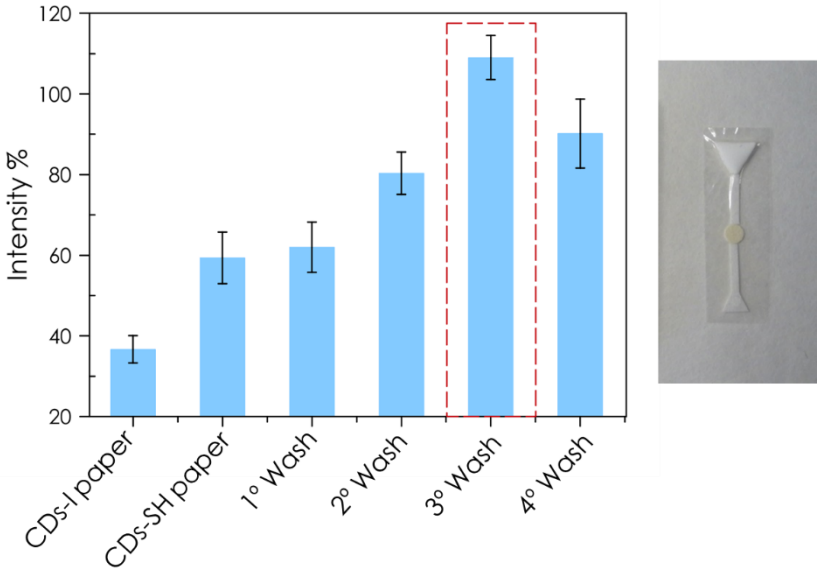

Fig esm 11. optimization of the washing steps for biothiol determination by the µpad. three µpads were used to know the influence of washing steps in the fluorescence intensity of cds-i paper. 5 µl of gsh solution 500 µm were added in the sampling area of the µpad. after 30 min reaction of reaction under nitrogen atmosphere 10 µl of milliq water was added in the sampling area of the µpads. the procedure was repeated three times. the washing steps influences were evaluated taking a picture of the µpads with digital camera working at iso 1250.

REFERENCES

[1] L.-M. Fu and Y.-N. Wang, "Detection methods and applications of microfluidic paper-based analytical devices," *TrAC Trends Anal. Chem.*, vol. 107, pp. 196–211, Oct. 2018.

[2] S. Ge, L. Zhang, Y. Zhang, F. Lan, M. Yan, and J. Yu, "Nanomaterials-modified cellulose paper as a platform for biosensing applications," *Nanoscale*, vol. 9, no. 13, pp. 4366–4382, 2017.

[3] J. Y. Liang, L. Han, S. G. Liu, Y. J. Ju, N. B. Li, and H. Q. Luo, "Carbon dots-based fluorescent turn off/on sensor for highly selective and sensitive detection of Hg2+ and biothiols," *Spectrochim. Acta Part A Mol. Biomol. Spectrosc.*, vol. 222, p. 117260, Nov. 2019.

[4] F. Yuan, S. Li, Z. Fan, X. Meng, L. Fan, and S. Yang, "Shining carbon dots: Synthesis and biomedical and optoelectronic applications," *Nano Today*, vol. 11, no. 5, pp. 565–586, Oct. 2016.

[5] Y. Song *et al.*, "Recent Progress in Microfluidics-Based Biosensing," *Anal. Chem.*, vol. 91, Nov. 2018.

[6] M. Farré, L. Kantiani, and D. Barceló, "Microfluidic Devices," in *Chemical Analysis of Food: Techniques and Applications*, Elsevier, 2012, pp. 177–217.

[7] S. Keshipour and A. Maleki, "Modification of Cellulose," 2019, pp. 435–486.

[8] Y. Xia, J. Si, and Z. Li, "Fabrication techniques for microfluidic paper-based analytical devices and their applications for biological testing: A review.," *Biosens. Bioelectron.*, vol. 77, pp. 774–789, Mar. 2016.

[9] A. M. López-Marzo and A. Merkoçi, "Paper-based sensors and assays: a success of the engineering design and the convergence of knowledge areas," *Lab Chip*, vol. 16, no. 17, pp. 3150–3176, 2016.

[10] Y. Yang, E. Noviana, M. P. Nguyen, B. J. Geiss, D. S. Dandy, and C. S. Henry, "Paper-Based Microfluidic Devices: Emerging Themes and Applications," *Anal. Chem.*, vol. 89, no. 1, pp. 71–91, Jan. 2017.

[11] C. S. Kosack, A.-L. Page, and P. R. Klatser, "A guide to aid the selection of

diagnostic tests," *Bull. World Health Organ.*, vol. 95, no. 9, pp. 639–645, Sep. 2017.

[12] L. Hu, Jie Wang, ShuQi Wang, B. Li, Fei Pingguan-Murphy, and F. Lu, Tian Jian Xu, "Advances in paper-based point-of-care diagnostics," *Biosens. Bioelectron.*, vol. 54, pp. 585–597, 2014.

[13] S. NISHAT, F. R. AWAN, and S. Z. BAJWA, "Nanoparticle-based Point of Care Immunoassays for in vitro Biomedical Diagnostics," *Anal. Sci.*, vol. 35, no. 2, pp. 123–131, Feb. 2019.

[14] A. M. López-Marzo and A. Merkoçi, "Paper-based sensors and assays: a success of the engineering design and the convergence of knowledge areas," *Lab Chip*, vol. 16, no. 17, pp. 3150–3176, 2016.

[15] S. Y. Lim, W. Shen, and Z. Gao, "Carbon quantum dots and their applications," *Chem. Soc. Rev.*, vol. 44, no. 1, pp. 362–381, 2015.

[16] J. Zhang and S.-H. Yu, "Carbon dots: large-scale synthesis, sensing and bioimaging," *Mater. Today*, vol. 19, no. 7, pp. 382–393, Sep. 2016.

[17] L. Liang, F. Lan, X. Yin, S. Ge, J. Yu, and M. Yan, "Metal-enhanced fluorescence/visual bimodal platform for multiplexed ultrasensitive detection of microRNA with reusable paper analytical devices," *Biosens. Bioelectron.*, vol. 95, pp. 181–188, Sep. 2017.

[18] S.-W. Hu, S. Qiao, B.-Y. Xu, X. Peng, J.-J. Xu, and H.-Y. Chen, "Dual-Functional Carbon Dots Pattern on Paper Chips for Fe 3+ and Ferritin Analysis in Whole Blood," *Anal. Chem.*, vol. 89, no. 3, pp. 2131–2137, Feb. 2017.

[19] C. He, Chao Ji, Haifeng Qian, Yihui Wang, Qian Liu, Xiaoling Zhao, Weifeng Zhao, "Heparin-based and heparin-inspired hydrogels: size-effect, gelation and biomedical applications," *J. Mater. Chem. B*, vol. 7, no. 8, pp. 1186–1208, 2019.

[20] J. Yu, Arthur Shang, B. A. Cheng, Fang Paik, and D. M. Kaplan, Justin M. Andrade, Rodrigo B. Ratner, "Biofunctional Paper via the Covalent Modification of Cellulose," *Langmuir*, vol. 28, no. 30, pp. 11265–11273, Jul. 2012.

[21] Y. Dong, Yongqiang Wang, Ruixue Li, Hao Shao, Jingwei Chi and G. Lin, Xiaomei Chen, "Polyamine-functionalized carbon quantum dots for chemical

sensing," *Carbon N. Y.*, vol. 50, no. 8, pp. 2810–2815, 2012.

[22] M. J. Salinas-Castillo, Alfonso Ariza-Avidad, Maria Pritz, Christian Camprubí-Robles, Maria Fernández, Belen Ruedas Rama and L. F. Megia-Fernández, Alicia Lapresta-Fernández, Alejandro Santoyo-Gonzalez, Francisco Schrott-Fischer, Annelies Capitan-Vallvey, "Carbon dots for copper detection with down and upconversion fluorescent properties as excitation sources," *Chem. Commun.*, vol. 49, no. 11, p. 1103, 2013.

[23] Y. You, H. Zhang, Y. Liu, and B. Lei, "Solid-state fluorescent composite phosphor based on cellulose grafted with carbon dots for temperature sensing," *RSC Adv.*, vol. 6, no. 93, pp. 90126–90131, 2016.

[24] D. Guo, Jiaqi Liu, S. Filpponen, Ilari Johansson, Leena-Sisko Malho, Jani-Markus Quraishi, and O. J. Liebner, Falk Santos, Hélder A. Rojas, "Photoluminescent Hybrids of Cellulose Nanocrystals and Carbon Quantum Dots as Cytocompatible Probes for in Vitro Bioimaging," *Biomacromolecules*, vol. 18, no. 7, pp. 2045–2055, Jul. 2017.

[25] K. Junka, J. Guo, I. Filpponen, J. Laine, and O. J. Rojas, "Modification of Cellulose Nanofibrils with Luminescent Carbon Dots," *Biomacromolecules*, vol. 15, no. 3, pp. 876–881, Mar. 2014.

[26] S. Ahmed and A. Abbas, "Paper-based Chemical and Biological Sensors: Engineering Aspects," *Biosens. Bioelectron.*, vol. 77, Sep. 2015.

[27] W. Xi, T. F. Scott, C. J. Kloxin, and C. N. Bowman, "Click Chemistry in Materials Science," *Adv. Funct. Mater.*, vol. 24, no. 18, pp. 2572–2590, May 2014.

[28] J.-L. Huang, C.-J. Li, and D. G. Gray, "Functionalization of cellulose nanocrystal films via 'thiol–ene' click reaction," *RSC Adv.*, vol. 4, no. 14, p. 6965, 2014.

[29] L. Nongbe, Medy C. Bretel, Guillaume Ekou, M. Ekou, Tchirioua Robitzer, and F.-X. Le Grognec, Erwan Felpin, "Cellulose paper azide as a molecular platform for versatile click ligations: application to the preparation of hydrophobic paper surface," *Cellulose*, vol. 25, no. 2, pp. 1395–1411, Feb. 2018.

[30] C. Gaucher, A. Boudier, J. Bonetti, I. Clarot, P. Leroy, and M. Parent, "Glutathione: Antioxidant Properties Dedicated to Nanotechnologies.,"

Antioxidants (Basel, Switzerland), vol. 7, no. 5, Apr. 2018.

[31] A. P. Mazzetti, M. C. Fiorile, A. Primavera, and M. Lo Bello, "Glutathione transferases and neurodegenerative diseases," *Neurochem. Int.*, vol. 82, pp. 10–18, Mar. 2015.

[32] P. Diaz-Vivancos, A. de Simone, G. Kiddle, and C. H. Foyer, "Glutathione – linking cell proliferation to oxidative stress," *Free Radic. Biol. Med.*, vol. 89, pp. 1154–1164, Dec. 2015.

[33] F. Yan, Q. Ye, J. Xu, J. He, L. Chen, and X. Zhou, "Carbon dots-bromoacetyl bromide conjugates as fluorescence probe for the detection of glutathione over cysteine and homocysteine," *Sensors Actuators B Chem.*, vol. 251, pp. 753–762, Nov. 2017.

[34] S. Gogoi and R. Khan, "NIR upconversion characteristics of carbon dots for selective detection of glutathione," *New J. Chem.*, vol. 42, no. 8, pp. 6399–6407, 2018.

[35] S. Lee, J. Li, X. Zhou, J. Yin, and J. Yoon, "Recent progress on the development of glutathione (GSH) selective fluorescent and colorimetric probes," *Coord. Chem. Rev.*, vol. 366, pp. 29–68, Jul. 2018.

[36] W. Dungchai, Y. Sameenoi, O. Chailapakul, J. Volckens, and C. S. Henry, "Determination of aerosol oxidative activity using silver nanoparticle aggregation on paper-based analytical devices," *Analyst*, vol. 138, no. 22, p. 6766, 2013.

[37] D. M. Cate, W. Dungchai, J. C. Cunningham, J. Volckens, and C. S. Henry, "Simple, distance-based measurement for paper analytical devices," *Lab Chip*, vol. 13, no. 12, p. 2397, 2013.

[38] J. C. Koziar and D. O. Cowan, "Photochemical heavy-atom effects," *Acc. Chem. Res.*, vol. 11, no. 9, pp. 334–341, Sep. 1978.

[39] M. Salemi, Giuseppe Gueli and I. D'Amelio, Marco Saia, Valentina Mangiapane, P Aridon, Paolo Ragonese, Paolo Lupo, "Blood levels of homocysteine, cysteine, glutathione, folic acid, and vitamin B12 in the acute phase of atherothrombotic stroke," *Neurol. Sci.*, vol. 30, pp. 361–364, Jun. 2009.

[40] G. Wu, Di Li, N. Chen, Xuefeng Qiu, G. Shi, Xuexiang Chen, and Y. Sun, Zhiwei

You, Jinmao Wu, "Fluorometric determination and imaging of glutathione based on a thiol-triggered inner filter effect on the fluorescence of carbon dots," *Microchim. Acta*, vol. 184, no. 7, pp. 1923–1931, Jul. 2017.

[41] Y. Tang, H. Song, Y. Su, and Y. Lv, "Turn-on Persistent Luminescence Probe Based on Graphitic Carbon Nitride for Imaging Detection of Biothiols in Biological Fluids," *Anal. Chem.*, vol. 85, no. 24, pp. 11876–11884, Dec. 2013.

[42] N. Zhang, F. Qu, H. Q. Luo, and N. B. Li, "Sensitive and selective detection of biothiols based on target-induced agglomeration of silvernanoclusters," *Biosens. Bioelectron.*, vol. 42, pp. 214–218, Apr. 2013.

[43] B. Han, J. Yuan, and E. Wang, "Sensitive and Selective Sensor for Biothiols in the Cell Based on the Recovered Fluorescence of the CdTe Quantum Dots−Hg(II) System," *Anal. Chem.*, vol. 81, no. 13, pp. 5569–5573, Jul. 2009.

[44] W. Zhao, M. Sun, T. Lei, X. Liu, Q. Zhang, and C. Zong, "An indicator-displacement assay based on the Murexide-Hg2+ system for fluorescence turn-on detection of biothiols in biological fluids," *Sensors Actuators B Chem.*, vol. 249, pp. 90–95, Oct. 2017.

[45] K. S. Park, M. Il Kim, M.-A. Woo, and H. G. Park, "A label-free method for detecting biological thiols based on blocking of Hg2+-quenching of fluorescent gold nanoclusters," *Biosens. Bioelectron.*, vol. 45, pp. 65–69, Jul. 2013.

[46] M. Lafuente, J. Solà, and I. Alfonso, "A Dynamic Chemical Network for Cystinuria Diagnosis.," *Angew. Chem. Int. Ed. Engl.*, vol. 57, no. 28, pp. 8421–8424, Jul. 2018.

ÍNDICE DE FIGURAS

Capítulo 5

Figure 1. Microfluidic paper-based analytical device for biothiols. **(a)** Drawing of the µPAD indicating dimensions. **(b)** Picture of the µPAD for biothiols determination inside of a homemade accessory. 256

Figure 2. (A) Dependence of the intensity of the fluorescence with the biothiols concentration. (B) Linearization of calibration functions for biothiols. Data points are the mean of 3 assays. Conditions: paper disk with $1.72x10^{-6}$ mg·mL^{-1} of immobilized CDs and functionalized with 120 mM of IAA; 5 µL phosphate buffer pH 7.4 10 mM; 5 µL of sample (GSH, Cys or Hcys); reaction time 30 min. 258

Figure 3. Comparison of the response of 5 µM Cys, Hcy and GSH, 5 µM GSH in the presence of 5 µM Cys, 5 µM of GSH in presence of 5 µM Hcy and 5 µM GSH en 5 µM Cys and Hcy. Coloured bar indicates theoretical values for the binary and tertiary systems obtained from the individual contribution of each biothiol according to the calibration function. Data points are the mean of 3 assays. Conditions: paper disk with $1.72x10^{-6}$ mg·mL^{-1} of immobilized CDs and functionalized with 120 mM of IAA; 5 µL phosphate buffer pH 7.4 10 mM; 5 µL of sample; reaction time 30 min. 260

Figure 4. Response of GSH, Cys and Hcy and interferences (100 µM). Data points are the mean of 3 assays. Conditions: paper disk with $1.72x10^{-6}$ mg·mL^{-1} of immobilized CDs and functionalized with 120 mM of IAA; 5 µL phosphate buffer pH 7.4 10 mM; 5 µL of interferent; reaction time 30 min. 261

Fig ESM 1. Characterization of the CDs by HRTEM. **A)** HR-TEM image, **B)** Size distribution for CDs and **C)** EDX spectrum. 264

Fig ESM 2. The measurement system consists of a digital camera located at a distance of 10 cm from the UV transilluminator. The µPAD is placed inside the homemade accessory in the UV transilluminator. The captured images were converted to grayscale using a MATLAB script to obtain the region of interest (ROI) and with them the calibration function was calculated. 264

Fig ESM 3. Optimization of ISO for digital camera. Blue bars: **CDs-I.-paper**; orange bars: GSH 250 µM; gray bars: GSH 750 µM. The paper circles were put in a homemade accessory on the UV transilluminator and a picture was taken. The intensity of the papers

was obtained using ISO ranging between 400–4000. Data points are the mean of 3 assays. Conditions: paper disk with $1.72x10^{-6}$ mg·mL^{-1} of immobilized CDs and functionalized with 120 mM of IAA; paper disks were buffered with phosphate buffer pH 7.4 10 mM, after that were dipped in GSH solutions; reaction time 30 min; λ_{exc}= 365 nm. 265
Fig ESM 4. Fluorescence profile of different commercial filter papers and nylon membranes: 1240, 1242, 1254, 1244, Whatman 1, PC1, Nytran SPC, Biodyne Plus, Biodyne C. Disks were placed in a homemade accessory, illuminated with a 365 nm wavelength UV lamp transilluminator and imaged with a digital camera (ISO 1250, shutter speed 1/80 s, aperture value f/3.2 and focal length of 4 mm). Inset: Image of the fluorescence emitted by the different substrates studied and the image in gray scale. Data points are the mean of 3 assays for each type of paper or nylon membranes. 266
Fig ESM 5. Evaluation of immobilization methodology by Cu^{2+} quenching. **A)** Physical adsorption of CDs: Fluorescence intensity of a disk paper with CDs. **B)** Maintenance of fluorescence intensity after treatment of a disk paper with water **C)** Graphical comparative of fluorescence intensity along the diameter of paper disk prior (blue dots) and after (yellow dots) the treatment with water. 267
Fig ESM 6. Evaluation of immobilization methodology. **A** Fluorescence intensity of a disk paper. **B** Fluorescence intensity of a disk paper with CDs immobilized. **C** Maintenance of fluorescence intensity after treatment of a disk paper with a IAA. **D** Fluorescence intensity of a disk paper after GSH reaction. **E** Graphical comparative of fluoresce intensity for a disk paper (red dots) CDs-paper (green dots), CDs-I-paper (yellow dots) and CDs-paper@GSH (blue dots) with a 500 µM GSH solution. 268
Fig ESM 7. XPS spectra. **A) VS-paper**, Inset: high resolution S_{2p} peak: 168 eV; **B) CDs-paper**, Inset: high resolution N_{1s} peak: 400 eV. **C) CDs-I-paper**, Inset: high resolution I_{3d} peak: 620 and 635 eV. **D) CDs-I-paper@GSH;** Inset: high resolution S_{2p} peak:165 eV. 269
Fig ESM 8. Elemental mapping by scanning transmission electron microscopy. **A) VS-paper; B) CDs-I-paper**; **C) CDs-I-paper** after GSH reaction. 271
Fig ESM 9. Fluorescence emission spectrum of **CDs-paper** and **CDs-I-paper** using an excitation wavelength of 330 nm. Inset: Images of **CDs-paper** and **CDs-I-paper.** 271
Fig ESM 10. Optimization of parameters: **A)** [CDs]: twenty disks of **VS-paper**, PBS buffer (1 mL, pH 7.4, 10 mM) and different concentrations of CDs 0.008 mg·mL^{-1}; **B)** [IAA]: twenty disks of **CDs-paper,** (30 mL); DCC (4.12 mg), DIPEA (2.58 mg) and different concentrations of IAA; **C)** pH. Conditions: disk of **CDs-paper**, IAA (120 mM)

and GSH (500 µM); **D)** Reaction time for fabrication of **CDs-I-paper:** disk of **CDs-paper** and IAA (120 mM); **E)** Reaction time for conjugation of GSH: **CDs-paper,** IAA (120 mM), GSH (500 µM), PBS buffer (pH 7.4, 10 mM). All parameters were evaluated with a digital camera at ISO 1250. 273
Fig ESM 11. Optimization of the washing steps for biothiol determination by the µPAD. Three µPADs were used to know the influence of washing steps in the fluorescence intensity of **CDs-I paper**. 5 µL of GSH solution 500 µM were added in the sampling area of the µPAD. After 30 min reaction of reaction under nitrogen atmosphere 10 µL of MilliQ water was added in the sampling area of the µPADs. The procedure was repeated three times. The washing steps influences were evaluated taking a picture of the µPADs with digital camera working at ISO 1250. 274

ÍNDICE DE TABLAS

Capítulo 5

Table 1. Analytical characteristics of µPAD for GSH, Cys and Hcy determination. .. 259
Table 2. Comparison between some selected assays for biothiols determination. 261

Capítulo 6

IONOPHORE-BASED OPTICAL SENSOR FOR URINE CREATININE DETERMINATION

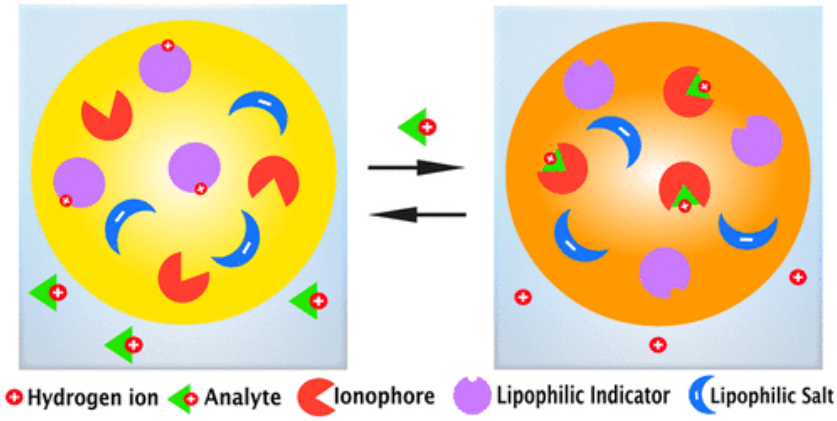

Published in ACS Sensor, 2019 4, 2, 421-426

CAPÍTULO 6: IONOPHORE-BASED OPTICAL SENSOR FOR URINE CREATININE DETERMINATION

Miguel M. Erenas[1,2], Inmaculada Ortiz-Gomez[1,2], Ignacio de Orbe-Paya[1,2], Daniel Hernandez-Alonso[3,4], Pablo Ballester[3,4,5], Pascal Blondeau[3,4], Francisco J. Andrade[3,4,5], Alfonso Salinas-Castillo[1,2] and Luis Fermín Capitan-Vallvey[1,2]

[1]ECsens, Department of Analytical Chemistry and [2]Unidad de Excelencia de Química aplicada a biomedicina y medioambiente of the University of Granada Campus Fuentenueva, Faculty of Sciences, University of Granada, 18071 Granada, Spain

[3]Institute of Chemical Research of Catalonia (ICIQ), The Barcelona Institute of Science and Technology, Av. Països Catalans, 16, 43007 Tarragona, Spain

[4]Catalan Institution for Research and Advanced Studies (ICREA), Pg. Lluís Companys 23, 08010 Barcelona, Spain

[5]Departament de Química Analítica i Química Organica, Universitat Rovira i Virgili (URV), C/Marcel lí Domingo 1, 43007Tarragona, Spain

Planteamiento

Hoy en día resulta muy importante el desarrollo de métodos de detección para el análisis clínico que satisfagan las crecientes demandas como es la determinación de ciertos biomarcadores de forma no invasiva en muestras biológicas así de orina, saliva, y el sudor tal y como se describe en el apartado 2.2.4 de la introducción de esta Memoria.

En este contexto, la determinación de creatinina en orina es de vital importancia para diagnosticar enfermedades crónicas renales y poder controlar su progreso. La creatinina es un producto de desecho del músculo resultante de la deshidratación enzimática de creatina o de la desfosforilación de fosfocreatina [1], [2]. Por lo general, la creatinina se excreta del cuerpo a través de la filtración glomerular en orina ya que no tiene utilidad biológica, siendo la cantidad de creatinina excretada proporcional a la masa muscular del individuo. De este modo, niveles anormales de excreción de creatinina indican un mal funcionamiento del riñón de lo que deriva la importancia de su determinación [3], [4].

Hasta la fecha, los métodos más utilizados para la determinación de creatinina en orina en los laboratorios clínicos y toxicológicos se basan en la reacción colorimétrica de Jaffe y/o en ensayos enzimáticos [5], [6], [7]. En la reacción de Jaffe la creatinina forma un complejo coloreado con ácido pícrico en una solución básica de forma que se produce un cambio de color de la disolución que se relaciona con la concentración de creatinina en la muestra y que es registrada mediante una medida espectrofotométrica. Sin embargo, la reacción de Jaffe presenta una baja especificidad debido a la interferencia de otros metabolitos presentes en la orina. En contraposición, los métodos enzimáticos han mejorado la especificidad del ensayo mediante la utilización de enzimas que permiten la determinación selectiva de creatinina. No obstante, la utilización de enzimas supone también un aumento significativo de los costos de detección. Por todo ello, resulta de especial interés el desarrollo de nuevos métodos de análisis que permitan mejorar las características de los métodos ya existentes. En consecuencia, una gran cantidad de métodos para la determinación de creatinina en orina han sido reportados en los últimos años entre los que se encuentran, técnicas de inyección en flujo (FIA), electroforesis capilar, cromatografía líquida, [8]–[13] etc. Sin embargo, estos métodos presentan múltiples desventajas, incluidas laboriosas etapas de preparación de la muestra, empleo de reactivos tóxicos para el medio ambiente, así como la necesidad de emplear instrumentación de laboratorio que puede ser sofisticada y costosa. De este modo, el desarrollo de nuevos métodos de análisis que permitan una determinación selectiva, rápida, de bajo coste y que permita una descentralización de las medidas bioquímicas presenta un gran interés.

Objetivo

En base a lo expuesto anteriormente en el sexto capítulo de esta Memoria se describe el desarrollo y validación de un nuevo sensor óptico desechable para la determinación espectrofotométrica de creatinina en orina.

Para conseguir este fin se ha utilizado el ionoforo calix[4]pirrol síntetizado por el grupo de investigación *Laboratory of nanosensors* de la Universidad Rovira i Virgili de

Tarragona. Seguidamente se diseñó y preparó una membrana para el reconocimiento del ion creatininio y se estudió el mecanismo de respuesta. Esta membrana se preparó sobre una lámina de PET para poder llevar a cabo la determinación espectrofotométrica de creatinina y se establecieron y optimizaron los factores influyentes. Se caracterizó analíticamente el sensor desarrollado y se estudió la selectividad del mismo frente a otras moléculas presentes en la orina que pudieran actuar como interferentes en esta determinación. Por otro lado, se llevó a cabo la validación del sensor en la determinación de creatinina y por último, se realizó una determinación de creatinina en muestras de orina para demostrar la aplicabilidad del sensor óptico desarrollado.

En conclusión, las etapas de las que consta este trabajo son:

1. Fabricación de la membrana sensora e implementación de la misma sobre una lámina de PET.
2. Optimización de las condiciones experimentales para la determinación de creatinina.
3. Caracterización analítica del sensor óptico.
4. Estudio de la selectividad de la membrana sensora.
5. Validación del sensor óptico.
6. Determinación de creatinina en muestras de orina.

IONOPHORE-BASED OPTICAL SENSOR FOR URINE CREATININE DETERMINATION

ABSTRACT

Creatinine is a metabolite present in urine, and its concentration is used to diagnose and monitor kidney performance. For that reason, the development of new sensors to analyze this metabolite and obtain accurate results in a short period of time is necessary. An optical disposable sensor for monitoring creatinine levels in urine is described. The system, based on a new aryl-substituted calix[4]pyrrole synthetic receptor, has an unusual coextraction scheme. Due to the low pKa values of creatininium (pKa 4.8), a careful selection of a lipophilic pH indicator that works in acid medium is required. The sensor components were optimized, and the new sensor displays a good response time to creatinine (approximately 3 min) over a wide dynamic range (from 1 × 10–5 to 1 × 10–2 M). Moreover, the optical selectivity coefficients obtained for creatinine over common cations present in urine meet the requirements for real sample measurements. With a good sensor-to-sensor reproducibility (RSD, 5.1–6.9% in the middle of the range), this method provides a simple, quick, cost-effective, and selective alternative to the conventional methodology based on Jaffé's reaction.

Keywords: Disposable sensor · Host-guest chemistry · Biofluids · Calix[4]pyrrole · Spectrometry · Optode

1. Introduction

The determination of creatinine in urine and blood is among the most requested clinical tests worldwide. As a metabolic byproduct of the muscles that is toxic for the cells, creatinine must be transported by the bloodstream and eliminated through renal filtration. For this reason, the levels of creatinine in blood (0.4 × 10–5–1.1 × 10–5 M) and urine (0.3 × 10–3–2.5 × 10–3 M) are used by doctors to calculate the glomerular filtration rate (GFR), a value that is universally used to diagnose and monitor kidney performance. Thus, at a time when social and demographic changes are sharply increasing kidney-

related conditions, [14] the development of new tools for the determination of this substance is highly relevant.

The current approaches for the determination of creatinine have some important complications. Jaffe's reaction, which has been (and still is) the most used approach for more than a century, is a kinetic method with significant interferences. The same is true for bioassays, which either by colorimetric or electrochemical detection require the use of multiple enzymes and present some interference issues. The gold standard isotope dilution gas chromatography is not applicable in routine assays. As a result, studies in laboratories in different countries show disappointing levels of variability with serious medical implications [15].

To overcome some of these issues, alternative colorimetric and electrochemical sensors for creatinine have been proposed, but in most cases they have significant drawbacks when dealing with real samples [16], [17]. More recently, an ionophore for creatinine has been reported by some of us, and its application in an ion-selective potentiometric sensor with the ability to quantify creatinine in urine and serum samples was demonstrated [18], [19].The improvements on the limits of detection allow for sample dilution, avoiding the typical matrix interferences of real samples. These results encourage further exploration of the use of this ionophore with alternative detection schemes.

Ionophore-based optical sensors (optodes) rely on the combination of ionophores and indicators present in lipophilic environments in different formats [20]. The selective extraction of a charged analyte along with a reference ion (typically proton) either by ion-exchange, in the case of cations, or coextraction, in the case of anions, triggers the optical signal. For the most part, molecular absorption (but also molecular emission) changes in the refractive index [21] or color [22] are used. The signal is usually obtained under equilibrium, although kinetic conditions with dynamic or exhaustive change [23] approaches–can be used. Most of the optodes developed so far have focused on the detection of inorganic cations and, to a lesser extent, anions. Very few examples of optodes for organic ions or ionizable organic compounds have been reported, and, to the best of our knowledge, none of them have been validated with real samples [24]–[29]. On the one hand, there are very few selective receptors for this kind of target based on host–guest chemistry [17], [30]. Indeed, once integrated in the sensors, the limited selectivity commonly hampers real application in biological fluids, environmental samples, and so forth. On the other hand, a challenge results from the type of signal output, i.e. the

availability of indicators capable of protonation/deprotonation at suitable pH conditions. Indeed, most of these systems rely on ammonium-based moieties, whose acidity constant dictates the range of pH working conditions. In short, the detection of organic cations with this type of indicator in acidic media is a highly challenging task. In the case of creatinine, for example, the low pKa (4.8) requires working in very unusual conditions when considering the typical ion-exchange scheme for cations. At present, no such system has been characterized and reported to work with real samples.

Therefore, considering the importance of the determination of creatinine, we anticipated that the use of the novel ionophore in a system with optical detection would be highly significant. This work proposes the use of the new synthetic receptor for creatinine as ionophore in an optode. The results show the feasibility of building a new disposable device for the determination of creatinine in urine. Optimization of the analytical parameters and the signal treatment allows for the detection of creatinine with excellent sensitivity and limits of detection.

2. Experimental section

2.1. Reagent and materials

All reagents used were analytical-grade and were obtained from Sigma-Aldrich (Sigma-Aldrich Química S.A., Madrid, Spain). Doubly deionized water (18.2 MΩ cm resistance) was obtained from a Milli-RO 12 plus Milli-Q station (Millipore, Bedford, MA, USA). Aqueous creatinine standard solutions were prepared by proper dilution of a 0.5 M stock solution of creatinine hydrochloride. Stock solutions (1.0 M) of the following species were also used: K^+, Na^+, NH_4^+ as chlorides. Acetic acid/sodium acetate buffer (0.1 M) at different pH values was prepared from acetic acid and NaOH. HCl (0.1 M) was used for the activation of the membranes. Poly(vinyl chloride) (PVC; high molecular weight), 4′,5′-dibromofluorescein octadecyl ester (ETH7075), o-nitrophenyl octyl ether (NPOE), potassium tetrakis [3,5-bis(trifluoromethyl) phenyl]borate (KTFPB), tridodecyl methyl ammonium chloride (TDMAC), and tetrahydrofuran (THF) purchased from Sigma-Aldrich were used to make the sensing film. The ionophore calix[4]pyrrole (Figure S1) for creatinine was synthesized in our laboratories [19].

2.2. Intruments and software

Sensing membranes were prepared by spin-coating using WS-400Bz-6NNP/LITE equipment from Laurell Technologies Corporation (PA, USA). The characterization of the creatinine-selective sensing membranes was done with a Hewlett-Packard diode array spectrophotometer (model 8453; Norwalk, CT, USA). The film thickness of membranes was measured with the Dektak XT Stimulus Surface Profiling System contact profilometer (Bruker Corporation, Coventry, UK).

2.3. Membrane preparation

The membrane cocktail was prepared from a batch of 31.9 mg (31.5 wt %) of PVC, 63.9 mg (63.0 wt %) of NPOE, 3.2 mg (3.2 wt %) of ionophore, 0.9 mg (0.9 wt %) of ETH7075, and 1.5 mg (1.5 wt %) of KTFPB all dissolved in 1 mL of freshly distilled THF. KTFPB was selected because it is a noncompetitive counterion for the creatininium cation [19].

The sensing membranes were casted by dropping 15 μL of cocktail on a 14 mm × 40 mm × 0.5 mm thick polyester sheet on the spin-coating device spinning at 190 rpm. Then, the membranes were dried in THF atmosphere. The sensing layer appears as a solid and homogeneous yellow circular film 10 mm diameter and 4 μm thick and contains 37.1 $mmol \cdot kg^{-1}$ in ionophore, 12.4 $mmol \cdot kg^{-1}$ lipophilic pH indicator, and 17.4 $mmol \cdot kg^{-1}$ lipophilic salt. After these membranes are dried, they are ready to be used.

2.4. Measurement setup

The membrane is first activated by immersion in a 0.1 M HCl solution for 3 min, acquiring a yellow color (due to the positively charged species of ETH7075), and then is immersed in a 0.01 M acetic acid/acetate buffer at pH 3.8 for 3 min. After this step, the absorbance (AH_2I^+) at 455 nm is measured. Thereafter, the membrane is equilibrated for 3 min with standards or sample solution containing creatinine containing 0.01 M acetic acid/acetate buffer pH 3.8, and the absorbance (Ax) at the same wavelength is measured again. Finally, the membrane is introduced in 0.05 M creatinine solution containing 0.01 M acetic acid/acetate buffer pH 3.8 for 3 min to obtain the limiting absorbance (AHI) of

the neutral form (orange color) of the indicator. All these measurements were carried out at room temperature.

The extent of creatinine recognition is measured by the degree of protonation of the pH indicator (1−α). Since the indicator can exist in three forms (H_2I^+, HI, and I^-) but the recognition process only involves the positively charged (H_2I^+) and neutral (HI) forms, an experimental value (1−αeff) was used instead. Under the working conditions (pH 3.8), 1 – αeff can be calculated from the absorbance values measured at 455 nm of membranes equilibrated in buffer (AH_2I^+), in 5×10^{-2} M creatinine (AHI) solution, and in creatinine sample or standard (Ax) according to eq 1.

$$1 - \alpha_{\text{eff}} = \frac{A_x - A_{\text{HI}}}{A_{H_2I^+} - A_{\text{HI}}} \quad (1)$$

2.5. Analysis of real samples

Urine samples were obtained from healthy volunteers and were filtered before analysis. In order to evaluate the interferences and the matrix effects, samples were diluted at 1:50; 1:100; 1:150, and 1:200 ratios with the working buffer solution and measured in triplicate, selecting 1:150 dilution for creatinine determination in urine. The creatinine level predicted from the optode membrane was compared to that of Jaffé's method used as a reference [31].

3. Results and discussion

The sensing mechanism of this system is based on a host–guest interaction, where the creatininium ion is recognized by the ionophore present in the membrane and to preserve the electroneutrality a proton is exchanged with the lipophilic pH indicator (HI), producing a change on the absorption spectrum. Thus, HI acts as an optical transducer of the recognition event. Since the pK_a of creatinine is around 4.8, [32], [33] the pH of the solution must be well below this value to maximize the concentration of the creatininium ion. Therefore, beyond the lipophilicity, the pH indicator must also have a pK_a value low enough to work under these acidity conditions. For this reason, ETH7075 was selected as indicator, since it can show both acidic and basic properties [34], [35] and has a lower

pK_a value than other lipophilic pH indicators [36]. With the incorporation of ionic sites of different charges in the membrane, such as tetraphenyl borate or quaternary ammonium salts, positively charged H_2I^+ (yellow color membrane) or negatively charged I^- species of the indicator (pink color membrane) can be generated (Figure 1). In this work, the inclusion of tetraphenyl borate salt in the membrane makes the equilibrium between H_2I^+ and HI (yellow and orange membrane colors, respectively) possible.

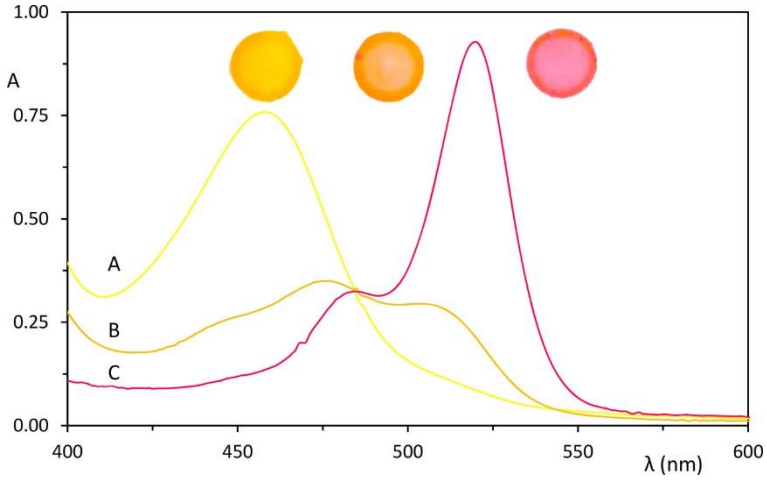

Figure 16. Absorption spectra of PVC-NPOE membranes containing 4′,5′-dibromofluorescein octadecyl ester (ETH7075). A: Membrane with ionophore (3.2 wt %) and KTFPB (1.5 wt %) after equilibration with 0.1 M HCl; B: Same membrane after equilibration with 50 mM creatinine in pH 3.8 buffer; C: Membrane with ionophore (3.2 wt %) and TDMAC (0.9 wt %) after equilibration with 0.1 M NaOH.

Assuming that the membrane contains (indicated as barred species) the ionophore (L), the pH indicator (H_2I^+), and the lipophilic anion (R^-), the reaction with creatininium ions (HC^+) in solution proceeds to form the HCL_p^+ complex with p stoichiometry, as represented in eq 2:

$$\overline{pL} + \overline{H_2I^+} + \overline{R^-} + HC^+ \leftrightarrow \overline{HI} + \overline{HCL_p^+} + \overline{R^-} + H^+ \qquad (2)$$

The experimental parameter used to describe the behavior of the sensor is the deprotonation degree α ([HI]/IC) measured by the normalized absorbance measured at 455 nm. Through an ion-exchange constant K_{exch}, this 1 – αeff experimental value is related to the analytical concentrations of ionophore CL, pH indicator CI, and lipophilic

salt CR, as well as the activities of creatininium and H^+ in aqueous medium according to eq 3 [21].

$$K_{exch} = \frac{1}{a_{HC^+}}\left(\frac{a_{H^+}\cdot\alpha_{eff}}{1-\alpha_{eff}}\right)\frac{C_R-(1-\alpha_{eff})C_I}{(C_L-p(C_R-(1-\alpha_{eff})C_I))^p} \quad (3)$$

The ionophore used in this work is an aryl-substituted monophosphonate-bridged calix[4]pyrrole (L), recently reported by some of us as a creatininium receptor. It includes a functionalized aromatic polar cavity that allows for multiple host–guest interactions with a creatininium ion based on hydrogen-bonding, CH–π, π–π, and hydrophobic interactions resulting in a good fit considering the size and bond complementarity [19], [18].

3.1. Optimization of the response

3.1.1. Membrane optimization

An ionophore:lipophilic salt molar ratio (L:R^- = 3:1) previously established in the study of the potentiometric sensor [18] was initially used. First, the influence of the pH indicator (HI) was studied. Membrane cocktails with L:HI:R^- molar ratios of 3:1:1, 3:2:1, and 3:3:1 were evaluated. The results show that an excess HI:R^- ratio reduces the linear range, although the limit of detection (LOD) remains constant around 6×10^{-5} M (Figure 2).

After this, different lipophilic salt molar ratios, namely, 3:1:1, 3:1:1.25, 3:1:1.5, and 3:1:1.75 (L:HI:R^-), were tested (Figures S2–S5). A 3:1:1.5 molar ratio gives the best results in terms of LOD (1×10^{-5} M) compared to the other compositions.

Once the chromoionophore:lipophilic salt ratio is optimized and considering that the theoretical model predicts an increase in sensitivity with ionophore concentration, cocktails from 3:1:1.5 to 5:1:1.5 (L:HI:R–) were tested (Figure S6). Results shows an improvement in sensitivity around 10% in the best case that does not justify the considerable increase in calix[6]pyrrole ionophore consumption, the reason as to why the 3:1:1.5 ratio was maintained.

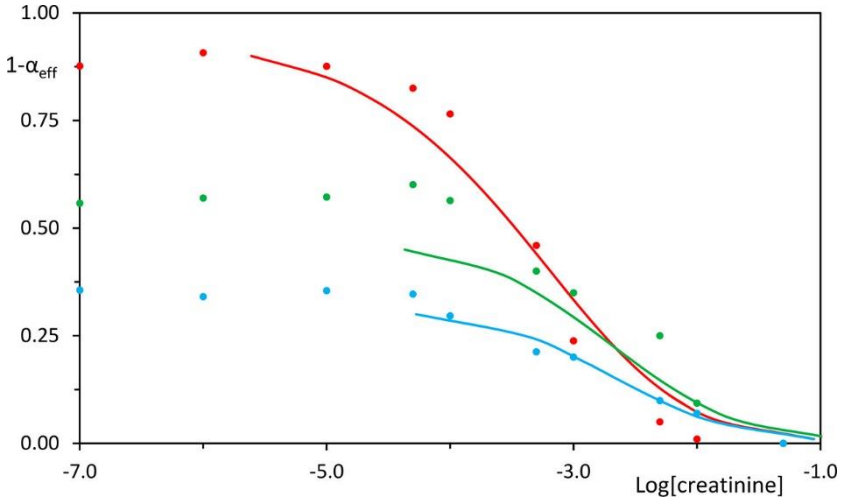

Figure 17. Theoretical model and experimental data (n = 3) obtained using different molar ratios of L:HI:R^-: 3:1:1 (red data), 3:2:1 (green data), and 3:3:1 (blue data).

In this way, the optimized sensing membrane was prepared from a cocktail including 3.2 mg of ionophore, 1.5 mg of KTFPB, 0.9 mg of ETH 7075, 63.9 mg of NPOE, and 31.9 mg of PVC in 1 mL of freshly distilled THF. The circular membrane prepared by spin-coating at 190 rpm is 4 μm thick across the membrane surface (Figure S7).

3.2. Reaction parameters

One characteristic of ionophore-based optical sensors that include a pH indicator in the membrane is pH cross-sensitivity due to cations with a competitive ion-exchange process. In this work, the pH must be low enough to displace the equilibrium toward the generation of the creatininium ion. Thus, to study the influence of the pH, two experiments were performed using membranes equilibrated in a set of 0.01 M acetic acid/acetate buffers of different pH's containing a constant concentration of 0.1 mM creatinine in one case and without it in the other. In the absence of creatinine (Figure S8B), the absorbance at 455 nm corresponding to $H2I^+$ species is constant until a pH around 4 and then decreases by deprotonation. In the presence of creatinine (Figure S8A), the absorbance decreases until 4.25 and remains constant thereafter. A pH = 3.8 was chosen as the optimum value, since the indicator is still completely in its cationic form and most of the creatinine is protonated (creatininium fraction at this pH of 90.9%, Figure S8C). Thus, at this pH, the signal only depends on the presence of creatininium.

The nearly constant value of absorbance from pH 4.25 onward in the presence of creatinine can be explained by the combination of two opposite effects: the reduction of the ion-exchange due to the reduction in the amount of creatininium present and the displacement of the pH indicator equilibrium.(21,22) The selected pH (3.8) is in good agreement with the working pH used for the potentiometric sensor based on the same ionophore [18].

In order to evaluate the stoichiometry of ionophore:creatinine, the fit of experimental data with eq 2 for stoichiometric index p of 0.5, 1, and 2 was studied. The effect of the stoichiometry on the theoretical response curve is small, except for p = 2, hindering a clear distinction between 0.5 and 1 stoichiometric index. Additionally, the summation of residual squares (srs) for the adjustment of experimental data to each theoretical model (eq 3) (p: 1; srs: 0.44; p: 2; srs: 0.85; p: 0.5; srs: 0.42) does not help to solve this issue. This difficulty evaluating the stoichiometry for the ionophore:creatinine complex has also appeared when studying the potentiometric sensor for creatinine based on the same ionophore [18]. The fit by least-squares of the experimental data in the maximum slope zone of the response curve makes it possible to calculate a value of 0.7 ± 0.3 for Kexch, which suggests a 1:1 stoichiometry.

3.3. Analytical characterization

The response of the ionophore-based optical sensors has the usual sigmoidal shape adjusting the data set to a Boltzmann (eq 4) where A1 and A2 represent the initial and final value, A3 is the inflection point, and A4 is the width. The fit of the experimental data to the Boltzmann equation provides a R2 = 0.987, as shown in Figure 3. The calculated limit of detection is 1×10^{-5} M, obtained as the intersection of the linear calibration function adjusted in the maximum slope zone and a linear function adjusted in the minimum slope zone at low analyte concentration (Table1).

$$1 - \alpha_{\text{eff}} = \frac{A_1 - A_2}{1 + e^{\log[\text{creatinine}] - A_3/(A_4)}} + A_2 \qquad (4)$$

The reproducibility of the measurement was evaluated at two different creatinine concentrations, located in the maximum slope zone of the calibration function, 5×10^{-4} M and 5×10^{-5} M. Coefficients of variation of 5.1 and 6.9% (n = 5) were obtained, respectively.

Table 10. Analytical Parameters of the Sensing Membrane for Creatinine Determination.

Analytical Parameters	
Boltzmann equation (see eq 4)	
A_1	0.996
A_2	0.030
A_3	–3.990
A_4	0.457
R^2	0.986
Limit of detection	1×10^{-5} M
Dynamic range	1×10^{-5} – 1×10^{-2} M
Intermembrane precision (n = 5)	
5×10^{-4} M	5.1%
5×10^{-5} M	6.9%

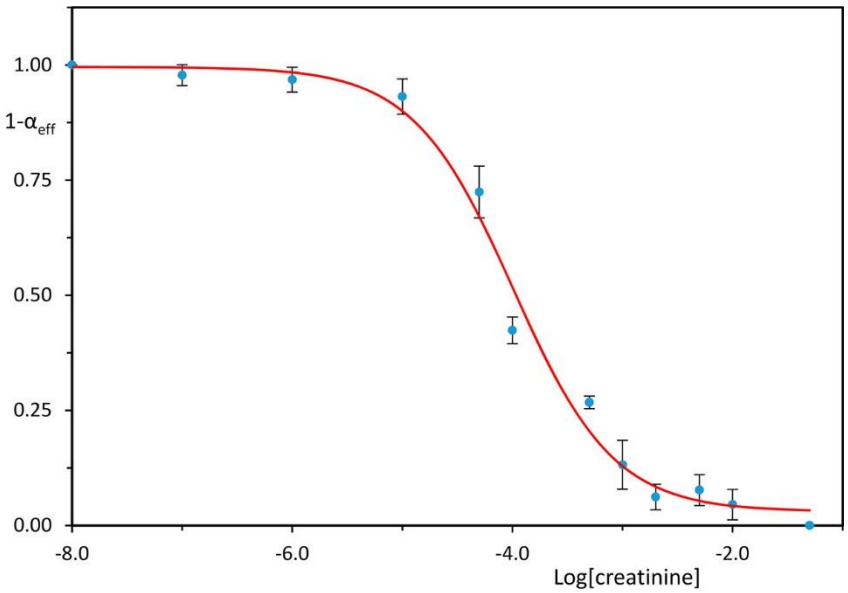

Figure 18. Calibration function of creatinine sensing membrane (n = 3).

The influence of different interfering species typically found in urine was studied using the separate solutions method. This method is typically used to study selectivity in this type of sensors, [21] and it is carried out obtaining a calibration for each interfering considered (Figure S10), obtaining the K_{exch} for each one. Finally, eq S1 is applied to obtain the log $K_{C,j}$ for creatinine and the considered interfering, being this value is a measurement of the difference between the K_{exch} of the analyte and the interfering. Seven different interfering solutions containing different concentrations of interfering species from 1×10^{-6} to 0.1 M were tested. The K_{exch} calculated for interferents (Table 2) is, at least, 3 orders of magnitude lower than that obtained for creatinine (0.7). This indicates that the selectivity coefficient obtained by the separate solution method in terms of log $K_{C,j}$ is always lower than −3. Finally, considering that the maximum tolerable error (PIJ) in urine is around 10%, [37] the required selectivity coefficient for 1, 10, and 100% was calculated (Table2). In the case of K^+ and Na^+, the error is under 10%, and in the case of NH_4^+ and creatine it is even below 1%. The selectivity coefficients found for K^+ and Na^+ are similar to the ones found by the same ionophore in an ISE [18], but in the case of NH_4^+ and creatine, the selectivity coefficients are better when using the same ionophore included in an optode.

Table 11. K_{exch} selectivity as Log $K_{creatinine,j}$ calculated using the separated solution method and $P_{creatinine,j}$ required for the interferents present in urine at different tolerable errors (1, 10, and 100%).

			required $P_{creatinine,j}$		
interfering	K_{exch}	log $K_{creatinine,j}$	**1%**	**10%**	**100%**
K^+	7.0×10^{-4}	–3.0	–3.3	–2.3	–1.3
Na^+	2.5×10^{-4}	–3.4	–3.6	–2.6	–1.6
NH_4^+	2.9×10^{-5}	–4.4	–2.6	–1.6	–0.6
creatine	2.9×10^{-6}	–5.4			

Additionally, we studied the potential interference of other compounds usually present in urine as are aspartic and glutamic acids. In both cases we found no answer at their maximum physiological value in urine ($1 - \alpha_{eff} = 0.91$ for 2 × 10–3 M in aspartic acid and $1 - \alpha_{eff} = 0.99$ for 2×10^{-3} M in glutamic acid). We attribute the selectivity of the sensing

membrane toward creatinine due to both the calix[4]pyrrole ionophore and the permselectivity of the membrane by including an anionic lipophilic salt. At the working pH both aspartic and glutamic acids have negative net charge.

A comparison table of recently developed creatinine determination methods (see Table S1) shows some analytical parameters, as well as types of measurement and recognition. We observe that the detection limit and dynamic range are similar to other methods previously published, are mainly electrochemical methods, and, in terms of response time, permit a faster analysis than other optical methods.

3.4. Analysis of real samples

The direct analysis of urine samples is affected by unspecific interferences. Thus, considering the good sensitivity of the proposed sensor, the influence of the dilution factor on the prediction of creatinine was studied. Optimum values for 1:150 dilution factors were found (Table S2), since lower dilutions (1:50 and 1:100) affect the predicted values due to the matrix effect and higher dilution (1:200) makes the creatinine concentration too low and out of the dynamic range of the sensor. Analysis of real urine samples yields recovery values from 81 to 112% (Table3). High creatinine concentration values were tested by spiking samples at the 15 mM level, obtaining recoveries in the range of 85 to 113% (Table S3).

Table 12. Determination of creatinine in urine samples using the sensor and reference methods (n = 3).

Sample	Sensor mM	Reference mM	Recovery (%)
1	6.3 ± 0.2	5.5 ± 0.2	114
2	6.1 ± 0.3	7.5 ± 0.3	81
3	1.9 ± 0.3	1.7 ± 0.1	112
4	4.5 ± 0.4	4.1 ± 0.1	110

4. Conclusiones

This work reports on the implementation of a calix[4]pyrrole ionophore for the optical detection of creatinine in disposable format, being one of the first creatinine optical sensing membranes based on a ionophore-chromoionophore scheme. The sensing membrane components as well as the working pH were first optimized to establish a suitable analytical performance. The sensor selectivity was assessed considering the common cations and species present in urine, and the obtained coefficients allowed for a maximum tolerable error between 1 and 10%. Based on the results in buffer, real sample measurements were achieved by proper dilution, making suitable recovery for biofluid detection possible. With the development of low-cost optical sensors based on paper and integration with a smartphone reader, the system developed here provides new opportunities as a decentralized analytical platform [38].

5. Electronic supporting information

5.1. Calix[4]pyrrole ionophore structure

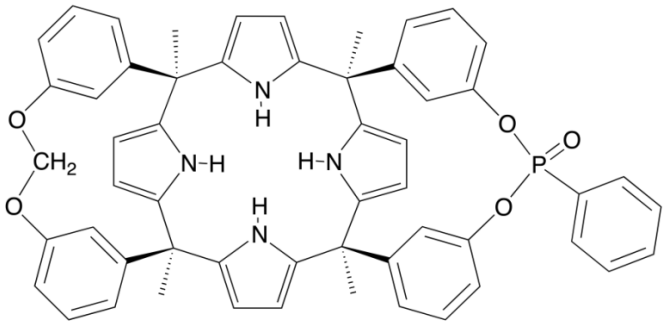

Figure S11. Calix[4]pyrrole ionophore structure.

5.2. Anionic salt optimization

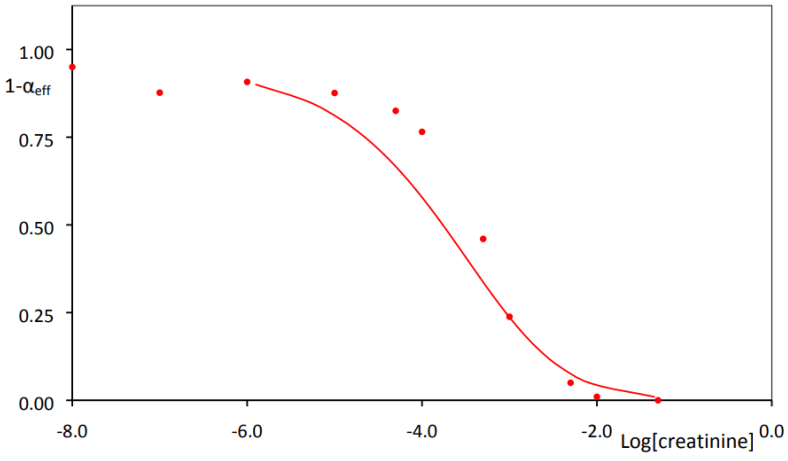

Figure S12. Experimental data and theoretical model of sensing membrane for 3:1:1 L:I:R ratio.

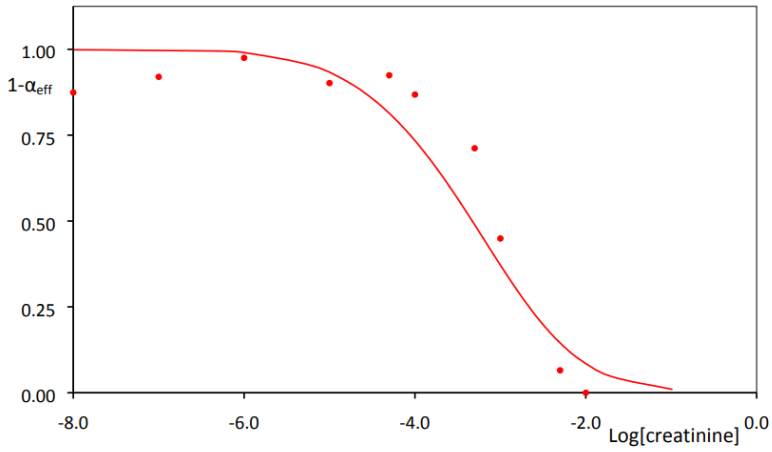

Figure S13. Experimental data and theoretical model of sensing membrane for 3:1:1.25 L:I:R ratio.

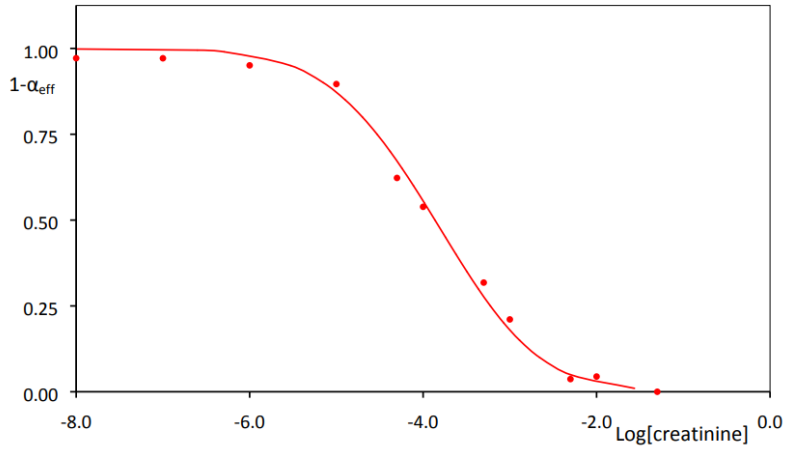

Figure S14. Experimental data and theoretical model of sensing membrane for 3:1:1.5 L:I:R ratio.

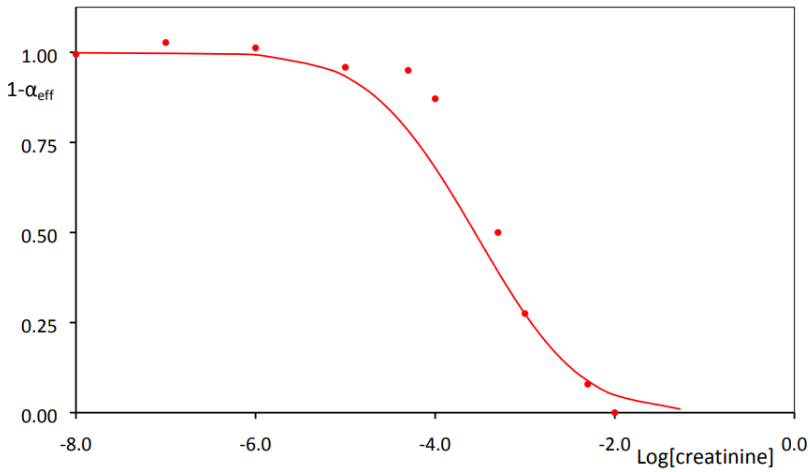

Figure S15. Experimental data and theoretical model of sensing membrane for 3:1:1.75 L:I:R ratio.

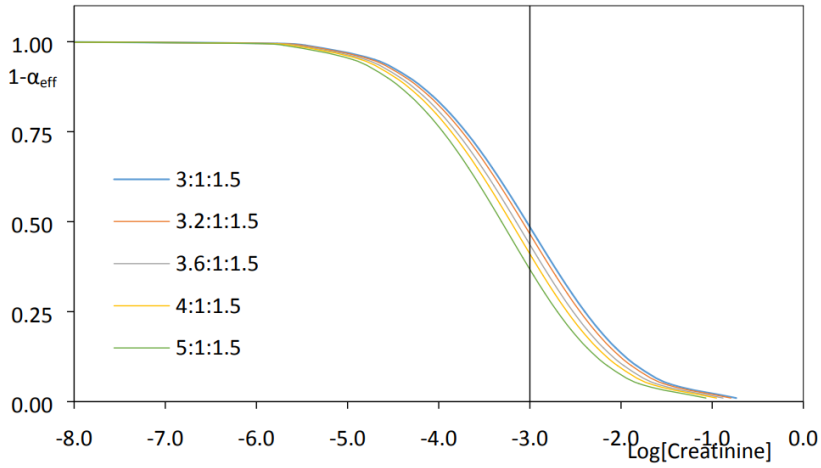

Figure S16. Theoretical influence of ionophore ratio increase on sensing membrane response. Membranes prepared with 3:1:1.5, 3:2:1:1,5, 3.6:1:1.5, 4:1:1,5 and 5:1:1.5 (L:HI:R^-) were tested against 10^{-3} M of creatinine obtaining 1- α_{eff} values of 0.485, 0.470, 0.440, 0.415 and 0.368.

5.3. Membrane thickness

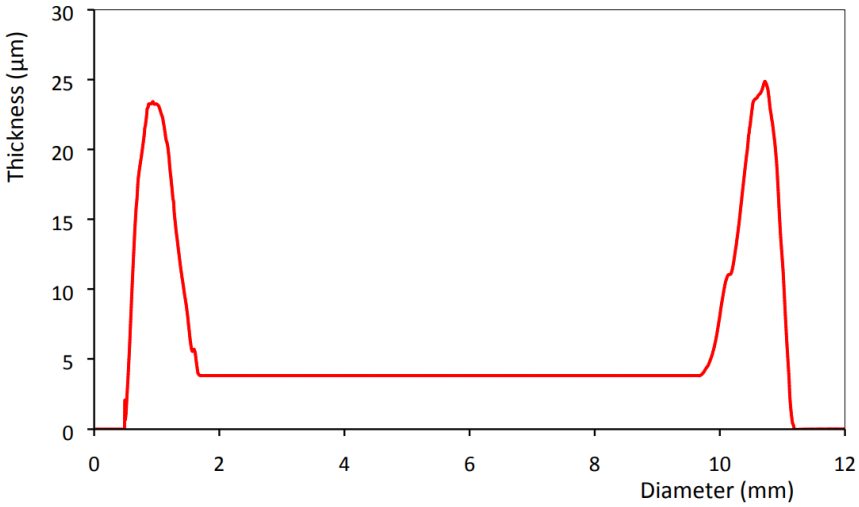

Figure S17. Variation of membrane thickness along the diameter of the circular sensing membrane measured by contact profilometry.

5.4. pH optimization

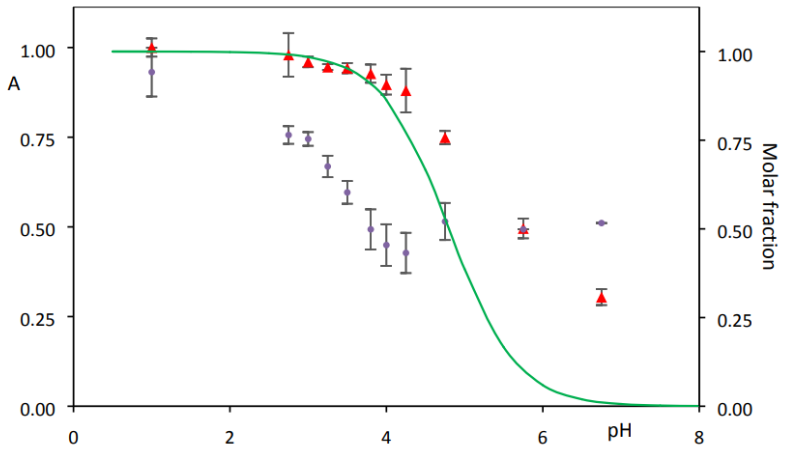

Figure S18. pH influence on the absorbance of sensing membranes. A: With creatinine (0.1 mM, blue dots); B: Without creatinine (red triangles); C: Evolution of creatininium fraction with pH (green line).

5.5. Response time

The time course of the creatinine response to the sensor was studied at three different creatinine concentrations: $1 \cdot 10^{-3}$, $1 \cdot 10^{-4}$ and $1 \cdot 10^{-5}$ M. After activation in 0.1 M HCl, the membrane was placed on one side of a 10 mm path length optical cell after which 2 mL of creatinine solution buffered to pH 3.8 in 0.01 M acetic acid/acetate buffer was added, recording the absorbance change over time for 300 s. Figure S6 shows that the reaction proceeds quickly, with only 180 s needed to reach equilibrium, this being the time used for the procedure.

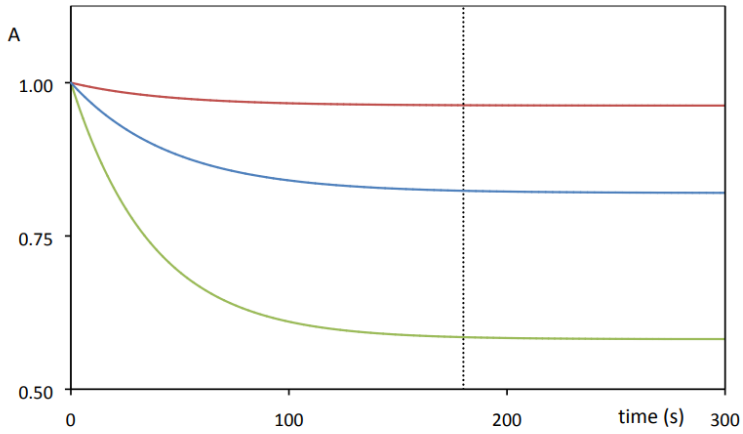

Figure S19. Variation of the absorbance (455 nm) over time for the creatinine sensor at different analyte concentrations: $1 \cdot 10^{-3}$ M (green line), $1 \cdot 10^{-4}$ M (blue line) and $1 \cdot 10^{-5}$ M (red line).

5.6. Selectivity study and maximum tolerable error

To calculate the selectivity coefficients for the sensing membrane studied, the separate solution method was used. The response curves for creatinine, Na(I), K(I), NH4 (I) and creatine were obtained following the procedure indicated in the Creatine assay section, and measuring six solutions with concentrations ranging from $1 \cdot 10^{-6}$ to 0.1 M in pH 3.8 acetic acid/acetate 10^{-2} M buffer (Figure S7). The corresponding exchange constant for S7 each equilibrium was calculated using Equation S1, assuming that the stoichiometric index is p = 1. The selectivity factor was calculated using Equation S11:

$$k_{IJ}^{opt} = \frac{v}{z}\frac{K_e^{JL_q}}{K_e^{IL_p}}\left(\frac{a_{H^+}\alpha}{1-\alpha}\right)^{z-v}\frac{C_L - \frac{1}{v}C_R - (1-\alpha)C_C}{C_L - \frac{1}{z}C_R - (1-\alpha)C_C} \qquad \text{(equation S1)}$$

Where is the protonic activity in the sample, C_R, C_I aH^+ and C_L are the molal concentration of the lipophilic salt, liphophilic pH indicator and ionophore, respectively, p the stoichiometric index for the complex ionophore-analyte (1:1 in this case), z is the analyte charge, and v is the interfering ion charge.

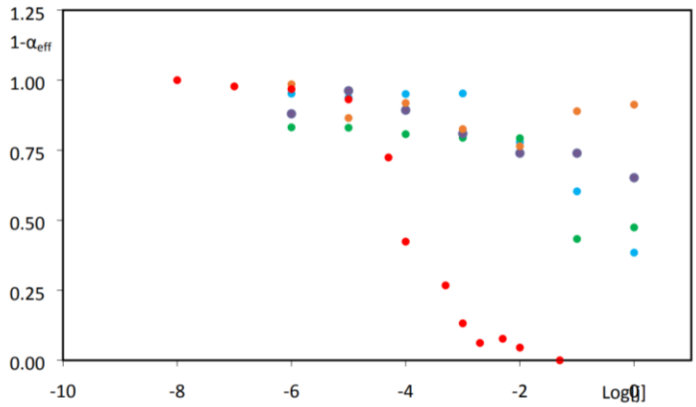

Figure S20. Data obtained calibrating the sensing membrane against creatinine and the interferences considered (j). Creatinine (red dots), Na^+ (blue dots), K^+ (green dots), NH_4^+ (purple dots) and creatine (orange dots).

The required selectivity factor was calculated using equation S2:

$$K^{opt}_{ij,\,max} = \frac{a_{i,\,min}}{(a_{j,max})} \cdot \frac{P_{ij}}{100} \qquad \text{(equation S2)}$$

where $K^{opt}_{ij,max}$ is the highest tolerable value of the selectivity factor, ai,min the lowest expected activity of the creatininium ion, aj,max the highest expected activity of the S8 interfering ion and Pij the highest tolerable error in the activity ai due to interference of aj . The concentrations considered to calculate the error at 1, 10 and 100% were 5 mM creatinine, 100 mM K^+ , 200 mM Na^+ and 20mM NH_4^+. Creatine error in not calculated because is not present in urine of healthy individuals [39].

5.7. Method comparison

Table S1. Comparison of the developed method with previous published creatinine methods.

Measurement	Detection based chemistry	LOD	Range	Response time	Reference
Amperometry	Sarcosine oxidase, creatinase and creatininase	7.8 µM	0.5 mM	8 s	[40]
Differential Pulse Voltammetry	Ni@PANI NP	0.2 nM	0.004 – 0.8 µM	30 min	[41]
Amperometry	Copper-creatinine complex	74.6 nM	6 – 378 µM	-	[42]
Dynamic Light Scattering	Calix[4]arene-Au NP	2.16 Nm	10 – 100 nM	60 s	[43]
Colorimetry	Citrate stabilized AuNP	0.08 mM	0.1 – 20 mM	24 min	[44]
Colorimetry	Plasmonic AuNP	19.8 nM	15 – 35 µM	-	[45]
UV-Vis Spectrophotometry	AgNP	3 nM	0.01 – 1.00 µM	5 min	[46]
Amperometry	HRP-conjugated creatinine antibody	40 mM	40 – 990 mM	5 min	[47]
Potentiometry	Calix[4]pyrrol ISE	0.63 µM	0.001 – 10 mM	5 min	[18]
UV-Vis Spectrophotometry	Calix[4]pyrrol ionophore chromoionophore	10 µM	$1 \cdot 10^{-2}$ – 10 mM	3 min	This paper

5.8. Real sample analysis

Table S2. Creatinine value predicted according to urine dilution.

Urine dilution	Creatinine concentration mM		Recovery (%)
1:50	13.7 ± 1.3	5.5 ± 0.2	250
1:100	9.5 ± 0.9		173
1:150	5.3 ± 0.4		96
1:200	-		-

Table S3. Recovery study in urine samples spiked at 15 mM level (n=3).

. Sample	Detected mM	Spiked mM	Recovery (%)
1	12.8	15.0	85
2	14.1	15.0	94
3	17.0	15.0	113
4	13.4	15.0	89
5	13.8	15.0	92

REFERENCES

[1] K. Spencer, "Analytical Reviews in Clinical Biochemistry: The Estimation of Creatinine," *Ann. Clin. Biochem. An Int. J. Biochem. Lab. Med.*, vol. 23, no. 1, pp. 1–25, Jan. 1986.

[2] E. P. Randviir and C. E. Banks, "Analytical methods for quantifying creatinine within biological media," *Sensors Actuators B Chem.*, vol. 183, pp. 239–252, 2013.

[3] D. B. Barr, L. C. Wilder, S. P. Caudill, A. J. Gonzalez, L. L. Needham, and J. L. Pirkle, "Urinary Creatinine Concentrations in the U.S. Population: Implications for Urinary Biologic Monitoring Measurements," *Environ. Health Perspect.*, vol. 113, no. 2, pp. 192–200, Feb. 2005.

[4] T. Arndt, "Urine-creatinine concentration as a marker of urine dilution: Reflections using a cohort of 45,000 samples," *Forensic Sci. Int.*, vol. 186, no. 1–3, pp. 48–51, Apr. 2009.

[5] E. P. Randviir, D. K. Kampouris, and C. E. Banks, "An improved electrochemical creatinine detection method via a Jaffe-based procedure," *Analyst*, vol. 138, no. 21, p. 6565, 2013.

[6] H. Yamato, M. Ohwa, and W. Wernet, "A Polypyrrole/Three-Enzyme Electrode for Creatinine Detection," *Anal. Chem.*, vol. 67, no. 17, pp. 2776–2780, Sep. 1995.

[7] S. Hanif, P. John, W. Gao, M. Saqib, L. Qi, and G. Xu, "Chemiluminescence of creatinine/H2O2/Co2+ and its application for selective creatinine detection," *Biosens. Bioelectron.*, vol. 75, pp. 347–351, Jan. 2016.

[8] R. T. Ambrose, D. F. Ketchum, and J. W. Smith, "Creatinine determined by 'high-performance' liquid chromatography.," *Clin. Chem.*, vol. 29, no. 2, pp. 256–259, Feb. 1983.

[9] E. M. K. Leung and W. Chan, "A novel reversed-phase HPLC method for the determination of urinary creatinine by pre-column derivatization with ethyl chloroformate: comparative studies with the standard Jaffé and isotope-dilution mass spectrometric assays," *Anal. Bioanal. Chem.*, vol. 406, no. 6, pp. 1807–1812, Feb. 2014.

[10] J. Jen, "Simultaneous determination of uric acid and creatinine in urine by an eco-

friendly solvent-free high performance liquid chromatographic method," *Talanta*, vol. 58, no. 4, pp. 711–717, Oct. 2002.

[11] N. A. Devenport, D. J. Blenkhorn, D. J. Weston, J. C. Reynolds, and C. S. Creaser, "Direct Determination of Urinary Creatinine by Reactive-Thermal Desorption-Extractive Electrospray-Ion Mobility-Tandem Mass Spectrometry.," *Anal. Chem.*, vol. 86, no. 1, pp. 357–361, Jan. 2014.

[12] J. Chen, Suming Chen, Li Wang, Jianing Hou, Jian He, Qing Liu, Jian'an Wang and Z. Xiong, Shaoxiang Yang, Guoqiang Nie, "2,3,4,5-Tetrakis(3′,4′-dihydroxylphenyl)thiophene: A New Matrix for the Selective Analysis of Low Molecular Weight Amines and Direct Determination of Creatinine in Urine by MALDI-TOF MS," *Anal. Chem.*, vol. 84, no. 23, pp. 10291–10297, Dec. 2012.

[13] C. Burton, H. Shi, and Y. Ma, "Simultaneous Detection of Six Urinary Pteridines and Creatinine by High-Performance Liquid Chromatography-Tandem Mass Spectrometry for Clinical Breast Cancer Detection," *Anal. Chem.*, vol. 85, no. 22, pp. 11137–11145, Nov. 2013.

[14] D. W. Bello, A. K.; Levin, A.; Tonelli, M.; Okpechi, I. G.; Feehally, J.; Harris, D.; Jindal, K.; Salako, B. L.; Rateb, A.; Osman, M. A.; Qarmi, B.; Saab, S.; Lunney, M.; Wiebe, N.; Ye, F.; Johnson, *Global Kidney Health Atlas: A report by the International Society of Nephrology on the current state of organization and structures for kidney care across the globe*. Brussels, Belgium: International Society of Nephrology, 2017.

[15] A. Delanghe, Joris R. Cobbaert, Christa Galteau, Marie-Madeleine Harmoinen, B. Jansen, Rob Kruse, Rolf Laitinen, Päivi Thienpont, Linda M. Wuyts, and M. Weykamp, Cas Panteghini, "Trueness verification of actual creatinine assays in the European market demonstrates a disappointing variability that needs substantial improvement. An international study in the framework of the EC4 creatinine standardization working group," *Clin. Chem. Lab. Med.*, vol. 46, no. 9, Jan. 2008.

[16] M. A. F. Elmosallamy, "New potentiometric sensors for creatinine," *Anal. Chim. Acta*, vol. 564, no. 2, pp. 253–257, Apr. 2006.

[17] P. Bühlmann and W. Simon, "Neutral hosts for the complexation of creatinine," *Tetrahedron*, vol. 49, no. 35, pp. 7627–7636, Aug. 1993.

[18] F. J. Guinovart, Tomàs Hernández-Alonso, Daniel Adriaenssens, Louis Blondeau, Pascal Rius, F. Xavier Ballester, Pablo Andrade, "Characterization of a new ionophore-based ion-selective electrode for the potentiometric determination of creatinine in urine," *Biosens. Bioelectron.*, vol. 87, pp. 587–592, Jan. 2017.

[19] P. Guinovart, Tomàs Hernández-Alonso, Daniel Adriaenssens, Louis Blondeau, Pascal Martínez-Belmonte, Marta Rius, F. Xavier Andrade, Francisco J. Ballester, "Recognition and Sensing of Creatinine," *Angew. Chemie Int. Ed.*, vol. 55, no. 7, pp. 2435–2440, Feb. 2016.

[20] X. X. Bakker Eric, "Ion selective optodes: from the bulk to the nanoscale," *Anal. Bioanal. Chem.*, vol. 407, no. 14, pp. 3899–3910, May 2015.

[21] E. Bakker, P. Bühlmann, and E. Pretsch, "Carrier-Based Ion-Selective Electrodes and Bulk Optodes. 1. General Characteristics," *Chem. Rev.*, vol. 97, no. 8, pp. 3083–3132, Dec. 1997.

[22] M. M. Erenas, I. de Orbe-Payá, and L. F. Capitan-Vallvey, "Surface Modified Thread-Based Microfluidic Analytical Device for Selective Potassium Analysis," *Anal. Chem.*, vol. 88, no. 10, pp. 5331–5337, May 2016.

[23] G. Mistlberger, G. A. Crespo, and E. Bakker, "Ionophore-Based Optical Sensors," *Annu. Rev. Anal. Chem.*, vol. 7, no. 1, pp. 483–512, Jun. 2014.

[24] P. Holý, W. E. Morf, K. Seller, W. Simon, and J.-P. Vigneron, "Enantioselective Optode Membranes with Enantiomer Selectivity for (R)- and (S)-l-Phenylethylammonium Ions," *Helv. Chim. Acta*, vol. 73, no. 5, pp. 1171–1181, Aug. 1990.

[25] H. He, G. Uray, and O. S. Wolfbeis, "Enantioselective optodes," *Anal. Chim. Acta*, vol. 246, no. 2, pp. 251–257, Jun. 1991.

[26] M. Choi, "Nicotine derivative optode membrane with nonactin as ionophore," *Talanta*, vol. 56, no. 6, pp. 1027–1038, Apr. 2002.

[27] M. M. F. Choi, X. J. Wu, and Y. R. Li, "Optode Membrane for Determination of Nicotine via Generation of Its Bromoethane Derivative," *Anal. Chem.*, vol. 71, no. 7, pp. 1342–1349, Apr. 1999.

[28] W. H. Chan, A. W. M. Lee, and K. Wang, "Design of a primary amine-selective

optode membrane based on a lipophilic hexaester of calix[6]arene," *Analyst*, vol. 119, no. 12, p. 2809, 1994.

[29] K. J. Cash and H. A. Clark, "In Vivo Histamine Optical Nanosensors," *Sensors*, vol. 12, no. 9, pp. 11922–11932, Aug. 2012.

[30] Y. Bell, T. Hou, Z Luo and A. Drew, M. Chapoteau, E Czech, B. Kumar, "Detection of creatinine by a designed receptor," *Science (80-.).*, vol. 269, no. 5224, pp. 671–674, Aug. 1995.

[31] J. M. Pizzolante, "Stabilized alkaline picrate reagent for Jaffe creatinine determination," 1989.

[32] A. K. Grzybowski and S. P. Datta, "31. The ionisation constant of the protonated form of creatinine," *J. Chem. Soc.*, p. 187, 1964.

[33] J. Gao, Y. Hu, S. Li, Y. Zhang, and X. Chen, "Tautomeric equilibrium of creatinine and creatininium cation in aqueous solutions explored by Raman spectroscopy and density functional theory calculations," *Chem. Phys.*, vol. 410, pp. 81–89, Jan. 2013.

[34] Y. Mi, "Lipophilic Ionic Sites for Solvent Polymeric Membrane pH Electrodes Based on 4′,5′-Dibromofluorescein Octadecylester as Electrically Charged Carrier," *J. Electrochem. Soc.*, vol. 144, no. 2, p. L27, 1997.

[35] Y. Mi, C. Green, and E. Bakker, "Polymeric Membrane pH Electrodes Based on Electrically Charged Ionophores," *Anal. Chem.*, vol. 70, no. 24, pp. 5252–5258, Dec. 1998.

[36] Y. Qin and E. Bakker, "Quantitive binding constants of H+-selective chromoionophores and anion ionophores in solvent polymeric sensing membranes," *Talanta*, vol. 58, no. 5, pp. 909–918, Nov. 2002.

[37] W. Oesch, U.; Ammann, D.; Simon, "Ion-selective membrane electrodes for clinical use," 1986.

[38] L. F. Lopez-Ruiz, Nuria Curto, Vincenzo F. Erenas, Miguel M. Benito-Lopez, Fernando Diamond, Dermot Palma, Alberto J. Capitan-Vallvey, "Smartphone-based simultaneous pH and nitrite colorimetric determination for paper microfluidic devices.," *Anal. Chem.*, vol. 86, no. 19, pp. 9554–9562, Oct. 2014.

[39] Carl A Burtis; Edward R Ashwood; David E Bruns; Norbert W Tietz, *Tietz fundamentals of clinical chemistry*. Elsevier, 2008.

[40] M. J. Pannell, E. E. Doll, N. Labban, M. B. Wayu, J. A. Pollock, and M. C. Leopold, "Versatile sarcosine and creatinine biosensing schemes utilizing layer-by-layer construction of carbon nanotube-chitosan composite films," *J. Electroanal. Chem.*, vol. 814, pp. 20–30, Apr. 2018.

[41] Y. Rao, Hanbing Lu, Zhiwei Ge, Hongwei Liu, Xin Chen, Bingyao Zou, Ping Wang, Xianxiang He, Hua Zeng, Xianyin Wang, "Electrochemical creatinine sensor based on a glassy carbon electrode modified with a molecularly imprinted polymer and a Ni@polyaniline nanocomposite," *Microchim. Acta*, vol. 184, no. 1, pp. 261–269, Jan. 2017.

[42] J. Raveendran, R. P.E., R. T., B. G. Nair, and T. G. Satheesh Babu, "Fabrication of a disposable non-enzymatic electrochemical creatinine sensor," *Sensors Actuators B Chem.*, vol. 243, pp. 589–595, May 2017.

[43] P. G. Sutariya, A. Pandya, A. Lodha, and S. K. Menon, "A simple and rapid creatinine sensing via DLS selectivity, using calix[4]arene thiol functionalized gold nanoparticles," *Talanta*, vol. 147, pp. 590–597, Jan. 2016.

[44] Y. He, X. Zhang, and H. Yu, "Gold nanoparticles-based colorimetric and visual creatinine assay," *Microchim. Acta*, vol. 182, no. 11–12, pp. 2037–2043, Aug. 2015.

[45] B. Du, Jianjun Zhu and X. Leow, Wan Ru Chen, Shi Sum, Tze Chien Peng, Xiaojun Chen, "Colorimetric Detection of Creatinine Based on Plasmonic Nanoparticles via Synergistic Coordination Chemistry," *Small*, vol. 11, no. 33, pp. 4104–4110, Sep. 2015.

[46] S. Mohammadi and G. Khayatian, "Highly selective and sensitive photometric creatinine assay using silver nanoparticles," *Microchim. Acta*, vol. 182, no. 7–8, pp. 1379–1386, Jun. 2015.

[47] S. Wei, Fang Cheng, E. F. Korin, Yael Reed, and J. Gjertson, David Ho, Chih-ming Gritsch, H. Albin Veale, "Serum Creatinine Detection by a Conducting-Polymer-Based Electrochemical Sensor To Identify Allograft Dysfunction," *Anal. Chem.*, vol. 84, no. 18, pp. 7933–7937, Sep. 2012.

ÍNDICE DE FIGURAS

Capítulo 6

Figure 1. Absorption spectra of PVC-NPOE membranes containing 4′,5′-dibromofluorescein octadecyl ester (ETH7075). A: Membrane with ionophore (3.2 wt %) and KTFPB (1.5 wt %) after equilibration with 0.1 M HCl; B: Same membrane after equilibration with 50 mM creatinine in pH 3.8 buffer; C: Membrane with ionophore (3.2 wt %) and TDMAC (0.9 wt %) after equilibration with 0.1 M NaOH. 295
Figure 2. Theoretical model and experimental data (n = 3) obtained using different molar ratios of L:HI:R^-: 3:1:1 (red data), 3:2:1 (green data), and 3:3:1 (blue data). 297
Figure 3. Calibration function of creatinine sensing membrane (n = 3). 299

Figure S1. Calix[4]pyrrole ionophore structure..... 302
Figure S2. Experimental data and theoretical model of sensing membrane for 3:1:1 L:I:R ratio. 303
Figure S3. Experimental data and theoretical model of sensing membrane for 3:1:1.25 L:I:R ratio. 303
Figure S4. Experimental data and theoretical model of sensing membrane for 3:1:1.5 L:I:R ratio. 304
Figure S5. Experimental data and theoretical model of sensing membrane for 3:1:1.75 L:I:R ratio. 304
Figure S6. Theoretical influence of ionophore ratio increase on sensing membrane response. Membranes prepared with 3:1:1.5, 3:2:1:1,5, 3.6:1:1.5, 4:1:1,5 and 5:1:1.5 (L:HI:R^-) were tested against 10^{-3} M of creatinine obtaining 1- α_{eff} values of 0.485, 0.470, 0.440, 0.415 and 0.368. 305
Figure S7. Variation of membrane thickness along the diameter of the circular sensing membrane measured by contact profilometry. 305
Figure S8. pH influence on the absorbance of sensing membranes. A: With creatinine (0.1 mM, blue dots); B: Without creatinine (red triangles); C: Evolution of creatininium fraction with pH (green line). 306
Figure S9. Variation of the absorbance (455 nm) over time for the creatinine sensor at different analyte concentrations: $1 \cdot 10^{-3}$ M (green line), $1 \cdot 10^{-4}$ M (blue line) and $1 \cdot 10^{-5}$ M (red line). 307

Figure S10. Data obtained calibrating the sensing membrane against creatinine and the interferences considered (j). Creatinine (red dots), Na^+ (blue dots), K^+ (green dots), NH_4^+ (purple dots) and creatine (orange dots). 308

ÍNDICE DE TABLAS

Capítulo 6

Table 1. Analytical Parameters of the Sensing Membrane for Creatinine Determination. 299

Table 2. K_{exch} selectivity as Log $K_{creatinine,j}$ calculated using the separated solution method and $P_{creatinine,j}$ required for the interferents present in urine at different tolerable errors (1, 10, and 100%). 300

Table 3. Determination of creatinine in urine samples using the sensor and reference methods (n = 3). 301

Table S1. Comparison of the developed method with previous published creatinine methods. 309

Table S2. Creatinine value predicted according to urine dilution. 309

Table S3. Recovery study in urine samples spiked at 15 mM level (n=3). 309

Capítulo 7

LUMINESCENT CALCIUM PHOSPHATE NANOPARTICLES DOPED WITH EUROPIUM FOR THE QUANTIFICATION OF CREATININE

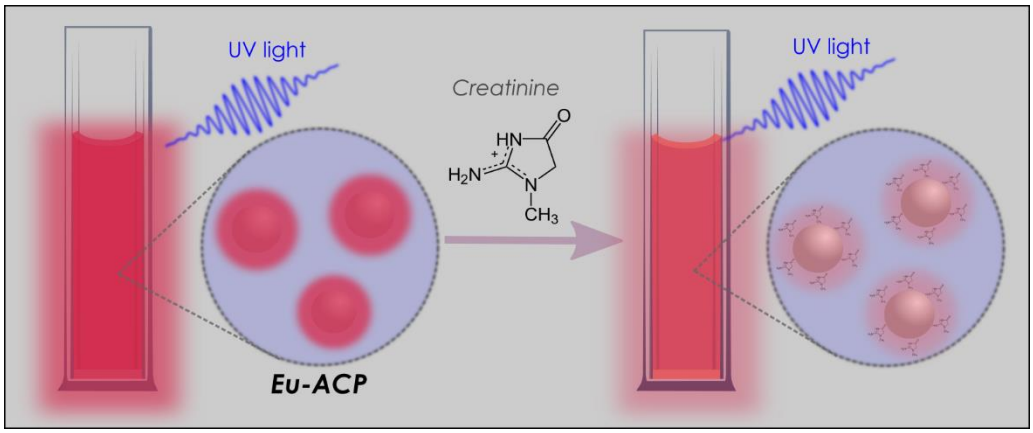

Submitted to Colloids and Surface B

CAPÍTULO 7: LUMINESCENT CALCIUM PHOSPHATE NANOPARTICLES DOPED WITH EUROPIUM FOR THE QUANTIFICATION OF CREATININE

Inmaculada Ortiz-Gómez,[a,c] Gloria B. Ramírez-Rodríguez,[b,c] Luis F. Capitán-Vallvey,[a,c] Alfonso Salinas-Castillo[a,c] and José M. Delgado-López[b,c]

[a]Department of Analytical Chemistry, University of Granada, Faculty of Science, Av. Fuente Nueva, s/n, 18071 Granada, Spain.

[b]Department of Inorganic Chemistry, University of Granada, Faculty of Science, Av. Fuente Nueva, s/n, 18071 Granada, Spain.

[c]Unit of Excellence in Chemistry applied to Biomedicine and the Environment of the University of Granada, Spain.

Planteamiento

Como se ha puesto de manifiesto en el capítulo anterior, el desarrollo de nuevos métodos que permitan la detección y cuantificación de creatinina en muestras de orina de forma rápida, con una alta selectividad y a un bajo coste presenta una gran importancia. Existen numerosas publicaciones científicas en las que se pone de manifiesto el desarrollo de métodos ópticos para la determinación de creatinina [1]–[5]. La mayoría de las publicaciones se centran en métodos colorimétricos basados en el método de Jaffé o métodos enzimáticos para la determinación de creatinina. Sin embargo, como se ha venido comentando anteriormente, estos métodos de determinación pueden presentar ciertos inconvenientes como una baja selectividad en el caso de la reacción de Jaffé y un elevado precio en el análisis por el empleo de enzimas. Por todo ello, surge la necesidad de investigar sobre nuevos métodos de determinación de forma que se pueda llevar a cabo una rápida, selectiva y de bajo coste determinación de creatinina. En este sentido, los métodos de análisis basados en luminiscencia satisfacen estas necesidades debido a la alta selectividad que presentan, así como la simplicidad y reducido coste que supone la realización de estos ensayos. Existen numerosas publicaciones científicas en las que se propone el empleo de nanomateriales funcionalizados con propiedades luminiscentes para la detección de creatinina [6], [7]. Normalmente, se trata de mecanismos de

detección basados en la atenuación de las propiedades lumínicas del nanomaterial como consecuencia de la aparición de creatinina en la muestra. No obstante, el empleo de nanomateriales como nanopartículas funcionalizadas en la determinación de creatinina puede conllevar algunos inconvenientes como la baja estabilidad química de las nanopartículas dificultando por tanto su uso en aplicaciones clínicas. Por todo ello, en este Capítulo proponemos un nuevo método luminiscente basado en la utilización de nanopartículas de fosfato de calcio dopadas con europio para la determinación de creatinina. Se trata de una detección fosforimétrica por perdida de las propiedades lumínicas de las nanopartículas en presencia de creatinina. Este método de determinación permite una detección rápida, selectiva, y a un bajo coste de creatinina en muestras de orina. Además, el empleo de nanopartículas de fosfato de calcio dopadas con europio presenta una buena estabilidad química y coloidal adecuada para su empleo en el desarrollo de sensores químicos.

Objetivo

El séptimo capítulo de esta Memoria se centra en el desarrollo de un nuevo método luminiscente para la determinación de creatinina en orina basado en el empleo de nanopartículas de hidroxiapatito de calcio dopadas con europio. Teniendo en cuenta este objetivo se llevó a cabo la síntesis y caracterización estructural de las nanopartículas de fosfato de calcio dopadas con europio. Además, se llevó a cabo un estudio para conocer la citotoxicidad de las nanopartículas. Seguidamente, evaluó las propiedades luminiscentes de las nanopartículas y se caracterizó analíticamente el sistema para la detección de creatinina. También, se evaluó la fotoluminiscencia de las nanopartículas, así como las variables influyentes en la determinación de creatinina. Por último, se comprobó la selectividad del método desarrollado frente a otras sustancias que podrían actuar como interferentes en esta determinación y se llevó a cabo la determinación de creatinina en muestras de orina.

En resumen, los objetivos de este capítulo son:

1. Síntesis y caracterización estructural de nanopartículas de fosfato de calcio dopadas con europio.
2. Estudio de la citotoxicidad de las nanopartículas de fosfato de calcio dopadas con europio.
3. Evaluación de las propiedades luminiscentes de las nanopartículas de fosfato de calcio dopadas con europio.
4. Optimización de las variables influyentes en la determinación de creatinina.
5. Caracterización analítica del sistema.
6. Estudio de la selectividad del método de determinación.
7. Determinación de creatinina en muestras de orina.

LUMINESCENT CALCIUM PHOSPHATE NANOPARTICLES DOPED WITH EUROPIUM FOR THE QUANTIFICATION OF CREATININE

Abstract

The determination of creatinine levels is essential for the detection of renal and muscular dysfunction. Luminescent nanoparticles are emerging as fast, cheap and highly selective sensors for the detection and quantification of creatinine. Nevertheless, current nanosensors only have a short shelf life due to their poor chemical and colloidal stability, which limits their clinical functionality. In this work, we have developed a highly stable, selective and sensitive nanosensor based on europium-doped, amorphous calcium phosphate nanoparticles (Eu-ACP) for the phosphorimetric determination of creatinine. The colloidal stability of Eu-ACP nanoparticles in aqueous solutions was optimised to ensure a constant phosphorescent signal after up to 4 months in storage. The phosphorescence of Eu-ACP decreased linearly with the creatinine concentration over the range of 1-120 μM (R^2 = 0.995). This concentration–response relationship was used to determine creatinine levels in real urine samples resulting in good recovery percentages. Significantly, selectivity assays indicated that none of the potential interfering species provoked discernible changes in phosphorescence intensity. The Eu-ACP nanoparticles demonstrated good cytocompatibility against a mouse melanoma cell line, which paves the way for their potential clinical application.

Keywords: Nanoparticles · Europium · Calcium phosphate · Luminescent · Creatinine sensor

1. Introduction

Creatinine, a waste product of muscle metabolism, is released into the bloodstream, undergoes glomerular filtration in the kidneys and is eventually excreted in the urine. Creatinine blood serum or urine concentration is indeed one of the most important and most requested clinical analyses when studying kidney function [8]. Generally,

abnormally high creatinine levels are often a clinical sign of severe kidney dysfunction, thyroid dysfunction or a muscle disorder [8]. Rapid, highly sensitive and selective analytical tests are therefore required for the quantitative determination of creatinine in body fluids in order to monitor the evolution of patients suffering from kidney disease [9]. The most extensively used technique for creatinine quantification in clinical laboratories is a colorimetric method based on the Jaffe reaction. This is an inexpensive and straightforward method based on the reaction between creatinine and picrate in a basic medium to form an orange product [8], [10]. However, this colorimetric method is prone to error associated with the sample colour and common interferences such as numerous metabolites and drugs found in biological samples [8], [10]. On the other hand, highly sensitive and selective conventional methods for creatinine determination such as chromatography, mass spectrometry, surface-enhanced Raman scattering (SERS), IR spectroscopy, potentiometry and electrochemical techniques are time-consuming and commonly require relatively complex sample pre-treatment and medium/high-cost instrumental set-ups [11], [12].

These limitations can be solved with the use of luminescent chemo-/biosensors, which commonly offer high specificity, sensitivity, easy sample preparation, fast response time and robust analyte detection [6], [13]. In fact, creatinine determination through luminescent techniques is an emerging research area [6], [13]–[17]. Quantum dots [14]–[16], copper nanoclusters [13] and Pd-naphthalimide complexes [6], [17] have been used to detect creatinine with results confirming the different materials' high sensitivity and selectivity. Nonetheless, these nanodevices still present some inherent limitations [18], [19] such as poor photochemical stability and photobleaching thresholds, high toxicity or poor colloidal stability, which hamper their implementation in clinical applications.

Photoluminescent inorganic nanoparticles such as lanthanide-based nanophosphors exhibit a long luminescence lifetime, high luminescence quantum yield, sharp emission bands, colour tuning and good resistance to photobleaching [19]. Among phosphate hosts, biomimetic calcium phosphate nanoparticles similar to those found in calcified tissues (e.g., bone and teeth) are additionally highly cytocompatible and biodegradable [20]–[22]. Owing to this, europium-doped hydroxyapatite nanoparticles (Eu-HA) have been used as fluorescence nanoplatforms in diagnostics (imaging and biosensors) [23]–[29] and theragnostic [26]–[28], [30]. However, the doping of amorphous calcium phosphate

(ACP), the precursor mineral phase of apatite nanocrystals in bone [31], has not received as much attention [32], [33], although it is known that ACP has a greater capacity to incorporate foreign ions than HA [34]. In the present work, we have doped amorphous calcium phosphate with europium to yield non-toxic, luminescent nanoparticles (Eu-ACP). We have also studied the nanosystem's photochemical and colloidal stability upon storage in aqueous solutions. Finally, we present the evaluation of the system's analytical performance (selectivity and sensitivity) in the detection and quantification of creatinine, including in real urine samples.

2. Experimental

2.1. Chemicals and reagents

Calcium chloride dihydrate ($CaCl_2 \cdot 2H_2O$, ≥99.0%), potassium citrate ($K_3(C_6H5O_7) \cdot 2H_2O$, ≥ 99.0% pure), potassium phosphate dibasic anhydrous (K_2HPO_4, ≥99.0% pure), potassium hydroxide (KOH, ≥99.0%), sodium hydroxide (NaOH, ≥97.0%), sodium chloride (NaCl, ≥99.5%), potassium chloride (KCl, ≥99.0%), ferrous sulphate ($FeSO_4$, ≥99.0%), europium chloride hexahydrate ($EuCl_3 \cdot 6H_2O$, ≥99.0% pure), creatinine ($C_4H_7N_3O$, ≥99.0%), glucose ($C_6H_{12}O_6$, ≥99.5%), ascorbic acid ($C_6H_8O_6$, ≥99.0%), urea (CH_4N_2O, ≥99.0%), and glutamic acid ($C_5H_9NO_4$, ≥99.0%) were purchased from Sigma Aldrich. All the solutions were prepared with ultrapure water (0.22 µS/cm, 25 °C, MilliQ©, Millipore). The colloidal stability of the nanoparticles was also studied in citric/citrate buffered solutions (0.1 M) at pH 7.4.

2.2. Synthesis of europium-doped amorphous calcium phosphate

The synthesis of Eu-ACP was carried out by pouring 100 mL of an aqueous solution containing calcium, citrate and Eu(III) ions (200 mM $CaCl_2$ + 200 mM $K_3(C_6H_5O_7)$ + 10 mM $EuCl_3$) on a phosphate-containing solution of equal volume (120 mM K_2HPO_4, pH = 12, adjusted with KOH). After mixing during 5 minutes at room temperature, the precipitate was collected by centrifugation (5000 rpm), washed three times with ultrapure water and stored at 4 °C. Non-doped nanoparticles (hereafter referred to as ACP) were

prepared through the same protocol without adding Eu^{3+} ions into the calcium-containing solution.

2.3. Characterisation of the nanoparticles

X-ray powder diffraction (XRPD) patterns were collected on a Bruker D2 phaser diffractometer (Bruker, Karlsruhe, Germany) equipped with an energy dispersive LYNXEYE XE-T detector. Measurements were carried out using Cu Kα radiation (λ = 1.5406 Å) generated at 30 kV and 10 mA. Patterns were recorded in the 2θ range with a step size (2θ) of 0.02. Fourier transform infrared (FTIR) spectra were collected on a Bruker Tensor 27 spectrometer under attenuated total reflection (ATR) configuration with spectral resolution of 2 cm^{-1} by accumulating 25 scans.

The morphology of Eu-ACP nanoparticles was evaluated with a transmission electron microscope (TEM, LIBRA 120 PLUS, Carl Zeiss SMT) and a high-resolution scanning electron microscope (FESEM; Zeiss SUPRA40VP) of the Centre for Scientific Instrumentation (University of Granada, CIC-UGR). For TEM observations, a copper grid covered with thin amorphous carbon films was passed through nanoparticle suspension several times and then let dry in a filter paper. Dry powdered sample was deposited on aluminium stubs using a carbon tape for SEM analysis.

High-resolution Transmission Electron Microscopy (HRTEM) images and compositional analysis (Ca, P and Eu) of selected areas were acquired with a 300 kV FEI TITAN G2 60–300 microscope equipped with a HAADF detector and a SuperR-X Energy dispersive X-ray (EDS) detector (Thermo Fisher Scientific, Waltham, MA, USA) of the Centre for Scientific Instrumentation, University of Granada (CIC-UGR). Images were analyzed with the Velox software (Thermo Fisher Scientific, Waltham, MA, USA). Nanoparticles were dispersed in pure ethanol and some drops of the slurry were deposited on 200-mesh copper grids with lacey carbon films.

X-ray Photoelectron Spectroscopy (XPS) analyses were performed on a Kratos Axis Ultra-DLD, equipped with a focused monochromatic Al Kα X-ray irradiation source.
The chemical composition of ACP and Eu-ACP nanoparticles (Ca, P and Eu weight percentage, %wt.) was analysed by inductively coupled plasma optical emission

spectrometry (ICP-OES, Perkin-Elmer® Optima™ 8300, CIC-UGR). The sample (20 mg) was totally dissolved in 2 mL of ultrapure nitric acid and then diluted up to 100 mL with Milli-Q water. The emission wavelength for the quantification of each element was 317.93 nm (Ca), 213.62 nm (P) and 381,967 nm (Eu). Three replicates were analysed and data are expressed as mean ± standard deviation.

Hydrodynamic diameter distributions of Eu-ACP in water and citrate buffer were measured by dynamic light scattering (DLS) with a Zetasizer Nano ZS (Malvern Instruments) with a 630 nm laser and a detection angle of 90°. For each sample, we performed three repetitions of 10 runs, 30 s each.

The cytotoxicity of Eu-ACP nanoparticle suspension was evaluated against mouse melanoma cell line (B16-F10, CRL-6322 from the Banco de Células, CIC-UGR). B16-F10 cells were grown in Dulbecco's Modified Eagle Medium (DMEM) supplemented with 2 mM glutamine and 10% Foetal Bovine Serum (FBS). After reaching full confluence, cells were detached from culture flasks by trypsinization, centrifuged and resuspended. The cells were seeded at a density of 10^4 cells/well in a 96 flat transparent well. After 48 hours of pre-incubation (37 °C with 5% CO_2), the cell culture medium was replaced by serial dilutions (10, 25, 50, 100, 150 and 250 mg/L) of the Eu-ACP nanoparticles in cell culture media. Cells cultured in media without nanoparticles were used as control. Cell viability after 48 hours of culture was determined using colorimetric MTS assays (CellTiter 96® AQ_{ueous} One Solution Cell Proliferation Assay, Promega), following the manufacturer's instructions. 20 µL of MTS reagent were added to each well and incubated at 37 ºC for 4 hours. Then, the absorbance at 490 nm was measured with a spectrophotometer (Infinite® 200 PRO NanoQuant, CIC-UGR). The absorbance at 490 nm is proportional to the number of living cells.

2.4. Luminescence measurements

Photo-luminescence (PL) emission spectra of Eu-ACP was recorded on a Varian Cary Eclipse fluorescence spectrophotometer (Palo Alto, CA, USA) in the range 200–800 nm with xenon lamp as excitation source. PL of Eu-ACP in aqueous media was measured using the following conditions: λ_{ex}= 240 nm and λ_{em}= 616 nm, gate time (t_g) 5 ms and delay time (t_d) 0.2 ms, the photomultiplier voltage was set at 800 V and excitation and

emission slits of 10 nm were used. All experiments were performed in a quartz cuvette with a path length of 10 mm and volume of 3500 µL (Hellma).

The release of Eu^{3+} from the nanoparticles to the media was measured by PL at scheduled times (1, 2, 3, 4 weeks and 4 months) to determine the long-term stability of the doping. To this aim, the nanoparticles were collected by centrifugation (13500 rpm, 15 min) at the scheduled time and the PL of the supernatant, filtered with a 0.1 µm MF-Millipore MCE membrane (MILLEX®GS), was measured. The PL intensity was related to Eu3+ concentration by means of a calibration linear plot previously determined at the following Eu^{3+} concentrations 0.25, 0.5, 1, 2.5 and 5 ppm in citrate buffer.

2.5. Creatinine quantification

Detection and quantification of creatinine was performed at room temperature. 5.0 µL of creatinine at different concentrations was added to the Eu-ACP suspension in citrate buffer. After incubating for 1 minute, PL intensity was measured at 616 nm under excitation at 240 nm. A calibration curve was obtained by measuring the PL intensity of 10 creatinine standards (3 replicates each). Creatinine was also quantified in human urine samples from three healthy volunteers. Briefly, 5.0 µL of filtered (0.22 µm, Millipore) urine was mixed with 2.5 mL of Eu-ACP in citrate buffer (0.1M, pH7.4) and creatinine at a final concentration of 0, 40 and 100 µM. The PL intensity of the mixture was measured after 1 min of incubation at room temperature.

3. Results and discussion

3.1. Synthesis and detailed characterisation of eu-acp

Calcium phosphate nanoparticles, mimicking composition and morphology of the amorphous precursor phase found in bone, and thus with excellent cyto-compatibility and biodegradability [20]–[22], were doped with Eu^{3+} ions to obtain non-toxic, luminescent nanoparticles. To this aim, we adapted a previous bio-inspired synthesis [35] of amorphous calcium phosphate in the presence of citrate, an important component of bone mineral [36] to incorporate Eu^{3+} ions. XRD patterns (Fig. 1a) of non-doped nanoparticles show the characteristic broad band centred at approximately 30º (2θ) in the X-ray powder

diffraction pattern (Fig. 1a) [37]. The addition of Eu3+ did not affect the pattern. Importantly, the absence of (sharp) Bragg peaks ruled out the precipitation of other crystalline phases, including europium chloride, europium oxide(s) or europium phosphate. The FTIR-ATR spectra of non-doped ACP also display the characteristic, poorly defined phosphate vibrational bands of amorphous calcium phosphate with the additional peaks corresponding to citrate and water [38], [39] (Fig. 1b). These vibrational features were neither affected by the addition of Eu (III) ions (Figs. 1b).

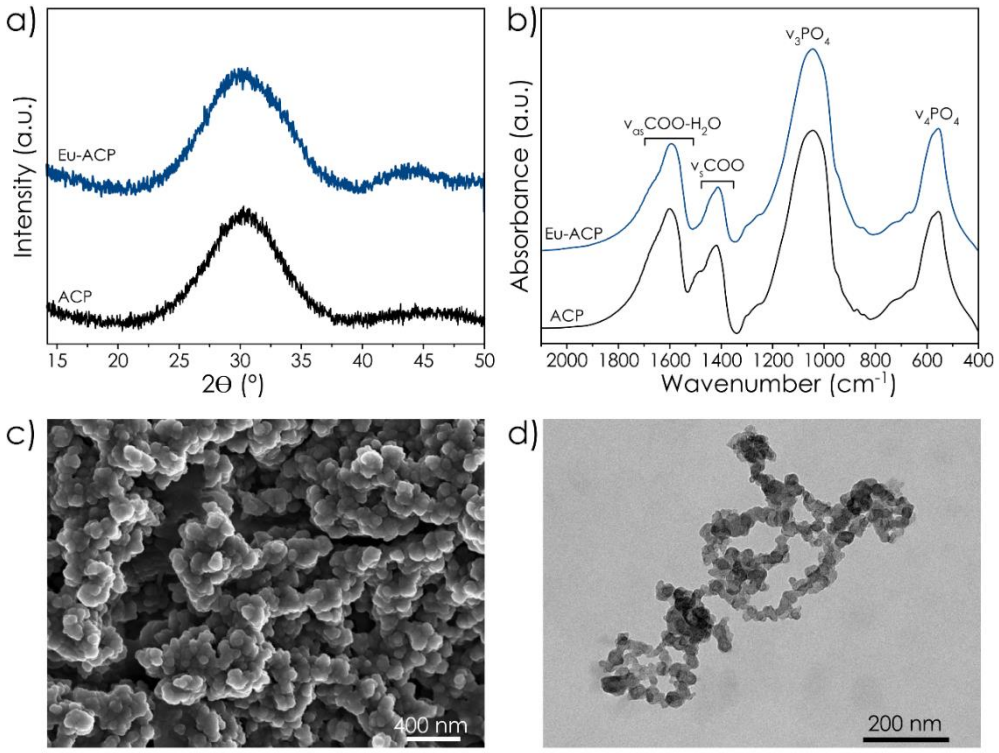

Figure 19. (a) XRD patterns, (b) FTIR spectra, (c) SEM and (d) TEM images of dried europium-doped amorphous calcium phosphate (Eu-ACP) nanoparticles.

The morphology of the Eu-doped nanoparticles was analysed by SEM and TEM (Figs. 1c-d). Eu-ACP nanoparticles exhibited the typically round morphology of amorphous calcium phosphate nanoparticles with diameters ranging between 50 and 100 nm. Different morphologies associated with other calcium phosphate phase or other Eu-containing compounds were not observed, which is in line with XRD results.

Table 13. Chemical composition (analysed by ICP-OES) of Eu-ACP and ACP nanoparticles. Data are expressed as mean ± standard deviation.

	Ca (wt.%)	P (wt.%)	Eu (wt.%)	Ca/P (Molar ratio)
Eu-ACP	27.9 ± 1.7	13.4 ± 0.9	5.6 ± 0.4	1.61 ± 0.01
ACP	33.9 ± 1.5	16.2 ± 0.7	-	1.61 ± 0.02

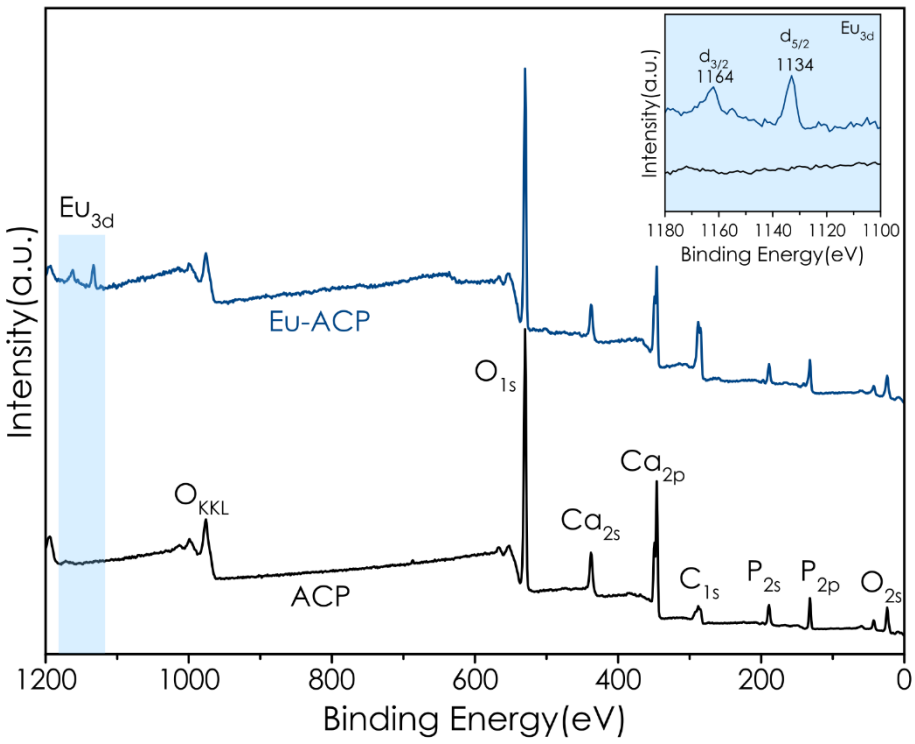

Figure 20. XPS spectra of ACP and Eu-ACP with signals of O (1s), Ca (2s, 2p), and P (2s, 2p) of ACP. The inset shows the Eu 3d region of Eu-ACP with the 3d doublets, that is $d_{3/2}$ and $d_{5/2}$, resulting from spin-orbit coupling and appearing at binding energies of 1134 eV and 1164 eV, respectively.

Table 1 summarizes the chemical composition (Ca, P and Eu) of ACP and Eu-ACP nanoparticles, as extracted by ICP-OES. The weight percentage of Eu was 5.6 wt.%. Importantly, the Ca/P ratio was not affected after the doping, maintaining a value of 1.61, which falls within range typically found for amorphous calcium phosphate (1.33-1.67) [37]. We used XPS to confirm the precipitation of Eu-doped ACP as the unique phase. The XPS spectra of ACP and EuACP were very similar (Figure 2). They show the presence of the main atomic elements of ACP: O (1s), Ca (2s, 2p) and P (2s, 2p), in agreement with the XPS spectra of ACP reported elsewhere [40]. The peak of C 1s is due

to adsorbed citrate ions. The spectrum of Eu-ACP additionally exhibited a doublet at 1164 eV and 1134 eV resulting from Eu 3d spin-orbit coupling, *i.e.*, $d_{3/2}$ and $d_{5/2}$ [41]. Additionally, chemical maps (Figure 3) obtained by EDS indicated that Eu (magenta) is homogenously distributed within the ACP nanoparticles, along with Ca (blue) and P (green). These results confirm the effective doping of ACP with Eu^{3+} ions. From XPS data, we can also exclude the presence of Eu^{2+} since the $d_{3/2}$ and $d_{5/2}$ doublet, typically appearing at 1155 eV and 1125 eV, respectively, was not observed (Figure 2). It is important to highlight that Eu incorporation did not introduce toxicity to the nanoparticles. Indeed, cell viability of B16-F10 murine melanoma cells was not affected by the addition of Eu-ACP at 250 mg/L, confirming the high cytocompatibility of the nanoparticles even after the Eu doping.

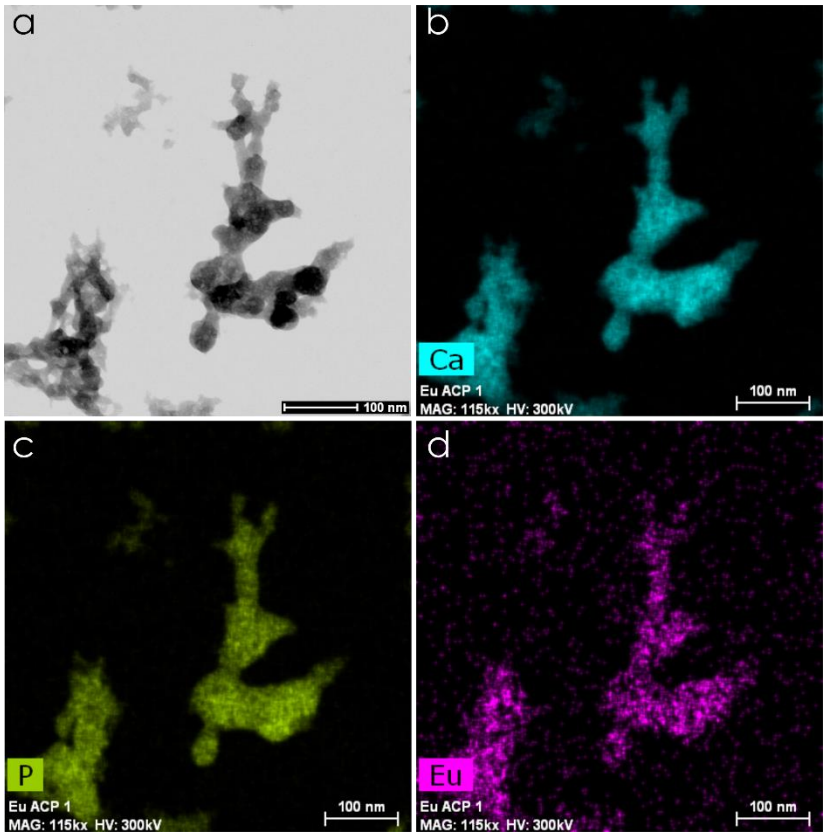

Figure 21. TEM micrograph of Eu-ACP (a) and corresponding EDS maps with Ca (b), P (c), and Eu (d) distributions.

3.2. Optimizing the photo-luminescence emission of Eu-ACP

Europium doping confers the nanoparticles with the capability of emitting persistent red light under UV excitation (240 nm). Concretely, the emission spectrum of Eu-ACP in water under excitation at 240 nm exhibited four line-like emission bands at about 593, 616, 653 and 700 nm (Fig. 3a). The most intense peak at 616 nm corresponds to the 5D0 → 7F2 transition within Eu^{3+} ions, while other peaks at 593, 653 and 700 nm correspond to 5D0 → 7F1, 5D0 → 7F3 and 5D0 → 7F4 transitions, respectively [42].

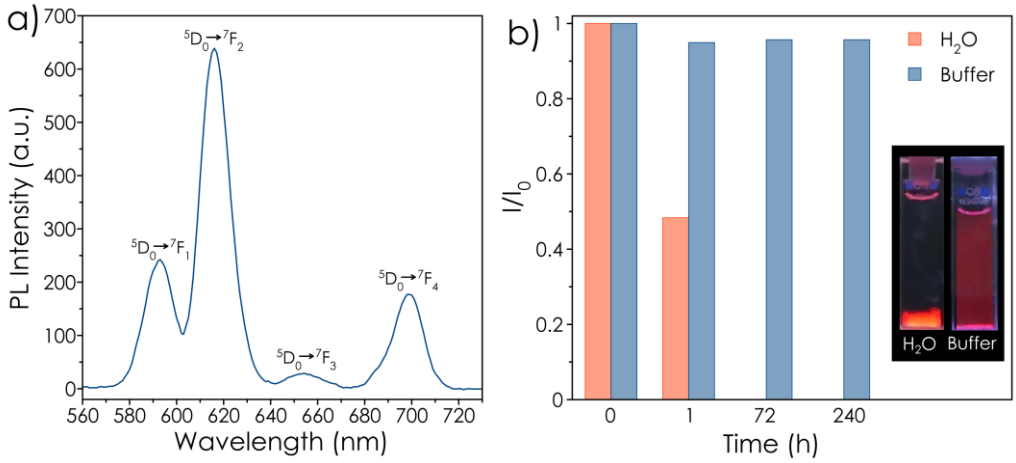

Figure 22. (a) PL emission (λexc =240 nm) spectra of Eu-ACP nanoparticle in ultrapure water (250 mg/L) just after preparation. (b) Temporal evolution of normalized luminescence intensity of Eu-ACP (250 mg/L) in ultrapure water (orange vertical bars) and citrate buffer (blue vertical bars). I0 and I refer, respectively, to the intensity of the emission peak at 616 nm at t0 (just after preparation) and at scheduled times. The inset shows PL photographs (under UV irradiation at 265 nm) of Eu-ACP in water and citrate buffer (250 mg/L), collected 240 hours after the preparation.

The long-term stability of this PL signal is crucial to ensure the success of the nano-device for clinical applications [43] and one of the main limitation of current luminescent sensors (Table 3) for creatinine quantification [13], [13]. Therefore, the evolution of the PL intensity of Eu-ACP in water was monitored. The normalized PL intensity of the most intense peak at 616 nm (I/I0, where I0 is the PL intensity just after preparation) drastically decreased after 1 hour of preparation, being practically negligible after 72 hours (Fig. 3b, orange vertical bars). The sedimentation of large aggregates of Eu-ACP (red under UV irradiation, inset of Fig. 3b) was evident after few hours. Indeed, DLS measurements confirm the formation of micrometric aggregates in few minutes in water (Fig. 4). The poor colloidal stability of lanthanide-doped calcium phosphate nanoparticles in aqueous

solutions is indeed the main limiting factor for its use as fluorescent probe [44]. Surface functionalization with organic moieties such as polyacrilic acid (PAA), [45] DNA [46] and 2-aminoethylphosphonic acid (AEP) [47], [48] has been demonstrated to maintain the colloidal stability of lanthanide-doped HA in aqueous media. Citrate ions have been also proposed as an ideal dispersant of HA nanocarriers for applications in drug delivery [49]–[51]. Following this strategy, we achieved stable emission at 616 nm from Eu-ACP nanoparticles in citrate buffer (0.1 M, pH7.4) up to 240 hours (Fig. 3b), which confirm the positive effect of adding citrate to improve the colloidal stability of the nanoparticles. DLS measurements in this media showed a broad size distribution with mean average around 100 nm (Fig. 4).

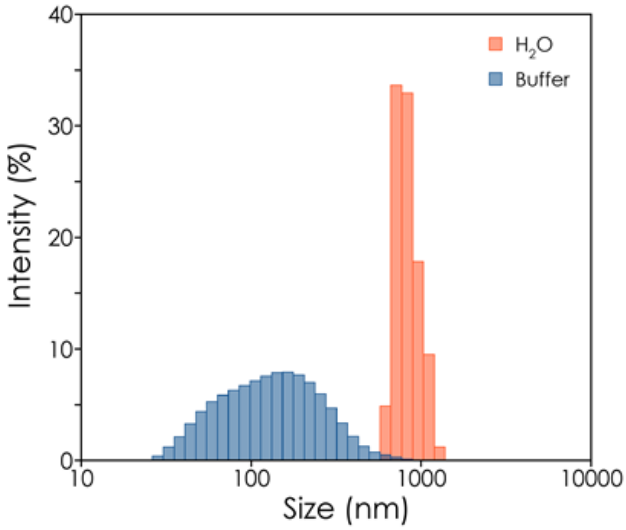

Figure 23. Size distribution of Eu-ACP nanoparticles (250 mg/L) in water (orange bars) and citrate buffer (blue bars) as obtained from DLS.

Nanoparticle concentration is another important factor for consideration when trying to find the ideal balance between PL intensity and PL signal stability. A high nanoparticle concentration (1000 mg/L) results in an abrupt decay of the PL signal over time (Fig. 6a) due to the formation of large aggregates which sediment at this concentration, despite being suspended in a citrate buffer solution. The PL signal at a Eu-ACP concentration of 500 mg/L is constant for up to 4 weeks (Fig. 6a). The best performance was achieved for Eu-ACP at 250 mg/L, for which we observed a constant PL signal even after 4 months (124 days) of storage at 4 °C (Fig. 6a), outstripping the short-term storage capacity of current luminescence sensors for creatinine determination [13], [15]. During this time, we

also evaluated the stability of the doping by measuring the release of Eu^{3+} to the media. We found that 2.3 wt.% of total europium of Eu-ACP was released after 1 week. The released Eu^{3+} slightly increased up to 3.6 wt.% after 4 months of storage. This means that nanoparticles retained most of the europium (< 96 wt.%) even after a long storage time

Since ionic strength can have a strong influence on the emission of luminophores [52], we measured the PL intensity of Eu-ACP suspensions (250 mg/L in citrate buffer) at increasing NaCl concentrations (Fig. 6b). The addition of NaCl, up to a final concentration of 1 M, did not affect emission intensity.

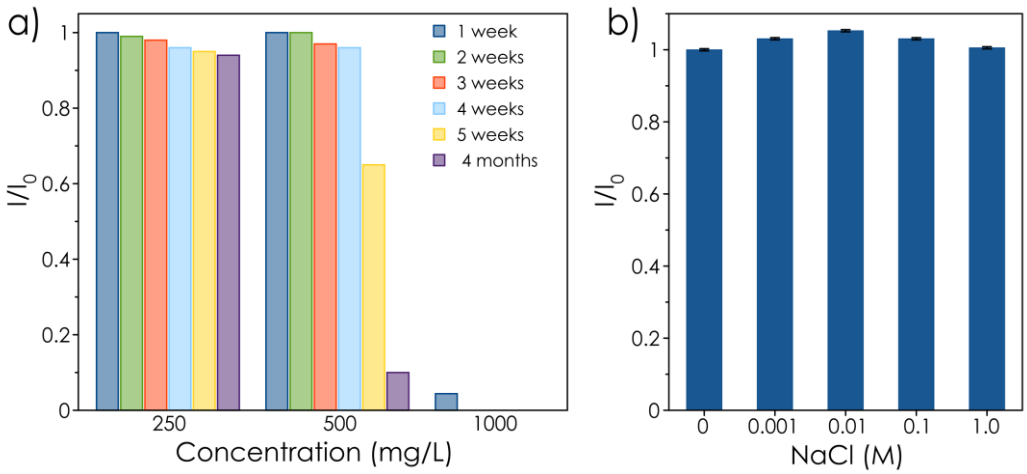

Figure 24. (a) Temporal evolution of normalized luminescence intensity of Eu-ACP nanoparticle in citrate buffer at different concentrations (250, 500 and 1000 mg/L). I0 and I refer, respectively, to the PL intensity at t0 (just after preparation) and at scheduled times. (b) Effect of ionic strength on PL intensity of Eu-ACP at 250 mg/L in citrate buffer. I0 and I correspond to the PL intensity in the absence and presence of NaCl, respectively.

3.3. Analytical performance of Eu-ACP

We evaluated the sensitivity of the Eu-ACP nanoparticles with respect to creatinine by photoluminescence spectroscopy. Figure 7a shows the emission spectra for Eu-ACP as a function of creatinine concentration. The emission wavelengths were not affected by creatinine concentration, but PL intensity decreased steadily and linearly as creatinine concentration increased (Fig. 7b). Creatinine absorbs photons of the excitation beam (240 nm), acting as an internal filter, which results in a concentration-responsive quenching of the PL emission from the nanoparticles. We indeed observed a good linear relationship

with a R^2 coefficient of 0.995 between the normalised luminescence intensity (I_0/I) and creatinine concentration in the range of 1-120 µM (Fig. 7b). This linear PL intensity–concentration dependence can be used to determine important analytical parameters (Table 2). The limits of detection (LOD) and quantification (LOQ) of Eu-ACP for creatinine were 0.07 and 0.22 µM, respectively, as determined in accordance with the ± 3σ criteria. Measurement reproducibility was evaluated at two different creatinine concentrations, *i.e.*, 40 and 100 µM, and revealed good coefficients of variation (1.8% and 1.2%, respectively). The linear range and limit of detection are in the same range of other luminescence creatinine sensors (Table 3). However, PL signal of our nanodevice is stable for very long storage periods of up to 4 months (124 days, Table 3).

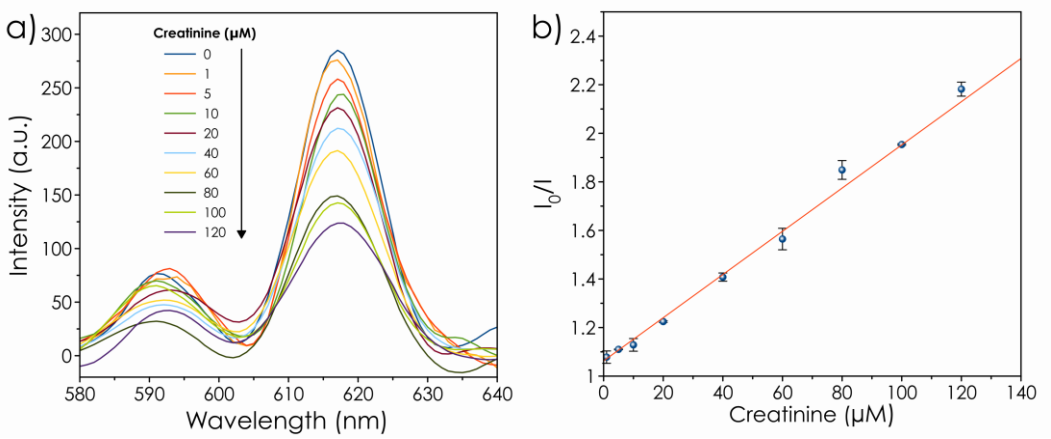

Figure 25. (a) Emission spectral response of Eu-ACP in the absence and presence of creatinine at increasing concentrations (1, 5, 10 20, 40, 60, 80, 100 and 120 µM). (b) Plot of normalized luminescence response of Eu-ACP as a function of creatinine concentration. I0 and I are the PL intensity in the absence and in the presence of creatinine, respectively. The solid line represents the linear fitting of the experimental data (symbols). S.E.M. are shown as error bars.

Table 14. Analytical characterization of Eu-ACP for creatinine determination.

Analytical parameter	Value
Measurement range (µM)	1-120
Slope (μM^{-1})	0.008
Intercept (a.u.)	1.062
LOD (µM)	0.07
LOQ (µM)	0.22
Precision (%) 40 µM	1.8
Precision (%) 100 µM	1.2

Table 15. Comparison of analytical parameters of several creatinine luminescent sensors.

Sensor	Measurement Range (µM)	LOD (µM)	Storage Time (days)	Ref.
TGA capped ZnS:Mn/ZnS quantum dots	0.07-3.4	0.007	5	[53]
Naphthalimide-based fluorescence light-up probe	1-10	0.3	N.M.	[6]
Gold-Quantum clusters stabilized with gluten	20-520	0.002	N.M	[16]
BSA-modified copper nanoclusters	5-60	0.050	18	[13]
Ethoxy ethanol-naphthalimide-Pd	1-70	0.16	N.M.	[54]
Eu-ACP	1-120	0.07	124	This work

3.4. Selectivity assay

One of the major challenges in the determination of creatinine is the selectivity required in the presence of interfering ions and organic species commonly found in biological samples [55]. To evaluate whether this approach is highly specific for creatinine, emission spectra of Eu-ACP suspension in citrate buffer were recorded in the presence of different interfering species typically found in urine samples, i.e., glutamic acid, ascorbic acid, glucose, urea, NH_4^+, K^+, Fe^{2+}, Fe^{3+}, Na^+ and Ca^{2+} (final concentration of 40 µM). Any of these species elicited discernible effect on luminescence response of Eu-ACP (Fig. 7). Only creatinine caused a significant decrease of luminescence emission of Eu-ACP respect to the control sample (Fig. 7). These results confirm that neither inorganic nor organic analytes found in urine interfere with our assay, validating the selectivity of Eu-ACP towards creatinine.

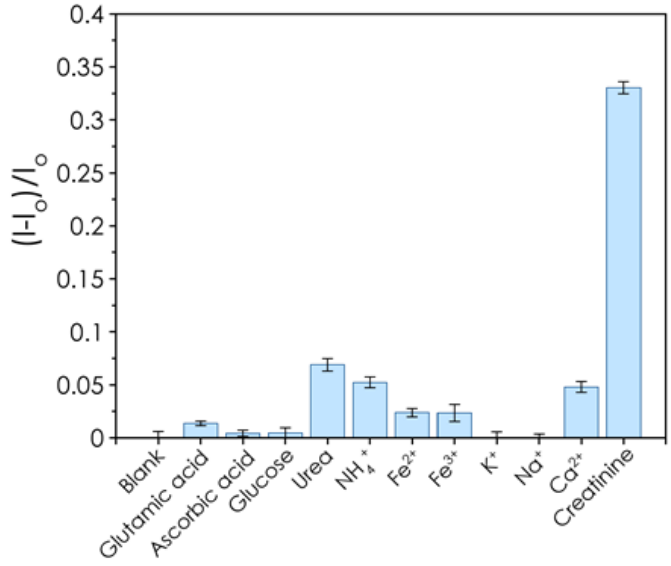

Figure 26. Normalised luminescence emission intensities for Eu-ACP suspensions in the presence of glutamic acid, ascorbic acid, glucose, urea, NH_4^+, K^+, Fe^{2+}, Fe^{3+}, Na^+, Ca^{2+} or creatinine. The final concentration of each analysed species was 40 µM. A blank experiment in the absence of interfering species was also measured (Blank, I_0).

3.5. Detection of creatinine in human urine

Despite the previous results, the problem of nonspecific interferences is hard to tackle due to the compositional complexity inherent to real biological samples. To validate the Eu-ACP nanoparticles' selectivity for the determination of creatinine in urine, we diluted (1:500) and analysed samples from three healthy human volunteers. Our method

measured creatinine concentrations of 8.3-9.4 µM (Table 4). These values fall within the limit of detection for our system (0.07 µM, Table 2). Considering the dilution factor (1:500), the creatinine concentration in urine was between 4.2-4.7 mM, which is within the expected range for healthy individuals [11], [56]. Moreover, quantification after adding a known amount of creatinine (40 and 100 µM) to diluted urine samples showed good recovery percentages (Table 4). These results demonstrated the high accuracy of Eu-ACP nanoparticles when used to quantify the amount of creatinine in human urine.

Table 16. Creatinine quantification in real urine samples.

	Concentration of creatinine, µM			
Samples	**Detected**	**Added**	**Total found**	**Recovery[a] %**
Urine 1	9.4	40	46.3	92.3
		100	119.3	109.9
Urine 2	8.3	40	46.6	95.8
		100	110.3	102.0
Urine 3	8.6	40	43.4	87.1
		100	114.8	106.2

[a] % Recovery = (Total found – Detected) / Added * 100

4. CONCLUSION

In this work we have demonstrated that doping amorphous calcium phosphate nanoparticles with europium (III) ions is a promising strategy in attempts to produce selective and sensitive luminescent sensors for detecting and quantifying creatinine in human urine samples. The nanoparticles were synthesised through a biomimetic route mimicking bone mineralisation and using citrate as a dispersing agent to ensure long-term phosphorescent stability (up to 4 months in storage). Based on emission quenching, our Eu-ACP nanoparticles showed good sensitivity in terms of creatinine detection in human urine samples. Moreover, common and potentially interfering species found in urine had practically no effect whatsoever on the intensity of luminescence emission from the Eu-ACP nanoparticles, thus confirming the good selectivity towards creatinine. These results demonstrate the reliability and accuracy of this new nanosensor for creatinine determination and its stability for longer storage time than current creatinine nanosensor [6], [13], [15]–[17]. Furthermore, the good cytocompatibility of Eu-ACP nanoparticles provides even greater prospects for their potential application in clinical diagnostics.

REFERENCES

[1] D. Heinegård and G. Tiderström, "Determination of serum creatinine by a direct colorimetric method," *Clin. Chim. Acta*, vol. 43, no. 3, pp. 305–310, 1973.

[2] A. K. Parmar, N. N. Valand, K. B. Solanki, and S. K. Menon, "Picric acid capped silver nanoparticles as a probe for colorimetric sensing of creatinine in human blood and cerebrospinal fluid samples," *Analyst*, vol. 141, no. 4, pp. 1488–1498, 2016.

[3] S. Masaru and Y. Mitsutaka, "A new enzymatic serum creatinine measurement based on an endogenous creatine-eliminating system," *Clin. Chim. Acta*, vol. 143, no. 2, pp. 147–155, 1984.

[4] K. Talalak, J. Noiphung, T. Songjaroen, O. Chailapakul, and W. Laiwattanapaisal, "A facile low-cost enzymatic paper-based assay for the determination of urine creatinine," *Talanta*, vol. 144, pp. 915–921, 2015.

[5] C.-C. Tseng, R.-J. Yang, W.-J. Ju, and L.-M. Fu, "Microfluidic paper-based platform for whole blood creatinine detection," *Chem. Eng. J.*, vol. 348, pp. 117–124, 2018.

[6] S. Pal, S. Lohar, M. Mukherjee, P. Chattopadhyay, and K. Dhara, "A fluorescent probe for the selective detection of creatinine in aqueous buffer applicable to human blood serum," *Chem. Commun.*, vol. 52, no. 94, pp. 13706–13709, 2016.

[7] R. Rajamanikandan and M. Ilanchelian, "Protein-protected red emittive copper nanoclusters as a fluorometric probe for highly sensitive biosensing of creatinine," *Anal. Methods*, vol. 10, no. 29, pp. 3666–3674, 2018.

[8] A. J. Killard and M. R. Smyth, "Creatinine biosensors: principles and designs," *Trends Biotechnol.*, vol. 18, no. 10, pp. 433–437, Oct. 2000.

[9] A. S.-C. L. F. C.-V. Manuel J Arroyo, Miguel M Erenas, Ignacio de Orbe-Payá, Kevin Cantrell, Jose A Dobado, Pablo Ballester, Pascal Blondeau, "Thread based microfluidic platform for urinary creatinine analysis," *Sensors Actuators B Chem.*, vol. 305, p. 127407, Feb. 2020.

[10] E. Mohabbati-Kalejahi, V. Azimirad, M. Bahrami, and A. Ganbari, "A review on creatinine measurement techniques," *Talanta*, vol. 97, pp. 1–8, Aug. 2012.

[11] Erenas, Miguel M Ortiz-Gómez, Inmaculada de Orbe-Payá, Ignacio Hernández-Alonso, Daniel Ballester and L. F. Blondeau, Pascal Andrade, Francisco J Salinas-Castillo, Alfonso Capitán-Vallvey, "Ionophore-based optical sensor for urine creatinine determination," *ACS sensors*, vol. 4, no. 2, pp. 421–426, 2019.

[12] C. S. Pundir, S. Yadav, and A. Kumar, "Creatinine sensors," *TrAC Trends Anal. Chem.*, vol. 50, pp. 42–52, Oct. 2013.

[13] R. Rajamanikandan and M. Ilanchelian, "Protein-protected red emittive copper nanoclusters as a fluorometric probe for highly sensitive biosensing of creatinine," *Anal. methods*, vol. 10, no. 29, pp. 3666–3674, 2018.

[14] R. V Nair, P. R. P. Suma, and R. S. Jayasree, "A dual signal on-off fluorescent nanosensor for the simultaneous detection of copper and creatinine," *Mater. Sci. Eng. C*, vol. 109, p. 110569, 2020.

[15] N. Tajarrod, M. K. Rofouei, M. Masteri-Farahani, and R. Zadmard, "A quantum dot-based fluorescence sensor for sensitive and enzymeless detection of creatinine," *Anal. Methods*, vol. 8, no. 30, pp. 5911–5920, 2016.

[16] M. S. Mathew and K. Joseph, "Green synthesis of gluten-stabilized fluorescent gold quantum clusters: application as turn-on sensing of human blood creatinine," *ACS Sustain. Chem. Eng.*, vol. 5, no. 6, pp. 4837–4845, 2017.

[17] X. Du, Fangkai Li, Mengru Wei, Yanye Huang, Donglian Zhou, Yan Yang, Lifang Chen, Jian Liu, Shaogang Tan, "A water-soluble fluorescent probe for detecting creatinine in totally aqueous media and imaging exogenous creatinine in living cells," *Anal. Bioanal. Chem.*, vol. 411, no. 12, pp. 2545–2553, May 2019.

[18] J. Li and J.-J. Zhu, "Quantum dots for fluorescent biosensing and bio-imaging applications," *Analyst*, vol. 138, no. 9, pp. 2506–2515, 2013.

[19] F. Wang, W. B. Tan, Y. Zhang, X. Fan, and M. Wang, "Luminescent nanomaterials for biological labelling," *Nanotechnology*, vol. 17, no. 1, p. R1, 2005.

[20] R. Gómez-Morales, Jaime Verdugo-Escamilla, Cristóbal Fernández-Penas, F. Parra-Milla, Carmen Maria Drouet, Christophe Iafisco, Michele Oltolina, and J. F. Prat, Maria Fernández-Sánchez, "Bioinspired crystallization, sensitized luminescence and cytocompatibility of citrate-functionalized Ca-substituted

europium phosphate monohydrate nanophosphors," *J. Colloid Interface Sci.*, vol. 538, pp. 174–186, 2019.

[21] S. V. Dorozhkin and M. Epple, "Biological and Medical Significance of Calcium Phosphates," *Angew. Chemie Int. Ed.*, vol. 41, no. 17, pp. 3130–3146, Sep. 2002.

[22] M. Epple, "Review of potential health risks associated with nanoscopic calcium phosphate," *Acta Biomater.*, vol. 77, pp. 1–14, Sep. 2018.

[23] Y. Li, C. Shen, X. Li, M. Yang, and C. Shao, "Hydroxyapatite nanoparticle based fluorometric determination and imaging of cysteine and homocysteine in living cells," *Microchim. Acta*, vol. 185, no. 5, p. 271, 2018.

[24] Y. Li, X. Li, D. Wang, C. Shen, and M. Yang, "Hydroxyapatite nanoparticle based fluorometric turn-on determination of dipicolinic acid, a biomarker of bacterial spores," *Microchim. Acta*, vol. 185, no. 9, p. 435, 2018.

[25] K. Zhang, K. Zeng, C. Shen, S. Tian, and M. Yang, "Determination of protein kinase A activity and inhibition by using hydroxyapatite nanoparticles as a fluorescent probe," *Microchim. Acta*, vol. 185, no. 4, p. 225, 2018.

[26] I. A. Neacsu, A. E. Stoica, B. S. Vasile, and E. Andronescu, "Luminescent Hydroxyapatite Doped with Rare Earth Elements for Biomedical Applications," *Nanomaterials*, vol. 9, no. 2, p. 239, Feb. 2019.

[27] T. S. H. Perera, Y. Han, X. Lu, X. Wang, H. Dai, and S. Li, "Rare earth doped apatite nanomaterials for biological application," *J. Nanomater.*, vol. 2015, p. 5, 2015.

[28] C. Qi, J. Lin, L.-H. Fu, and P. Huang, "Calcium-based biomaterials for diagnosis, treatment, and theranostics," *Chem. Soc. Rev.*, vol. 47, no. 2, pp. 357–403, 2018.

[29] F. A. Tesch, Annemarie Wenisch, Christoph Herrmann, Karl-Heinz Reichenbach, Jürgen R. Warncke, Paul Fischer, Dagmar Müller, "Luminomagnetic Eu3+- and Dy3+-doped hydroxyapatite for multimodal imaging," *Mater. Sci. Eng. C*, vol. 81, pp. 422–431, Dec. 2017.

[30] S. P. Victor, M. G. Gayathri Devi, W. Paul, V. M. Vijayan, J. Muthu, and C. P. Sharma, "Europium Doped Calcium Deficient Hydroxyapatite as Theranostic Nanoplatforms: Effect of Structure and Aspect Ratio," *ACS Biomater. Sci. Eng.*,

vol. 3, no. 12, pp. 3588–3595, Dec. 2017.

[31] L. Mahamid, Julia Aichmayer, Barbara Shimoni, Eyal Ziblat, Roy Li, Chenghao Siegel, Stefan Paris, Oskar Fratzl, Peter Weiner, Steve Addadi, "Mapping amorphous calcium phosphate transformation into crystalline mineral from the cell to the bone in zebrafish fin rays," *Proc. Natl. Acad. Sci.*, vol. 107, pp. 6316–6321, 2010.

[32] Y.-J. Chen, Feng Zhu and X.-M. Zhang, Kui-Hua Wu, Jin Wang, Ke-Wei Tang, Qi-Li Mo, "Europium-doped amorphous calcium phosphate porous nanospheres: preparation and application as luminescent drug carriers," *Nanoscale Res. Lett.*, vol. 6, p. 67, 2011.

[33] P. Chen, Feng Huang, B.-Q. Qi, Chao Lu, C. Zhao, Xin-Yu Li, and Y.-J. Wu, Jin Cui, Da-Xiang Zhu, "Multifunctional biodegradable mesoporous microspheres of Eu 3+-doped amorphous calcium phosphate: microwave-assisted preparation, pH-sensitive drug release, and bioimaging application," *J. Mater. Chem. B*, vol. 2, no. 41, pp. 7132–7140, 2014.

[34] J. M. Ramírez-Rodríguez, Gloria B. Dal Sasso, Gregorio Carmona, Francisco J. Miguel-Rojas, Cristina Pérez-de-Luque, Alejandro Masciocchi, Norberto Guagliardi, Antonietta Delgado-López, "Engineering Biomimetic Calcium Phosphate Nanoparticles: A Green Synthesis of Slow-Release Multinutrient (NPK) Nanofertilizers," *ACS Appl. Bio Mater.*, vol. 3, no. 3, pp. 1344–1353, Mar. 2020.

[35] J. M. Chatzipanagis, Konstantinos Iafisco, Michele Roncal Herrero, Teresa Bilton, Matthew Tampieri, Anna Kröger, Roland Delgado-López, "Crystallization of citrate-stabilized amorphous calcium phosphate to nanocrystalline apatite: a surface-mediated transformation," *CrystEngComm*, vol. 18, pp. 3170–3173, 2016.

[36] Y. Y. Hu, A. Rawal, and K. Schmidt-Rohr, "Strongly bound citrate stabilizes the apatite nanocrystals in bone," *Proc. Natl. Acad. Sci. U. S. A.*, vol. 107, pp. 22425–22429, 2010.

[37] S. V Dorozhkin, "Amorphous calcium (ortho)phosphates," *Acta Biomater.*, vol. 6, pp. 4457–4475, 2010.

[38] J. Delgado-López, José Manuel Iafisco, Michele Rodríguez, Isaac Tampieri, Anna

Prat, Maria Gómez-Morales, “Crystallization of bioinspired citrate-functionalized nanoapatite with tailored carbonate content,” *Acta Biomater.*, vol. 8, pp. 3491–3499, 2012.

[39] C. Combes and C. Rey, “Amorphous calcium phosphates: Synthesis, properties and uses in biomaterials,” *Acta Biomater.*, vol. 6, no. 9, pp. 3362–3378, Sep. 2010.

[40] V. Uskoković, “X-ray photoelectron and ion scattering spectroscopic surface analyses of amorphous and crystalline calcium phosphate nanoparticles with different chemical histories,” *Phys. Chem. Chem. Phys.*, vol. 22, no. 10, pp. 5531–5547, 2020.

[41] M. Yahyaoui, A. Bouchama, B. Anak, C. Chiter, A. Djedouani, and F. Rabilloud, “Synthesis, molecular structure analyses and DFT studies on new asymmetrical azines based Schiff bases,” *J. Mol. Struct.*, vol. 1177, pp. 69–77, Feb. 2019.

[42] F. S. Richardson, “Terbium(III) and europium(III) ions as luminescent probes and stains for biomolecular systems,” *Chem. Rev.*, vol. 82, no. 5, pp. 541–552, Oct. 1982.

[43] C. S. Pundir, P. Kumar, and R. Jaiwal, “Biosensing methods for determination of creatinine: A review,” *Biosens. Bioelectron.*, vol. 126, pp. 707–724, Feb. 2019.

[44] T. S. H. Perera, Y. Han, X. Lu, X. Wang, H. Dai, and S. Li, “Rare Earth Doped Apatite Nanomaterials for Biological Application,” *J. Nanomater.*, vol. 2015, pp. 1–6, 2015.

[45] A. Escudero, M. E. Calvo, S. Rivera-Fernández, J. M. de la Fuente, and M. Ocaña, “Microwave-Assisted Synthesis of Biocompatible Europium-Doped Calcium Hydroxyapatite and Fluoroapatite Luminescent Nanospindles Functionalized with Poly(acrylic acid),” *Langmuir*, vol. 29, no. 6, pp. 1985–1994, Feb. 2013.

[46] S. P. Mondéjar, A. Kovtun, and M. Epple, “Lanthanide-doped calcium phosphate nanoparticles with high internal crystallinity and with a shell of DNA as fluorescent probes in cell experiments,” *J. Mater. Chem.*, vol. 17, no. 39, p. 4153, 2007.

[47] A. Lebugle, F. Pellé, C. Charvillat, I. Rousselot, and J. Y. Chane-Ching, “Colloidal and monocrystalline Ln3+ doped apatite calcium phosphate as biocompatible

fluorescent probes," *Chem. Commun.*, no. 6, p. 606, 2006.

[48] A. Al-Kattan, P. Dufour, J. Dexpert-Ghys, and C. Drouet, "Preparation and Physicochemical Characteristics of Luminescent Apatite-Based Colloids," *J. Phys. Chem. C*, vol. 114, no. 7, pp. 2918–2924, Feb. 2010.

[49] M. Sandhöfer, Benedikt Meckel, Marian Delgado-López, José Manuel Patrício, Tatiana Tampieri, Anna Rösch, Frank Iafisco, "Synthesis and Preliminary in Vivo Evaluation of Well-Dispersed Biomimetic Nanocrystalline Apatites Labeled with Positron Emission Tomographic Imaging Agents," *ACS Appl. Mater. Interfaces*, vol. 7, no. 19, pp. 10623–10633, May 2015.

[50] X. Jin, J. Zhuang, Z. Zhang, H. Guo, and J. Tan, "Hydrothermal synthesis of hydroxyapatite nanorods in the presence of sodium citrate and its aqueous colloidal stability evaluation in neutral pH," *J. Colloid Interface Sci.*, vol. 443, pp. 125–130, Apr. 2015.

[51] S. C. G. Leeuwenburgh, I. D. Ana, and J. A. Jansen, "Sodium citrate as an effective dispersant for the synthesis of inorganic–organic composites with a nanodispersed mineral phase," *Acta Biomater.*, vol. 6, no. 3, pp. 836–844, Mar. 2010.

[52] J. R. Lakowicz, *Principles of Fluorescence Spectroscopy*. Springer US, 2007.

[53] R. A. Almotiri, K. J. Ham, V. M. Vijayan, and S. A. Catledge, "Molecularly Imprinted Polyacrylamide with Fluorescent Nanodiamond for Creatinine Detection," *Materials (Basel).*, vol. 12, no. 13, p. 2097, Jun. 2019.

[54] X. Du, Fangkai Li, Mengru Wei, Yanye Huang, Donglian Zhou, Yan Yang, Lifang Chen, Jian Liu, Shaogang Tan, "A water-soluble fluorescent probe for detecting creatinine in totally aqueous media and imaging exogenous creatinine in living cells," *Anal. Bioanal. Chem.*, vol. 411, no. 12, pp. 2545–2553, 2019.

[55] P. Erenas, Miguel M. Ortiz-Gómez, Inmaculada de Orbe-Payá, Ignacio Hernández Alonso, Daniel Ballester and L. F. Blondeau, Pascal Andrade, Francisco J. Salinas-Castillo, Alfonso Capitán-Vallvey, "Ionophore-Based Optical Sensor for Urine Creatinine Determination," *ACS Sensors*, vol. 4, no. 2, pp. 421–426, Feb. 2019.

[56] D. B. Barr, L. C. Wilder, S. P. Caudill, A. J. Gonzalez, L. L. Needham, and J. L. Pirkle, "Urinary Creatinine Concentrations in the U.S. Population: Implications for

Urinary Biologic Monitoring Measurements," *Environ. Health Perspect.*, vol. 113, no. 2, pp. 192–200, Feb. 2005.

ÍNDICE DE FIGURAS

Capítulo 7

Figure 1. (a) XRD patterns, (b) FTIR spectra, (c) SEM and (d) TEM images of dried europium-doped amorphous calcium phosphate (Eu-ACP) nanoparticles. 330
Figure 2. XPS spectra of ACP and Eu-ACP with signals of O (1s), Ca (2s, 2p), and P (2s, 2p) of ACP. The inset shows the Eu 3d region of Eu-ACP with the 3d doublets, that is $d_{3/2}$ and $d_{5/2}$, resulting from spin-orbit coupling and appearing at binding energies of 1134 eV and 1164 eV, respectively. 331
Figure 3. TEM micrograph of Eu-ACP (a) and corresponding EDS maps with Ca (b), P (c), and Eu (d) distributions. 332
Figure 4. (a) PL emission (λexc =240 nm) spectra of Eu-ACP nanoparticle in ultrapure water (250 mg/L) just after preparation. (b) Temporal evolution of normalized luminescence intensity of Eu-ACP (250 mg/L) in ultrapure water (orange vertical bars) and citrate buffer (blue vertical bars). I0 and I refer, respectively, to the intensity of the emission peak at 616 nm at t0 (just after preparation) and at scheduled times. The inset shows PL photographs (under UV irradiation at 265 nm) of Eu-ACP in water and citrate buffer (250 mg/L), collected 240 hours after the preparation. 333
Figure 5. Size distribution of Eu-ACP nanoparticles (250 mg/L) in water (orange bars) and citrate buffer (blue bars) as obtained from DLS. 334
Figure 6. (a) Temporal evolution of normalized luminescence intensity of Eu-ACP nanoparticle in citrate buffer at different concentrations (250, 500 and 1000 mg/L). I0 and I refer, respectively, to the PL intensity at t0 (just after preparation) and at scheduled times. (b) Effect of ionic strength on PL intensity of Eu-ACP at 250 mg/L in citrate buffer. I0 and I correspond to the PL intensity in the absence and presence of NaCl, respectively. 335
Figure 7. (a) Emission spectral response of Eu-ACP in the absence and presence of creatinine at increasing concentrations (1, 5, 10 20, 40, 60, 80, 100 and 120 μM). (b) Plot of normalized luminescence response of Eu-ACP as a function of creatinine concentration. I0 and I are the PL intensity in the absence and in the presence of creatinine, respectively. The solid line represents the linear fitting of the experimental data (symbols). S.E.M. are shown as error bars. 336
Figure 8. Normalised luminescence emission intensities for Eu-ACP suspensions in the presence of glutamic acid, ascorbic acid, glucose, urea, NH_4^+, K^+, Fe^{2+}, Fe^{3+}, Na^+, Ca^{2+}

or creatinine. The final concentration of each analysed species was 40 µM. A blank experiment in the absence of interfering species was also measured (Blank, I_0)..... 338

ÍNDICE DE TABLAS

Capítulo 7

Table 1. Chemical composition (analysed by ICP-OES) of Eu-ACP and ACP nanoparticles. Data are expressed as mean ± standard deviation. 331
Table 2. Analytical characterization of Eu-ACP for creatinine determination..... 337
Table 3. Comparison of analytical parameters of several creatinine luminescent sensors. 337
Table 4. Creatinine quantification in real urine samples. 339

ANEXO

WEARABLE POTENTIOMETRIC ION PATCH FOR ON-BODY ELECTROLYTE MONITORING IN SWEAT: A VALIDATION STRATEGY TO ENSURE PHYSIOLOGICAL RELEVANCE

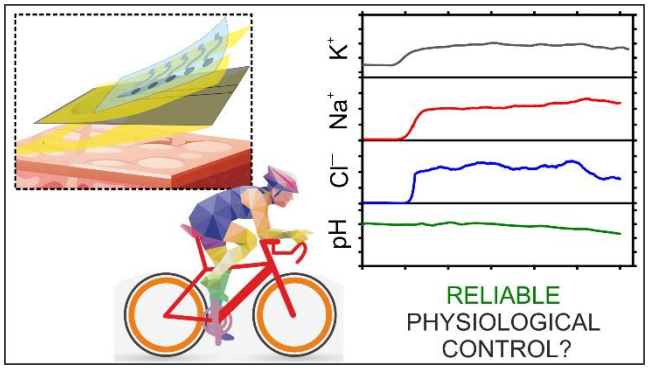

Published in Analytical Chemistry, 2019, 91, (13), 8644-8651

ANEXO: WEARABLE POTENTIOMETRIC ION PATCH FOR ON-BODY ELECTROLYTE MONITORING IN SWEAT: A VALIDATION STRATEGY TO ENSURE PHYSIOLOGICAL RELEVANCE

Marc Parrilla[+], Inmaculada Ortiz-Gómez[+], Rocio Canovas[+], Alfonso Salinas-Castillo[†], Maria Cuartero[+], Gaston A. Crespo[+]

+Department of Chemistry, School of Engineering Science in Chemistry, Biochemistry and Health, KTH Royal Institute of Technology, Teknikringen 30, SE-100 44, Stockholm, Sweden.

[†]Department of Analytical Chemistry, Campus Fuentenueva, Faculty of Sciences, University of Granada, 18071, Spain.

Planteamiento

Como se ha puesto de manifiesto en la sección 3 de la Introducción de esta Memoria, cada vez se hace mayor la necesidad de mejorar los servicios de atención sanitaria de forma que puedan detectarse enfermedades de forma más rápida y sencilla, ya que la instrumentación convencional empleada supone un costo económico elevado, debido a la especialización de los equipos que se utilizan en el diagnóstico de enfermedades y al tiempo de espera de los resultados del análisis clínico que, en ocasiones, es demasiado largo [1].

Aprovechando los avances en el desarrollo de sensores portátiles de bajo costo, pueden realizarse tanto la detección de enfermedades como el tratamiento de las mismas reduciendo los costos considerablemente y obteniendo unas buenas prestaciones. El empleo de dispositivos de análisis en tiempo real puede eludir la necesidad de biopsias o análisis por patólogos expertos, que suelen ser costosos y escasos en países en desarrollo. De este modo, en los últimos años ha habido un elevado crecimiento del desarrollo de dispositivos POC que permiten realizar ensayos clínicos proporcionando resultados inmediatos, haciendo más fácil la toma de decisiones referentes al diagnóstico y la monitorización del tratamiento. Se trata de sistemas compactos y de bajo costo que se pueden vincular a redes de teléfonos móviles de forma que los resultados lleguen de inmediato a especialistas [2]. En este sentido, los sensores biométricos tales como pulseras, relojes, parches para la piel, cintas para la cabeza y ropa permiten la detección

de problemas de salud o enfermedades de forma discreta y pasiva gracias a su diseño unificador [3]. Además, estos dispositivos tienen la capacidad de rastrear y transferir todos los datos biométricos sin interrupciones, de forma que se pueden compartir con el personal sanitario, los investigadores, los miembros de la familia o las redes sociales.

Por todo ello, nos resulta de interés desarrollar nuevos dispositivos que permitan la descentralización de las medidas bioquímicas y que permitan bajar los costes de la sanidad. Así, el desarrollo de dispositivos de diagnóstico que se adapten a la piel y permitan la detección no invasiva o mínimamente invasiva de biomarcadores del cuerpo presentes en fluidos como el sudor, fluidos intersticiales o heridas presentan una gran importancia en este campo de aplicación [4], [5]. La utilización de este tipo de dispositivos supone una mayor rapidez y simplicidad en el análisis [6], [7]. De esta forma el desarrollo de parches, pegatinas o apósitos adhesivos para el análisis de biomarcadores en el cuerpo resulta mucho más cómodo para los usuarios que la realización de ensayos de laboratorio o pruebas hospitalarias, ya que en estos casos se requiere de muchos pasos en el manejo de las muestras fuera del cuerpo [8]. Además, el análisis de la muestra por un usuario con experiencia e instrumentación específica se hace imprescindible lo que supone un incremento en el coste total del análisis.

Objetivo

Teniendo en cuenta todas las consideraciones anteriores, el objetivo de este trabajo ha sido el desarrollo y la validación de un parche potenciométrico estirable para la recogida de sudor y la monitorización de pH, K^+, Na^+ y Cl^-.

Para este objetivo se llevaron a cabo las siguientes etapas secuenciales:

1. Impresión por serigrafía de los electrodos sobre un sustrato de poliuretano empleando tinta de carbono estirable.
2. Implementación de las membranas selectivas de iones en los electrodos.
3. Diseño y fabricación de la celda de muestreo para la recogida y análisis del sudor.
4. Caracterización analítica de los electrodos.
5. Estudio de estabilidad y robustez de los electrodos dentro y fuera del parche.
6. Doble validación del parche potenciométrico *in situ* y *ex situ*.

WEARABLE POTENTIOMETRIC ION PATCH FOR ON-BODY ELECTROLYTE MONITORING IN SWEAT: A VALIDATION STRATEGY TO ENSURE PHYSIOLOGICAL RELEVANCE

ABSTRACT

Herein, the reproducibility and a double validation of on-body measurements provided by new wearable potentiometric ion sensors (WPISs) is presented. Sweat collected during sport practice was first analyzed using the developed device, the pH-meter, and ion chromatography (IC) prior to onbody measurements (off-site validation). Subsequently, the accuracy of onbody measurements accomplished by the WPISs was evaluated by comparison with pH-meter readings and IC after collecting sweat (every 10−12.5 min) during sport practice. The developed device contains sensors for pH, Cl^-, K^+, and Na^+ that are embedded in a flexible sampling cell for sweat analysis. The electrode array was fabricated employing MWCNTs (as an ion-to-electron transducer) and stretchable materials that have been exhaustively characterized in terms of analytical performance, presenting Nernstian slopes within the expected physiological range of each ion analyte (Cl^-, 10−100 mM; K^+, 10−10 mM; and Na^+, 10− 100 mM and pH, 4.5−7.5), drift suitable for midterm exercise practice (0.3 ± 0.2 mV h^{-1}), fast response time, adequate selectivity for sweat measurements, and excellent reversibility. Besides that, the designed sampling cell avoids any sweat contamination and evaporation issues while supplying a passive sweat flow encompassing specifically the individual's perspiration. The interpretation of ion concentration profiles may permit the identification of personal dynamic patterns in sweat composition while practicing sport.

1. Introduction

The ability to monitor chemical events in a continuous and periodic manner has become of general interest in many fields, especially in environmental sensing and healthcare. [1] Analytical devices that can be on-bodily worn without disturbing the individual's status are key players as interfaces between vital chemical events and the digitalization of related observations. [2] Today, these gadgets are actively proposed in the literature in the form of wristbands, textiles and skin patches, among others, [3] giving rise to new

opportunities for the digitalization of unique data that was inaccessible before this recent paradigm shift.

The growth experienced in the field of wearable chemical sensors over the past decade is undoubtedly connected to increasing market expectations. [5] Thus, market outlooks predict that the immediate revenue from electronic skin patches will reach $10bn by 2023 and $15bn by 2028. [6] However, these numbers are primarily based on the unquestionable success of physical sensors (i.e., temperature, pressure, and movement) over chemical ones. Considering that the information provided by these two kind of sensors is different while complementary, it is absolutely necessary a breakthrough in wearable chemical sensors by demonstrating reliable operability in real scenarios.

Electrochemical sensors are the most convenient platform to develop wearable chemical sensors as inferred from the large number of scientific contributions.[7] These sensors allow for the monitoring of critical biomarkers, such as biomolecules (e.g., glucose, lactate, and drugs), through amperometric readout and ions (K^+ and Na^+) using potentiometry. [8] Indeed, the wellestablished all-solid-state technology offers a broad range of advantages in terms of technical specifications, such as simplicity, miniaturization, and low consumption of resources and power, that are essential toward a potential commercialization.

Regarding the value of the chemical information monitored by electrochemical devices, so-called wearable potentiometric ion sensors (WPISs) may particularly enable unique observations related to applied human physiology and health care by measuring ion levels in sweat (and other biological fluids). [9] From a medical perspective, WPISs are striving to supply data suitable for diagnosis of cystic fibrosis and other diseases that involve electrolyte imbalance disorders. [10], [11]

These devices are also useful from a fitness perspective, permitting the monitoring of certain indicators of the dehydration status of the individual (through sodium and chloride concentrations), [12] muscle activity (potassium), [13] exercise intensity (ammonium), [14] acid−base equilibria (pH), [15] or muscle strength (magnesium). [16] Recently, certain reviews in the field of WPISs have reported the key requirements for the development of WPISs toward a successful on-body application. [9] These include (i) fast response time to obtain real-time electrolyte dynamics; (ii) reversibility of the electrode response to detect any fluctuations of the ion analyte as a result of physiological events;

(iii) resiliency and stability of the electrode response during the wearability; [17] (iv) appropriate calibration protocol to minimize any possible error in the calculation of the electrolyte concentration (number of points, comparison between preand postcalibration, concentration versus activity, possibility of calibration-free sensor, influence of the sweat rate, etc.); [18] (v) the noninvasive nature of the device and sampling strategy; (vi) the provision of a sampling approach (i.e., sampling cell) that allows for obtaining a constant sweat flow without the influence of any evaporation or contamination issue; [19]−[22] and (vii) proper validation of on-body measurements. Hence, the inappropriate fulfillment of any of the mentioned requirements may lead to important errors in the calculation of the concentration of the tested ions, therefore ending in a mistaken decision-making process by the physician (medical purpose) or coach (fitness perspective) (Figure 1).

Figure 1. Illustration of the question formulated in this manuscript. Is it currently reliable the on-body data provide by WPISs? Which is the proper validation protocol to evaluate the reliability of the real-time observations?

Concerning the validation of on-body measurements, the collection of enough sample volume suitable for later analysis utilizing a standard technique (i.e., ion chromatography (IC) and others) justifies the validation of on-body measurements only at longer sampling times (1 h of monitoring). This has resulted in a lack of validation criteria of the reported data despite the developed devices being promising. [23], [24]

We propose herein a new protocol to validate on-body measurements provided by any WPISs. Indeed, we have developed a novel design for pH, Cl^-, K^+, and Na^+ detection in sweat and use it as proof-of-concept. It is worth mentioning, that the developed wearable device incorporates a sampling cell for constant sweat flow specifically tailored for an individual's perspiration while avoiding any evaporation and contamination issues. In the final part of the work, validated on-body data demonstrate the potential of the WPISs in supplying reproducible (n = 3) and reliable data during the monitoring of physical activity

of different subjects in a total of 9 on-body tests (T1−T9). To the best of our knowledge, this is the first time that such deep validation of on-body measurements provided by WPISs as well as its reproducibility is reported.

2. Experimental section

2.1. Fabrication of the electrode array

Figure 2a illustrates the procedure for the fabrication of the electrode array on a flexible polyurethane (PU) substrate. The electrodes consisted of five circular patterns prepared with stretchable carbon ink (CI-2051, Engineered Conductive Materials, Inc.) that were in turn connected to a serpentine track made of stretchable silver ink (CI-1036, Engineered Conductive Materials, Inc.). The electrodic path was fabricated on the PU substrate with the screen-printing technique (SPR-45 Automated SMT Stencil Printer, DDM Novastar, Inc., USA). Subsequently, the electrodes were modified first with a layer of multiwalled carbon nanotubes (MWCNTs) and thereafter with the selective membrane on top (see Table S1 for the compositions). For more details, the reader should refer to the Supporting Information.

First, the analytical performances of the selective electrodes were characterized against a commercial Ag/AgCl reference electrode (6.0726.100, Metrohm Nordic, Sweden) when they were immersed in a beaker. The electrodes displayed a Nernstian slope as well as limits of detection (LODs) and linear ranges of responses (LRRs) suitable to detect the selected ions in sweat (Table S1). Interestingly, the expected physiological range for the tested ions during sport monitoring were for chloride 10−100 mM, potassium 3−10 mM, sodium 20−100 mM, and pH 4−7.5.9 Between-electrode reproducibility (n = 3), response repeatability, medium-term drift, and selectivity were also adequate (Figures S1 and S2 and Tables S2 and S3). Indeed, other sensors already reported in the literature using conventional materials featured similar values (Table S3).

The reference electrode was prepared by modifying the method proposed by Bühlman et al. [25] in order to provide stretchability and durability by avoiding the use of a plasticizer (see the Supporting Information). Figure S3 displays the characterization of the analytical performances of this new reference electrode in terms of membrane composition (Table

S4), interferences, medium-term stability, and the influence of light on the electrode response. The optimal condition obtained was the use of a PU without a plasticizer, which exhibits higher stability that is likely explained by the decrease of the leaching of the membrane components. [26]

2.2. Implementation of the electrodes into the sampling cell for on-body measurements

The electrode array was then coupled to the sampling cell (Figure 2b). A circular collection zone allowed for the eccrine glands to collect sweat, which passively flows through the sensing channel up to the outlet of the sampling cell (Figure 2c) (see the Supporting Information for specific details). For example, as the total volume is 8.8 μL, the collected sweat will begin to flow through the sensing channel after 4.8 min of an individual sweating at a rate of 1 μL cm^{-2} min^{-1}, which is a typical rate for a midintensity sport in several parts of the body. [27], [28]

All the zones and channels of the sampling cell have rounded shapes to enhance the homogenization of the sample. [29] The sampling cell is attached to the electrode array by adhesive transfer tape, thereby avoiding any possible leaking of sweat and allowing for an adequate pressure from the eccrine glands [14] (Figure 2d). Finally, the device (electrode array + sampling cell) is attached to the skin for on-body measurements through adhesive transfer tape.

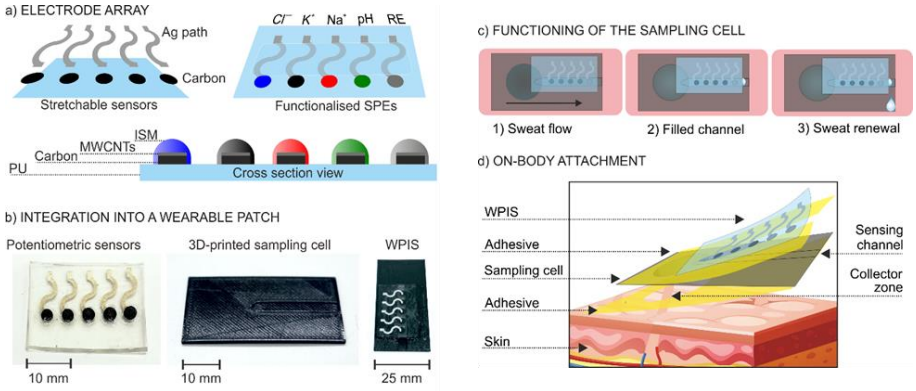

Figure 2. Illustration of the WPIS). (a) Representation of the electrodes before and after functionalization. (b) Pictures of the electrode array, the sampling cell and the entire wearable device (sensors + sampling cell). (c) Scheme of the functioning of the sweat flow in the sampling cell once it is attached to the skin. (d) WPISs attached into the skin by using adhesive transfer tape. ISM = ion-selective membrane.

3. Results and discussion

3.1. In vitro performance of the WPISs

The analytical performances of the electrode array incorporating all-solidstate sensors for Cl^-, K^+, Na^+, and pH, together with the reference electrode, were evaluated in water and artificial sweat before and after the implementation of the sampling cell. Figure S4 depicts the observed individual calibration graphs as well as the carry-over response, which is important for confirming the reversibility of the electrode response. The obtained calibration parameters (Tables S5 and S6) were similar to those displayed using the commercial reference electrode, pointing out the correct functioning of the reference electrode.

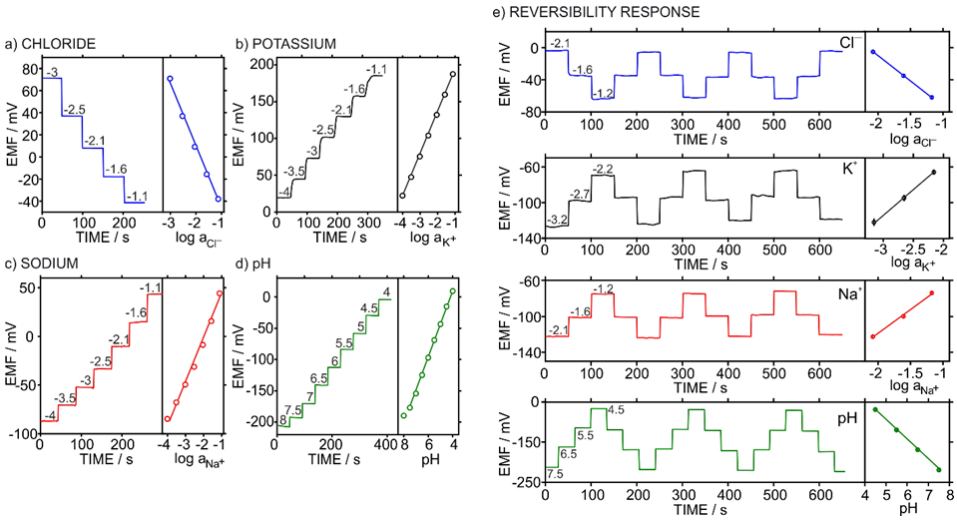

Figure 3 Dynamic responses and corresponding calibration graphs in water for (a) Cl^-, (b) K^+, (c) Na^+ and (d) pH, using the electrode array. The numbers in the dynamic response indicate the logarithm activity reached in each step. (e) Dynamic response and corresponding calibration graph observed in artificial sweat during the reversibility test accomplished by increasing and decreasing the activity of each ion.

Thus, the electrodes displayed a reproducible Nernstian slope (−63.0 ± 2.4 mV for Cl^-, 56.8 ± 2.5 mV for K^+, 54.2 ± 1.3 mV for Na^+, and 50.1 ± 0.5 mV for H^+) within the same LRRs (1−100 mM, Cl^-; 0.1−100 mM, Na^+ ; 0.1−100 mM, K^+ ; and 4−7.5, pH), which include the physiological ranges expected for these ions in sweat. In addition, the electrodes showed robust response (reversibility) even under different types of mechanical stress. This latter is crucial as any change caused by the sensors' portability during on-body measurements while practicing any sport activity may lead to important errors in the quantification of the analyte concentration. In this sense, the development of advanced materials with the ability to provide resiliency to the electrode response while maintaining the rest of the analytical performances is being actively explored by many authors. [30], [31]

In the present work, the entire WPIS device (electrodes + sampling cell) has been engineered with elastomeric materials that confer elasticity while maintaining the analytical characteristics of the potentiometric sensors.

Figure S5 portrays the calibration curves of the developed electrode array under linear stretching (up to 50% elongation) and during the bending effort (up to 80°). Importantly, these resiliency tests largely emulate the mechanical strain that the electrodes may experience during on-body measurements. Although, in some of the cases, it was found

that the applied deformation modified the analytical behavior up to 30% (Table S7), this is unlikely to be experienced during on-body tests.

3.2. Off-site evaluation of the wpiss performance

The strategy applied for sweat-sampling coupled to the WPISs is one of the major concerns when dealing with the accuracy of on-body sweat analysis. Accordingly, potentiometric sensors must be embedded in a gadget that offers (i) effective sweat renewal encompassed through the individual's perspiration during sport practice in order to allow for the real-time monitoring of the ion analytes; (ii) no risk of sweat evaporation that leads to biased results towing to the analyte enrichment in the fluid; (iii) no risk of sample contamination; and (iv) compatibility with different sweating rates. [4], [9]

Regarding this latter requirement, elite athletes usually have high sweat rates (0.7−5.9 μL cm^{-2} min^{-1}) [28] that may require a larger capacity of the sampling cell in order to negate excessive pressure from the eccrine sweat glands. This may lead to modifications of physiological sweating behavior in the skin zone (e.g., hydromeiosis events), therefore masking the onbody observations. [24], [32] In contrast, WPISs for medical diagnostics should involve microfluidic cells with tiny sampling in order to be coupled to lower sweat rates provoked by iontophoresis approaches (198−354 nL cm^{-2} min^{-1}). [11], [33] The design of the sampling cell (Figure 2b, c) was here conceived to fulfill all the aforementioned necessities. First, the microfluidic cell was 3D-printed with the PU substrate to confer conformability to the gadget for further attachment to the human body. The dimensions of the cell were engineered to provide a constant and passive flow of sweat through the sensing channel while the individual is sweating during sport practice. Hence, it is necessary that the sweat fills in first the collecting zone (volume of 8.8 μL), and then the sensing channel (volume of 12.6 μL) will be able to begin the potentiometric measurements. The total time needed slightly depends on the sweating rate of the individual. For example, considering active perspiration of the back during midintensity physical activity, a sweating rate close to 1 μL cm^{-2} min^{-1} will occur. [24], [27] This sweat flow would involve 4.8 min to fill the collection zone and 7 min more to completely fill the sensing zone. After ca. 12 min, a continuous sweat renewal takes place in a passive manner while the subject is sweating (see Figure 2c). This was experimentally confirmed by flowing artificial sweat at 4 μL min^{-1} by means of a peristaltic pump. This flow rate

mimics the sweating rate of 2 μL cm^{-2} min^{-1} considering an area of 2 cm^2, achieved under extreme conditions during on-body tests. [27]

The sampling cell was additionally designed to isolate the collected sweat from the environment, hence avoiding any evaporation or contamination of sweat during on-body tests. Moreover, the entire device was fixed onto a subject's skin by means of adhesive transfer tape (3 M 9471LE), which is commonly used for the attachment of wearable sensors to the body. [19], [21]

The analytical performance of the WPISs were also evaluated under flow conditions by means of a peristaltic pump. Figure 3a displays the potential response of three pH electrodes when the sample pH was increased by almost one pH unit to assess the response time of the device. A time of 5 min is necessary for the electrodes to sense this change in pH at a flow rate of 4 μL min^{-1}. Indeed, each electrode starts to respond 30 s after the other according to its order along the sensing channel.

The influence of the flow rate on electrode response was assessed, as sporadic changes in the sweating rate of the individual are expected during the workout. Moreover, the perspiration rate may substantially change with the region of the body. [28] This behavior was studied by measuring the potential of a solution at pH 5.6 while successively increasing and decreasing (4, 8, and 16 μL cm^{-2} min^{-1}) the flow rate of the pump (Figure 3b). These flow rates were chosen to mimic high sweat rates that may exist in the body during sport practice, e.g., forehead sweat rate of 5.9 ± 3.0 μL cm^{-2} min^{-1}, [28] which means a flow rate of 16.0 μL min^{-1} according to the area of the collection zone of the sampling cell developed herein. A negligible change was determined for the potentiometric response under these conditions, manifesting such that the WPISs could be used in any part of the body at any intensity of physical activity. No influence was found for the entire calibration graph (pH 7.5−4.7), maintaining even the response reversibility (Figure 3c). Therefore, the same calibration graph may be suitable for the calculation of pH in sweat despite any change on the perspiration rate.

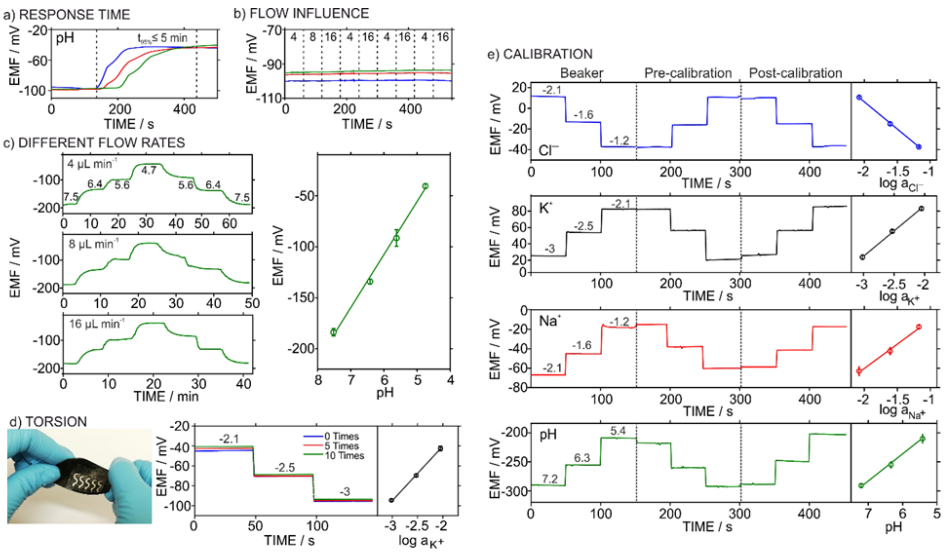

Figure 27. (a) Response of three pH electrodes for a pH change from 5.6 to 4.7. Flow rate = 4 µL min-1. Dotted lines indicate the response time. (b) Response of three pH electrodes in a solution of pH 5.6 at different flow rates: 4, 8 and 16 µL min-1. (c) Calibrations using a pH electrode at different flow rates: 4, 8 and 16 µL min^{-1}. (d) WPISs under torsion deformation. Response of a K^+ electrode after applying different torsion deformations. (e) Calibrations using WPISs for Cl^-, Na^+, K^+, pH before and after the incorporation of the sampling cell, and after on-body measurements. All the calibration curves were performed in artificial sweat. The pre-calibration graph was accomplished from higher to lower concentrations in order to assess the sensors' reversibility.

In this sense, the average of the six calibration graphs presented in Figure 3c obtained at different flow rates and with a carry-over evaluation leads to a slope and intercept of 51.7 ± 0.6 mV pH−1 and 201.5 ± 4.4 mV, respectively. Considering the standard deviations for the calibration parameters, the maximum error expected in the pH calculation is 1−3% considering this curve as one that is universal. This level of error is generally considered acceptable in measurements involving the screening of the physiological status of an individual. [5] Notably, the errors in slope and E0 for the pH sensor were calculated under drastic changes of pH and flow rates. That is, the pH sensor will show uncertainty of 3% at much. But this level of uncertainty will be even lower for onbody measurements, as the sensors were calibrated before and after its portability, see below. A similar behavior was observed for the Cl^-, K^+ , and Na^+ electrodes, and therefore, no influence of the perspiration rate on the response of the entire electrode array was detected (as an example, the response of three K^+ electrodes are shown in Figure S6). Indeed, even though any influence in the diffusion process of the ion analyte when its activity is changed in the bulk solution (such as solution stirring and flow rate) may affect the response of the potentiometric sensors, [34] this is here unnoticeable based on the very low flow rates.

Figure 3d presents a resiliency test of K^+ sensors implemented with the sampling cell (i.e., WPISs only containing K^+ sensors) based on applying different torsion strains to the device. The calibration graph did not change under these conditions (slope of 53.7 ± 1.4 mV with an intercept of 67.0 ± 4.9). Besides that, and to confirm that any corporal movement during on-body portability does not affect the electrode response, the electrode array was calibrated for every ion analyte before and after on-body measurements. No changes were observed in the calibration graphs (Figure 3e). Furthermore, the calibration graphs are the same as those obtained in the beaker before the implementation of the sampling cell, which were determined without stirring by immersing the electrodes in separate solutions (Figure 3e). As a result, either of these three calibration graphs (i.e., in the beaker, or in the WPISs before and after the test) can be used to calculate on-body electrolyte concentration.

3.3. Validation of the WPISs

As mentioned in the Introduction section, yet, there is not an established protocol for the validation of WPISs, and only some recent papers attempted to perform a few additional measurements to establish its accuracy. [35], [36]

Current methods for sweat analysis performed in physiology laboratories related to sport performance consist of collecting sweat during the workout using either the regional absorbent patch method (REG) or whole-body wash down technique (WBW), [13], [28] with the subsequent use of different analytical techniques, such as IC, [28] ion-selective electrodes (ISE), [37] or inductively coupled plasma-mass spectrometry (ICP-MS), [36] to analyze electrolyte concentration. In principle, it is worthy to base the validation of the WPISs in these approaches. In this sense, we propose a double validation of the WPISs operating first out of the body by pumping the sweat toward the WPIS (off-body validation) and then during on-body measurements, comparing the results with IC and a pH meter.

The protocol employed to convert the profiles of the potentiometric signal observed with the WPISs into ion analyte concentrations is seen in Figure S7. Briefly, raw data (dynamic recording of the electrode potential) is converted into ion activity using the precalibration. Subsequently, the ion concentration is calculated from the activity coefficient, which is

determined by the ionic strength of artificial sweat (see the Supporting Information). Importantly, while the direct use of ion concentration in the calibration graph shortens the practical calculations, it is not formally correct and may induce additional errors, as demonstrated in the following. First, human sweat was collected at different times following the REG method from the back of a subject, as described in the Supporting Information, and the samples were analyzed by the WPISs operating by means of a peristaltic pump (i.e., off-site the body), IC, and the pH meter. Briefly, REG consists of attaching a cotton pad (oval-shaped pads of 85 × 70 mm and circular-shaped pads of 58 mm diameter) on the skin with hydrofilm tape, and after a certain length of time, the pad is detached from the skin, demounted from the tape, and finally centrifuged (5.000 rpm) to extract the sweat. The back of individuals participating in this study was chosen as the local region to fix the WPISs during all the on-body tests to maximize the collected volume [27], [28] (10−80 μL, 100−700 μL, and 1−3 mL after 5, 10, and 60 min of sweating, respectively). These ranges may slightly vary between subjects, but still, this volume is enough for analysis with the pH meter or IC after dilution (1:100).

Figure S8 displays the correlation plots for all the tested ions using the off-body validation. As a general trend, samples collected over a short time (5−10 min) exhibited over concentrated values, i.e., concentrations outside of the physiological ranges of K^+, Na^+, and Cl^- (delimited with colored squares). However, samples collected over longer times (60 min) were within physiological ranges (see below). In addition, whatever the collection time was, excellent correlations were observed between WPISs and gold standard techniques (Figure S8, Pearson correlation coefficient of 0.97 for Cl^-, 0.89 for K^+, 0.91 for Na^+, and 0.94 for pH). This indicates that the overestimation issue is related to how the sample is collected in/from the pad, as the same samples were analyzed with different techniques obtaining similar values.

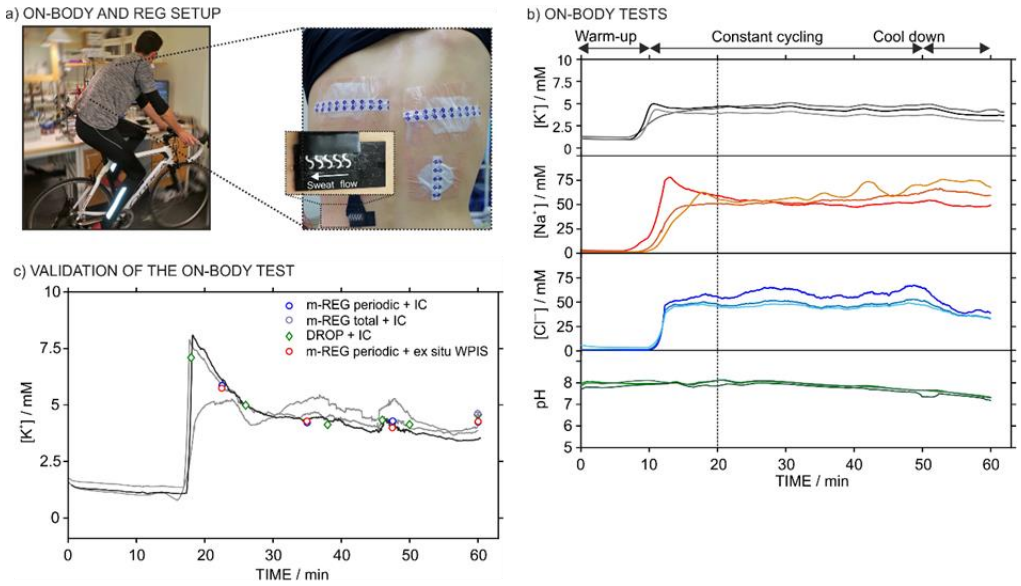

Figure 28. (a) Pictures of a subject during cycling exercise with the WPISs and absorbent patches attached to the back. (b) Concentration profiles observed with the WPISs during 60 min of cycling workout (10 min of warming-up, 40 min of mid to high intensity cycling and 10 min of cooling-down). WPISs contained three twin electrodes for each ion. (c) Profile of K^+ concentration during on-body measurements. IC measurements were additionally accomplished for validation.

The second part of the validation comprised the comparison of on-body measurements with the gold standard techniques (IC and pH meter) along a 1-h workout. The WPISs and absorbent pads (3 pads of 85 × 70 mm and/or 58 mm diameter dimensions) were attached to the low and medium back of the subjects to collect enough sample volume during sport practice using a professional bike kept in a static trainer (Figure S9). Importantly, every ion was individually measured through a wearable device comprising three twin electrodes and two reference electrodes (one acting as a reference and the other a regular working electrode). This allowed for evaluating the reproducibility of the developed sensors for the first time, as far as we know, during on-body measurements.

Figure 4a depicts the on-body concentration profiles for $Cl^–$, K^+, Na^+, and pH obtained with independent devices for each ion during a 1-h workout. The reproducibility among the three replicates was additionally evaluated, exhibiting relative standard deviations of 12.5 ± 3.2% for $Cl^–$, 11.3 ± 6.1% for Na^+, 11.5 ± 2.1 for K^+ n and 0.9 ± 0.4% for pH (see the dynamic profile of the RSD in Figure S10), which are really appropriate values considering possible variability implied in any kind of in situ measurements. Furthermore, as in the case of the previous off-site validation of the WPISs, the values yielded by IC every 5 or 10 min were always higher than those measured on the body

(i.e., Cl^- > 100 mM, K^+ > 8 mM, and Na^+ > 100 mM) and rendered of nonphysiological meaning unless the subject experienced unhealthy conditions (see Table S8). Thus, we confirmed the incompatibility of the application of the REG method for short collection times of 5−10 min, as they gave rise to values very different between the IC and the WPISs (ca. 60−300% of difference), and because the values measured with IC were totally outside the ranges expected in healthy volunteers.

Therefore, we modified the REG method (m-REG) to minimize evaporation issues of the sample during its collection and manipulation, which may be the cause for an over concentration of the ion analytes (Figure S9). Briefly, (i) the period of sweat collection was increased to 10−12.5 min; (ii) the absorbent pad was squeezed by means of a syringe immediately after removal from the body rather than the traditional centrifugation process; and (iii) sample dilution (1:100) was then quickly accomplished, and the sample was immediately stored in the fridge (4 °C). This method permitted gathering from 100 to 500 μL of sweat depending on the perspiration rate. Figure 4b portrays the on-body profile (n = 3) for K^+ concentrations with the analysis of the samples obtained from the IC and WPISs additionally operating out of the body (in a flow mode with the peristaltic pump) after sweat sampling employing the new m-REG method (every 12.5 min), and one pad collecting sweat during the entire exercise. Now, all the measurements analyzed with the IC fit within the physiological range of ions and agreed with the on-body profiles. Indeed, this agreement was also observed with the WPISs coupled to the peristaltic pump (Pearson correlation of 0.99, Figure S11a). In addition, the sweat at the outlet of the sampling cell was collected during the on-body test and analyzed in the IC for comparative purposes (DROP). The results were also in line with the on-body profile, K^+ concentration of 7.1 mM at 18 min, 4.0mM at 30 min, 5.0 mM at 36 min, 4.1 mM at 38 min, 4.3 mM at 46 min, 4.1 mM at 50 min, and 4.6 mM at 60 min, which correspond to the differences of 17.9, 6, 13.8, 3.7, 1.4, and 18.8%, respectively, calculated from the WPISs and collected drop. An analogous experiment was accomplished for on-body Na+ detection providing the same conclusions (Figure S11b, on-body test T6).

Conveniently, the assessment of the calibration graph in artificial sweat permits the use of coefficient activities for the formal construction of the potentiometric calibration graph used for the final calculation of the concentrations (see Figure S7). Otherwise, either the application of a calibration graph based on concentration rather than activity or the comparison of activity with the concentrations found with other gold standard techniques

(i.e., IC) introduced greater error in the observed values (see Table S9 for a comparison between different tests). Table 1 shows the calculated concentrations during the validation of on-body measurements by comparison with IC and the pH-meter. In addition, the same samples were measured by WPISs operating out of the body (Table S10). Whether the data from the gold standard techniques are considered as the true concentrations in sweat, these differences serve as accuracy in terms of error of the developed WPISs. The error across all the tests was below 16% with an average of 7.9 ± 4.7%, which is acceptable with respect to a reliable decision-making process based on real-time measurements assessed in real scenarios. A proper agreement with the WPISs operating out of the body was also observed (Table S10).

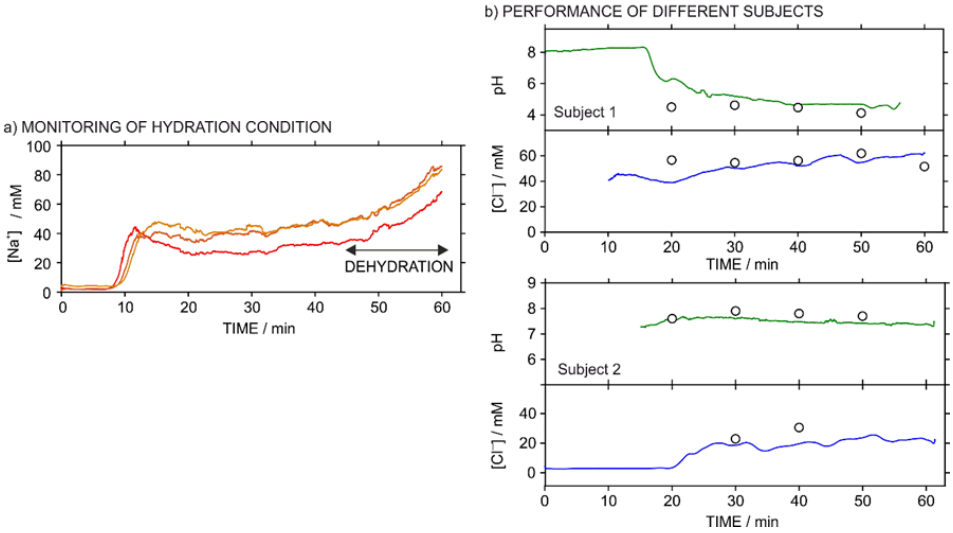

Figure 29. Electrolyte dynamics observed during on-body tests: (a) Na^+ concentration of an individual subjected to 1-h cycling at high-intensity. (b) Cl^- and pH monitoring in two different individuals subjected to the same physical activity (22°C, 1-h cycling, high intensity). The dots indicate the concentrations of sweat analyzed by IC after sweat collection by m-REG.

Finally, the WPISs were evaluated under different conditions, (i) Na^+ profile of one subject under high physical activity (constant workload at level 7−8 out of 10 exercise intensity) and without any water intake during the practice (on-body test T7), and (ii) Cl^- and pH profiles of 2 different individuals subjected to the same activity conditions but under hydration conditions (22 °C, 1 h cycling, medium intensity, on-body tests T8 and T9). In the case of the exercise practice without any water intake (Figure 5a), after 45 min of cycling, there was a gradual increase in Na^+ concentration that may suggest a dehydration status of the subject, as previously reported. [8], [12] However, this

information may be carefully interpreted as the observed increase in Na^+ may be a consequence of the local increase of skin temperature, change in the exercise intensity or other factors. Therefore, further onbody tests (i.e., massive validation) are needed to confirm this finding and others from a physiological point of view.

Regarding the second experiment (Figure 5b), subject 1 had more acidic pH levels, with Cl^- concentrations within the common healthy range (10−100 mM), while subject 2 showed more basic pH levels and lower Cl^- concentrations. These differences may be associated with the diet, the fitness condition of each subject, and hydration status. However, the interpretation of these results is far beyond the scope of this work. Overall, these observations encourage the further testing of WPISs in athletes at known physiological conditions to assess the differences in electrolyte dynamics.

Table 17. Concentrations obtained during the ex situ and in situ validation of the WPISs using the m-REG method.

	Period (min)	WPISs (mM or pH)	IC (mM) or pH meter	IC-WPISs difference(%)
K^+	10 – 22.5	6.3 ± 1.4	5.9	7.4
	22.5 – 35	4.9 ± 0.5	4.2	15.3
	35 – 47.5	4.5 ± 0.4	4.3	5.9
	47.5 – 60	4.0 ± 0.4	4.2	5.3
	10 – 60	4.7 ± 0.9	4.6	1.4
Na^+	10 – 22.5	79.9 ± 10.1	84.8	5.8
	22.5 – 35	79.7 ± 5.9	83.7	4.9
	35 – 47.5	77.8 ± 6.1	89.5	13.1
	47.5 – 60	72.4 ± 6.6	83.5	13.3
	10 – 60	76.9 ± 7.4	85.0	9.4
Cl^-	20 – 30	46.0 ± 3.9	54.6	15.8
	30 – 40	52.7 ± 1.7	56.2	6.1
	40 – 50	56.7 ± 2.9	61.9	8.4
	50 – 60	59.1 ± 1.9	51.6	14.6
pH	20 – 30	8.0 ± 0.1	7.5	7.3
	30 – 40	7.9 ± 0.1	7.6	4.3
	40 – 50	7.7 ± 0.1	7.7	0.5
	50 – 60	7.5 ± 0.1	7.3	3.0

[a]The corresponding experiments are shown in **Figure 6c, Figure S10b, Figure 7b (subject 1)** and **Figure 6c** for K^+, Na^+, Cl- and pH respectively. [b]The concentrations were calculated as the average corresponding to the collection time.

4. Conclusions

We have demonstrated, for the first time, the reproducibility and reliability of on-body measurements accomplished by new WPISs for pH, Cl^-, K^+, and Na^+ analysis in sweat. The validation of these measurements has been advantageously assessed through a two-step protocol, considering, first, the offsite performance of the WPISs and then on-body operation. All measurements were compared with the results from gold standard techniques, such as IC and a pH meter. The incorporation of an innovative sampling cell additionally permitted the realization of on-body measurements in real time through the provision of a continuous and passive sweat flow encompassing the subjects' perspiration. Overall, it is here demonstrated, the potential of the developed WPISs for providing reliable physiological and personal data of body status during sports activity. It is expected, that the advances presented in this article will contribute to the appropriate validation of future wearable chemical sensors that will constitute the next generation of digital health solutions for personalized hydration and recovery strategies in sport performance and wellbeing.

REFERENCES

[1] S. A. Boppart and R. Richards-Kortum, “Point-of-care and point-of-procedure optical imaging technologies for primary care and global health,” *Sci. Transl. Med.*, vol. 6, no. 253, pp. 253rv2-253rv2, Sep. 2014.

[2] J. Heikenfeld, J. Jajack, A. Rogers, J. Gutruf, P. Tian, L. Pan, T. Li, R. Khine, M. Kim, J. Wang, J. Kim, “Wearable sensors: modalities, challenges, and prospects,” *Lab Chip*, vol. 18, no. 2, pp. 217–248, 2018.

[3] M. Bariya, H. Y. Y. Nyein, and A. Javey, “Wearable sweat sensors,” *Nat. Electron.*, vol. 1, no. 3, pp. 160–171, Mar. 2018.

[4] M. Parrilla, Marc Cuartero, N. Padrell Sánchez, Sara Rajabi, Mina Roxhed, and G. A. Niklaus, Frank Crespo, “Wearable All-Solid-State Potentiometric Microneedle Patch for Intradermal Potassium Detection,” *Anal. Chem.*, vol. 91, no. 2, pp. 1578–1586, Jan. 2019.

[5] R. Cánovas, M. Parrilla, P. Blondeau, and F. J. Andrade, “A novel wireless paper-based potentiometric platform for monitoring glucose in blood,” *Lab Chip*, vol. 17, no. 14, pp. 2500–2507, 2017.

[6] M. Parrilla, J. Ferré, T. Guinovart, and F. J. Andrade, “Wearable Potentiometric Sensors Based on Commercial Carbon Fibres for Monitoring Sodium in Sweat,” *Electroanalysis*, vol. 28, no. 6, pp. 1267–1275, Jun. 2016.

[7] M. Parrilla, M. Cuartero, and G. A. Crespo, “Wearable potentiometric ion sensors,” *TrAC Trends Anal. Chem.*, vol. 110, pp. 303–320, Jan. 2019.

[8] M. Parrilla, R. Cánovas, I. Jeerapan, F. J. Andrade, and J. Wang, “A Textile-Based Stretchable Multi-Ion Potentiometric Sensor,” *Adv. Healthc. Mater.*, vol. 5, no. 9, pp. 996–1001, May 2016.

[9] J. Kim, A. S. Campbell, B. E.-F. de Ávila, and J. Wang, “Wearable biosensors for healthcare monitoring,” *Nat. Biotechnol.*, 2019.

[10] G. Kaya, Tolga Liu, K. Ho, Jenny Yelamarthi, and A. Miller, Kevin Edwards, Jeffrey Stannard, "Wearable Sweat Sensors: Background and Current Trends," *Electroanalysis*, 2018.

[11] W. Gao, G. A. Brooks, and D. C. Klonoff, "Wearable Physiological Systems and Technologies for Metabolic Monitoring," *J. Appl. Physiol.*, vol. 124, no. 3, pp. 548–556, 2018.

[12] A. K. Yetisen, J. L. Martinez-Hurtado, B. Ünal, A. Khademhosseini, and H. Butt, "Wearables in Medicine," *Adv. Mater.*, vol. 1706910, p. 1706910, 2018.

[13] J. Hayward, "Electronic Skin Patches 2018-2028: Technologies, Players & Markets, IDTechEx," 2018.

[14] J. Heikenfeld, J. Jajack, A. Rogers, J. Gutruf, P. Tian, L. Pan, T. Li, R. Khine, M. Kim, J. Wang, J. Kim, "Wearable sensors: modalities, challenges, and prospects," *Lab Chip*, vol. 18, pp. 217–248, 2018.

[15] K. Gao, Wei Emaminejad, Sam Nyein, Hnin Yin Yin Challa, Samyuktha Chen and A. Peck, Austin Fahad, Hossain M. Ota, Hiroki Shiraki, Hiroshi Kiriya, Daisuke Lien, Der-Hsien Brooks, George A. Davis, Ronald W. Javey, "Fully integrated wearable sensor arrays for multiplexed in situ perspiration analysis," *Nature*, vol. 529, no. 7587, pp. 509–514, 2016.

[16] M. Parrilla, M. Cuartero, and G. A. Crespo, "Wearable Potentiometric Ion Sensors," *TrAC - Trends Anal. Chem.*, vol. 110, pp. 303–320, 2019.

[17] P. C. Choi, Dong Hoon Thaxton, Abigail Jeong, In cheol Kim, Kain Sosnay, Patrick R. Cutting, Garry R. Searson, "Sweat test for cystic fibrosis: Wearable sweat sensor vs. standard laboratory test," *J. Cyst. Fibros.*, vol. 17, no. 4, pp. e35–e38, 2018.

[18] M. Cuartero, M. Parrilla, and G. A. Crespo, "Wearable potentiometric sensors for medical applications," *Sensors (Basel).*, vol. 19, no. 363, 2019.

[19] R. M. Morgan, M. J. Patterson, and M. a. Nimmo, “Acute effects of dehydration on sweat composition in men during prolonged exercise in the heat,” *Acta Physiol. Scand.*, vol. 182, no. 1, pp. 37–43, 2004.

[20] L. B. Baker, J. R. Stofan, A. A. Hamilton, and C. A. Horswill, “Comparison of regional patch collection vs . whole body washdown for measuring sweat sodium and potassium loss during exercise,” *J. Appl. Physiol.*, vol. 107, pp. 887–895, 2009.

[21] R. Sonner, Z. Wilder, E. Heikenfeld, J. Kasting, G. Beyette, F. Swaile, D. Sherman, F. Joyce, J. Hagen, J. Kelley-Loughnane, N. Naik, “The microfluidics of the eccrine sweat gland, including biomarker partitioning, transport, and biosensing implications,” *Biomicrofluidics*, vol. 9, no. 3, p. 4921039, 2015.

[22] S. M. Ali and G. Yosipovitch, “Skin pH: From basic science to basic skin care,” *Acta Derm. Venereol.*, vol. 93, no. 3, pp. 261–267, 2013.

[23] C. H. Bohl and S. L. Volpe, “Magnesium and exercise,” *Crit. Rev. Food Sci. Nutr.*, vol. 42, no. 6, pp. 533–563, 2002.

[24] M. Parrilla, R. Cánovas, I. Jeerapan, F. J. Andrade, and J. Wang, “A Textile-Based Stretchable Multi-Ion Potentiometric Sensor.,” *Adv. Healthc. Mater.*, vol. 5, no. 9, pp. 996–1001, May 2016.

[25] M. Parrilla, J. Ferré, T. Guinovart, and F. J. Andrade, “Wearable Potentiometric Sensors Based on Commercial Carbon Fibres for Monitoring Sodium in Sweat,” *Electroanalysis*, vol. 28, no. 6, pp. 1267–1275, 2016.

[26] R. Alizadeh, Azar Burns, Andrew Lenigk, Ralf Gettings and M. Ashe, Jeffrey Porter, Adam McCaul, Margaret Barrett, Ruairi Diamond, Dermot White, Paddy Skeath, Perry Tomczak, “A wearable patch for continuous monitoring of sweat electrolytes during exertion,” *Lab Chip*, vol. 18, pp. 2632–2641, 2018.

[27] G. B. Nyein, Hnin Yin Yin Tai, Li-chia Ngo, Quynh Phuong Chao, Minghan Zhang, H. Gao, Wei Bariya, Mallika Bullock, James Kim, and A. Fahad, Hossain

M Javey, “A Wearable Microfluidic Sensing Patch for Dynamic Sweat Secretion Analysis,” *ACS Sensors*, vol. 3, no. 5, pp. 944–952, 2018.

[28] J. Sempionatto, Juliane R Martin, Aida García-Carmona, Laura Barfidokht, Abbas Kurniawan, Jonas F Moreto, Jose R Tang, Guangda Shin, Andrew Liu, Xiaofeng Escarpa, Alberto Wang, “Skin-Worn Soft Microfluidic Potentiometric Detection System.”

[29] B. Anastasova, S. Crewther, V. Bembnowicz, P. Curto, and G. Z. Ip, H. M. Rosa, B. Yang, “A wearable multisensing patch for continuous sweat monitoring,” *Biosens. Bioelectron.*, vol. 94, no. June 2016, p. 730, 2017.

[30] C. E. Dziedzic, M. L. Ross, G. J. Slater, and L. M. Burke, “Variability of Measurements of Sweat Sodium Using the Regional Absorbent-Patch Method,” *Int. J. Sport Physiol. Perform.*, vol. 9, pp. 832–838, 2014.

[31] L. B. Baker, “Sweating Rate and Sweat Sodium Concentration in Athletes: A Review of Methodology and Intra/Interindividual Variability,” *Sport. Med.*, vol. 47, no. s1, pp. 111–128, 2017.

[32] J. Hu, K. T. Ho, X. U. Zou, W. H. Smyrl, A. Stein, and P. Buhlmann, “All-solid-state reference electrodes based on colloid-imprinted mesoporous carbon and their application in disposable paper-based potentiometric sensing devices,” *Anal. Chem.*, vol. 87, no. 5, pp. 2981–2987, 2015.

[33] M. Cuartero, G. A. Crespo, and E. Bakker, “Polyurethane Ionophore-Based Thin Layer Membranes for Voltammetric Ion Activity Sensing,” *Anal. Chem.*, vol. 88, no. 11, pp. 5649–5654, 2016.

[34] G. Smith, Caroline J.Havenith, “Body mapping of sweating patterns in male athletes in mild exercise-induced hyperthermia,” *Eur. J. Appl. Physiol.*, vol. 111, no. 7, pp. 1391–1404, 2011.

[35] J. R. Baker, Lindsay B. Ungaro, Corey T. Sopeña, Bridget C. Nuccio, Ryan P.

Reimel, Adam J. Carter, James M. Stofan and K. A. Barnes, “Body map of regional vs. whole body sweating rate and sweat electrolyte concentrations in men and women during moderate exercise-heat stress,” *J. Appl. Physiol.*, vol. 124, no. 5, pp. 1304–1318, 2018.

[36] C. K. Dixit, K. Kadimisetty, and J. Rusling, “3D-printed miniaturized fluidic tools in chemistry and biology,” *TrAC - Trends Anal. Chem.*, vol. 106, pp. 37–52, 2018.

[37] J. Kim, R. Kumar, A. J. Bandodkar, and J. Wang, “Advanced Materials for Printed Wearable Electrochemical Devices: A Review,” *Adv. Electron. Mater.*, vol. 3, no. 1, p. 1600260, 2017.

[38] R. Cánovas, M. Parrilla, P. Mercier, F. J. Andrade, and J. Wang, “Balloon-Embedded Sensors Withstanding Extreme Multiaxial Stretching and Global Bending Mechanical Stress: Towards Environmental and Security Monitoring,” *Adv. Mater. Technol.*, vol. 1, no. 5, p. 1600061, 2016.

[39] M. Bariya, H. Y. Y. Nyein, and A. Javey, “Wearable sweat sensors,” *Nat. Electron.*, vol. 1, no. 3, pp. 160–171, 2018.

[40] K. Sato, W. H. Kang, K. Saga, and K. T. Sato, “Biology of sweat glands and their disorders. I. Normal sweat gland function.,” *J. Am. Acad. Dermatol.*, vol. 20, no. 4, pp. 537–563, 1989.

[41] W. Emaminejad, Sam Gao and R. W. Wu, Eric Davies, Zoe A. Yin Yin Nyein, Hnin Challa, Samyuktha Ryan, Sean P. Fahad, Hossain M. Chen, Kevin Shahpar, Ziba Talebi, Salmonn Milla, Carlos Javey, Ali Davis, “Autonomous sweat extraction and analysis applied to cystic fibrosis and glucose monitoring using a fully integrated wearable platform,” *Proc. Natl. Acad. Sci.*, vol. 114, no. 18, p. 201701740, 2017.

[42] K. Tóth, J. Fucskó, E. Lindner, Z. Fehér, and E. Pungor, “Potentiometric detection in flow analysis,” *Anal. Chim. Acta*, vol. 179, pp. 359–370, 1986.

[43] F. Cazalé, A. Sant, W. Ginot and P. Launay, J.-C. Savourey, G. Revol-Cavalier, F. Lagarde, J.M. Heinry, D. Launay, J. Temple-Boyer, "Physiological stress monitoring using sodium ion potentiometric microsensors for sweat analysis," *Sensors Actuators B Chem.*, vol. 225, pp. 1–9, 2016.

[44] W. Nyein, Hnin Yin Yin Gao and A. Shahpar, Ziba Emaminejad, Sam Challa, Samyuktha Chen, Kevin Fahad, Hossain M. Tai, Li-Chia Ota, Hiroki Davis, Ronald W. Javey, "A Wearable Electrochemical Platform for Noninvasive Simultaneous Monitoring of Ca 2+ and pH," *ACS Nano*, vol. 10, no. 7, pp. 7216–7224, 2016.

[45] L. B. Baker, C. T. Ungaro, K. A. Barnes, R. P. Nuccio, A. J. Reimel, and J. R. Stofan, "Validity and reliability of a field technique for sweat Na+and K+analysis during exercise in a hot-humid environment," *Physiol. Rep.*, vol. 2, no. 5, p. e12007, 2014.

[46] R. J. Maughan and S. M. Shirreffs, "Development of individual hydration strategies for athletes," *Int. J. Sport Nutr. Exerc. Metab.*, vol. 18, no. 5, pp. 457–472, 2008.

[47] G. A. Pankratova, Nadezda Cuartero, Maria Jowett, Laura A. Howe, Ethan N.W. Gale, Philip A. Bakker, Eric Crespo, "Fluorinated tripodal receptors for potentiometric chloride detection in biological fluids," *Biosens. Bioelectron.*, vol. 99, no. February 2017, pp. 70–76, 2018.

[48] C. Callewaert, B. Buysschaert, E. Vossen, V. Fievez, T. Van de Wiele, and N. Boon, "Artificial sweat composition to grow and sustain a mixed human axillary microbiome," *J. Microbiol. Methods*, vol. 103, pp. 6–8, 2014.

[49] P. C. Meier, "Two-parameter debye-hückel approximation for the evaluation of mean activity coefficients of 109 electrolytes," *Anal. Chim. Acta*, vol. 136, no. C, pp. 363–368, 1982.

[50] E. Bakker and E. Pretsch, "Modern potentiometry.Bakker, E., & Pretsch, E.

(2007). Modern potentiometry. Angewandte Chemie (International Ed. in English), 46(30), 5660–8. doi:10.1002/anie.200605068," *Angew. Chem. Int. Ed. Engl.*, vol. 46, no. 30, pp. 5660–8, 2007.

[51] E. Bakker, E. Pretsch, and P. Bühlmann, "Selectivity of Potentiometric Ion Sensors," *Anal. Chem.*, vol. 72, no. 6, pp. 1127–1133, Mar. 2000.

[52] G. A. Crespo, S. Macho, and F. X. Rius, "Ion-selective electrodes using carbon nanotubes as ion-to-electron transducers.," *Anal. Chem.*, vol. 80, pp. 1316–1322, 2008.

[53] *C. of E. European Council of Human Rights, "European Convention on Human Rights."* 1953.

[54] O. Hamulák, D. R. Troitiño, and A. Chochia, "The charter of fundamental rights of the european union and the social rights," *Estud. Const.*, vol. 16, no. 1, pp. 167–186, 2018.

[55] L. Baker, K. Barnes, M. Anderson, D. Passe, and J. Stofan, "Normative data for regional sweat sodium concentration and whole-body sweating rate in athletes," *J. Sports Sci.*, vol. 34, pp. 1–11, Jun. 2015.

[56] K. Baker, Lindsay Ungaro, Corey Nuccio, Ryan Reimel, Adam Carter, James Stofan, John Barnes, "Body Map of Regional versus Whole Body Sweating Rate and Sweat Electrolyte Concentrations in Men and Women during Moderate Exercise-Heat Stress," *J. Appl. Physiol.*, vol. 124, Feb. 2018.

[57] M. Novell, M. Parrilla, G. A. Crespo, F. X. Rius, and F. J. Andrade, "Paper-based ion-selective potentiometric sensors," *Anal. Chem.*, vol. 84, no. 11, pp. 4695–4702, 2012.

[58] T. Guinovart, M. Parrilla, G. A. Crespo, F. X. Rius, and F. J. Andrade, "Potentiometric sensors using cotton yarns, carbon nanotubes and polymeric membranes," *Analyst*, vol. 138, no. 18, pp. 5208–15, 2013.

[59] J. Zhu, X. Li, Y. Qin, and Y. Zhang, “Single-piece solid-contact ion-selective electrodes with polymer-carbon nanotube composites,” *Sensors Actuators, B Chem.*, vol. 148, no. 1, pp. 166–172, 2010.

5. Electronic supplementary material

5.1. Reagents, materials and instrumentation

Multiwalled carbon nanotubes (MWCNTs), valinomycin (potassium ionophore I, selectophore grade), sodium ionophore X (selectophore grade), chromoionophore I (selectophore grade), potassium tetrakis (4-chlorophenyl) borate (KTClPB) with >98% purity, sodium tetrakis[3,5-bis(trifluoromethyl)phenyl]borate (NaTFPB) with >98% purity, tridodecylmethylammonium chloride (TDMACl), bis(2-ethylhexyl)sebacate (DOS) with ≤97% purity, 2-nitrophenyl octyl ether (o-NPOE) 99% purity, polyurethane Tecoflex SG-80A (PU), dodecyl 2-nitrophenyl ether (DNPE), ionic liquid 1-methyl-3-octylimidazolium bis(trifluoromethylsulfonyl)imid [C8min^{+}][C1C1N^{-}], and tetrahydrofuran (THF) were purchased from Sigma-Aldrich. Chloride ionophore I was synthetized as described elsewhere.[47] Analytical grade chloride salts of ammonium, calcium, lithium, magnesium, potassium, sodium, as well as sodium carbonate and sodium phosphate were purchased also from Sigma-Aldrich. Stretchable silver (Ag) ink (CI-1036) and stretchable carbon ink (CI-2051) were obtained from Engineered Conductive Materials, Inc. (U.S.A.). The 3M XYZ 9712 electrically conductive tape and 3M 9471LE adhesive transfer tape were employed for the assembly of the WPISs. Polyurethane polymer ClearFlex used as the electrode substrate was obtained from Smooth-on, Inc., USA. PU filament for the 3D printing of the sampling cell, TPU 95A, Ultimaker Material 1756 was obtained from Ultimaker B.V., the Netherlands.

A 100 mg mixture of ionophore, ion-exchanger, PU and plasticizer in 1ml of THF was used to prepare the cocktails for the ion-selective membranes (ISMs). Table S1 presents all the ISM compositions. The cocktail for the reference membrane (RM) was prepared by dissolving ionic liquid, plasticizer and PU in THF according to the compositions shown in Table S4, as previously described in the literature. [32]

All solutions were prepared in 18.2 MΩ cm^{-1} doubly deionized water (Milli-Q water systems, Merck Millipore). Artificial sweat was prepared according to the recipe previously described in the literature but without containing the analyte of interest in each of the corresponding WPIS evaluation.[48] Briefly, the artificial sweat composition was

50 mM NaCl, 6 mM KCl, 5 mM NH_4Cl, 0.08 mM $MgCl_2$, 2.6 mM $NaHCO_3$ and 0.04 mM Na_2HPO_4.

Electromotive force (EMF) was measured with a high input impedance (10^{15} Ω) EMF16 multichannel data acquisition device (Lawson Laboratories, Inc.) against either a double-junction Ag/AgCl/sat. KCl/1M LiOAc reference electrode (6.0726.100, Metrohm Nordic, Sweden) or the solid-state reference electrode herein developed.

A semi-automatic screen-printer machine (SPR-45 Automated SMT Stencil Printer, DDM Novastar, inc., USA) was used to print the electrodes over the PU substrate. Stencils were designed with Corel Draw software and fabricated at Coated Screens Scandinavian AB, Sweden.

Silhoutte Cameo cutter, USA, was employed to sharply cut the adhesive transfer tape. 3D printer Ultimaker 3, Ultimaker B.V., the Netherlands was used for the printing of the sampling cell. The design of the sampling cell was performed by Solid Edge ST9 solid modelling software (Siemens PLM software, Inc., USA).

The pH measurements were performed with a pH-meter (914 pH/Conductometer, 2.914.0020, Metrohm) or a micropH electrode (biotrode, 6.0224.100, Metrohm) coupled to the previous pH meter. Sweat samples were additionally analysed by ion chromatography (850 Professional IC with a conductivity detector, Metrohm) using Metrosep C6 150/4.0 (6.1051.420) column for cation analysis and Metrosep A Supp 5 105/4.0 (6.1006.520) column for anion analysis, and, a micropH electrode (biotrode, 6.0224.100, Metrohm) coupled to the previous pH meter. All this instrumentation was purchased in Metrohm Nordic, Sweden.

For the regional absorbent patch method (REG), commercial cotton pads where obtained from a local store (oval – shaped pads, 85 x 70 mm and circular – shaped pads, 58 mm

diameter). Hydrofilm roll water-resistant tape (10 cm x 10 m) (Hartmann GmbH, Germany) was purchased from a local pharmacy.

5.2. Potentiometric measurements

All experiments for the evaluation of the ion-selective electrodes were carried out at room temperature of 22±1°C and under constant stirring of 300 rpm (stirrer IKA COLOR SQUID S000, IKA, Germany). Calibrations in the beaker were assessed by the separate solution calibration protocol. Calibration curve using the sensor (working and reference electrode) were performed by immersing the electrode into the corresponding solution. For the flow measurements, the solution flows through the sampling cell by means of a tubing (Tygon LMT-55, ISMATEC, Cole-Parmer GmbH, Germany) connected to a peristaltic pump (ISMATEC IPC series, Cole-Parmer GmbH, Germany). The screen-printed electrodes (both working and reference electrodes) were connected to aluminium wires by employing a conductive tape (3M XYZ 9712 electrically conductive tape), and subsequently to the potentiometer through electrical clamps and BNC outputs. The activity coefficients were calculated using a two-parameter Debye-Hückel approximation from the experimental concentrations. [49] Each logarithmic activity was then plotted against the corresponding steady-state potential and the data were fitted to the Nernst equation.[50]

The selectivity was evaluated using the separate solution method according to Bakker *et al*. [51] Thus, individual calibration graphs were accomplished for the primary ion and the interfering ones and the logarithmic selectivity coefficients were calculated by extrapolating the response to a_I = 1 M using the portion of the calibration curve close to Nernstian response.

For the on-body tests, the activity obtained from the real-time analysis of sweat was converted into concentration in order to have a comparable validation with the standard method. The activity coefficient for each ion analyte was calculated according to a mean

value from the electrolytes found in sweat (i.e., 50 mM NaCl, 6 mM KCl, 5 mM NH_4Cl, 0.08 mM $MgCl_2$, 2.6 mM $NaHCO_3$ and 0.04 mM Na_2HPO_4).[48]

The potential obtained during the on-body tests was smoothed by means of the smooth data option of MATLAB (MathWorks) with a span of 50 in order to remove spikes in the potential response produced during the movements of the subject running on a bike.

5.3. Fabrication of the all-solid-state wearable potentiometric ion sensors

The wearable patch consists of screen-printed electrodes over a stretchable PU substrate (ClearFlex, Smooth-on Inc., USA). First, the PU substrate was prepared by mixing equal volume of reagents A and B as detailed by the manufacturer and spreading the mixture in a rectangular container for the curing process. A time of 5 min vacuum was applied over the mixture to remove bubbles produced during the mixing process. The curing process took place first for 16 h at room temperature. Subsequently, the PU substrate was introduced in an oven at 60°C for 5 h in order to eliminate sticky surface. Finally, the PU substrate was cut into pieces (100 x 50 mm) suitable for the screen-printing process.

The second step involved the screen-printing of the electrodes. The conductive path was printed by employing stretchable silver ink (CI-1036, Engineered Conductive Materials, Inc.) and was then cured at 120°C for 10 min. Afterthought, the stretchable carbon ink (CI-2051, Engineered Conductive Materials, Inc.) was printed to define the circular electrode surface, being cured at 80°C for 5 min. Subsequently, a layer of PU substrate (without curing) was applied over the conductive patterns, being without covering one part (1.5 mm long) to define the connections to the reader and the carbon electrode surface (2.5 mm circle) for later modification to provide ion-sensing properties. This PU covering was also cured at room temperature for 16 h. Overall, the size of the wearable patch was 30 x 20 x 1.5 mm which includes the patterning of 5 electrodes based on serpentine shape to allow the stretchability of the conductive track (10 x 4 mm) and a circular carbon electrode (2.5 mm diameter).

The third step involved the modification of the carbon electrodes to obtain the corresponding working electrodes (WE) and/or reference electrodes (RE). A first film of multiwalled carbon nanotubes (MWCNTs), acting as ion-to-electron transducer, [52] was deposited on top of the carbon electrodes by drop casting 10 x 2 µL of a MWCNTs dispersion in ethanol (1 mg mL^{-1}), waiting 2 min for each drop to be totally dried (i.e. ethanol evaporation). Subsequently, the corresponding ISM or reference membrane was deposited by drop casting 8 x 4 µL (for ISM cocktails) or 5 x 5 µL (for RM cocktail) on top on the MWCNTs layer. Each layer was dried for 2 min before depositing the next drop. Finally, the ISMs and RM were left to dry at room temperature for 5 h (see Table S1 and S4 for the tested membrane compositions). After that, the working and reference electrodes were conditioned overnight in 100 mM NaCl, 10 mM KCl and pH 4.5, respectively for each primary ion.

5.4. Implementation of the sampling cell

A microfluidic sampling cell based on PU (TPU 95A, Ultimaker Material 1756, Ultimaker B.V., the Netherlands) is fabricated using 3D printing technology (Ultimaker 3, Ultimaker B.V., the Netherlands). The optimized microfluidic cell (45 x 25 mm) consists of a hole (1 mm diameter) connected to a sensing channel where the sensor array is placed (24 mm x 3.5 mm x 0.15 mm). This represents a volume of 12.6 µL. A circular collection zone of 15 mm diameter and 50 µm thickness made by the adhesive transfer tape (3M™ 9471LE) (shape cut with Cameo cutter) is also implemented for attachment into the skin while allowing the eccrine glands to deliver sweat towards the sensing channel.

Before on-body tests, the WPISs were tested at controlling flow conditions (i.e. sensor array integrated with the sampling cell). The emulation of the perspiration rate was performed using a peristaltic pump (ISMATEC IPC series, Cole-Parmer GmbH, Germany). The tubing from the pump was fixed to inlet of the sampling cell by adhesive transfer tape.

5.5. On-body tests

The on-body evaluation of the wearable device was performed in compliance with European and Swedish legislations and fundamental ethical principles, including those reflected in the Charter of Fundamental Rights in the European Union and the European Convention on Human Rights and its Supplementary Protocols. [39], [53], [54] Moreover, an informed consent was agreed with each subject before the on-body tests. This informed consent describes the aims, methods and implications of the research, the nature of the research and any benefits, risks or discomfort that may ensue during the test. The main objective of this document is to explicitly state that the participation is voluntary and that anyone has the right to refuse to participate at any time of the process without any consequences. Finally, this informed consent will state how data will be treated (anonymously), used and protected during the project.

The on-body test consists of applying the WPISs on the back of the subject by attachment with adhesive transfer tape. Subsequently, the subject performed constant workload cycle in a professional road bike over a static trainer to produce active perspiration during 1-h. This trial consists of a 10 min ramp up, 40 min of medium-high activity and 10 min of cooling down. The WPISs are connected through conventional cables to the reader close to the static bike (see Figure 6a in the main manuscript). Three different subjects performed the on-body tests, which included different repetitions of the exercise during different days.

The WPISs were previously calibrated with the microfluidic pump in order to calculate the electrolyte dynamics during the on-body trial. Before the WPISs attachment to the skin, the sensing channel was filled with the lowest concentration of the target analyte within the physiological range (i.e., 10 mM NaCl, 1 mM KCl and pH 7.5) to close the potentiometric cell and avoid electrical noise until the microfluidic channel is filled by sweat. When the subject starts the perspiration, the channel will renew the standard with the sweat for the real-time analysis of the electrolytes. This process will be manifested as a sharped change in the potentiometric response of the electrodes, which allows the identification of the starting point of the real measurements.

5.6. Sweat collection

In the first on-body experiments reported herein, the regional absorbent patch (REG) method was used for sweat collection. However, this method may vary depending on the laboratory where the analysis is performed and there is not a universal protocol for this purpose.[30], [31], [55] The description of the method points out the use of 'an absorbent material' that is placed on the skin and 'attached through water-resistant tapes'. Thereafter, the absorbent pad is centrifuged to collect the sweat for further analysis. Because we identified that this method is not compatible with short collection times, we have adapted it as described in the main text. We have called it as modified REG (m-REG).

Commercial cotton pads (oval – shaped pads, 85 x 70 mm and circular – shaped pads, 58 mm diameter) were attached to the skin by Hydrofilm water-resistant tape (120 x 100 mm). After the first 10 min of cycling, when the perspiration was identified in the subject back, the skin was cleaned first with deionized water and dried with a sterile gauze before the pad was fixed. After a certain period of sweat collection, the patch is unstuck form the skin, the pad demounted from the tape and then kept in Falcon tubes, and subsequently, it is centrifuged at 5000 rpm and 4°C for 5 min. Each Falcon tube incorporates a porous platform to allow sweat flowing due to gravitational forces and keep the absorbent material at the upper part of the tube. Finally, the sweat sample was extracted from the tube, aliquoted into Eppendorf tubes, and refrigerated at 4°C for later analysis.

Cotton pads of 85 x 70 mm or 58 mm diameter where previously rinsed with double distilled water, dried in the oven at 80 °C for 2 h and placed on the skin, close to the region where the wearable device is attached. This aims to minimize any differences coming from the sweat in different parts of the body. [56]

On-body validation consisted of the analysis of sweat obtained from the REG or m-REG method by the standard methods (pH meter or ion chromatography) and compare the values with the profiles obtained by the wearable patch during the on-body tests.

Off-body validation consisted of the analysis of sweat obtained from REG or m-REG by the standard methods (pH meter or ion chromatography) and compared with the values obtained by the wearable patch with the same sweat collected by the REG or m-REG and analysed using the microfluidic pump setting.

Table S1. Compositions of ion-selective membranes (isms). Values in parenthesis show the mmol kg^{-1} of the corresponding compound in the membrane.

ISM	PU / wt%	Plasticizer / wt%	Ion-exchanger / wt%	Ionophore / wt%
Cl^-	33	DNPE / 64.85	TDMACl / 0.3 (5)	1.85 (20)
K^+	33	DOS / 64.5	KTClPB / 0.5 (10)	2 (18)
Na^+	33	NPOE / 65.86	NaTFPB / 0.44 (5)	0.7 (7)
pH	33	NPOE / 65.5	KTClPB / 0.5 (10)	1 (17)

Table S2. Analytical performances of the solid-state ion-selective electrodes for potassium, sodium, chloride and pH (n=3). Reference electrode=Ag/AgCl/sat. KCl/1M LiOAc reference electrode (6.0726.100, Metrohm Nordic, Sweden).

ISE	Reproducibility		Repeatability		LOD	LRR	Drift
	Slope (mV)	Intercept (mV)	Slope (mV)	Intercept (mV)	(activity)	(activity)	(mV h^{-1})[a]
Cl^-	-55.9 ± 0.4	29.2 ± 5.2	-54.6 ± 0.3	12.1 ± 5.2	$10^{-5.1}$	10^{-4} – $10^{-1.1}$	0.3 ± 0.2
K^+	60.0 ± 0.3	377.5 ± 5.7	59.8 ± 0.2	294.7 ± 0.5	$10^{-6.1}$	10^{-5} – $10^{-1.1}$	0.3 ± 0.1
Na^+	54.4 ± 2.2	188.3 ± 12.7	56.7 ± 0.2	191.0 ± 1.0	$10^{-5.1}$	$10^{-4.5}$ – $10^{-1.1}$	0.6 ± 0.0
pH	51.1 ± 0.5	576.0 ± 4.6	45.6 ± 0.6	551.3 ± 6.9	–	$10^{-7.5}$ – $10^{-4.5}$	0.2 ± 0.1

[a]Drift values were obtained in 10 mM solution of NaCl and KCl, and pH 6.5 over a period of 12 h.

Table S3. Logarithmic selectivity coefficients for the screen-printed electrodes developed in this work. Other values reported in the literature are included for comparison. The sensors already reported in the literature are referred according to the citation list in the supporting information. Reference electrode=Ag/AgCl/sat. KCl/1M LiOAc reference electrode (6.0726.100, Metrohm Nordic, Sweden).

$logK_{i,j}^{pot}$	**This work**[a]	**Paper-based** [b] [57]	**Yarn-based** [b] [58]	[a]**Au-based**[59]
$logK_{K,Na}^{pot}$	-3.7 ± 0.0	−2.8 ± 0.1	-3.6	−3.2 ± 0.2
$logK_{K,Li}^{pot}$	-3.5 ± 0.0	−2.7 ± 0.1	-4.4	−4.4 ± 0.1
$logK_{K,NH_4}^{pot}$	-1.8 ± 0.1	−1.9 ± 0.1	-1.8	–
$logK_{K,Mg}^{pot}$	-3.9 ± 0.0	−4.1 ± 0.1	–	−4.9 ± 0.2
$logK_{K,Ca}^{pot}$	-3.7 ± 0.1	−3.9 ± 0.1	-4,6	−4.7 ± 0.1
$logK_{Na,K}^{pot}$	-1.5 ± 0.1	–	–	−2.4 ± 0.2
$logK_{Na,Li}^{pot}$	-2.0 ± 0.1	–	–	−3.7 ± 0.1
$logK_{Na,NH_4}^{pot}$	-1.9 ± 0.1	–	–	–
$logK_{Na,Mg}^{pot}$	-3.0 ± 0.1	–	–	−4.4 ± 0.2
$logK_{Na,Ca}^{pot}$	-2.8 ± 0.3	–	–	−4.0 ± 0.1
$logK_{Cl,pyruvate}^{pot}$	-1.2 ± 0.1	–	–	–
$logK_{Cl,urate}^{pot}$	-2.7 ± 0.0	–	–	–
$logK_{Cl,lactate}^{pot}$	-2.0 ± 0.1	–	–	–
$logK_{Cl,HPO_4^{2-}}^{pot}$	-1.4 ± 0.3	–	–	–
$logK_{Cl,HCO_3^-}^{pot}$	-0.2 ± 0.1	–	–	–
$logK_{Cl,ClO_4^-}^{pot}$	-0.3 ± 0.2	–	–	–

[a]Separate solution method; [b]Fixed interference method.

Table S4. Analytical performances of the developed reference electrode (RE) using different membrane compositions (n=5).

Membrane composition[a]	**Slope (mV log a_i^{-1})**[b]	**Drift (mV h^{-1}) / Time of test (h)** [c]
R1: 60 mg PU, 60 mg o-NPOE, 30 mg IL	3.0 ± 0.9	–
R2: 60 mg PU, 30 mg IL	1.3 ± 0.5	3.9 ± 0.8 / 5.5
R3: 90 mg PU, 30 mg IL	3.7 ± 1.6	2.8 ± 0.5 / 8.5
R4: 120 mg PU, 30 mg IL	1.2 ± 1.3	0.2 ± 0.1 / 8.5

[a]All the reagents were dissolved in 1 mL THF. [b]Slope calculated from the additions of KCl from 0.1 to 100 mM.

Table S5. Analytical parameters of the all-solid-state potentiometric sensors (including working and reference electrode in the array) for potassium, sodium, chloride and pH (n=3).

ISE	Slope (mV)	Intercept (mV)	LRR (activity)
Cl^-	-57.2 ± 3.0	-105.1 ± 6.8	$10^{-3} – 10^{-1.1}$
K^+	57.6 ± 0.1	250.5 ± 2.3	$10^{-4} – 10^{-1.1}$
Na^+	53.5 ± 0.9	107.6 ± 0.3	$10^{-3} – 10^{-1.1}$
pH	54.5± 0.5	216.3±12.5	$10^{-7.5} – 10^{-4.5}$

Table S6. Carry-over tests of the all-solid-state potentiometric sensor (including working and reference electrode in the same array) for potassium, sodium, chloride and pH (n=6).

ISE	Slope (mV)	Intercept	LRR (activity)
Cl^-	-63.0 ± 2.4	-136.4 ± 4.0	$10^{-2.1} – 10^{-1.2}$
K^+	56.8 ± 2.5	56.4 ± 5.8	$10^{-3.2} – 10^{-2.2}$
Na^+	54.2 ± 1.3	-11.4 ± 2.8	$10^{-2.1} – 10^{-1.2}$
pH	50.1 ± 0.5	156.8 ± 3.1	$10^{-7.5} – 10^{-4.5}$

Table S7. Calibration parameters obtained during resiliency tests of the all-solid-state potentiometric sensor (including working and reference electrode in the same array) for potassium, sodium, chloride and pH.

ISE	Test	Slope (mV)	Intercept (mV)
Cl^-	Stretching	-53.9 ± 2.4	-97.8 ± 2.2
	Bending	-53.2 ± 1.3	-60.0 ± 5.0
K^+	Stretching	52.2 ± 1.4	140.9 ± 6.1
	Bending	52.3 ± 0.7	136.1 ± 3.5
Na^+	Stretching	53.5 ± 0.9	102.3 ± 0.5
	Bending	54.4 ± 1.0	34.8 ± 2.5
pH	Stretching	57.6 ± 1.3	405.4 ± 5.7
	Bending	52.7 ± 0.5	179.3 ± 1.8
*K^+	Twisting	53.7 ± 1.4	67.0 ± 4.9

***Mechanical test carried by twisting the WPISs (electrode array + sampling cell).

Table S8. IC values from sweat samples obtained by the REG method and comparison to the concentrations obtained by WPISs (profiles exhibited on Figure 6b, average of 3 working electrodes). Table shows data from chloride, potassium and sodium. IC = ion chromatography.

Analyte	Period (min)	IC (mM)	WPISs (mM)	Error (%)
Cl^-	10 – 20	161.4	41.2 ± 16.2	292.1
	20 – 25	126.3	49.5 ± 5.3	155.3
	25 – 30	175.8	53.8 ± 7.1	226.8
	30 – 35	175.3	51.4 ± 6.5	241.2
	35 – 40	171.1	48.1 ± 5.3	255.9
	40 – 45	192.9	50.4 ± 5.7	282.9
	45 – 50	224.0	54.1 ± 7.3	314.1
	50 – 55	192.8	46.0 ± 6.6	318.9
	55 – 60	135.2	37.0 ± 2.4	265.8
Na^+	10 – 20	158.2	46.7 ± 19.1	239.1
	20 – 25	137.2	53.3 ± 2.5	157.4
	25 – 30	186.2	53.0 ± 1.4	251.0
	30 – 35	185.7	53.3 ± 2.9	250.6
	35 – 40	186.6	54.4 ± 4.3	243.0
	40 – 45	201.8	58.0 ± 8.1	248.1
	45 – 50	229.8	58.9 ± 5.9	290.4
	50 – 55	200.0	63.2 ± 9.0	216.3
	55 – 60	145.2	60.9 ± 10.2	138.4
K^+	10 – 20	7.0	4.2 ± 0.4	67.7
	20 – 30	7.1	4.4 ± 0.4	59.5
	30 – 40	8.2	4.3 ± 0.4	88.7
	40 – 50	7.0	4.2 ± 0.5	65.7
	50 – 60	6.3	3.9 ± 0.5	59.6

Table S9. Error obtained by using directly the activity readout or by converting the activity from the WPISs to concentration.

Analyte	Period (min)	IC (mM)	WPIS – concentration (mM)	WPIS – activity	Error (%) WPIS concentration	Error (%) WPIS activity
K^+	35 – 47.5	4.3	4.4 ± 0.2	3.4 ± 0.2	2.3	20.2
	47.5 – 60	4.2	3.9 ± 0.2	3.0 ± 0.2	8.6	28.7
Na^+	22.5 – 35	83.7	85.1 ± 2.0	63.8 ± 1.5	1.6	23.8
	35 – 47.5	89.5	83.7 ± 1.3	62.8 ± 1.0	6.5	29.9
	47.5 – 60	83.5	78.6 ± 2.2	59.0 ± 1.7	5.9	29.4
Cl^-	20 – 30	54.6	46.0 ± 3.9	37.2 ± 3.2	15.8	31.8
	30 – 40	56.2	52.7 ± 1.7	42.7 ± 1.4	6.1	24.0
	40 – 50	61.9	56.7 ± 2.9	45.9 ± 2.3	8.4	25.8

*Data corresponding to the on-body tests on Figure 6a, Figure S9b, Figure 7b (Subject 1).

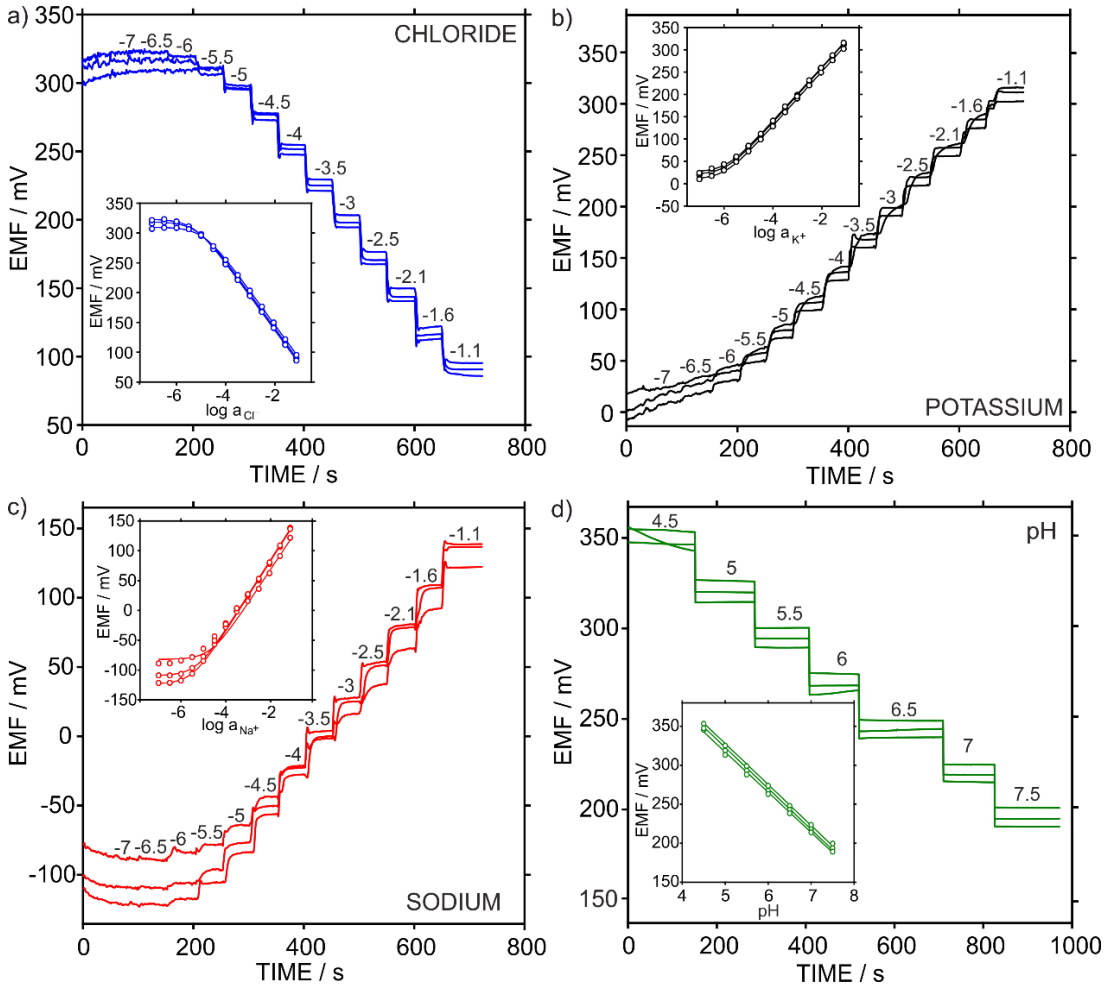

Figure S21. Reproducibility of the solid-state potentiometric sensors. Dynamic response of (a) chloride-selective electrodes (n=3), (b) potassium-selective electrodes and (n=3), (c) sodium-selective electrodes (n=3) and (d) pH electrodes (n=3) in MQ water. Inset plots: corresponding calibration curves fitted to the Nernst equation.

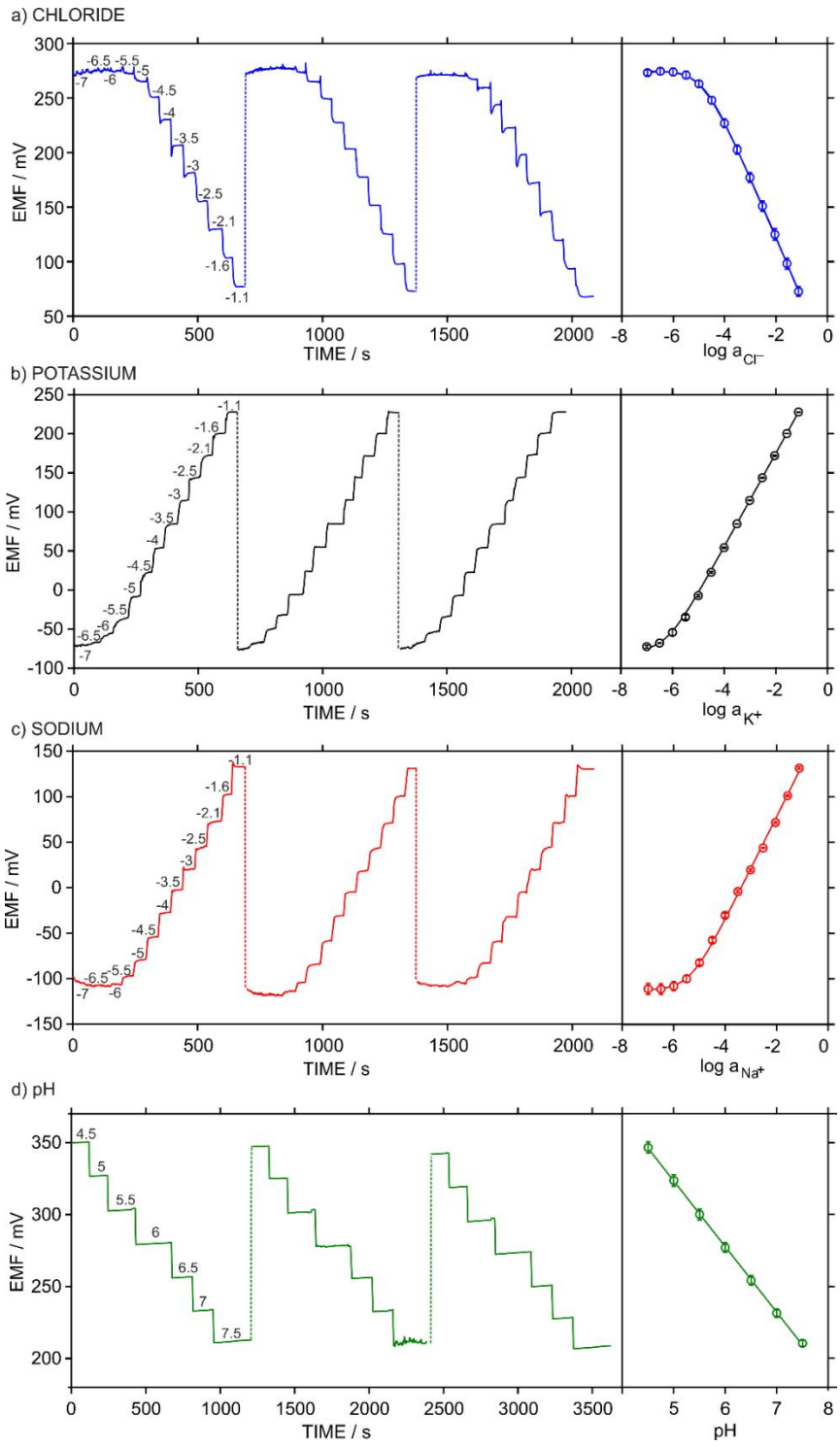

Figure S22. Repeatability of the solid-state potentiometric electrodes: (a) chloride, (b) potassium, (c) sodium and (d) pH. The assay consists of running three consecutive calibration curves. The dynamic response is displayed for each ion-selective electrode on the left with the corresponding calibration curve on the right.

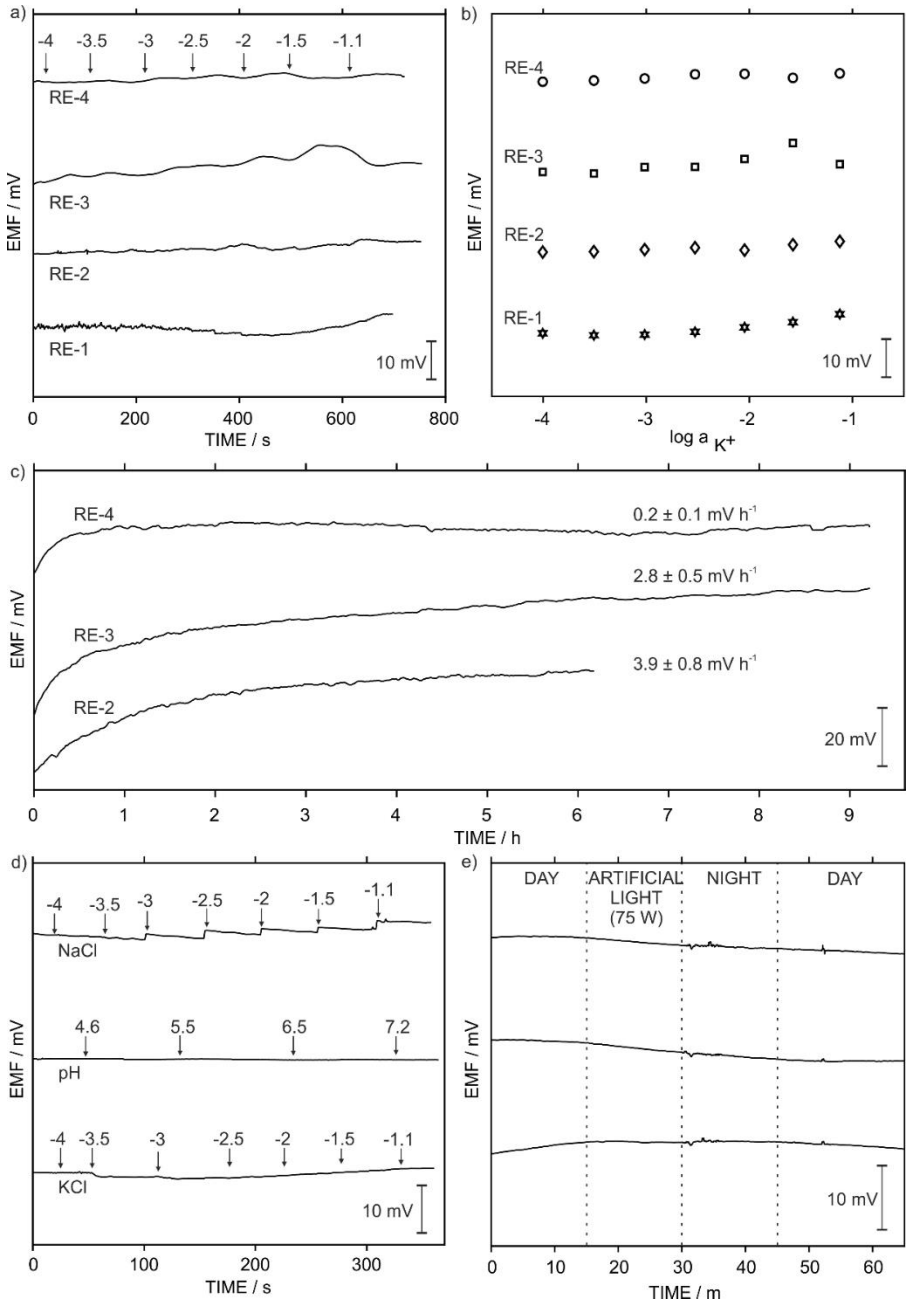

Figure S23. Characterization of the solid-state reference electrodes. a) Dynamic potentiometric response of different compositions of reference membranes towards KCl from 10^{-4} to $10^{-1.1}$ in aqueous solution. b) Plots of logarithmic activity vs. potential. Note that the potentiometric responses have been offset by a few mV to avoid overlapping of the displayed signal. c) Medium-term drift in 10 mM KCl. d) Dynamic potentiometric response of the optimal reference membrane towards NaCl, KCl from 10^{-4} to $10^{-1.1}$ in aqueous solution and change in pH from 4.6 to 7.2 with acetate buffer and phosphate buffer at 10 mM ionic strength. e) Light sensitivity (ambient light, darkness and artificial light using a bulb of 75W).

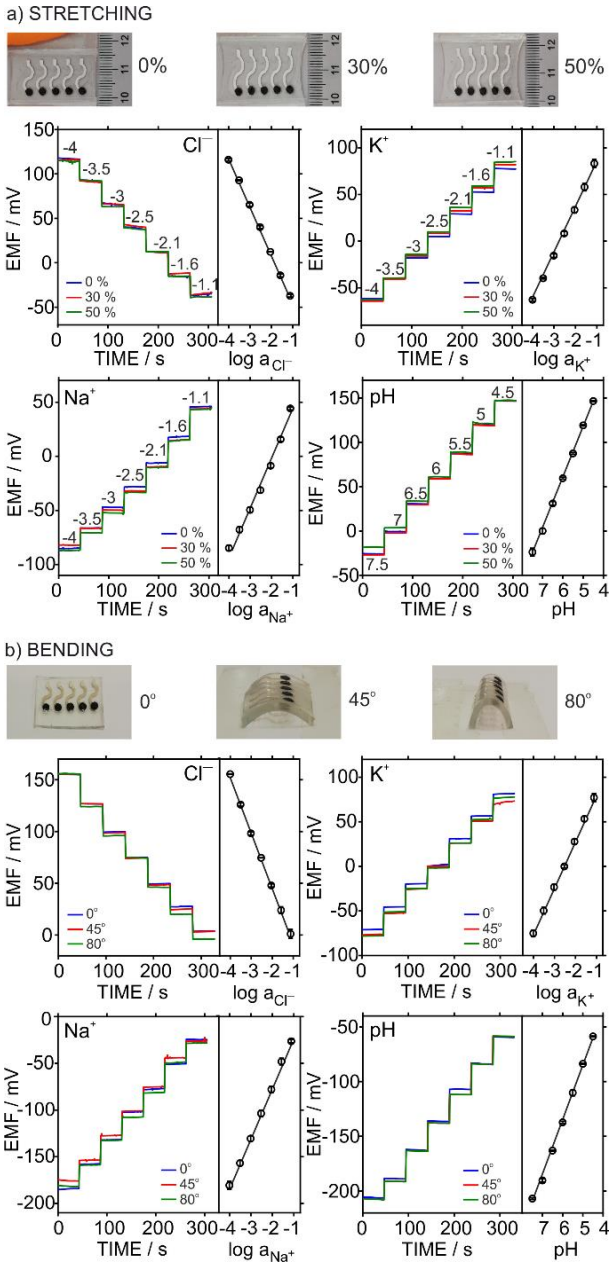

Figure S24. (a) Images of the stretchability force upon the application of 30 and 50 % of linear deformation. Observed dynamic responses for increasing concentrations of each ion analyte together with the corresponding calibration curve. (b) Images of the bending force upon the application of 45° and 80° of curvilinear deformation. Observed dynamic responses for increasing concentrations of each ion together with the corresponding calibration curve. Each resiliency test consisted of 10 repetitions of the corresponding deformation. All the calibrations were performed in water.

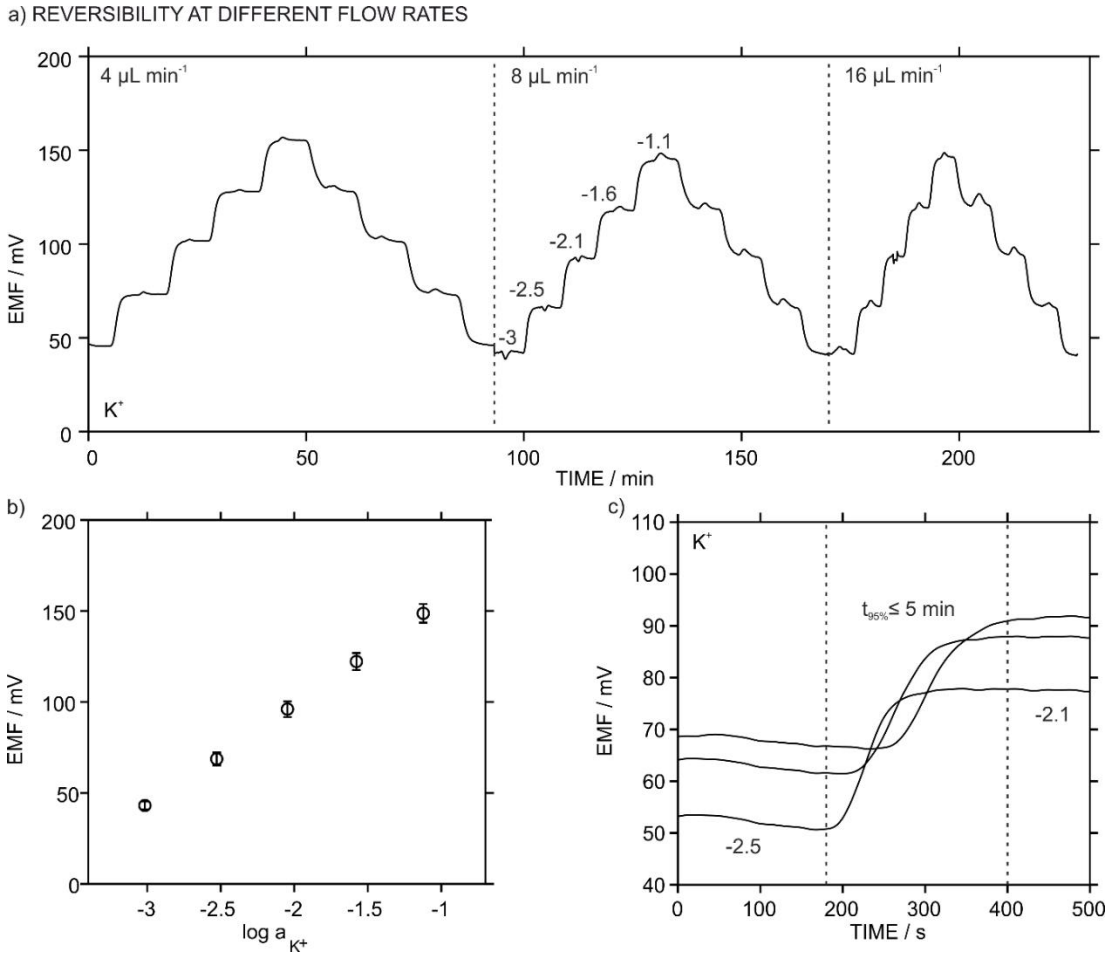

Figure S25. Effect of the flow rate in the potassium response using WPISs (sensors array + sampling cell). a) Reversibility of the dynamic response for potassium under 4, 8 and 16 µL min^{-1}. b) Calibration graph obtained as the average of the dynamic profiles displayed in (a). c) Response time after changing K^+ concentration from $10^{-2.5}$ to $10^{-2.1}$ at 4 µL min^{-1}.

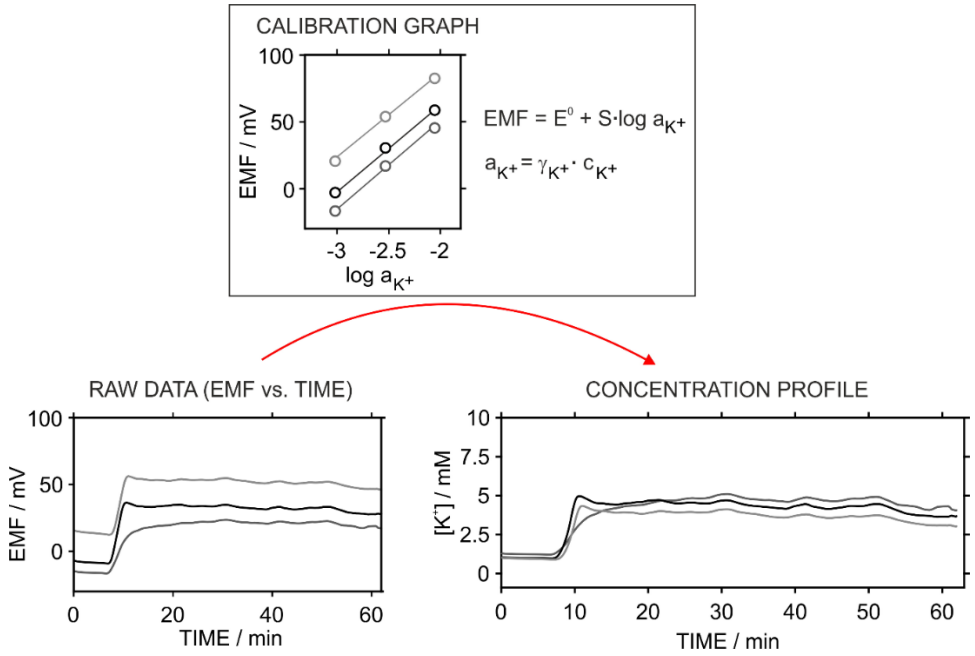

Figure S26. The dynamic plot electromotive force (EMF) versus time gathered with potassium electrodes during an on-body test is translated into concentration versus time by using the previous calibration graph (logarithmic activity versus EMF) of each electrode. Finally, the ion activity is transformed into concentration by considering the ionic strength of the solution, in this case, calculated by the artificial sweat composition. Potassium profiles are shown as an example.

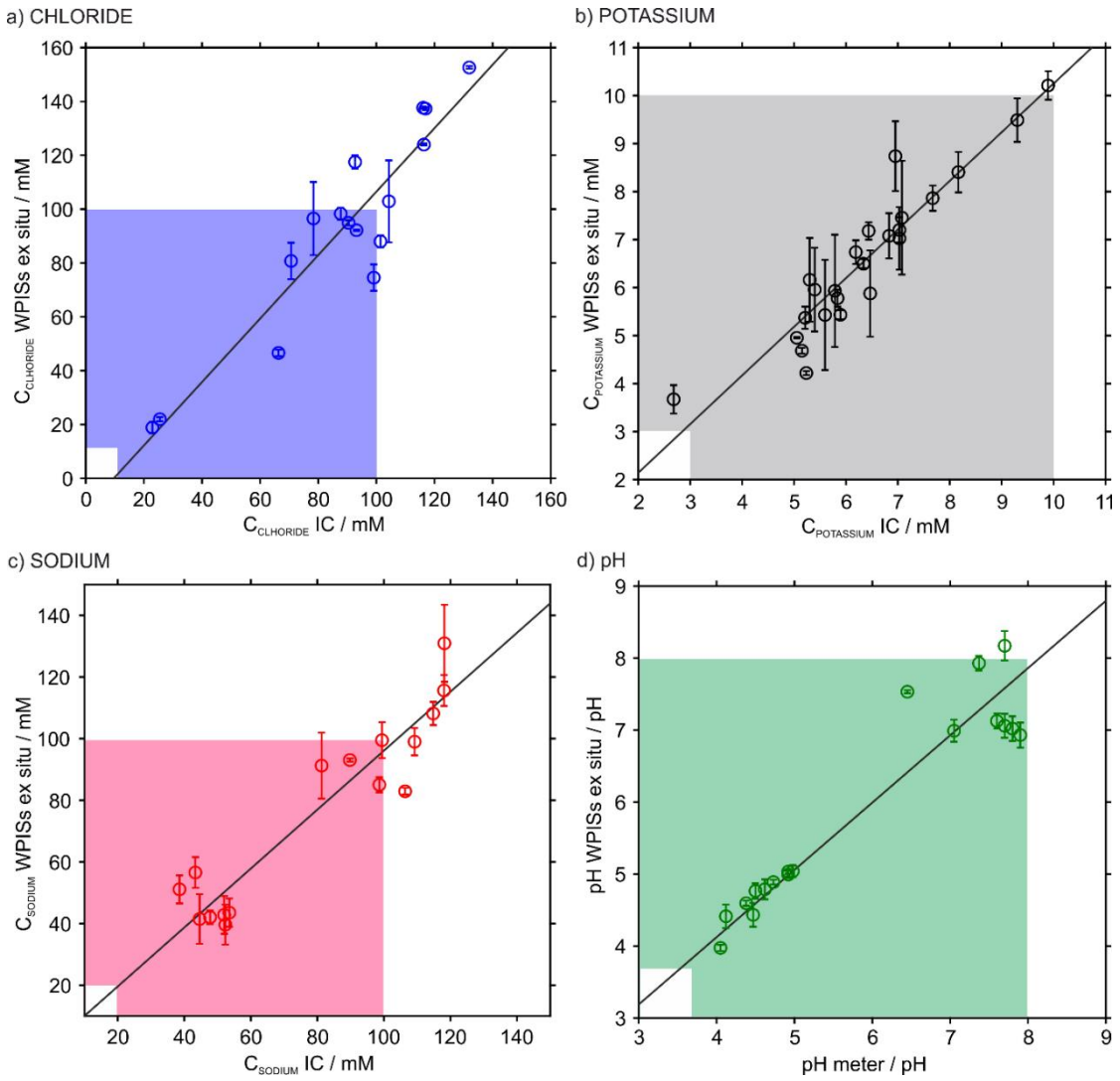

Figure S27. Validation of the WPISs operating ex situ. a) Correlation between the Cl^- concentrations obtained by the WPISs (n=3) and ion chromatography (IC). b) Correlation between the K^+ concentrations obtained by the WPISs (n=3) and IC. c) Correlation between the Na^+ concentrations obtained by the WPISs (n=3) and IC. d) Correlation between the pH obtained by the WPISs (n=3) and a pH micro-electrode. All the samples were diluted (1:100) in MQ water for IC analysis. The observed Pearson correlation coefficients were 0.93 for Cl^- (n = 16 samples), 0.94 for K^+ (n = 24 samples), 0.94 for Na^+ (n = 16 samples) and 0.95 for pH (n = 18 samples). The common physiological levels of the analyte are displayed in the colorful square inside each plot.

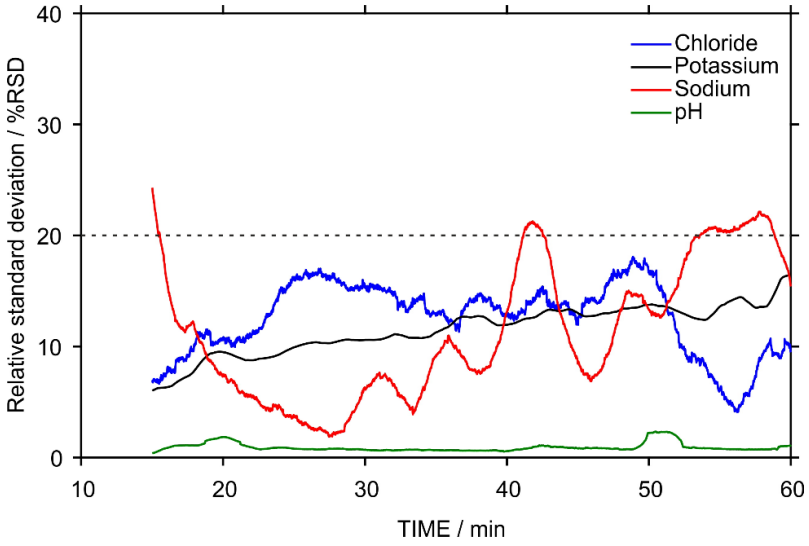

Figure S28. Reproducibility of the WPISs (3 working electrodes) from each of the on-body tests at Figure 6b. The plot shows the dynamic relative standard deviation (%RSD) from the 3 replicates at each time (every second during the on-body test) for the chloride, potassium, sodium and pH WPISs.

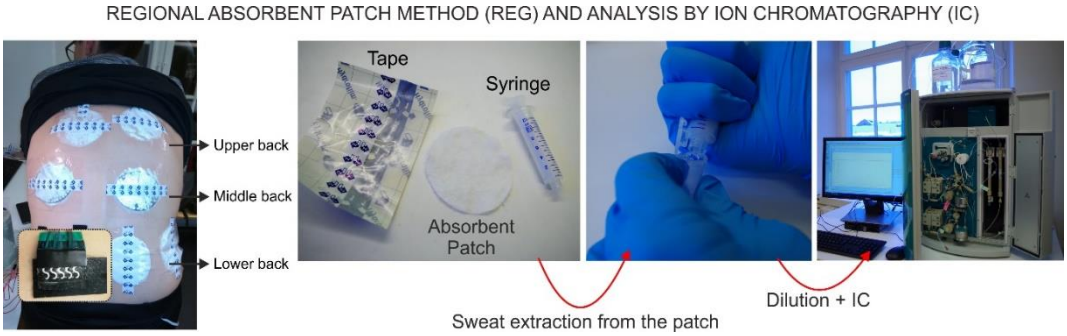

Figure S29. Illustration of the protocol based on the modified regional absorbent patch method (m-REG) for sweat sampling and subsequent IC analysis. After sweat collection during a certain time by means of commercial cotton pads (85 x 70 mm dimensions) fixed in the back of the subject with Hydrofilm tape, the absorbent pad is removed from the tape and inserted in a syringe (12 mL). The pad is then squeezed by applying pressure by the syringe, which allows to collect the sample into an Eppendorf tube. Finally, the sample is diluted prior to its analysis in the IC.

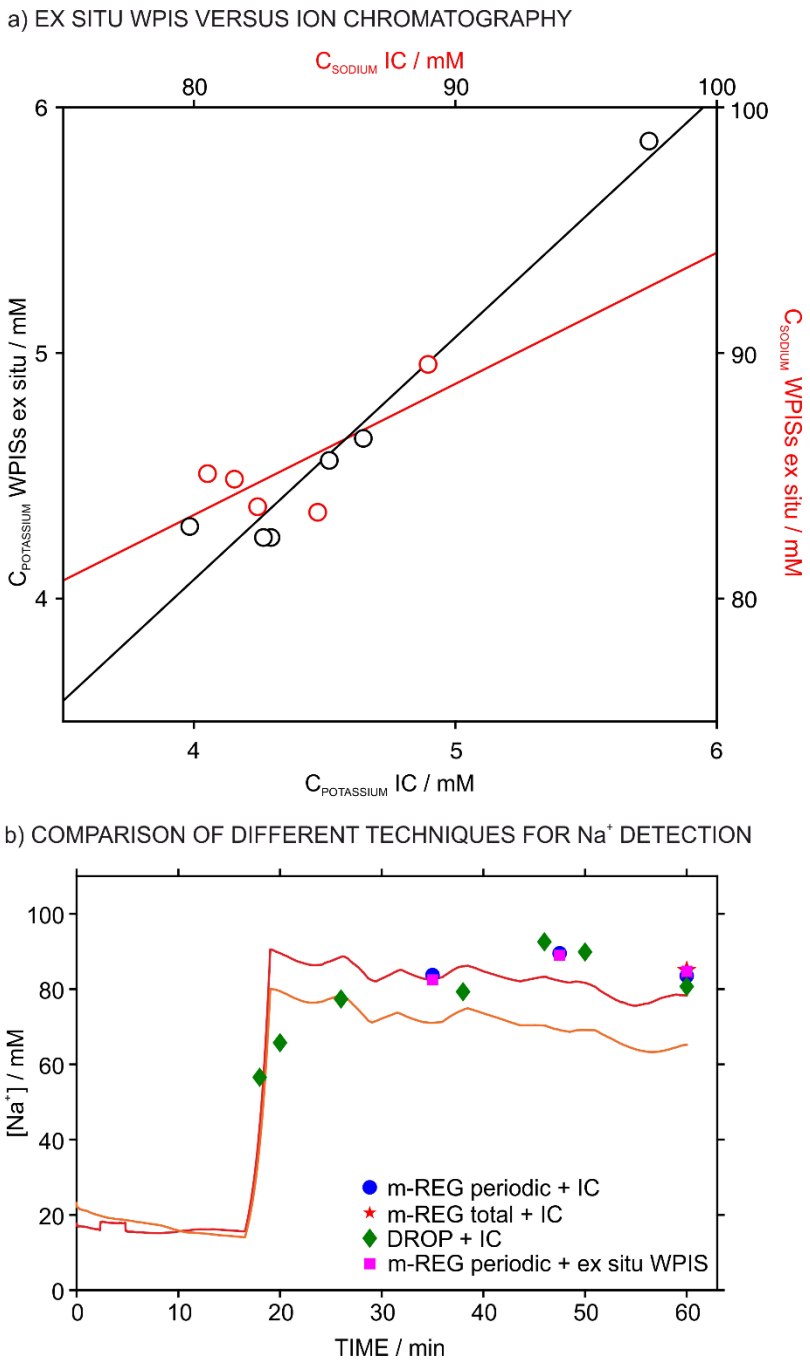

Figure S30. (a) Correlation between WPISs performing ex situ and IC analysis of sweat samples collected by the m-REG method. Pearson correlation coefficient of 0.99. (b) Concentration profile of two WPISs for sodium during on-body measurements. Sweat samples were collected with the m-REG method and measured with IC and the WPISs operating ex situ. In addition, the sweat was collected at the outlet of the sampling cell (DROP) and analyzed with IC for comparison.

REFERENCES

[1] S. A. Boppart and R. Richards-Kortum, "Point-of-care and point-of-procedure optical imaging technologies for primary care and global health," *Sci. Transl. Med.*, vol. 6, no. 253, pp. 253rv2-253rv2, Sep. 2014.

[2] J. Heikenfeld, J. Jajack, A. Rogers, J. Gutruf, P. Tian, L. Pan, T. Li, R. Khine, M. Kim, J. Wang, J. Kim, "Wearable sensors: modalities, challenges, and prospects," *Lab Chip*, vol. 18, no. 2, pp. 217–248, 2018.

[3] M. Bariya, H. Y. Y. Nyein, and A. Javey, "Wearable sweat sensors," *Nat. Electron.*, vol. 1, no. 3, pp. 160–171, Mar. 2018.

[4] M. Parrilla, Marc Cuartero, N. Padrell Sánchez, Sara Rajabi, Mina Roxhed, and G. A. Niklaus, Frank Crespo, "Wearable All-Solid-State Potentiometric Microneedle Patch for Intradermal Potassium Detection," *Anal. Chem.*, vol. 91, no. 2, pp. 1578–1586, Jan. 2019.

[5] R. Cánovas, M. Parrilla, P. Blondeau, and F. J. Andrade, "A novel wireless paper-based potentiometric platform for monitoring glucose in blood," *Lab Chip*, vol. 17, no. 14, pp. 2500–2507, 2017.

[6] M. Parrilla, J. Ferré, T. Guinovart, and F. J. Andrade, "Wearable Potentiometric Sensors Based on Commercial Carbon Fibres for Monitoring Sodium in Sweat," *Electroanalysis*, vol. 28, no. 6, pp. 1267–1275, Jun. 2016.

[7] M. Parrilla, M. Cuartero, and G. A. Crespo, "Wearable potentiometric ion sensors," *TrAC Trends Anal. Chem.*, vol. 110, pp. 303–320, Jan. 2019.

[8] M. Parrilla, R. Cánovas, I. Jeerapan, F. J. Andrade, and J. Wang, "A Textile-Based Stretchable Multi-Ion Potentiometric Sensor," *Adv. Healthc. Mater.*, vol. 5, no. 9, pp. 996–1001, May 2016.

[9] J. Kim, A. S. Campbell, B. E.-F. de Ávila, and J. Wang, "Wearable biosensors for healthcare monitoring," *Nat. Biotechnol.*, 2019.

[10] G. Kaya, Tolga Liu, K. Ho, Jenny Yelamarthi, and A. Miller, Kevin Edwards, Jeffrey Stannard, "Wearable Sweat Sensors: Background and Current Trends," *Electroanalysis*, 2018.

[11] W. Gao, G. A. Brooks, and D. C. Klonoff, "Wearable Physiological Systems and Technologies for Metabolic Monitoring," *J. Appl. Physiol.*, vol. 124, no. 3, pp. 548–556, 2018.

[12] A. K. Yetisen, J. L. Martinez-Hurtado, B. Ünal, A. Khademhosseini, and H. Butt, "Wearables in Medicine," *Adv. Mater.*, vol. 1706910, p. 1706910, 2018.

[13] J. Hayward, "Electronic Skin Patches 2018-2028: Technologies, Players & Markets, IDTechEx," 2018.

[14] J. Heikenfeld, J. Jajack, A. Rogers, J. Gutruf, P. Tian, L. Pan, T. Li, R. Khine, M. Kim, J. Wang, J. Kim, "Wearable sensors: modalities, challenges, and prospects," *Lab Chip*, vol. 18, pp. 217–248, 2018.

[15] K. Gao, Wei Emaminejad, Sam Nyein, Hnin Yin Yin Challa, Samyuktha Chen and A. Peck, Austin Fahad, Hossain M. Ota, Hiroki Shiraki, Hiroshi Kiriya, Daisuke Lien, Der-Hsien Brooks, George A. Davis, Ronald W. Javey, "Fully integrated wearable sensor arrays for multiplexed in situ perspiration analysis," *Nature*, vol. 529, no. 7587, pp. 509–514, 2016.

[16] M. Parrilla, M. Cuartero, and G. A. Crespo, "Wearable Potentiometric Ion Sensors," *TrAC - Trends Anal. Chem.*, vol. 110, pp. 303–320, 2019.

[17] P. C. Choi, Dong Hoon Thaxton, Abigail Jeong, In cheol Kim, Kain Sosnay, Patrick R. Cutting, Garry R. Searson, "Sweat test for cystic fibrosis: Wearable sweat sensor vs. standard laboratory test," *J. Cyst. Fibros.*, vol. 17, no. 4, pp. e35–e38, 2018.

[18] M. Cuartero, M. Parrilla, and G. A. Crespo, "Wearable potentiometric sensors for medical applications," *Sensors (Basel).*, vol. 19, no. 363, 2019.

[19] R. M. Morgan, M. J. Patterson, and M. a. Nimmo, "Acute effects of dehydration on sweat composition in men during prolonged exercise in the heat," *Acta Physiol. Scand.*, vol. 182, no. 1, pp. 37–43, 2004.

[20] L. B. Baker, J. R. Stofan, A. A. Hamilton, and C. A. Horswill, "Comparison of regional patch collection vs . whole body washdown for measuring sweat sodium and potassium loss during exercise," *J. Appl. Physiol.*, vol. 107, pp. 887–895, 2009.

[21] R. Sonner, Z. Wilder, E. Heikenfeld, J. Kasting, G. Beyette, F. Swaile, D. Sherman, F. Joyce, J. Hagen, J. Kelley-Loughnane, N. Naik, "The microfluidics of the eccrine sweat gland, including biomarker partitioning, transport, and biosensing implications," *Biomicrofluidics*, vol. 9, no. 3, p. 4921039, 2015.

[22] S. M. Ali and G. Yosipovitch, "Skin pH: From basic science to basic skin care," *Acta Derm. Venereol.*, vol. 93, no. 3, pp. 261–267, 2013.

[23] C. H. Bohl and S. L. Volpe, "Magnesium and exercise," *Crit. Rev. Food Sci. Nutr.*, vol. 42, no. 6, pp. 533–563, 2002.

[24] M. Parrilla, R. Cánovas, I. Jeerapan, F. J. Andrade, and J. Wang, "A Textile-Based Stretchable Multi-Ion Potentiometric Sensor.," *Adv. Healthc. Mater.*, vol. 5, no. 9, pp. 996–1001, May 2016.

[25] M. Parrilla, J. Ferré, T. Guinovart, and F. J. Andrade, "Wearable Potentiometric Sensors Based on Commercial Carbon Fibres for Monitoring Sodium in Sweat," *Electroanalysis*, vol. 28, no. 6, pp. 1267–1275, 2016.

[26] R. Alizadeh, Azar Burns, Andrew Lenigk, Ralf Gettings and M. Ashe, Jeffrey Porter, Adam McCaul, Margaret Barrett, Ruairi Diamond, Dermot White, Paddy Skeath, Perry Tomczak, "A wearable patch for continuous monitoring of sweat electrolytes during exertion," *Lab Chip*, vol. 18, pp. 2632–2641, 2018.

[27] G. B. Nyein, Hnin Yin Yin Tai, Li-chia Ngo, Quynh Phuong Chao, Minghan Zhang, H. Gao, Wei Bariya, Mallika Bullock, James Kim, and A. Fahad, Hossain M Javey, "A Wearable Microfluidic Sensing Patch for Dynamic Sweat Secretion Analysis," *ACS Sensors*, vol. 3, no. 5, pp. 944–952, 2018.

[28] J. Sempionatto, Juliane R Martin, Aida García-Carmona, Laura Barfidokht, Abbas Kurniawan, Jonas F Moreto, Jose R Tang, Guangda Shin, Andrew Liu, Xiaofeng Escarpa, Alberto Wang, "Skin-Worn Soft Microfluidic Potentiometric Detection System."

[29] B. Anastasova, S. Crewther, V. Bembnowicz, P. Curto, and G. Z. Ip, H. M. Rosa, B. Yang, "A wearable multisensing patch for continuous sweat monitoring," *Biosens. Bioelectron.*, vol. 94, no. June 2016, p. 730, 2017.

[30] C. E. Dziedzic, M. L. Ross, G. J. Slater, and L. M. Burke, "Variability of Measurements of Sweat Sodium Using the Regional Absorbent-Patch Method," *Int. J. Sport Physiol. Perform.*, vol. 9, pp. 832–838, 2014.

[31] L. B. Baker, "Sweating Rate and Sweat Sodium Concentration in Athletes: A Review of Methodology and Intra/Interindividual Variability," *Sport. Med.*, vol. 47, no. s1, pp. 111–128, 2017.

[32] J. Hu, K. T. Ho, X. U. Zou, W. H. Smyrl, A. Stein, and P. Buhlmann, "All-solid-state reference electrodes based on colloid-imprinted mesoporous carbon and their application in disposable paper-based potentiometric sensing devices," *Anal.*

Chem., vol. 87, no. 5, pp. 2981–2987, 2015.

[33] M. Cuartero, G. A. Crespo, and E. Bakker, "Polyurethane Ionophore-Based Thin Layer Membranes for Voltammetric Ion Activity Sensing," *Anal. Chem.*, vol. 88, no. 11, pp. 5649–5654, 2016.

[34] G. Smith, Caroline J.Havenith, "Body mapping of sweating patterns in male athletes in mild exercise-induced hyperthermia," *Eur. J. Appl. Physiol.*, vol. 111, no. 7, pp. 1391–1404, 2011.

[35] J. R. Baker, Lindsay B. Ungaro, Corey T. Sopeña, Bridget C. Nuccio, Ryan P. Reimel, Adam J. Carter, James M. Stofan and K. A. Barnes, "Body map of regional vs. whole body sweating rate and sweat electrolyte concentrations in men and women during moderate exercise-heat stress," *J. Appl. Physiol.*, vol. 124, no. 5, pp. 1304–1318, 2018.

[36] C. K. Dixit, K. Kadimisetty, and J. Rusling, "3D-printed miniaturized fluidic tools in chemistry and biology," *TrAC - Trends Anal. Chem.*, vol. 106, pp. 37–52, 2018.

[37] J. Kim, R. Kumar, A. J. Bandodkar, and J. Wang, "Advanced Materials for Printed Wearable Electrochemical Devices: A Review," *Adv. Electron. Mater.*, vol. 3, no. 1, p. 1600260, 2017.

[38] R. Cánovas, M. Parrilla, P. Mercier, F. J. Andrade, and J. Wang, "Balloon-Embedded Sensors Withstanding Extreme Multiaxial Stretching and Global Bending Mechanical Stress: Towards Environmental and Security Monitoring," *Adv. Mater. Technol.*, vol. 1, no. 5, p. 1600061, 2016.

[39] M. Bariya, H. Y. Y. Nyein, and A. Javey, "Wearable sweat sensors," *Nat. Electron.*, vol. 1, no. 3, pp. 160–171, 2018.

[40] K. Sato, W. H. Kang, K. Saga, and K. T. Sato, "Biology of sweat glands and their disorders. I. Normal sweat gland function.," *J. Am. Acad. Dermatol.*, vol. 20, no. 4, pp. 537–563, 1989.

[41] W. Emaminejad, Sam Gao and R. W. Wu, Eric Davies, Zoe A. Yin Yin Nyein, Hnin Challa, Samyuktha Ryan, Sean P. Fahad, Hossain M. Chen, Kevin Shahpar, Ziba Talebi, Salmonn Milla, Carlos Javey, Ali Davis, "Autonomous sweat extraction and analysis applied to cystic fibrosis and glucose monitoring using a fully integrated wearable platform," *Proc. Natl. Acad. Sci.*, vol. 114, no. 18, p. 201701740, 2017.

[42] K. Tóth, J. Fucskó, E. Lindner, Z. Fehér, and E. Pungor, "Potentiometric detection in flow analysis," *Anal. Chim. Acta*, vol. 179, pp. 359–370, 1986.

[43] F. Cazalé, A. Sant, W. Ginot and P. Launay, J.-C. Savourey, G. Revol-Cavalier, F. Lagarde, J.M. Heinry, D. Launay, J. Temple-Boyer, "Physiological stress monitoring using sodium ion potentiometric microsensors for sweat analysis," *Sensors Actuators B Chem.*, vol. 225, pp. 1–9, 2016.

[44] W. Nyein, Hnin Yin Yin Gao and A. Shahpar, Ziba Emaminejad, Sam Challa, Samyuktha Chen, Kevin Fahad, Hossain M. Tai, Li-Chia Ota, Hiroki Davis, Ronald W. Javey, "A Wearable Electrochemical Platform for Noninvasive Simultaneous Monitoring of Ca 2+ and pH," *ACS Nano*, vol. 10, no. 7, pp. 7216–7224, 2016.

[45] L. B. Baker, C. T. Ungaro, K. A. Barnes, R. P. Nuccio, A. J. Reimel, and J. R. Stofan, "Validity and reliability of a field technique for sweat Na+and K+analysis during exercise in a hot-humid environment," *Physiol. Rep.*, vol. 2, no. 5, p. e12007, 2014.

[46] R. J. Maughan and S. M. Shirreffs, "Development of individual hydration strategies for athletes," *Int. J. Sport Nutr. Exerc. Metab.*, vol. 18, no. 5, pp. 457–472, 2008.

[47] G. A. Pankratova, Nadezda Cuartero, Maria Jowett, Laura A. Howe, Ethan N.W. Gale, Philip A. Bakker, Eric Crespo, "Fluorinated tripodal receptors for potentiometric chloride detection in biological fluids," *Biosens. Bioelectron.*, vol. 99, no. February 2017, pp. 70–76, 2018.

[48] C. Callewaert, B. Buysschaert, E. Vossen, V. Fievez, T. Van de Wiele, and N. Boon, "Artificial sweat composition to grow and sustain a mixed human axillary microbiome," *J. Microbiol. Methods*, vol. 103, pp. 6–8, 2014.

[49] P. C. Meier, "Two-parameter debye-hückel approximation for the evaluation of mean activity coefficients of 109 electrolytes," *Anal. Chim. Acta*, vol. 136, no. C, pp. 363–368, 1982.

[50] E. Bakker and E. Pretsch, "Modern potentiometry.Bakker, E., & Pretsch, E. (2007). Modern potentiometry. Angewandte Chemie (International Ed. in English), 46(30), 5660–8. doi:10.1002/anie.200605068," *Angew. Chem. Int. Ed. Engl.*, vol. 46, no. 30, pp. 5660–8, 2007.

[51] E. Bakker, E. Pretsch, and P. Bühlmann, "Selectivity of Potentiometric Ion Sensors," *Anal. Chem.*, vol. 72, no. 6, pp. 1127–1133, Mar. 2000.

[52] G. A. Crespo, S. Macho, and F. X. Rius, "Ion-selective electrodes using carbon nanotubes as ion-to-electron transducers.," *Anal. Chem.*, vol. 80, pp. 1316–1322, 2008.

[53] *C. of E. European Council of Human Rights, "European Convention on Human Rights."* 1953.

[54] O. Hamulák, D. R. Troitiño, and A. Chochia, "The charter of fundamental rights of the european union and the social rights," *Estud. Const.*, vol. 16, no. 1, pp. 167–186, 2018.

[55] L. Baker, K. Barnes, M. Anderson, D. Passe, and J. Stofan, "Normative data for regional sweat sodium concentration and whole-body sweating rate in athletes," *J. Sports Sci.*, vol. 34, pp. 1–11, Jun. 2015.

[56] K. Baker, Lindsay Ungaro, Corey Nuccio, Ryan Reimel, Adam Carter, James Stofan, John Barnes, "Body Map of Regional versus Whole Body Sweating Rate and Sweat Electrolyte Concentrations in Men and Women during Moderate Exercise-Heat Stress," *J. Appl. Physiol.*, vol. 124, Feb. 2018.

[57] M. Novell, M. Parrilla, G. A. Crespo, F. X. Rius, and F. J. Andrade, "Paper-based ion-selective potentiometric sensors," *Anal. Chem.*, vol. 84, no. 11, pp. 4695–4702, 2012.

[58] T. Guinovart, M. Parrilla, G. A. Crespo, F. X. Rius, and F. J. Andrade, "Potentiometric sensors using cotton yarns, carbon nanotubes and polymeric membranes," *Analyst*, vol. 138, no. 18, pp. 5208–15, 2013.

[59] J. Zhu, X. Li, Y. Qin, and Y. Zhang, "Single-piece solid-contact ion-selective electrodes with polymer-carbon nanotube composites," *Sensors Actuators, B Chem.*, vol. 148, no. 1, pp. 166–172, 2010.

ÍNDICE DE FIGURAS

Anexo

Figure 1. Illustration of the question formulated in this manuscript. Is it currently reliable the on-body data provide by WPISs? Which is the proper validation protocol to evaluate the reliability of the real-time observations? 357

Figure 2. Illustration of the WPIS). (a) Representation of the electrodes before and after functionalization. (b) Pictures of the electrode array, the sampling cell and the entire wearable device (sensors + sampling cell). (c) Scheme of the functioning of the sweat flow in the sampling cell once it is attached to the skin. (d) WPISs attached into the skin by using adhesive transfer tape. ISM = ion-selective membrane. 360

Figure 3. Dynamic responses and corresponding calibration graphs in water for (a) Cl^-, (b) K^+, (c) Na^+ and (d) pH, using the electrode array. The numbers in the dynamic response indicate the logarithm activity reached in each step. (e) Dynamic response and corresponding calibration graph observed in artificial sweat during the reversibility test accomplished by increasing and decreasing the activity of each ion. 361

Figure 4. (a) Response of three pH electrodes for a pH change from 5.6 to 4.7. Flow rate = 4 µL min-1. Dotted lines indicate the response time. (b) Response of three pH electrodes in a solution of pH 5.6 at different flow rates: 4, 8 and 16 µL min-1. (c) Calibrations using a pH electrode at different flow rates: 4, 8 and 16 µL min^{-1}. (d) WPISs under torsion deformation. Response of a K^+ electrode after applying different torsion deformations. (e) Calibrations using WPISs for $Cl^–$, Na^+, K^+, pH before and after the incorporation of the sampling cell, and after on-body measurements. All the calibration curves were performed in artificial sweat. The pre-calibration graph was accomplished from higher to lower concentrations in order to assess the sensors' reversibility. 364

Figure 5. (a) Pictures of a subject during cycling exercise with the WPISs and absorbent patches attached to the back. (b) Concentration profiles observed with the WPISs during 60 min of cycling workout (10 min of warming-up, 40 min of mid to high intensity cycling and 10 min of cooling-down). WPISs contained three twin electrodes for each ion. (c) Profile of K^+ concentration during on-body measurements. IC measurements were additionally accomplished for validation. 367

Figure 6. Electrolyte dynamics observed during on-body tests: (a) Na^+ concentration of an individual subjected to 1-h cycling at high-intensity. (b) $Cl^–$ and pH monitoring in two different individuals subjected to the same physical activity (22°C, 1-h cycling, high

intensity). The dots indicate the concentrations of sweat analyzed by IC after sweat collection by m-REG. 369

Figure S1. Reproducibility of the solid-state potentiometric sensors. Dynamic response of (a) chloride-selective electrodes (n=3), (b) potassium-selective electrodes and (n=3), (c) sodium-selective electrodes (n=3) and (d) pH electrodes (n=3) in MQ water. Inset plots: corresponding calibration curves fitted to the Nernst equation. 393

Figure S2. Repeatability of the solid-state potentiometric electrodes: (a) chloride, (b) potassium, (c) sodium and (d) pH. The assay consists of running three consecutive calibration curves. The dynamic response is displayed for each ion-selective electrode on the left with the corresponding calibration curve on the right..... 394

Figure S3. Characterization of the solid-state reference electrodes. a) Dynamic potentiometric response of different compositions of reference membranes towards KCl from 10^{-4} to $10^{-1.1}$ in aqueous solution. b) Plots of logarithmic activity vs. potential. Note that the potentiometric responses have been offset by a few mV to avoid overlapping of the displayed signal. c) Medium-term drift in 10 mM KCl. d) Dynamic potentiometric response of the optimal reference membrane towards NaCl, KCl from 10^{-4} to $10^{-1.1}$ in aqueous solution and change in pH from 4.6 to 7.2 with acetate buffer and phosphate buffer at 10 mM ionic strength. e) Light sensitivity (ambient light, darkness and artificial light using a bulb of 75W)..... 395

Figure S4. (a) Images of the stretchability force upon the application of 30 and 50 % of linear deformation. Observed dynamic responses for increasing concentrations of each ion analyte together with the corresponding calibration curve. (b) Images of the bending force upon the application of 45° and 80° of curvilinear deformation. Observed dynamic responses for increasing concentrations of each ion together with the corresponding calibration curve. Each resiliency test consisted of 10 repetitions of the corresponding deformation. All the calibrations were performed in water..... 396

Figure S5. Effect of the flow rate in the potassium response using WPISs (sensors array + sampling cell). a) Reversibility of the dynamic response for potassium under 4, 8 and 16 µL min^{-1}. b) Calibration graph obtained as the average of the dynamic profiles displayed in (a). c) Response time after changing K^+ concentration from $10^{-2.5}$ to $10^{-2.1}$ at 4 µL min^{-1}..... 397

Figure S6. The dynamic plot electromotive force (EMF) versus time gathered with potassium electrodes during an on-body test is translated into concentration versus time by using the previous calibration graph (logarithmic activity versus EMF) of each electrode. Finally, the ion activity is transformed into concentration by considering the ionic strength of the solution, in this case, calculated by the artificial sweat composition. Potassium profiles are shown as an example. 398
Figure S7. Validation of the WPISs operating ex situ. a) Correlation between the Cl^- concentrations obtained by the WPISs (n=3) and ion chromatography (IC). b) Correlation between the K^+ concentrations obtained by the WPISs (n=3) and IC. c) Correlation between the Na^+ concentrations obtained by the WPISs (n=3) and IC. d) Correlation between the pH obtained by the WPISs (n=3) and a pH micro-electrode. All the samples were diluted (1:100) in MQ water for IC analysis. The observed Pearson correlation coefficients were 0.93 for Cl^- (n = 16 samples), 0.94 for K^+ (n = 24 samples), 0.94 for Na^+ (n = 16 samples) and 0.95 for pH (n = 18 samples). The common physiological levels of the analyte are displayed in the colorful square inside each plot. 399
Figure S8. Reproducibility of the WPISs (3 working electrodes) from each of the on-body tests at Figure 6b. The plot shows the dynamic relative standard deviation (%RSD) from the 3 replicates at each time (every second during the on-body test) for the chloride, potassium, sodium and pH WPISs. 400
Figure S9. Illustration of the protocol based on the modified regional absorbent patch method (m-REG) for sweat sampling and subsequent IC analysis. After sweat collection during a certain time by means of commercial cotton pads (85 x 70 mm dimensions) fixed in the back of the subject with Hydrofilm tape, the absorbent pad is removed from the tape and inserted in a syringe (12 mL). The pad is then squeezed by applying pressure by the syringe, which allows to collect the sample into an Eppendorf tube. Finally, the sample is diluted prior to its analysis in the IC. 400
Figure S10. (a) Correlation between WPISs performing ex situ and IC analysis of sweat samples collected by the m-REG method. Pearson correlation coefficient of 0.99. (b) Concentration profile of two WPISs for sodium during on-body measurements. Sweat samples were collected with the m-REG method and measured with IC and the WPISs operating ex situ. In addition, the sweat was collected at the outlet of the sampling cell (DROP) and analyzed with IC for comparison. 401

ÍNDICE DE TABLAS

Anexo

Table 1. Concentrations obtained during the ex situ and in situ validation of the WPISs using the m-REG method. 371

Table S1. Compositions of ion-selective membranes (ISMs). Values in parenthesis show the mmol kg^{-1} of the corresponding compound in the membrane. 388

Table S2. Analytical performances of the solid-state ion-selective electrodes for potassium, sodium, chloride and pH (n=3). Reference electrode=Ag/AgCl/sat. KCl/1M LiOAc reference electrode (6.0726.100, Metrohm Nordic, Sweden). 388

Table S3. Logarithmic selectivity coefficients for the screen-printed electrodes developed in this work. Other values reported in the literature are included for comparison. The sensors already reported in the literature are referred according to the citation list in the supporting information. Reference electrode=Ag/AgCl/sat. KCl/1M LiOAc reference electrode (6.0726.100, Metrohm Nordic, Sweden). 389

Table S4. Analytical performances of the developed reference electrode (RE) using different membrane compositions (n=5). 389

Table S5. Analytical parameters of the all-solid-state potentiometric sensors (including working and reference electrode in the array) for potassium, sodium, chloride and pH (n=3). 390

Table S6. Carry-over tests of the all-solid-state potentiometric sensor (including working and reference electrode in the same array) for potassium, sodium, chloride and pH (n=6). 390

Table S7. Calibration parameters obtained during resiliency tests of the all-solid-state potentiometric sensor (including working and reference electrode in the same array) for potassium, sodium, chloride and pH. 390

Table S8. IC values from sweat samples obtained by the REG method and comparison to the concentrations obtained by WPISs (profiles exhibited on Figure 6b, average of 3 working electrodes). Table shows data from chloride, potassium and sodium. IC = ion chromatography. 391

Table S9. Error obtained by using directly the activity readout or by converting the activity from the WPISs to concentration. 392

CONCLUSIONES

CONCLUSIONES GENERALES

En la presente Memoria de esta Tesis Doctoral se han desarrollado diferentes sensores químicos para la detección óptica de determinados analitos de interés dentro del campo del análisis clínico, alimentario y medioambiental, mediante la utilización y/o implementación de nanomateriales novedosos en dispositivos microfluídicos capilares. Las principales conclusiones derivadas de la presente Tesis Doctoral pueden resumirse en los siguientes puntos:

1. Se ha llevado a cabo el diseño, desarrollo y caracterización de un dispositivo microfluídico basado en papel para la determinación colorimétrica de nitrito en agua, por lo que se sintetizó y caracterizó la tetrazina 1, 2-dihidro-3, 6-bis (3, 5-dimetil-1H-pirazol-1-il) 1, 2, 4, 5-tetrazina (DHBPTz) empleada como reactivo cromogénico en ésta determinación. Se han optimizado las condiciones experimentales necesarias para la determinación colorimétrica de nitrito. La coordenada de saturación S del espacio de color HSV ha sido utilizada como parámetro analítico en esta determinación. Además, se ha establecido experimentalmente la función de calibrado y las características analíticas del procedimiento de análisis llevado a cabo. Por otra parte, se ha estudiado el efecto de los iones más comunes presentes en agua que pueden actuar como interferentes en la reacción de determinación de nitrito. Así, se ha llevado a cabo la determinación de nitrito en diferentes tipos de agua. Por último, se han comparado los resultados obtenidos en esta determinación empleando un Smartphone como dispositivo analítico frente a los resultados obtenidos empleando una cámara fotográfica, observando que los resultados son similares y que por tanto el Smartphone puede ser utilizado como dispositivo de imagen en ésta determinación.

2. Se ha evaluado un nuevo dispositivo microfluídico basado en papel para la determinación colorimétrica de glucosa en muestras de suero y orina mediante la implementación del MOF Fe-MIL-101, mimético del enzima HRP, en papel. Para ello se ha realizado la síntesis y caracterización del MOF Fe-MIL-101 en papel. Además, se han optimizado las condiciones experimentales necesarias para el desarrollo del dispositivo. Por otro lado, se ha estudiado la actividad mimética del MOF Fe-MIL-101 frente al enzima HRP. Así, se ha establecido

experimentalmente la función de calibrado y las características analíticas del procedimiento de medida empleando como parámetro analítico la coordenada de saturación S del espacio de color HSV. Se ha estudiado el efecto de las sustancias más comunes presentes en el suero y la orina que pueden actuar como interferentes en la reacción de determinación de glucosa. Del mismo modo, se ha aplicado éste método de determinación de glucosa en dos fluidos biológicos diferentes como son el suero y la orina. Por último, se han comparado los resultados obtenidos para la determinación colorimétrica de glucosa empleando un Smartphone como dispositivo analítico frente a los resultados obtenidos empleando una cámara fotográfica, observando resultados similares.

3. Se ha establecido un nuevo método de síntesis in situ de silicon nanodots fluorescentes sobre un dispositivo microfluídico de papel para la determinación de glucosa y fructosa en muestras biológicas de suero y orina, así como en zumos y tés comerciales. Para ello se ha implementado al dispositivo microfluídico un calentador portátil fabricado a partir de grafeno inducido por láser que suministra al papel la energía necesaria para poder llevar a cabo la síntesis de los silicon nanodot. Por otro lado, se han optimizado las variables influyente en la reacción de determinación de monosacáridos reductores, y se ha realizado la caracterización analítica del dispositivo en la determinación de glucosa y fructosa. De este modo, una fotografía del µPAD bajo una lámpara UV es adquirida utilizando un Smartphone como dispositivo de imagen. A continuación, la fotografía es analizada de forma que se ha establecido como parámetro analítico en la determinación de azúcar la media de las coordenadas R, G y B del espacio de color RGB expresadas en escala de grises. Asimismo, se ha evaluado la respuesta de los compuestos más comunes presentes en muestras biológicas que pueden actuar como interferentes en ésta reacción de determinación de azúcar. Por último, se ha llevado a cabo la determinación de glucosa en muestras de suero y orina, así como la determinación de azúcar en zumos y tés comerciales.

4. Se ha puesto a punto un µPAD para la determinación colorimétrica de glutation basado en la oxidación del reactivo cromogénico 3,3’,5,5’-tetrametilbencidina (TMB) por Ag(I). Esta oxidación se hace notable por un cambio de color, de

incoloro a azul, al pasar de la forma reducida a la forma oxidada del TMB. De este modo, se ha puesto de manifiesto que la presencia de glutation en el medio puede formar complejos con la Ag(I) dificultando o impidiendo la oxidación del reactivo cromógeno. Así, la determinación de glutation puede llevarse a cabo mediante la relación de la saturación del color azul del compuesto oxidado con la concentración de glutation de una muestra. Para ello esta plataforma de análisis está dotada de una etiqueta NFC que permite la conexión con un Smartphone, de forma que suministra al dispositivo los resultados de la medida de glutation presentes en la muestra. Una vez que el Smartphone recibe la información obtenida se muestran los resultados en la pantalla del teléfono pudiéndose realizar la interpretación y el almacenamiento de los resultados, así como, el envió de datos a través de Internet. De este modo, se han estudiado las variables influyentes en el µPAD y se ha realizado una caracterización analítica del mismo. Por otro lado, se ha evaluado la selectividad del µPAD frente a otros compuestos que pueden actuar de interferentes en esta determinación. Por último, se ha llevado a cabo la determinación de glutation en muestras de suero con el fin de demostrar la aplicabilidad del dispositivo desarrollado.

5. Se ha desarrollado µPAD para la determinación fluorométrica de biotioles basada en un mecanismo off/on empleando carbon dots fluorescentes inmovilizados covalentemente al papel. Para ello, se ha llevado a cabo la unión covalente de carbon dots al papel de celulosa empleando divinilsulfona mediante una adición oxa-Michael. A continuación, se ha procedido a la posterior funcionalización de los carbon dots inmovilizados generando la pérdida de sus propiedades luminiscentes. Seguidamente, se ha realizado la optimización de las variables influyentes en la reacción de determinación de biotioles. También, se ha llevado a cabo la caracterización analítica del dispositivo microfluídico desarrollado en la determinación de glutation, cisteína y homocisteina. Se ha empleado como parámetro analítico la intensidad de fluorescencia de los carbon dots expresada en escala de grises. Para ello, se ha realizado y analizado una fotografía del µPAD utilizado una cámara fotográfica y un Smartphone. Por último, se ha llevado a cabo la validación del método propuesto para la determinación de glutation en muestras de orina.

6. Se ha descrito un sensor óptico desechable basado en cambios de color para la monitorización de los niveles de creatinina en orina. Para ello se ha fabricado una membrana selectiva de iones contiendo el ionoforo calix[4]pyrrol que actúa como elemento de reconocimiento del ión creatininio en la determinación de creatinina. Además, un indicador de pH lipofílico, que actúa como transductor óptico, ha sido implementado en la membrana de reconocimiento para preservar la electroneutralidad permitiendo un intercambio de protones que produce un cambio en el espectro de absorción de la membrana. En este sentido, se ha llevado a cabo la optimización de la membrana selectiva de iones y las diferentes variables influyentes en la reacción de determinación de creatinina. Además, se ha caracterizado analíticamente la respuesta del sensor óptico y se ha estudiado la influencia de diferentes especies presentes en la orina que pueden actuar como interferentes en ésta determinación. Por último, se ha llevado a cabo la validación del sensor mediante la determinación la concentración de creatinina en muestras de orina y se han comparado los resultados obtenidos con un método de referencia, demostrándose así su aplicabilidad.

7. Se ha presentado nuevo método óptico para la determinación luminiscente de creatinina en orina. Se ha descrito el empleo de nanopartículas luminiscentes de fosfato de calcio dopadas con europio para la determinación de creatinina en orina. En este caso la determinación de creatinina tiene lugar por la pérdida de las propiedades luminiscentes de las nanopartículas de fosfato de calcio como consecuencia de un proceso de filtro interno. En este caso, se ha llevado a cabo la síntesis y la caracterización morfológica de las nanopartículas de fosfato de calcio dopadas con europio. Se han optimizado las variables influyentes en la reacción de determinación de creatinina. Además, se ha caracterizado analíticamente el sistema de detección de creatinina y se ha estudiado la posible interferencia de otras especies comunes en orina que pudieran afectar a la determinación. En último lugar, se ha llevado a cabo la cuantificación de creatinina en muestras de orina demostrando la buena precisión del sensor desarrollado en ésta determinación.

8. Se ha diseñado, fabricado y validado un parche potenciométrico reutilizable para la recogida de sudor y el análisis multi-iónico de electrolitos. El dispositivo desarrollado cuenta una celda de muestreo flexible, cuatro electrodos dotados con membranas selectivas para pH, Cl^-, K^+ y Na^+ y un electrodo de referencia. Los electrodos se han fabricados sobre un sustrato flexible de poliuretano mediante serigrafia utilizando tinta de carbono estirable. Además, se ha evaluado la composición de las diferentes membranas selectivas de iones implementadas en los electrodos. Asimismo, se ha comprobado la robustez de los electrodos potenciométricos y se ha verificado la efectividad de la celda de muestreo en la recogida del sudor para evitar problemas de evaporación y contaminación de la muestra durante el proceso de análisis. También, se ha estudiado la respuesta del sensor potenciométrico en función de velocidad de flujo de la muestra que entra en el parche. Se llevado a cabo una caracterización analítica del sensor potenciométrico antes y después de su incorporación a la celda de muestreo. Del mismo modo, se ha comprobado la selectividad de cada una de las membranas frente a diferentes iones presentes en el sudor que podrían suponer una interferencia en la determinación de cada uno de los analitos. Por último, se ha evaluado la precisión de las medidas realizadas por el parche potenciométrico en el cuerpo en comparación con los resultados obtenidos para las mismas muestras por un cromatografo de iones y un pHmetro.

MAIN CONCLUSIONS

MAIN CONLUSIONS

In this Thesis, different chemical sensors have been developed for the optical detection of certain analytes of interest on the clinical, food and environmental analysis, through the use and/or implementation of novel nanomaterials in paper-based microfluidic devices. Thus, the following conclusions have been derived:

1. The design, development and characterization of a paper-based microfluidic device for the colorimetric determination of nitrite in water has been carried out. Thus, 1, 2-dihydro - 3, 6 – bis (3, 5 – dimethyl - 1H – pyrazol - 1- yl) 1, 2, 4, 5-tetrazine (DHBPTz), used as a chromogenic reagent in this determination, has been synthetized and characterized. The experimental conditions necessary for the colorimetric determination of nitrite have been optimized. The saturation coordinate S of the HSV colour space have been used as an analytical parameter. Furthermore, the calibration function and the analytical characteristics of the analysis procedure carried out have been experimentally established. On the other hand, the effect of the most common ions present in water that can act as interferers in the nitrite determination reaction has been studied. Thus, nitrite determination has been carried out in different types of water. Finally, the results obtained in this determination using a Smartphone, as an analytical device, have been compared with the results obtained using a photographic camera, observing that the results are similar so, Smartphone can be used as an imaging device in this determination.

2. A new paper-based microfluidic device has been evaluated for the colorimetric determination of glucose in serum and urine samples through the implementation of MOF Fe-MIL-101 on paper, as mimic of the HRP enzyme. Thus, the synthesis and characterization of MOF Fe-MIL-101 on paper has been carried out. In addition, the experimental conditions necessary for the development of this device have been optimized. On the other hand, the mimetic activity of MOF Fe-MIL-101 against HRP enzyme has been studied. Thus, the calibration function and the analytical characteristics of the measurement procedure have been experimentally established using the saturation coordinate S of the HSV colour space as the analytical parameter. The effect of the most common compounds present in serum and urine which can act as interferers in the glucose determination has been

studied. In the same way, this method of glucose determination has been applied in two different biological fluids such as serum and urine. Finally, the results obtained for the colorimetric determination of glucose using a Smartphone, as an analytical device, have been compared with the results obtained using a photographic camera, and similar results have been observed.

3. A µPAD for the fluorometric determination of biothiols based on an off/on mechanism using fluorescent carbon dots immobilized covalently to the paper has been developed. For this, the covalent bonding of carbon dots to the cellulose paper has been carried out using divinylsulfone by the click oxa-Michael addition to the hydroxyl groups of cellulose paper. Subsequently, the intrinsic fluorescence of carbon dots have been turned off via the heavy atom effect of an introduced iodo group. Subsequently, the optimization of the influencing variables in the biothiols determination was carried out. Also, the analytical characterization of the microfluidic device to the determination of glutathione, cysteine and homocysteine has been carried out. The fluorescence intensity of the carbon dots expressed in gray scale has been used as an analytical parameter. Thus, a photograph of the µPAD has been taken and analysed using a photographic camera and a Smartphone. Finally, the validation of the proposed method for the determination of glutathione in urine samples has been carried out.

4. A new method of in situ synthesis of fluorescent silicon nanodots has been established on a paper microfluidic device for the determination of glucose and fructose in biological samples, such as serum and urine, as well as in commercial juices and teas. Thus, the microfluidic device has been implemented in a portable heater fabricated by laser-induced grapheme, which supplies the energy necessary to carry out the synthesis of silicon nanodot on paper. On the other hand, the influence of different variables in reducer monosacarides determination have been optimized, and the analytical characterization of the device has been carried out to the determination of glucose and fructose. Thus, a photograph of the µPAD under a UV lamp is acquired using a Smartphone as the imaging device. Next, the photograph is analysed so, the average of the R, G and B coordinates of the RGB colour space was expressed in grayscale to establish as an analytical parameter in glucose and fructose determination. Likewise, the response of the most common

compounds present in biological samples which can act as interferers in the sugar determination method has been evaluated. Finally, glucose determination in serum and urine samples has been carried out, as well as glucose and fructose determination in commercial juices and teas.

5. A μPAD for the colorimetric determination of glutathione based on the oxidation of the chromogenic reagent 3, 3', 5, 5'-tetramethylbenzidine (TMB) by Ag (I) has been developed. This oxidation is based on the fact that the oxidized TMB present a blue colour and reduced TMB is colourless. Thus, it has been shown that the presence of glutathione in the medium can cause the reduction of oxidized TMB and it can also combine with Ag (I) hindering or preventing the oxidation of TMB. Thus, the determination of glutathione can be carried out by relating the saturation of the blue colour of the oxidized TMB with the concentration of glutathione in a sample. For this, this platform of analysis is implemented with an NFC tag which allows connection with a Smartphone, so that it supplies the device with the results of the glutathione measurement present in the sample. Once the Smartphone receives the information obtained, the results are displayed on the phone screen, being able to interpret and store the results, as well as sending data on Internet. Thus, the influencing variables in μPAD have been studied and an analytical characterization of it has been carried out. On the other hand, the selectivity of μPAD against other compounds which can act as interferers in this determination has been evaluated. Finally, glutathione determination in serum samples has been carried out in order to demonstrate the applicability of the developed device.

6. A disposable optical sensor based on colour changes has been described for monitoring urine creatinine levels. Thus, an ion selective membrane has been fabricated which contain the ionophore calix [4] pyrrol which acts as a recognition element of the creatininium ion in the determination of creatinine. In addition, a lipophilic pH indicator, which acts as an optical transducer, has been implemented in the recognition membrane to preserve electroneutrality allowing a proton exchange that produces a change in the absorption spectrum of the membrane. In this sense, the optimization of ion selective membrane and the different influencing variables in the creatinine determination have been carried out. In addition, the response of the optical sensor has been analytically characterized and

the influence of different species present in the urine which can act as interferers in this determination has been studied. Lastly, the validation of the sensor was carried out by determining the concentration of creatinine in urine samples and the results obtained were compared with a reference method, thus demonstrating its applicability.

7. The use of europium doped calcium phosphate nanoparticles for the determination of creatinine in urine has been described. In this case, the creatinine determination takes place due to the loss of the luminescent properties of the nanoparticles as a consequence of an internal filter process. In this case, the synthesis and morphological characterization of europium-doped calcium phosphate nanoparticles has been carried out. The influencing variables in the creatinine determination have been optimized. In addition, the creatinine detection system has been analytically characterized and the possible interference of other common species in urine which could affect the determination has been studied. Lastly, creatinine quantification in urine samples was carried out, demonstrating the good precision of the sensor developed in this determination.

8. A wearable potentiometric ion patch for on-body electrolyte monitoring in sweat has been designed, manufactured and validated. The developed device has a flexible sampling cell, four electrodes implemented with selective membranes for pH, Cl^-, K^+ and Na^+ and a reference electrode. The electrodes have been fabricated employing a stretchable polyurethane materials and carbon ink by screen printing. Furthermore, the composition of the different ion selective membranes implemented in the electrodes has been evaluated. Likewise, the robustness of the potentiometric electrodes has been verified and the effectiveness of the sampling cell to collect sweat has been verified to avoid evaporation problems and contamination of the sample during the analysis process. Also, the response of the potentiometric sensor as a function of the flow rate of the sample in the wearable patch has been studied. An analytical characterization of the potentiometric sensor was carried out before and after its incorporation into the sampling cell. Similarly, the selectivity of each membranes against different ions present in sweat has been verified, which could cause interference in the determination of each of the

analytes. Finally, the precision of the measurements of the potentiometric patch on the body has been evaluated by comparison with the results obtained for the same samples by an ion chromatograph and a pH meter.

ACRÓNIMOS

Acronimos

AA	Ascorbic Acid
ABTS	**2,2′-Azino-bis(3-ethylbenzothiazoline-6-sulfonic acid) diammonium salt**
AFM	Atomic Force Microscopy
AKD	Alkyl Ketene Dimer
Arg	Arginine
Asn	Asparagine
ASSURED	Affordable, Sensitive, Specific, User friendly, Rapid and robust, Equipment-free and Delivered
AWB	Auto White Balance
BSI-CMOS	Back Side Illumination Complementary Metal Oxide Semiconductor
CA	Citric Acid
CCD	Charge Coupled Device
CDs	Carbon Dots
CE	Counter Electrode
CMOS	Complementary Metal Oxide Semiconductor
CNT	Nanotubos de Carbono
Cys	Cysteine
DCC	**N,N-dicyclohexylcarbodiimide**
DCM	Dichloromethane
DHBPTz	1,2-dihydro-3,6- bis(3,5-dimethyl-1H-pyrazol-1-yl)-1,2,4,5-tetrazine
DIPEA	**N,N-diisopropylethylamine**
DL	Detection Limit
DLS	Dynamic Light Scattering
DVS	Divinylsulfone
EDX	Engergy Dispersive X-ray Spectroscopy
FTIR	Fourier Transform Infrared Spectroscopy
GOx	Glucose Oxidase
GSH	Glutathione
Hcys	Homocysteine
His	Histidine
HRP	Horseradish Peroxidase

HRTEM	High Resolution Transmission Electron Microscopy
HSV	Hue, saturation and value
IAA	Iodoacetic Acid
ICDD	International Centre for Diffraction
ISO	International Organization for Standarization
LOC	Lab On a Chip
LOD	Limit Of Detection
LOQ	Limit of Quantification
LQ	Limit of Quantification
Lys	Lysine
Man	Mannose
MIP	Molecular Imprinted Polymer
MOF	Metal Organic Framework
MOS	Metal Oxide Semiconductor
µPAD	Microfluidic Paper-based Analytical Device
µTAD	Microfluidic Tread-based Analytical Device
NED	N-(1-naphthyl)-ethylenediamine
NFC	Near Field Communication
NPs	Nanopartículas
OPD	O-Phenylenediamine dihydrochloride
PEDs	Paper-based Electrochemical Devices
PEI	Polyethylenimine
PET	Polyethylene Terephthalate
PMMA	Poly (methyl methacrylate)
POC	Point Of Care
POCT	Point Of Care Test
PoN	Point of Need
PP	Polypropylene
PS	Polystyrene
QDs	Quantum Dots

RE	Reference Electrode
RGB	Red, Green and Blue
RMN	Resonancia Magnética Nuclear
ROI	Region OF Interest
RSD	Relative Standard Deviation
SEM	Scanning Electron Microscopy
SER	Serine
SPR	Surface Plasmon Resonance
STEM	Scanning Transmission Electron Microscopy
TEA	Triethylamine
TEM	Transmission Electron Microscopy
TMB	Tetranethylbenzidine
UV-vis	Ultraviolet-Visible Spectroscopy
VS	Vinyl Sulfone
XPS	X-ray Photoelectron Spectroscopy
XRD	X-ray Diffraction
WE	Working Electrode
WHO	World Health Organization

INFORME DEL FACTOR DE IMPACTO

INFORME DEL FACTOR DE IMPACTO

De acuerdo con el Reglamento de los Estudios de Doctorado de la Universidad de Granada, para presentar la Tesis Doctoral como compendio de publicaciones la normativa exige incluir en la presente Memoria un informe indicando el factor de impacto de las publicaciones presentadas junto con un detalle informativo sobre la calidad de las mismas de forma que se refleje el índice de impacto y la posición que ocupa la revista dentro de una determinada categoría. En base a lo expuesto anteriormente, a continuación, se incluye una tabla donde se recogen los criterios mencionados.

Tabla 1. Relación de las publicaciones derivadas del trabajo realizado durante la Tesis. Datos obtenidos del Journal Citations Reports®.

Referencia	Índice de impacto JCR 2018	Categoría	Citas
Talanta 160, 2016, 721-728	4.916	Química Analítica	11/84
Microchimica Acta 185, 2018, 1-8	5.479	Química Analítica	9/84
En escritura para su publicación en Sensor and Actuator B	6.393	Química Analítica	11/75
En escritura para su publicación en Sensors and Actuator B-Chemical	6.393	Química Analítica	4/84
Aceptado en Microchimica Acta	5.479	Química Analítica	9/84
ACS Sensor 4, 2019, 421-426	6.944	Química multidisciplinar Química Analítica Nanociencia y Nanotecnología	4/84
Enviado para su publicación en Colloids and Surfaces B-biointerfaces	3.973	Física Química Biofísica Ciencia de los Materiales y biomateriales	5/14
Analytical Chemistry 91, 2019, 8644 - 8651	6.350	Química Analítica	7/84